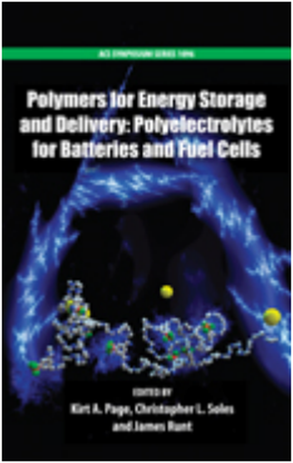

ACS SYMPOSIUM SERIES 1096

Polymers for Energy Storage and Delivery: Polyelectrolytes for Batteries and Fuel Cells

EDITED BY

Kirt A. Page, Christopher L. Soles
and James Runt

Downloaded by 89.163.35.42 on June 14, 2012 | http://pubs.acs.org
Publication Date (Web): May 7, 2012 | doi: 10.1021/bk-2012-1096.fw001

Polymers for Energy Storage and Delivery: Polyelectrolytes for Batteries and Fuel Cells

In Polymers for Energy Storage and Delivery: Polyelectrolytes for Batteries and Fuel Cells; Page, K., et al.;
ACS Symposium Series; American Chemical Society: Washington, DC, 2012.

Downloaded by 89.163.35.42 on June 14, 2012 | http://pubs.acs.org
Publication Date (Web): May 7, 2012 | doi: 10.1021/bk-2012-1096.fw001

ACS SYMPOSIUM SERIES **1096**

Polymers for Energy Storage and Delivery: Polyelectrolytes for Batteries and Fuel Cells

Kirt A. Page, Editor
National Institute of Standards and Technology

Christopher L. Soles, Editor
National Institute of Standards and Technology

James Runt, Editor
The Pennsylvania State University

Downloaded by 89.163.35.42 on June 14, 2012 | http://pubs.acs.org
Publication Date (Web): May 7, 2012 | doi: 10.1021/bk-2012-1096.fw001

Sponsored by the
ACS Division of Polymer Chemistry
ACS Division of Polymeric Materials: Science and Engineering

American Chemical Society, Washington, DC

Distributed in print by Oxford University Press, Inc.

Downloaded by 89.163.35.42 on June 14, 2012 | http://pubs.acs.org
Publication Date (Web): May 7, 2012 | doi: 10.1021/bk-2012-1096.fw001

Library of Congress Cataloging-in-Publication Data

Polymers for energy storage and delivery : polyelectrolytes for batteries and fuel cells / Kirt A. Page, editor ; Christopher L. Soles, editor ; James Runt, editor.
p. cm. -- (ACS symposium series ; 1096)
"Sponsored by the ACS Division of Polymer Chemistry and ACS Division of Polymeric Materials: Science and Engineering."
Includes bibliographical references and index.
ISBN 978-0-8412-2631-9 (alk. paper)
1. Storage batteries--Materials--Congresses. 2. Polyelectrolytes--Congresses. 3. Electronic polymers--Congresses. 4. Polymers--Electric properties--Congresses. I. Page, Kirt A. II. Soles, Christopher L. III. Runt, James P. (James Patrick), 1953-
TK2941.P65 2012
621.31’2424--dc23
2012010049

The paper used in this publication meets the minimum requirements of American National Standard for Information Sciences—Permanence of Paper for Printed Library Materials, ANSI Z39.48n1984.

Copyright © 2012 American Chemical Society

Distributed in print by Oxford University Press, Inc.

All Rights Reserved. Reprographic copying beyond that permitted by Sections 107 or 108 of the U.S. Copyright Act is allowed for internal use only, provided that a per-chapter fee of $40.25 plus $0.75 per page is paid to the Copyright Clearance Center, Inc., 222 Rosewood Drive, Danvers, MA 01923, USA. Republication or reproduction for sale of pages in this book is permitted only under license from ACS. Direct these and other permission requests to ACS Copyright Office, Publications Division, 1155 16th Street, N.W., Washington, DC 20036.

The citation of trade names and/or names of manufacturers in this publication is not to be construed as an endorsement or as approval by ACS of the commercial products or services referenced herein; nor should the mere reference herein to any drawing, specification, chemical process, or other data be regarded as a license or as a conveyance of any right or permission to the holder, reader, or any other person or corporation, to manufacture, reproduce, use, or sell any patented invention or copyrighted work that may in any way be related thereto. Registered names, trademarks, etc., used in this publication, even without specific indication thereof, are not to be considered unprotected by law.

PRINTED IN THE UNITED STATES OF AMERICA

Foreword

The ACS Symposium Series was first published in 1974 to provide a mechanism for publishing symposia quickly in book form. The purpose of the series is to publish timely, comprehensive books developed from the ACS sponsored symposia based on current scientific research. Occasionally, books are developed from symposia sponsored by other organizations when the topic is of keen interest to the chemistry audience.

Before agreeing to publish a book, the proposed table of contents is reviewed for appropriate and comprehensive coverage and for interest to the audience. Some papers may be excluded to better focus the book; others may be added to provide comprehensiveness. When appropriate, overview or introductory chapters are added. Drafts of chapters are peer-reviewed prior to final acceptance or rejection, and manuscripts are prepared in camera-ready format.

As a rule, only original research papers and original review papers are included in the volumes. Verbatim reproductions of previous published papers are not accepted.

ACS Books Department

Downloaded by 89.163.35.42 on June 14, 2012 | http://pubs.acs.org
Publication Date (Web): May 7, 2012 | doi: 10.1021/bk-2012-1096.fw001

Preface

Polymeric materials have been and continue to be a focus of research in the development of materials for energy conversion, storage and delivery applications (fuel cells, batteries, photovoltaics, capacitors, *etc.*). A Web of Science^{SM} search for polymer research as applied to various energy applications over the past 47 years yields a significant number of results as can be seen in the Figure below. From this historical perspective one can see that significant growth in this area started in the early 1990s and has continued to grow quite substantially since that time. In fact, approximately 90% of the volume of work has been produced in the last 10 years and more than 60% just in the last 5 years. The amount of work produced in just the areas of fuel cells and batteries is nearly 60% of polymer related work in the field of energy conversion, storage and delivery. While this is not meant to serve as a detailed quantitative analysis of the growth in the field, it certainly demonstrates the prominent place that polymeric materials now have in energy research.

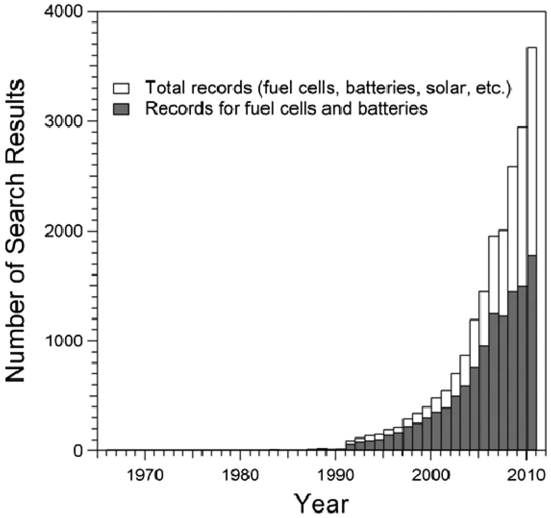

For polymers, particularly polyelectrolytes, being used in fuel cell and battery applications, the importance of *chain microstructure, chain dynamics, and nanoscale morphology* on the overall performance characteristics of these materials cannot be overstated. As further advancements are made in polymer

Downloaded by 89.163.35.42 on June 14, 2012 | http://pubs.acs.org
Publication Date (Web): May 7, 2012 | doi: 10.1021/bk-2012-1096.pr001

chemistry, control of nanostructure and characterization, there is a necessity for organized forums that foster cross-fertilization of knowledge and ideas between experts in polymer chemistry, chemical engineering, and polymer physics. This volume is the result of such a forum. Most of the chapters in this book are based on a cross-section of the oral presentations in a symposium on *Polymers for Energy Storage and Delivery* held in March of 2011 as part of the 241st ACS National Meeting & Exposition (Anaheim, CA). The symposium was organized by ACS Division of Polymer Chemistry (POLY) and co-sponsored by the ACS Division of Polymeric Materials: Science & Engineering (PMSE).

The book contains 17 chapters and is presented in two parts. Part one focuses on polymers for battery applications and will cover theory and modeling, novel materials, and materials characterization. Professor Janna Maranas has provided an excellent review of the current state of understanding in polyelectrolytes as ion conductors in batteries. Part two will focus on polymers for fuel cells and will cover novel materials, transport, and materials characterization with a brief introduction into the history of polyelectrolytes for fuel cells and the classes of materials being pursued. Realizing the common role that nanostructure plays in both battery and fuel cell applications, Professor Moon Jeong Park and co-workers have also contributed a chapter demonstrating the role of nanostructured polyelectrolyte systems in energy storage and delivery. In addition, we are pleased to have a chapter—contributed by Professor Howard Wang and staff scientists of the NIST Center for Neutron Research—on the most state-of-art, *in-situ* neutron methods for studying lithium ion batteries.

We would like to thank the authors for their efforts and the high quality of the work they have produced. This book would not have been possible if it were not for the caliber of research they carry out day-to-day in an area of such great importance and, of course, for their willingness to participate in the symposium and the exigency of manuscript preparation, submission, and revision. Thanks are also due to the support of the ACS Divisions of Polymer Chemistry (POLY) and Polymeric Materials: Science & Engineering (PMSE). In addition, the editors would like to thank Tim Marney, Arlene Furman, and Lou Larsen at ACS Books for all of their support throughout the publication process.

It is our hope that scientists and engineers who are engaged in research and development in the structure, dynamics, and transport of ions in polyelectrolytes for use in energy applications find this book to be a valuable reference.

Downloaded by 89.163.35.42 on June 14, 2012 | http://pubs.acs.org
Publication Date (Web): May 7, 2012 | doi: 10.1021/bk-2012-1096.pr001

Downloaded by 89.163.35.42 on June 14, 2012 | http://pubs.acs.org
Publication Date (Web): May 7, 2012 | doi: 10.1021/bk-2012-1096.pr001

The cover art design and concept were created by Kirt A. Page (NIST) and Kevin G. Yager (Brookhaven National Laboratory Center for Functional Nanomaterials), the graphics and artwork were created by Kevin G. Yager. The molecule shown is the result of a molecular dynamics simulation of a polyethylene oxide-based, single-ion conductor (see below) and was provided by Professor Janna Maranas and her student Kan-Ju Lin (Ph. D. candidate) from the Department of Chemical Engineering at The Pennsylvania State University.

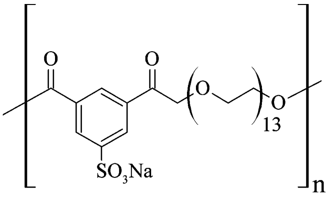

Chemical Structure of the simluated PEO-based Single-Ion Conductor

Kirt A. Page

Energy and Electronics Materials Group
Polymers Division
Material Measurement Laboratory
National Institute of Standards and Technology
Gaithersburg, MD 20899-8542, USA

Christopher L. Soles

Leader, Energy and Electronics Materials Group
Polymers Division
Material Measurement Laboratory
National Institute of Standards and Technology
Gaithersburg, MD 20899-8542, USA

James Runt

Department of Materials Science and Engineering
The Pennsylvania State University
325C Steidle Building
University Park, PA 16802, USA

Downloaded by CORNELL UNIV on June 14, 2012 | http://pubs.acs.org
Publication Date (Web): May 7, 2012 | doi: 10.1021/bk-2012-1096.ot001

Editors' Biographies

Kirt Page

Kirt Page is a staff scientist in the Polymers Division at NIST working on the Energy Storage and Delivery Project within the Energy and Electronics Materials Research Group. He completed his Ph.D. in Polymer Science and Engineering (2005) at The University of Southern Mississippi and then came to NIST as a National Academy of Sciences, National Research Council Post-doctoral Fellow. His research interests are in the area of structure/property relationships and molecular dynamics in polymer systems for energy applications. Kirt is a former Fulbright Fellow and a practitioner of Vipassana Meditation.

Christopher Soles

Christopher Soles leads the Energy and Electronics Materials Research Group in the NIST Polymers Division. He received his Ph D in 1998 in Materials Science and Engineering from the University of Michigan and then joined NIST as a NRC Postdoctoral Research Fellow. His research interests include thin films and polymers in confinement, polymer dynamics, lithographic pattering, porous materials, organic semiconducting materials, and ion containing polymers for energy storage and delivery. He has over 110 peer-reviewed publications and received several awards, including the Presidential Early Career Award for Science and Engineering (2006) and the United States Department of Commerce Bronze (2006, 2008) and Silver (2006) Medals, and the Arthur S. Flemming Award from the George Washington University (2010). From 2007 to 2010 he was a Technical Program Chair for the PMSE Division of the American Chemical Society and is a Fellow of the American Physical Society.

James Runt

James Runt is currently Professor of Polymer Science in the Materials Science and Engineering Department at Penn State University. Jim is the author of more than 180 peer-reviewed publications and book chapters, and is a Fellow of the American Physical Society and the American Institute of Medical and Biological Engineers. He is an editor of the ACS Professional Reference Series book: *Dielectric Spectroscopy of Polymeric Materials: Fundamentals and Applications*, and is a member of the Board of Directors of the International Dielectrics Society.

In Polymers for Energy Storage and Delivery: Polyelectrolytes for Batteries and Fuel Cells; Page, K., et al.;
ACS Symposium Series; American Chemical Society: Washington, DC, 2012.

Downloaded by 89.163.35.42 on June 14, 2012 | http://pubs.acs.org
Publication Date (Web): May 7, 2012 | doi: 10.1021/bk-2012-1096.ch001

Chapter 1

Polyelectrolytes for Batteries: Current State of Understanding

Janna K. Maranas[*]

Department of Chemical Engineering, The Pennsylvania State University
[*]jmaranas@engr.psu.edu

Lithium ion batteries are widely used in portable electronics. The electrolyte in commercial Li ion batteries is an organic liquid with dissolved Li salt. Polymer electrolytes offer several advantages and have been investigated for over 30 years. This chapter introduces the polymer electrolyte, outines the factors which influence ionic conductivity, discusses novel material choices, and overviews characterization techniques.

In 1988, when I was an undergraduate, one of my two best friends bought a cell phone. She would call me on her commute from Orange County to Los Angeles using what seemed to me an unreachable technology. At the time the Motorola DynaTAC 8500XL sold for $2,500. It weighed 29 oz., with much of that weight coming from the six 1.2 V NiCd rechargeable [secondary] batteries. In 1996 the Motorola StarTAC, the worlds first flip phone, weighed ten times less and was 56 times smaller [by volume]. Between 1988 and 1996 came the introduction of the Li ion secondary battery by Sony in 1990. The use of a single 3.7 Li ion secondary cell was responsible for much of the difference in size and weight between the DynaTAC and the StarTAC. In 1988, there were 800,000 cell phones in use in the US. In December 2010 there were over 300 million: 96% of the US population. I bought my first cell phone in 2002, when I was an assistant professor and realized that since some of the graduate students had cell phones, they must be affordable. Now I feel uneasy if I forget my phone on a 20 minute trip to the grocery store!

There is no question that the rise of cell phones and other portable devices has been governed by the Li ion battery. The first secondary cell based on Li technology was commercialized the same year my friend bought her cell phone: 1988. It was a Li/Li_xMoS_2 cell based on the pioneering intercalation work of

In Polymers for Energy Storage and Delivery: Polyelectrolytes for Batteries and Fuel Cells; Page, K., et al.;
ACS Symposium Series; American Chemical Society: Washington, DC, 2012.

Whittingham on Li_xTiS_2 (*1*). The anode was extremely reactive Li metal, which ultimately led to safety issues and recall of the batteries. The cell commercialized by Sony in 1990 avoided this problem with an anode that incorporated lithium within a carbon structure[LiC_6]. The Li_xCoO_2 cathode had been suggested by Goodenough 10 years earlier (*2*). The electrolyte in both cells was $LiPF_6$ dissolved in organic carbonates, which remains the electrolyte in today's Li ion batteries.

Despite the safety issues, the energy density obtained by use of a Li metal anode can be more than 10 times greater than that in commercialized Li ion batteries. The Li air battery, with Li metal as the anode and air as the cathode, realizes a large weight reduction because the 6 carbon atoms for each Li atom are removed from the anode, and the cathode requires only a porous support. This is important for vehicle applications not only because of the reduced weight, but also because it will require less cycles to achieve the same lifetime: a battery that runs 200 miles in a charge will cycle 1000 times to achieve a lifetime of 200,000 miles, whereas one that runs 400 miles per charge would only require 500 cycles] The theoretical energy density of the Li air battery not including weight of O_2 (11,140 Wh/kg) is two orders of magnitude greater than that of the Li ion battery, and approaches that of the gasoline air engine (11,860 Wh/kg). The practical energy density including the weight of O_2 (1,700 Wh/kg) is still over 10 times greater than that of the Li ion battery. Although Li metal is used in primary Li batteries, the high reactivity and formation of dendrites on recycling limits use in secondary batteries. The use of a solid electrolyte can begin to address problems due to high reactivity and dendrite formation of Li metal [although dendrite formation is still an issue], and offers other advantages, such as eliminating the need for a separator, retaining contact with the electrode/electrolyte interface as state of charge varies, and allowing for flexible devices as containment of the electrolyte is no longer required. Ceramic electrolytes such as β-alumina are called "solid electrolytes": to differentiate polymer-based electrolytes that are also solid, they are referred to as "solid polymer electrolytes" or SPEs.

In 1973, a letter appeared in Polymer reporting the first observation of ionic conductivity in complexes of salts in poly(ethylene oxide) (*3*). These complexes were first proposed as SPEs in 1979 by Michel Armand (*4*), around the same time that Goodenough proposed the Li_xCoO_2 cathode. The major drawback to SPEs is their low conductivity compared to liquid electrolytes: conductivity drops by six orders of magnitude compared to $LiPF_6$ in carbonates, and is three orders of magnitude smaller than that required for practical use. Even so, their potential use with Li metal anodes, and other practical features have spurred a large amount of research. A Web of Science search on "solid polymer electrolytes" finds 1507 articles in the last five years, 21% of the articles found for "lithium ion battery" over the same time period.

Although other materials have been investigated [examples include PVDF (*5*), PVC (*6*), PVA (*7*), and PMMA (*8*)] most studies on SPEs are based on poly ethylene oxide [PEO] because its ether oxygens and the tendency of the chain towards local helical structure provides solvation of Li, similar to the behavior of crown ethers. Compared to liquid electrolytes, SPEs are complicated by several features: crystallization, coupling of lithium and polymer motions, and significant contribution of the anion to conductivity. PEO is a semicrystalline polymer at

Downloaded by 89.163.35.42 on June 14, 2012 | http://pubs.acs.org
Publication Date (Web): May 7, 2012 | doi: 10.1021/bk-2012-1096.ch001

room temperature. Although it readily crystallizes, the final state contains both amorphous and crystalline regions with the extent of crystallization and crystal size influenced by thermal history. PEO-based SPEs also form crystal phases that involve the salt: phases with 6 and 3 ether oxygens to Li have been identified. We denote the EO to Li ratio as 6:1, and the specific crystal structure with composition 6:1 as PEO_6. An example of the phase diagram of an SPE is given in Figure 1 (*9*). Depending on the temperature and salt composition, three crystal phases are possible. Under most conditions, either two crystal phases or one crystal phase and liquid coexist. At concentrations of less than 6:1 and temperatures above 65 °C, the SPE is entirely liquid [note that although it is liquid in a thermodynamic sense, it is quite viscous and still behaves as a solid]; it is in this region where the conductivity reaches practical values. As temperature is lowered from 65 °C, either PEO or PEO_6 form, depending on whether the composition is above or below the eutectic composition of 10:1. Even below 50 °C, it is possible to observe crystallization of only pure PEO because its crystallization kinetics are fast compared to those of PEO_6. While PEO will crystalize within minutes, PEO_6 crystallizes over 1-3 weeks (*10–12*). Formation of both phases will influence the composition of the remaining amorphous regions: for example, the concentration of the amorphous regions in an SPE with overall composition of 14:1 and 31% PEO crystallization will be 8:1.

Downloaded by 89.163.35.42 on June 14, 2012 | http://pubs.acs.org
Publication Date (Web): May 7, 2012 | doi: 10.1021/bk-2012-1096.ch001

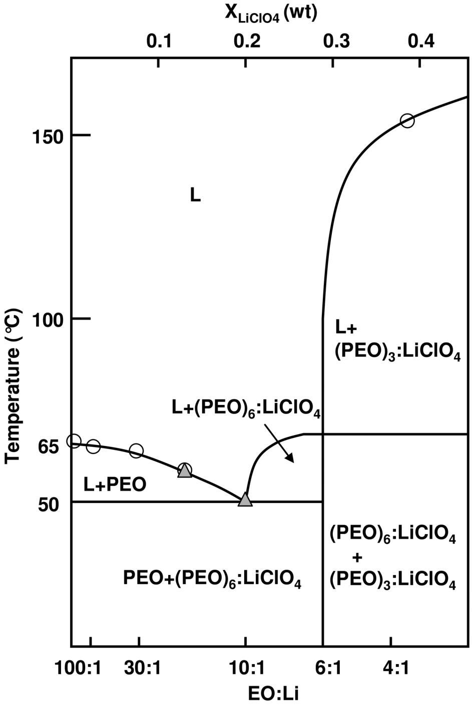

Figure 1. Phase diagram for the PEO/$LiClO_4$ SPE. Reproduced with permission from reference (9).

The eutectic composition may be important with respect to conductivity of SPEs. At this composition the liquid, the PEO crystal and the PEO_6 crystal are in equilibrium. This can lead to many local configurations with similar energies – exactly what is required for Li to rapidly move from one configuration to another. As a result, the SPE conductivity is often maximized at the eutectic composition. Figure 2 compares the composition at the eutectic (*13–16*) with that of maximum conductivity (*17–20*) for four SPE systems. Over a range of eutectic compositions [10:1 to 20:1], the maximum conductivity occurs at or near the eutectic. Note that the $PEO/LiCF_3SO_3$ system exhibits two maxima: one at the eutectic composition of 100:1, and the other at 18:1. This data is not included in the figure because the highest conductivity occurs at 18:1 (*13*). The coincidence between eutectic concentration and concentration of maximum conductivity persists even above the melting temperature, suggesting that concentration fluctuations preceding the eutectic may play a role in conduction. This may mean that an inaccessible liquid-liquid spinodal is buried within the crystalline region.

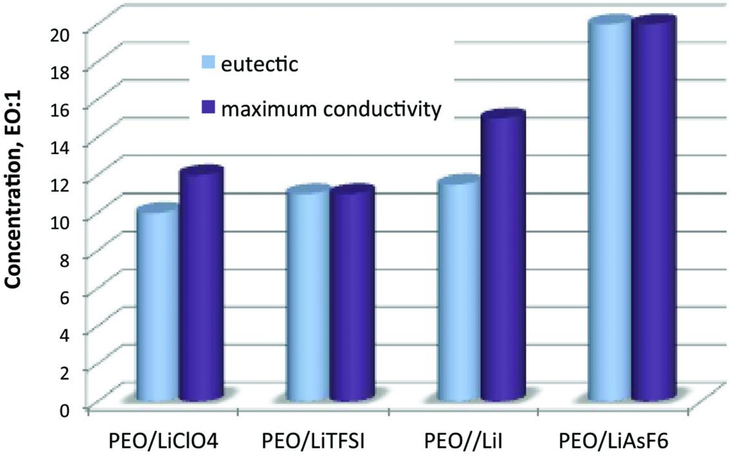

Figure 2. Comparison of eutectic and maximum conductivity concentrations. Y-axis: X in x:1, where x is the EO concentration. Data: eutectic: $PEO/LiClO_4$ (13), PEO/LiTFSI (14, 15), PEO/LiI (16), $PEO/LiAsF_6$ (13); maximum conductivity: $PEO/LiClO_4$ (13, 17), PEO/LiTFSI (18), PEO/LiI (19, 20), $PEO/LiAsF_6$ (13). Maximum conductivity for LiI is from computer simulation.

Lithium transport is generally accepted to occur via the amorphous regions, where the diffusion of lithium is coupled to the segmental motion of the polymer. Lithium may be "single" [complexed only to PEO ether oxygens], paired to the anion, or a part of larger aggregates. The single lithium ions, also referred to as free ions, are the conducting species, with pairs and neutral aggregates contributing little to conductivity. Charged aggregates could potentially contribute to conductivity. For ion contents near the conductivity maximum, the single ion content in PEO-based SPEs is between 20% and 60% (*21–23*) depending on anion, and temperature (*24–26*). Single lithium ions are coordinated by 5-7 ether

Downloaded by 89.163.35.42 on June 14, 2012 | http://pubs.acs.org
Publication Date (Web): May 7, 2012 | doi: 10.1021/bk-2012-1096.ch001

oxygens (*27*), and the local structure even above the melting point resembles the underlying crystal structures (*28*). Motion takes place as the PEO chain undergoes segmental motion: this causes some or all of the ether oxygens coordinating a given lithium to turn over, thus propelling the ion to a new location. Because a single lithium ion can complex ether oxygens from different PEO chains, it serves as a transient cross-link, with the average lifetime estimated at 13-40 ns from computer simulation (*24*, *29*). These cross-links slow the segmental motion of the polymer, as demonstrated using quasi-elastic neutron scattering (*17*, *30–34*). The slowing is concentration dependent, and thus attempts to increase the number of charge carriers by increasing the salt concentration will decrease conductivity by slowing the polymer. This is another reason for a maxiumum in conductivity with salt concentration. Significant slowing appears between 14:1 and 8:1, also the most common location of the eutectic concentration. As mentioned above, the conductivity of PEO/$LiCF_3SO_3$ exhibits two maxima (*13*): the maxima at 18:1 presumably occurs due to slowing of polymer motion. Below the melting point [between 50 and 65 °C depending on concentration], formation of pure PEO crystals serves to increase the lithium concentration in the amorphous regions, contributing to the rapid decrease of conductivity with crystallization. In some cases, the lithium salt introduces a second process, slower than segmental motion and not observed in neat PEO. This process has been attributed to turnover of transient cross links (*30*, *33*, *34*), and rotation of a local cylindrical structure resembling the PEO_6 crystal (*17*).

Although most studies support conduction via the amorphous domains, it has been demonstrated that conduction can occur in fully crystalline SPEs (*35–38*) In all cases, the crystal structure is PEO_6, in which two chains of PEO wrap around a column of lithium ions, and the anions are located between the PEO/Li cylinders (*35*, *37*, *133*). This structure highlights the solvent separated pair, in which a PEO chain is located between the anion and cation. This stable structure also occurs in the liquid phase. Crystalline SPEs are fundamentally different from SPEs in which transport occurs in the amorphous phase, and from ceramic electrolytes. Unlike polymer-based systems, the conductivity is uncoupled from polymer motion and thus follows an Arrhenius, rather than Vogel, temperature dependence (*35–37*, *39*). In this way, the fully crystalline SPE is more like a ceramic electrolyte. Cyrstalline SPEs differ from ceramic electrolytes in mechanical properties as they remain soft solids. Although conductivity is greater than the amorphous counterpart, it remains too low to be practical. As this has received less attention, it is more likely that further research will improve the situation. Rather than increasing polymer motion by lowering Tg, crystalline polymer electrolytes require introduction of defects. This can occur from chain ends [short polymers], polydispersity, or the addition of a second salt. Reference (*40*) provides a good review of crystalline polymer electrolytes.

Not all of the measured conductivity arises from lithium, as the anion can also contribute. The fraction of conductivity from lithium [quantified by transference number] for SPEs falls in the range of 20-30% (*40*), implying faster motion from the anion than lithium. When the anion is mobile, it can accumulate near the electrodes, decreasing performance via electrode polarization (*41*, *42*). To reduce this issue, large, heavy anions such as TFSI are desirable.

Downloaded by 89.163.35.42 on June 14, 2012 | http://pubs.acs.org
Publication Date (Web): May 7, 2012 | doi: 10.1021/bk-2012-1096.ch001

Even in this case transference numbers of unity [lithium conduction only] are not achieved. The largest reduction in anion mobility occurs when the anion is incorporated in the polymer chain. Such “single ion conductors” have transference numbers near unity (*43–56*) [note that this is also achieved with crystalline polymer electrolytes (*35*)]. Such a system belongs to a class of materials termed ionomers [note that ionomer is used for charged polymers at low ion content, while polyelectrolyte is used for charged polymers at high ion content], often limited for synthetic reasons to low ion content. Whereas ionomers often microphase separate into ion-containing and non ion-containing regions (*57–60*), PEO based single ion conductors do not always exhibit such behavior (*61*). As in polymer/salt SPEs, the PEO segment solvates the cations. Although distinct phase separation does not always occur, single ion conductors do have more ion pairing and aggregation than their SPE counterparts. The single ion content of PEO-sulfonates has been estimated at less than 1% using dielectric relaxation spectroscopy (*62*), and no single ions are observed in FTIR (*63*). Aggregation in single ion conductors complicates polymer mobility because it provides another mechanism for inter-chain cross linking. Both PEO solvated cations and aggregated cations will slow polymer dynamics, whereas only PEO solvated cations slow polymer dynamics in PEO/salt systems. As a result, the conductivity maximum occurs at lower ion content in single ion conductors [as low as 100:1] (*64*). Although the transference number in single ion conductors approaches unity, their conductivity is low compared to the best current SPEs, even when adjusted for the greater contribution for lithium conduction. Because of temperature dependent aggregation (*61*) that includes the polymer chain, the mechanisms and design principles for single ion conductors differ from polymer salt/systems, and are not yet understood.

Another way to increase the transport number is through use of an anion receptor – a molecule that is added to the system to “trap” the anion in a complex so it cannot conduct. This is similar to the interaction of lithium with the PEO chain [crown ethers act as cation receptors]. Anions have little interaction with PEO, and thus use of an anion receptor could be expected to provide interaction sites for the anion to balance those provided for lithium by PEO. The ideal anion receptor would have a very strong interaction with the anion, such that it formed a long lived complex. Although anion receptors have been added to SPEs, with transference numbers approaching unity, significant increases in conductivity have not been observed (*65–67*).

Although micron size fillers had been added to SPEs to improve mechanical properties, the first demonstration that fillers can improve conductivity came when the particles were decreased to nanometer dimensions (*68*). The idea became widely investigated following a publication in Nature in 1998 (*69*). In addition to increasing conductivity, nanoscale fillers are reported to increase the transport number as high as 0.5 (*70*). The observation that nanoscale fillers improve conductivity whereas micron size filler do not suggests that the improvement is related to increased polymer/particle surface area. Effective fillers are oxides: TiO_2 (*69*, *71*), Al_2O_3 (*9*, *69*, *72–76*), SiO_2 (*72*, *77–79*), ZrO_2 (*80–82*), $LiAlO_2$ (*83*), Y_2O_3 (*84*), MgO (*85*, *85*), ZnO (*86*), $BaTiO_3$ (*87*), $PbTiO_3$ (*88*), $LiNbO_3$ (*88*), and Fe_3O_4 (*89*). Polymer segmental dynamics are influenced

Downloaded by 89.163.35.42 on June 14, 2012 | http://pubs.acs.org
Publication Date (Web): May 7, 2012 | doi: 10.1021/bk-2012-1096.ch001

near surfaces out to ~30nm (*90*), with the direction of the change dependent on the polymer-particle interaction. PEO wets the surface of oxide particles, meaning that the polymer-particle interaction is attractive and expected to decrease PEO mobility. In the presence of salt, the situation is somewhat more complicated, because the PEO already interacts with lithium, also an attractive interaction that slows segmental motion of the polymer. Depending on whether the polymer, the lithium or the anion interacts with the particle surface, and the strength of these interactions, polymer mobility could increase, decrease or stay the same. Both a small decrease (*91*) and no change (*9*) in segmental mobility have been observed. Since it appears unlikely that increased polymer motion is responsible for the improvement in conductivity, the mechanism must be related to surface chemistry of the filler. In particular, a surface chemistry with Lewis acids [-OH groups] leads to the most improvement in conductivity (*9*, *81*, *82*). In this case, the PEO ether oxygens interact with the particle surface and one might imagine the PEO would form a tunnel-like structure, with the lithium ions placed between the PEO and the particle surface, as illustrated in Figure 3. In this schematic, the filler surface replaces one of the polymer chains in the PEO_6 crystal structure, which is comprised of two PEO chains each of which forms a half cylinder (*92*). This mechanism is consistent with the observation that PEO mobility is decreased, and results in a region of enhanced Li mobility surrounding the particle surface: the conducting pathways illustrated in reference (*40*). In this case, one might expect that the conductivity of a nano-filled system would be similar to that of the corresponding crystalline system: such a comparison is presented in Figure 4. A similar improvement in conductivity is observed for 10 wt% Al_2O_3 nanofilled and fully crystalline $PEO_xLiTFSI$ (*36*, *93*). The presence of enhanced mobility near the filler surface implies that spherical particles would not perform optimally when well dispersed; stringlike aggregates would be better. Such aggregates have been observed (*94*) using small angle neutron scattering. At the volume fraction corresponding to the optimal 10wt% loading, percolation theory (*95–97*) [ref] suggests a structure with 18:1 aspect ratio. The best type of filler may have high aspect ratio, although both cellulose nanowhiskers (*98*, *99*) and Al_2O_3 (*100*) have been tried and do not improve conductivity.

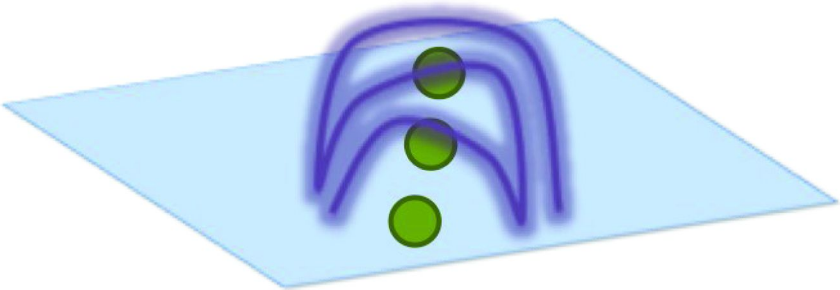

Figure 3. Schematic of a SPE interacting with a filler surface. Blue: filler. Green: lithium ions. Purple: PEO chain. Anions would be located outside the PEO chain.

Downloaded by 89.163.35.42 on June 14, 2012 | http://pubs.acs.org
Publication Date (Web): May 7, 2012 | doi: 10.1021/bk-2012-1096.ch001

Downloaded by 89.163.35.42 on June 14, 2012 | http://pubs.acs.org
Publication Date (Web): May 7, 2012 | doi: 10.1021/bk-2012-1096.ch001

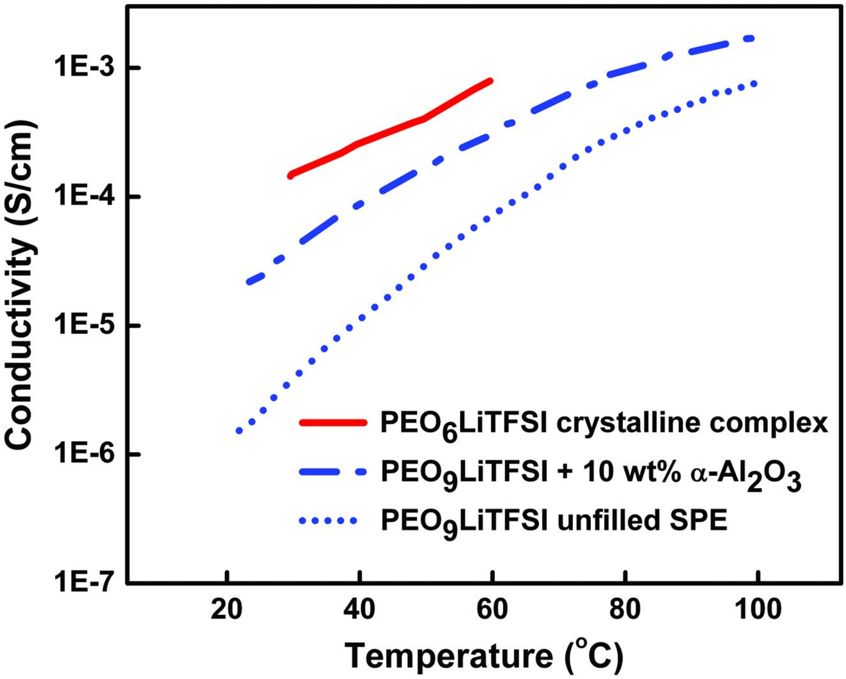

Figure 4. The increase in conductivity when adding nanoparticles [blue curves] is similar to the difference between amorphous and crystalline PEOxLiTFSI [red curves]. Crystalline $PEO_6LiTFSI$*: ref (33). Unfilled* $PEO_9LiTFSI$ *+ 10 wt%* α*-*Al_2O_3*: ref (92). Unfilled* $PEO_9LiTFSI$*: ref (92).*

To effectively and safely use lithium metal in secondary batteries, the formation of dendrites must be prevented. Although a polymer electrolyte could achieve this in theory, the shear modulus required is orders of magnitude above that of PEO (*101–103*). This problem is not easily circumvented, since the coupling of ionic conductivity to polymer motion leads to the requirement of a soft [low modulus] material for reasonable conductivity. Block copolymers have been proposed to address this issue: they combine a soft ion conducting block with a hard insulating block, and thus result in a polymer with appropriate mechanical properties and reasonable conductivity (*104–115*). A good overview of work before 2007 is provided in reference (*110*). An interesting feature of these systems is that the presence of salt significantly alters the phase behavior of the copolymer (*116–120*). In addition to improved mechanical properties, better cycling (*121*, *122*) and higher capacity (*123*) has been reported, although conductivity is sometimes decreased (*124–126*). This decrease is expected based on the reduction in the conducting fraction of the material, the continuity of the conducting phase, and orientation (*113*, *115*).

The performance of SPEs depends on morphology and local structure, thermal behavior and history, polymer dynamics, ion diffusion, and interfacial properties at the electrodes. Thus a large range of techniques have been used for their study. Morphology includes the size and shape of crystalline regions, microphase separation in ionomers or block copolymers, and dispersion of nanoscale fillers. Microphase separation and lamellae size within crystalline regions are nanoscale features, and most appropriately studied by small angle scattering using X-rays (*57*, *61*, *110*, *111*, *117*, *118*, *125*) and neutrons (*17*, *119*). Recently the patterning of Li within one domain of a block copolymer was observed using energy filtered TEM (*127*). Well dispersed nanoscale fillers may also be characterized with small angle scattering (*9*, *94*), although aggregation often occurs to sizes beyond the limit of these techniques. Relevant morphology above nanoscale dimensions includes crystallinity and filler aggregation. Crystallinity is observed under a polarizaing microscope (*10*, *11*, *128–130*); these measurements are effective when combined with X-ray diffraction to identify the crystalline phase under observation (*129*), or with kinetic studies to determine the time evolution of the PEO and PEO_6 phases (*11*). Local structures important to SPEs are the crystal structures of PEO and PEO_6 and the immediate Li environment above the melting point. X-ray diffraction is used for crystal structures (*92*, *131*, *132*), although single crystal and power diffraction were unable to solve the structure of PEO_6, which required a simulated annealing/Monte Carlo procedure to create trial structural models (*133*). An elegant way to investigate local structures in amorphous SPEs is neutron diffraction combined with Li labeling. Several such studies have shown that the local coordination of Li varies from 3.5:1 to 5:1 (*134–136*), and provide evidence for the solvent separated pair. Computer simulation is a powerful method to observe local structure in SPEs, and fully atomistic, polarizable force fields for several such systems are available (*19*, *24–26*, *137*, *138*). Molecular dynamics enforces both the Li:EO ratio obtained from neutron diffraction, and the importance of the solvent separated pair. It is also possible to directly observe ion pairing and aggregation, and to estimate the fraction of free ions, given a specific definition of free. Experimentally, ion association state may be investigated using vibrationa spectroscopy [FTIR and Raman] (*139–148*). These studies often focus on the anion, because internal modes of several anions [for example CF_3SO_3 and CLO_4] depend on the number of coordinated cation. However, ion solvation may also be evaluated from the cation-dependent polymer modes.

Dynamic processes that are relevant to SPEs are the segmental motion of the polymer and the diffusion and mechanism of both anion and cation. Segmental motion of the polymer is best observed using Quasi-Elastic Neutron Scattering because this technique follows the self correlation of hydrogen atoms on the polymer backbone (*9*, *17*, *30–34*). Information about the slowing of polymer mobility due to interaction between Li ions and the polymer backbone and the presence of a second polymer motion slower than segmental motion has been obtained using this technique. Computer simulation is an important source of mechanistic information on SPEs. The lifetimes of Li-EO bonds range from 100ps-1ns, and are temperature dependent (*19*). Ion motion occurs by hopping from sites with 5-7 such bonds, and thus involves breaking multiple bonds in succession or at the same time. Thus times for hopping are considerably longer than Li-EO bond lifetimes. Ion motion is heterogenous, and includes motion

Downloaded by 89.163.35.42 on June 14, 2012 | http://pubs.acs.org
Publication Date (Web): May 7, 2012 | doi: 10.1021/bk-2012-1096.ch001

along a single polymer chain, interchain hopping, diffusion with a polymer host, and movement through aggregates. Motion along a polymer chain is the fastest, with infrequent interchain hopping (*29*). Some decoupling of polymer and ion motion is observed (*19*): understanding the origin of this decoupling is important, as it may provide a route to significant improvement in SPE conductivity. Direct measurement of ion motion can be performed using Li NMR (*149*, *150*), and such measurements were used to establish the dependence of conductivity on polymer motion (*151–153*). Conductivity may be extracted from from NMR self diffusion coefficients using the Nernst-Einstein relation: this overestimates conductivity by an order of magnitude (*154–158*). The difference occurs due to correlated movement of charge. For example, ion pairs moving together will contribute to the self diffusion of each species, with no contribution to conductivity. Computer simulations where both self and collective diffusion is directly computed also show that collective diffusion is an order of magnitude less than self diffusion (*19*, *29*), and the effect is larger when more ion aggregates are present (*29*). Although the presence of ion aggregates is observed to decrease conductivity through correlated motion, nothing precludes increased conductivity due to aggregates. In this case, charge could move through an aggregate by local rearrangement of bonds, similar to the Grotthus mechanism of proton conduction. Such a mechanism has not been observed in SPEs. If NMR is also feasible for the anion, this can be used to establish the transference number. The transference number has also been reported from impedance spectroscopy combined with steady-state current technique (*159*, *160*), and from computer simulation (*19*). A recent and novel use of NMR monitors in-situ formation of dendrites (*161*). This will enable indentification and testing of the factors that might control or eliminate the formation of dendrites. Dendrite formation and other interfacial phenomena are not easily monitored with in-situ experimental techniques. The electrochemical interface is thus an important target for computational approaches, and some work has appeared aimed at Li electrolyte/electrode interfaces (*162*, *163*).

The drastic and unimagined proliferation of cell phones and other portable electronic devices since my friend bought her cell phone in 1988 has been propelled by the commercialization of the rechargeable lithium ion battery [liquid electrolyte]. It is reasonable to ask what role lithium ion batteries in general, and lithium ion batteries with solid polymer electrolytes in particular will play in the future. The next main hurdle for batteries is applications requiring more power than consumer electronics, such as the fully electric or electric hybrid vehicle. The 2011 Motor Trend car of the year is the Chevy Volt, a plug-in electric hybrid that has been on the market since December 2010. The Volt uses a 16 kW-hr lithium ion battery pack with 288 individual cells, similar to the ones in todays cell phones. Also first available in December 2010, the Nissan Leaf is a fully electric vehicle and the 2011 World Car of the Year. The Leaf's 24 kW-hr battery pack consists of 192 lithium ion cells. Power density is particularly important for vehicle applications, and thus the increase promised by lithium metal anode is particularly important. This requires solving the dendrite problem. SPEs alone do not achieve this, as preventing dendrite formation requires a material with modulus higher than that of PEO (*101*). However, several approaches discussed in this chaper could raise the modulus while maintaining reasonable

Downloaded by 89.163.35.42 on June 14, 2012 | http://pubs.acs.org
Publication Date (Web): May 7, 2012 | doi: 10.1021/bk-2012-1096.ch001

conductivity. Block copolymers introduce a hard block that can prevent dendrites while maintaining a soft PEO block for conduction. Fully crystalline SPEs could conduct and prevent dendrites if their conductivity could be maintained at high molecular weight. Nanoscale fillers significantly impact mechanical properties, including the modulus. Direction of the PEO_6 crystal structure with appropriately patterned fillers may offer high conductivity in combination with improved mechanical properties. Perhaps in 2012, one of my friends will purchase a Chevy Volt, and in 2035 its 435 lb lithium ion battery pack will have been replaced with a 40 lb lithium metal battery which costs considerably less and is far smaller. In reality, it is unlikely that we can imagine what the batteries of the future might enable in a vehicle or other applications, just as it was not possible in 1988 to imagine that in 2011 I could check my email on my phone while waiting in line at the grocery store.

Downloaded by 89.163.35.42 on June 14, 2012 | http://pubs.acs.org
Publication Date (Web): May 7, 2012 | doi: 10.1021/bk-2012-1096.ch001

References

1. Whittingham, M. S. *Science* **1976**, *192*, 1126–1127.
2. Mizushima, K.; Jones, P. C.; Wiseman, P. J.; Goodenough, J. B. *Mater. Res. Bull.* **1980**, *15*, 783–789.
3. Fenton, D. E.; Parker, J. M.; Wright, P. V. *Polymer* **1973**, *14*, 359–367.
4. Armand, M. B.; Chabagno, J. M.; Duclot, M. J. In *Fast Ion Transport in Solids*; Vashishta, P., Ed.; North Holland: New York, NY, 1979; p 131.
5. Jacob, M. M. E.; Prabhakaran, S. R. S.; Radhakrishna, S. *Solid State Ionics* **1997**, *104*, 267–276.
6. Wang, X. J.; Kang, J. J.; Wu, Y. P.; Fang, S. B. *Electrochem. Commun.* **2003**, *12*, 1025–1029.
7. Rajendran, S.; Sivakumar, M.; Subhadevi, R. *J. Appl. Polym. Sci.* **2003**, *90*, 2794–2800.
8. Ramesh, S.; Wen, L. C. *Ionics* **2010**, *16*, 255–262.
9. Fullerton-Shirey, S. K.; Maranas, J. K. *J. Phys. Chem. C* **2010**, *114*, 9196–9206.
10. Choi, B.-K. *Solid State Ionics* **2004**, *168*, 123–129.
11. Marzabtowicz, M.; Dygas, J. R.; Krok, F.; Nowiński, J. L.; Tomaszewska, A.; Florjańczyk, Z.; Zygadlo-Monikowska, E. *J. Power Sources* **2006**, *159*, 420–430.
12. Henderson, W. A.; Passerini, S. *Electrochem. Commun.* **2003**, *5*, 575–578.
13. Robitaille, C. D.; Fauteux, D. *J. Electrochem. Soc.* **1986**, *133*, 315–325.
14. Edman, L.; Ferry, A.; Doeff, M. M. *J. Mater. Res.* **2000**, *15*, 1950–1954.
15. Labrèche, C.; Léveque, I.; Prud'homme, J. *Macromolecules* **1996**, *29*, 7795–7801.
16. Fateux, D. Phase Equlibria. In *Polymer Electrolyte Reviews*; MacCallum, J. R., Vincent, C. A., Eds.; Elsevier Applied Science: New York, NY, 1987.
17. Fullerton-Shirey, S. K.; Maranas, J. K. *Macromolecules* **2009**, *42*, 2142–2156.
18. Lascaud, S.; Perrier, M.; Vallée, A.; Besner, S.; Prud'homme, J. *Macromolecules* **1994**, *27*, 7469–7477.

Downloaded by 89.163.35.42 on June 14, 2012 | http://pubs.acs.org
Publication Date (Web): May 7, 2012 | doi: 10.1021/bk-2012-1096.ch001

19. Borodin, O.; Smith, G. D. *Macromolecules* **2000**, *33*, 2273–2283.
20. Müller-Plathe, F.; van Gunsteren, W. F. *J. Chem. Phys.* **1995**, *103*, 4745–4756.
21. Schantz, S. *J. Chem. Phys.* **1991**, *94*, 6296–6306.
22. Schantz, S.; Sandahl, J.; Börjesson, L.; Torell, L. M. *Solid State Ionics* **1988**, *28−30*, 1047–1053.
23. Edman, L. *J. Phys. Chem. B* **2000**, *104*, 7254–7258.
24. Borodin, O.; Smith, G. D. *Macromolecules* **2006**, *39*, 1620–1629.
25. Borodin, O.; Smith, G. D.; Jaffe, R. L. *J. Comput. Chem.* **2001**, *22*, 641–654.
26. Borodin, O.; Smith, G. D *Macromolecules* **1998**, *31*, 8396–8406.
27. Gadjourova, Z.; Martín y Marero, D.; Andersen, K. H.; Andreev, Y. G.; Bruce, P. G. *Chem. Mater.* **2001**, *13*, 1282–1285.
28. Frech, R.; Chintapalli, S.; Bruce, P. G.; Vincent, A. *J. Chem. Soc. Chem. Commun.* **1997**, 157–158.
29. Borodin, O.; Smith, G. D *J. Phys. Chem. B* **2003**, *107*, 6824–6837.
30. Mao, G.; Perea, R. F.; Howells, W. S.; Price, D. L.; Saboungi, M.-L. *Nature* **2000**, *405*, 163–165.
31. Mao, G.; Saboungi, M.-L.; Price, D. L.; Armand, M.; Mezei, F.; Pouget, S. *Macromolecules* **2000**, *35*, 415–419.
32. Mos, B.; Verkerk, P.; Pouget, S.; van Zon, A.; Bel, G. J.; de Keeuw, S. W.; Eisenbach, D. C. *J. Chem. Phys.* **2000**, *113*, 4–7.
33. Triolo, A.; Arrighi, V.; Triolo, R.; Passerini, S.; Mastragostina, M.; Lechner, R. E.; Ferguson, R.; Borodin, O.; Smith, G. D. *Physica B* **2001**, *301*, 163–167.
34. Triolo, A.; Lo Celso, F.; Passerini, S.; Arrigi, V.; Lechner, R. E.; Frick, B.; Triolo, R. *Appl. Phys. A* **2002**, *74*, S493–S495.
35. Gadjourova, Z.; Andreev, Y. G.; Tunstall, D. P.; Y., G; Bruce, P. G. *Nature* **2001**, *412*, 520–523.
36. Christie, A. M.; Lilley, S. J.; Staunton, E.; Andreev, Y. G.; Bruce, PG. *Nature* **2005**, *433*, 50–53.
37. Stoeva, Z.; Martin-Litas, I.; Staunton, E.; Andreev, Y. G.; Bruce, P. G. *J. Am Chem. Soc* **2003**, *125*, 4619–4626.
38. Staunton, E.; Andreev, Y. G.; Bruce, P. G. *Faraday Discuss.* **2007**, *134*, 143–156.
39. Zhang, C.; Staunton, E.; Andreev, Y. G.; Bruce, P. G. *J. Am. Chem. Soc.* **2005**, *127*, 18305–18308.
40. Armand, M. B.; Bruce, P. G., Forsyth, M. Scrosati, B., Wieczorek, W. In *Energy Materials*; Bruce, D. W., O'Hare, D., Walton, R. I., Eds.; John Wiley & Sons: United Kingdom, 2011, pp 1−31.
41. Gray, F. M. *Polymer Electrolytes*; The Royal Society of Chemistry: Letchworth, U.K., 1997.
42. Xu, K. *Chem. Rev.* **2004**, *104*, 4304–4417.
43. Hamaide, T.; Ledeore, C. *Polymer* **1993**, *34*, 1038–1046.
44. Rawsky, G. C.; Fujinami, T.; Shriver, D. F. *Chem. Mater.* **1994**, *6*, 2208–2209.
45. Sun, X.-G.; Kerr, J. B. *Macromolecules* **2005**, *39*, 362–372.

46. Sun, X.-G.; Kerr, J. B.; Reeder, C. L.; Liu, G.; Han, Y. *Macromolecules* **2004**, *37*, 5133–5135.
47. Ito, K.; Ohno, H. *Solid State Ionics* **1995**, *79*, 300–305.
48. Bronstein, L. M.; Karlinsey, R. L.; Stein, B.; Yi, Z.; Carini, J.; Zwanziger, J. W. *Chem. Mater.* **2006**, *18*, 708–715.
49. Ito, K.; Ohno, H. *Solid State Ionics* **1995**, *79*, 300–305.
50. Ito, K.; Nishina, N.; Tominaga, Y.; Ohno, H. *Solid State Ionics* **1996**, *86−88*, 325–328.
51. Zhou, G.; Khan, I.; Smid, J. *Macromolecules* **1993**, *26*, 2202–2208.
52. Ohno, H.; Kobayashi, N.; Takeoka, S.; Ishizaka, H.; Tsuchida, E. *Solid State Ionics* **1990**, *40-41*, 655–658.
53. Tsuchida, E.; Ohno, H.; Kobayashi, N.; Ishizaka, H. *Macromolecules* **1989**, *22*, 1771–1775.
54. Klein, R. J.; Runt, J. *J. Phys. Chem. B* **2007**, *111*, 13188–13193.
55. Doeff, M. M.; Reed, J. S. *Solid State Ionics* **1998**, *113*, 109–115.
56. Kobayashi, N.; Uchiyama, M.; Tsuchida, E. *Solid State Ionics* **1985**, *17*, 307–311.
57. Seitz, M. E.; Chan, C. D.; Opper, K. L.; Baughman, T. W.; Wagener, K. B.; Winey, K. I. *J. Am. Chem. Soc.* **2010**, *132*, 8165–8174.
58. Peiffer, D. G.; Weiss, R. A.; Lundberg, R. D. *J. Polym. Sci., Part B: Polym. Phys. Ed.* **1982**, *20*, 1503–1509.
59. Lantman, C. W.; MacKnight, W. J.; Lundberg, R. D. *Annu. Rev. Mater. Sci.* **1989**, *19*, 295–317.
60. Eisenberg, A.; Kim, J.-S. *Introduction to Ionomers*; John Wiley & Sons: New York, 1998
61. Wang, W.; Tudryn, G. J.; Colby, R. J.; Winey, K. I. *J. Am. Chem. Soc.* **2011**, *133*, 10826–10831.
62. Fragiadakis, D.; Dou, S.; Colby, R. H.; Runt, J. *Macromolecules* **2008**, *41*, 5723–5728.
63. Lu, M.; Runt, J.; Painter, P. *Macromolecules* **2009**, *42*, 6581–6587.
64. Sinha, K.; Maranas, J. K. *Macromolecules* **2011**, *44*, 5381–5391.
65. Blazejczyk, A.; Szczupak, M.; Wieczorek, W.; Cmoch, P.; Appetecchi, G. B.; Scrosati, B.; Kovarsky, R.; Golodnitsky, D.; Peled, E. *Chem. Mater.* **2005**, *17*, 1535–1547.
66. Blazejczyk, A.; Wieczorek, W.; Kovarsky, R.; Goloditsky, D.; Peled, E.; Scanlon, L. G.; Appetecchi, G. B.; Scrosati, B. *J. Electrochem. Soc.* **2004**, *10*, A1762–A1766.
67. Golodnitsky, D.; Kovarsky, R. k; Mazor, H.; Rosenberg, Yu.; Lapides, I.; Peled, E.; Wieczorek, W.; Plewa, A.; Siekierski, M.; Kalita, M.; Settimi, L.; Scrosati, B.; Scanlon, L. G. *J. Electrochem. Soc.* **2007**, A547–A553.
68. Krawiec, W.; Scanlon, L. G., Jr.; Fellner, J. P.; Vaia, R. A.; Vasudevan, S.; Giannelis, E. P. *J. Power Sources* **1995**, *54*, 310–315.
69. Croce, F.; Appetecchi, G. B.; Persi, L.; Scrosati, B. *Nature* **1998**, *394*, 456–458.
70. Chung, S. H.; Wang, Y.; Persi, L.; Croce, F.; Greenbaum, S. G.; Scrosati, B.; Plichta, E. *J. Power Sources* **2001**, *97-98*, 644–648.

Downloaded by 89.163.35.42 on June 14, 2012 | http://pubs.acs.org
Publication Date (Web): May 7, 2012 | doi: 10.1021/bk-2012-1096.ch001

71. Ahn, J. H.; Wang, G. X.; Liu, H. X.; Dou, S. X. *J. Power Sources* **2003**, *119*, 422–426.
72. Johansson, P.; Ratner, M. A.; Shriver, D. F. *J. Phys. Chem. B* **2001**, *105*, 9016–9021.
73. Jayathilaka, P. A. R. D.; Dissanayake, M. A. K. L.; Albinsson, I.; Mellander, B.-E. *Electrochim. Acta* **2002**, *47*, 3257–3268.
74. Wieczorek, W.; Stevens, J. R.; Florjańczyk, Z. *Solid State Ionics* **1996**, *85*, 67–72.
75. Tambelli, C. C.; Bloise, A. C.; Rosário, A. V.; Pereira, E. C.; Magon, C. J. *Electrochim. Acta* **2002**, *47*, 1677–1682.
76. Dissanayake, M. A. K. L.; Jayathilaka, P. A. R. D.; Bokalawala, R. S. P.; Albinsson, I.; Mellander, B.-E. *J. Power Sources* **2003**, *119*, 409–414.
77. Capiglia, C.; Mustarelli, P.; Quartarone, E.; Tomasi, C.; Magistris, A. *Solid State Ionics* **1999**, *118*, 73–79.
78. Scrosati, B.; Croce, F.; Persi, L. *J. Electrochem. Soc.* **2000**, *147*, 1718–1721.
79. Tominaga, Y.; Asai, S.; Sumita, M.; Panero, S.; Scrosati, B. *J. Power Sources* **2005**, *146*, 402–406.
80. Derrien, G.; Hassoun, J.; Simone Sacchetti, S.; Stefania Panero, S. *Solid State Ionics* **2009**, *180*, 1267–1271.
81. Croce, F.; Sacchetti, S.; Scrosati, B. *J. Power Sources* **2006**, *161*, 560–564.
82. Croce, F.; Settimi, L.; Scrosati, B. *Electrochem. Commun.* **2006**, *8*, 364–368.
83. Wen, Z.; Itoh, T.; Ikeda, M.; Hirata, N.; Kubo, M.; Yamamoto, O. *J. Power Sources* **2000**, *90*, 20–26.
84. Liang, G.; Xu, J.; Xu, W.; Shen, X.; Zhang, H.; Yao, Mu. *Polym. Compos.* **2011**, *32*, 1–8.
85. Kumar, R.; A. Subramania, A.; Sundaram, N. T. K.; Kumar, G. V.; Baskaran, I. *J. Membr. Sci.* **2007**, *300*, 104–110.
86. Xiong, H.-M.; Zhao, X.; Chen, J.-S. *J. Phys. Chem. B* **2001**, *105*, 10169–10174.
87. Sun, H. Y.; Sohn, H.-J.; Yamamoto, O.; Takeda, Y.; Imanishi, N. *J. Electrochem. Soc.* **1999**, *146*, 1672–1676.
88. Sun, H. Y.; Takeda, Y.; Imanishi, N.; Yamamoto, O.; Sohn, H.-J. *J. Electrochem. Soc.* **2000**, *147*, 2462–2467.
89. Reddy, J. P.; Chu, P. P.; Kumar, J. S.; Rao, U. V. S. *J. Power Sources* **2006**, *161*, 535–540.
90. Ellison, C. J.; Torkelson, J. M. *Nat. Mater.* **2003**, *2*, 695–700.
91. Karlsson, C.; Best, A. S.; Swenson, J.; Howells, W. S.; Börjesson, L. M. *J. Chem. Phys.* **2003**, *118*, 4206–4212.
92. MacGlashan, G. S.; Andreev, Y. G.; Bruce, P. G. *Nature* **1999**, *398*, 792–794.
93. Dissanayake, M. A. K. L. *Ionics* **2004**, *10*, 221–225.
94. Karlsson, C.; Best, A. S.; Swenson, J.; Kohlbrecher, J.; Börjesson, L. *Macromolecules* **2005**, *38*, 6666–6671.
95. Takayanagi, M.; Uemura, S.; Minami, S. *J. Polym. Sci., Part C* **1964**, *5*, 113–122.
96. Ouali, N.; Cavaillé, J. Y.; Perez, J. *Plast., Rubber Compos., Process. Appl.* **1991**, *16*, 55–60.

Downloaded by 89.163.35.42 on June 14, 2012 | http://pubs.acs.org
Publication Date (Web): May 7, 2012 | doi: 10.1021/bk-2012-1096.ch001

97. Favier, V.; Canova, G. R.; Shrivastava, S. C.; Cavaille, J. Y. *Polym. Eng. Sci.* **1997**, *37*, 1732–1739.
98. Samir, M. A. S. A.; Alloin, F.; Gorecki, W.; Sanchez, J.-Y.; Dufresne, A. *J. Phys. Chem. B* **2004**, *108*, 10845–10852.
99. Alloin, F.; D'Aprea, A.; Kissi, N. E.; Dufresne, A.; Bossard, F. *Electrochim. Acta* **2010**, *55*, 5186–5194.
100. Wen, Z.; Wu, M.; Itoh, T.; Kubo, M.; Lin, Z.; Yamamoto, O. *Solid State Ionics* **2002**, *148*, 185–191.
101. Monroe, C.; Newman, J. *J. Electrochem. Soc.* **2005**, *152*, A396–A404.
102. Monroe, C.; Newman, J. *J. Electrochem. Soc.* **2004**, *151*, A880–A886.
103. Monroe, C.; Newman, J. *J. Electrochem. Soc.* **2003**, *150*, A31377–A1384.
104. Gray, F. M.; MacCallum, J. R.; Vincent, C. A.; Giles, J. R. M. *Macromolecules* **1988**, *21*, 393–397.
105. Giles, J. R. M.; Gray, F. L.; MacCallum, J. R.; Vincent, C. A. *Polymer* **1987**, *28*, 1977–1981.
106. Soo, P. P.; Huang, B.; Jang, Y.-I.; Chiang, Y.-M.; Sadoway, D. R.; Mayes, A. M. *J. Electrochem. Soc.* **1999**, *146*, 32–37.
107. Jannasch, P. *Chem. Mater.* **2002**, *14*, 2718–2724.
108. Kishimoto, K.; Hoshio, M.; Mukai, T.; Yoshizawa, M.; Ohno, H.; Kato, T. *J. Am. Chem. Soc.* **2003**, *125*, 3196–3197.
109. Nitani, T.; Shimada; Kawamura, K.; Dokko, K.; Rho, Y.-H.; Kamamura, K. *Electrochem. Solid State Lett.* **2005**, *8*, A385–A388.
110. Singh, M.; Odusanya, O.; Wilmes, G. M.; Eitouni, H. B.; Gomez, E. D.; Patel, A. J.; Chen, V. L.; Park, M. J.; Fragouli, P.; Iatrou, H.; Hadjichristidis, N.; Cookson, D.; Balsara, N. *Macromolecules* **2007**, *40*, 4578–4585.
111. Ioannou, E. F.; Mountrichas, G.; Pispas, S.; Kamitsos, E. I.; Floudas, G. *Macromolecules* **2008**, *41*, 6183–6190.
112. Xiao, Q.; Wang, X.; Li, W.; Li, Z.; Zhang, T.; Zhang, H. *J. Membr. Sci.* **2009**, *334*, 117–122.
113. Panday, A.; Mullin, S.; Gomez, E. D.; Wnankule, N.; Chen, V. L.; Hexemar, A.; Pople, J.; Balsara, N. P. *Macromolecules* **2009**, *42*, 4632–4637.
114. Ghosh, A.; Wang, C.; Kofinas, P. *J. Electrochem. Soc.* **2009**, *157*, A846–A849.
115. Mullin, S. A.; Stone, G. M.; Panday, A.; Balsara, N. P. *J. Electrochem. Soc.* **2011**, *158*, A619–A627.
116. Cho, B.-K.; Jain, A.; Gruner, S. M.; Weisner, U. *Science* **2004**, *305*, 1598–1601.
117. Epps, T. H., III; Bailey, T. S.; Waletzko, R.; Bates, F. S. *Macromolecules* **2003**, *36*, 2873–2881.
118. Wanakule, N. S.; Panday, A.; Mullin, S. A.; Gann, E.; Hexemer, A.; Balsara, N. P. *Macromolecules* **2009**, *42*, 5642–5651.
119. Ruzette, A.-V. G.; Soo, P. P.; Sadoway, D. R.; Mayes, A. M. *J. Electrochem. Soc.* **2001**, *148*, A537–A543.
120. Ohtake, T.; Ogasawara, M.; Ito-Akita, K.; Nishina, N.; Ujie, E.; Ohno, H.; Kato, T. *Chem. Mater.* **2000**, *12*, 782–789.

Downloaded by 89.163.35.42 on June 14, 2012 | http://pubs.acs.org
Publication Date (Web): May 7, 2012 | doi: 10.1021/bk-2012-1096.ch001

121. Trapa, P. E.; Huang, B.; Won, Y.-Y.; Sadoway, D. R.; Mayes, A. M. *Electrochem. Solid State Lett.* **2002**, *5*, A85–A88.

122. Trapa, P. E.; Won, Y.-Y.; Mui, S. C.; Olivetti, E. A.; Huang, B.; Sadoway, D. R.; Mayes, A. M.; Dallek, S. *J. Electrochem. Soc.* **2005**, *152*, A1–A5.

123. Arbizzaqni, C.; Mastragostino, M.; Hamaide, T.; Guyot, A. *Electrochim. Acta* **1990**, *35*, 1781–1785.

124. Wang, C.; Sakai, T.; Watanabe, O.; Hirahara, K.; Nakanishi *J. Electrochem. Soc.* **2003**, *153*, A1166–A1170.

125. Kosonen, H.; Valkama, S.; Hartikainen, J.; Eerikäinen, H.; Torkkeli, M.; Jokela, K.; Serimaa, R.; Sundholm, F; ten Brinke, G.; Ikkala, O. *Macromolecules* **2002**, *35*, 10149–10154.

126. Khan, I. M.; Fish, K.; Delaviz, Y.; Smid, J. *Makromol. Chem.* **1989**, *190*, 1069–1078.

127. Gomez, E. D.; Panday, A.; Feng, E. H.; Chen, V.; Stone, G. M.; Minor, A. M; Kisielowski, C.; Kowning, K. H.; Borodin, O.; Smith, G. D.; Balsara, N. P. *Nano Lett.* **2009**, *9*, 1212–1216.

128. Marzantowicz, M; Dygas, J. R.; Krok, F.; Łasińska, A.; Florjańczyk, Z.; Zygadło-Monikowska, E. *Electrochim. Acta* **2006**, *51*, 1713–1727.

129. Marzantowicz, M; Dygas, J. R.; Krok, F.; Florjańczyk, Z.; Zygadło-Monikowska, E. *Electrochim. Acta* **2007**, *53*, 1518–1526.

130. Lin, J.-H.; Woo, E. M.; Huang, Y.-P. *J. Polym. Sci., Part B: Polym. Phys.* **2006**, *44*, 3357–3368.

131. Lightfoot, P.; Mehta, M. A.; Bruce, P. G. *Science* **1993**, *262*, 883–885.

132. Andreev, Y. G.; MacGlashan, G. S.; Bruce, P. G. *Phys. Rev. B* **1997**, *55*, 12011–12017.

133. MacGlashan, G. S.; Andreev, Y. G.; Bruce, P. G. *Nature* **1999**, *398*, 792–794.

134. Mao, G.; Saboungi, M.-L.; Badyal, Y. S.; Fischer, H. E. *Europhys. Lett.* **2001**, *54*, 347–353.

135. Mao, G.; Saboungi, M.-L.; Price, D. L; Armand, M. B.; Howells, W. S. *Phys. Rev. Lett.* **2000**, *84*, 5536–5539.

136. Londono, J. D.; Anis, B. K.; Habenschuss, A.; Borodin, O.; Smith, G. D; Turner, J. Z.; Soper, A. K. *Macromolecules* **1997**, *30*, 7151–7157.

137. Borodin, O.; Smith, G. D.; Douglas, R. *J. Phys. Chem. B* **2003**, *107*, 6824–6837.

138. Diddens, D.; Heuer, A.; Borodin, O. *Macromolecules* **2009**, *43*, 2028–2036.

139. Huang, W.; Frech, R.; Wheeler, R. A. *Spectrochim. Acta* **1994**, *50A*, 985–996.

140. Bishop, A. G.; MacFarlane, D. R.; McNaughton, D.; Forsyth, M. *J. Phys. Chem.* **1996**, *100*, 2237–2243.

141. Wensjo, A.; Lindgren, J.; Thomas, J. O.; Farrington, G. C. *Solid State Ionics* **1992**, *53−56*, 1077–82.

142. Bernson, A.; Lindgren, J. *Solid State Ionics* **1993**, *60*, 31–36.

143. Yang, L.; Lin, J.; Wang, Z.; Zhou, R.; Liu, Q. *Solid State Ionics* **1990**, *40−41*, 616–619.

144. Kakihani, M.; Schantz, S.; Torell, L. M. *Solid State Ionics* **1990**, *40−41*, 641–644.

Downloaded by 89.163.35.42 on June 14, 2012 | http://pubs.acs.org
Publication Date (Web): May 7, 2012 | doi: 10.1021/bk-2012-1096.ch001

145. Papke, B. L.; Ratner, M. A.; Shriver, D. F. *J. Electrochem. Soc.* **1982**, *129*, 1434–1438.
146. Petersen, G.; Torell, L. M.; Panero, S.; Scosati, B.; da Silva, C. J.; Smith, M. *Solid State Ionics* **1993**, *60*, 55–60.
147. Huang, W.; Frech, R.; Wheeler, R. A. *J. Phys. Chem.* **1994**, *98*, 100–110.
148. Huang, W.; Frech, R. *Polymer* **1994**, *35*, 235–242.
149. Judeinstein, P.; Reichert, D.; deAzevedo, E. R.; Bonagamba, T. J. *Acta Chim. Slov.* **2005**, *52*, 349–360.
150. Reddy, M. J.; Chu, P. P. *J. Power Sources* **2004**, *135*, 1–8.
151. Paneroa, S.; Scrosati, B.; Greenbaum, S. G. *Electrochim. Acta* **1992**, *37*, 1533–153.
152. Chung, S. H.; Jeffrey, K. R.; Stevens, J. R. *J. Chem. Phys.* **1991**, *94*, 1803–1811.
153. Tunstall, D. P.; Tomlin, A. S.; MacCallum, J. R.; Vincent, C. A. *J. Phys C: Solid State Phys.* **1988**, *21*, 1039–1048.
154. Walls, H. J.; Fedkiw, P. S.; Zawodzinski, T. A., Jr.; Khan, S. A. *J. Electrochem. Soc.* **2003**, *150*, E165–E174.
155. G. Fleischer, G.; Scheller, H.; Karger, J.; Reiche, A.; Sandner, B. *J. Non-Cryst. Solids* **1998**, *235*, 742–747.
156. Ferry, A.; Oradd, G.; Jacobsson, P. *J. Chem. Phys.* **1998**, *108*, 7426–7433.
157. Williamson, M. J.; Hubbard, H. V. S. A.; Ward, I. M. *Polymer* **1999**, *40*, 7177–7185.
158. Ward, I. M.; Boden, N.; Cruickshank, J.; Leng, S. A. *Electrochim. Acta* **1995**, *40*, 2071–2076.
159. Bruce, P. G.; Vincent, C. A. *J. Electroanal. Chem.* **1987**, *225*, 1–17.
160. Riley, M.; Fedkiw, P. S.; Khan, S. A. *J. Electrochem. Soc.* **2002**, *149*, A667–A674.
161. Bhattacharyya, R.; Key, B.; Chen, H.; Best, A. S; Hollenkamp, A. F.; Grey, C. P. *Nat. Mater.* **2010**, *9*, 504–510.
162. Smith, G. D.; Borodin, O.; Russo, S. P.; Rees, R. J.; Hollenkamp, A. F. *Phys. Chem. Chem. Phys.* **2009**, *11*, 9884–9897.
163. Vatamanu, J.; Borodin, O.; Smith, G. D. *Phys. Chem. Chem. Phys.* **2010**, *12*, 170–182.

Downloaded by 89.163.35.42 on June 14, 2012 | http://pubs.acs.org
Publication Date (Web): May 7, 2012 | doi: 10.1021/bk-2012-1096.ch001

Downloaded by CORNELL UNIV on June 14, 2012 | http://pubs.acs.org
Publication Date (Web): May 7, 2012 | doi: 10.1021/bk-2012-1096.ch002

Chapter 2

First Principles Design of Ionomers for Facile Ion Transport

Wenjuan Liu,[a,c,d] Michael J. Janik,[b] and Ralph H. Colby[a,c,*]

[a]Department of Materials Science and Engineering, Pennsylvania State University, University Park, PA 16802
[b]Department of Chemical Engineering, Pennsylvania State University, University Park, PA 16802
[c]Materials Research Institute, Pennsylvania State University, University Park, PA 16802
[d]Current Address: Dow Chemical Company, Midland, MI 48674
[*]rhc@plmsc.psu.edu

Ab initio calculations have been performed for the association of lithium and sodium cations with various carboxylate, sulfonate, phosphonate and borate anions, with a particular emphasis on the effects of perfluorinating the anions. Fluorinating the benzene ring on benzene carboxylate, benzene sulfonate or benzene phosphonate makes the pair and positive triple ion binding less favorable by 5-10% due to the electron-withdrawing F placing more of the negative charge on the ring, effectively softening these anions. However, fluorinating the four benzene rings of tetraphenyl borate has a significantly stronger electron-withdrawing effect, destabilizing the pair and positive triple ion energies by 20-30%. We also explore two methods to account for the effects of a surrounding polar medium on ion interactions. The polarizable continuum model was studied with six ion pairs to account for the dielectric constant of the surroundings. We also model specific local solvation of poly(ethylene oxide) on Li^+ and Na^+ with two anions (benzene sulfonate and triflate) and also their ion pairs, by surrounding these with explicit dimethyl ether (DME) molecules. We find a strong local solvation effect on the cations that is particularly strong for Li^+ with four DME in the first solvation shell. There is very little specific solvation of anions

In Polymers for Energy Storage and Delivery: Polyelectrolytes for Batteries and Fuel Cells; Page, K., et al.;
ACS Symposium Series; American Chemical Society: Washington, DC, 2012.

by DME and the ion pairs fill their first solvation shell with three DME, with all four ion pairs studied showing very similar solvated pair interactions.

1. Introduction

Ion-containing polymers are of interest for use as electrolytes in lithium ion batteries, fuel cell membrane electrode assemblies, supercapacitors, sensors and actuators. Ion conduction may be achieved by dispersing a Li or Na salt in poly(ethylene oxide) (PEO) (*1*) however, salt doped PEO suffers from undesirable concentration polarization, since the anions generally have higher mobility than Li^+ or Na^+ (*1–3*), and the anions accumulate at the electrode/electrolyte interface over time in either lithium or sodium batteries. This build-up lowers the field the cations see and also can serve to trap/delay cations locally and place enormous stress on the electrolyte/electrode interface, since the anions cannot transfer their charge to the electrode (*2*). Covalent bonding of the anions to the polymer to form an ionomer ('single-ion conductors' in the electrochemical literature) can overcome these difficulties (*3–7*). Covalent attachment of the anions to the polymer chain means that only the cations are able to migrate over long distances on reasonable time scales, and a cation transference number very close to unity can be achieved. For cation conductors, the choices for composition of the covalently bound anionic group, polymer backbone, and additional side chains or functional groups are extensive, and cannot be efficiently sampled through experiment. We are therefore motivated to develop a rational bottom-up design strategy of superior ionomers for facile ion transport using computational methods.

Ionomer membranes transport different counterions in various applications. The ion is often bulky in actuators, often Li^+ or Na^+ in advanced batteries, and often either H_3O^+ or OH^- in fuel cell membrane-electrode assemblies. In each application, conductivity is enhanced by increasing the concentration of conducting counterions, defined as the (often small) fraction of counterions that simultaneously participate in conduction. Unfortunately, for poly(ethylene oxide)-based sulfonate ionomers with Li^+ or Na^+ counterions, only a fraction, $< 10^{-3}$, of the counterions are simultaneously participating in conduction (*4–7*). While the conductivity benchmark for useful Li or Na salts in PEO is 10^{-3} S/cm, since the anions in these systems move 5-10X faster than the cations, the benchmark for single-ion conductors is 10^{-4} S/cm (*3*). Current conductivities of the best ionomers are roughly 100X too small for practical applications. Since they also have less than 1/1000th of their countercations simultaneously participating in conduction there is a genuine opportunity to meet the benchmark by higher participation of counterions in conduction. The small fraction of conducting counterions arises because the interaction energy between oppositely charged ions is large. With PEO-based sulfonate ionomers, this forces the vast majority of Li^+ counterions to be less than 4 Å from the S in the sulfonate group, with binding energy of order 25 kJ/mol (*4*).

Downloaded by CORNELL UNIV on June 14, 2012 | http://pubs.acs.org
Publication Date (Web): May 7, 2012 | doi: 10.1021/bk-2012-1096.ch002

Ab initio methods allow for direct quantitative examination of the potential energy surface for pairwise interactions between species. Figure 1 schematically illustrates the perturbations of a hypothetical anion-cation potential energy surface with compositional changes in an ionomeric system. Ion conduction would be enhanced by *softening* (lowering the magnitude of) the cation-anion interaction (ΔE_{pair}) to allow a higher fraction of ions to participate in conduction. This might be accomplished by a combination of the three modifications illustrated schematically in Figure 1:

1) delocalize the anionic charge and sterically hinder cation access to the anion (red dotted curve)
2) raise the dielectric constant of the surrounding ionomer medium (blue solid curve)
3) locally solvate (stabilize) the conducting ions relative to the ion pair (green solid curve).

Downloaded by CORNELL UNIV on June 14, 2012 | http://pubs.acs.org
Publication Date (Web): May 7, 2012 | doi: 10.1021/bk-2012-1096.ch002

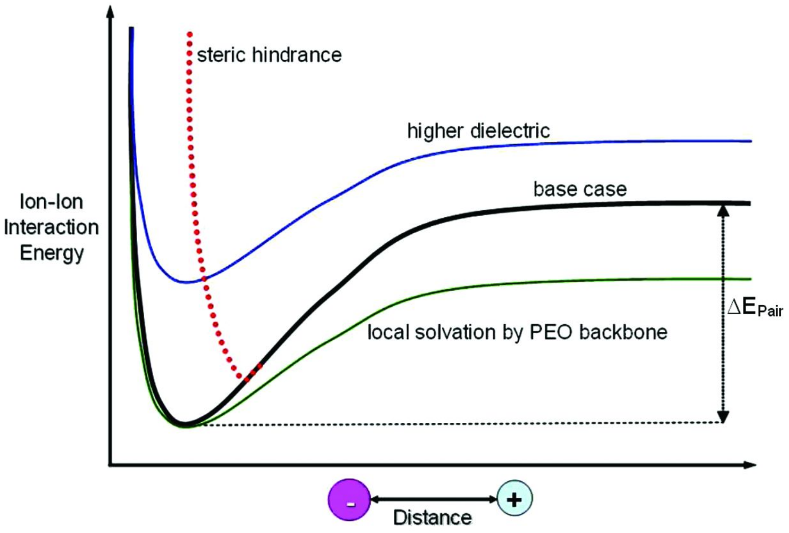

Figure 1. Schematic anion-cation interaction potential energy surface (black curve) including perturbations introduced by changes in the ionomer composition that sterically hinder ions (red dashed), raise dielectric constant ε (blue) or solvate ions (green).

Ab initio methods have been previously applied to explore interactions between ions in vacuum (*8–11*). The majority of these studies have evaluated methodological choices in comparison with experimental data or sought to explain observed experimental behavior through detailed electronic structure studies. Many studies have employed *ab initio* methods to guide the choice of counteranion in lithium ion salts (*12–27*), but the application of these methods for large scale evaluation and design of complex ionomer compositions has not been previously attempted.

Downloaded by CORNELL UNIV on June 14, 2012 | http://pubs.acs.org
Publication Date (Web): May 7, 2012 | doi: 10.1021/bk-2012-1096.ch002

Though *ab initio* methods are limited in the time and length scales accessible, they will serve to evaluate interaction energies and these values then guide design choices to 1) provide insight into the interactions and molecular level phenomena that impact conductivity; 2) establish relationships between interactions of ions and polar functional groups to guide rational design; and 3) identify promising compositions/combinations of polymer backbone repeat units, functional groups and attached anions. In this paper, we study various common ionomer anions: sulfonates, phosphonates, and carboxylates, as well as highly delocalized borates, and the effect of the dielectric constant of the surrounding medium. We use *ab initio* calculations to evaluate the interaction energies that drive ion pairing and clustering, and consider approaches to including specific local solvation effects of ether oxygen atoms on these interaction energies.

2. Computational Methods

All the calculations reported in this paper were carried out with the Gaussian03 program (*28*). Density-functional theory (DFT) calculations used Becke's three-parameter hybrid method employed with the B3LYP exchange - correlation functional (*29–32*) and a split valence plus diffuse and polarization functions 6-31+G* basis set. For method validation, B3LYP/6-31+G* was compared with Møller-Plesset 2nd order perturbation theory (MP2) molecular orbital calculations with the triple split valence plus diffuse and polarization functions 6-311+G* basis set. The magnitude of the interaction energy (ΔE_{int}) between Li^+ or Na^+ cations and neutral or anionic species was evaluated as the difference in the energies of the coordination complexes ($E_{complex}$) to that of the isolated species (E_{cation} and $E_{anion/neutral}$):

$$\Delta E_{int} = E_{cation} + E_{anion\,/\,neutral} - E_{complex} \qquad (1)$$

More positive ΔE_{int} values represent a stronger attractive interaction between species. Structural optimization was continued until convergence criteria of maximum and root mean squared atomic forces and distance variation were met. The default convergence values invoked by the "Opt" keyword were used. Vibrational frequency calculations were performed both to confirm that the obtained structures were true minima on the potential energy surfaces and to add zero-point vibrational energy (ZPVE), thermal enthalpy, and thermal free energy corrections to the total energy. For calculations in which Li^+ or Na^+ cations were paired with neutral or anionic species, multiple local minima were located and the reported results reflect the most stable structure located. Extensive sampling of the potential energy surface was done for each cation with one anion of each type (i.e., with one sulfonate, one phosphonate) and the minimum energy configuration was utilized as the starting point for the same ion state of the same cation with other anions of the same type.

To study global solvation effects, we performed solvation calculations (SCRF) with the polarizable continuum model (PCM), originally developed by Tomasi, and coworkers (*33–38*) and implemented by Gaussian03, for six salts in 22 solvents. This method is a straightforward extension of the 1936 Onsager

Downloaded by CORNELL UNIV on June 14, 2012 | http://pubs.acs.org
Publication Date (Web): May 7, 2012 | doi: 10.1021/bk-2012-1096.ch002

model (*39*) to ions and ion clusters of non-spherical shapes, creating the solute cavity via a series of overlapping spheres within the solvent reaction field. Solvated interaction energies attempt to include both the electronic energy and electrostatic solute-solvent interactions within the PCM model. The polarizable continuum model has the advantage of incorporating extended solute-solvent interactions with minimal computational requirements and without concerns as to the detailed solvation structure adopted. Disadvantages of this approach include the lack of molecular structure inherent in the use of a continuum, difficulties in determining the proper definition of the solute cavity within the polarizable continuum, and the need to approximate a dielectric constant representative of a specific polar group. In using the PCM model, only the electrostatic terms in the solute-solvent interaction were included in determining the forces for geometry optimization and the total energies.

To examine the accuracy of the methods employed, we compared calculated and experimental values of the dipole moments of various species of interest as well as the interaction energies of Li^+ and Na^+ cations with various species. The dipole moment is compared among B3LYP/6-31+G* and MP2/6-311+G* methods and experimentally measured values for neutral polar small molecules. Table 1 lists the dipole moment of 16 neutral polar small molecules calculated by both method/basis sets and the measured values (*40*). Figure 2 illustrates the correlation of calculated and experimental values.

Table 1. Comparison of calculated dipole moments with vapor phase measurements (*40*) for small polar molecules.

Polar Small Molecules	*Dipole Moment (Debye)*			*Polar Small Molecules*	*Dipole Moment (Debye)*		
	Meas.	*MP2*	*DFT*		*Meas.*	*MP2*	*DFT*
Toluene	0.37	0.38	0.40	Pyridine	2.21	2.45	2.38
Diethyl ether	1.15	1.44	1.23	Oxirane	1.89	2.47	2.15
Phenol	1.22	1.56	1.42	Acetaldehyde	2.75	3.30	2.87
1-Propanol	1.55	1.84	1.70	Acetone	2.88	3.55	3.19
1-Butanol	1.66	1.91	1.76	Benzeneacetonitrile	3.5	4.23	4.03
Fluorobenzene	1.60	1.99	1.75	Acetonitrile	3.92	4.27	4.07
Methyl acetate	1.72	2.04	1.96	Dimethylformamide	3.82	4.59	4.41
Methanol	1.70	2.09	1.94	Benzonitrile	4.18	5.10	4.77

Downloaded by CORNELL UNIV on June 14, 2012 | http://pubs.acs.org
Publication Date (Web): May 7, 2012 | doi: 10.1021/bk-2012-1096.ch002

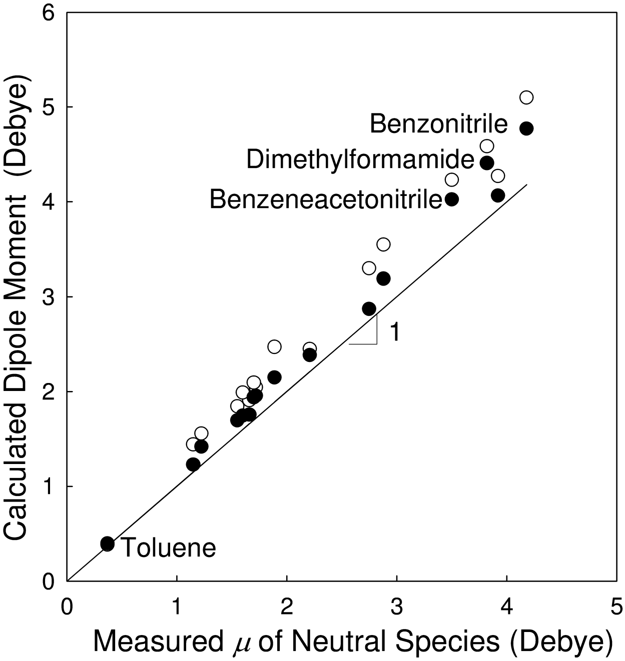

Figure 2. Dipole moment of neutral polar small molecules calculated by B3LYP/6-31+G (filled circles) and MP2/6-311+G* (open circles) plotted versus experimentally measured values in the vapor phase.*

Both basis sets systematically overestimate the dipole moments, but within the experimental error in most cases, estimated to be 15% (*40*). The results generated by B3LYP/6-31+G* show better agreement with measured values, with the largest deviation being 13.5%. The theoretical overestimation increases as the molecule becomes more polar, such as for dimethylformamide (DMF) (13.4%), benzene acetonitrile (13.5%), and benzonitrile (12.4%). The disagreement with experiment may, in part, be caused by experimental error due to the presence of aggregates of two or more polar molecules lowering the measured value.

We also compared calculated and experimentally measured interaction energies between Li^+ cations and a series of solvents in the gas phase. Experimental gas phase heats of interaction ($\Delta H_r°$) and free energies of interaction ($\Delta G_r°$) were taken from a NIST database [from original refs (*41–45*)]. In adjusting the 0 K electronic energy differences to temperature dependent free energy differences, all species were assumed to be free of accessible excited electronic states. Enthalpic and entropic terms associated with vibration and molecular rotation were treated with harmonic oscillator and rigid rotor models in the ideal gas limit. The ΔE_{int} values (Equation 1) refer to 0 K, non-ZPVE corrected interaction energies. The symbols ΔH_{int} and ΔG_{int} are used to refer to the ZPVE and thermally corrected values at standard state conditions (298.15 K, 1.0 atm)

In Polymers for Energy Storage and Delivery: Polyelectrolytes for Batteries and Fuel Cells; Page, K., et al.;
ACS Symposium Series; American Chemical Society: Washington, DC, 2012.

calculated equivalently to Equation 1 for the 0 K values. In Table 2 and Figure 3, the calculated and experimental interaction enthalpies and free energies are compared.

Downloaded by CORNELL UNIV on June 14, 2012 | http://pubs.acs.org
Publication Date (Web): May 7, 2012 | doi: 10.1021/bk-2012-1096.ch002

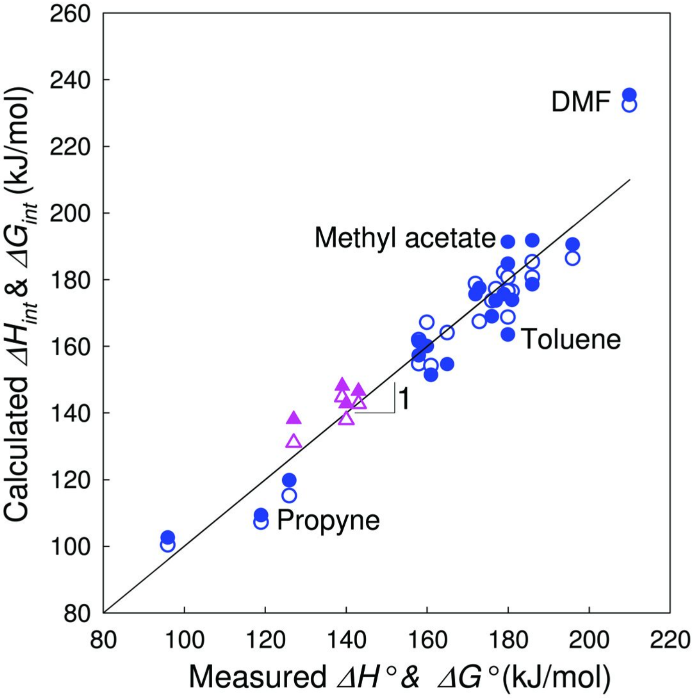

Figure 3. Comparison of calculated and experimental interaction enthalpies and free energies (41–45) between neutral polar small molecules with a Li^+ cation. Filled symbols are calculated with B3LYP/6-31+G and open symbols with MP2/6-311+G*. Blue circles represent interaction enthalpies and pink triangles represent interaction free energies, both with zero-point vibrational energy.*

Most of the interaction energies generated by the two sets of calculations are within 7% of experimental values. The sole exception is dimethylformamide, the most polar solvent that we could find Li^+ interaction energy data for. We evaluated the mean squared error of the calculated data sets from the experimental data, as reported in Table 3. Though the MP2/6-311+G* basis set does slightly better than B3LYP/6-31+G* on interaction enthalpies, the difference is slight and the DFT method does better on the free energies. Throughout the remainder of the study, all values are calculated with DFT (B3LYP/6-31+G*).

Downloaded by CORNELL UNIV on June 14, 2012 | http://pubs.acs.org
Publication Date (Web): May 7, 2012 | doi: 10.1021/bk-2012-1096.ch002

Table 2. Interaction energies of a Li$^+$ cation with a series of polar species. Values calculated with B3LYP/6-31+G* and MP2/6-311+G* with zero-point vibrational energy correction and thermal corrections are compared with experimentally measured dissociation enthalpies and free energies (*41–45*) in kJ/mol.

Solvent	*DFT (B3LYP/6-31+G*)*			*MP2 (MP2/6-311+G*)*			*Measured*	
	ΔE_{int}	ΔH_{int}	ΔG_{int}	ΔE_{int}	ΔH_{int}	ΔG_{int}	$\Delta H°$	$\Delta G°$
Propene (*42*)	105	103	74	100	100	72	96	
Propyne (*42*)	111	109	83	105	107	79	119	
Fluorobenzene (*44*)	121	120	96	122	115	90	147 ± 21	
Phenol (*44*)	154	151	127	161	154	127	178 ± 17	
Pyrazine (*45*)	161	157	127	157	155	125	149 ± 14	
Methanol (*43*)	164	160	131	171	167	138	159	127
Dimethoxyethane (*41*)	165	161	132	163	162	134	158 ± 4	
Dimethylether (*43*)	166	155	125	168	164	136	165	131
Toluene (*44*)	168	163	127	172	169	134	183 ± 17	
Trimethylamine (*43*)	174	169	138	171	174	143	176	140
2-Propanol (*41*)	178	174	145	181	176	150	173 ± 8	
Dimethylamine (*43*)	179	174	143	176	177	147	177	143
1-Propanol (*41*)	180	176	146	184	182	151	171 ± 8	
Methylamine (*43*)	182	176	145	179	179	148	172	139

Downloaded by CORNELL UNIV on June 14, 2012 | http://pubs.acs.org
Publication Date (Web): May 7, 2012 | doi: 10.1021/bk-2012-1096.ch002

Solvent	***DFT (B3LYP/6-31+G*)***			***MP2 (MP2/6-311+G*)***			***Measured***	
	ΔE_{int}	ΔH_{int}	ΔG_{int}	ΔE_{int}	ΔH_{int}	ΔG_{int}	$\Delta H°$	$\Delta G°$
1-Butanol (*41*)	183	179	149	186	185	152	178 ± 8	
Acetaldehyde (*42*)	183	177	152	195	167	142	173	
Acetonitrile (*42*)	187	185	155	191	177	147	180	
Pyridine (*45*)	195	190	160	193	186	156	181 ± 15	
Methyl acetate (*42*)	195	191	163	203	181	150	180	
Acetone (*42*)	198	192	167	207	181	156	186	
Dimethylformamide (*42*)	244	235	209	250	232	198	210	

Table 3. The mean squared error of the calculated enthalpies and free energies of interaction versus experimental values for the DFT (B3LYP/6-31+G*) and MP2/6-311+G* basis sets.

	$\Delta H_{int} \leftrightarrow \Delta H°$	$\Delta G_{int} \leftrightarrow \Delta G°$
B3LYP/6-31+G*	9.09	3.70
MP2/6-311+G*	7.85	7.52

3. Interactions and Dipoles of Isolated Ion Pairs

We chose a series of 6 sulfonate, 6 phosphonate and 6 carboxylate anions with methyl, ethyl and phenyl functional groups and 3 borate anions, many of which are the perfluorinated versions of these anions to evaluate interactions with Li^+ and Na^+. All the 21 anions are chemically stable and most of them are commercially available, though synthesis of ionomers containing each anion has not yet been demonstrated. The interaction energies (ΔE_{int}), and dipole moments (μ) of the Li and Na ion pairs with these 21 anions are listed in Table 4, along with two measures of the anion-cation distance. The distance between the Li atom and the sulfur, phosphorus, carbon or boron atom of the anion is labeled $d_{cation\text{-}S/P/C/B}$. A second distance, derived from the dipole moment, is labeled $d \equiv \mu/e$, representing the charge separation distance implied by the dipole moment if the anion and cation are assumed to retain their full unit charge in the paired state.

Figure 4 illustrates a subset of the optimized structures. For sulfonates and phosphates, a Li cation prefers to interact with two oxygen atoms, along the edge of the tetrahedron. For the carboxylates, a Li cation interacts with both oxygen atoms. Comparison with structures with a Li cation interacting with one or three oxygen atoms confirmed that the illustrated configurations represent the minimum energy structure. For the tetraphenylborate anion, the optimal Li position is 3.0 Å from the central B atom, equally spaced between two phenyl rings. This position is preferred in comparison to a structure where Li interacts more directly with a single phenyl ring.

Comparing Na^+ and Li^+, with sulfonates, phosphonates, and carboxylates, the pair energy is consistently about 17% larger for the smaller Li^+. Comparing sulfonates, phosphonates, and carboxylates, for all anion substituents, the interaction with Na^+ and Li^+ is always weakest for sulfonates, intermediate for phosphonates and strongest for carboxylates. The borates considered show weaker interaction with Na^+ and Li^+ cations than all other anions. Comparing Na^+ and Li^+, with the borates, the pair energy shows an even larger effect of cation, 26% larger for the smaller Li^+ for tetrabutyl borate, 15% larger for tetraphenylborate and 22% larger for perfluorinated tetraphenylborate. Fluorinating the anion (replacing all C-H with C-F) significantly lowers the interaction energy of anions with Li^+ or Na^+ due to the electron-withdrawing nature of F atoms; fluorinating significantly increases the dipole moment of the ion pair while not significantly changing the cation-P/S/C distance. If weaker pair

Downloaded by CORNELL UNIV on June 14, 2012 | http://pubs.acs.org
Publication Date (Web): May 7, 2012 | doi: 10.1021/bk-2012-1096.ch002

interactions are presumed to predict the extent to which the conducting cation will be "freed" from the anion in the ionomer, these trends suggest borate or sulfonate anions would produce the greatest amount of Li^+ or Na^+ cations participating in conduction. The cation-P/S/C distances do not correlate with interaction energies and are not sensitive to changing the anion substituents. These distances reflect size differences of the central P/S/C atom rather than the Coulombic interaction distance, as expected since the negative charge of the anions is localized on the oxygen atoms and not the central atom. Larger dipole moments (and dipole moment derived distances) generally indicate weaker interactions. The ratio of distances $ed_{cation-S,P,C,B}/\mu$ provides a crude measure of 'covalency'. Non-fluorinated carboxylates and phosphonates have the most covalent character to their ionic bonds and perfluorinating the anion always makes the ionic bond less covalent, since the electron-withdrawing F atoms leave less negative charge for these anions to share.

Downloaded by CORNELL UNIV on June 14, 2012 | http://pubs.acs.org
Publication Date (Web): May 7, 2012 | doi: 10.1021/bk-2012-1096.ch002

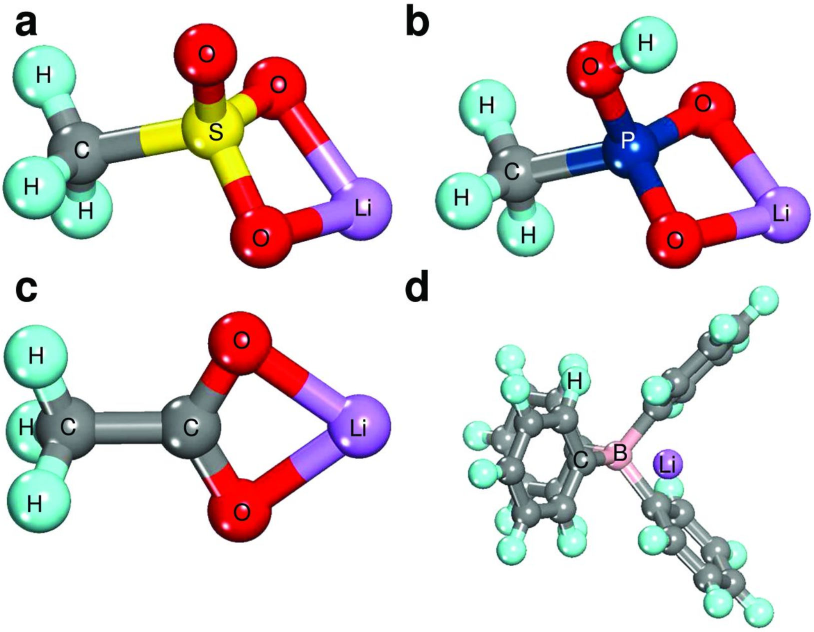

Figure 4. Equilibrium pair structures of a) Li-methyl sulfonate, b) Li-methyl phosponate, c) Li-methyl carboxylate, and d) Li-tetraphenylborate.

In Polymers for Energy Storage and Delivery: Polyelectrolytes for Batteries and Fuel Cells; Page, K., et al.;
ACS Symposium Series; American Chemical Society: Washington, DC, 2012.

Downloaded by CORNELL UNIV on June 14, 2012 | http://pubs.acs.org
Publication Date (Web): May 7, 2012 | doi: 10.1021/bk-2012-1096.ch002

Table 4. Ion pair interaction energies (ΔE_{int}) without ZPVE correction, dipole moment (μ), distance calculated from dipole moment ($d \equiv \mu/e$, where e is the elementary charge) and the distance of the Li^+ or Na^+ cation from the sulfur or phosphorus or carbon or boron ($d_{cation\text{-}S/P/C/B}$) of 21 anions.

Anion Name	*Chemical Formula*	*ΔE_{int} (kJ/mol)*		*μ (Debye)*		*$d \equiv \mu / e$ (Å)*		*$d_{cation\text{-}S/P/C/B}$ (Å)*	
		Li^+	*Na^+*	*Li^+*	*Na^+*	*Li^+*	*Na^+*	*Li^+*	*Na^+*
Methyl sulfonate	$CH_3SO_3^-$	654	558	5.68	7.66	1.18	1.59	2.37	2.74
Ethyl sulfonate	$C_2H_5SO_3^-$	656	559	5.52	7.47	1.15	1.56	2.37	2.74
Benzene sulfonate	$C_6H_5SO_3^-$	641	545	5.74	7.77	1.19	1.62	2.37	2.74
Trifluoromethane sulfonate	$CF_3SO_3^-$	592[a]	506	6.56	9.20	1.37	1.92	2.38	2.75
Pentafluoroethane sulfonate	$C_2F_5SO_3^-$	584	499	6.28	9.30	1.31	1.94	2.38	2.75
Pentafluorobenzene sulfonate	$C_6F_5SO_3^-$	604	516	5.82	8.31	1.21	1.73	2.37	2.75
Methyl phosphonate	$CH_3PHO_3^-$	689	587	3.27	5.55	0.68	1.16	2.32	2.68
Ethyl phosphonate	$C_2H_5PHO_3^-$	689	587	3.20	5.48	0.67	1.14	2.32	2.68
Benzene phosphonate	$C_6H_5PHO_3^-$	667	570	2.61	5.24	0.54	1.09	2.31	2.67
Trifluoromethane phosphonate	$CF_3PHO_3^-$	620	532	4.81	7.38	1.00	1.54	2.32	2.68
Pentafluoroethane phosphonate	$C_2F_5PHO_3^-$	612	525	4.94	7.59	1.03	1.58	2.32	2.68
Pentafluorobenzene phosphonate	$C_6F_5PHO_3^-$	625	535	3.76	6.28	0.78	1.31	2.31	2.67
Methyl carboxylate	$CH_3CO_2^-$	718	617	3.29	5.59	0.68	1.16	2.12	2.49
Ethyl carboxylate	$C_2H_5CO_2^-$	716	614	3.35	5.70	0.70	1.19	2.12	2.49
Benzene carboxylate	$C_6H_5CO_2^-$	697	596	3.20	5.92	0.67	1.23	2.12	2.50

Downloaded by CORNELL UNIV on June 14, 2012 | http://pubs.acs.org
Publication Date (Web): May 7, 2012 | doi: 10.1021/bk-2012-1096.ch002

Anion Name	***Chemical Formula***	***ΔE_{int} (kJ/mol)***		***μ (Debye)***		***$d \equiv \mu / e$ (Å)***		***$d_{cation\text{-}S/P/C/B}$ (Å)***	
		Li^+	***Na^+***	***Li^+***	***Na^+***	***Li^+***	***Na^+***	***Li^+***	***Na^+***
Trifluoromethane carboxylate	$CF_3CO_2^-$	635	547	6.40	8.77	1.33	1.83	2.12	2.48
Pentafluoroethane carboxylate	$C_2F_5CO_2^-$	625	538	6.58	9.03	1.37	1.88	2.12	2.49
Pentafluorobenzene carboxylate	$C_6F_5CO_2^-$	630	540	6.00	8.89	1.25	1.85	2.12	2.50
Tetrabutylborate	$(C_4H_9)_4B^-$	585	464	4.68	7.17	0.97	1.49	1.98	2.50
Tetraphenylborate	$(C_6H_5)_4B^-$	555[b]	484	4.83	10.2	1.00	2.13	2.16	2.66
Tetra(pentafluorophenyl)borate	$(C_6F_5)_4B^-$	448	366	7.35	10.7	1.53	2.23	2.90	3.57

[a] 595 kJ/mol in ref (*22*) using B3LYP/6-311+G*. [b] 558 kJ/mol in ref (*22*) using B3LYP/6-311+G*.

Downloaded by CORNELL UNIV on June 14, 2012 | http://pubs.acs.org
Publication Date (Web): May 7, 2012 | doi: 10.1021/bk-2012-1096.ch002

4. Polarizable Continuum Model for Solvation and Dielectric Constant

The interaction enthalpies in Table 4 (without temperature effects; at 0 K in vacuum) do not consider the extended interactions between the ions and their surroundings that would occur in the ionomer. We refer to these extended interactions as solvating the ion or ion pair state. To examine the effect of solvation on ion pairing interactions, we calculated the interaction energy using the polarizable continuum model (PCM) (*33–38*). PCM-solvated interaction energies were studied for 6 salts in 22 solvents by computing the energy of the separated and paired ions within the solvent. The six salts were chosen to be able to provide a more transferable definition of separation distance d. The six salts are lithium fluoride (LiF, $d \equiv d_{Li\text{-}F}$), lithium trifluoromethanesulfonate (Li[TfO], $d \equiv d_{Li\text{-}S}$), lithium tetrafluoroborate (Li[BF_4], $d \equiv d_{Li\text{-}B}$), tetramethylammonium fluoride ([TMA]F, $d \equiv d_{N\text{-}F}$), tetramethylammonium tetrafluoroborate ([TMA][BF_4], $d \equiv d_{N\text{-}B}$) and tetramethylammonium trifluoromethanesulfonate ([TMA][TfO], $d \equiv d_{N\text{-}S}$). Ideally, the distance measurement for each of these would provide a measure of the distance of charge separation, were the bonding between ions purely ionic and the charge on each ion perfectly symmetric (no polarization). These distances should be taken as an approximate measure of this idealized charge separation. Comparison among anions, even in the consideration of a purely ionic pair binding, should consider the spatial distribution of negative charge in the anion. The structure of the ion pair was re-optimized for each solvent, and therefore the value of d increases somewhat as dielectric constant is increased (by only about 7% for LiF and [TMA][TfO] but by about 12% for [TMA]F and [TMA][BF_4], while d increases significantly more for Li[TfO] and Li[BF_4], as discussed below). Table 5 lists the 22 solvents and their ambient dielectric constants ε. There are other parameters used to define solvents within the PCM, such as solvent radius, density and optical dielectric constant which are not listed but these were left at their standard (default) values in the Gaussian03 package.

Examples of the cavities that Gaussian03 uses for the PCM solvation calculations are shown in Figure 5. In all cases we used the default mode of Gaussian03's implementation of the PCM, which generates a cavity based on overlapping atom-centered spheres and adjusts this cavity as atomic distances vary during structural optimization. Figure 6 illustrates the correlation of pair interaction energy with the reciprocal dielectric constant of the solvent. For a purely Coulombic interaction between ions, a linear correlation with a zero intercept is expected by the Coulomb energy (Equation 2) for each ion pair:

$$\Delta E_{pair} = \frac{e^2}{4\pi\varepsilon_0 \varepsilon d} \qquad (2)$$

[TMA]F, [TMA][BF_4] and [TMA][TfO] indeed have linear trends producing intercepts very close to zero, as expected by Equation 2. However, while the $\varepsilon < 3$ points have nearly zero intercept for LiF, the ion pair energies for more polar solvents are systematically *above* this line, resulting in a substantial positive intercept for LiF. Conversely, Li[BF_4] and Li[TfO] points with $\varepsilon < 3$ have linear trends with a strongly negative intercept and the points themselves reach a pair energy near zero at $\varepsilon \approx 10$, with more polar solvents showing $\Delta E_{pair} \approx 0$ for Li[BF_4] and Li[TfO]. One possible source of the non-zero intercept is variations in d with dielectric constant, as the inter-ion spacing was allowed to reoptimize in each solvent.

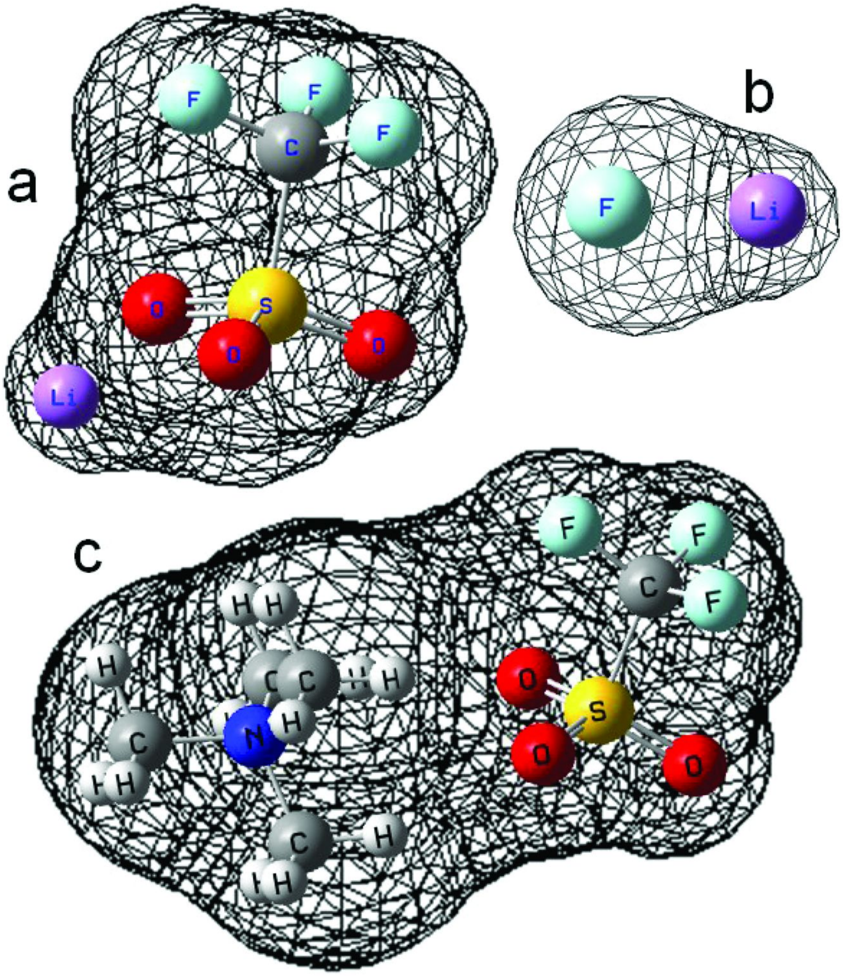

Figure 5. The PCM molecular cavities of three ion pairs a) Li[TfO], b) LiF, and c) [TMA][TfO] in the presence of diethylether. The meshed surface denotes the cavity created in the PCM in which the quantum mechanically treated ion pairs are located.

Downloaded by CORNELL UNIV on June 14, 2012 | http://pubs.acs.org
Publication Date (Web): May 7, 2012 | doi: 10.1021/bk-2012-1096.ch002

Downloaded by CORNELL UNIV on June 14, 2012 | http://pubs.acs.org
Publication Date (Web): May 7, 2012 | doi: 10.1021/bk-2012-1096.ch002

Table 5. **The names and dielectric constants of the 22 solvents used for PCM solvation calculations.**

Solvent	Argon	Heptane	Cyclohexane	Carbontetrachloride	Benzene
$\varepsilon_{solvent}$	1.43	1.92	2.02	2.23	2.25
Solvent	Toluene	Ether	Chloroform	Chlorobenzene	Aniline
$\varepsilon_{solvent}$	2.38	4.34	4.90	5.62	6.89
Solvent	THF[a]	Dichloromethane	Quinoline	Dichloroethane	Isoquinoline
$\varepsilon_{solvent}$	7.58	8.93	9.03	10.36	10.43
Solvent	Acetone	Ethanol	Methanol	Acetonitrile	Nitromethane
$\varepsilon_{solvent}$	20.70	24.55	32.63	36.64	38.20
Solvent	DMSO[b]	Water			
$\varepsilon_{solvent}$	46.70	78.39			

[a] THF = Tetrahydrofuran, [b] DMSO = Dimethylsulfoxide

Downloaded by CORNELL UNIV on June 14, 2012 | http://pubs.acs.org
Publication Date (Web): May 7, 2012 | doi: 10.1021/bk-2012-1096.ch002

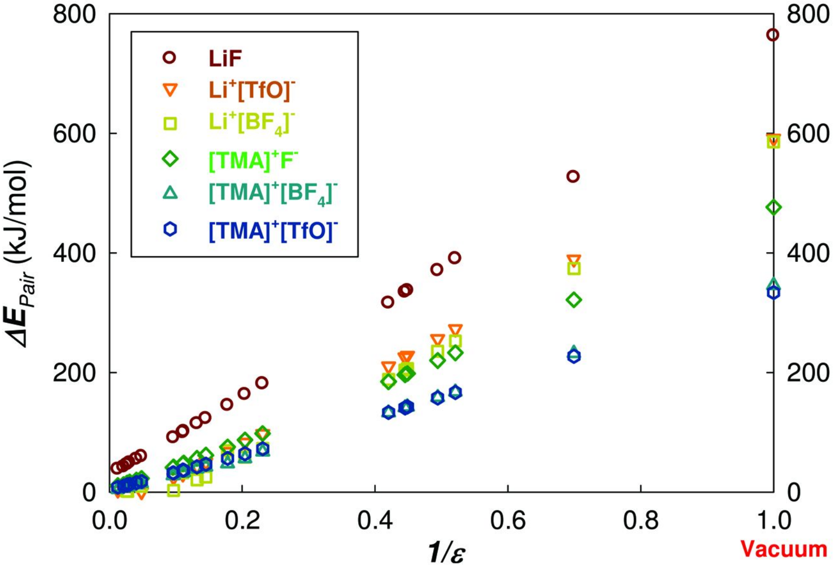

Figure 6. Ion pairing energies with no ZPVE correction for six salts as a function of reciprocal dielectric constant of the PCM medium.

Figure 7 illustrates the correlation of pair interaction energies with the reciprocal dielectric constant multiplied by the cation-anion distance. Ion pair interaction energies are linearly correlated with $1/(\varepsilon d)$, as expected by the Coulomb energy (Equation 2), and the data for the various ion pairs come closer to collinear. Non-zero intercepts are still seen for LiF, Li[TfO] and Li[BF_4]. At this time it is not clear whether these non-zero intercepts reflect (1) real ion pair character in different surroundings, (2) problems with B3LYP or (3) problems with Gaussian03's implementation of the PCM. Li[TfO] and Li[BF_4] progressively change their configurations with dielectric constant, from a tightly bound Li that is close to the central atom, allowing interaction with multiple O or F in less polar media, to a highly extended structure that has Li only interacting with a single O or F in polar media. Contributing to this are difficulties in defining *d*, the partial covalency in the anion-cation interactions, as well as variations in the solute cavity structure among anions or with varying *d* values. The Coulomb energy of Equation 2 appears to only approximately describe the pair interaction energy. One cause of this is that the definition of *d* used does not precisely translate to that in Equation 2, as the negative charge is distributed differently in each anion. Additionally, the bonding interaction is not purely ionic, as pairing will cause a redistribution of charge in each ion which can be described as a combination of polarization and charge transfer. The approximate reduction of all ion pairs to the single line in Figure 7 provides a simplistic picture of solvation effects based solely on the dielectric constant. However, this solvation model lacks variations in the local solvation interactions among solvents, which limits its accuracy. Local solvation considerations are discussed in Section 5.

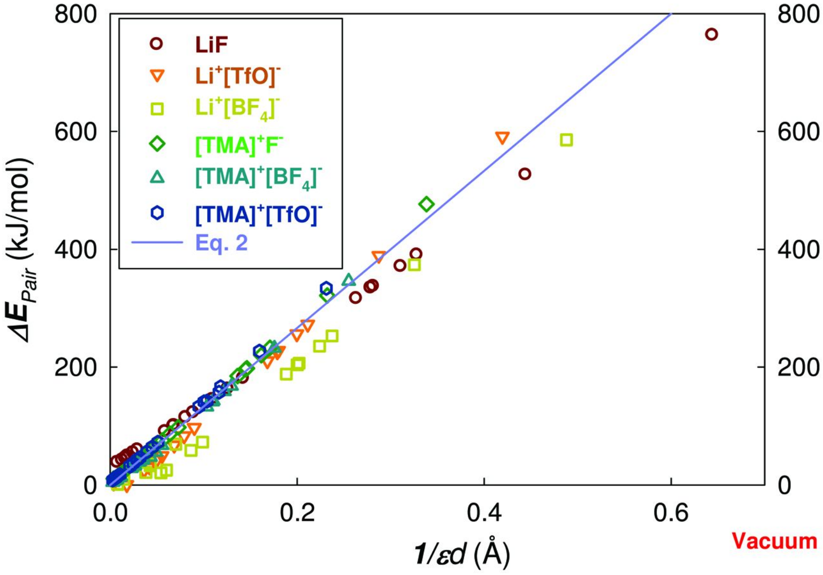

Figure 7. PCM calculated ion interaction energies with no ZPVE correction for six salts as a function of reciprocal of the product of dielectric constant ε and cation-anion distance d, defined carefully in the first paragraph of Section 4. The line is the Coulomb energy (Equation 2).

Downloaded by CORNELL UNIV on June 14, 2012 | http://pubs.acs.org
Publication Date (Web): May 7, 2012 | doi: 10.1021/bk-2012-1096.ch002

Analysis of the inclusion of PCM solvation clearly indicates that the strength of the binding interaction between pairs will be altered by interactions within the extended medium of the ionomer. A greater solvation, offered by a larger dielectric constant, will weaken pair interaction and possibly free more cations to participate in conduction. The analysis above illustrates that the quantum/PCM calculations generally provide results that indicate a simple scaling of interactions assuming a purely Coulombic interaction is reasonable, though complexities arise both due to the non-point charge nature of the ions and the partial covalency in ion pairing. Further, the PCM solvation model does not take into account the local solvation offered, for example, by ether oxygen – Li^+ interactions, that could differentially impact pairing among a series of Li-anion combinations.

5. Specific Solvation with Dimethyl Ether

The PCM solvation model has the disadvantage of neglecting the specific interactions between the solute and the first solvation shell. To explore the impact of specific solvation interactions on ion interaction energies, the stabilization offered by ion interaction with ether oxygens was evaluated. Li^+ ions are known to coordinate with 4-6 ether oxygen atoms in PEO (*46*, *47*). To mimic the local specific solvation by PEO, 1~6 dimethyl ether molecules were explicitly included in the DFT model and the stabilization energy was determined. The explicit solvent model has the advantage of directly considering the impact of PEO on interactions with isolated cations, anions and their pairs, and by explicitly including the "solvent" molecules within the *ab initio* calculation, a full quantum treatment is provided to the ion-"solvent" interaction. Disadvantages include the concern that global minima on a potential energy surface might not be located, that transitions between solute-solvent and solvent-solvent interactions are difficult to identify, and that computational time requirements will limit the ability to consider large ion-solvent systems. A stabilization energy of a single ion or ion pair ($\Delta E_{stabilization}$), given for the example of a Li^+ cation, is defined as:

$$\Delta E_{stabilization} = E_{Li^+-nDME} - E_{Li^+} - nE_{DME} \tag{3}$$

Figure 8 plots the cumulative specific solvation interactions (stabilization energy of Equation 3) of 1-6 dimethyl ether (DME) molecules with Li^+ cation, Na^+ cation, benzene sulfonate and triflate anions and their ion pairs. The stabilization energies were found to increase steeply up to four DME around the cations, suggesting that their first solvation shell is filled after about four dimethyl ether molecules. The cations have the strongest solvation, particularly for Li^+ as the smallest cation can get closest to the lone electron pairs on the DME oxygen. In contrast, the anions are barely solvated at all by DME, as expected. Anions show a gradual increase with little change in slope, reflecting the lack of a significant specific interaction. The ion pairs show solvation intermediate between the cations and anions, filling the first shell around the cations with about three DME molecules with a specific solvation of 153-186 kJ/mol for all four ion pairs, nearly independent of the choice of ions. Whereas for anions the specific solvation from three DME in the first shell is 52-64 kJ/mol, for Li^+ the specific solvation from the four DME in the first solvation shell is 458 kJ/mol and for Na^+ it is 333 kJ/mol.

The pair interaction energy including specific solvation $\Delta E_{pair+DME}$, for any value of n, can be calculated by correcting the pair interaction energy ΔE_{pair} in vacuum by the cumulative solvation interaction.

$$\Delta E_{pair+DME} = \Delta E_{pair} + \Delta E_{stabilization,pair} - \Delta E_{stabilization,cation} - \Delta E_{stabilization,anion} \tag{4}$$

In Figure 9, the pair interaction energies that include specific solvation are plotted versus the number of DME solvating (n), where each of the stabilization energies in Equation 4 are calculated with the same value of n. The net solvated pair interaction energy decreases with the number of dimethyl ethers, from ion-specific values (506 - 641 kJ/mol) with zero dimethyl ethers to a less ion-dependent value of approximately 340 kJ/mol with three DME around the ion pairs, for Li^+ or Na^+ ion pairs with benzene sulfonate or triflate. While not identical, the spread in

In Polymers for Energy Storage and Delivery: Polyelectrolytes for Batteries and Fuel Cells; Page, K., et al.;
ACS Symposium Series; American Chemical Society: Washington, DC, 2012.

Downloaded by CORNELL UNIV on June 14, 2012 | http://pubs.acs.org
Publication Date (Web): May 7, 2012 | doi: 10.1021/bk-2012-1096.ch002

pair interaction energies for these four ion pairs that include specific solvation are within our estimates of uncertainties the same for $3 \leq n \leq 6$, which all have the first solvation shell around the cation filled with anion + 3 DME. Consequently, we conclude that specific solvation is vital for understanding ion interactions (Equation 2 without specific solvation is insufficient) and that specific solvation is in some sense the great equalizer; the ~100 kJ/mol reduction in pair interaction energy per DME added to the first solvation shell is sufficiently strong to soften the ion interactions significantly. Though large differences in pairing energy in vacuum calculations might suggest substantial differences in the relative concentrations of pairs and separated ions, these results suggest that solvation significantly diminishes these differences, such that concentrations are expected to be quite similar among large anions in PEO-based ionomer systems.

Downloaded by CORNELL UNIV on June 14, 2012 | http://pubs.acs.org
Publication Date (Web): May 7, 2012 | doi: 10.1021/bk-2012-1096.ch002

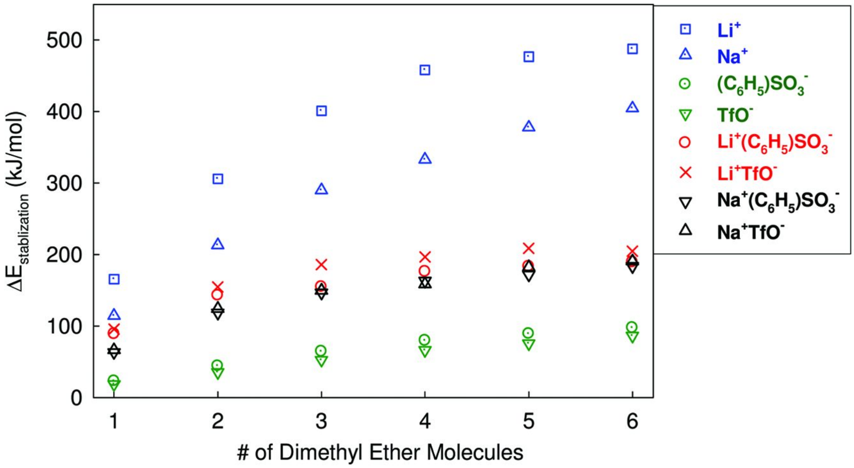

Figure 8. The cumulative specific solvation energy from interaction with 1 to 6 explicit dimethyl ether molecules for cations (blue) Li^+ and Na^+; anions (green) $C_6H_5SO_3^-$ (benzene sulfonate) and $CF_3SO_3^-$ (triflate) and their four ion pairs (red and black) in the gas phase (no PCM). The interaction of Li^+ with 1-3 dimethyl ether molecules has been reported by Blint (48) to be 165 kJ/mol (we calculate 166 kJ/mol) for one DME, 304 kJ/mol (we calculate 306 kJ/mol) for two DME and 397 kJ/mol (we calculate 401 kJ/mol) for three DME.

Downloaded by CORNELL UNIV on June 14, 2012 | http://pubs.acs.org
Publication Date (Web): May 7, 2012 | doi: 10.1021/bk-2012-1096.ch002

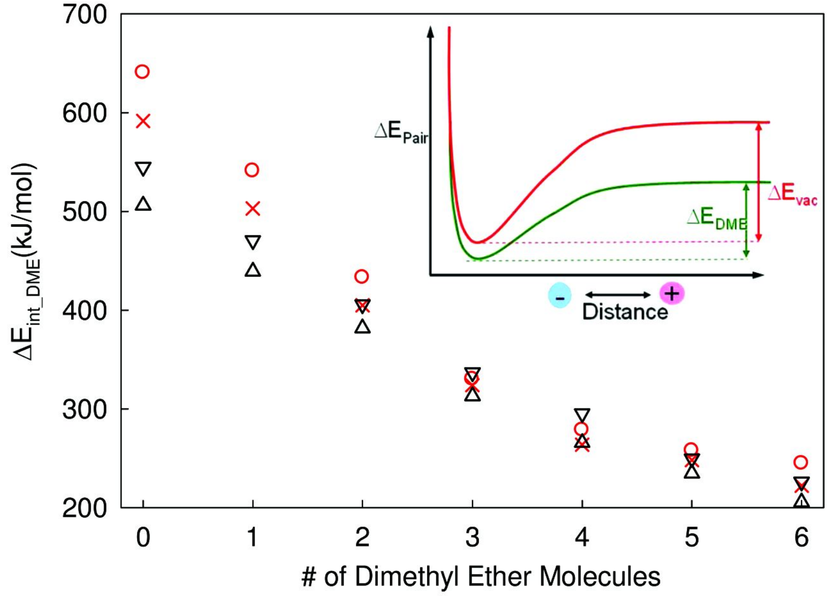

Figure 9. The specifically solvated pair interaction energy of Li^+ $C_6H_5SO_3^-$ (red circles), Li^+ $CF_3SO_3^-$ (red crosses), Na^+ $C_6H_5SO_3^-$ (black down triangles) and Na^+ $CF_3SO_3^-$ (black up triangles), in the gas phase (no PCM) as functions of the number of dimethyl ether molecules interacting with the ions and the ion pairs.

6. A Simple Four-State Model based on 0 K Interactions in Vacuum

The interaction energy of ions at 0 K in vacuum that is directly measured by *ab initio* methods gets diminished by three effects in real ionomer systems.

1) Global Solvation – The dielectric constant of the surroundings directly lowers the Coulomb energy and that effect is enhanced by the fact that the ion separations also increase as dielectric constant increases.
2) Local (specific) Solvation – Favorable interactions of polar functional groups on the polymer (or solvent) act to break up the ion associations because of the steric effect that more specific solvation is able to occur for a given ion when there are fewer other ions nearby.
3) Temperature – The higher T of real systems allows for thermal motions that increase the average ion separation and lower the effective Coulomb interaction. However, the dielectric constant of liquids generally also decreases roughly proportional to 1/T (*39*), complicating the effect of temperature.

Downloaded by CORNELL UNIV on June 14, 2012 | http://pubs.acs.org
Publication Date (Web): May 7, 2012 | doi: 10.1021/bk-2012-1096.ch002

These three effects are actually quite similar for different ionic species and that observation allows us to make use of the 0 K/vacuum *ab initio* energies with no solvation, temperature or dielectric constant effects, to compare different ions for their propensity to aggregate. In this crude way, we can use Gaussian03 as a design tool to select ions worthy of ionomer synthesis. Table 6 lists the *ab initio* vacuum interaction energies for four ion states of interest relative to the free (isolated ions). The triple ion states denote the combination of two cations with an anion ("triple+") or two anions with a cation ("triple-"). The quadrupole state is composed of two pairs interacting, and is representative of larger aggregates that can form in ionomer systems. Each of these states was optimized, with multiple geometries considered, to locate global minimum energy structures. The quadrupole and triple ion interaction energies are defined similarly to Equation 1, with the number of isolated anions and cations in the reference state adjusted. All of these ion states are significantly more stable than free isolated ions based on these 0 K energetics. The substantial binding energy associated with these states, in comparison to an anticipated small entropic driving force for dissociation in the ionomeric system, suggests that charged aggregates such as the positive triple ion (*49–58*) will represent the conducting species.

Table 6. Interaction energies of ion pairs, positive triple ions, negative triple ions and quadrupoles for Li^+ and Na^+ cations with various aromatic anions and their perfluorinated counterparts and also tetrabutyl borate for comparison.

	Li^+				***Na^+***			
Energy (kJ/mol)	ΔE_{Pair}	ΔE_{Tr+}	ΔE_{Tr-}	ΔE_{Quad}	ΔE_{Pair}	ΔE_{Tr+}	ΔE_{Tr-}	ΔE_{Quad}
$(C_6H_5)SO_3^-$	641	892	846	1474	545	758	737	1280
$(C_6F_5)SO_3^-$	604	819	772	1380	516	701	696	1187
$(C_6H_5)HPO_3^-$	667	934	860	1515	570	785	741	1335
$(C_6F_5)HPO_3^-$	625	864	821	1335	535	747	712	1150
$(C_6H_5)CO_2^-$	697	927	894	1588	596	783	800	1360
$(C_6F_5)CO_2^-$	630	864	838	1451	540	715	738	1245
$(C_4H_9)_{4B}^-$	585	788	>592	1148	464	616	507	925
$(C_6H_5)_4B^-$	555	860[a]	--	>1126	484	737[a]	>547	>952
$(C_6F_5)_4B^-$	448	611[a]	--	--	366	498[a]	--	--

[a] optimization was performed with "loose" criteria in Gaussian03.

As noted in section 3, regardless of whether the cation is Li^+ or Na^+ or whether the anion is perfluorinated or not, the pair energies increase in the order SO_3^- < HPO_3^- < CO_2^-. The carboxylates, phosphonates and sulfonates are really quite similar in their interactions with Li^+ and Na^+, and this persists for the triple ion energies and quadrupole energies. The four ion states are illustrated in Figure 10 for the Li-(C_6H_5)SO_3 salt. As observed for methyl sulfonate, a Li cation prefers to interact with two oxygen atoms in the benzene sulfonate pair and triple ion states. In the quadrupole state, each Li cation interacts with two oxygen atoms on one anion and a single oxygen atom on the other anion. The last three entries in Table 6, tetrabutyl borate, tetraphenyl borate and perfluorinated tetraphenyl borate, have significantly lower interaction energies because of the highly delocalized nature of these borate anions.

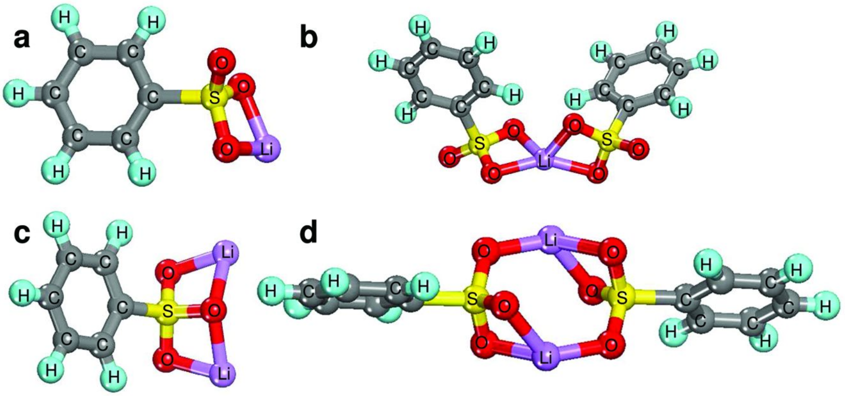

Figure 10. Equilibrium structures of Li-(C_6H_5)SO_3 species, a) pair, b) negative triple ion, c) positive triple ion, and d) quadrupole.

In contrast to the direct interaction with oxygen atoms, the negative charge center in the sulfonate, the interaction between lithium and the borate species is more difficult to define. In the pair, the Li cation approaches the B atom center. However, in the aggregated states, the Li ion moves further from the boron atom and interacts with the delocalized negative charge. B has significantly lower electronegativity (2.01) compared with C (2.5), making the B of these anions have an effective positive charge and the net negative charge of these anions is distributed on the hydrocarbon or fluorocarbon exterior. The pair and positive triple ions of the borates converged to global minima but the negative triple ions and quadrupoles (i.e., all ion states with two borate anions) did not necessarily converge to global minima and are indicated as lower bounds on the energies with > sign in Table 6. With perfluorinated tetraphenyl borate, optimization of negative triple ions and quadrupoles did not converge to a stable structure after extensive testing starting from multiple initial molecular geometries. Difficulties in finding a converged structure likely indicate the relatively broad, shallow potential energy surface associated with the cation interacting with the diffuse negative charge among multiple borate anions. The lack of a distinguished and deep minima for the aggregated state possibly indicates that this most-delocalized anion may be unlikely to aggregate under any conditions. The effect of fluorination is particularly strong for tetraphenyl borate: Fluorinating the benzene ring on benzene carboxylate, sulfonate or phosphonate lowers the pair and positive triple

Downloaded by CORNELL UNIV on June 14, 2012 | http://pubs.acs.org
Publication Date (Web): May 7, 2012 | doi: 10.1021/bk-2012-1096.ch002

In Polymers for Energy Storage and Delivery: Polyelectrolytes for Batteries and Fuel Cells; Page, K., et al.;
ACS Symposium Series; American Chemical Society: Washington, DC, 2012.

ion energies by 5-10% but fluorinating the four benzene rings of tetraphenyl borate lowers the pair and positive triple ion energies by 20-30%. For these reasons, a synthesis goal in our current research is to attach perfluorinated tetraphenyl borate to low-T_g polymer backbones to create a perfluorinated tetraphenyl borate ionomer as a single-ion conductor of Li^+ or Na^+.

7. Conclusion

Calculated values of the dipole moments of common polar small molecules compare favorably with reported measurements (*40*) using two basis sets. Calculated vapor phase interaction enthalpy and also free energy of Li^+ with various individual common polar small molecules also compare favorably with reported measurements (*41–45*). Ion pair interaction energies are estimated in vacuum and via the Polarizable Continuum Model in 22 solvents of different dielectric constant. Those ion pair interaction energies are roughly correlated with $1/(\varepsilon d)$ as expected by the Coulomb energy, but with significant data scatter owing to the difficulties in properly defining the cation – anion separation distance d. The specific solvation interactions of 1-6 dimethyl ether molecules with Li^+, Na^+ and their ion pairs with benzene sulfonate and triflate anions are studied and found to significantly lower the effective pair interaction energy. The net solvated pair interaction energy is found to decrease with the number of dimethyl ethers, from ion-specific values (506 - 641 kJ/mol) with zero dimethyl ethers to an approximately ion-independent value of 340 kJ/mol with three dimethyl ethers around the ion pairs, for Li^+ or Na^+ ion pairs with benzene sulfonate or triflate. Specific solvation is vital to include, and seems to be the great equalizer once the first solvation shell is filled. For this reason, we are developing a hybrid model that includes specific solvation in the first shell, all inside a PCM cavity.

Downloaded by CORNELL UNIV on June 14, 2012 | http://pubs.acs.org
Publication Date (Web): May 7, 2012 | doi: 10.1021/bk-2012-1096.ch002

Acknowledgments

This work is supported by the Department of Energy, Office of Basic Energy Sciences, under Grant No. DE-FG02-07ER46409.

References

1. Bruce, P. G.; Gray, F. M. In *Solid State Electrochemistry*; Bruce, P. G., Ed.; Cambridge University Press: 1995.
2. Armand, M.; Tarascon, J.-M. *Nature (London)* **2008**, *451*, 652.
3. Kerr, J. B. In *Lithium Batteries*; Nazri, G.-A., Pistoia, G.; Kluwer: 2004; p 574.
4. Fragiadakis, D.; Dou, S.; Colby, R. H.; Runt, J. *J. Chem. Phys.* **2009**, *130*, 064907.
5. Fragiadakis, D.; Dou, S.; Colby, R. H.; Runt, J. *Macromolecules* **2008**, *41*, 5723.
6. Dou, S.; Zhang, S.; Klein, R. J.; Runt, J.; Colby, R. H. *Chem. Mater.* **2006**, *18*, 4288.

7. Klein, R. J.; Zhang, S.; Dou, S.; Jones, B. H.; Colby, R. H.; Runt, J. *J. Chem. Phys.* **2006**, *124*, 144903.
8. Kollman, P.; Rothenberg, S. *J. Am. Chem. Soc.* **1977**, *99*, 1333.
9. Smith, S. F.; Chandrasekhar, J.; Jorgensen, W. L. *J. Phys. Chem.* **1982**, *86*, 3308.
10. Jarek, R. L.; Miles, T. D.; Trester, M. L.; Denson, S. C.; Shin, S. K. *J. Phys. Chem. A* **2000**, *104*, 2230.
11. Fujii, T. *Mass Spectrom. Rev.* **2000**, *19*, 111.
12. Johansson, P. *J. Phys. Chem. A* **2001**, *105*, 9258.
13. Johansson, P.; Jacobsson, P. *J. Phys. Chem. A* **2001**, *105*, 8504.
14. Johansson, P.; Jacobsson, P. *Electrochim. Acta* **2001**, *46*, 1545.
15. Johansson, P.; Tegenfeldt, J.; Lindgren, J. *Polymer* **2001**, *42*, 6673.
16. Kerr, J. B.; Liu, G.; Curtiss, L. A.; Redfern, P. C. *Electrochim. Acta* **2003**, *48*, 2305.
17. Markusson, H.; Tokuda, H.; Watanabe, M.; Johansson, P.; Jacobsson, P. *Polymer* **2004**, *45*, 9057.
18. Markusson, H.; Johansson, P.; Jacobsson, P. *Electrochem. Solid-State Lett.* **2005**, *8*, A215.
19. Johansson, P.; Jacobsson, P. *Solid State Ionics* **2006**, *177*, 2691.
20. Johansson, P.; Jacobsson, P. *J. Power Sources* **2006**, *153*, 336.
21. Paddison, S. J.; Kreuer, K. D.; Maier, J. *Phys. Chem. Chem. Phys.* **2006**, *8*, 4530.
22. Johansson, P. *Phys. Chem. Chem. Phys.* **2007**, *9*, 1493.
23. Armand, M.; Johansson, P. *J. Power Sources* **2008**, *178*, 821.
24. Scheers, J.; Johansson, P.; Szczecinski, P.; Wieczorek, W.; Armand, M.; Jacobsson, P. *J. Power Sources* **2010**, *195*, 6081.
25. Scheers, J.; Niedzicki, L.; Zukowska, G. Z.; Johansson, P.; Wieczorek, W.; Jacobsson, P. *Phys. Chem. Chem. Phys.* **2011**, *13*, 11136.
26. Angenendt, K.; Johansson, P. *J. Phys. Chem. B* **2011**, *115*, 7808.
27. Izgorodina, E. I. *Phys. Chem. Chem. Phys.* **2011**, *13*, 4189.
28. Frisch, M. J.; et al.; *GAUSSIAN 03*, Revision B.05; Gaussian Inc.: Pittsburgh, PA, 2003.
29. Becke, A. D. *J. Chem. Phys.* **1993**, *98*, 1372.
30. Becke, A. D. *Phys. Rev. A* **1988**, *38*, 3098.
31. Lee, C.; Yang, W.; Parr, R. G. *Phys. Rev. B* **1988**, *37*, 785.
32. Stephens, P. J.; Devlin, F. J.; Chabalowski, C. F.; Frisch, M. J. *J. Phys. Chem.* **1994**, *98*, 11623.
33. Miertus, S.; Scrocco, E.; Tomasi, J. *Chem. Phys.* **1981**, *55*, 117.
34. Cancès, M. T.; Mennucci, B.; Tomasi, J. *J. Chem. Phys.* **1997**, *107*, 3032.
35. Cossi, M.; Barone, V.; Mennucci, B.; Tomasi, J. *Chem. Phys. Lett.* **1998**, *286*, 253.
36. Mennucci, B.; Tomasi, J. *J. Chem. Phys.* **1997**, *106*, 5151.
37. Cossi, M.; Scalmani, G.; Rega, N.; Barone, V. *J. Chem. Phys.* **2002**, *117*, 43.
38. Tomasi, J. *Theor. Chem. Acc.* **2004**, *112*, 184.
39. Onsager, L. *J. Am. Chem. Soc.* **1936**, *58*, 1486.
40. *CRC Handbook of Chemistry and Physics*, 87th ed.; Lide, D. R., Ed.; CRC Press: 2006.

Downloaded by CORNELL UNIV on June 14, 2012 | http://pubs.acs.org
Publication Date (Web): May 7, 2012 | doi: 10.1021/bk-2012-1096.ch002

41. Rodgers, M. T.; Armentrout, P. B. *Mass Spectrom. Rev.* **2000**, *19*, 215.
42. Staley, R. H.; Beauchamp, J. L. *J. Am. Chem. Soc.* **1975**, *97*, 5920.
43. Woodin, R. L.; Beauchamp, J. L. *J. Am. Chem. Soc.* **1978**, *100*, 501.
44. Amunugama, R.; Rodgers, M. T. *J. Phys. Chem. A* **2002**, *106*, 9718.
45. Amunugama, R.; Rodgers, M. T. *Int. J. Mass Spectrom.* **2000**, *195/196*, 439.
46. Mao, G.; Saboungi, M.-L.; Price, D. L.; Armand, M. B.; Howells, W. S. *Phys. Rev. Lett.* **2000**, *84*, 5536.
47. Borodin, O.; Smith, G. D. *Macromolecules* **2006**, *39*, 1620.
48. Blint, R. J. *J. Electrochem. Soc.* **1995**, *142*, 696.
49. Fuoss, R. M.; Kraus, C. A. *J. Am. Chem. Soc.* **1933**, *55*, 2387.
50. Fuoss, R. M.; Hsia, K.-L. *Proc. Nat. Acad. Sci. U.S.A.* **1967**, *57*, 1550.
51. Onishi, S.; Farber, H.; Petrucci, S. *J. Phys. Chem.* **1980**, *84*, 2292.
52. Hojo, M.; Imai, Y. *Bull. Chem. Soc. Jpn.* **1983**, *56*, 1963.
53. Barthel, J.; Gerber, R.; Gores, H.-J. *Ber. Bunsen-Ges. Phys. Chem.* **1984**, *88*, 616.
54. Hojo, M.; Takiguchi, T.; Hagiwara, M.; Nagai, H.; Imai, Y. *J. Phys. Chem.* **1989**, *93*, 955.
55. Barthel, J. M. G.; Krienke, H.; Kunz, W. *Physical Chemistry of Electrolyte Solutions*; Springer: 1998.
56. Petrucci, S.; Masiker, M. C.; Eyring, E. M. *J. Sol. Chem.* **2008**, *37*, 1031.
57. Hojo, M.; Ueda, T.; Hamada, H.; Chen, Z.; Umetani, S. *J. Mol. Liq.* **2009**, *145*, 24.
58. Roy, M. N.; Chanda, R.; Bhattacharjee, A. *Fluid Phase Equilib.* **2009**, *280*, 76.

Downloaded by CORNELL UNIV on June 14, 2012 | http://pubs.acs.org
Publication Date (Web): May 7, 2012 | doi: 10.1021/bk-2012-1096.ch002

Chapter 3

Redox-Active Radical Polymers for a Totally Organic Rechargeable Battery

Takeo Suga[1,2] and Hiroyuki Nishide[1,*]

[1]Department of Applied Chemistry, Waseda University,
Tokyo 169-8555, Japan
[2]Research Institute for Science and Engineering, Waseda University,
Tokyo 169-8555, Japan
[*]nishide@waseda.jp

Downloaded by UNIV OF GUELPH LIBRARY on June 14, 2012 | http://pubs.acs.org
Publication Date (Web): May 7, 2012 | doi: 10.1021/bk-2012-1096.ch003

"Radical polymers" bearing a high density of unpaired electrons in a pendant, non-conjugated fashion on each repeating unit were utilized as cathode- and anode-active materials in a totally organic-based rechargeable battery. Careful molecular design of radical polymers such as nitroxide and galvinoxyl derivatives produced remarkably stable p- and n-type redox couples, which provided three different battery configurations. The power-rate performance of these cells was excellent (360 C rate, 10 sec charge/discharge), as a result of the rapid redox process of the organic radical moieties in the amorphous polymer layer. Organic polymer-based electrodes also allowed their utilization to a flexible, paper-like, and transparent rechargeable energy-storage device.

Introduction

There is increasing demand for new development of energy storage and delivery technologies (batteries, fuel cells, capacitors, etc). A lithium-ion battery has been successfully and widely used as power sources for portable electric devices such as cellular phones and laptop computers, and are currently explored to target high power applications, *e.g.* electric vehicles (*1*). While lithium transition-metal oxide materials have revolutionized rechargeable battery technology with their extraordinarily high charge density (150 mAh/g), high voltage (3.5 V), and long cycle life (> 500 cycles). Among inorganic-based

In Polymers for Energy Storage and Delivery: Polyelectrolytes for Batteries and Fuel Cells; Page, K., et al.;
ACS Symposium Series; American Chemical Society: Washington, DC, 2012.

electrode-active materials, a kinetic problem caused by the slow diffusion of Li-ions in electrodes has limited the battery's use in high power applications. To overcome the tradeoff between high energy density and high power-rate performance, extensive studies of nano-sized electrode fabrication have attracted much interest in recent years (*2*, *3*). However, the research of the nanostructured electrode materials are underway and will face cost issues (*4*). A series of overheating accidents of Li-ion batteries, some leading to ignition, evoked inherent safety concerns of lithium-ion batteries (*5*). Limited natural resources of rare metals, such as cobalt, will be also potential issues for the increasing battery market. Current Li-ion battery technology still has these technical challenge.

In addition to the improvement of battery performance, there is another demand for the next generation energy-storage devices which merit light-weight, flexibility, and environmental friendliness. Emerging technologies with plastic-based, ubiquitous portable electronic devices, such as flexible displays, smart memory, radio-frequency identification tags, and organic solar cells, has attracted intense interest in the research toward more powerful, slim and flexible (wearable) energy storage devices (*6*, *7*). For those applications, organic polymer-based materials have significant inherent advantages in comparison with inorganic materials, regarding flexibility and environmental friendliness. Since the discovery of electrically conducting polymers, various conducting polymers (*8*) and sulfur-based derivatives (*9*), have been examined for their safety advantages, but they have not led to commercialization because of the following limitations: low doping levels resulting in small theoretical capacity, and slow kinetics of electrode reactions impeding the power-rate performance. Here we focused on the reversible and rapid one-electron redox reaction of organic radical species (oxidation and reduction are regarded as a p-type and an n-type redox reaction, respectively, Figure 1), because we anticipated that organic radicals are potentially useful as electrode-active, charge-storage materials (*10*–*15*). Robust organic radicals such as nitroxides with an NO-centered unpaired electron and galvinoxyls with an O-centered unpaired electron, in which the unpaired electron is stabilized by the effective delocalization and/or bulky substituents, have been extensively studied for use in functional materials, such as organic ferromagnets (*16*, *17*), metal-free redox mediators for synthetic applications (*18*, *19*), and electron- and hole-transport materials in organic devices (*20*). However, despite extensive research on their redox processes, the idea of using robust organic radicals as electrode-active materials for rechargeable batteries had never been proposed until our recent reports (*13*, *14*). The radical polymers we use in our batteries are polymers with aliphatic backbones and numerous pendant redox groups. As a result, the densely populated and yet redox-isolated groups permit rapid and quantitative charge/discharge at a constant output voltage (plateau voltage). The theoretical redox capacity, which is based on the formula weight of the repeating unit, was in the range of 50 – 110 mAh/g (Figure 1).

We have extensively explored the redox properties of a series of organic radical derivatives, and here we mainly focus on our recent efforts to fabricate a totally organic-based battery consisting of radical polymer electrodes. For this purpose, the exploration of n-type redox-active (n-dopable) polymers was inevitable. However, few reports on n-type redox polymers have been published,

Downloaded by UNIV OF GUELPH LIBRARY on June 14, 2012 | http://pubs.acs.org
Publication Date (Web): May 7, 2012 | doi: 10.1021/bk-2012-1096.ch003

most likely because of the instability of the n-doped state (*21*). We successfully synthesized the n-type redox polymer by the molecular design of n-type radical polymers, and constructed organic batteries with three configurations: p-type cathode and n-type anode (Type I); p- and n-type redox of the same polymer for the both electrodes (symmetrical configuration, Type II); n-type cathode and n-type anode (configuration with rocking chair-type migration of counterions, Type III) (*22*).

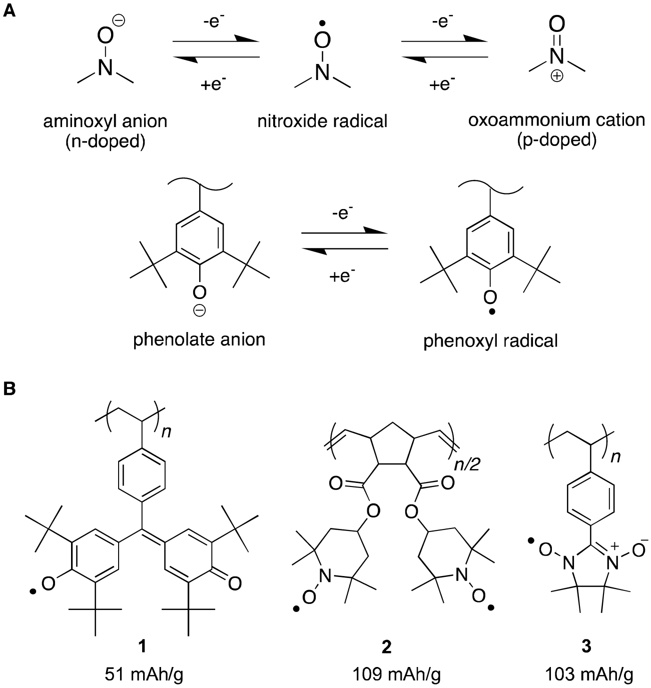

*Figure 1. (**A**) Redox reactions of nitroxide and phenoxyl radicals. (**B**) Radical polymers, in which theoretical redox capacities (Q) were calculated from the formula weight (M_W) of the monomer repeating unit, and the number of radicals in the repeating unit (n), using the following equation: $Q = 96485 \times n / (M_w \times 3600)$ (mAh/g).*

p, n-Type Redox-Active Radical Polymers for a Totally Organic Battery

Radical polymers with different redox potentials can be employed as the cathode- and anode-active materials in all organic-based batteries. The representative combination was the poly(galvinoxylstyrene) **1** for the anode and the poly(TEMPO-substituted norbornene) **2** for the cathode (Type

Downloaded by UNIV OF GUELPH LIBRARY on June 14, 2012 | http://pubs.acs.org
Publication Date (Web): May 7, 2012 | doi: 10.1021/bk-2012-1096.ch003

Downloaded by UNIV OF GUELPH LIBRARY on June 14, 2012 | http://pubs.acs.org
Publication Date (Web): May 7, 2012 | doi: 10.1021/bk-2012-1096.ch003

I). Poly(galvinoxylstyrene) **1** was synthesized via radical polymerization of non-radical precursors followed by chemical oxidation to generate the corresponding radical polymers (*15*). Poly(TEMPO-substituted norbornene) **2** was prepared by ring-opening metathesis polymerization of the radical monomers with Grubbs 2nd generation catalyst. ESR and SQUID measurements estimated the radical density for both polymers **1** and **2** to be 0.91 and 1.97 unpaired electrons per monomer unit, respectively, which were almost equal to the theoretical density. Poly(galvinoxylstyrene) **1** was suitably modified via cross-linking with tetraethyleneglycol diacrylate, to impede its dissolution into the electrolyte solution. Poly(TEMPO-substituted norbornene) **2** was photo-crosslinked with bisazide (*23*).

Electrochemical studies of the polymer film **1** have revealed its reversible redox behavior at $E^{f}_{\mathbf{1},\,\mathrm{n}} = 0.06$ V vs. Ag/AgCl in the presence of an organic base additive such as tetrabutylammonium hydroxide and alkali butoxide in the electrolyte solution (Figure 2A). Narrow peak-to-peak separations (ca. 50 mV) and an increase of the peak current in proportion to the scan rate in the cyclic voltammogram of polymer film **1** proved that the redox site was confined on the current collector with high density and had undergone rapid charge transfer. *In-situ* electrochemical ESR spectra revealed the n-type redox reaction corresponding to the reduction of the galvinoxyl radical to the galvinolate anion (Figure 2A).

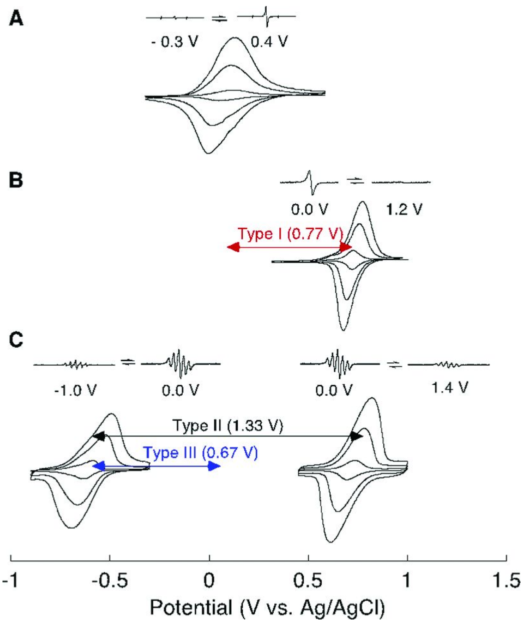

Downloaded by UNIV OF GUELPH LIBRARY on June 14, 2012 | http://pubs.acs.org
Publication Date (Web): May 7, 2012 | doi: 10.1021/bk-2012-1096.ch003

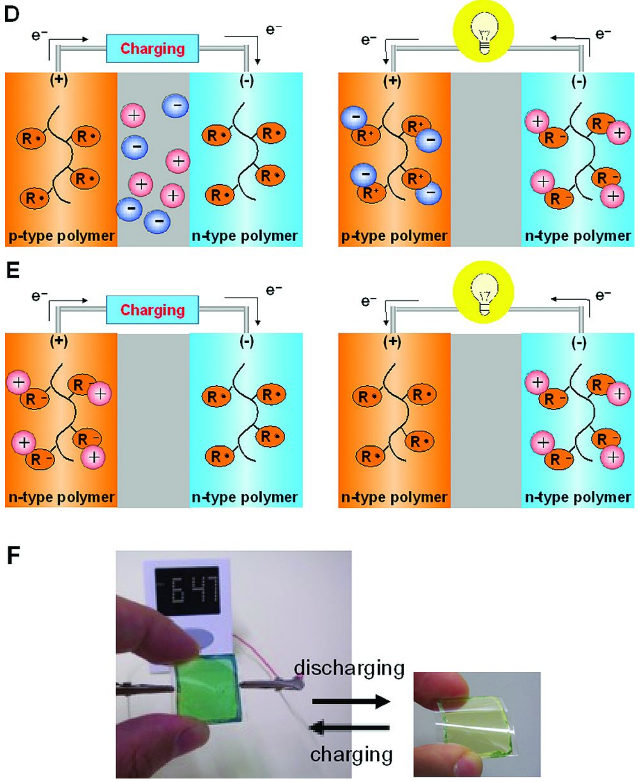

*Figure 2. Cyclic voltammograms of (**A**) poly(galvinoxylstyrene) **1**, (**B**) poly(TEMPO-substituted norbornene) **2**, and (**C**) poly(nitronylnitroxylstyrene) **3** films on the ITO/glass substrate in 0.2 M $(C_4H_9)_4NClO_4$ acetonitrile solution with 0.01 M tetrabutylammonium hydroxide. Scan rate = 1, 5, 10 mV/s in ascending order. Inset: electrolytic ESR spectra of **1** – **3** under the applied potentials vs. Ag/AgCl, which were standardized by the formal potential of Fc/Fc^+ (0.45 V). (D) Configuration for Battery Types I and II (symmetrical configurations). (E) Configuration for Battery Type III. (F) A see-through paper-like battery; blue in charged state (galvinolate anion) and light-yellow in discharged state (galvinoxyl).*

Charge/discharge curves of the fabricated cell utilizing cathode **1** and anode **2** (Type I, Figure 2D) showed a plateau voltage at 0.66 V, which agreed well with the potential gap between the two redox couples, $E^f_{\mathbf{2},p} - E^f_{\mathbf{1},n}$ (Figure 3, Type I). The charge capacity was 32 mAh/g (per total loaded amount of cathode and anode), which corresponded to 92% of the available capacity (34.8 mAh/g). Based on the current-rate performance measurement, the fabricated cell exhibited a strikingly high current capability, allowing rapid charging within 10 sec and large discharge currents (360 C rate, where 1 C rate is defined as the current density at which the charging or discharging of the battery takes 1 h.) without substantial loss of output voltages; this capability can be attributed to the rapid electrode reaction of the radicals and the efficient charge propagation within the polymer layer (ca. 500 nm) that has diffusion coefficients (D_{app}) on the order of 10^{-8} cm^2/s (*24*). Such rapid redox processes of the polymer electrodes suggest the rapid incorporation and release of charge-compensating counterions, which can be attributed to the amorphous nature of the radical polymers, in contrast to the slow lithium insertion process in the conventional Li-ion battery (*24*). Our radical battery has the high power-rate capability comparable to that of supercapacitors, but the constant output voltage and the high charge capacity are advantageous compared to them. It also should be noted that the cycle performance of the radical battery during charging and discharging at the cut-off voltages of 0.0 and 1.2 V, respectively, displayed no significant deterioration in capacity at more than 250 cycles.

Downloaded by UNIV OF GUELPH LIBRARY on June 14, 2012 | http://pubs.acs.org
Publication Date (Web): May 7, 2012 | doi: 10.1021/bk-2012-1096.ch003

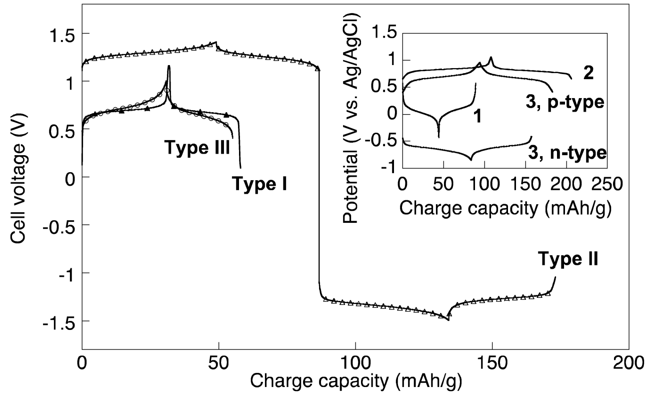

*Figure 3. Charge/discharge curves of the three types of the totally organic battery. Type **1** is composed of cathode **2** and anode **1**; Type II is composed of both cathode and anode **3**; and Type III is composed of cathode **1** and anode **3**.. All types were composed in 0.5 M $(C_4H_9)_4NClO_4$ acetonitrile solution with 0.01 M $(C_4H_9)_4NOH$, current density = 10 C rate. The capacity of each cell was calculated per total weight of the loaded amount of cathode- and anode-active materials. Inset: Chronopotentiogram of the half-cell for each polymer in 0.2 M $(C_4H_9)_4NClO_4$ acetonitrile solution with 0.01 M $(C_4H_9)_4NOH$, Pt auxiliary electrode, Ag/AgCl reference electrode, current density = 10 C rate. The inset potentiograms supported that all electrodes exhibited the quantitative charging/discharging behavior in a half-cell, respectively.*

In addition, the amorphous radical polymers make it easy to fabricate flexible, thin-film, paper-like energy-storage devices by wet or solution-based processing techniques. An exciting feature of our work was the fabrication of a see-through, flexible battery by preparing a radical thin film on an ITO-coated glass or PET substrate. The blue color in the charged state resulting from the galvinoxyl anion reverted dramatically to a light yellow color of the galvinoxyl radical in the discharged state (Figure 2F). *In-situ* electrochemical UV spectroscopy revealed reversible and rapid color change with distinct isosbestic points during the redox reactions. In a see-through battery, the color change, accompanied by radical redox reactions, can be used as an indicator of the charging level.

In the interest of simplifying the battery configuration, we explored a symmetrical configuration utilizing the same polymer for both electrodes. We focused on nitronylnitroxide as a p- and n-type bipolar redox-active material. Poly(4-nitronylnitroxylstyrene) **3** was synthesized via radical polymerization of the silyl-protected monomer, followed by deprotection and chemical oxidation (0.96 unpaired electrons per monomer unit). As seen in the cyclic voltammograms of Figure 2C, the polymer film **3** displayed two reversible redox behaviors at –0.61 and 0.72 V vs. Ag/AgCl, which were attribeuted to the p- and n-type redox reactions. All organic-based batteries consisting of the same polymer **3** for both electrodes exhibited a plateau voltage of 1.3 V, which corresponded to the potential gap of $E^{f}_{\mathbf{3},p} - E^{f}_{\mathbf{3},n}$, for concurrent reduction and oxidation of the same nitronylnitroxide at the anode and the cathode, respectively (Figure 3, Type II). When the direction of the battery was reversed, the charge/discharge curves displayed a plateau voltage of oppositely signed –1.3 V, which indicated that the polymer **3** electrode performed a dual function as either a cathode or an anode.

In a final study, we focused on the potential difference between the n-type redox couples for poly(galvinoxylstyrene) **1** and poly(nitronylnitroxylstyrene) **3**, and we constructed a Type III test cell (Figure 2E), in which **1** and **3** were used as the cathode- and anode-active material, respectively. Because of the n-type redox couples in both electrodes, only counter cation (*e.g.* tetrabutylammonium ion) was exchanged at both electrodes during the charge/discharge cycle, giving rise to the "rocking chair" type migration of cations, which ultimately reduces the electrolytes down to the minimum amount necessary to allow current flow. This "rocking chair" type migration downsizes the overall battery while maintaining the charge capacity. The test cell fabricated with **1** and **3** exhibited an output cell voltage at 0.6 V, a charge capacity of 29 mAh/g (91% of the available capacity), 90% of the original capacity maintained at 120 C rate, and good cycle performance exceeding 250. It should be stressed that the unprecedented configuration of the Type III battery was made possible by our successful molecular design of n-type radical polymers **1** and **3**.

Conclusions and Future Prospects

Radical polymers have proven to be a new class of redox polymers suitable for electrode-active materials in a rechargeable battery. Robust but redox-active organic radicals allow fully reversible one-electron redox reactions featuring fast electrode kinetics, high cyclability, and relatively high battery electrode capacity. Our exploration of the n-type redox-active radical polymers enabled a "totally organic-based radical battery" with various configurations including a rocking-chair battery. In addition, the radical polymers are produced from more abundant natural resources, and no use of harmful/toxic heavy metals or rare metals also leads to a low environmental impact compared to current Li ion-based batteries. The radical polymer-based electrodes provide good processability

Downloaded by UNIV OF GUELPH LIBRARY on June 14, 2012 | http://pubs.acs.org
Publication Date (Web): May 7, 2012 | doi: 10.1021/bk-2012-1096.ch003

and shape flexibility, leading to the paper-like and wearable energy-storage devices, which were widely applicable in battery on the chip and RFID tags. The integrated printable electronics technology will enable facile fabrication of the battery in the future.

Besides the application to charge-storage materials, inspired from the rapid and reversible redox activity, the robust organic radicals are now being explored for other electronics applications. For instance, we also reported a battery-inspired nonvolatile organic memory by sandwiching a dielectric material poly(vinylidene fluoride) with the radical polymers. The "radical memory" showed unique electroconductive bistability (ON-OFF ratio: 10^4, >1000 cycles) and opened up the high potential of redox-active radical even in a dry electronic device (*25*, *26*). The mediator capability of the TEMPO derivatives has been also proposed as an alternative system for iodide/triiodide redox couple in the dye-sensitized solar cells (*27*, *28*). In view of "redox-activity", the robust organic radical polymers allow us to challenge yet unexplored energy-related applications.

Downloaded by UNIV OF GUELPH LIBRARY on June 14, 2012 | http://pubs.acs.org
Publication Date (Web): May 7, 2012 | doi: 10.1021/bk-2012-1096.ch003

Acknowledgments

The authors acknowledge financial support from the Grants-in-Aid for Scientific Research (No. 17350061, 19105003, and 19655043) and the Global COE Program from MEXT, Japan and the NEDO Project on "Radical Battery for Ubiquitous Power". The authors appreciate the technical discussions we had with staff of the Nano Electronics Research Laboratories, NEC Co. T. S. acknowledges financial support from the Grants-in Aid for Young Scientists (B)(A09324100) and the Grants-in-Aid for Scientific Research (No. 23550139), and RISE, Waseda University.

References

1. Service, R. F. *Science* **2011**, *332*, 1494–1496.
2. Winter, M.; Brodd, R. J. *Chem. Rev.* **2004**, *104*, 4245–4269.
3. Scrosati, B. *Nat. Nanotechnol.* **2007**, *2*, 598–599.
4. Chiang, Y.-M. *Science* **2010**, *330*, 1485–1486.
5. Tullo, A. *Chem. Eng. News* **2006**, *84* (34), 11.
6. Nishide, H.; Oyaizu, K. *Science* **2008**, *319*, 737–738.
7. Nyholm, L.; Nystrom, G.; Mihranyan, A.; Stromme, M. *Adv. Mater.* **2011**, *23*, 3751–3769.
8. Novák, P.; Müller, K.; Santhanam, K. S. V.; Haas, O. *Chem. Rev.* **1997**, *97*, 207–281.
9. Oyama, N.; Tatsuma, T.; Sato, T.; Sotomura, T. *Nature* **1995**, *373*, 598–600.
10. Suga, T.; Nishide, H. In *Stable Radicals*; Hicks, R. G., Ed.; John Wiley & Sons: West Sussex, UK, 2010; pp 507−519.
11. Nakahara, K.; Oyaizu, K.; Nishide, H. *Chem. Lett.* **2011**, *40*, 222–227.
12. Nishide, H.; Suga, T. *Electrochem. Soc. Interface* **2005**, *14* (4), 32–36.
13. Nishide, H.; Iwasa, S.; Pu, Y.-J.; Suga, T.; Nakahara, K.; Satoh, M. *Electrochim. Acta* **2004**, *50*, 827–831.

14. Nakahara, K.; Iwasa, S.; Satoh, M.; Morioka, Y.; Iriyama, J.; Suguro, M. *Chem. Phys. Lett.* **2002**, *359*, 351.
15. Suga, T.; Ohshiro, H.; Sugita, S.; Oyaizu, K.; Nishide, H. *Adv. Mater.* **2009**, *21*, 1627–1630.
16. Kaneko, T.; Makino, T.; Miyaji, H.; Teraguchi, M.; Aoki, T.; Miyasaka, M.; Nishide, H. *J. Am. Chem. Soc.* **2003**, *125*, 3554.
17. Fukuzaki, E.; Nishide, H. *J. Am. Chem. Soc.* **2006**, *128*, 996–1001.
18. Semmelhack, M. F.; Schmid, C. R.; Cortés, D. A.; Chou, C. S. *J. Am. Chem. Soc.* **1984**, *106*, 3374–3376.
19. Dijksman, A.; Marino-González, A.; Payeras, A. M. I.; Arends, I. W. C. E.; Sheldon, R. A. *J. Am. Chem. Soc.* **2001**, *123*, 6826–6833.
20. Kurata, T.; Koshika, K.; Kato, F.; Kido, J.; Nishide, H. *Chem. Commun.* **2007**, 2986–2988.
21. Suga, T.; Pu, Y.-J.; Kasatori, S.; Nishide, H. *Macromolecules* **2007**, *40*, 3167–3173.
22. Suga, T.; Sugita, S.; Ohshiro, H.; Oyaizu, K.; Nishide, H. *Adv. Mater.* **2011**, *23*, 751–754.
23. Suga, T.; Konishi, H.; Nishide, H. *Chem. Commun.* **2007**, 1730–1732.
24. Oyaizu, K.; Ando, Y.; Konishi, H.; Nishide, H. *J. Am. Chem. Soc.* **2008**, *130*, 14459–14461.
25. Yonekuta, Y.; Susuki, K.; Oyaizu, K.; Honda, K.; Nishide, H. *J. Am. Chem. Soc.* **2007**, *129*, 14128–14129.
26. Suga, T.; Takeuchi, S.; Ozaki, T.; Sakata, M.; Oyaizu, K.; Nishide, H. *Chem. Lett.* **2009**, *38*, 1160–1161.
27. Zhang, Z.; Chen, P.; Murakami, T. N.; Zakeeruddin, S. M.; Gratzel, M. *Adv. Funct. Mater.* **2008**, *18*, 341–346.
28. Murakami, T.; Kato, F.; Oyaizu, K.; Nishide, H. *J. Photopolym. Sci. Technol.* **2010**, *23*, 353–355.

Downloaded by UNIV OF GUELPH LIBRARY on June 14, 2012 | http://pubs.acs.org
Publication Date (Web): May 7, 2012 | doi: 10.1021/bk-2012-1096.ch003

Downloaded by STANFORD UNIV GREEN LIBR on June 14, 2012 | http://pubs.acs.org
Publication Date (Web): May 7, 2012 | doi: 10.1021/bk-2012-1096.ch004

Chapter 4

Effect of Lithium Salt Content on the Performance of Thermoset Lithium Battery Electrolytes

Markus Willgert,[1] Maria H. Kjell,[2] and Mats Johansson[1],*

[1]KTH Royal Institute of Technology, School of Chemical Science and Engineering, Department of Fibre and Polymer Technology, SE-100 44 Stockholm, Sweden
[2]KTH Royal Institute of Technology, School of Chemical Science and Engineering, Department of Chemical Engineering and Technology, Applied Electrochemistry, SE-100 44 Stockholm, Sweden
***Corresponding author. Tel. +46(0)8 790 92 87; fax: +46(0)8 790 82 83.**
E-mail address: matskg@kth.se (Mats Johansson)

Series of solid poly(ethylene glycol)-methacrylate electrolytes have successfully been manufactured in a solvent free process with an aim to serve in a multifunctional battery, both as mechanical load carrier as well as lithium ion conductor. The electrolytes have been studied with respect to mechanical and electrical properties. The thermoset series differs with respect to crosslink density and glass transition temperature (T_g). The results show that the conductivity increases, with salt content exhibiting similar trends, although at overall levels that differ if measured above or below the T_g of the system. The T_g transition on the other hand is more affected by the salt content for loosely crosslinked thermosets. The coordination of a lithium salt to the PEG-segments play a more important role for the physical state of the material when there are less restrictions due to crosslinking of the PEG-chains. The overall performance of the electrolyte at different temperatures will thus be more affected.

In Polymers for Energy Storage and Delivery: Polyelectrolytes for Batteries and Fuel Cells; Page, K., et al.;
ACS Symposium Series; American Chemical Society: Washington, DC, 2012.

Downloaded by STANFORD UNIV GREEN LIBR on June 14, 2012 | http://pubs.acs.org
Publication Date (Web): May 7, 2012 | doi: 10.1021/bk-2012-1096.ch004

Introduction

There is an increasing demand of possibilities to store electrical energy since this energy is by a growing extent to be used in portable applications. As of today, lithium-ion batteries are considered to be the primary storage medium for electrical energy in for instance a Smartphone which, due to the rapid development of portable devices, typically uses significantly more electrical energy than its precursor because of the many new applications. This development calls for new solutions to store the energy, since batteries tend to possess a significant part of the total item weight, a highly disadvantegous property in a portable device (*1*). Additionally the batteries often occupy a considerable space in a product such as a mobile phone or an electric vehicle (EV) or hybrid electric vehicle (HEV).

Earlier work has investigated the possibility to let the battery itself be a mechanical load bearing component in the total construction (*1–3*). This would significantly reduce the overall weight since the battery in this case not only provide for energy storage, but also replaces a load bearing component in the structure (*4*, *5*). Previous work accounts for the possibility to build polymer electrolytes composed by poly(ethylene-glycol), (PEG) segments (*3*, *6*). These are the most considered polymers within this context, since the glycol units in such a polymer are known to be able to coordinate to a Li^+ ion (*7–9*). The PEG segments can then be crosslinked for instance by acrylate or methacrylate functional groups attached to these segments, forming a thermoset network. This action both enhances the mechanical properties dramatically, but also suppresses crystallization of the PEG, which would be detrimental for the ability to conduct lithium ions (*10*, *11*). Extensive work within the field has for instance been conducted by Snyder et al, where PEG-based solid polymer electrolytes (SPEs) that are able to possess ionic conductivities (σ) of almost up to 10^{-5} $S \times cm^{-1}$ or a storage modulus (E') of around 2 GPa have been manufactured (*6*). However, these two properties are counteracting one another, since a densely crosslinked thermoset may possess excellent mechanical properties at the cost of ion conductivity and vice versa. This is believed to stem from a number of reasons, short distances between the crosslinks and by that a low mobility of the backbone polymers which needs to be able to move to promote ion transportation throughout the electrolyte (*10*), but also a severe decrease in free volume in the network (*12*), which is a drawback since transport of the lithium-ion is coupled to the local mobility of the PEG chains (*13*). It can also be assumed that the polymer chain mobility itself is affected by the presence of lithium ions that coordinate to the chain segments. We have in earlier work showed that the concentration of the lithium salt in the electrolyte had little effect on either the ionic conductivity nor the mechanical properties for densely crosslinked systems when the electrolyte is below its T_g, as defined by the tanδ peak value, when using intermediate levels of salt content (*14*). It is however not fully clear how the balance between crosslink density, coordination strength, coordination sites per unit volume, and mobility of polymer segments between crosslinks affect the ion conductivity in relation to mechanical properties. There is thus a lack of full understanding in what mechanisms are critical in controlling the lithium ion diffusion in these systems, and the present work aims to investigate this further. Improved understanding of these mechanisms and the main factors behind them is an essential objective on the way of designing structural batteries and to find advantageous trade-offs when designing the same.

There are several polymerization techniques available for crosslinking of methacrylated or acrylated PEGs, where thermal initiation (*3*) or photoinduced initiation through UV irradiation (*15*) is the most common techniques used . Photoinduced polymerization reactions are known to be rapid, induce low thermal impact, and result in well defined networks (*16*). The technique is well established for solid polymer electrolytes (SPEs) (*17*, *18*) and is the polymerization route used in this study.

Previous studies on crosslinked PEG-methacrylate electrolytes have shown that increased crosslink density has a significant impact on the conductivity when the T_g transition increases above ambient conditions (*6*, *18*) i.e. the temperature at which the ionic conductivity is measured plays a mayor role (*19*). It has also been shown that the lithium salt content has rather small effect on the conductivity below T_g for a specific thermoset (*14*). It is however not clear if the same relationship between conductivity and salt content is valid in the rubbery state i.e. above T_g for these systems and at what level of salt content that the SPE becomes conductive. The present study aim to reveal more details on this and how the lithium salt content affect the properties above T_g.

Downloaded by STANFORD UNIV GREEN LIBR on June 14, 2012 | http://pubs.acs.org
Publication Date (Web): May 7, 2012 | doi: 10.1021/bk-2012-1096.ch004

Experimental

Materials

Tetraethylene glycol dimethacrylate (SR209), and methoxy polyethylene glycol (350) monomethacrylate (SR550), both displayed as **A** and **B** respectively in Figure 1, were kindly supplied by Sartomer Company, Europe. 2,2-dimethoxy-2-phenylaceto-phenone (DMPA) was obtained by Ciba Specialty Chemicals (Switzerland). Lithium trifluoromethanesulfonate (lithium triflate) (97%) (Figure 1) was purchased from Chemtronica AB (Sweden). All chemicals were used as delivered.

Techniques

Procedures and Test Series, Photopolymerization

Test specimens for two different test series were produced using a general procedure. The monomer/salt mixtures were weighed into small vials in proportions given in Table I. The vials were sealed and put on a shaking table overnight to allow complete mixing of the components. 1 weight-% photoinitiator relative to the monomer amount was then added to the mixture. 0.3 ml of the mixture was then transferred into a Teflon mould (15×20×1 mm) using a syringe and then cured under UV-irradiation at 15 cm distance from the UV light source using a total dose of 1.25 J×cm^{-2}. The light source used for curing was a Blak Ray B-100AP (100 W, 365 nm) Hg UV lamp with an intensity of 5.2 mW×cm^{-2} as determined with an Uvicure Plus High Energy UV Intergrating Radiometer (EIT,

In Polymers for Energy Storage and Delivery: Polyelectrolytes for Batteries and Fuel Cells; Page, K., et al.;
ACS Symposium Series; American Chemical Society: Washington, DC, 2012.

Downloaded by STANFORD UNIV GREEN LIBR on June 14, 2012 | http://pubs.acs.org
Publication Date (Web): May 7, 2012 | doi: 10.1021/bk-2012-1096.ch004

USA), measuring UVA at 320-390 nm. The temperature of the cured samples did not exceed 42 °C during cure. After curing, the cured solids were taken out of the moulds and cut into pieces of appropriate size, using a scalpel, for further characterization. The sample mixtures were prepared and UV-cured in a glove box under dry conditions, (<0,05 ppm H_2O), in argon atmosphere.

Electrical Impedance Spectroscopy (EIS)

To determine the electrochemical performance, the SPE samples, which measure 15×20×1 mm were placed in a four-electrode test cell. The test cell was constituted of four gold wires (two working electrodes with a separating distance of 20 mm and two reference electrodes with 5 mm separation) and two Plexiglas plates with screws to hold the samples in place. The impedance was measured potentiostatically in the frequency range 1 Hz to 300 kHz, at 10 points per decade using a Gamry Series G 750 Potentiostat/Galvanostat/ZRA interface. The measurements were carried out under argon environment in a glove box, (less than 0.05 ppm H_2O), at ambient temperature.

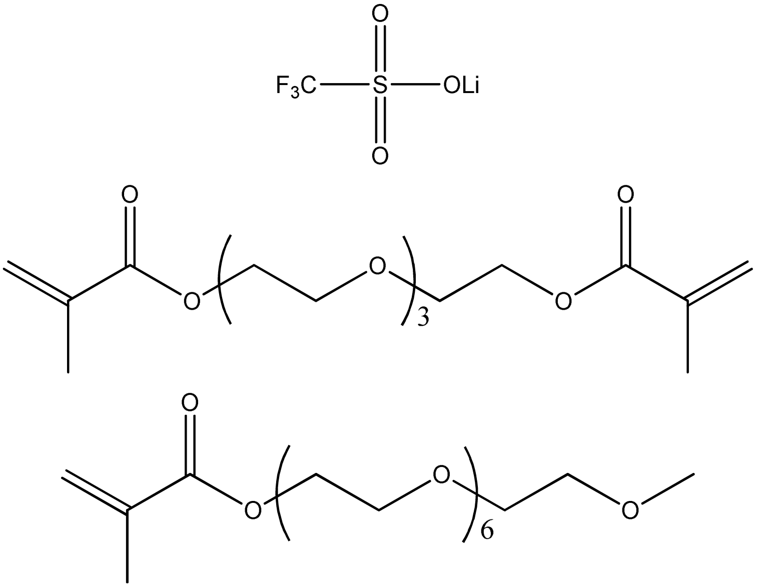

*Figure 1. Chemical structure of the lithium triflate salt as well as monomers **A** and **B** used.*

Downloaded by STANFORD UNIV GREEN LIBR on June 14, 2012 | http://pubs.acs.org
Publication Date (Web): May 7, 2012 | doi: 10.1021/bk-2012-1096.ch004

Table I. Data on the test series prepared and a summary of the results

Sample number	Monomer composition [% w/w]		Li-salt content [% w/w]	$\sigma_{20°C}$ [S×cm^{-1}]	T_g [°C]	$E'_{0°C}$ [MPa]	$E'_{20°C}$ [MPa]
	A	B					
1.1	20	80	0	$-\infty$	0	30	9
1.2	20	80	2	2.6×10^{-7}	0	50	11
1.3	20	80	4	7.2×10^{-7}	5	90	15
1.4	20	80	8	1.2×10^{-6}	5	80	12
1.5	20	80	12	1.1×10^{-6}	11	280	20
1.6	20	80	16	1.2×10^{-6}	15	290	21
2.1	50	50	0	$-\infty$	51	930	490
2.2	50	50	2	8.1×10^{-9}	52	930	470
2.3	50	50	4	3.2×10^{-8}	54	1280	630
2.4	50	50	8	5.0×10^{-8}	59	1800	820
2.5	50	50	12	5.5×10^{-8}	55	2000	770
2.6	50	50	16	4.2×10^{-8}	61	2260	1130

Note: all samples are given a dose of 1.25 J×cm^{-2} through UV irradiation, which results in a conversion ≥92%.

Dynamical Mechanical Analysis (DMA)

Dynamical mechanical analysis (DMA) tests were performed on a TA instruments DMA, model Q800 (tensile mode). Samples were processed from the initial UV cured sample pieces from the curing, giving them a geometry of 7×5×1 mm. The specimens were tightened in the clamps of the sample holder, and the temperature was then decreased to and held at the starting temperature (-50 °C) for 5 minutes before the temperature was increased and data was recorded. The temperature was then increased by 5 °C/min up to a top value of 150 °C. The oscillation frequency was held at 1 Hz at constant amplitude of 10.0 µm. DMA measurements gave values for storage modulus (E′), loss factor (tan δ) and T_g for the electrolytes presented in Table I. Loss modulus (E″) was also obtained from the DMA measurements, although not presented here.

Fourier-Transform Infrared Spectroscopy (FT-IR)

FT-IR analysis was carried out using a Perkin-Elmer Spectrum 2000 FT-IR instrument (Norwalk, CT). The instrument was equipped with a heat-controlled, single reflection (ATR: attenuated total reflection) accessory unit (Golden Gate) from Graseby Specac Ltd. (Kent, England). The degree of conversion was determined by measurements of the vinyl stretch peak at 1637 cm^{-1} relative to the carbonyl peak from the ester group at 1715 cm^{-1}.

Results and Discussion

Two different series of thermosets electrolytes having different crosslink densities have been evaluated with respect to mechanical and electrochemical properties, Table I. The lithium salt content was in both series varied from 0 up to 16 weight%. FT-IR analysis revealed that all cured samples were to full conversion i.e. no detectable amount of residual unsaturation could be found. A previous study on similar systems revealed that a dose of 1.25 J×cm^{-2} is sufficient to obtain full conversion (*14*).

Downloaded by STANFORD UNIV GREEN LIBR on June 14, 2012 | http://pubs.acs.org
Publication Date (Web): May 7, 2012 | doi: 10.1021/bk-2012-1096.ch004

Effect of Lithium Salt Content on the Mechanical Properties of Thermosets below and above T_g

The mechanical properties are, as expected, widely affected by the crosslink density as can be seen in Figures 2 to 5. However, the difference in these properties depending on salt content are less pronounced, although a slightly larger dependence in this regard can be seen on the samples above T_g (Figure 2) than to the series below T_g (Figure 3). This can also be noted from Table I, since the variation span in series 1.1-1.6 is 15 °C, while the same span in series 2.1-2.6 is approximately 10 °C.

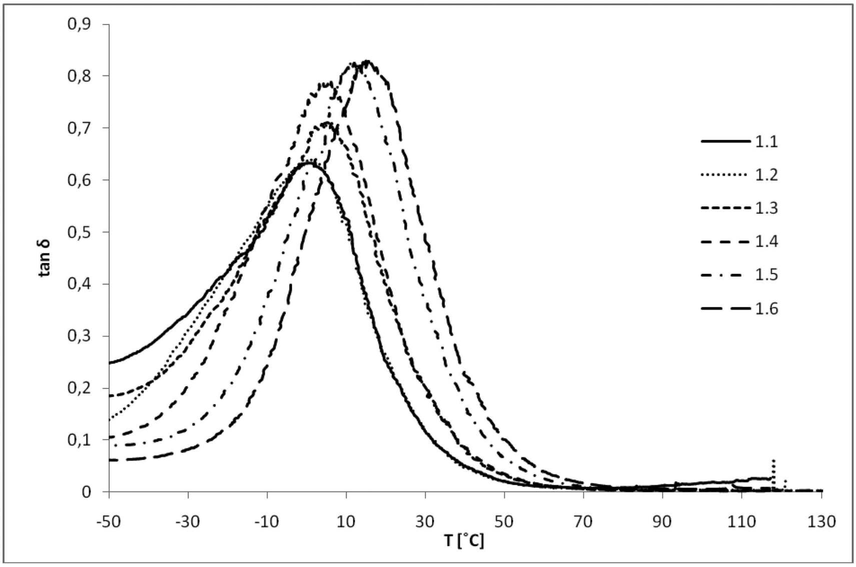

Figure 2. tan δ (E''/E') vs. temperature for samples 1.1-1.6.

Downloaded by STANFORD UNIV GREEN LIBR on June 14, 2012 | http://pubs.acs.org
Publication Date (Web): May 7, 2012 | doi: 10.1021/bk-2012-1096.ch004

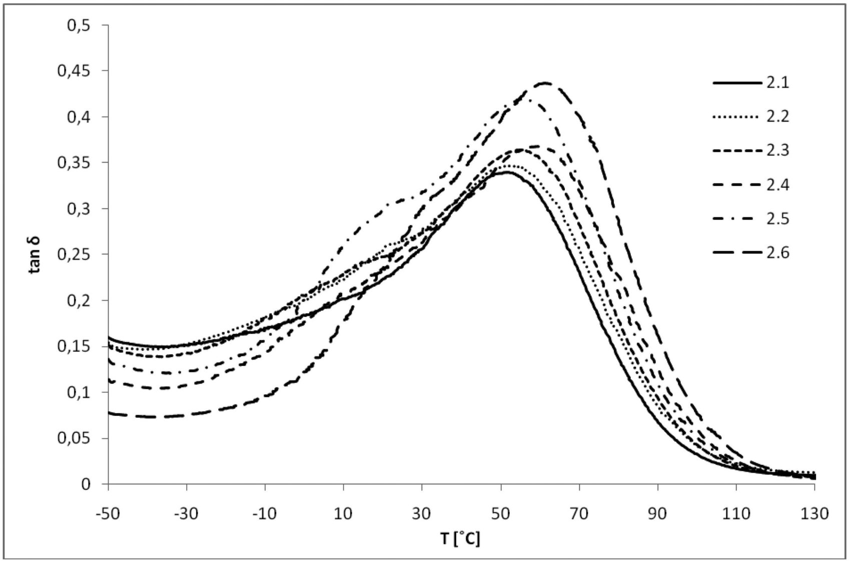

Figure 3. tan δ (E''/E') vs. temperature for samples 2.1-2.6.

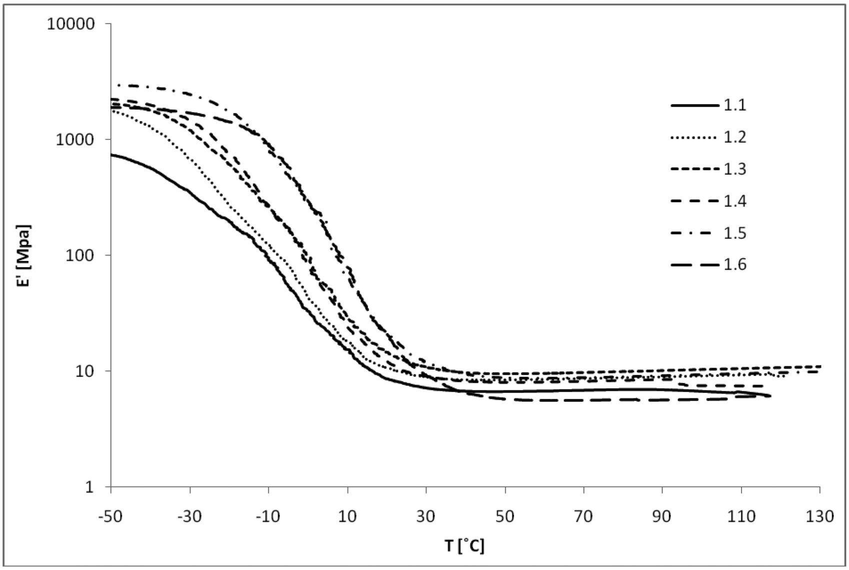

Figure 4. E' vs. temperature for samples 1.1-1.6

In Polymers for Energy Storage and Delivery: Polyelectrolytes for Batteries and Fuel Cells; Page, K., et al.;
ACS Symposium Series; American Chemical Society: Washington, DC, 2012.

Downloaded by STANFORD UNIV GREEN LIBR on June 14, 2012 | http://pubs.acs.org
Publication Date (Web): May 7, 2012 | doi: 10.1021/bk-2012-1096.ch004

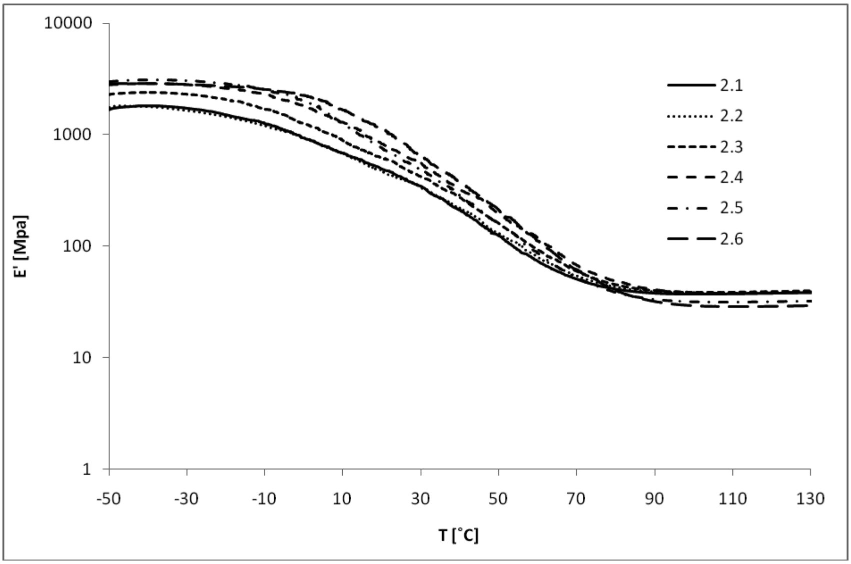

Figure 5. E' vs. temperature for samples 2.1-2.6

Furthermore, looking at the storage modulus dependence of lithium salt concentration, differences can be seen within the T_g-transition range. The more densily crossslinked serie 2 has a wider T_g transition with only small changes depending on the salt content (Figure 5). The less crosslinked series 1, exhibit a more narrow transition where significant differences in modulus with salt content within the transition is seen (Figure 4). This indicate that the lithium ion coordination strength affects the modulus of the electrolyte when going from the glassy state to the rubbery state more, when the PEG chain segments have less restriction in mobility due to crosslinking i.e. segment rigidity and secondary forces between chain segments play a more dominating role. These findings are of importance when considering the change in temperature that occurs in the final application while subjecting a structural battery to a mechanical load.

Effect of Lithium Salt Content on the Conductivity of Thermosets below and above T_g

In Figures 6 and 7, the lithium ion conductivity versus the lithium salt content is depicted. Samples without any lithium salt, sample 1.1 and 1.2, is not ion conducting at all.

Downloaded by STANFORD UNIV GREEN LIBR on June 14, 2012 | http://pubs.acs.org
Publication Date (Web): May 7, 2012 | doi: 10.1021/bk-2012-1096.ch004

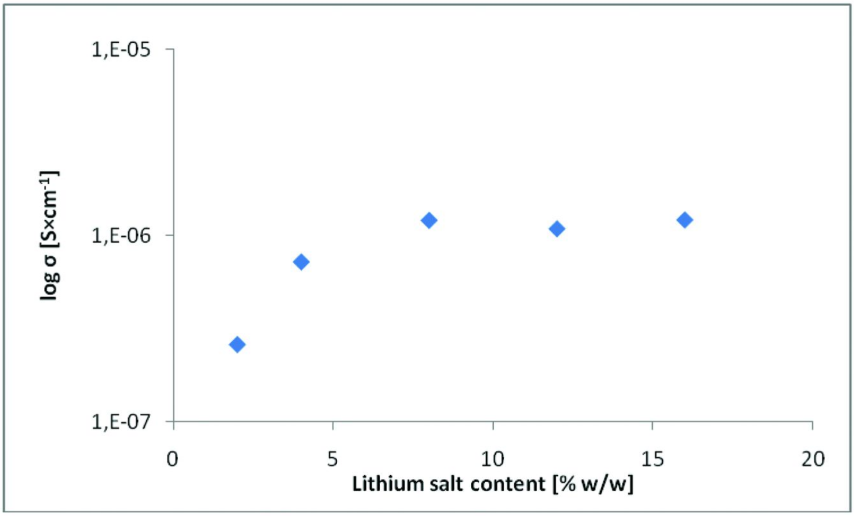

Figure 6. σ vs. amount of lithium salt for samples 1.2-1.6. Sample 1.1 without any lithium salt is not ion conducting.

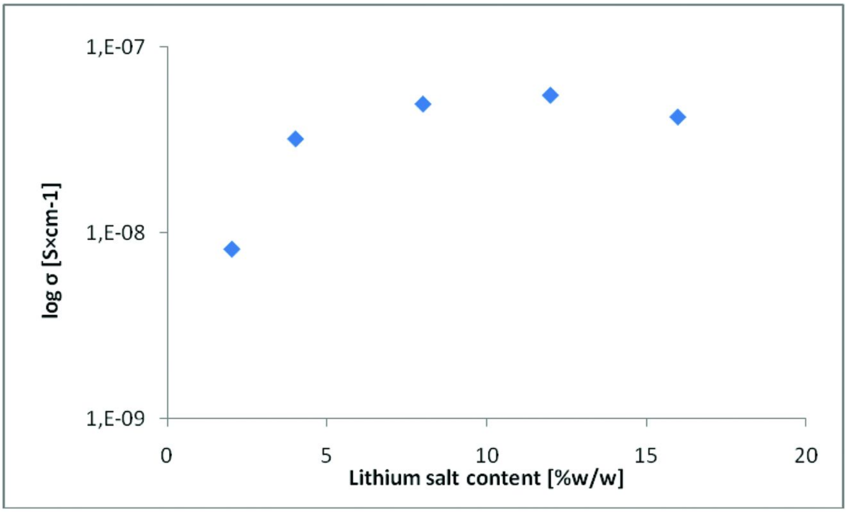

Figure 7. σ vs. amount of lithium salt for samples 2.2-2.6. Sample 2.1 without any lithium salt is not ion conducting.

The trend of increased conductivity with salt content in series 1.2-1.6 and 2.2-2.6 is about the same, with about 1.5 decades separating the series. It should be noted that a threshold value around 4 percent lithium triflate salt is seen, above which the conductivity is only slightly increased with a further increase in salt content. All this together suggests that the main limiting factor for the lithium ion transport is whether the material is above or below its T_g.

Since the physical state i.e. the T_g transition is to a larger extent depending on the salt content for loosely crosslinked networks (Figures 4 and 5) this indicates that the salt content influence on the conductivity will be larger for less crosslinked systems when changes in temperature around the T_g transtion occur.

Downloaded by STANFORD UNIV GREEN LIBR on June 14, 2012 | http://pubs.acs.org
Publication Date (Web): May 7, 2012 | doi: 10.1021/bk-2012-1096.ch004

Conclusions

Two series of PEG-based thermoset lithium battery electrolytes with varied lithium salt content have been studied with respect to mechanical and electrical properties. The thermoset series differs with respect to crosslink density and T_g transition. The less crosslinked system has a T_g below, and the more crosslinked a T_g above room temperature. Similar trends of an increase in conductivity with increased lithium salt content are seen in both series. The overall levels of conductivity however differ significantly, with a higher level for the low T_g series. The salt content also affects the T_g transition by shifting the T_g upwards with increasing salt content. This effect is more significant for the low T_g system with a low crosslink density. The coordination of a lithium salt to the PEG-segments is seen to play an important role for the physical state of the material especially when there is less restriction due to crosslinking of the PEG-chains.

Acknowledgments

Funding by the Swedish Foundation for Strategic Research (SSF), framework grant RMA08-0002 is gratefully acknowledged. The monomers were supplied by Sartomer Company, which is thankfully acknowledged. Finally, the entire KOMBATT group is acknowledged for valuable and giving discussions.

References

1. Ekstedt, S.; Wysocki, M.; Asp, L. *Plast., Rubber Compos.* **2010**, *39* (3/4/5), 148–150.
2. Wetzel, E. D. *AMPTIAC Quarterly* **2004**, *8* (4), 91–95.
3. Snyder, J. F.; Carter, R. H.; Wetzel, E. D. *Chem. Mater.* **2007**, *19* (15), 3793–3801.
4. Liu, P.; Sherman, E.; Jacobsen, A. *J. Power Sources* **2009**, *189* (1), 646–650.
5. Thomas, J. P.; Qidwai, M. A. *JOM* **2005**, *57* (3), 18–24.
6. Snyder, J. F.; Wetzel, E. D.; Watson, C. M. *Polymer* **2009**, *50* (20), 4906–4916.
7. Fenton, D. E.; Parker, J. M.; Wright, P. V. *Polymer* **1973**, *14* (11), 589.

8. Berthier, C.; Gorecki, W.; Minier, M.; Armand, M. B.; Chabagno, J. M.; Rigaud, P. *Solid State Ionics* **1983**, *11* (1), 91–5.
9. Wright, P. V. *Br. Polym. J.* **1975**, *7* (5), 319–27.
10. MacCallum, J. R.; Smith, M. J.; Vincent, C. A. *Solid State Ionics* **1984**, *11* (4), 307–312.
11. Wakihara, M.; Nakayama, M.; Kato,Y. In *Lithium Ion Rechargeable Batteries*, 1st reprint; Ozawa, K., Ed.; Wiley-VCH Verlag GmbH & Co. KGaA: Weinheim, 2009; pp 213−255.
12. Killis, A.; LeNest, J. F.; Cheradame, H.; Gandini, A. *Makromol. Chem.* **1982**, *183* (11), 2835–2845.
13. Zhang, H.; Kulkarni, S.; Wunder, S. L. *J. Phys. Chem. B* **2007**, *111* (14), 3583–3590.
14. Willgert, M.; Kjell, M. H.; Jacques, E.; Johansson, M.; Behm, M.; Lindbergh, G. *Eur. Polym. J.* **2011**, submitted.
15. Kwisnek, L.; Heinz, S.; Wiggins, J. S.; Nazarenko, S. *J. Membr. Sci.* **2011**, *369* (1−2), 429–436.
16. Decker, C. *Prog. Polym. Sci.* **1996**, *21* (4), 593–650.
17. Choi, Y.; Kim, S. K.; Chang, K. H.; Lee, M. H. *J. Appl. Electrochem.* **1997**, *27* (9), 1118–1121.
18. Nair, J. R.; Gerbaldi, C.; Destro, M.; Bongiovanni, R.; Penazzi, N. *React. Funct. Polym.* **2011**, *71* (4), 409–416.
19. Watanabe, M.; Sanui, K.; Ogata, N.; Inoue, F.; Kobayashi, T.; Ohtaki, Z. *Polym. J.* **1984**, *16* (9), 711–716.

Downloaded by STANFORD UNIV GREEN LIBR on June 14, 2012 | http://pubs.acs.org
Publication Date (Web): May 7, 2012 | doi: 10.1021/bk-2012-1096.ch004

Downloaded by UNIV OF DELAWARE MORRIS LIB on June 14, 2012 | http://pubs.acs.org
Publication Date (Web): May 7, 2012 | doi: 10.1021/bk-2012-1096.ch005

Chapter 5

Inelastic Neutron Scattering on Polymer Electrolytes for Lithium-Ion Batteries

**Hua-Gen Peng,[1] Madhusudan Tyagi,[2,3] Kirt A. Page,[1]
and Christopher L. Soles[1,*]**

**[1]Polymers Division, National Institute of Standards and Technology,
Gaithersburg, MD 20899
[2]NIST Center for Neutron Research, National Institute of Standards and
Technology, Gaithersburg, MD 20899
[3]Dept. of Materials Science and Engineering, University of Maryland,
College Park, MD 20742
*csoles@nist.gov**

The relationship between ion transport and polymer dynamics is central to the pursuit of solid polymer electrolytes for lithium batteries. This understanding is critical to achieve solid polymer electrolyte systems of sufficiently high ion conductivities. Solid polymer electrolytes are highly attractive from the perspective of their mechanical properties and low flammability compared to current electrolytes, however their ionic conductivities are typically an order of magnitude lower than the liquid electrolytes that are used today in commercial Li^+ ion battery systems. Here we introduce inelastic neutron scattering (INS) as a tool to quantify the coupling between the local dynamics in the polymer electrolyte with the ion mobility through this ion transport media. INS technqiues are well suited for this task as they are primarily sensitive to the dynamics of the hydrogen rich polymer electrolyte and not the Li^+ ions themselves. This is complimentary to dielectric or impedance measurements which in battery systems loaded with ionic charge carriers are primarily senstive to the dynamics if these ions; the impedance contribution from the organic electrolyte is usually overshadowed by the ions. The combination of INS and dielectric measurements provides the opportunity to directly correlate ion dynamics with the dynamics of the host

In Polymers for Energy Storage and Delivery: Polyelectrolytes for Batteries and Fuel Cells; Page, K., et al.;
ACS Symposium Series; American Chemical Society: Washington, DC, 2012.

> electrolyte to better understand this complicated ion transport process. In this chapter we briefly introduce some of the basic INS techniques that can be used for these studies and review the current literature focused on understanding the dynamics in organic and polymer electrolytes for Li^+ ion batteries.

Introduction

Lithium-ion rechargeable batteries are widely used in portable electronics and are quickly becoming critical power sources for current and future electric vehicles, primarily due to their high energy density, light weight, and high operational voltage (*1*). Current lithium-ion batteries utilize organic liquid electrolytes such as propylene carbonate or ethylene carbonate that come with several shortcomings which limit their wide-spread usage in large load applications such as electric vehicles and stationary power. These liabilities are safety related and include electrolyte leakage, decomposition, flammability, and a propensity to develop catastrophic short circuits from lithium dendrites (*2*, *3*). Solid polymer electrolyte (SPE) rechargeable lithium batteries offer several potential advantages over current battery technologies based on liquid electrolytes. Easy containment of the solid electrolyte allows for more latitude in designing the battery shape, an ability to handle higher energy densities, and reduced environmental hazards and flammability (*1*, *2*). However, these potential advantages have not been fully realized after decades of research due to the generally low conductivities of SPEs compared to liquid electrolytes.

Poly(ethylene oxide) (PEO) is the most prominent example of a SPE due to its ability to solvate and transport lithium-ions. However, PEO is semi-crystalline with a high degree of crystallinity (> 70%) and the Li-ion transport is limited primarily to the minor domains of the mobile amorphous phase. The result is that unmodified PEO has a low Li-ion conductivity (10^{-6} S/cm) below its melting temperature ($T_m = \sim 65$ °C) (*4*, *5*) . This is far below the target of 10^{-3} S/cm that is required for current battery applications (*3*, *6*, *7*). There are several strategies to suppress crystallization of PEO and improve conductivity. One approach has been to decrease the crystalline fraction through the incorporation of propylene oxide (PO) units into the PEO backbone (*5*). While this prevents crystallization, the Li-ion conductivity of these polymers is not substantially improved. It is thought that the nonpolar propyl groups also reduces the solubility of Li-ions in the polyelectrolyte and thus the mobile charge carriers (*3*). An analogous approach has be to graft oligo(ethylene glycol) units to other flexible polymers, resulting in comb-branched architectures that will solvate Li-ions (*3*, *8*, *9*). There have also been attempts to swell polyether polymers with small polar molecules, such as propylene carbonate and ethylene carbonate. While effective at improving conductivity, these gel-type systems still have safety issues related to the leakage of liquid additives (*5*, *10*). Cross-linked and branched polymers have also been explored as polymer electrolytes (*11–13*), but their Li-ion conductivities remain well below the threshold of 10^{-3} S/cm. As a rule of thumb the ionic conductivity of typical SPEs with Li^+ ions are approximately 10^{-4} S/cm, about an order of

Downloaded by UNIV OF DELAWARE MORRIS LIB on June 14, 2012 | http://pubs.acs.org
Publication Date (Web): May 7, 2012 | doi: 10.1021/bk-2012-1096.ch005

Downloaded by UNIV OF DELAWARE MORRIS LIB on June 14, 2012 | http://pubs.acs.org
Publication Date (Web): May 7, 2012 | doi: 10.1021/bk-2012-1096.ch005

magnitude lower than the organic liquid electrolytes that are used in current Li^+ ion battery technologies. Dramatic increases in ionic conductivity are needed to realize SPE Li^+ ion batteries. This is not an entirely unrealistic goal by any means. Beta alumina is a solid ceramic electrolyte that can conduct Na^+ ions with mobilities on the order of 10^{-2} S/cm (*14*). However, to get to this point with SPEs requires the understanding of Li^+ ion conduction mechanism.

It is generally accepted that the Li^+ ion conduction is regulated through cooperative motions of the polymer chain (*5*). The exact nature of this coupling on the molecular level is still not completely understood. It is generally acknowledged that the hopping rate of the charge carriers is directly influenced by fast local motions of the chain segments. In this chapter we describe inelastic neutron scattering (INS) as a powerful tool to quantify dynamics on the time and length scales that are relevant for ion transport. INS has long been used to investigate the dynamics in polymeric, ceramic, and biological materials (*15–18*). The application expanded to polymer electrolytes about a decade and half ago. The first part of this chapter will focus on describing the basics of several different INS measurement techniques while the second half will focus on examples of applying INS measurements to Li^+ ion battery electrolytes. The primary objective of this chapter is to enlighten the battery field about INS and stimulate broader application of INS. However, the methodology is general and can be applied to a range of systems where ions or small molecules must pass through a dynamically active membrane. Other relevant examples include fuel cell membranes, flow batteries, and reverse osmosis membranes for water filtration.

Inelastic Neutron Scattering

INS is a versatile and powerful tool for quantifying the dynamics in biological and soft materials. The basis of the technique is illustrated schematically in Figure 1. A beam of neutrons with a narrow, well-defined energy distribution is focused onto the sample of interest. Different INS spectrometers vary in their ability to monochromate the energies of the incident neutron, but typically (for the sake of illustration) the beam can be focused into a narrow Gaussian energy distribution centered on E_0. The solid lines in Figure 1 indicate such a distribution. When the incident beam of neutrons collides with the atomic nuclei in the sample, the strong nuclear interactions scatter the neutrons in various directions. The energy distribution of the scattered neutrons changes in comparison to the initial distribution. Some of the neutrons gain or lose energy through the dynamic interactions with the sample while others are scattered elastically, with no energy exchange. Figure 1 shows that there are generically two types of INS events. The left panel depicts scattering from a vibrating atomic nucleus, the motion confined within a well-defined potential energy minimum. The well-defined minimum leads to a distinct peak in the scattered energies. The shift in scattered peak from the incident energy indicates the energy of the excitation and this type of scattering is typically referred to as pure inelastic scattering. The second type of scattering is depicted in the right panel of Figure 1 where there is a diffusive motion of the atomic nucleus from one location to another. This results in a diffuse broadening of the incident energy distribution. In the right panel of Figure 1 the narrow Gaussian distribution broadens into something more resembling a Lorentzian (as an example). Conventionally this diffuse broadening is referred to as quasielastic scattering (QES), although it is technically still a form of INS. By understanding the energy exchange between the sample and the neutrons, it is possible to perceive the atomic or molecular dynamics in the sample.

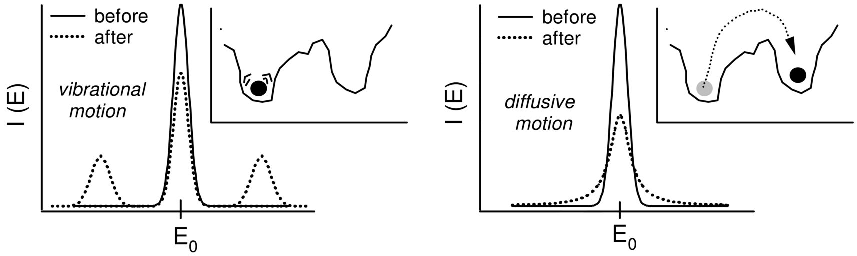

Figure 1. A cartoon depicting the two general types of energy exchange between a sample and a neutron for vibrational (left) and relaxational (right) molecular motions.

This type of inelastic scattering to measure sample dynamics is used with both light and X-rays in addition to neutrons. However, there are several attributes that make neutron scattering ideal for quantifying dynamics in biological and/or soft materials. First, the wavelength of most neutrons is between 1 Å and 10 Å, commensurate with many of the interatomic or intermolecular distances in soft organic materials. The length scale of the motions over which a motion is probed is given by the scattering vector $Q = 4\pi\sin(\theta)/\lambda$. In this expression θ is scattering angle and λ is the neutron wavelength. With most INS instruments it is reasonable to probe scattering over a range of angles that encompass a reciprocal space domain of $0.2\ \text{Å}^{-1} < Q < 2.0\ \text{Å}^{-1}$. In real space that corresponds to length scales approximately 3 Å to 30 Å, well suited for characterizing local atomic and molecular motions in organic materials.

The second property of neutrons that makes them useful for measuring polymer dynamics is their energy. Most cold neutrons that have passed through a liquid He moderator have energies that are on the order of a few meVs, on the same order of magnitude as the activation energies for many of the solid state excitations, molecular relaxations, and dynamic processes that occur in polymeric and soft materials. This means that when a neutron gains or loses energy from a dynamic interaction with the sample, the change in the energy of the neutron is usually a significant fraction of the initial neutron energy. This means that it is relatively easy to ascertain if a neutron has changed energy upon scattering. In contrast, X-rays in most scattering experiments have energies on the order of a

Downloaded by UNIV OF DELAWARE MORRIS LIB on June 14, 2012 | http://pubs.acs.org
Publication Date (Web): May 7, 2012 | doi: 10.1021/bk-2012-1096.ch005

few keV. This is at least 6 to 7 orders of magnitude greater than the typical solid and liquid state excitations that occur in most polymeric materials. Most X-rays scatter or penetrate polymers with very little change in the energy of the incident beam. To discriminate a meV change in the energy of a keV source requires extremely sensitive energy discrimination.

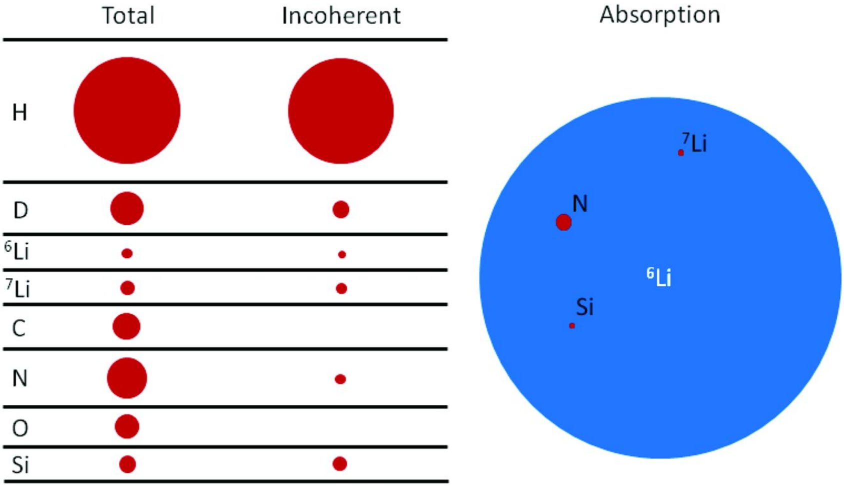

Figure 2. A series of circles are shown for different elements that are commonly encountered in the electrolyte media for Li-ion batteries. The areas of the circles have been scaled to reflect the differences in their neutron cross-sections, including the total scattering, incoherent scattering, and neutron absorption cross-sections.

Downloaded by UNIV OF DELAWARE MORRIS LIB on June 14, 2012 | http://pubs.acs.org
Publication Date (Web): May 7, 2012 | doi: 10.1021/bk-2012-1096.ch005

The final reason why neutrons are ideal for measuring dynamics in organic and polymeric materials, especially in battery systems, is related to the scattering cross-section of the elements commonly present in these components, such as C, O, N, Li, H, and Si. With X-rays the scattering is dominated by the heavier elements and the scattering cross-section increases with atomic number. However, the strength of the nuclear interactions changes in more of a random manner with atomic number. Fortunately, hydrogen has the largest incoherent scattering cross-section of all the elements for neutron scattering. This is shown graphically in Figure 2 where the area of the circle represents the magnitude of the different scattering cross-sections; H rich moieties will dominate an inelastic scattering experiment. This is quite useful because H dynamics are difficult to quantify with complimentary optical and X-ray scattering techniques that are often insensitive to the lighter elements. The utility of neutron scattering is further enhanced by the fact that the isotopic switch from hydrogen (H) to deuterium (D) greatly reduces this massive scattering cross-section. From a chemistry point of view, the switch from H to D is usually trivial in terms of modifying the physical properties, meaning that powerful isotopic labeling schemes can be devised. By selectively replacing certain H with D, one can study the dynamics isolated to a certain species or selected side group or moiety of the macromolecule. A similar analogy could be made with the radioisotope labeling schemes often used in nuclear magnetic resonance (NMR) measurements.

It is also notable that Li, in either its natural state of ^{6}Li or in its readily available isotope of ^{7}Li, does not have an appreciable incoherent scattering cross-section compared to H. This means that inelastic neutron scattering is naturally more sensitive to the dynamics of the hydrogenous electrolyte material than the mobile Li^+ ions that carry the charge. This is in contrast to dielectric or impedance spectroscopy in which the signal is dominated by the strong charges on theionic species. Impedance spectroscopy is well-suited to characterize dynamics of the charged ionic species. As the ions typically are inorganic or lack H, inelastic neutron scattering is more sensitive to the dynamics in the polymer organic electrolyte. As we discuss later, these measurements turn out to be very complimentary. Additionally, there is a very big difference between the neutron absorption cross sections between ^{6}Li and ^{7}Li. Although we do not discuss it here, this becomes extremely useful in adapting neutron reflectivity and depth profiling techniques to quantify Li distributions across an interface. These methods are discussed in greater detail in other chapters of this book.

The combination of a large scattering cross-section with incident beam energies that are comparable to the intrinsic excitation energies means that hydrogen rich organic and polymeric materials scatter neutrons with large changes in the energy of the incident neutron beam. Using spectrometers that are sensitive to these energy changes, it is easy to quantify the energy gain/loss from the scattered neutrons. From energy and angular dependencies of the scattered neutrons, it is possible to determine the time and length scales of the dynamic processes in polymers. This is the fundamental basis for inelastic neutron scattering.

The neutron scattering cross-section of an element can be broken into its coherent and incoherent components (there is also an absorption cross-section which is unrelated to scattering which we will not address here). The cross-section reflects the number of neutrons scattered from a unit volume divided by the flux of the incident neutron beam. For coherent scattering events, there is a spatial correlation between the scattering from different nuclei of the same type. These spatial correlations allow us to determine the Van Hove or the pair-pair correlation function, i.e., the spatial correlations between the different atoms. For incoherent scattering events this spatial correlation is lost and there is no relation between scattering events between different pairs of atoms. However, the energy gained or lost by the scattered neutron is still perceivable. By converting the energy exchange into the time domain one can determine the Van Hove self-correlation function. This tells us that at a time, t (defined by the energy exchange), how far the nucleus has moved from its initial position at t = 0. From the energy and angular dependence of the incoherent scattering one can determine the time and length scale of the relaxations or other dynamic motions in a polymeric system.

Downloaded by UNIV OF DELAWARE MORRIS LIB on June 14, 2012 | http://pubs.acs.org
Publication Date (Web): May 7, 2012 | doi: 10.1021/bk-2012-1096.ch005

Above, we mention that hydrogen has the largest scattering cross-section of all the elements. Its cross-section is nearly all incoherent; the coherent scattering from hydrogen is negligible. Figure 2 displays a series of circles whose areas are scaled proportionally to both the total and incoherent scattering cross-section of the nuclei they represent. From this representation it is apparent that inelastic neutron scattering is primarily sensitive to the dynamics of the hydrogen containing chemical groups or moieties. As most polymers are hydrocarbons, their incoherent scattering is very strong. Inelastic neutron scattering is one of the most direct methods to quantify the time and length scales of polymer dynamics.

The dynamic processes and relaxations that occur in polymers span a broad range of time and length scales. It is generally not possible to access the full phase space of time and length scales of these processes in a single inelastic neutron scattering experiment. Different types of experiments are sensitive to different regions of this phase space, as illustrated in Figure 3. The three primary techniques that have been utilized with respect to battery materials include neutron spin echo spectroscopy (NSE), backscattering spectroscopy (BS), and time-of-flight spectroscopy (TOF). The primary difference among the three techniques is the time and length scale of the dynamics probed. The NSE is sensitive to the slowest motions of the three spectrometers, perceiving dynamic processes on a time scale of 10^{-7} sec to 10^{-10} sec or dynamics in the micro- to nano-second range. To place the NSE technique in context, most solid state NMR instruments are sensitive to dynamic processes on the order of a microsecond and slower. As larger objects tend to move slower, NSE is also sensitive to the longer range motions; length scales on the order of 0.1 nm to 25 nm are common on NSE experiments. At these time and length scales, NSE can be used to monitor diffusive motions of polymer chains or large scale collective motions that span across tens to hundreds of atoms. By comparison, BS measurements are sensitive to slightly faster and shorter range motions. Most backscattering spectrometers are only sensitive to those motions faster than a nanosecond (slower motions appear as static or elastic scattering) at length scales that are comparable to most wide angle X-ray diffraction experiments. This spans molecular and atomic displacements nominally in the 1 Å to 30 Å range, which includes not just atomic vibrations but also some of the segmental motions. In polymers these often include side group motions, such as methyl rotations or crank shaft motions of chain segments. TOF spectrometers are sensitive to the fastest dynamics of the three instruments, perceiving dynamics on the order of picoseconds and faster over comparable length scales as in the BS instrument. At these time scales the dynamical processes probed in TOF experiments are typically atomic or molecular vibrations. Many of the same modes seen in infrared or Raman spectroscopy are also evidenced by TOF spectroscopy. Yet unlike infrared or Raman, there are no optical selection rules as to which modes are visible; the closest equivalent of would be the scattering cross section. In this respect, TOF can be regarded as more sensitive to the vibrational and high frequency relaxation processes of the hydrogenous moieties in the sample. To properly interpret experimental neutron scattering data for polymers under strong states of confinement, it is important to remain cognizant of the time and length scales of the motions that the spectrometer is sensitive to.

Downloaded by UNIV OF DELAWARE MORRIS LIB on June 14, 2012 | http://pubs.acs.org
Publication Date (Web): May 7, 2012 | doi: 10.1021/bk-2012-1096.ch005

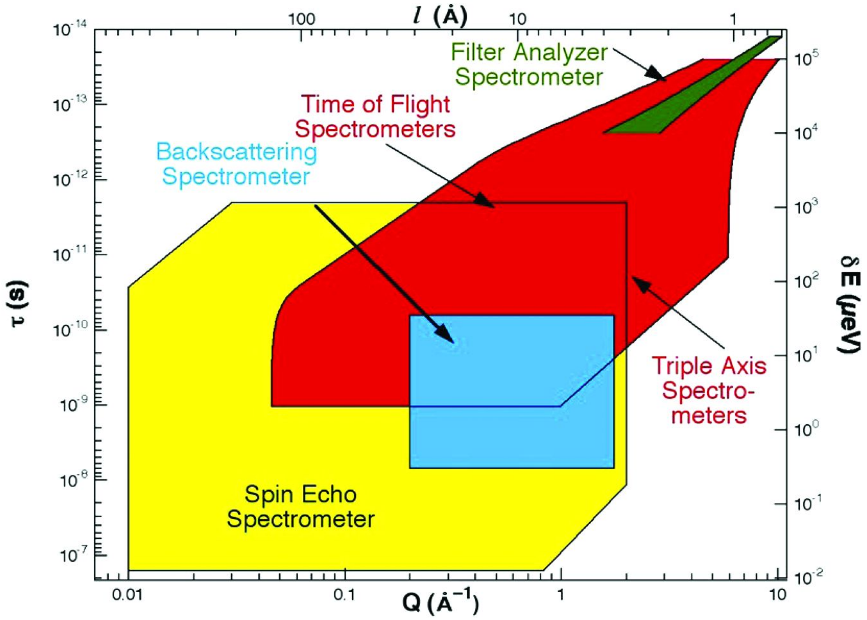

Figure 3. This figure maps out the length and energy scales that are accessible with the different types of inelastic neutron scattering techniques. In this chapter we have limited our discussion to the time of flight spectrometers, backscattering spectrometers, and spin echo spectrometers. Figure obtained from the NIST Center for Neutron Research Website (19).

Neutron Scattering Instrumentation

INS experiments require access to a neutron scattering facility. While there are only a handful of these in most major countries, access is often encouraged and most users find the facilities open to the scientific and research communities in general. The measurements described in this chapter put an emphasis on the NIST Center for Neutron Research (NCNR). The NCNR is a federally funded facility that is open to the general public. The user community at the NCNR spans academic, industrial, and government scientists from the United States and all over the world. Information about utilizing the NCNR facilities can be found through the NCNR's website (*19*). This chapter will mainly discuss the three types of INS spectrometers at the NCNR which were already mentioned above: the Time-of-Flight Spectrometer (TOF) (*20*), the High Flux Backscattering Spectrometer (HFBS) (*21*), and the Neutron Spin-Echo Spectrometer (NSE). Analogs of these are instruments are commonly found at most major neutron scattering facilities around the world, so the discussion is not limited to the NCNR. In the following section we briefly review the way in which these three instruments operate.

The TOF spectrometer is conceptually straightforward. It operates on the principal that when scattered neutrons gain energy, they speed up. Likewise, when

Downloaded by UNIV OF DELAWARE MORRIS LIB on June 14, 2012 | http://pubs.acs.org
Publication Date (Web): May 7, 2012 | doi: 10.1021/bk-2012-1096.ch005

neutrons loose energy, they slow down. By measuring the time of flight of the scattered neutron across a fixed length from the sample to the detector, the energy of the scattered neutron can be determined. A schematic in Figure 3 depicts how a typical TOF spectrometer operates. The neutron beam enters a monochromator that only allows neutrons of a well-defined wavelength, and therefore a well defined energy distribution, to pass through. This ideally mono-energetic beam of neutrons comes from a "chopper" that periodically releases pulses of neutrons onto the sample. The distance from the chopper to the sample and then from the sample to the detectors is accurately known for each TOF spectrometer. Since the energy or speed of the incident beam of neutrons is known (defined by the monochromator), it is straightforward to predict how long it should take a given pulse of neutrons to leave the chopper, scatter from the sample elastically, and then reach the detector. If the actual time of arrival at the detector is sooner than predicted, the neutrons have gained energy. If the time of arrival is later, the neutrons have lost energy through the scattering event. As Figure 4 shows, there are actually several detectors equidistant from the sample, spread out in a semicircle. This allows the dynamics to be probed over a large *Q* range, or range of different length scales.

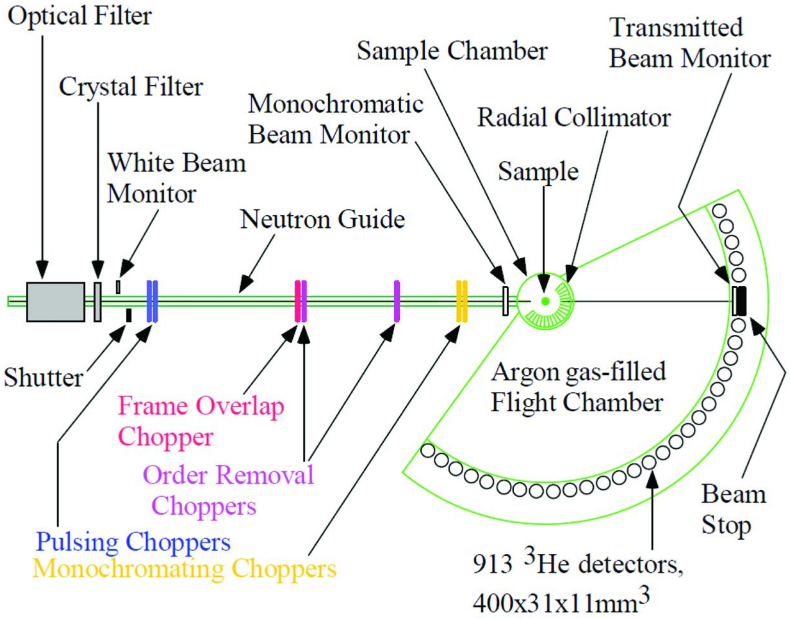
Optical Filter
Crystal Filter
White Beam Monitor
Neutron Guide
Monochromatic Beam Monitor
Sample Chamber
Transmitted Beam Monitor
Radial Collimator
Sample
Shutter
Frame Overlap Chopper
Order Removal Choppers
Pulsing Choppers
Monochromating Choppers
Argon gas-filled Flight Chamber
Beam Stop
913 ^{3}He detectors, 400x31x11mm^3

Figure 4. A schematic representation of the Disc Chopper Spectrometer time-of-flight inelastic neutron spectrometer available through the NCNR (19). The neutrons fly down the guide into the energy monochromator and then are periodically pulsed onto the sample at well-defined intervals. By precisely knowing the distance from the chopper to the sample and the flight path to the detector, one can quantify the neutron time-of-flight and thus the energy gained or lost in the scattering event.

Downloaded by UNIV OF DELAWARE MORRIS LIB on June 14, 2012 | http://pubs.acs.org
Publication Date (Web): May 7, 2012 | doi: 10.1021/bk-2012-1096.ch005

Downloaded by UNIV OF DELAWARE MORRIS LIB on June 14, 2012 | http://pubs.acs.org
Publication Date (Web): May 7, 2012 | doi: 10.1021/bk-2012-1096.ch005

Typically, the incident energy distribution of such instruments, described by the full-width at half maximum (FWHM), is on the order of 10 to 100 μeV. This energy resolution means that the instrument is sensitive to motions faster than approximately 5 GHz. A better energy resolution would mean that slower motions could be detected. As a scale of reference, these motions are a few orders of magnitude faster than the KHz to MHz processes that can be probed by NMR. It may also be useful to think of these energy resolutions in terms of wave numbers. The Disc Chopper TOF spectrometer at NCNR can see modes higher in energy than approximately 0.1 cm^{-1} (1 meV = 8 cm^{-1}).

The NIST HFBS spectrometer is a fixed final energy spectrometer. The details of this spectrometer are described in Figure 5. A beam of neutrons travels down the converging guide and bounces backwards off of a phase space transformation (PST) chopper, toward monochromator. The phase space chopper allows only those neutrons with a wavelength of 6.271 Å to pass onto the the Si-<111> monochromator. The monochromator reflects these 6.271 Å neutrons (in yellow) back towards the phase space chopper and into the sample (in red). When the neutrons hit the sample, they scatter at different angles into the Debye-Scherrer ring of reflectors. The Debye-Scherrer rings composed of Si-111 also reflect only those neutrons with a wavelength of 6.271 Å back towards a bank of ^{3}He detectors that resides just behind and slightly above the sample. Given that all of the neutron optics in this system is designed for 6.271 Å neutrons, only elastically scattered neutrons reach the detectors when the monochromator is static. The key to detecting dynamics (inelastic neutrons) with the HFBS spectrometer is that the monochromator can oscillate back and forth relative to the incident neutron beam. This Doppler shifts the reflected neutrons; some slightly increase in energy and some slightly decrease. If the frequency and stroke of the Doppler drive oscillation are known, it is possible to calculate the broadened energy distribution of the Doppler-shifted, initially monochromatic neutron beam. However, only those Doppler shifted neutrons that change back to their original incident 6.271 Å wavelength after scattering are able reflect off of the Debye-Scherrer ring and into the detectors. From this it is possible to determine the energy distribution of the scattered neutrons.

The NIST High Flux BS spectrometer is capable of detecting much smaller neutron energy exchanges with the sample, and therefore slower dynamics than the TOF spectrometer. The incident energy beam can be collimated to 0.85 μeV FWHM in terms of an elastic energy resolution. This means that motions faster than 205 MHz can be seen by the HFBS spectrometer; slower motions appear as static. This energy resolution is much closer to the frequencies accessible in through a NMR measurement. In terms of wave numbers, the HFBS is sensitive to modes of 0.007 cm^{-1} and higher in energy. In addition, the maximum energy gain or loss HFBS can detect, the so-called energy window, is defined by the Doppler driver. The energy window of the NCNR HFBS is ±36 μeV. All scattering events outside of the energy window, associated with fast relaxation processes, appear as background under the scattering spectrum.

In Polymers for Energy Storage and Delivery: Polyelectrolytes for Batteries and Fuel Cells; Page, K., et al.;
ACS Symposium Series; American Chemical Society: Washington, DC, 2012.

Downloaded by UNIV OF DELAWARE MORRIS LIB on June 14, 2012 | http://pubs.acs.org
Publication Date (Web): May 7, 2012 | doi: 10.1021/bk-2012-1096.ch005

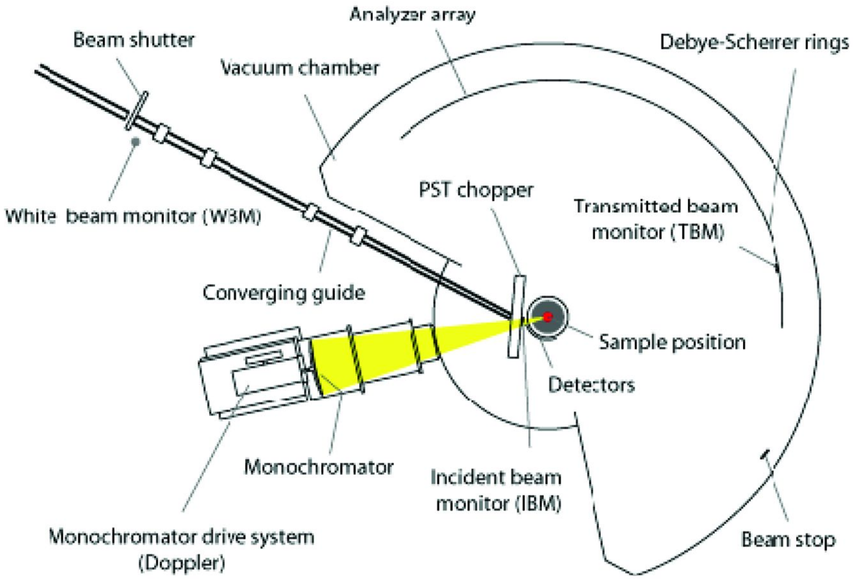
Analyzer array
Beam shutter
Vacuum chamber
Debye-Scherrer rings
White beam monitor (WBM)
PST chopper
Transmitted beam monitor (TBM)
Converging guide
Sample position
Detectors
Monochromator
Incident beam monitor (IBM)
Monochromator drive system (Doppler)
Beam stop

Figure 5. A schematic representation of the High Flux Backscattering Spectrometer available through the NCNR (19). The neutrons fly down the incident guide and converge on the PST chopper which reflects them into the Doppler drive monochomator. This redirects the neutrons back onto the sample where they scatter into the analyzer crystals located on the Debye-Scherrer rings. Only those neutrons with the appropriate energy are reflected back into the detector bank located right behind the sample.

Another INS technique, neutron spin echo (NSE), employs neutron's spin and magnetic moment in a magnetic field. Polarized neutrons are sent through two symmetric magnetic fields before and after the sample. At the sample a π spin flip occurs by a flipper. If the scattering process is strictly elastic the Larmor precession angles in the two fields are equal and opposite, so that full polarization is recovered, irrespective of the initial neutron velocity (energy) distribution. Quasielastic scattering with the sample leads to a change in the neutron energy and one in the precession angle of the outgoing beam, resulting in a decrease in the polarization. Basically, NSE is also time-of-flight technique and it achieves high energy resolution (as small as neV) by encoding the neutron energy into neutron spin Larmor precession angle. With the manipulation of the neutron spin, NSE spectrometers directly measure the real part of the intermediate function S(Q,t) by scanning the magnetic fields in the coils and measuring the polarization. Another important property of NSE is its ability to distinguish coherent from incoherent scattering. The incoherent INS, which alters both the spin and energy of the neutrons, provides only the background or noise in NSE measurement. More details about this instrument can be found on NCNR website (*19*).

INS Data Interpretation

To understand the nature of the motion in a polymeric or soft organic material, the Q and ω (frequency) dependence of the scattered neutrons must be modeled to extract the characteristic lengths and time scales of the motion. Q is the space Fourier transform of the relevant length scales while ω is the Fourier transform of the time scales of the motion into the frequency (or energy) domain. The Q and ω dependence of the scattered neutrons contain all the spatial and temporal characteristics information of the dynamics that fall within the energy and Q resolution of the spectrometer. It can be challenging to extract the proper details of the motion given inverse problem (loss of phase information) in the scattering process. Therefore, the experimental data must be modeled and inherent assumptions or limitations are often implied by the nature of the model. Most INS measurements in polymeric materials focus on the incoherent neutron scattering given that the incoherent cross-section dominates the scattering for hydrogenous materials and, therefore, provide self correlation function of the hydrogens. A common starting point for most dynamic models is the one-phonon approximation:

$$S_{inc}(Q,\omega) = \frac{3N\hbar}{2M} e^{-2W} Q^2 \frac{n(\omega)+1}{\omega} g(\omega) \tag{1}$$

where $S_{inc}(Q, \omega)$ is proportional to the number of neutrons (i.e., intensity) scattered at a wave vector Q with a frequency ω, and $g(\omega)$ is the density of states, $n(\omega)+1$ is the Bose population factor, and e^{-2W} is the Debye-Waller factor. In this expression, $W = (1/6)Q^2\langle u^2\rangle$, with $\langle u^2\rangle$ denoting the mean-square atomic displacement. The prefactor $3N\hbar/2M$ contains all the information about the total number of scattering nuclei in the sample and their representative scattering cross sections. The process of choosing an appropriate model for the motion is beyond the scope of this chapter. However, there are several excellent textbooks dedicated to this subject (*15*, *17*, *18*). In the following we present a few of the most simple models, but sufficient to illustrate the power of the technique.

Quantitative analysis of the INS spectra from a polymeric material can be challenging since in most cases one is unable to work out an exact model for the scattering function to be compared with the experimental data, as is frequently done, e.g., in molecular crystals. In many instances the polymeric material is disordered or amorphous, as is often the case with polymer electrolytes with a lithium salt complex system. This leads to a broad spectrum of relaxation processes whose characteristic times range from picoseconds to seconds. INS is a microscopic method sensitive to fast local motions in the pico to nano second region. Typically, these are side group rotations or stochastic motions of chain segments. The data fitting and analysis often requires trial and error to achieve fitting results that are *mathematically* acceptable and make *physical* sense. The general equation to model the INS data contains three different terms (*17*):

$$S_{theo}(Q,\omega)=DWF\{A_0(Q)\delta(\omega)+[1-A_0(Q)]S_{QE}(Q,\omega)\}+BKG \tag{2}$$

Downloaded by UNIV OF DELAWARE MORRIS LIB on June 14, 2012 | http://pubs.acs.org
Publication Date (Web): May 7, 2012 | doi: 10.1021/bk-2012-1096.ch005

Downloaded by UNIV OF DELAWARE MORRIS LIB on June 14, 2012 | http://pubs.acs.org
Publication Date (Web): May 7, 2012 | doi: 10.1021/bk-2012-1096.ch005

where DWF is the usual Debye Waller factor discussed above, $A_0(Q)$ is the so-called elastic incoherent structure factor (EISF), $\delta(\omega)$ is the Dirac delta function at zero frequency, $S_{QE}(Q,\omega)$ is the quasi-elastic scattering model function and BKG is the background. EISF approaches zero for purely diffusive or diffusive-like processes and the data analysis becomes much simpler. The Delta function in eq.2 accounts for any processes that are slower than the instrumental resolution and the background accounts for faster dynamical processes that are outside the dynamical range of the instrument. Equation 2 should also should be convoluted with instrumental resolution before it can be fitted to the measured experimental data; The first commonly used approach is to treat the QE signal, $S_{QE}(Q,\omega)$, by a single Lorentzian function. A Lorentzian function can describe many types of molecular motions such as diffusion and rotation (*17*). Futhermore, the fourier transform of an exponential decay function, $\exp[-t/\tau]$, is also a Lorentzian function. Thus, a Lorentzian function can be interpreted as pure exponential relaxation process with a single relaxation time τ. However, for the polymer segmental motion, a single Lorentzian is, often, not enough and, usually, a stretched-exponential function or Kohlraush William Watts (KWW) function (*22*) fits the data well. The KWW function, in the time domain, is given by:

$$\Phi(t) \approx \exp\{-(t/\tau)^{\beta}\} \qquad (3)$$

where τ is the characteristic relaxation time and β ($0<\beta<1$) is the stretched exponental parameter defining the non-exponential behaviour of the relaxation. The KWW function has been used to describe the dynamics of amorphous liquids and polymer segmental motions in literature by many researchers. The KWW model can be thought of a distribution of relaxation times and has also been interpreted in heterogeneous and homogeneous scenarios of the molecular dynamics (*23*). However, fitting the QENS data to KWW function is not free from challenges. As the QENS data is typically available in energy domain (for the TOF and BS spectrometers, but not the NSE spectrometer) and the KWW function has no exact functional form other than β=0.5 (*24*), Fourier transform of the KWW function has to be performed before it can be fitted to experimental data. However, such analysis only works if all the other components that contribute to the scattering besides the KWW function are known. For example, if there is an elastic contribution, then the shape parameter β and relaxation time τ will be strongly coupled to the a priori unknown elastic intensity or $A_0(Q)$. On the other hand, one can perform inverse Fourier transform of $S(Q,\omega)$ to obtain $S(Q,t)$ and then fit the data in time domain. Unfortunately, the truncation errors involved in Fourier transform due to the limited frequency range in the experimental data can be overwhelming. In addition, shape parameter and relaxation time are strongly coupled and the correlation matrix has to be examined carefully before analysing the results (*25*). Fortunately though, in polymer systems theshape parameter β is found to be Q independent which makes the fitting procedure relatively easier as one can fix the shape parameter to average values and determine the relaxation times with better accuracy.

Another form of data obtained from INS measurements, almost entirely HFBS measurements, that is not discussed above is the so-called fixed window scan

Downloaded by UNIV OF DELAWARE MORRIS LIB on June 14, 2012 | http://pubs.acs.org
Publication Date (Web): May 7, 2012 | doi: 10.1021/bk-2012-1096.ch005

(FWS). In FWS, the Doppler driver of the HFBS spectrometer in Figure 5 is held stationary and only the intensity of the elastically scattered neutrons are measured. Dynamic processes and inelastic scattering that are within the energy window of the spectrometer also result in a loss of the elastic scattering intensity. Typical FWS experiments are done by heating or cooling the sample at a certain rate and recording the elastic intensity as a function of Q. As the total scattering (elastic plus inelastic) is conserved, a decrease in the elastic intensity infers an increase in the inelastic intensity. As only the elastic intensities ($\omega = 0$) are considered, the Q dependence of the normalized elastic intensity I_{inc} can be quantified in terms of a Debye-Waller factor approximation (*26*) where the hydrogen weighted mean-square atomic displacement $<u^2>$ is given by:

$$I_{inc}(Q,T)/I_{T0}(Q) = \exp\{-Q^2 <u^2(T)>/3\} \tag{4}$$

In the above eq., $I_{T0}(Q)$ is the purely elastic intensity and can usually be measured on a sample at low temperatures, approaching 0 K, where no dynamics are expected on the time scale of backscattering instrument. With this assumption, a plot of $\ln(I_{inc}/I_{T0})$ versus Q^2 is linear and the slope provides value of the mean square displacement $<u^2>$ at a given temperature. Although most atomic motions in soft condensed matter are admittedly anharmonic, this approximation has been useful for characterizing the dynamics of polymers and other glass formers. In the following sections, we will review some of the literature on the dynamics of polymer electrolytes and learn about some of the progress that has recently been made using INS.

Relaxations in Polymer Electrolytes with Lithium Salt

Although the conduction mechanism of Li^+ ions in polymer electrolytes is not yet fully understood, it is commonly accepted that the hoping rate of the charge transfer is directly influenced by local and segmental motion of the polymer. In order to understand the coupling between the charge transfer and the molecular motions in the polymer electrolytes, it is necessary to understand the polymer relaxation processes. When a lithium salt is solvated by polymers such as poly(ethylene oxide) (PEO), each Li^+ ion is coordinated with several ether oxygen atoms on single or perhaps multiple polymer chains. The Li^+ ion transport in the electrolytes involves re-coordination of the charge with neighboring oxygen-bearing groups. The formation and disruption of these coordination sites must be accompanied by relaxation of the local polymer segments. The main focus of existing measurements is to see how the polymer motion changes upon the addition of the lithium salt. Below we summarize the different attempts by researchers in this field to analyze their INS data on such systems. Most of the data thus far has been obtained on TOF and BS spectrometers, but there have also been a few reports utilizing NSE spectrometers.

Some of the first INS studies on polymer electrolyte system were reported on PPO (polypropylene oxide) and its salt blends (*25*, *27*). In these systems, fixed center of mass methyl group rotations are activated at a lower temperatures than the longer range segmental motion associated with the glass transition; these

Downloaded by UNIV OF DELAWARE MORRIS LIB on June 14, 2012 | http://pubs.acs.org
Publication Date (Web): May 7, 2012 | doi: 10.1021/bk-2012-1096.ch005

methyl group rotations must be considered when fitting the spectra measured at higher temperatures. Carlsson et al accounted for the methyl group rotation using a well-established jump rotational model, after which the segmental motion was described in terms of a stretched exponential relaxation (*27*). In comparison to neat PPO, the segmental motion of the blend with $LiClO_4$ (O:Li = 10:1) was found to be slower and moved outside of the experimental time window of the TOF measurements. However, the characteristic times for methyl group rotation were not affected. These results suggest that the coordination of ether oxygen atoms to the Li^+ ions constrains the segmental motion, but does not affect the methyl group rotation. This is not surprising since the non-polar methyl groups do not interact strongly with the ions and their rotation is fixed center of mass movement; they should not have a strong influence on ion transport. However, since the scattering from the methyl group rotation is very pronounced, it can dominate the spectra; methyl rotation can become a nuisance when trying to analyze INS data for diffusive motions that are more relevant to transport. A much simpler system to work with is PEO and its lithium salt blends, on which the vast majority of the INS measurement have focused on.

The INS spectra of neat PEO can be readily fit with the KWW function. Mao et al have argued that this KWW relaxation in neat PEO is translational in nature (*28*). In the presence of Li salts, these relaxations show quite a different nature in a way that depends on the type of anions. For the PEO-$LiClO_4$ system, data was modeled to an elastic peak and a simple Lorentzian function to capture the relaxation process. The FWHM of the Lorentzian for the PEO fast relaxation did not show any Q dependence in the presence of $LiClO_4$, indicating that the translational motions had become localized. On the other hand, the spectra of PEO blended with LiTFSI (lithium bis(trifluoromethanesulfonyl)imide) required the addition of one more exponential decay process (one more Lorentzian function) to adequately fit the data. These fast single exponential components were attributed to rotational motions stemming from rapid conformal fluctuations of the chain segments between Li coordination sites. These fluctuations were thought be associated with the making and breaking of the coordination bonds that assist the Li^+ ion transport in these electrolytes. Mao et al also argued that the appearance of the elastic component in PEO complexed with the Li salts reflected a slowing down of the translational motion of the chain segments. Both NSE measurements and molecular dynamics simulation support this notion (*29*, *30*). The intermediate scattering function from the NSE measurements show that adding salt increases the polymer relaxation times by 2-3 orders of magnitude, accompanied by a decrease in the stretching parameters by a factors of 2-3; this suggests a broader distribution of characteristic time scales. In a related study by Triolo et al, a combination of a KWW function for the segmental motion and a Lorentzian function for librational modes was used to model the TOF data of pure PEO (*31*). For the dynamics of PEO with lithium salt, Triolo et al found that a slower relaxation process was needed to fit the data and they attributed this additional process to the segmental dynamics of the restricted PEO chains involved in Li^+ ion coordination. In general the notion that the addition of Li^+ ions that interact with multiple ether oxygen segments leads retarded dynamics of the PEO and increased elastic scattering seems very reasonable.

Downloaded by UNIV OF DELAWARE MORRIS LIB on June 14, 2012 | http://pubs.acs.org
Publication Date (Web): May 7, 2012 | doi: 10.1021/bk-2012-1096.ch005

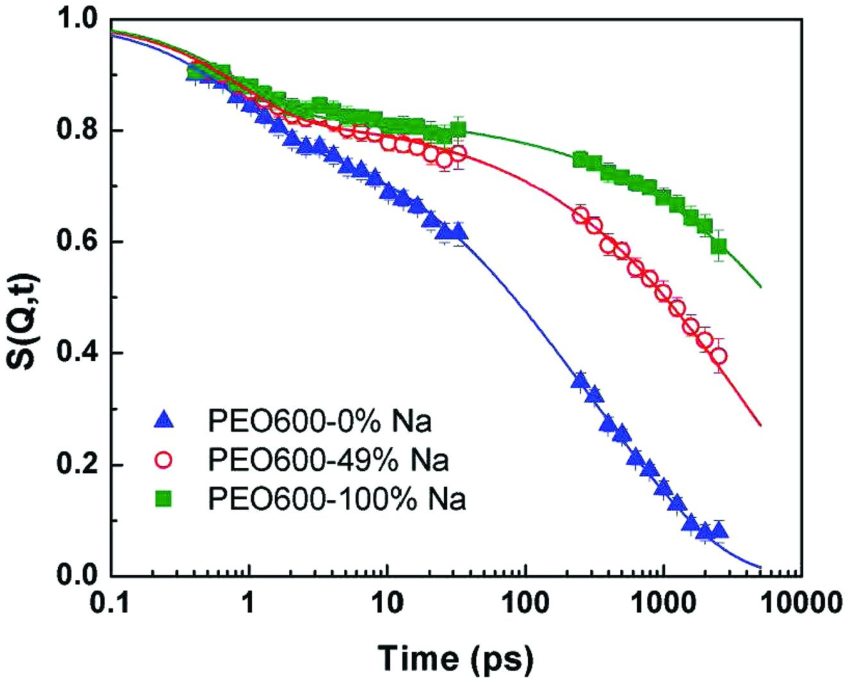

Figure 6. Intermediate scattering function, S(Q,t), for three polyester single ion conductors (33). The percentage number indicates the degree of the isophthalate groups that were substituted with sodium sulfonate. The data symbols are derived from Fourier transform of the TOF (less than 100 ps) and of HFBS (beyond 100 ps) INS data. The lines are fits to the sum of two KWW functions.

Fullerton-Shirey et al studied the dynamics of PEO in its neat form and in blends with $LiClO_4$ for varying ratios of O:Li using both the TOF and BS spectrometers (*32*). In their approach, the intermediate scattering functions, S(Q,t), were obtained via a frequency domain Fourier transform of the reduced S(Q,ω) data. Two KWW functions were found to be necessary to fit the combined QENS data covering a time span from 0.4 ps to 2.5 ns. The faster KWW process, with Q dependent relaxation times was attributed to the segmental mobility of PEO while the slower KWW process, with Q independent relaxation time was attributed to of the restricted rotation of protons around the Li^+ ions. Assuming that the ether oxygen atoms on PEO chains coordinate with Li^+ ions, they proposed a rotational model with non-uniform distribution. The most surprising result of this study was that the segmental mobility of PEO chains was found to decouple from the ionic conductivity. As these measurements were only sensitive to the local motions in the amorphous phase, Fullerton et al interpreted this decoupling as the consequence of ion conduction through the crystalline phase only. This is intriguing as ion transport is largely believed to be limited to the amorphous regions. In continuation, Sinha et al measured PEO electrolytes with a polyester single ion conductor (*33*). The polyester single ion conductor was composed of PEO spacers, separated by isophthalate groups, with varying degrees to which a sodium sulfonate group was attached. The combined intermediate scattering function again required two KWW processes (as shown in Figure 6) to fit the experimental data. The faster process was attributed to the PEO units away from the ions; the dynamic features of this process were very similar to the segmental motion observed in neat PEO and its lithium salt blends discussed above. The slower process appeared to be related to the PEO units close to the ions. The significant increase in the relaxation time of the slow process with the increase of ion content was explained in terms of ionic cluster formation.

Fixed window scan (FWS) are also used to study the dynamics of polymer electrolytes for battery applications. Later in this manuscript we will discuss some of our own traditional FWS measurements on hyperbranched PEO molecules that inhibit crystallization. In a unique backscattering spectrometer, Russina et al used a monochromator made of <111> oriented $Si_{0.9}Ge_{0.1}$ crystals, instead of the conventional <111> Si crystals that are used in typical backscattering spectrometers (*34*). The lattice spacing of the their monochromator was slightly different from that of the conventional <111> Si analyzer by an amount that corresponds to an energy transfer of -14.5 μeV. With the modified analyzer the FWS measurements only detect neutrons that are scattered inelastically with an energy of -14.5 μeV; this measurement is more appropriately referred to as an inelastic fixed window (IFW) scan. Russina et al measured both neat and LiTFSI doped PEO-PPO random copolymer using this technique. The IFW data were modeled with a Cole-Davidson (CD) type susceptibility for the relaxation process and the relaxation times were assumed to follow the usual Vogel-Fulcher-Tammann (VFT) type temperature dependence. In agreement with previous results, Russina et al found that the methyl group dynamics were unaffected by the salt addition. However, they discovered that the segmental motions of the salt blend were bimodal, including a faster process that is identical to the relaxation process in the neat polymer and the slower one corresponding to the relaxation of the polymer segments involved in the Li^+ ion complexation (see Figure 7).

Dynamics in Nanocomposite Polymer Electrolytes

The influence of nano-composites on the ionic conductivity of a polymer electrolyte was first reported in the seminal work of Croce et al (*35*). They reported that the addition of inorganic nanoparticles such as Al_2O_3 and TiO_2 can increase the polymer electrolyte conductivity several fold, both below and above the PEO melting temperature. The increased conductivity below the PEO melting temperature might be understood by the nanoparticles reducing the crystallinity of the PEO. However, the ten-fold increase in conductivity above the PEO melting temperature appeared to suggest that the charge transport mechanism or the polymer dynamics were fundamentally modified. This spurred significant interest, both experimentally and theoretically, to uncover the mechanism behind the increased ion conductivity. Fullerton-Shirey et al employed INS measurements to quantify the dynamics of the PEO electrolytes both with and

Downloaded by UNIV OF DELAWARE MORRIS LIB on June 14, 2012 | http://pubs.acs.org
Publication Date (Web): May 7, 2012 | doi: 10.1021/bk-2012-1096.ch005

Downloaded by UNIV OF DELAWARE MORRIS LIB on June 14, 2012 | http://pubs.acs.org
Publication Date (Web): May 7, 2012 | doi: 10.1021/bk-2012-1096.ch005

without Al_2O_3 nanoparticles (*36*). These measurements suggested that both the PEO segmental motions and the rotational motion of the Li coordination sites that they had previously reported (*32*) were unaltered by the presence of nano-fillers. The only exception was that the rotation modes became slightly restricted at a concentration where O:Li ratio was 8:1. However, unlike the Croce et al., their measurements generally did not show improved ion conductivity upon adding Al_2O_3 nanoparticles. The only exception was when the O:Li ratio was 10:1, a specific loading that corresponds to an eutectic concentration. In agreement with their previous work (*32*), the increased conductivity could not be associated with enhanced polymer dynamics and the two were found to be decoupled.

In order to discriminate between the effect of nanoparticles on crystallinity and other confinement effects, such as changes in segmental mobility as discussed above, Karlsson et al used QENS to investigate a system based on a completely amorphous polymer trihydroxy poly(ethylene oxide-co-propylene oxide) (3PEG) (*37*). In this study, the diffusive segmental motions of the bulk polymer, the methyl group rotation, and fast local chain motions were modeled by several Lorentzian functions, while an elastic component was added to account for the slow relaxations (not in the window of the spectrometer) of immobilized chain segments. These measurements showed that the elastic peak increased in intensity upon the addition of TiO_2 nano-fillers. Karlsson et al proposed that there was an immobilized layer of polymer surrounding the nano-fillers. They calculated the thickness of this layer to be approximately 4-5 nm, thereby accounting for about 5% of the total polymer volume. Interestingly, the fast processes remained unchanged in all samples, suggesting polymer dynamics did not contribute to the increased ion conductivity in the nanocomposite polymer electrolytes.

In all the studies discussed thus far, the information of the ionic motions have been deduced indirectly by analyzing the dynamics of the polymer electrolyte as the Li^+ ions themselves do not have appreciable neutron scattering cross section; they do not contribute significantly to the observed neutron scattering intensity. Eijck et al performed interesting INS experiments on the mixture of deuterated PEO oligomer and NH_4I, both with and without TiO_2 nanoparticles (*38*). The purpose of these experiments was to make the PEO oligomer molecules practically invisible in QENS measurements so that the cation dynamics could be observed directly. Interestingly, the QENS spectra showed a significant increase of the quasi-elastic scattering intensity in the nanocomposite polymer electrolyte. Van Eijck et al proposed that the addition of nano-fillers increased the population of mobile NH_4^+ cations which also resulted in the enhanced ion conductivity. Although an extension of these results, obtained from a model cation system, cannot be directly made to the Li^+ ion PEO systems, the results are entirely consistent with the observed increase in conductivity upon the addition of nanoparticles. The increased conductivity of polymer electrolytes upon the addition of nanoparticles could be due to reduced interaction strength between the ether-oxygen and the cations, rather than the increase in polymer dynamics. This notion is also in agreement with the conclusions of Karlsson et al (*37*).

Downloaded by UNIV OF DELAWARE MORRIS LIB on June 14, 2012 | http://pubs.acs.org
Publication Date (Web): May 7, 2012 | doi: 10.1021/bk-2012-1096.ch005

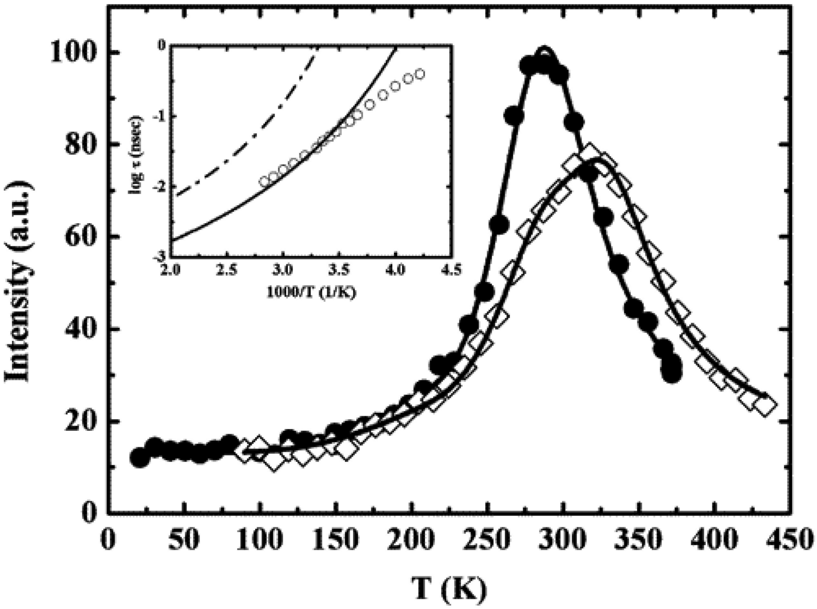

Figure 7. Comparison between the inelastic fixed window energy scans on the neat (filled circles) and lithium salt doped (open diamonds) PEO-PPO random block copolymer (34).

Relationship between Fast Segmental Motion and Ion Transport

In most of the examples discussed thus far, the focus has been on relating the quasielastic or inelastic scattering that describes the relaxation processes in the polymer to the ion conductivity. This requires fitting the scattering data with the appropriate relaxation models that describe the motion. For complicated motions, this fitting can be very complicated as the number of processes and fitting parameters increases. In the field of polymers, biological materials, and soft matter, it has also been realized that the temperature and Q dependence of the elastic scattering, which is trivial to characterize, can provide a very meaningful approximation for the polymer dynamics with very few fitting parameters (*39*). This analysis is based on the Debye-Waller approximation presented in Equation 4. The elastic scattering experiment that measures mean square displacement of a system, also provides a simplified but direct measure of the molecular mobility. As an example, a correlation between viscosity and the atomic mean-square displacement was first proposed by Buchenau and Zorn (*40*). For this purpose, the authors defined, $\langle u_2 \rangle_{loc}$, as the difference between the mean-square displacement of the disordered phase (amorphous and liquid) and the ordered phase (crystalline):

$$\langle u^2\rangle_{\mathrm{loc}} = \langle u^2\rangle_{\mathrm{disord}} - \langle u^2\rangle_{\mathrm{ord}} \quad (5)$$

The inverse of the newly defined $<u^2>_{loc}$ which measures only the part of the mean-square displacement that corresponds to localized modes in the disordered phase, shows a linear relationship with logarithm of viscosity. The above relationship, which was reported for selenium and polybutadiene, can be generalized to amorphous liquids and solids by defining $<u^2>_{loc} = <u^2>_{liq} + <u^2>_{hard}$ where $<u^2>_{liq}$ is the mean-square displacement for motion faster than the instrumental resolution and $<u^2>_{hard}$ takes into account only the typical lattice vibrational frequencies. According to the Nernst-Einstein relation, the ion conductivity should be directly related to the viscosity. Therefore, atomic mean square displacements can provide useful insight of the ion conductivity as they seem to be related.

One of the biggest problems in using PEO as a polymer electrolyte is that it crystallizes below 50° - 60°C. This significantly lowers the room temperature conductivity as the ion transport is largely limited to amorphous phase of the semi-crystalline morphology. As mentioned previously, there have been several strategies to suppress crystallization of PEO and improve conductivity at room temperature (*3*, *5*, *8–13*). Hyperbranching of a polymer chain is one effective way to suppress crystallization. To better understand the effects of fast polymer dynamics on the ion transport, we studied a series of hyperbranched PEO (hbPEO) with varying degrees of branching, both with and without lithium salts (*41*). As expected, the hyperbranching suppressed the crystallization and the salt containing samples were found to be amorphous above 0° C, confirmed with differential scanning calorimetry. The temperature dependence of ionic conductivity for different hbPEOs and linear PEO with the lithium salt, LiTFSI, are shown in Figure 8. The Li^+ ion conductivity showed strong variations with the glycidol (G) branching comonomer content. We investigated hyperbranched PEO copolymers with 8, 16, and 50% glycidol, denoted as hbPEO-G8, hbPEO-G16, and hbPEO-G50, respectively. The *hb*PEO-G8 displayed the highest conductivity at room temperature and there was a very small decrease in conductivity when moving from 8% to 16% glycidol content, followed by a more significant drop at 50% glycidol (see Fig. 8). The decrease in conductivity at higher glycidol fractions probably reflects the increase in the hydroxyl content with the introduction of the glycidol branching moieties. For each glycidol unit of the copolymer, exactly one additional hydroxyl group is introduced, leading to the formation of a hydrogen-bonded network with increased branching. This was consistent with the visual observation that the room temperature viscosity increases from a viscous liquid that readily flows for *hb*PEO-G8 to an elastomer-like gel for the *hb*PEO-G50 sample. In breaking up this hydrogen-bonded network, we also investigated a permethylated version of the hbPEO-G16 where the –OH groups were replaced with $-OCD_3$ to break up the hydrogen bonds between the polymer termini. The methyl group was deuterium substituted to eliminate the contribution from methyl rotors in the

Downloaded by UNIV OF DELAWARE MORRIS LIB on June 14, 2012 | http://pubs.acs.org
Publication Date (Web): May 7, 2012 | doi: 10.1021/bk-2012-1096.ch005

neutron scattering. As expected, the permethylated sample shows a significant increase in the Li-ion conductivity as shown in Figure 8.

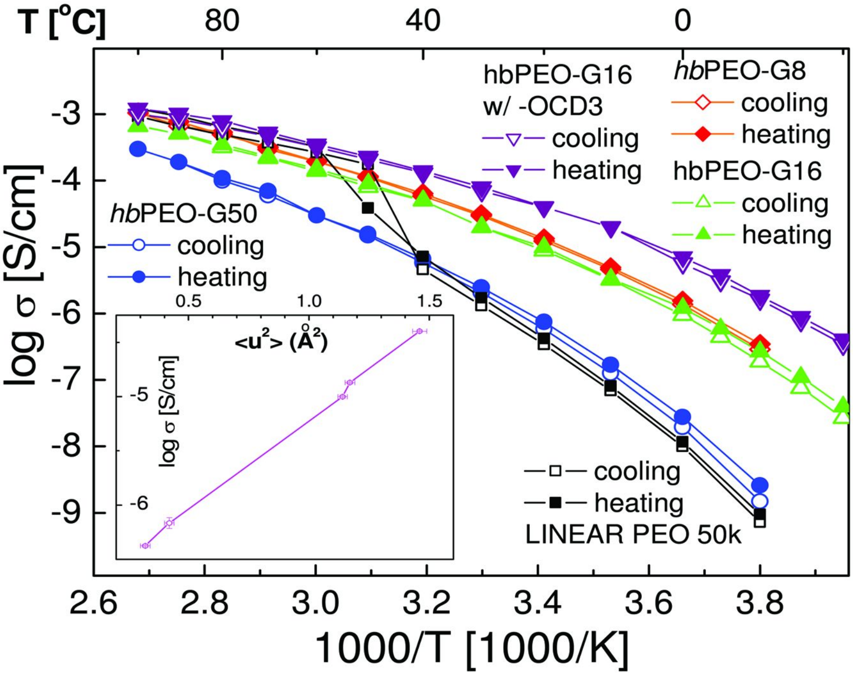

Figure 8. Temperature-dependent Li^+ ion conductivity for hbPEO samples with varying glycidol branching contents and permethylation, as compared with linear PEO, blended with LiTFSI salt in molar ratio O:Li of 25:1.13 The inset shows a direct correlation between the Li^+ ion conductivity and the hydrogen weighted mean-square displacement $<u^2>$ as measured by INS at ambient termperature. Figure reproduced from reference (41).

The atomic mean square displacement was obtained from FWS measurements on the HFBS at the NIST Center for Neutron Research, as described in the INS data interpretation section. The inset of Figure 8 shows a well defined relationship between $<u^2>$ and the logarithm of conductivity. This is analogous (but admitedly not identical to) the studies of Buchanea and Zorn that showed an exponential relationship between viscosity and $1/<u^2>$. It is, however, of particular significance that there is a direct correlation between the high frequency segmental dynamics of hbPEOs blended with Li salts probed by the INS measurements and the slower motions of the Li^+ ions in these polymers. It is generally believed that the Li^+ ions move through PEO by the Grotthus hopping mechanism (*42*) from one association site to the next, involving a catch-and-release process of Li^+ ions association/dessociation by the PEO segments. The Grotthus mechanism is then strongly coupled to the segmental reorganization dynamics of the polymer involving the Li^+ ions. These findings

Downloaded by UNIV OF DELAWARE MORRIS LIB on June 14, 2012 | http://pubs.acs.org
Publication Date (Web): May 7, 2012 | doi: 10.1021/bk-2012-1096.ch005

suggest that the transport of Li^+ ions is closely coupled to the pico- to nanosecond dynamics of polymer chains. The implication is that one should be able to increase the Li^+ ion conductivity of polymer electrolytes by enabling faster local dynamics, as demonstrated here with hbPEO-G16-OCD3.

Summary

In this chapter we have introduced the use of INS techniques as a quantitative tool to better understand the mechanisms of Li^+ ion transport through polymeric electrolyte media. We have introduced the concept of inelastic neutron scattering and provided a basic understanding of the types of motions and atomic species to which it is sensitive. We have also provided a brief background on the different types of INS spectrometers that can be used to study the dynamics of different polymers used as electrolytes. The case has been made that the INS measurements of the dynamics in the polymers provide very complimentary measurements to e.g. dielectric measurerments that directly quantify ion mobility. Quantifying the dynamics of both the ionic species and the host transport media are important for undertanding this complicated transport problem. In particular, we introduced results from the literature indicating that the dynamics of a polymer electrloyte are impacted upon the addition of a Li salt. Typically the segmental or translational relaxations slow down while fixed center of mass motions involving non-polar or non-solvating groups such as methyl rotations are unaffected by the presence of the ions. This generally supports the notion Li^+ ions agregattinng with multiple polymer chains in a way that can slow down the molecular and ionic mobility of the entire system; the Li^+ ions act as transient cross-links. The literature reported herein, with a few exceptions, also appears to support a general correlation between the level of molecular mobility within the polymer electroytes and the ionic conductivity through the the electrolyte media. These polymers with enhanced anharmonic or translational relaxation process in the presence of the Li salts also appear to posses increased ionic conductivity. Unfortunately though, polymer dynamics alone were unable to fully explain some of the empirical observations of enhanced conductivity in polymer electrolytes upon the addition of nanoparticle fillers. This underscores the importance of understanding the role of all the interactions between the mobile ions, their counter ions, the polymer electrolyte, and any additional additives is important. In general though, a positive correlation between ion conductivity and viscosity/mobility on the macroscopic scale makes intuitive sense through empirical relations like the Nernst-Einstein equation. The utility of inelastic neutron scattering is that one can focus on the detailed mechanisms at the nanosecond and picosecond time scale to better understand how molecular mobility translates to ion motion. This should provide better insight for understanding ion conductivty in complicated systems and molecular design cues for desiging higher mobility solid polymer electrolytes.

Downloaded by UNIV OF DELAWARE MORRIS LIB on June 14, 2012 | http://pubs.acs.org
Publication Date (Web): May 7, 2012 | doi: 10.1021/bk-2012-1096.ch005

References

1. Wakihara, M.; Yamamoto, O. *Lithium Ion Batteris*; Kodansha Ltd.: Tokyo; Wiley-VCH: Weinheim, 1998.
2. Agrawal, R. C.; Pandey, G. P. *J. Phys. D: Appl. Phys.* **2008**, *41*, 223001.
3. Gray, F. M. *Polymer Electrolytes*; Materials Monographs; Royal Society of Chemistry: Cambridge, 1997.
4. Armand, M. B. *Annu. Rev. Mater. Sci.* **1986**, *16*, 245.
5. MacCallum, J. R.; Vincent, C. A. *Polymer Electrolyte Reviews 1*; Elsevier Applied Science: 1987.
6. Meyer, W. H. *Adv. Mater.* **1998**, *10*, 439.
7. Murata, K.; Izuchi, S.; Yoshihisa, Y. *Electrochim. Acta* **2000**, *45*, 1501.
8. Allcock, H. R.; O'Connor, S. J. M.; Olmeijer, D. L.; Napierala, M. E.; Cameron, C. G. *Macromolecules* **1996**, *29*, 7544.
9. Hooper, R.; Lyons, L. J.; Mapes, M. K.; Schumacher, D.; Moline, D. A.; West, R. *Macromolecules* **2001**, *34*, 931.
10. Abraham, K. M.; Choe, H. S.; Pasquariello, D. M. *Electrochim. Acta* **1998**, *43*, 2399.
11. Nishimoto, A.; Agehara, K.; Furuya, N.; Watanabe, T.; Watanabe, M. *Macromolecules* **1999**, *32*, 1541.
12. Hawker, C. J.; Chu, F.; Pomery, P. J.; Hill, D. J. T. *Macromolecules* **1996**, *29*, 3831.
13. Marzantowicz, M.; Dygas, J. R.; Krok, F.; Tomaszewska, A.; Florjanczyk, Z.; Zygadlo-Monikowska, E.; Lapienis, G. *J. Power Sources* **2009**, *194*, 51.
14. Briant, J. L.; Farrington, G. C. *J. Solid State Chemistry* **1980**, *33*, 385–390.
15. Higgins, J. S.; Benoît, H. C. *Polymers and Neutron Scattering*; Oxford, 1994.
16. Frick, B.; Richter, D. *Science* **1995**, *267*, 1939.
17. Bee, M. *Quasi-elastic Neutron Scattering*; Adam Hilger: Bristol, 1988.
18. Roe, R. J. *Methods of X-Ray and Neutron Scattering in Polymer Science*; Oxford University Press: New York, 2000.
19. http://www.ncnr.nist.gov.
20. Copley, J. R. D.; Cook, J. C. *Chem. Phys.* **2003**, *292*, 477.
21. Meyer, A.; Dimeo, R. M.; Gehring, P. M.; Neumann, D. A. *Rev. Sci. Instrum.* **2003**, *74*, 2759.
22. Williams, G.; Watts, D. C. *Trans. Faraday Soc.* **1970**, *66*, 80.
23. Arbe, A.; Colmenero, J.; Monkenbusch, M.; Richter, D. *Phys. Rev. Lett.* **1998**, *81*, 590.
24. Rajagopal, A. K.; Ngai, K. L. *Relaxations in Complex Systems*; North Holland, Amsterdam, 1991.
25. Zajac, W.; Gabrys, B. J.; McGreevy, R.; Mattssons, B. *Physica B* **1996**, *226*, 144.
26. Zorn, R. *Nucl. Instrum. Methods Phys. Res.* **2007**, *572*, 874.
27. Carlsson, P; Mattsson, B.; Swenson, J.; Torell, L. M.; Kall, M.; Borjesson, L.; McGreevy, R.; Mortensen, K.; Gabrys, B. *Solid State Ionics* **1998**, *113−115*, 139.
28. Mao, G.; Perea, R. F.; Howells, W. S.; Price, D. L.; Saboungi, M.-L. *Nature* **2000**, *405*, 163.

Downloaded by UNIV OF DELAWARE MORRIS LIB on June 14, 2012 | http://pubs.acs.org
Publication Date (Web): May 7, 2012 | doi: 10.1021/bk-2012-1096.ch005

In Polymers for Energy Storage and Delivery: Polyelectrolytes for Batteries and Fuel Cells; Page, K., et al.;
ACS Symposium Series; American Chemical Society: Washington, DC, 2012.

Downloaded by UNIV OF DELAWARE MORRIS LIB on June 14, 2012 | http://pubs.acs.org
Publication Date (Web): May 7, 2012 | doi: 10.1021/bk-2012-1096.ch005

29. Saboungi, M.-L.; Price, D. L.; Mao, G.; Fernandez-Perea, R.; Borodin, O.; Smith, G. D.; Armand, M.; Howells, W. S. *Solid State Ionics* **2002**, *147*, 225.
30. Mos, B.; Verkerk, P.; Pouget, S.; Zon, A. V.; Bel, G. J.; de Leeuw, S. W.; Eisenbach, C. D. *J. Chem. Phys.* **2000**, *113*, 4–7.
31. Triolo, A.; Celso, F. Lo; Passerini, S.; Arrighi, V.; Lechner, R. E.; Frick, B.; Triolo, R. *Appl. Phys. A* **2002**, *74*, S493.
32. Fullerton-Shirey, S. K.; Maranas, J. *Macromolecules* **2009**, *42*, 2142.
33. Sinha, K.; Maranas, J. K. *Macromolecules* **2011**, *44*, 5381.
34. Russina, O.; Triolo, A.; Aihara, Y.; Telling, M. T. F.; Grimm, H. *Macromolecules* **2004**, *37*, 8653.
35. Croce, F.; Appetecchi, B.; Persi, L.; Scrosati, B. *Nature* **1998**, *394*, 456.
36. Fullerton-Shirey, S. K.; Maranas, J. K. *J. Phys. Chem. C* **2010**, *114*, 9196.
37. Karlsson, C.; Best, A. S.; Swenson, J.; Howells, W. S.; Borjesson, L. *J. Chem. Phys.* **2003**, *118*, 4206.
38. Eijck, L.; Best, A. S.; Stride, J.; Kearley, G. *J. Chem. Phys.* **2005**, *317*, 282.
39. Zaccai, G. *Science* **2000**, *288*, 5471.
40. Buchenau, U.; Zorn, R. *Europhys. Lett.* **1992**, *18*, 523.
41. Lee, S-Il; Schomer, M.; Peng, H.; Page, K. A.; Wilms, D.; Frey, H.; Soles, C. L.; Yoon, D. Y. *Chem. Mater.* **2011**, *23*, 2685.
42. de Grotthuss, C. J. T. *Ann. Chim.* **1806**, *58*, 54.

Downloaded by UNIV OF DELAWARE MORRIS LIB on June 14, 2012 | http://pubs.acs.org
Publication Date (Web): May 7, 2012 | doi: 10.1021/bk-2012-1096.ch006

Chapter 6

In Situ Neutron Techniques for Studying Lithium Ion Batteries

Howard Wang,[1,2,5,*] R. Gregory Downing,[2] Joseph A. Dura,[3] and Daniel S. Hussey[4]

[1]Institute for Material Research and Department of Mechanical Engineering, State University of New York, Binghamton, NY 13902
[2]Material Measurement Laboratory, National Institute of Standards and Technology, Gaithersburg, MD 20899
[3]NIST Center for Neutron Research, National Institute of Standards and Technology, Gaithersburg, MD 20899
[4]Physical Measurement Laboratory, National Institute of Standards and Technology, Gaithersburg, MD 20899
[5]Department of Materials Science and Engineering, University of Maryland, College Park, MD 20742
***email: wangh@binghamton.edu**

We review *in situ* neutron techniques for studying lithium ion batteries. Four neutron measurement techniques, neutron depth profiling, neutron reflectivity, small angle neutron scattering, and neutron imaging are discussed in this chapter. They are used to quantify the real-time distribution and transport of Li in active battery components during battery operation, and gain new insights in the function and failure of battery systems. We demonstrate that *in situ* neutron diagnoses offer new opportunities in better understanding the performance and lifetime of secondary batteries.

Introduction

Efficient energy storage will be an integral part of future energy solutions, in which alternative energy sources such as solar and wind will be extensively used, transportation with hybrid cars or all-electric vehicles will be the everyday norm, and portable devices and standalone electronics will be ubiquitous. Rechargeable

In Polymers for Energy Storage and Delivery: Polyelectrolytes for Batteries and Fuel Cells; Page, K., et al.; ACS Symposium Series; American Chemical Society: Washington, DC, 2012.

Downloaded by UNIV OF DELAWARE MORRIS LIB on June 14, 2012 | http://pubs.acs.org
Publication Date (Web): May 7, 2012 | doi: 10.1021/bk-2012-1096.ch006

Li-ion batteries (LIBs) are a promising technology for efficient energy storage owing to the potential for high energy capacity, long cycle life, and low cost. Since the initial proposal by Whittingham in the 1970s (*1*), Li-ion batteries have evolved over three decades and have been commonly used in portable electronics such as laptop computers and mobile phones. However, to meet the high demands in large-scale energy storage needs such as plug-in hybrid electric vehicles (PHEV), renewable energy management, and power grid applications, battery technologies need to overcome many daunting challenges in order to significantly increase the energy and power capacities as well as safety and lifetime (*2–4*). Because of the transient and non-equilibrium nature of the materials and processes in a working LIB, much of the critical structural information is not easily accessible, greatly impeding the advances in the field. Precise, *in situ* diagnostic techniques will play a critical role in materials and process innovation, system optimization, safety analysis, failure diagnosis, and lifetime prediction in developing next generation LIBs.

Researchers have applied microscopy, spectroscopy, x-ray tomography, and scattering techniques to better understand the structure and performance of LIB systems. Particularly, insights are now gleaned from innovative use of *in situ* transmission electron microscopy (*5*, *6*), scanning probe microscopy (*7*, *8*), nuclear magnetic resonance spectroscopy (*9*, *10*), and synchrotron x-ray diffraction (*11*, *12*). Applications of neutron techniques for *in situ* diagnosis of LIBs are relatively new; however, they can be very powerful because of neutron's high penetration power and its relatively high sensitivity to lithium isotopes. Recently, *in situ* neutron diffraction has been successfully used to reveal changes in the crystal structures of electrode materials during battery operation (*13–20*).

There are many neutron measurement methods that are less frequently used by the battery research community. In this Chapter, four *in situ* neutron techniques are discussed: neutron depth profiling (NDP), neutron reflectivity (NR), small angle neutron scattering (SANS), and neutron imaging (NI). In addition to introducing fundamentals and physical principles of each technique, their potential applications to studying battery systems are illustrated with specific examples. Together they provide multi-scale measurements of the Li distribution and transport in active LIBs to yield valuable new insights in the performance and failure of battery systems.

Neutron Depth Profiling

As most LIBs operate with the so called rocking chair mechanism, in which Li ions are shuttled back and forth between cathode and anode layers, it is of great interest to directly visualize the distribution of the mobile ingredient, Li, in a LIB during its operation. Simultaneous space- and time-resolved Li measurements allow for direct comparison of ionic motion in the battery with the electric current in the external circuit, which would provide irreplaceable insights in addressing issues related to transport mechanisms, structure integrity, normalcy of performance, and reliability of operation. Based on the neutron activation and the energy loss spectrum of energetic ions in matter, NDP has been applied to resolving nano- to micro-scale lithium distributions in working battery systems during charge/discharge cycles.

NDP is an analytical technique for quantitative measurements of a list of technologically important elements (Li, B, N, He, Na, etc) as a function of depth into a solid surface (*21*). Initially developed in the early 1970's for measuring boron distributions in silicon wafers (*22*), and until recently applied mostly to studying electronics materials, NDP is now a mature technique, increasingly used to measure lithium distributions in modern battery technologies (*23–28*).

The NDP setup is schematically illustrated in Figure 1. This arrangement is typical of the instrument operated at the National Institute of Standards and Technology (NIST) (*21*). In an NDP measurement, a flux of cold neutrons coming out of a neutron guide pass through a Li-containing specimen and react with the isotope ^{6}Li to generate two highly energetic charged particles, $^6\text{Li} + \text{n} \rightarrow \alpha + {}^3\text{H}$. Both the charged particle energy spectrum and the total neutron fluence that passes through each sample are monitored and recorded with surface barrier detectors. The majority of neutrons that enter the chamber pass through the sample, exit the sample chamber, and are absorbed by the beam stop. Because the incoming energy of the neutron is negligible (< 4 meV) and the interaction rate is small, typically < 0.01% of the incoming fluence, NDP is considered a non-destructive technique, an obvious advantage in battery studies.

Downloaded by UNIV OF DELAWARE MORRIS LIB on June 14, 2012 | http://pubs.acs.org
Publication Date (Web): May 7, 2012 | doi: 10.1021/bk-2012-1096.ch006

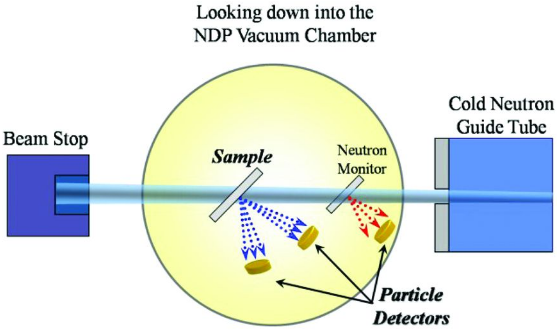

Figure 1. Schematic illustration of NDP setup.

The tritium and the recoil α particles emitted from the reaction each have a well-known energy determined by the reaction kinematics (2727 keV and 2054 keV respectively). The total number of charged particles emitted from the sample is proportional to the product of the neutron fluence that impinges upon the sample, the reaction cross-section of the nuclides (*ca.* 2089 barns for ^{6}Li and 4 meV neutrons), and the nuclidic abundance throughout the illuminated volume. Using cold neutrons enhances the reaction cross-section and enables measurement at higher rates or better statistics. The charged particles travel diametrically away from the reaction center, and lose energy to the matrix at a rate (the stopping power) that depends on the energy of ions and the electronic structures of the matrix (*21*). The energy of the detected particles is used to determine the initial location of the activation reaction; the normalized counts are used to measure the abundance of elements at the corresponding depth.

NDP has similarities to ion beam techniques, such as forward recoil spectrometry (FRES) and Rutherford backscattering spectrometry (RBS), it enables the measurement of depth profiles of flat solid specimens over an area of *ca.* 1 mm^2 to >10^2 mm^2, conveniently defined by the aperture of a mask covering the sample. The full depth range of the profile varies from a few micrometers to 10s of micrometers, depending on the atomic composition of the specimen as well as the particle of detection, α or ^{3}H. Likewise, the depth resolution varies from a few nanometers to a few hundred nanometers. There are also important differences in the abovementioned techniques that make them complimentary. RBS is most useful for determining heavy elements in low atomic number matrix materials. As both FRES and NDP are good for profiling light elements, FRES requires the use of an energetic (MeV) ion beam of heavier elements to knock out the light elements for measurements, whereas NDP uses an meV neutron beam which causes little energy deposition, avoiding heating and damaging the specimen. Another consequence of the nuclear activation *vs.* ion beam is that NDP has superior energy resolution to those techniques because the well-defined kinetic energies of detecting particles at the reaction. In addition, the selective nature of nuclear activation ensures that Li spectra are clean, being free of interference from other elements. These differences represent a significant advantage of NDP for continuous *in situ* measurement of Li transport during prolonged battery operation.

The distribution of Li in working batteries undergoing charge/discharge cycles has been measured using *in situ* NDP at NIST. One example of *in situ* NDP real-time assessment on the battery operation is shown in Figure 2. The battery was fabricated by sputter deposition of thin films, with a layered structure of mica / Pt (200 nm) / $LiCoO_2$ (5 µm) / LiPON (2 µm) / Li (4 µm) / Pt (200 nm) / mica, where $LiCoO_2$ is the cathode and Li metal is the anode. The mica encapsulating window has to be thinned down to *ca.* 15 µm in order for the $^3H^+$ to escape the packaging layers and reach the detector. NDP spectra recorded during the charge/discharge are shown in Figures 2(a) and 2(b), respectively. Each spectrum was collected during a period of 15 min and consecutive spectra are 75 min apart (one of every five spectra plotted for clarity). The Li metal layer is shown as a prominent peak around 1200 keV, while the $LiCoO_2$ layer is shown as the plateau about 1700 keV to 2100 keV. In the charge cycle, Li is pumped out from the $LiCoO_2$ cathode layer and deposited in the anode, while in discharge, Li flows back from the anode to cathode.

Figure 3(a) shows the potential profiles of the battery during several cycles of charge/discharge. Using SRIM software to calculate the stopping power of $^3H^+$ in different battery layers (*29*), NDP data are quantitatively analyzed to yield lithium depth profiles, allowing for direct comparison of Li transport inside the battery and the electric current flow in the external circuit. Figure 3(b) compares the Li ion density in the cathode measured by NDP (symbols) and displaced electric charge recorded by the potentiostat (lines). (Note: throughout this chapter error bars represent a one sigma standard deviation.) A good match is maintained till the instability occurs as indicated by the erratic responses of current and potential during the second discharge, which may relate to sudden structural changes in the battery. The discrepancy between the ionic transport in the cathode and the electric

Downloaded by UNIV OF DELAWARE MORRIS LIB on June 14, 2012 | http://pubs.acs.org
Publication Date (Web): May 7, 2012 | doi: 10.1021/bk-2012-1096.ch006

transport in the external circuit could be a powerful indicator of the onset of battery failure, which is illustrated here using time-resolved NDP.

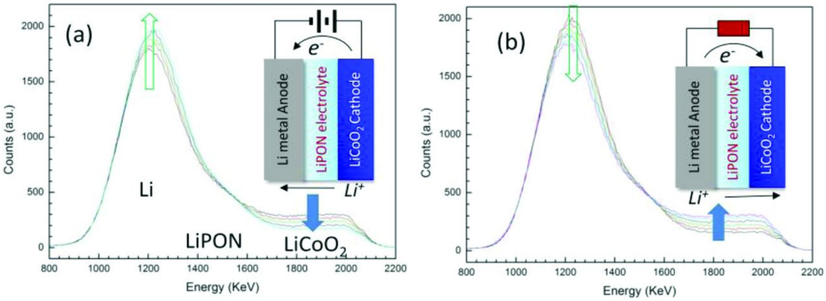

Figure 2. Time-resolved in situ NDP on a thin film battery during (a) charging and (b) discharging. The assignment of electrode ane electrolyte layers in the spectra are labeled. Arrows indicate the flow of Li in each electrode.

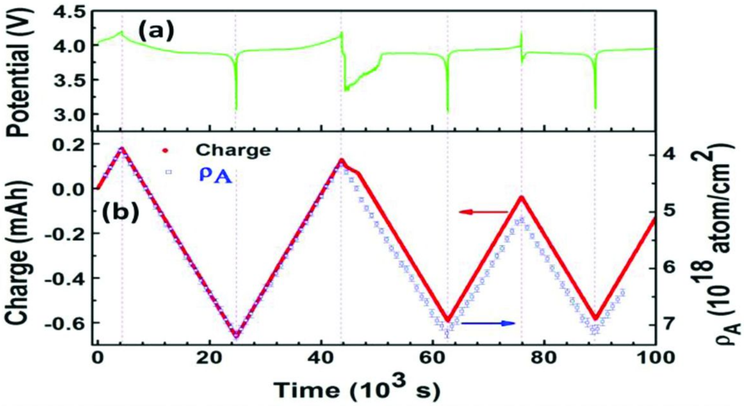

Figure 3. Time-resolved (a) potential profile, and (b) electric vs. ionic charge displacement. The potential anomaly at the beginning of the second discharge coincides with the mismatched charge at the same time.

Although thin film solid state batteries are used here to illustrate the utility of *in situ* NDP, the technique can be readily applied to any Li-containing batteries prepared in layered structures and operatable in vacuume. With higher neutron flux and better detection capability, NDP could be further improved to become a powerful tool to probe the reliability and lifetime of Li-containing batteries under real operation circumstances. Fast NDP measurement will be particularly useful for understanding battery performance at high charge/discharge rates, which is critical for vehicle applications.

Downloaded by UNIV OF DELAWARE MORRIS LIB on June 14, 2012 | http://pubs.acs.org
Publication Date (Web): May 7, 2012 | doi: 10.1021/bk-2012-1096.ch006

Downloaded by UNIV OF DELAWARE MORRIS LIB on June 14, 2012 | http://pubs.acs.org
Publication Date (Web): May 7, 2012 | doi: 10.1021/bk-2012-1096.ch006

Neutron Reflectivity

Most lithiation and delithiation processes involve compositional and structural changes in electrode materials, most notably volume expansion and retraction. Precise measurements are needed in order to quantify these variations at sub-nanometer levels particularly near interfaces. As the bulk of a crystalline structure expands, a lattice parameter change or phase transition can be measured with diffraction techniques, which, however, do not readily quantify amorphous materials. Furthermore, the composition and structure across interfaces between different components in batteries are of critical importance to the transport of Li ions and electrons. Precisely measuring these structures to sub-nanometer scales is critical to understanding interfacial phenomena.

One prominent example is the structure and composition of the solid electrolyte interface (SEI) layer that forms on electrodes from the breakdown of the electrolyte, which is crucial for the reliable operation of batteries. Recent NR measurements are the first of their kind in determining the thickness of the SEI as a function of potentiostatic voltage (*30*). The sensitivity of NR for light elements and for different isotopes of certain elements including H and Li makes it ideally suited for Li battery research. Furthermore, since single crystals such as Si are relatively transparent to the neutron beam, NR can be applied to *in situ* characterization of electrode films and their interfaces deposited onto a flat Si substrate and enclosed in wet chemical cells, similar to those developed for studying hybrid lipid bilayer membranes (*31*), except that a fully enclosed cell is often used in battery studies to avoid the corrosion of the substrate and the contamination of electrolytes.

NR is a high resolution technique for probing structure, composition and magnetism in thin films with sub-angstrom accuracy for films as thin as 1.5 nm (*32*, *33*). It is commonly used to measure liquid/gas interfaces (*34*), and biological (*35*, *36*), hydrogen related (*37*, *38*) polymer (*39*), water containing materials such as polymer electrolyte membranes (*40*), and magnetic thin films (*41*), or combinations of these phenomena (*42*). Typically thin films are characterized using specular neutron reflectometry (*43*, *44*), in which a monochromatic neutron beam of wavelength λ is directed onto thin layers on a flat substrate at a glancing angle, θ. The intensity of the reflected beam at the same angle relative to the sample [Figure 4(a)] is recorded as a function of the amplitude of momentum transfer vector normal to the film surface, Q_z, defined as: $Q_z = (4\pi / \lambda) \sin\theta$. NR data are used to determine the scattering length density (SLD) as a function of depth or $\rho(z)$ defined (ignoring magnetic contributions) as: $\rho(z) = \Sigma_j N_j(z)\, b_j$, where $N_j(z)$ is the number density of isotope j at depth z, b_j is the coherent nuclear scattering length of isotope j. The atomic dependence through b_j allows the SLD profile to be interpreted as a compositional profile when the constituent materials are known. Furthermore, the isotopic dependence of b_j allows for specific components of a system to be labeled during sample preparation and followed as the sample evolves during an experiment.

Specular NR is not sensitive to in-plane structures and interacts with the SLD which is averaged in the plane of the sample over any compositional variations within the neutron coherence length, as depicted by the dashed line in

In Polymers for Energy Storage and Delivery: Polyelectrolytes for Batteries and Fuel Cells; Page, K., et al.;
ACS Symposium Series; American Chemical Society: Washington, DC, 2012.

Downloaded by UNIV OF DELAWARE MORRIS LIB on June 14, 2012 | http://pubs.acs.org
Publication Date (Web): May 7, 2012 | doi: 10.1021/bk-2012-1096.ch006

the two dimensional rendition of a multilayer structure shown in Figure 4(a). The corresponding SLD depth profile is shown in Figure 4(b). Neutrons reflected from each interface in multilayered thin films interfere constructively or destructively as a function of Q_z, resulting in oscillatory reflectivity, whose periodicities are inversely proportional to the thickness of the layers that have caused the interference. As large surface and interfacial roughnesses seriously deteriorate the quality of NR spectra, it is essential to prepare films with sub-nanometer roughness in order to take advantage of the high resolution technique.

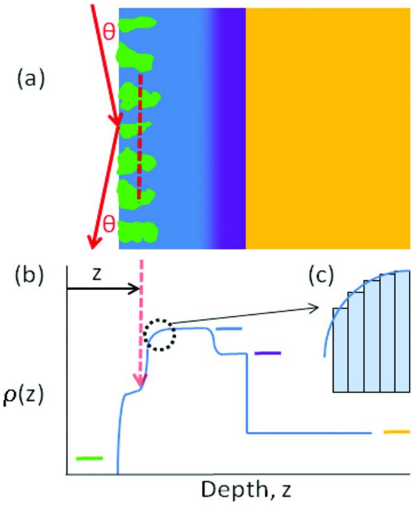

Figure 4. Schematics of NR measurement. (a) A cross section view of a multilayer structure, (b) the simulated SLD profile, and (c) details of the profile approximation.

Because NR measures the reflected intensity rather than the amplitude, the phase of the neutron wave is not measured; therefore, single NR spectra cannot be directly inverted to determine a SLD profile. Although approaches have been developed for direct inversion (*45*), the more widely used method of determining the depth profile is through model fitting. Simple structures can be modeled as single layers of constant SLD for each film. More complicated profiles, such as rough interfaces or compositional gradients, can be modeled as a stack of arbitrarily thin layers; this can be applied to approximate any SLD profile [Figure 4(c)]. In fitting, SLD profile models are created and iteratively adjusted through least square refinement until the simulated scattering plot matches the dataset. The software (*46*) used for this is based upon the Parratt formalism (*47*).

The battery assembly for *in situ* NR measurements is schematically illustrated in Figure 5(a). It consisted of a half cell of eleactron-beam evaporated Cu (5 nm) / a-Si (10 nm) / Al_2O_3 (2 nm) films on a Si substrate as the active electrode, Li metal as the counter and negative electrode, and 1 mol/L $LiPF_6$ in EC:DMC (1:1 by volume) solution as the electrolyte. The cell was sealed using a 0.7 mm thick viton gasket, and the electrodes were connected to a potentiostat through thin gold leaves. NR data were taken after the initial assembly (noted as open circuit, or OC), and after the first and sixth lithiation and delithiation, as shown in Figure 5(b). The curves through symbols are the calculated reflectivity from the best fits. The fitting results in Figure 6(a) show that the Si film swells from the initial thickness of 11 nm to 16 nm upon first lithiation, and shrinks back to 12 nm upon delithiation. Similar behaviors are observed upon sixth lithiation and delithiation. Corresponding Li compositions appear to be consistent with the Si film swelling/shrinking [Figure 6(b)]. The results indicate that increasing amounts of residual Li are left in the sample after delithiation as a function of the number of cycles. The integrity of both the a-Si and Al_2O_3 layer remains largely intact during the operation, presumably due to the shallowness of the lithiation/delithiation.

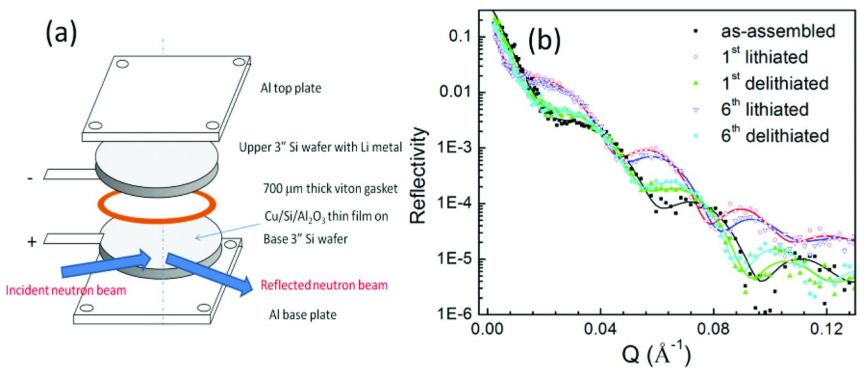

Figure 5. (a) schematics of battery assembly for in situ NR measurements, and (b) NR spectra at various charge states showing mostly reversible structural variations.

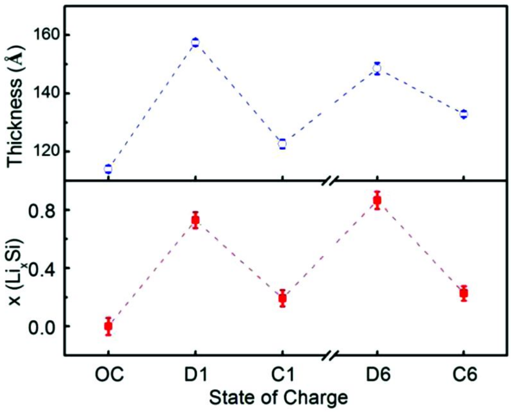

Figure 6. (a) The thickness of Si electrode, and (b) the Li composition at various charge states. The lines are a guide to the eye.

Downloaded by UNIV OF DELAWARE MORRIS LIB on June 14, 2012 | http://pubs.acs.org
Publication Date (Web): May 7, 2012 | doi: 10.1021/bk-2012-1096.ch006

As demonstrated in this example, NR offers the unique capability of sub-nanometer resolution measurements of buried interfaces and films, which are much needed for advancing fundamental understanding of LIB materials and systems. Critical LIB issues to be addressed using NR include the mechanism of lithiation/delithiation of active materials, the formation of solid electrolyte interface, degradation and dissolution of electrodes, and the structure of electrolytes near solid surfaces.

Small Angle Neutron Scattering

Nanoscale morphology has become an increasingly important topic in battery research since much of the transport behavior and structural integrity issues rely on details near surfaces and at nanoscales. Nanoscale engineering is also considered a key element in addressing the issue of the low power density of batteries (*48*) as large surface areas and small diffusion lengths assure fast charge/discharge kinetics. To avoid compromising the system-level energy and powder density, nanoscale materials need to be densely packed into bulk composites when included as active components in batteries. The structure variation of such materials is best monitored using small angle neutron scattering, SANS. In particular, SANS measures two aspects, direct structure measurement such as swelling and recovery of nanoscale grain in a bulk assembly, and the contrast changes due to the lithiation-induced scattering length density variation.

In a SANS measurement, incident neutrons with a wavelength λ, typically in the range of 5 Å to 20 Å, impinge on the sample, and scattered neutrons are counted using a 2-dimensional (2D) area detector (see Figure 7). Several measurements including the direct beam intensity, background noise, sample transmission, empty cell scattering, and detector efficiency, are needed to correctly obtain the sample scattering. The absorption of neutrons by Li is small in a typical SANS battery cell, and is quantitatively accounted for by the sample transmission. For samples with assumed isotropic pore geometry, the corrected 2D intensity is circularly averaged to yield the total scattering cross section of the sample, which includes the incoherent scattering (*49*). The scattering intensity, I, is obtained as a function of momentum transfer vector, Q=(4π / λ sinα/2), where α is the scattering angle. In a typical SANS experiment, several sample-to-detector distances from 1 m to 15 m can be used to obtain a wide Q-range (~0.001 Å^{-1} to ~0.5 Å^{-1}) covering structural length scales from ~ 1 nm to ~ 200 nm. The neutron wavelength dispersion is mainly responsible for the resolution of the SANS measurements.

SANS has been widely used to measure nanoscale structures in bulk phases. Time-resolved *in situ* SANS, TR-SANS, has found relatively limited applications in battery research because of the small neutron fluence rate and low scattering. In recent years, the increase in flux at the reactor-based NIST instruments and deployment of the spallation neutron source at ORNL make it possible to study nanoscale phenomena in LIB in real time. In the following example, TR-SANS measurements were performed with the NG-7 30 m SANS instrument at the NIST Center for Neutron Research.

Downloaded by UNIV OF DELAWARE MORRIS LIB on June 14, 2012 | http://pubs.acs.org
Publication Date (Web): May 7, 2012 | doi: 10.1021/bk-2012-1096.ch006

Downloaded by UNIV OF DELAWARE MORRIS LIB on June 14, 2012 | http://pubs.acs.org
Publication Date (Web): May 7, 2012 | doi: 10.1021/bk-2012-1096.ch006

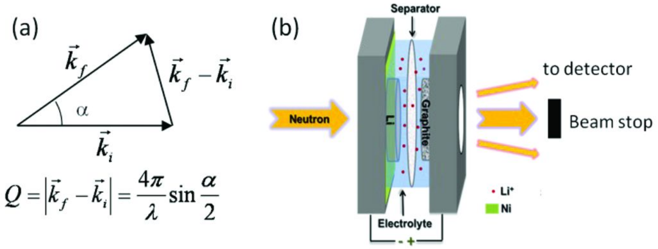

Figure 7. (a) Neutron momentum transfer in SANS; (b) schematics of a battery cell for SANS

The battery assembly consists of graphite composite *vs.* Li electrodes for studying lithiation and delithiation processes in the graphite electrode as schematically shown in Figure 7(b). A neutron beam passes through a stack of two 1 mm thick quartz plate windows, two 10 µm thick Ni foils as current collectors, 300 µm thick Li anode, 1 mol/L $LiPF_6$ in EC:DMC (1:1 by volume) solution as electrolyte, 25 µm thick polypropylene separator, and *ca.* 15 µm thick graphite composite electrode in the normal direction, with scattering occurring mostly from the graphite electrode, which is composed of platelet graphite particles of *ca.* 10 µm wide and 1-2 µm thick, carbon black, and polyvinylidene fluoride (PVDF). SANS spectra of the initial state (squares) and the fully lithiated state (triangles) are shown in Figure 8. The variation of the scattering intensity upon charge/discharge is small compared to the overall intensity. A dominant scattering feature in the Q-range is the $\sim Q^{-4}$ power law behavior, which is characteristic Porod scattering law due mostly to interfacial contributions.

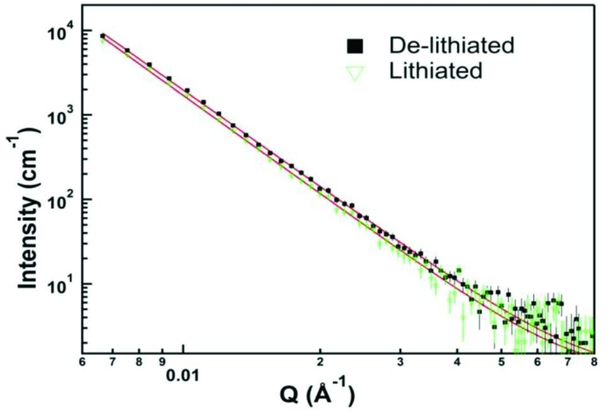

Figure 8. SANS spectra of delithiated (squares) and lithiated (down triangles) states.

Downloaded by UNIV OF DELAWARE MORRIS LIB on June 14, 2012 | http://pubs.acs.org
Publication Date (Web): May 7, 2012 | doi: 10.1021/bk-2012-1096.ch006

The charge/discharge current [Figure 9(a)], potential [Figure 9(b)], and electric charge displacement [Figure 9(c)] profiles recorded during SANS measurements indicate the typical performance of a graphite anode. The variation of integrated SANS intensity upon cyclic charge/discharge is shown in Figure 9(d), which rises and falls in apparently full synchronization with charge states. This is due to the contrast variation induced by lithiation/delithiation. As Li intercalates into graphite particles, the overall SLD decreases, reducing the contrast with the matrix, hence decreasing the scattering intensity, and vice versa with de-intercalation. However, as the charge transfer becomes shallower at higher cycling rates, the amplitude of the intensity variation becomes even larger. This is contradictory to the prediction that the contrast variation is the only source of the scattering intensity change. The excess scattering could result from new surfaces created due to fracturing of graphite particles.

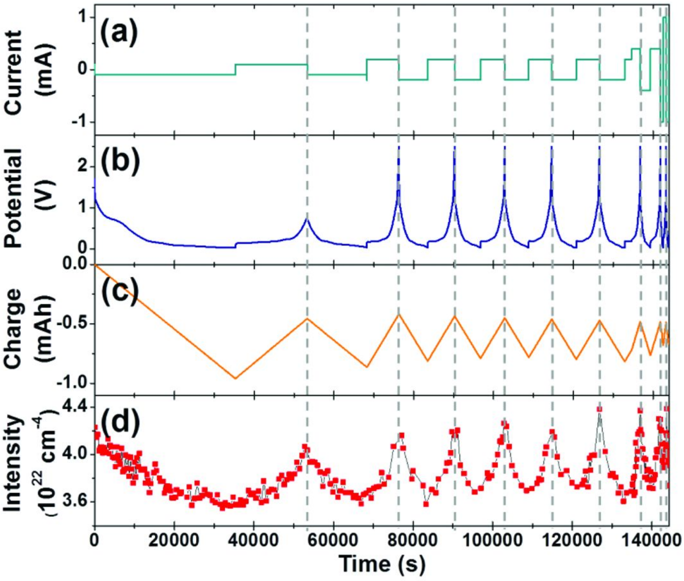

Figure 9. The evolution of (a) current, (b) potential, (c) charge displacement, and (d) integrated SANS intensity during charge/discharge cycles.

This observation is particularly interesting because fresh surfaces from the fracture will be immediately passivated by new SEI layers, which consume Li in the battery, resulting in the reduction of the reversible energy storage capacity. Lithiation-induced fracturing of graphite particles in the anode has been one cause of the irreversible capacity loss during LIB operation. Quantitative *in situ* monitoring of the generation of new surface areas will assist the development of materials and process recipes for improved cycle life. There are studies on this topic using *ex situ* Raman spectroscopy and electron microscopy (*50*). *In situ* diagnosis by scanning probe (*51*) acoustic emission measurement (*52*) has also been developed. Nevertheless, those techniques offer mostly indirect and qualitative measurements of fracture surfaces.

Although the case of graphite particle fracturing is discussed here, such approach can be applied to other electrode materials that are faceted and fracture brittlely. SANS can be a unique *in situ* technique for monitoring both the bulk and interfacial activities of individual grains in active components in batteries. In the example discussed above, hydrogenated electrolyte solvent was used; there is little contrast between the electrolyte and the SEI layer formed from the decomposition of the electrolyte molecules because of their similar overall isotopic compositions. However, by selective labeling of molecules in the electrolyte, SANS could be used to determine the reactivity of different species from the resultant interfacial scattering signals upon battery operation. Such capabilities for surface detection, together with its conventional strength for monitoring the size and shape of nanoscale structures in real time, *in situ* SANS could be a very powerful tool in understanding the operation of LIBs going through lithiation/delithiation cycles.

Neutron Imaging

The electrode of a practical LIB is a complex composite designed to facilitate ionic and electric transport while maintaining mechanical integrity. Non-uniform physical structures and processes, coupled with heterogeneous chemical activities at surfaces and in the bulk of battery materials result in the heterogeneity in electrochemical processes at both the electrode and individual grain levels. Much of the difficulty in accurate modeling of battery performance lies in the uncertainty of the ionic and electric transport pathways. That has led to recent efforts in the tomography of electrode materials (*53*). Visualization of non-uniformity is difficult, particularly in a real battery environment. Neutron imaging (or neutron radiography) offers the promise of direct visualization of hotspots and non-uniform fields of transport in lithiating electrodes.

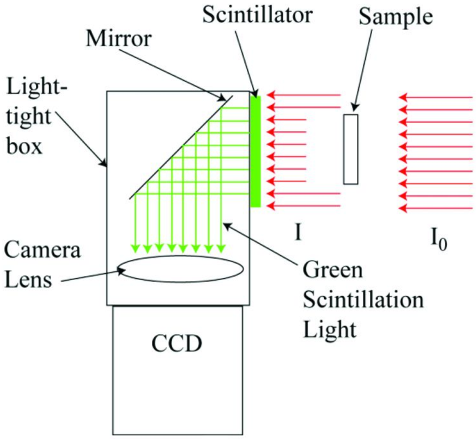

Figure 10. Schematic illustration of neutron imaging.

Downloaded by UNIV OF DELAWARE MORRIS LIB on June 14, 2012 | http://pubs.acs.org
Publication Date (Web): May 7, 2012 | doi: 10.1021/bk-2012-1096.ch006

Neutron radiography measures spatially the change in transmission of an object as a function of time compared to a reference state. A sketch of the sample area for neutron imaging is shown in Figure 10. Neutrons impinge on the sample from the right. The sample is mounted as close to the scintillator screen as possible and is exposed to ambient conditions. Neutrons are absorbed by Gadolinium in the gadoxysulfide scintillator, and the energetic conversion electrons result in the emission of green light. A camera lens attached to the charge-coupled device (CCD) collects and focuses light onto the sensor and enables tailoring the field of view and spatial resolution to the sample under study by varying the focal length. A mirror at 45° enables locating the radiation sensitive CCD camera out of the direct beam path of unabsorbed neutrons and gamma rays emanating from the reactor core. The scintillator, mirror, lens and camera are housed in a light-tight box to reduce the background. Neutron images are continuously recorded.

Neutron radiography is attractive for battery research due to the direct measurement of the change in Li concentration. There are applications of NI to battery studies (*54–57*), which take advantage of the high penetrating power of neutrons and the high contrast with Li containing materials, particularly with ^{6}Li isotope because of its large activation cross-section. It is possible to image at high spatial resolution or high time resolution, with a trade-off required to obtain a given uncertainty in the areal number density (*58*). At high spatial resolution (~10 μm), it is possible to independently observe the bulk through-plane variations in the Li-concentration during battery operation (*56*) with time resolution of order 20 min. At moderate spatial resolution of 50 μm, one can perform tomography on cylindrical cells as a function of the charge and discharge current (*55*).

To illustrate the utility of neutron imaging, a planar battery cell using highly oriented pyrolitic graphite (HOPG, dimension: 5 mm x 10 mm x 1 mm.) as the intercalating electrode and a piece of ^{6}Li metal as counter electrode was assembled. The two electrodes are separated laterally to avoid the overlap in neutron projection, and are in contact with 10 μm Ni foils on the opposing sides and connected to an external circuit. Neutron imaging was performed at the NIST neutron imaging facility, located on BT2 at the NIST Center for Neutron Research. In order to optimize the spatial resolution and measurement of the change in ^{6}Li concentration, the beam was set to have a collimation ratio of L/D = 600, which corresponds to a fluence rate of about $\Phi = 5 \times 10^6$ cm^{-2} s^{-1}. The CCD-lens system was configured to yield a field of view of about 4.5 cm × 4.5 cm with a spatial resolution of about 50 μm. Lithiation of HOPG at an electric current of -400 nA was captured using a time sequence picture framing of every 25 seconds over 20 hours.

The neutron image of the HOPG/^{6}Li cell is shown in Figure 11 (a). The attenuation of the neutron beam is the largest in regions of the highest ^{6}Li concentration; ^{6}Li appears dark and the pristine HOPG appears light. The images of HOPG upon lithiation for 5.9 min [Figure 11(b)], 41.0 min (c), 76.1 min (d), 111.2 min (e), 181.4 min (f), and 239.9 min (g) show highly non-uniform Li distribution in the HOPG, where the false-colored brighter regions are more concentrated in ^{6}Li. From a relatively Li-free initial state, 4 hotspots start to develop near the edge and at the surface of HOPG. As time goes by, more Li enter through those hotspots rather than creating new hotspots.

Downloaded by UNIV OF DELAWARE MORRIS LIB on June 14, 2012 | http://pubs.acs.org
Publication Date (Web): May 7, 2012 | doi: 10.1021/bk-2012-1096.ch006

Downloaded by UNIV OF DELAWARE MORRIS LIB on June 14, 2012 | http://pubs.acs.org
Publication Date (Web): May 7, 2012 | doi: 10.1021/bk-2012-1096.ch006

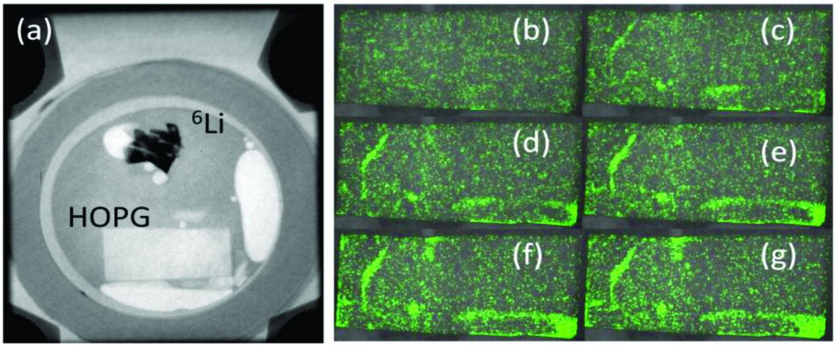

Figure 11. NI of HOPG lithiation (a) cell assembly, (b-g) time sequences of HOPG images

Considering that there are only 4 hotspots, each being of microscopic origin at the onset of lithiation, over the entire macroscopic HOPG crystal, we imagine that lithiation heterogeneity occurs over wide length scales, ranging from individual graphite particles in the order of 10 μm to the thickness of electrode layer to the dimension of battery cells. The activation and evolution of transport hotspots would pose new challenges in quantitative modeling of equivalent circuits and electrochemical performance of batteries. *In situ* NI can help construct more accurate circuit models for the design and optimization of the next generation secondary batteries.

Summary

The application of four *in situ* neutron measurement techniques for studying lithium ion batteries, neutron depth profiling (NDP), neutron reflectivity (NR), small angle neutron scattering (SANS), and neutron imaging (NI) are discussed in this chapter. In addition to introducing fundamentals and physical principles of each technique, their potential applications to studying battery systems are illustrated with specific examples. In each example, special battery cells were constructed and suitable charge/discharge rates were used to enable neutron measurements while maintaining the equivalent electrochemistry of battery operations. As those techniques together provide multi-scale measurements of the Li distribution and transport in active LIBs to yield valuable new insights in the performance and failure of battery systems, further development of neutron techniques is needed to meet the increasing demands in spatial, temporal and composition resolutions in battery research. Complementing other *in situ* and *ex situ* measurement techniques, neutron diagnoses could play a critical role in the design and development of future batteries with greater safety and reliability, higher energy and power density, and lower cost.

Downloaded by UNIV OF DELAWARE MORRIS LIB on June 14, 2012 | http://pubs.acs.org
Publication Date (Web): May 7, 2012 | doi: 10.1021/bk-2012-1096.ch006

Acknowledgments

HW acknowledges the financial support of General Motors Companry and University of Maryland through NIST-ARRA program.

References

1. Whittingham, M. S. *Science* **1976**, *192*, 1126–1127.
2. Whittingham, M. S. *MRS Bull.* **2008**, *33*, 411–419.
3. Tarascon, J. M.; Armand, M. *Nature* **2008**, *451*, 652–657.
4. Goodenough, J. B.; Kim, Y. *Chem. Mater* **2010**, *22*, 587–603.
5. Huang, J. Y.; et al. *Science* **2010**, *330*, 1515–1520.
6. Liu, X. H.; et al. *Nano Lett.* **2011**, *11*, 2251–2258.
7. Balke, N.; et al. *Nat. Nanotechnol.* **2010**, *5*, 749–754.
8. Kalinin, S. V.; et al. *ACS Nano* **2011**, *5*, 5683–5691.
9. Bhattacharyya, R.; et al. *Nat. Mater.* **2010**, *9*, 504–510.
10. Baris, K.; et al. *J. Am. Chem. Soc.* **2011**, *133*, 503–512.
11. Russenbeek, J.; et al. *J. Power Sources* **2011**, *196*, 2332–2339.
12. Shin, H. C.; et al. *Electrochim. Acta* **2011**, *56*, 1182–1189.
13. Sharma, N.; et al. *J. Power Sources* **2010**, *195*, 8258–8266.
14. Sharma, N.; et al. *Solid State Ionics* **2011**, *199-200*, 37–43.
15. Sharma, N.; et al. *J. Phys. Chem. C* **2011**, *115*, 21473–21480.
16. Rodriguez, M. A.; et al. *Electrochem Solid-State Lett.* **2004**, *7*, A8–10.
17. Rosciano, F.; Holzapfel, M.; Scheifele, W.; Novak, P. *J. Appl. Crystallogr.* **2008**, *41*, 690–694.
18. Colin, J. F.; Godbole, V.; Novák, P. *Electrochem. Comm.* **2010**, *12*, 804–807.
19. Du, G.; et al. *Adv. Funct. Mater.* **2011**, *21*, 3990–3997.
20. Bergstom, O.; Andersson, A. M.; Edstrom, K.; Gustafsson, T. *J. Appl. Cryst.* **1998**, *31*, 823–825.
21. Downing, R. G.; Lamaze, G. P.; Langland, J. K.; Hwang, S. T. *NIST J. Research* **1993**, *98*, 109.
22. Biersack, J. P.; Fink, D. *Nucl. Instr. Meth.* **1973**, *108*, 397–399.
23. Lamaze, G. P.; et al. *J. Power Sources* **2003**, *680*, 119–121.
24. Whitney, S. M.; Biegalski, S. R. F.; Downing, R. G. *J. Radioanal. Nucl. Chem.* **2009**, *282*, 173–176.
25. Whitney, S. M.; Biegalski, S. R.; Huang, Y. H.; Goodenough, J. B. *J. Electrochem. Soc.* **2009**, *156*, A886–A890.
26. Danilov, D.; Niessen, R. A. H.; Notten, P. H. L. *J. Electrochem. Soc.* **2011**, *158*, A215–A222.
27. Shrikant, C.; Nagpure, R.; Downing, R. G.; Bhushan, B.; Babu, S. S.; Cao, L. *Electrochimica Acta* **2011**, *56*, 4735–4743.
28. Oudenhoven, J. F. M.; Labohm, F.; Mulder, M.; Niessen, R. A. H.; Mulder, F. M.; Notten, P. H. L. *Advanced Materials* **2011**, *23*, 4103–4106.
29. Ziegler, J. F.; Ziegler, M. D.; Biersack, J. P. *Nucl Instrum Methods Phys Res B* **2010**, *268*, 1818–1823.
30. Owejan, J. E.; Owejan, J. P.; DeCaluwe S. C.; Dura J. A. (to be published)

In Polymers for Energy Storage and Delivery: Polyelectrolytes for Batteries and Fuel Cells; Page, K., et al.;
ACS Symposium Series; American Chemical Society: Washington, DC, 2012.

Downloaded by UNIV OF DELAWARE MORRIS LIB on June 14, 2012 | http://pubs.acs.org
Publication Date (Web): May 7, 2012 | doi: 10.1021/bk-2012-1096.ch006

31. Krueger, S.; Meuse, C. W.; Majkrzak, C. F.; Dura, J. A.; Berk, N. F.; Tarek, M.; Plant, A. L. *Langmuir* **2001**, *17*, 511.
32. Seah, M. P.; et al. *Surf. Interface Anal.* **2004**, *36*, 1269–1303.
33. Seah, M. P.; et al. *Surf. Interface Anal.* **2009**, *41*, 430–439.
34. Kent, M. S.; et al. *Macromolecules* **1992**, *25*, 6240–6247.
35. Majkrzak, C. F.; et al. In *Neutron Scattering in Biology: Techniques and Applications*; Fitter, J., Gutberlet, T., Katsaras, J., Eds.; Springer: 2006; pp 225–263.
36. Wacklin, H. P. *Curr. Opin. Colloid Interface Sci.* **2010**, *15*, 445–454.
37. Dura, J. A.; et al. *J. Appl. Phys.* **2011**, *109*, 093501.
38. Rehm, Ch.; Maletta, H.; Fieber-Erdmann, M.; Holub-Krappe, E.; Klose, F. *Phys. Rev. B* **2002**, *65*, 113404.
39. Russell, T. P. *Mater. Sci. Rep.* **1990**, *5*, 171–271.
40. Dura, J. A.; Murthi, V. S.; Hartman, M.; Satija, S. K.; Majkrzak, C. F. *Macromolecules* **2009**, *42*, 4769–4774.
41. Fitzsimmons M. R.; Majkrzak, C. F. In *Modern Techniques for Characterizing Magnetic Materials*; Zhu, Y., Ed.; Kluwer Acedemic Publishers: Boston, 2005.
42. Hjorvarsson, B.; et al. *Phys. Rev. Lett.* **1997**, *79*, 901.
43. Majkrzak, C. F. *Physica B* **1995**, *213*, 904.
44. Dura, J. A.; Pierce, D. J.; et al. *Rev. Sci. Instrum.* **2006**, *77*, 074301.
45. Majkrzak, C. F.; et al. *Physica B* **1998**, *248*, 338–342.
46. Kienzle, P. A.; O'Donovan, K. V.; Ankner, J. F.; Berk, N. F.; Majkrzak, C. F. http://www.ncnr.nist.gov/reflpak, 2000−2006.
47. Parratt, L. G. *Phys. Rev.* **1954**, *95*, 359.
48. Rolison, D. R.; Nazar, L. F. *MRS Bull.* **2011**, *36*, 486.
49. Details of SANS data analysis could be found in NIST wetsite: http://www.ncnr.nist.gov/programs/sans/data/red_anal.html.
50. Markervich, E.; Salitra, G.; Levi, M. D.; Aurbach, D. *J. Power Sources* **2005**, *146*, 146–150.
51. Aurbach, D.; Koltypin, M.; Teller, H. *Langmuir* **2002**, *18*, 9000–9009.
52. Rhodes, K.; Kirkham, M.; Meisner, R.; Parish, C. M.; Dudney, N.; Daniel, C. *Rev. Sci. Instrum.* **2011**, *82*, 075107.
53. Shearing, P. R.; Howard, L. E.; Jørgensen, P. S.; Brandon, N. P.; Harris, S. J. *Electrochem. Commun.* **2010**, *12*, 374–377.
54. Goers, D.; et al. *J. Power Sources* **2004**, *130*, 221–226.
55. Riley, G. V.; Hussey, D. S.; Jacobson, D. L. *ECS Trans.* **2009**, *25*, 75–83.
56. Siegel, J. B.; et al. *J. Electrochem. Soc.* **2011**, *158*, A523–A529.
57. Nikolay, K.; et al. *Mater. Today* **2011**, *14*, 248–256.
58. Hussey, D. S.; Jacobson, D. L.; Coakley, K. J.; Vecchia, D. F.; Arif, M. *ASME J. Fuel Cell Sci. Technol.* **2010**, *7*, 021024.

Downloaded by UNIV OF GUELPH LIBRARY on June 14, 2012 | http://pubs.acs.org
Publication Date (Web): May 7, 2012 | doi: 10.1021/bk-2012-1096.ch007

Chapter 7

Vanadium Redox Flow Batteries for Electrical Energy Storage: Challenges and Opportunities

R. Zaffou,* W. N. Li, and M. L. Perry

United Technologies Research Center, 411 Silver Lane, East Hartford, CT 06108
***e-mail: zaffour@utrc.utc.com**

A Flow-Battery System is an Electrical Energy Storage approach that was originally conceived by NASA during the energy crises of the 1970s. A flow battery utilizes reversible redox couples on two electrodes to store chemical energy. However, instead of storing the electrochemical reactants within the electrode, as in a conventional battery, the reactants are dissolved in electrolytic solutions and stored in tanks external to the flow battery stack. Flow batteries are emerging as a potential electricity storage technology to support a more efficient, reliable, and cleaner electrical energy market. Some of the promising applications of flow batteries are related to load management of large-scale electricity supply to the grid (*e.g.*, peak shaving, power quality, spinning reserves). Flow battery technology can also offer solutions to issues associated with the integration of intermittent renewable energy resources (*e.g.*, wind, solar) with the power grid by making these power resources more stable, dependable, and dispachable. The objective of this paper is to provide an overview, status, and challenges of the flow-battery technology with an emphasis on vanadium redox-based system, which will also include an examination of recent results demonstrated by the United Technologies Research Center. Progress in the area of membranes for vanadium redox flow battery applications will be highlighted including a discussion of the important membrane improvements that would enable significantly higher power density which is needed to accelerate the commercialization of flow-battery technology.

In Polymers for Energy Storage and Delivery: Polyelectrolytes for Batteries and Fuel Cells; Page, K., et al.;
ACS Symposium Series; American Chemical Society: Washington, DC, 2012.

Introduction

The interest in Electrical Energy Storage (EES) has risen considerably in recent years as the demand for efficient, dependable, and cleaner electricity has increased. The function of an EES device is to provide a temporary medium to store electricity which can then be released when needed. Traditionally, electricity is generated by an electricity generator that is driven by a heat engine consuming fossil fuels (*e.g.*, coal, natural gas) or driven by some other means such as turbines running on falling water or wind. Without an EES device, electricity cannot be stored and a real-time balance between electricity generation and demand is required at any given time to avoid any disruption that can result in poor power quality of the electrical supply system (*e.g.*, variations in frequency and/or voltage). If not controlled within acceptable limits, instability of power supply can lead to equipments failure and in some cases blackouts. Matching the electricity supply and demand is very challenging especially for grid-scale electrical supply, the largest supply system in the world. In the United States alone, the electrical grid includes 15,000 generators and about 5,600 distribution facilities serving millions of customers with a demand that is constantly changing at varying rates from hour-to-hour, day-to-day, and season-to-season (*1*). Currently, the generation and use are matched continuously by operating *peaking* generators in addition to the primary generators. These *peaking* generators run intermittently to meet the excess electricity demand and they remain underutilized during off-peak periods. When responding to peak demand, these generators are required to change their load output up or down within minutes to maintain stable power supply. This mode of operation forces the *peaking* generator to run inefficiently, therefore, increasing its consumption of fossil fuel as well as the release of more greenhouse gases. The ability to store electricity at a large-scale provides many significant benefits, for instance, *peaking* generators can be replaced by EES system that can provide a source for both storing excess electricity during low usage and also to provide power back to the grid when the generation capacity is exceeded. The deployment of EES technology can also eliminate greenhouse gas emissions from *peaking* generators. In addition, EES technology can enable large growth and penetration of renewable energy resources (*e.g.*, solar, wind) into the grid by making these power resources stable, dependable and dispachable (*2*). A number of in-depth studies to examin potential applications of energy storage technolgies for EES can be found elsewhere (*2*, *3*).

Energy storage for Grid-scale applications covers a wide spectrum of technologies that vary in power, energy capacity, and response time. The most mature and widely used storage technology for Grid-scale EES applications that require long discharge durations is pumped hydro. This form of storage technology is based on storing energy in the form of water. During off-peak periods, water is pumped to high elevation reservoirs which can be released during peak demand to operate turbines that generate electricity. Despite its reliability and cost effectiveness, the geographical constraints as well as environmental concerns limit the growth of pumped hydro technology to meet all of the requirements of EES for Grid-scale systems.

Downloaded by UNIV OF GUELPH LIBRARY on June 14, 2012 | http://pubs.acs.org
Publication Date (Web): May 7, 2012 | doi: 10.1021/bk-2012-1096.ch007

Rechargeable batteries are emerging as an attractive option for EES applications. Unlike pumped hydro, rechargeable batteries are deployable and have a fast response time. In addition, batteries, depending on their chemistries, can meet the needs for EES applications requiring a wide range of power and energy capacity. Batteries are devices that convert chemical energy into electricity in an electrochemical process by which an exchange of electrons between reactive materials takes place by means of redox (reduction and oxidation) reactions. This process is reversible which allows the battery system to be utilized for both storage and delivery of electricity. Amongst the well-known rechargeable battery technologies are lead-acid, lithium ion, and vanadium redox flow system. Due to their unique design, vanadium redox flow batteries (VRFBs) provide significant advantages over traditional batteries for Grid-scale EES applications (*2*, *4*). In response to the demand for large-scale EES, interest in VRFB technology has been renewed and the number of field demonstrations ranging from kW to MW scale has been on the rise (*5*). The goal of this paper is to provide an overview, status, and challenges of the flow-battery technology with an emphasis on VRFB-based systems. The discussion includes progress and opportunities namely in the area of membranes and cell designs that can enable much needed performance improvement to accelerate the commercialization of VRFB technology.

Downloaded by UNIV OF GUELPH LIBRARY on June 14, 2012 | http://pubs.acs.org
Publication Date (Web): May 7, 2012 | doi: 10.1021/bk-2012-1096.ch007

Flow-Battery Technology

A Flow-Battery System (FBS) is an EES approach that was originally conceived by NASA during the energy crises of the 1970s (*5*). Analogous to conventional rechargeable batteries, a flow battery utilizes reversible electrochemical couples on two electrodes to store chemical energy. However, instead of storing the electrochemical reactants within the electrode, as in a conventional battery, the reactants are dissolved in electrolytic solutions and stored in tanks external to the reactor. The reactor is a stack of cells; each cell contains sites where electrochemical electron-transfer reactions occur as the reactants flow through the cells, which is analogous to a fuel cell. Therefore, a FBS is a sort of hybrid of a conventional rechargeable battery and a regenerative fuel cell.

Because of its unique configuration of a separate reactor and reactant storage, a FBS offers some key advantages relative to conventional batteries. The most obvious advantage is that a FBS has inherent design flexibility because it is based upon two key modular components (*i.e.*, stacks and reactant tanks) that enable products with a wide range of power-to-energy ratios built upon common components. There are also some less obvious advantages to flow batteries. Conventional batteries rely on at least one solid active material, which limits the conductivity of the electrodes and therefore the amount of current that can flow through them, as well as the amount of active material that can be stored in each electrode. Since the active materials in flow batteries are stored in tanks, flow batteries can have extremely large energy capacities without using thick electrodes. In other words, a flow battery can theoretically offer both high power and energy density in a single device, whereas the design of conventional batteries always entails a trade-off between high power (thin electrodes) *or* high energy (thick electrodes). Additionally, as a conventional battery undergoes repeated charge/discharge cycles, the electrode materials expand and contract, which results in degradation over time and severely limits the cyclic lifetimes of conventional batteries; this is especially true for batteries with relatively thick electrodes (*i.e.*, high energy batteries) undergoing deep Depth-of-Discharge (DOD) cycles. Flow-battery electrodes are not required to undergo changes during cycles, since the changes are occurring in the active materials that are dissolved in solutions. Therefore, the cycle life of FBS cells is *not* dependent on DOD, and the utilization of the relatively expensive active materials can be very high without impacting cyclic life. Therefore, flow batteries can be designed to deliver rated power for multiple hours without having negative impacts on cycle life or power density of the flow-battery stack.

In summary, among the myriad of battery technologies, FBSs possess several key advantages that make them particularly, if not uniquely, suited for Grid-Scale EES. A FBS can undergo deep cycles on a daily basis with minimal degradation over years of operation. A FBS has inherent design flexibility that enables products with a wide range of power-to-energy ratios built upon common components. Additionally, flow batteries can have large energy capacities and high power capability in a single device. A FBS that offers both high energy *and* power capability can potentially be well suited for a wide range of EES applications.

Much like conventional batteries, there are multiple flow-battery chemistries. Flow-battery technologies that have also been developed, to various degrees of maturity, include zinc-bromine (*6*), polysulfide-bromide batteries (*7*), iron-chrome batteries (*6*), and VRFBs. Batteries operating on zinc-bromine are considered a type of hybrid FBS. During charge, zinc is deposited onto the negative electrode while bromine is formed at the positive electrode. The anolyte and catholyte solutions contain a zinc bromide salt dissolved in an aqueous solution. During discharge, metallic zinc is dissolved and stored again in the anolyte solution while bromine is converted back to bromide at the catholyte solution. While this type of battery has been attracting interest, the corrosiveness of bromine and the electroplating of zinc at the anode remain a major limitation for the zinc-bromine battery technology compared to other flow-battery technologies. Polysulfide-bromide batteries, unlike zinc-bromine batteries, are considered true flow battery systems since both anolyte and catholyte redox couples remain dissolved in the electrolyte during charge and discharge. Despite of this advantage, polysulfide-bromide batteries still suffer from durability issues due the corrosive nature of bromine as well as the sulfur precipitation resulting from bromine crossing over from cathode to anode during charge. Amongst the existing flow-battery technologies, VRFBs has especially attractive attributes for Grid-scale EES applications. The attractiveness of the vanadium-based FBSs stems from the fact that, in addition to being a true flow-battery system, the anolyte and catholyte solutions are the same species, hence the name all-vanadium flow battery is sometimes used. During charge, the oxidation state of the vanadium ions changes depending on whether these reactive species are present on the anode or cathode. Instead of being a durability issue, as in the case of

Downloaded by UNIV OF GUELPH LIBRARY on June 14, 2012 | http://pubs.acs.org
Publication Date (Web): May 7, 2012 | doi: 10.1021/bk-2012-1096.ch007

polysulfide-bromide batteries, the impact of cross-over contamination amongst the various vanadium ions between the anolyte and catholyte solutions is limited to system efficiency loss. Additionally, vanadium solutions have relatively low vapor pressure and are less corrosive especially when compared to zinc- bromine and polysulfide-bromide batteries. A comparison between conventional and flow battery based technologies for grid-scale EES is provided in Table I.

Table I. A comparison between conventional and flow battery-based technologies

Technology	*Major attributes*	*Major Issues*
Conventional rechargeable batteries (*e.g.,* lead-acid, Li-ion)	- High round-trip efficiencies - No precious-metal catalysts - High energy densities	- Power & energy not independent - Limited life cycle - Continuous self-discharge
Redox flow batteries (*e.g.*, vanadium, polysulfide-bromide)	- High round-trip efficiencies - No precious-metal catalysts - Energy and power independent - Long life cycle - Low self-discharge rates	- Complex (relative to conventional battery) - Low energy density(relative to batteries) - Low power density cells
Hybrid redox flow batteries (*e.g.*, Zn-Br)	- High round-trip efficiencies - Low self-discharge rates - Moderate energy densities	- Complex (relative to conventional battery) - Power & energy not independent - Limited life cycle (Zn electrode) - Precious-metal catalysts(Br electrode) - Vapor pressure of Br_2

Vanadium Redox Flow Battery Technology

The principle of operation of VRFB system is based on oxidation and reduction of various vanadium ions. During charge, at the anode electrode, vanadium (V^{3+}) is reduced to vanadium (V^{2+}) ion by accepting an electron resulting from the oxidation of vanadium (V^{4+}) to vanadium (V^{5+}) ion at the cathode in the presence of an external electrical source. The opposite reactions occur during discharge which enables the battery to provide electrical power back to an external load. Details of half-cell reactions occurring at the anode and cathode electrodes during charge are:

Downloaded by UNIV OF GUELPH LIBRARY on June 14, 2012 | http://pubs.acs.org
Publication Date (Web): May 7, 2012 | doi: 10.1021/bk-2012-1096.ch007

Positive Reaction:

$$VO^{2+} + H_2O - e^- \rightarrow VO_2^+ + 2H^+ \qquad E^\circ = 1.00V$$

Negative Reaction:

$$V^{3+} + e^- \rightarrow V^{2+} \qquad E^\circ = -0.255V$$

Net Reaction:

$$VO^{2+} + H_2O + V^{3+} \rightarrow VO_2^+ + 2H^+ + V^{2+} \quad E^\circ = 1.255V$$

A liquid containing a mixture of water and sulfuric acid, typically 1 to 3M H_2SO_4 solution, is used as an electrolyte to support the redox reactions, since protons are also consumed at the cathode during discharge, as well as to provide an ionically conductive medium for proton transport within the membrane and the electrodes. A VRFB cell contains two porous carbon-based layers (*e.g.*, carbon felt) to form anode and cathode electrodes. The primarily role of these carbon-based porous layers is to provide a path for reactant transport to the surface of the carbon where the electrochemical reactions can take place. Sandwiched between these electrodes is a separator, typically an ion-exchange membrane (*e.g.*, Nafion™). The basic function of the membrane separator is to enable conduction of protons for charge neutrality and to also minimize battery self-discharge due to mixing of charged vanadium ions between the anolyte and catholyte solutions. The electrolyte solutions are typically stored inside plastic tanks external to the battery. During operation, these solutions are supplied to the electrodes using a reactant delivery system provided by additional plates, referred to as bipolar plates, positioned next to the electrode layers. Additionally, these bipolar plates, which are electrically conductive (*e.g.*, solid graphite), provide mechanical support for the membrane and electrodes and also separate each cell in a stack assembly. Figure 1 illustrates the principle of assembly and operation of a VRFB cell. The size of the stack determines the power output (kW) of the system; specifically, the area of the electrodes determines the current (i.e., amps) and the number of cells determines the stack voltage. The total energy capacity (kWhr) of the flow-battery system is determined by the amount of vanadium ions present in the solutions, which is a function of the electrolyte volume and vanadium concentration. The module nature of a VRFB system makes this technology attractive for many applications with a wide range of power-to-energy ratio. For applications that require high power capacity, additional stack modules can be added, whereas, for high energy application that require long run time, larger electrolyte tanks can simply be employed.

Downloaded by UNIV OF GUELPH LIBRARY on June 14, 2012 | http://pubs.acs.org
Publication Date (Web): May 7, 2012 | doi: 10.1021/bk-2012-1096.ch007

Downloaded by UNIV OF GUELPH LIBRARY on June 14, 2012 | http://pubs.acs.org
Publication Date (Web): May 7, 2012 | doi: 10.1021/bk-2012-1096.ch007

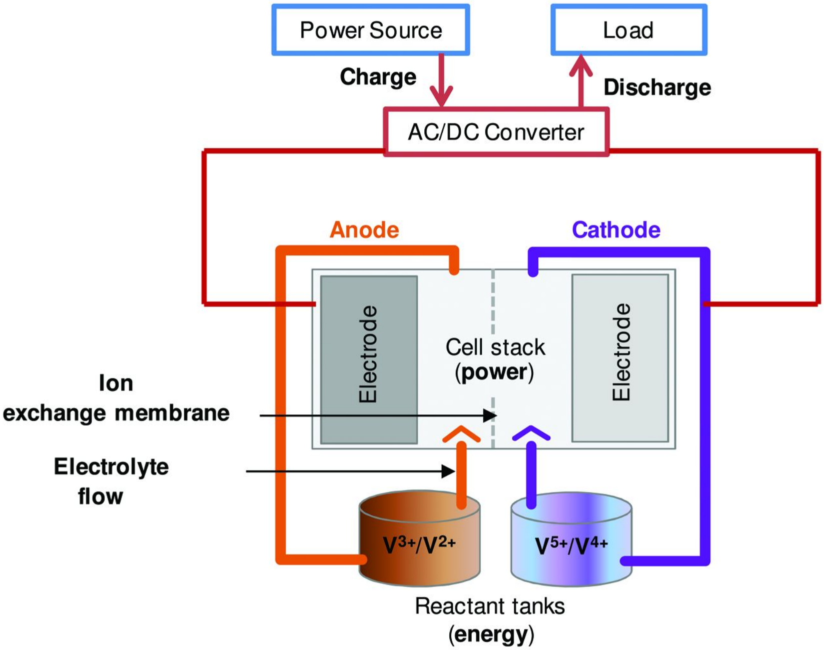

Figure 1. Principle of assembly and operation of a VRFB system

Despite all of these inherent advantages, the deployment of VRFB products has been limited to field demonstrations, which have shown that this technology is capable of long life; specifically, over 5 years of unmanned service with almost daily use (*3*) and thousands of deep charge/discharge cycles with high round-trip electrical efficiencies (*8*). The unsuccessful commercialization of the flow batteries, to date, is because this technology in general is best suited for large, stationary applications (such as those targeted by the Grid), which are known to have very challenging cost targets. This is because fossil-fueled "*peaking* plants" have been the primary means to close the gap between electricity supply and demand on the grid created primarily by fluctuations in demand. However, growing demand for cleaner, reliable, and secure sources of electricity have resulted in a renewed interest in flow-battery technologies. Despite this interest, the high cost of the flow batteries, including VRFB-based products, remains a major barrier towards their competiveness and their commercial-viability.

The heart of a VRFB system is the stack, which is also a major contributor to the cost of the overall flow-battery system. This is especially true at relatively low production volumes, since the stack is always a custom component built from hundreds of custom parts, whereas the rest of the system can be built from essentially off-the-shelf components (*e.g.*, pumps, valves, plumbing, controller, *etc*.). As is the case in conventional batteries, an essential means to significant cost reductions is to minimize the non-reactant materials, especially materials within the battery (*e.g.*, electrodes, separators, current collectors) since these materials are generally more expensive because they must be stable in an electrochemical environment (*e.g.*, be corrosion resistant). In a FBS, the electrolyte reservoirs are already as inexpensive as possible (*e. g.*, plastic tanks), so the key to reducing the amount of electrochemically-stable materials required is to reduce the size of the FBS stacks. The performance of flow batteries including VRFB is low (*e.g.*, typically ≤ 0.1 W/cm^2 of active area) (*6*), especially relative to fuel cells, which makes the cell-stack assembly large and expensive. Improving stack performance is a key to reducing the stack size and hence achieving a lower stack cost.

High Power Density VRFB System

Downloaded by UNIV OF GUELPH LIBRARY on June 14, 2012 | http://pubs.acs.org
Publication Date (Web): May 7, 2012 | doi: 10.1021/bk-2012-1096.ch007

The performance losses in a VRFB cell are originated from three major sources: activation overpotential, ohmic overpotential, and concentration overpotential. Activation overpotential is associated with sluggish kinetics and low catalyst activity towards the oxidation and reduction of the vanadium ions. Ohmic overpotential is associated with resistance to proton and/or electron transport. Concentration overpotential is associated with transport of reactive ions to the catalyst surface at the electrode layers. There are other sources of polarization, beyond the three major sources; these additional losses are associated with crossover of charged vanadium ions (*e.g.*, V^{2+}, V^{5+}) across the separator membrane resulting in battery self-discharge and hence loss in system efficiency. The rate of vanadium-ion crossover depends on the characteristics of the membrane separator and also the operating conditions (*e.g.*, temperature, concentration, membrane thickness). In addition, small current leaks can occur within a battery due to internal short circuits caused by an electrically conductive current path either through the membrane and/or through the electrolyte connecting different cells in a battery stack (*e.g.*, shunt current (*9*)). These currents are relatively small; however, their effect can be prevalent if the operating current is of the same order as the short current.

Conventional VRFB systems are known to operate at current densities of 50 to 80 mA/cm^2 (*10*); under these relatively low current densities, concentration as well as ohmic overpotentials are relatively small resulting in a VRFB performance that is limited primarily by kinetic losses. To achieve high current density operation, new vanadium flow-battery architecture that enables, in addition to high catalyst utilization, high reactant transport rates and low ohmic losses within the electrodes to support high current density rates, is critical.

Unlike conventional batteries, which operate at similar current densities (*e.g.*, 5 to 50 mA/cm^2 is not uncommon), flow batteries have the advantage of forced convection through the electrodes. The forced convection through the electrode can, in principle, support much higher current rates by enabling effective delivery of reactants to the reaction sites and hence reducing the transport losses that are expected to accompany high currents operation. Since the electrode layers are where all three major sources of overpotential are present, they are critical to the performance in a VRFB cell. Therefore, enhancing the performance of the electrodes is a key enabler towards improving the power density of VRFB system. These electrodes, which are 3-dimensional porous layers are typically made from

Downloaded by UNIV OF GUELPH LIBRARY on June 14, 2012 | http://pubs.acs.org
Publication Date (Web): May 7, 2012 | doi: 10.1021/bk-2012-1096.ch007

graphitized carbon fibers, for example, in the form of a non-woven structure (*e.g.*, carbon felt). These electrodes need to have high electrocatalytic activity towards vanadium redox reactions, be electrically conductive, be stable under the operating potentials and the acidic environment of the battery, as well as providing a porous medium to enable the transport of reactants to the catalyst surface (*e.g.*, carbon).

One approach to improving the power density of a VRFB system is to improve the operating current densities. UTRC has developed proprietary cell and electrode designs that enable much higher performance than has been demonstrated with conventional flow-battery cells. A comparison of power densities measured on UTRC's cells and conventional VRFB cells is shown in Figure 2. The improved performance enables order-of-magnitude higher current densities and substantially higher power densities at reasonable cell efficiencies. For example, on discharge, UTRC's VRFB system is capable of operating at 1.2 V (~80% voltage efficiency) at a current density of 0.6 A/cm^2, which reflects a ~ 6X improvement in the operating current density compared to conventional VRFB system at the same voltage efficiency. These dramatic performance improvements have been obtained using conventional VRFB materials and chemistries.

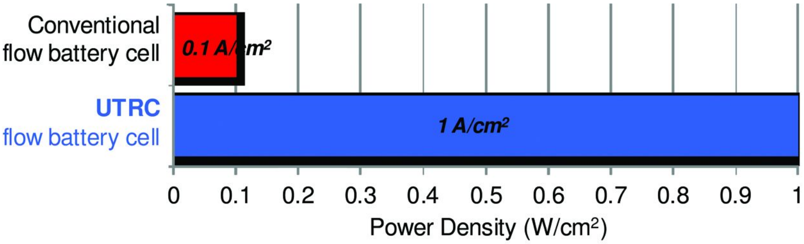

Figure 2. Comparison of power density during discharge of VRFB sub-scale cells (25-cm^2). UTRC cells utilize improved cell design.

While the commercialization of VRFB technology can benefit greatly from innovative design changes resulting in high power densities, further advancements in materials can certainly lead to even greater impact. Research in this area to date has been primarily dedicated to the development of potentially less expensive materials for VRFB system; however the impact of these efforts on system cost has been less than what can be obtained from an order-of-magnitude improvement in power density. To have the greatest impact on system cost, new and improved materials suitable for high power density VRFB cells should be developed. It is particularly important to note that the material requirements for this new class of VRFB cells vary from those in conventional cell designs. This difference is primarily driven by the high operating current density. A discussion of the requirements of these new materials, which vary depending on the functionality of each component within the VRFB cell, is beyond the scope of this paper, however, a review of recent research in the area of membrane separator with a discussion of important future direction is included here.

Downloaded by UNIV OF GUELPH LIBRARY on June 14, 2012 | http://pubs.acs.org
Publication Date (Web): May 7, 2012 | doi: 10.1021/bk-2012-1096.ch007

Membrane Separators for VRFB System

In addition to the electrode layers, the membrane separator is a key component in a VRFB system. Providing a barrier against transfer of water and vanadium ions between anolyte and catholyte solutions while allowing charge-carrier (*e.g.*, proton) transport are key functions of the separator. Cross-contamination is undesirable as it results in energy loss and decrease in system efficiency. Besides these transport requirements, the membrane separator must be chemically and mechanically stable.

The most commonly used and studied membrane for VRFBs is Nafion™ (*11*), an ion-exchange perfluorosulfonic acid membrane that incorporates a poly(tetrafluoroethylene), (*e.g.,* Teflon™), backbone with perfluorvinyl ether groups terminated with sulfonic groups (Figure 3) (*12*). The fluorocarbon backbone provides Nafion™ with good mechanical properties and the sulfonic groups make it an excellent ionic conductor. Nafion™ was invented in 1960 by DuPont where it was first used in chloro-alkali industry (*12*). Due to its high proton conductivity and excellent stability, the usage of Nafion™ membranes have expanded to other applications including electrolyzers, polymer-electrolyte fuel cells, and flow batteries (*e.g.*, VRFBs). Despite its excellent chemical and mechanical stability and its facile cation transport, the opposing membrane requirements for applications where Nafion™ is commonly used represents an opportunity to develop better membranes that are more optimized for the VRFB application. Table II summarizes the requirements for VRFB membrane compared to those found in polymer-electrolyte fuel-cell applications. For VRFB applications, the low selectivity to ion crossover and the high affinity to water are significant limitations of Nafion™ membranes. Figure 4 illustrates the crossover of different vanadium ions and their corresponding fluxes in an ion-exchange membrane (*13*, *14*). Furthermore, due to its relatively high cost, the use of Nafion™ membrane in VRFB products is commercially unattractive, since it currently constitutes the most expensive component in the stack (*14*, *15*). What is needed is a low cost new VRFB membrane having similar properties found in Nafion™ with regards to its mechanical and chemical stability meanwhile having high selectivity against crossover of ions and water while allowing facile proton transport.

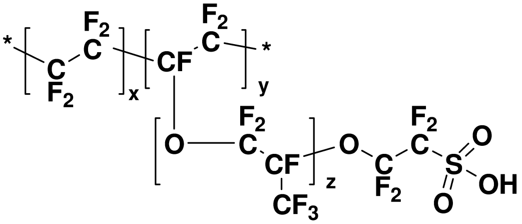

Figure 3. Structure of Nafion™

Downloaded by UNIV OF GUELPH LIBRARY on June 14, 2012 | http://pubs.acs.org
Publication Date (Web): May 7, 2012 | doi: 10.1021/bk-2012-1096.ch007

Table II. A comparison between operational requirement for membranes for VRFB and PEMFC applications[a]

Operational Requirements	*VRFB*	*PEMFC*
Low gas permeabiity	na	yes
Low liquid permeability	yes	na
High proton conductivity	not required in the presence of sulfuric acid	yes
Chemical stability	yes (VO_2^+ attack)	yes (peroxide attack)
Mechnical stability	yes	yes[b]
Operability under dry conditions	na	yes
Tolerance to low RH and high temperatures	na	yes[c]

[a] PEMFC: polymer electrolyte fuel cell RH: Relative humidity na: Not applicable. [b] Humidity cycling, which is not present for VRFBs, is a significant contributor to mechanical failure in Nafion™ for PEMFCs. [c] Only for high temperature PEMFCs (*e.g.*, T > 100°C, RH<30).

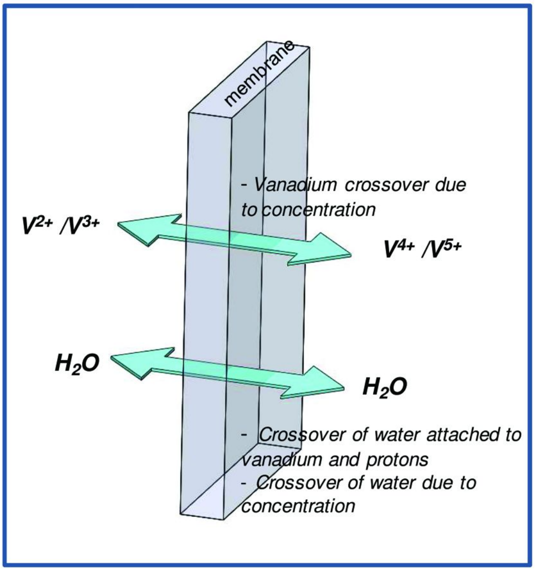
membrane
- Vanadium crossover due to concentration
V^{2+} /V^{3+}
V^{4+} /V^{5+}
H_2O
H_2O
- Crossover of water attached to vanadium and protons
- Crossover of water due to concentration

Figure 4. Illustration of water and vanadium ions crossover in a VRFB system (13, 16).

In recent years, many studies have been published on various approaches to mitigate issues related to Nafion™ for VRFB applications by either modifying the structure of Nafion™ or by using new class of membranes. The goal of the next section is to provide a highlight of some of the work published in this area. More detailed reviews can be found elsewhere (*11*, *15*). A summary of these studies is presented in Table III.

For Nafion™ modifications, by employing inorganic additives to impart membrane hydrophilicity, Xi, *et al.*, have successfully demonstrated a significant decrease in vanadium cross-diffusion through a Nafion™ membrane treated with SiO_2 nanoparticles without sacrificing its proton conductivity and stability (*17*). Other inorganic additives, such as titanium dioxides (TiO_2) and zirconium phosphate (ZrP) have also been investigated. TiO_2 linked with organic silica to form Nafion™ /Si/Ti hybrid membrane has also shown a reduction in vanadium permeability and water crossover compared to unmodified Nafion™ membrane (*18*). Similarly, ZrP/Nafion™ 1135 hybrid membrane was also found to effectively decrease VO^{2+} transport across membrane without any loss of proton conductivity (*19*). Vanadium transport was found to decrease by incorporating an organic layer with high selectivity to vanadium ion. Luo, *et al.*, proposed modification of Nafion™ based on Donnan exclusion to impede the absorption of multivalent cations like vanadium ions onto the membrane surface. A 2.5 percent and 5 percent Polyethylenimine (PEI)-based organic layer resulted in a decrease in vanadium diffusion by 95 percent and 86 percent, respectively (*20*). However, the PEI layer had a negative impact on the membrane resistance. The vanadium-ion selectivity was also enhanced by incorporating polyvinylidene fluoride (PVDF) to make a Nafion™/PVDF blend membrane (*21*). The miscibility of PVDF in Nafion™ allows the polymer blend to attain the mechanical and conductivity properties of Nafion™. It is believed that the increase of the ion selectivity observed in PVDF modification is a result of the decrease in swelling of Nafion™ membrane due to the crystallization of PVDF. Improved ion selectivity has also been reported on modified Nafion™ using pyrrole, sulfonated poly(tetramethydiphenyl ether ether ketone) (SPEEK), and layer-by-layer deposition with poly(diallydimethylammonium chloride-polyaion poly(sodium styrene sulfonate) (PDDA-PSS) (*22–24*). An *in-situ* sol-gel process was used for the synthesis of Nafion™/SiO_2 hybrid membrane, which has been applied by Teng, *et al.*, to prepare an organic silicate (ORMOSIL) modified Nafion™ 117 membrane (Nafion™/ORMISIL), which demonstrated nearly a 20 folds lower permeability of the VO^{2+} compared to untreated Nafion™ (*25*).

Besides Nafion™, other fluorocarbon-based polymers, such as poly(ethylene-co-tetrafluoroethylene) (ETFE) and PVDF have been explored as candidates for VRFB applications. Unfortunately, these membranes suffer from poor ionic conductivity (*26*). Recently, Qiu, *et al.*, has demonstrated improved ionic conductivity by incorporating ionic groups (styrene and maleic anhydride) into PVDF membrane via grafting (*26*).

Downloaded by UNIV OF GUELPH LIBRARY on June 14, 2012 | http://pubs.acs.org
Publication Date (Web): May 7, 2012 | doi: 10.1021/bk-2012-1096.ch007

Downloaded by UNIV OF GUELPH LIBRARY on June 14, 2012 | http://pubs.acs.org
Publication Date (Web): May 7, 2012 | doi: 10.1021/bk-2012-1096.ch007

Table III. Summary of membranes tested for VRFB systems[a]

Membrane Category	*Membrane Type*	*Chemical Composition*	*Thickness (μm)*	*Ionic Conductivity (mS/cm)*	*Water Uptake (%)*	*Ion Diffusion Coefficient (10^{-7} cm^2/min)*				*Chemical Stability*	*Ref*
						V^{2+}	V^{3+}	VO^{2+}	VO_2^+		
perfluorinated polymer	Nafion115	PFSA	127	-	-	52.61	19.33	40.95	35.38	Baseline	(*11*)
	Nafion117		183	58.7	26	-	38	36.9	7	Baseline	(*17*)
	Nafion1135		89	10	-	-	-	2.4	-	-	(*19*)
modified perfluorinated polymer	Nafion117/SiO2	Nafion + SiO2 nanoparticle	204	56.2	21.5	-	7.5	3.5	-	no decay of CE and EE up to 100cycles (60 mA/cm2)	(*17*)
	Nafion1135/ZrP	ZrP modified Nafion1135	99	6.9	-	-	-	0.19	-	-	(*19*)
	Nafion117/ ORMOSIL	morganic silicate modified Nafion	217	57.5	23.6	-	-	1.85	-	no decay of CE and EE > 100cycles (60 mA/cm^2)	(*25*)
	Nafion117/ organosilica-TiO2	Organic silica_TiO2 modified Nafion	225	17.9	22.5	-	-	4.3	-	no decay of CE and EE up to 100cycles (60 mA/cm^2)	(*18*)

Continued on next page.

In Polymers for Energy Storage and Delivery: Polyelectrolytes for Batteries and Fuel Cells; Page, K., et al.;
ACS Symposium Series; American Chemical Society: Washington, DC, 2012.

Downloaded by UNIV OF GUELPH LIBRARY on June 14, 2012 | http://pubs.acs.org
Publication Date (Web): May 7, 2012 | doi: 10.1021/bk-2012-1096.ch007

Table III. (Continued). Summary of membranes tested for VRFB systems[a]

Membrane Category	***Membrane Type***	***Chemical Composition***	***Thickness (µm)***	***Ionic Conductivity (mS/cm)***	***Water Uptake (%)***	***Ion Diffusion Coefficient (10^{-7} cm²/min)***				***Chemical Stability***	***Ref***
						V^{2+}	V^{3+}	VO^{2+}	VO_2^+		
	Nafion117/PEI	2.5% PEI	196	15.8	-	-	-	5.23	-	Stable OCV for >265hrs compared to 100hr for N117	(*20*)
		5% PEI	208	15.5	-	-	-	1.7	-	-	(*20*)
	Nafion /PDDA-PSS3	3 layers of PDDA-PSS	-	51.8	-	-	5.12	-		-	(*24*)
	Nafion /PDDA-PSS5	5 layers of PDDA-PSS	-	50.3	-	3.17	2.85	0.58		Stable OCV for 42hrs compared to 14hrs for N117	(*24*)
	Nafion /PDDA-PSS7	7 layers of PDDA-PSS	-	48.8	-	-	2.78	-	-	-	(*24*)
	Nafion /SPEEK	SPEEK modified Nafion	100	6.25	-	-	-	1.928	-	30 cycles (50 mA/cm²)	(*23*)

Downloaded by UNIV OF GUELPH LIBRARY on June 14, 2012 | http://pubs.acs.org
Publication Date (Web): May 7, 2012 | doi: 10.1021/bk-2012-1096.ch007

Membrane Category	***Membrane Type***	***Chemical Composition***	***Thick-ness (µm)***	***Ionic Con-ductivity (mS/cm)***	***Water Uptake (%)***	***Ion Diffusion Coefficient (10^{-7} cm^2/min)***				***Chemical Stability***	***Ref***
						V^{2+}	***V^{3+}***	***VO^{2+}***	***VO_2^+***		
Non-fluorinated polymer	Nafion /polypyrrole	Polypyrrole modified Nafion at 0 °C for 60min (electrodeposition)	-	7.83	-	-	-	5	-	-	(*22*)
	Daramic1	polyethylene 45% + silica 55%	190	23.8	48.6	-	-	-	-	-	(*29*)
	Daramic2		250	62.5	56.2	-	-	-	-	-	(*29*)
	SPEEK	40% sulfonation	90	7.4	26.7	-	-	0.36	-	Good performance up to 80cycles (60 mA/cm^2)	(*30*)
	SPEEK	50% sulfonation	85	7.7	31.8	-	-	-	-	-	(*30*)
	SPEEK	60% sulfonation	90	7.3	25.3	-	-	2.12	-	-	(*30*)
	SPEEK	-	100	7.9	-	-	-	2.432	-	-	(*23*)
	SPFEK	-	180	17.1	27.8	-	-	-	-	Good after 80cycles	(*32*)

Continued on next page.

Downloaded by UNIV OF GUELPH LIBRARY on June 14, 2012 | http://pubs.acs.org
Publication Date (Web): May 7, 2012 | doi: 10.1021/bk-2012-1096.ch007

Table III. (Continued). Summary of membranes tested for VRFB systems[a]

Membrane Category	*Membrane Type*	*Chemical Composition*	*Thick-ness (µm)*	*Ionic Con-ductivity (mS/cm)*	*Water Uptake (%)*	*Ion Diffusion Coefficient (10^{-7} cm²/min)*				*Chemical Stability*	*Ref*
						V^{2+}	V^{3+}	VO^{2+}	VO_2^+		
modified non-fluorinated polymer	S-Radel	-	115	100	37	-	-	2.07	-	1M V5+ sol for 15days, good performance at 40mA/cm²	(*31*)
	PVDF-g-PSSA-co-PMAc	-	70	15	7.2	-	1.12	0.73	0.11	Stable OCV for >33hrs	(*26*)
	SPTK	-		10.5	11.9	-	-	0.72	-	-	(*32*)
	SPTKK	-		13.6	19.3	-	-	1.86	-	-	(*32*)
	Daramic/DVB	Amberlite CG400 + divinylbenzen	230-250	14.0	-	-	-	-	-	-	(*27*)
	Daramic/Nafion1	5% Nafion modified	190	7.9	28.8	-	-	-	-	-	(*28*)
	Daramic/Nafion2	5% Nafion modified	250	10.4	31.2	-	-	-	-	-	(*28*)

[a] EE: energy efficiency CE: coulombic efficiency OCV: open circuit voltage

Downloaded by UNIV OF GUELPH LIBRARY on June 14, 2012 | http://pubs.acs.org
Publication Date (Web): May 7, 2012 | doi: 10.1021/bk-2012-1096.ch007

As an alternative to Nafion™ membrane, non-fluorinated porous hydrocarbon-based membranes have been investigated due to their low cost and tuned conductivity. The early research led by Skyllas-Kazacos focused on the commercially-available membranes, such as sulfonated polyethylene (PE), sulfonated polystyrene, and Daramic™ (45 wight percent polyethylene and 55 weight percent silica), which has been the focus of the most studies (*27*). These studies have been largely focused on improving the ionic conductivity, which has been the major limitation of Daramic™ membranes. By soaking the Daramic™ membrane in Nafion™ solution to produce a Daramic/Nafion™ composite membrane, Tian, *et al.*, showed a low membrane resistance while attaining the high ionic selectivity of Daramic™ membrane (*28*). Very recently, aromatic-type membranes, such as sulfonated poly(fluorenyl ether ketone), SPEEK, sulfonatd poly(phenylsulfone) (S-Radel), sulfonated poly(arylene thioether ketone) (SPTK) and sulfonated poly(arylene thioether ketone ketone) (SPTKK) have been investigated as potential substitutions for Nafion™ in VRFB applications. An order-of-magnitude lower vanadium permeability was demonstrated using SPEEK with various degrees of sulfonation (*29*). Similarly, significantly lower vanadium-ion permeability was achieved using S-Radel membrane. *In-situ* tests also demonstrated improved self-discharge, better capacity retention, as well as higher columbic efficiency when using S-Radel membrane. S-Radel is also significantly less expensive than Nafion™ (*30*). However, the durability of S-Radel needs to be demonstrated before this type of membrane can be a viable replacement to Nafion™ in VRFB applications. SPTK and SPTKK membranes showed an order-of-magnitude lower VO_2^+ permeabilities with similar proton conductivities measured in Nafion 117 membranes under the same conditions. Higher Coulombic efficiencies, compared to those found in Nafion 117, were also demonstrated using VRFB cells containing SPTK and SPTKK membranes (*31*).

Very recently, a group of researchers have successfully demonstrated high ionic selectivity using synthesized nano-filtration (NF) membranes in a VRFB system (*32*). The basic principle behind the ionic selectivity of NF membranes is based on pore-size exclusion that relies on pressure (*e.g.*, 0.3-4.0MPa) as a driving force for the separation process. Due to their relatively large size, the multivalent ions (vanadium ions) can be retained while monovalent ions such as protons with relatively small size are transported through the membrane. NF membranes based on polyacrylonitrile have exhibited good performance by achieving coulomic efficiencies up to 95 percent and an energy efficiency of 76 percent at 80 mA/cm^2 for more than 200 cycles (*32*).

Membrane Challenges and Opportunities for Advanced VRFBs

As mentioned in previous discussions, conventional VRFBs operate at relatively low current densities (50 to 80 mA/cm^2) due to inherent system and material limitations. Therefore, the vast majority of membrane studies are focused primarily on low crossover approaches, which are particularly important for relatively low operating currents. The most common membranes found in current VRFB products are relatively thick (*e.g.*, 175 μm), which is required to limit the impact of undesirable crossover of ions and water. The development of high power density VRFB systems to meet EES cost targets has also given rise to a need for development of low resistance membranes to enable high voltage efficiencies at high currents. Figure 5 shows an estimation of ohmic loss as a function of membrane thickness for two different operating current densities (80 and 1000 mA/cm^2) assuming a membrane conductivity of 0.1 S/cm and membrane resistance that is proportional to thickness. From an ohmic perspective, thick membranes pose a significant performance limitation at high current densities. For example, with a 175-µm thick membrane, the voltage loss in the membrane is 175 mV at 1000 mA/cm^2, which represents a voltage penalty of approximately 14 percent of the open-circuit voltage (OCV) of a VRFB cell. Whereas, this voltage loss is relatively small in the case of 25-µm thick membrane (*i.e.*, ~ 2 percent of OCV). These ohmic losses obtained at relatively low operating current densities are much less sensitive to membrane thickness.

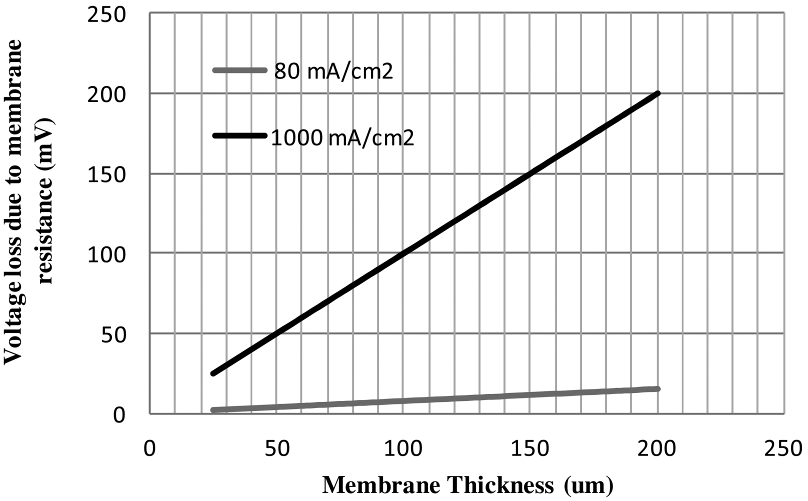

Figure 5. Relationship between voltage loss in the membrane, assuming a conductivity of 0.1 S/cm, and membrane thickness in the case of 80 and 1000 mA/cm^2.

Though thinner membranes offer a significant advantage in enabling low ohmic losses, and hence improved cell overpotentials, crossover can limit the use of thin membranes. Careful optimization in membrane design to achieve low resistance membrane while maintaining an acceptable crossover is very important. This is actually more difficult at lower operating currents, since reactant crossover is typically relatively independent of the operating current density (*i.e.,* reactant crossover is typically dominated by diffusion, due to concentration gradients, and not by osmotic drag (*33*)). Therefore, the impact of reactant crossover is less apparent at higher currents. Similarly, membranes having low interfacial resistance to minimize contact resistance between the membrane and the

Downloaded by UNIV OF GUELPH LIBRARY on June 14, 2012 | http://pubs.acs.org
Publication Date (Web): May 7, 2012 | doi: 10.1021/bk-2012-1096.ch007

electrodes can also result in considerable performance improvements at high current densities (*34*). Another significant element that impacts the membrane resistance towards proton transport is related to sulfuric acid as well as vanadium solution. In principle, ionic membranes are not required in a VRFB system, since sulfuric acid contained within the membrane pores is inherently conductive to protons. However, the interaction between the polymer and sulfuric acid can potentially have a considerable impact on proton conductivity within the membrane (*35*). The interactions between the polymer membranes and the reactant solutions and how that impacts proton-transport properties in VRFB membrane are not well understood. More sophisticated models and additional experiements are required to elucidate the transport mechanisms (*36*).

Downloaded by UNIV OF GUELPH LIBRARY on June 14, 2012 | http://pubs.acs.org
Publication Date (Web): May 7, 2012 | doi: 10.1021/bk-2012-1096.ch007

Summary

EES technology has the potential to make electricity market cleaner, more efficient, and dependable. For Grid-scale applications, EES can significantly enhance the power quality and reliability of the electricity supply system by lessening the constraints of real-time balance between electricity supply and demand. EES system can also enable large-scale deployment of stochastic renewable electricity generation such as solar and wind by making these power resources more stable and dispachable.

Amongst the host of battery technologies for EES, flow batteries, particulary those based on vanadium-redox systems, are considered the most suitable for large-scale EES applications with broad range of power and energy capacity ratings as well as fast response time. Despite their proven performance and reliability, the relatively high cost of VRFB systems remains the major barrier towards the commercialization of this technology. As the demand for EES continues to increase, the commercial competitiveness of VRFBs will necessitate large reduction in system capital cost which can only be achieved if the cost of the battery is substantially lowered. The process of achieving low stack cost that can have the desired impact on the overall system cost will require considerable improvements in stack power density (an-order-of magnitude or higher compared to conventional VRFB systems). Fundamental changes to VRFB cell architecture are required to enable aggressive improvements in system's operating power density. New cell designs with low resistance (ohmic, kinetic) that can also enable adequate convective reactants flow through the electrodes layers are particularly important. These new cell designs will have the greatest impact on system performance and hence overall system cost if combined with high performance materials (electrodes, membrane, bipolar plates) that are designed specifically to meet all the VRFB requirements.

References

1. Massoud, A.; John, S. The Electric Power Grid: Today and Tomorrow. *MRS Bull.* **2008**, 399–409.

2. *Electricity Energy Storage Options*; 1020676, EPRI Report; Palo Alto, CA, 2010.
3. Gyuk, I. *Energy Storage Applications for the Electric Grid*; . Niskayuna, NY, 2008.
4. Schoenung, S.; Hassenzahl, W. *Long- vs. Short-Term Energy Storage Technologies Analysis*; Sandia Report; Albuquerque, NM, 2003.
5. EPRI-DOE. *Handbook of Energy Storage for Transmission and Distribution Applications*; Palo Alto, CA, and U.S. Department of Energy, Washington, DC, 2003.
6. Linden, D.; Reddy, T. *Linden's Handbook of Batteries*, 4th ed.; McGraw-Hill: New York, 2011; Vol. 30, issue 6, pp 30−35.
7. Ge, S. H.; Yi, B. L.; Zhang, H. M. *J. Appl. Electrochem.* **2004**, *34*, 181.
8. Ponce de Leon, C.; Frias-Ferrer, A.; Gonzalez-Garcia, J.; Szanto, D.A.; Walsh, F.C. *J. Power Sources* **2006**, *160*, 716.
9. Katz, M. *J. Electrochem. Soc.* **2009**, *125* (4), 515.
10. Zhao, P.; Zhang, H. M; Zhou, H.; Chen, J.; Gao, S.; Yi, B. *J. Power Sources* **2006**, *162*, 1416.
11. Li, X.; Zhang, H.; Mai, Z.; Zhang, H.; Vankelecom, I. *Energy Eviron. Sci.* **2011**, *4*, 1147.
12. Heitner-Wirguin, C. *J. Membr. Sci.* **1996**, *120*, 1.
13. Sun, C.; Chen, J.; Zhang; Han, X.; Luo, Q. *J. Power Sources* **2010**, *195*, 890.
14. Sukkar, T.; Skyllas-Kazacos, M. *J. Appl. Electrochem.* **2004**, *34*, 137.
15. Yang, Z.; Zhang, J.; Kintner-Meyer, M. C. W.; Lu, X.; Choi, D.; Lemmon, J. P.; Liu, J. *Chem. Rev.* **2011**, *111* (5), 3577.
16. Sukkar, T.; Skyllas-Kazacos, M. *J. Membr. Sci.* **2003**, *222*, 235.
17. Xi, J.; Wu, Z.; Qiu, X.; Chen, L. *J. Power Sources* **2007**, *166*, 531.
18. Teng, X.; Zhao, Y.; Xi, J.; Wu, Z.; Qiu, X.; Chen, L. *J. Membr. Sci.* **2009**, *341*, 149.
19. Sang, S.; Wu, Q.; Huang, K. *J. Membr. Sci.* **2007**, *305*, 118.
20. Luo, Q.; zhang, H.; Chen, J.; Qian, P.; Zhai, Y. *J. Membr. Sci.* **2008**, *311*, 98.
21. Mai, Z.; Zhang, H.; Li, X.; XIao, S.; Zhang, H. *J. Power Sources* **2011**, *196*, 5737.
22. Zeng, J.; Jiang, C.; Wang, Y.; Chen, J.; Zhu, S.; Zhao, B.; Wang, R. *Electrochem. Commun.* **2008**, *10*, 372.
23. Luo, Q.; Zhang, H.; Chen, J.; You, D.; Sun, C.; Zhang, Y. *J. Membr. Sci.* **2008**, *325*, 553.
24. Xi, J.; Wu, Z.; Teng, X.; Zhao, Y.; Chen, L.; Qiu, X. *J. Mater. Chem.* **2008**, *18*, 1232.
25. Teng, X.; Zhao, Y.; Xi, J.; Wu, Z.; Qiu, X.; Chen, L. *J. Power Sources* **2009**, *189*, 1240.
26. Qiu, J.; Zhao, L.; Zhai, M.; Ni, J.; Zhou, H.; Peng, J.; Li, J.; Wei, G. *J. Power Sources* **2008**, *177*, 617.
27. Mohammadi, T.; Skyllas-Kazacos, M. *J. Membr. Sci.* **1995**, *98*, 11.
28. Tian, B.; Yan, C. W.; Wang, F. H. *J. Membr. Sci.* **2004**, *234*, 51.
29. Mai, Z.; Zhang, H.; Li, X.; Bi, C.; Dai, H. *J. Power Sources* **2011**, *196*, 482.
30. Kim, S.; Yan, J.; Schwenzer, B.; Zhang, J.; Li, L.; Liu, J.; Yang, Z.; Hickner, M. A. *Electrochem. Commun.* **2010**, *12*, 1650.

Downloaded by UNIV OF GUELPH LIBRARY on June 14, 2012 | http://pubs.acs.org
Publication Date (Web): May 7, 2012 | doi: 10.1021/bk-2012-1096.ch007

31. Chen, D.; Wang, S.; Xiao, M.; Meng, Y. *Energy Environ. Sci.* **2010**, *3*, 622.
32. Zhang, H.; Zhang, H.; Li, X.; Mai, Z.; Zhang, J. *Energy Environ. Sci.* **2011**, *4*, 1676.
33. Ren, X.; Gottesfeld, S. *J. Electrochem. Soc.* **2001**, *148* (1), A87.
34. Tsampas, M. N.; Pikos, A.; Brosda, S.; Katsaounis, A.; Vayenas, C. G. *Electrochim. Acta* **2006**, *51*, 2743.
35. Tang, Z.; Aaron, D. S.; Keith, R.; Papandrew, A. B.; Zawodzinski, T. A. Proton Exchange Membrane Performance in Vanadium Redox Flow Battery; ECS proceedings, Boston, MA, October 2011.
36. Sing, D. C.; Michael, P.; Meyers, J. P. Redox Flow Battery Simulations for Optimizaing Separator Membrane Performance; ECS proceedings, Boston, MA, October 2011.

Downloaded by UNIV OF GUELPH LIBRARY on June 14, 2012 | http://pubs.acs.org
Publication Date (Web): May 7, 2012 | doi: 10.1021/bk-2012-1096.ch007

Downloaded by UNIV OF GUELPH LIBRARY on June 14, 2012 | http://pubs.acs.org
Publication Date (Web): May 7, 2012 | doi: 10.1021/bk-2012-1096.ch008

Chapter 8

Role of Nanostructures in Polymer Electrolytes for Energy Storage and Delivery

Moon Jeong Park,[*] Jaewan Hong, and Seong Yeon Kim

**Department of Chemistry, Division of Advanced Materials Science (WCU),
Pohang University of Science and Technology (POSTECH), Pohang 790-784,
Korea
[*]Corrensponding Author (moonpark@postech.edu)**

This chapter describes recent developments in polymer electrolyte membranes (PEMs) for fuel cells and lithium batteries. The current progress in advancing transport properties of PEMs over the last five years will be summarized. It is beyond the scope of this chapter to give an extensive review of PEMs and we will focus on the morphology effects on transport properties of PEMs; how parameters such as self-assembled nanostructures, domain sizes, and domain orientations affect conductivities of PEMs will be presented. Challenges in obtaining well-defined morphologies and strategies to access improved transport properties will also be addressed. The contents of this chapter will illuminate the structure-transport relationships in PEMs to suggest promising avenues for designing next-generation polymers for energy storage and conversion technologies.

Introduction

The growing threat of an energy crisis is drawing major public attention in recent days. There are rising demands for developing more efficient energy materials to stem the depletion of fossil fuels. This has prompted significant research efforts on proton exchange fuel cells (*1*, *2*) and lithium batteries (*3*, *4*). These technologies increasingly rely upon polymer electrolyte membranes (PEMs) that transport ions from the anode to the cathode to balance the flow of electrons in an external circuit, and therefore play a central role in determing the

In Polymers for Energy Storage and Delivery: Polyelectrolytes for Batteries and Fuel Cells; Page, K., et al.;
ACS Symposium Series; American Chemical Society: Washington, DC, 2012.

efficiency of the devices (*5*, *6*); as ion transport is a kinetic bottleneck compared to electrical conductivity, enormous efforts have been devoted to improving the transport properties of PEMs.

In fact, advances in lithium-polymer batteries have played a transformative role in the area of portable small electronics. The use of lithium batteries comprising solid PEMs in vehicle upon complete replacement of gasoline will increase the energy density significantly since liquid electrolytes impede the direct utilization of lithium metal to batteries. However, the development of either fuel cells nor lithium batteries that can be used for medium-large sized electric power resources still appears distant.

Key challenges in advancing the performance of PEMs are improved conductivity combined with good mechanical properties. In light of this challenge, PEMs possessing nanoscale morphologies have received great interest owing to their improved structural integrity and unique electrochemical properties (*7–10*). It has been shown that phase separated hydrophobic phases can offer effective mechanical support while the hydrophilic domains facilitate ion transport by confinement. To realize the power of nanostructured PEMs, a variety of avenues are being explored. These include the rational design of new PEMs based on a molecular-level understanding of chemistry, morphology, and transport (*11–13*).

In following sections we describe the current state of understanding in the relationship between PEM morphologies and their transport properties. The chapter is organized as follows: the first section describes the mechanisms of ion transport across PEMs; the second section presents the current development of PEMs (mostly sulfonated PEMs) for proton exchange fuel cells and the role of nanostructures in achieving improved conductivities is discussed; the third section elucidates recent studies on polyethylene oxide (PEO) based PEMs for lithium batteries and opens up the debate on the issues of morphological effects on transport properties. At the end of second and third sections, a summary and outlook for future avenues toward the evolution of new PEMs are given.

Downloaded by UNIV OF GUELPH LIBRARY on June 14, 2012 | http://pubs.acs.org
Publication Date (Web): May 7, 2012 | doi: 10.1021/bk-2012-1096.ch008

Ion Transport Mechanisms in PEMs

Ion transport in sulfonated PEMs of fuel cells is commonly understood through a complicated combination of vehicular, hopping (Grotthus), and surface diffusion mechanisms (*14*, *15*). Under fully hydrated conditions, the water transport pathways swell considerably and both hopping and vehicular mechanisms become significant and effective proton transport occurs by interfering hydrogen bonds of water molecules as well as transferring protons from one side to the other side directly. At relatively low hydration levels, in contrast, most of the water molecules and hydronium (H_3O^+) ions are strongly bound to the $–SO_3H$ groups; proton transport is strongly coupled to and impeded by the structure of the membrane. At hydrophilic channels in PEMs, the fixed anion sites help proton transport through surface diffusion mechanism, however, this process needs high activation energy and the large reduction in proton conductivity is typically seen due to small proton mobility. Consequently, over the past decade, transport properties of sulfonated PEMs under hydrated conditions have been studied extensively by varying molecular designs to retain water molecules more effectively (*16*).

Whereas ion conduction mechanisms in solid PEMs (solvent-free systems) of lithium batteries are closely coupled to the segmental motion of the polymer chains, which promotes the ionic motions. As proposed by Vogel-Tammen-Fulcher (VTF), Arrhenius-type hopping (Grotthus), and Williams-Landel-Ferry (WLF, free volume model) mechanisms (*17–19*), one lithium ion and 4~6 oxygens in ether form can make a complex and the hopping of lithium ions from one complex to others occurs by relaxation/breathing and/or segmental motions of polymer segments. To date, salt-doped polyethylene oxide (PEO) exhibits reasonable high Li^+ mobility among different solid PEMs, which was first reported by Fenton in 1973 (*20*). On account of the high Li^+ conductivity of salt-doped PEO, current researches on PEMs for lithium batteries have concentrated on PEO based systems. It has been reported that ionic conductivity of Li salts/PEO based PEMs can be improved by optimizing the lithium ion mobility and the effective number of lithium ions, taking into account the ion-ion and ion-polymer interactions.

Recently, the effects of nanostructures on ionic conductivities of fuel cells and lithium batteries have been the subject of much debate (*14–16*, *21–25*). Perhaps the nanostructures play only a small role in improving the ion transport rate since the ions in PEMs always move back and forth. Nevertheless, the diverse observations of morphology dependent conductivity is motivation for exploring key parameters, which influence ion transport in nanostructured PEMs.

Downloaded by UNIV OF GUELPH LIBRARY on June 14, 2012 | http://pubs.acs.org
Publication Date (Web): May 7, 2012 | doi: 10.1021/bk-2012-1096.ch008

The Role of Nanostructures in Ion Transport: Fuel Cell

Nanostructures for Less Tortuous/More Efficient Ion Conduction Pathways

Proton exchange fuel cells comprising sulfonated PEMs and Pt electrodes, which generate power from water formation reaction and thus offer the prospect of supplying clean energy, have been the subject of extensive study (*26*). The most common route to acheive high conductivity in sulfonated PEMs is the solvation of phase separated $-SO_3H$ domains with water since the water molecules facilitate conveyance of protons dissociated from $-SO_3H$ groups by shuttling them between ionic moieties (*27*). In hydrated PEMs, it has been well-reported that the proton transport rate is heavily dependent on the water content within the membranes.

Among different kinds of sulfonated PEMs that have been studied for fuel cell applications, Nafion™ (Dupont) has been a benchmark polymer in many sulfonated PEMs studies. Nafion has a high conductivity, on order of 0.1 S/cm, under fully hydrated conditions despite the low ion exchange capacity (IEC) value of 0.9 meq/g (*27*). Although scattering experiments have attempted to quantify a phase-separated morphology for Nafion (*28*), the ill-defined, process-dependent, heterogeneous structures from the nano to microscale have not been particularly useful in establishing fundamental structure-transport relationships in this material which is considered an industry standard. In contrast, the use of sulfonated block and/or graft copolymers where well-defined nanostructures with tunable morphologies and domain sizes are readily achieved, are proving to provide extremely valuable insight into this optimization problem (*9*, *29–31*).

When the ionic domain structures of PEMs possessing well-defined nanostructures are compared against those of traditional PEMs lacking organizations, one may grasp the differences in connectivity of ionic domains, orientation of ionic domains, and average proximity of acid moieties at the same IEC, as schematically drawn in Figure 1. All of the factors mentioned above should strongly influence the proton conductivity of hydrated PEMs. It is generally believed now that the phase separated morphology between non-ionic and ionic domains is an effective way to generate continuous pathways where the local concentration of $-SO_3H$ within ionic channels of nanostructured PEMs is distinctly high. In particular, the high proximity of ionic groups appears to have positive effects on proton mobility since the tortuosity of the ion transport domains can be dramatically reduced.

Downloaded by UNIV OF GUELPH LIBRARY on June 14, 2012 | http://pubs.acs.org
Publication Date (Web): May 7, 2012 | doi: 10.1021/bk-2012-1096.ch008

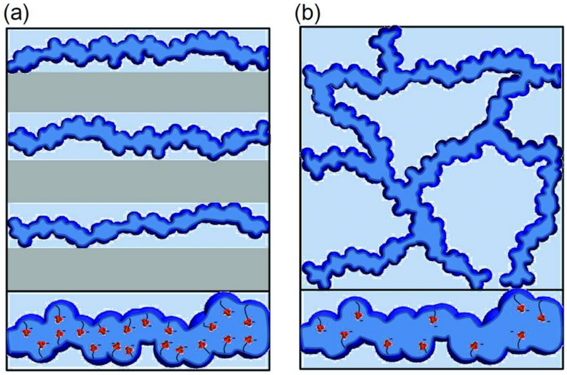

Figure 1. Schematic illustration of ionic domain structure within (a) PEMs possessing well-defined nanostructures and (b) PEMs lacking organizations. Different connectivities of ionic domains and dissimilar spatial proximities of neighboring $-SO_3H$ *groups at the same level of IEC are highlighted.*

Holdcroft et al. demonstrated PEM-dependent proton mobilities, as analyzed in hydrated PEMs followed by extrapolation of the data down to an infinite dilute condition (*32*). By comparing different sulfonated PEMs, i.e., sulfonated poly(arylene ether sulfone) (SPAEK), sulfonated polyimide, and Nafion, a two-fold difference in mobility was observed. The divergence in proton mobility was understood as a consequence of different proximity of acid groups. Recently, Park et al. have explored ionic domain size and shape-dependent proton mobility by employing both hydrated PEMs and polymer dilute solutions (*33*). The system of interest was a series of sulfonated poly(styrene-methylbutylene) (PSS-PMB) diblock copolymers. The proton transport in PSS-PMB copolymers was found to be facilitated by the decrease in the ionic domain sizes. In addition, the proton mobilities were largely determined by the ionic domain shape (spherical vs. cylindrical domains), which was rationalized by the different levels of tortuosity of acid groups.

In fact, early works by Holdcroft and coworkers already demonstrated that the creation of ion-rich domains in graft copolymers could enhance the proton conductivity over its random copolymer analogue at high hydration levels (*34*). This stimulated several efforts to synthesize sulfonic acid containing block or graft copolymers. These have coupled elements of material designs and controllable IEC values with a variety of self-assembled nanostructures (*35–38*). Elabd and Winey et al. followed this line of thinking and compared the conductivities of ordered sulfonated poly(styrene-isobutylene-styrene) (S-SIBS) triblock copolymers with analogous random copolymer containing PSS (*36*).

Their data revealed an order of magnitude enhanced conductivity for block copolymer based PEMs at the same level of IEC values and water contents, as shown in Figure 2a. It is worthwhile to note that morphological transition from lamellar to a co-continuous structure with an increase in the IEC values results in a discontinuous increase in conductivity as seen from the figure. The results of Moore et al., reproduced in Figure 2b (*37*), bear similarities with those of Elabd et al. even though a different system of PSS middle block containing triblock polymer, poly(hexylmethacrylate-styrenesulfonate-hexylmethacrylate), is employed; better order in the PEMs yields greater conductivity.

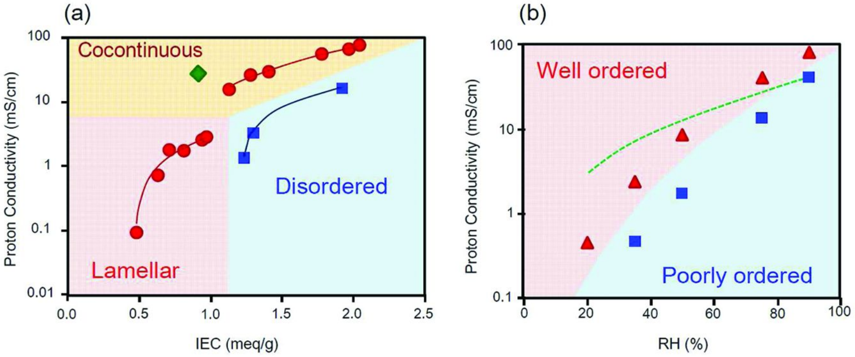

Figure 2. Conductivity vs IEC for PSS end block containing triblock copolymers (●) and PSS random copolymer (■) obtained under fully hydrated conditions. Conductivity of Nafion (♦) is given for reference. (b) Conductivity as a function of relative humidity for PSS middle block containing triblock copolymers with improved order (▲) and with lacking organization (■). The dotted lines are trend lines of Nafion conductivity. Reproduced from refs (36) and (37) with the permission of American Chemical Society and Royal Society of Chemistry, respectively.

More recently, Ingratta et al. have illustrated a more detailed structure-transport relationships for sulfonated poly(phenylene oxide) bearing polyfluorostyrene side chains (*38*). Their result indicates that the conductivity increase in the order of continuous > lamellar >> hexagonal > poorly ordered structures. This clearly illustrates of the morphology effects on proton transport properties in sulfonated PEMs.

Downloaded by UNIV OF GUELPH LIBRARY on June 14, 2012 | http://pubs.acs.org
Publication Date (Web): May 7, 2012 | doi: 10.1021/bk-2012-1096.ch008

McGrath et al. have shown higher water diffusion coefficients in block copolymers (well-ordered structure) than those of random copolymers (ill-defined morphology), as measured by nuclear magnetic resonance (NMR) (*39*). This would be one of the mechanisms by which block copolymer-based PEMs exhibit higher conductivities compared to their random analogs. The authors suggested that concentrating ionic groups in a highly sulfonated domain seems to have an influence on the water behavior, as discussed in Figure 1, which is intimately associated with proton transport in PEMs. For that reason, the strategy of creating phase separation at nanometer scales is now considered one of the promising routes to enhance the conductivity of PEMs.

Downloaded by UNIV OF GUELPH LIBRARY on June 14, 2012 | http://pubs.acs.org
Publication Date (Web): May 7, 2012 | doi: 10.1021/bk-2012-1096.ch008

Nanostructures for Guiding Ions to Targeted Pathways

Understaning of the morphology effects on conductivity prompted researchers toward investigating the alignment of ionic phases with promised rewards in achieving more efficient PEMs. Indeed, anisotropic transport properties have been widely observed not only in block/graft copolymer PEMs but also in random copolymer membranes such as Nafion. Anisotropic diffusion of water molecules within extruded Nafion membranes was revealed by ^{2}H-NMR spectroscopy by Madsen et al. (*40*). With increased alignment of Nafion membranes, substantial enhancement in water transport along the draw direction was seen. This is quite interesting since Nafion membranes do not possess a well-defined morphology. For practical applications, however, the alignment along through-plane is desirable for optimal conduction in PEMs, which has not yet been achieved with random copolymer PEMs.

In contrast, both in-plane and through-plane alignments in PEMs are achievable with the use of block copolymer PEMs. In fact, for many different PEMs, in-plane orientation of microdomains was readily attainable by solvent casting (*36*, *41*). Elabd and Winey et al. showed that the S-SIBS PEMs, prepared by solvent casting, indicates large reduction in through-plane conductivity compared with in-plane conductivity without altering IEC values (*36*).

Upon applying a variety of external stimuli such as shear flow, pressure, and electric field to lamellar forming PSS-PMB diblock copolymers, as demonstrated by Park and Balsara, an order of magnitude different in-plane and through-plane conductivities were observed (*41*). Although the disparity in the degree of alignment and connectivity across the PEMs was not controllable, the ability to tune the conductivity in targeted directions is interesting. Figure 3 summarizes the alignment effects on anisotropic conductivities.

Nanostructures to Break Up Ionic Aggregates: Confinement Effects

As a last category of morphology effects, the size of microdomain is found to be a crucial parameter in determining water uptake and proton conductivity (*16*, *42*). Park and Balsara et al. showed that the PSS-PMB diblock copolymers comprising hydrophilic phases with widths ranging from 2 to 5 nm effectively retain water at high temperature up to 90 °C regardless of relative humidity (see Figure 4a) (*16*). Hillmyer et al. confirmed the result using different sulfonated

Downloaded by UNIV OF GUELPH LIBRARY on June 14, 2012 | http://pubs.acs.org
Publication Date (Web): May 7, 2012 | doi: 10.1021/bk-2012-1096.ch008

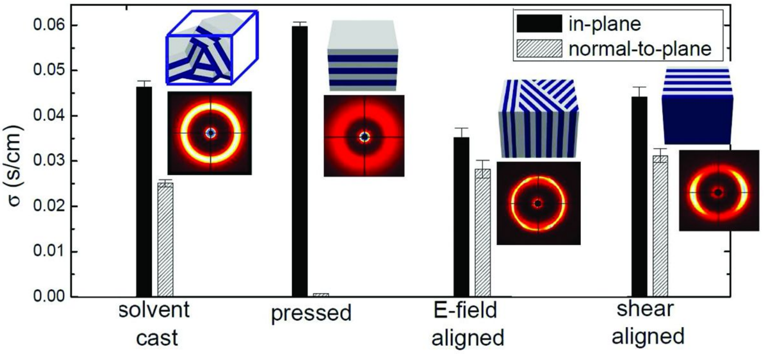

Figure 3. The effect of lamellar alignments on both in-plane and through-plane conductivities in PSS-PMB membrane. Reprinted from ref. (41) with the permission of the American Chemical Society.

PEMs, sulfonated poly(styrene-norbornenylethylstyrene) (PSS-PNS) diblock polymers (*42*). The conductivity of PSS-PNS copolymers was improved with the decrease in PSS domain size, as shown in Figure 4b.

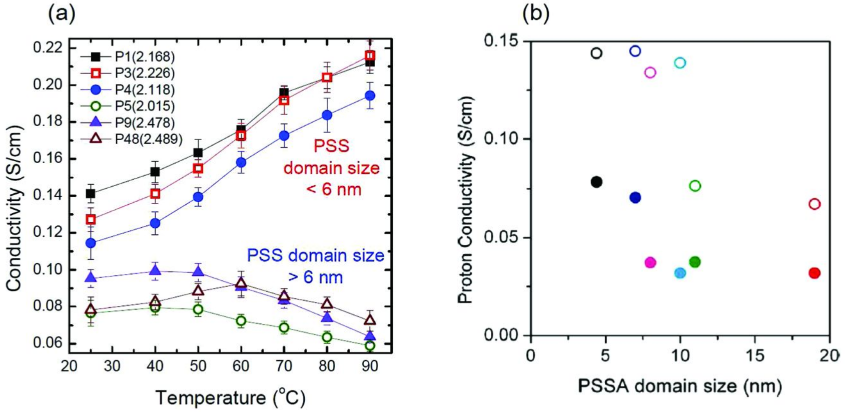

Figure 4. The effect of microdomain size on proton conductivity for (a) PSS-PMB and (b) PSS-PNS diblock copolymer PEMs under fully hydrated conditions. In (b) open symbols correspond to 80 °C while filled ones are obtained at 30 °C. Reprinted from refs (16) and (42) with the permission of the American Chemical Society.

Park et al. further explored the microdomain size effects by examining hydrated morphologies of PSS-PMB over a wide range of sulfonation levels, copolymer molecular weights, temperature, and humidity (*43*). It has been found that the nominally hydrophilic PSS domains contain a substructure periodically arranged water-rich domains. The 3-5 nm water domain spacing observed more-or-less universally in the PEMs owing to a balance between enthalpic gains (by a decrease in contacts between hydrophobic portions of the chains and water) and a free energy penalty (associated with the formation of watery domains). However, the water domain substructure ceases to exist when the hydrophilic PSS domain size is decreased to 6 nm over the entire range of temperature and humidity investigated. This implies that the homogeneous hydrophilic PSS phases caused by the finite size effects are responsible for the rapid proton transport and increased water retention at elevated temperatures.

Interestingly, it seems that the microdomain size effects on proton transport are not limited to the block copolymer PEMs. Holdcroft et al. described that when differently sized ionic clusters were created in graft copolymer PEMs by varying the grafting chain length, smaller ionic clusters in the long graft PEMs allowed the membranes to retain more water at low humidity conditions so high conductivity above 70 °C was attainable (*35*). Consequently, it is clear that a range of parameters, tied to morphology, impact transport performance of hydrated PEMs and a fundamental understanding of the synthetic control of morphologies in PEMs should be pursued further.

Downloaded by UNIV OF GUELPH LIBRARY on June 14, 2012 | http://pubs.acs.org
Publication Date (Web): May 7, 2012 | doi: 10.1021/bk-2012-1096.ch008

Nanostructures for Improving Anhydrous Ionic Conductivity in PEMs

To date, the operating temperature of fuel cells is constrained below 90 °C due to the role of water content on proton transport rates. One of the key challenges in advancing the technology lies in the long term stability and durability of the system. Major issues are carbon monoxide (CO) poisoning of the platinum catalyst at the anode side, the complexity of heat and water management in polymer electrolyte membranes (PEMs), and the enhancement of reaction kinetics at both electrodes (*44*, *45*).

Overcoming these issues may be simple if the operation performance of PEFCs is increased to above 120 °C and a low humidification condition is used. Above 120 °C, CO poisoning becomes negligible, and transport kinetics are significantly enhanced (*46*). Unfortunately, most PEMs suffer from membrane dehydration at temperatures above 100 °C. Therefore, there is a growing need to develop a new system that can operate above 120 °C by replacing water with solvents that are non-volatile, have high boiling points, and have high ionic conductivities to alleviate the durability concerns.

As a promising candidate toward high temperature PEMs, ionic liquids (ILs) have received enormous interest lately owing to their non-flammablility, chemical stability, and negligible vapor pressures (*47*). In particular, excellent ionic conductivity of ILs can open great possibilities in enhancing conductivity of IL-containing PEMs in the absence of water molecules. Under anhydrous conditions, proton transport mechanisms in PEMs are fully altered since the proton tunneling among hydrogen bonded water molecules is ruled out. In these systems, the reported conductivity values were considerably lower than the conductivities obtained with hydrated PEMs (*48*, *49*). Consequently, the fundamental understanding of ion transport mechanisms in anhydrous PEMs and the knowledge on morphology-transport relationship is urgently needed to develop advanced high temperature PEMs.

Park et al. reported anhydrous conductivity in alkylimidazolium-based IL incorporated PSS-PMB block copolymers (*8*). Strikingly, it has been found that

Downloaded by UNIV OF GUELPH LIBRARY on June 14, 2012 | http://pubs.acs.org
Publication Date (Web): May 7, 2012 | doi: 10.1021/bk-2012-1096.ch008

the composite PEMs with well-defined morphologies indicate a few orders of magnitude higher conductivities than the PEMs lacking organization (i.e., PSS random polymer/IL). This implies that the morphology also plays an important role in improving ion transport in PEMs under anhydrous conditions. The conduction mechanisms of IL-doped PSS-PMBs can be descrived as follows; 1) the proton transport occurs by the making and breaking of ionic bonds between acid groups and imidazolium cations. 2) the vehicular diffusion of ILs along the PSS domains becomes significant at the high IL concentrations. The authors further explored the anhydrous conductivity of composite PEMs by altering the anions of ILs while keeping the same imidazolium cations (*10*). It is noteworthy to address here that the use of different anions results in distinctly different morphologies and anisotropy, which impact ionic conductivity of composite PEMs. Among lamellar (LAM), hexagonal cylinder (HEX), and hexagonal perforated lamellar (HPL), and poorly organized spherical domains, it has been found that the HPL morphology has the highest conductivity in both in-plane and through-plane directions while the LAM exhibits the highest anisotropy in conductivity. Figure 5 summarizes the morphology effects on anhydrous conductivity.

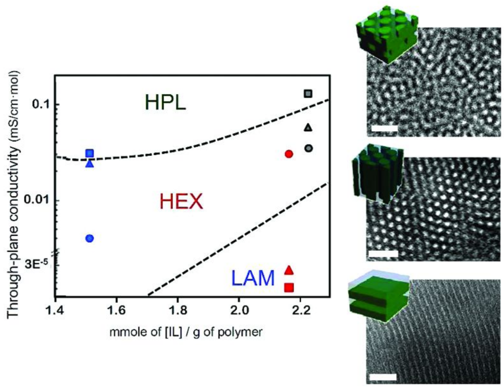

Figure 5. Through-plane conductivities of IL incorporated PSS-PMB copolymers obtained at 165 °C under anhydrous conditions. Three different PSS-PMBs (plotted with different symbols) and three different ILs (shown with different color) are used as indicated in the figure. The PSS domain in TEM images was darkened by RuO_4 staining and the scale bars represent 50 nm. Reprinted from ref. (10) with the permission of the American Chemical Society.

Elabd et al. also reported the morphology effects on ionic conductivity of IL doped PEMs (*50*). In this study, poly(styrene-b-methylmethacrylate) (PS-PMMA) copolymers were employed as matrix PEMs. In PS-PMMA, PMMA serves as hydrophilic domains for the selective incorporation of alkyl imidazolium based ILs and the conductivity is mostly affected by vehicular motion of the incorporated ILs, which can be expressed by the Vogel-Tamman-Fulcher (VTF) model (*51*). Significantly higher ionic conductivities can be achieved with

Downloaded by UNIV OF GUELPH LIBRARY on June 14, 2012 | http://pubs.acs.org
Publication Date (Web): May 7, 2012 | doi: 10.1021/bk-2012-1096.ch008

PS-PMMA/IL compared to PMMA/IL at the same IL contents (wt%), because the non-conductive PS microdomain excludes IL, which produces a higher local IL concentration in the conductive phase. Note that from a practical point of view, the real application of the PS-PMMA/IL composite PEMs to high temperature fuel cells does not seem to be viable since no protic sites are exist in this system.

In contrast, Segalman et al. found that conductivity is not affected by morphology if the value is normalized by the concentration of IL and glass transition temperature of the matrix polymer (*52*). The system investigated was poly(styrene-b-2-vinylpyridine) (PS-P2VP) block copolymer, which again does not contain any protic sites yet P2VP serves as specific sites for ion coordination. Instead, they employed protic imidazolium. A wide variety of nanostructures, i.e., LAM, closed packed spheres, cubic spheres, disordered micelles, were compared and no clear morphology effects were seen. This result would open up a debate on the issues of morphology effects on anhydrous conductivities of IL containing PEMs.

Concerning the long-term durability in composite PEMs, many researchers also have given attention to the synthesis and characterization of ion-tethered PEMs (*53*, *54*). In this way, one can minimize the migration of ions upon applying a DC bias. Interestingly, Hayward et al. showed distinct morphology effects on the conductivity in ion-tethered PEMs (*53*), as shown in Figure 6. The systems studied were benzotriazole-based polymers and when the polymer is only differed by the inclusion of a hydrophobic decyl chain, it exhibits organized supramolecular assemblies and shows a dramatic enhancement in anhydrous conductivity relative to analogous materials lacking organization.

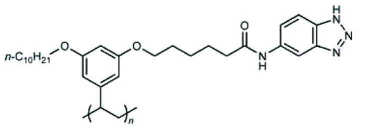

1

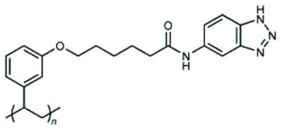

2

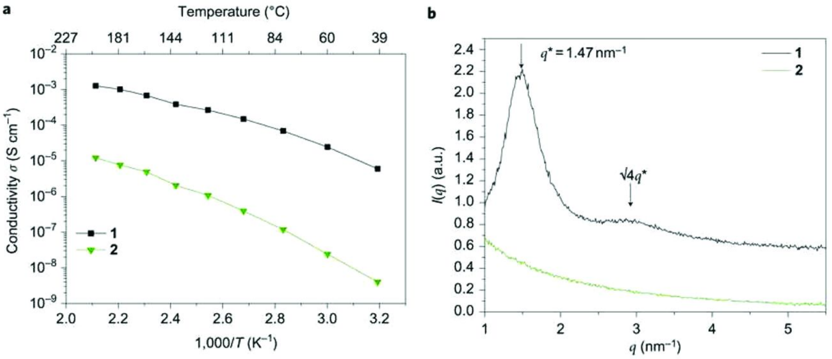

Figure 6. (a) Different conductivities and (b) scattering profiles from benzotriazole-based polymers that only differ by the inclusion of a decyl chain. Reprinted from ref. (53) by the permission from the Nature Publishing Group.

Downloaded by UNIV OF GUELPH LIBRARY on June 14, 2012 | http://pubs.acs.org
Publication Date (Web): May 7, 2012 | doi: 10.1021/bk-2012-1096.ch008

It should be noted here that the energy penalty for proton transfer was known to be highest for imidazole but lowest for phosphonic acid (*55*). Accordingly, the use of phosphonic acid functionalized polymers has received increased attention for anhydrous fuel cells (*56*–*59*). For example, Parvole et al. reported conductivity of 4.6 mS/cm at 130 °C in nominal dry condition with the use of poly(vinyl phosphonic acid) grafted PEMs, as shown in Figure 7a (*59*). However, low acidity of phosphonic acid limits the IEC window of PEMs so that the high proton conductivity would, likewise, suffer. One worthwhile system to be studied is Zwitterionic-type polymers where the polymers possess tethered cation and anion at the same polymer chains. Chemical structure of a representative Zwitterionic-type block polymer is shown in Figure 7b (*60*).

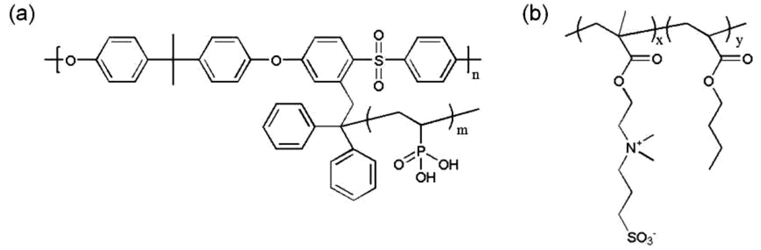

Figure 7. Chemical structures of (a) phosphonic acid grafted PEM and (b) Zwitterionic-type block copolymer.

Overall, it is not yet clear whether these systems could be successfully integrated into high temperature PEMs but the optimal structural designs of PEMs should be further pursued for the access of reasonable transport properties under anhydrous conditions.

Summary and Outlook: Fuel Cells

Nanostructured PEMs are having an impact on the development of proton exchange fuel cells. However, the quantitative understanding on the self-assembly phenomenon of ion containing polymers is lacking substantially and thus, more fundamental work is needed. It should be noted here that the future avenues of new PEMs are not limited to block/graft copolymer PEMs and the use of random copolymers such as SPAEK, acid-doped polyacrylamide and polybenzoimidazole would be certainly required. For these polymers, however, acquiring the equilibrium morphologies is known to be difficult, which has hampered the quantitative analysis of morphology-transport relationship.

There are many smart approaches under progress and it is fair to say that phase-separated structures have benefits for enhancing ion transport rate to some extent. However, the "ideal" morphology with the highest attainable ionic conductivity have not yet been determined. Alignment of ordered morphologies is known to improve the conductivity of membranes along targeted directions to a certain extent, but the details of how ions traverse grain boundaries, what is the role of grain size, and tortuosity effects of the ionic domains on ion transport properties require further study. As potential future directions in high temperature PEMs, the development of new materials that conduct only single ions effectively under anhydrous conditions is essential so as to enhance the electrochemical and mechanical stability of PEMs under fuel cell operation.

The Role of Nanostructures in Ion Transport: Lithium Batteries

Many attempts to improve the design of lithium batteries have dealt with the interface problems between electrolyte and electrode, but work is now focusing on the chemical and physical properties of the electrolyte. In particular, the replacement of flammable liquid electrolytes by solid PEMs has received considerable attention recently due to not only safety issues but also simple manufacturing process and flexible design. However, the major issue in utilizing solid PEMs in lithium ion batteries is arising from their relatively low ionic conductivity compared to liquid electrolytes.

As an key parameter determining Li^+ conductivity, the effective number of lithium ions can be enhanced by increasing the dissociation level of lithium salts and Li^+ transference number. (*61*). Recently, Kofinas et al. demonstrated that the use of nanostructured block copolymer, PEO-PMMA can increase the Li^+ transference number up to 0.9 at room temperature (*22*). This suggests that the nanoscale morphologies also impact the Li^+ conductivity, which has prompted us to explore the role of PEM nanostructures on the Li^+ transport properties for lithium batteries.

Nanostructures for More Efficient Ion Conduction Pathways

Currently, PEO or PEO derivatives are employed in commercially available lithium polymer batteries. PEO is a linear polymer and the regularity of the –(CH_2CH_2O)– unit allows a high degree of crystallinity over 80%. After salt doping, the salt itself acts as a plasticizer and the salt-doped PEO becomes amorphous (gel-like), which is responsible for ionic conductivity (*4*). However, poor mechanical properties of PEO systems potentially yield the fatal flaw of dendritic shorts and therefore, the development of new PEMs with improved mechanical and electrochemical properties is required (*62–65*). In light of such aspects, many PEO-based PEMs, typically in forms of block copolymers, graft copolymers, and polymer composites, have been proposed. However, their conductivity values are lower than PEO homopolymers, which limit the range of practical applications. To solve the low conductivity issues, additives have been utilized so the viscosity of PEM matrix can be lowered. However, it is important to point out here that additive-free PEMs are considered of prime importance in order to progress lithium batteries to increase the cyclability of the batteries.

How can one achieve enhanced conductivities while keeping high mechanical integrities? Organizing the ion-coordination sites (ether oxygens in PEO) of PEMs in such a way as to increase the local order would provide benefits. In particular, the inherent microphase separation characteristics in salt-doped PEO based block

Downloaded by UNIV OF GUELPH LIBRARY on June 14, 2012 | http://pubs.acs.org
Publication Date (Web): May 7, 2012 | doi: 10.1021/bk-2012-1096.ch008

and/or graft copolymer PEMs (if molecular weight is not too small) offer a way of increasing ion dissociation by partitioning anions and cations in two sub-phases.

The early work done by Wiesner et al. has demonstrated the morphology-dependent ionic conductivities of PEO-based dendrons (*23*). A variety of self-assembled morphologies of cubic, lamellar, hexagonal columnar, and gyroid morphologies were obtained via synthetic controls. Interestingly, discontinuous changes in conductivity were observed with the increase in temperature only if there exist phase transitions. For example, an abrupt increase in ionic conductivity was seen upon undergoing hexagonal columnar to gyroid (continous cubic morphology) phase transition. Figure 8 highlights the morphology effects on ionic conductivity in PEO-based dendrons.

Downloaded by UNIV OF GUELPH LIBRARY on June 14, 2012 | http://pubs.acs.org
Publication Date (Web): May 7, 2012 | doi: 10.1021/bk-2012-1096.ch008

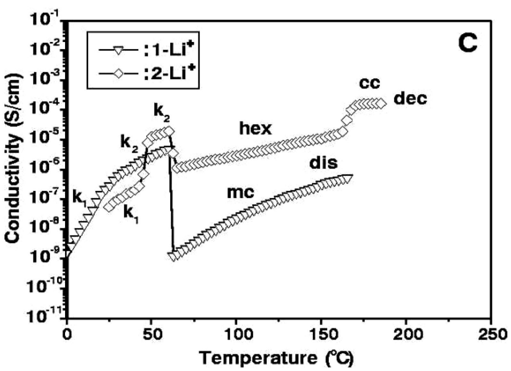

Figure 8. Ionic conductivity as a function of temperature for amphiphilic dendrons; hex: hexagonal columnar; cc: continuous cubic; dec: decomposition; mc: micellar; dis: disordered. Reprinted from ref. (23) with the permission of the American Association for the Advancement of Science.

Thereafter, the nanoscale morphology effects on Li$^+$ conductivity have been extensively investigated using a wide variety of PEO based PEMs. Among them, PS-PEO diblock copolymers have been considered as a model system because of the adequate mechanical strength provided by PS block and good salt-solvating properties of PEO chains. Lodge et al. utilized concentrated solutions of PS-PEO/IL by varying the volume fraction of PEO phases to obtain HEX (PS cylinders), LAM, and HEX (PEO cylinders), and cocontinuous structures (*24*). What is interesting is that when the obtained conductivity values are normalized by volume fraction of the conducting phases (PEO + IL), the results were much lower than theoretically expected values. The authors inferred that this is due to the randomly oriented microdomains that limit the direct ionic conduction through the samples. However, the sample having continuous ionic domains was significantly more conductive than others on account of a small number of grain boundaries.

In contrast, Balsara et al, reported non-significant morphology effects on ionic conductivity for several low molecular weight PS-PEO (*25*). As shown in Figure

Downloaded by UNIV OF GUELPH LIBRARY on June 14, 2012 | http://pubs.acs.org
Publication Date (Web): May 7, 2012 | doi: 10.1021/bk-2012-1096.ch008

9, with the increase in temperature, the samples exhibit order-disorder transitions from LAM-gyroid or LAM-disorder or HEX-disorder, however, no discontinuous changes in conductivity are seen across the phase boundaries. Therefore, in PEO based PEMs, it is fair to say that although the conductivity is known to scale with the relative volume fraction of PEO phase in the PEMs, the morphology effects on ionic conductivity are still under debate.

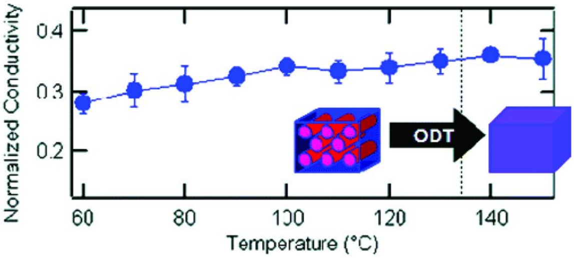

Figure 9. Ionic conductivity upon acrossing order-disorder transition for a low molecular weight PS-PEO diblock copolymer. Reprinted from ref. (25) with the permission of the American Chemical Society.

It is interesting to note here that Balsara et al. have revealed that the Li^+ conductivity in salt-doped PS-PEO is crucially dependent on the domain sizes of PEO phases (in turns, PEO molecular weights) where the ionic conductivity of the copolymers increases with M_{PEO} (*63*). This result is further confirmed by Lodge et al. (*24*). The authors have explained the increase in conductivity by an increase in ionic dissociation with localized Li^+ at the center of the PEO domains, as visualized by energy filtered transmission electron microscopy (*66*).

Nanostructures for Guiding Ions to Targeted Pathways

Lithium battery PEMs bear analogy to those of fuel cells in terms of the development of anisotropy and grain boundaries. The randomly oriented microdomains inherent in the samples limit the access of theoretical conductivity values. Therefore, alignment approaches are also ongoing in order to improve the ultimate ionic conductivity attainable for the nanostructured PEMs. For instance, Iyoda et al. exploited anisotropic ionic conductivity in PEO based liquid crystalline diblock copolymers, poly(ethyleneoxide-methacrylate) (PEO-PMA), so that perpendicular oriented columnar structure was developed (*67*). Isotropic-to-smectic phase transition is known to yield significant anisotropy in conductivity; through-plane conductivity was a few orders of magnitude larger than in-plane conductivity, as shown in Figure 10.

True lithium batteries comprising nanostructured PEMs may still be some way off. To achieve the most optimal transport properties in solid PEMs in the absence of additives, the optimal material designs of PEMs to minimize grain boundaries and maximize ion mobilities should be pursued in future research.

Downloaded by UNIV OF GUELPH LIBRARY on June 14, 2012 | http://pubs.acs.org
Publication Date (Web): May 7, 2012 | doi: 10.1021/bk-2012-1096.ch008

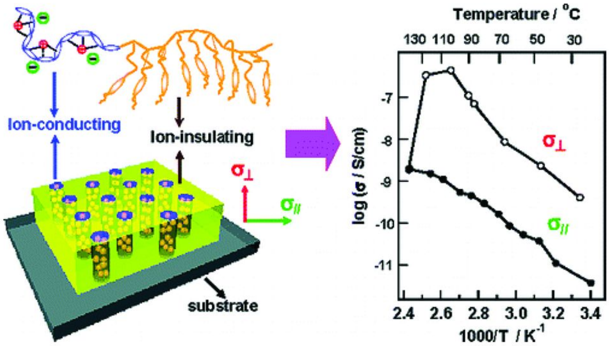

Figure 10. Perpendicular alignment of PEO-PMA block copolymers and anisotropic ion conductivity of salt-doped PEO-PMA as a function of temperature. Large reduction in in-plane conductivity is seen. Reprinted from ref. (67) with the permission of the American Chemical Society.

Summary and Outlook: Lithium Batteries

Although the use of lithium batteries comprising solid PEMs will increase the energy density significantly by allowing the direct use of lithium metal anode, it is not yet clear whether the nanostructure solid PEMs will be successfully integrated into next generation of batteries. We need to carry out fundamental studies on thermodynamics, morphologies, and transport of model PEMs to suggest new trends and ideas toward future avenues. One potential avenue would be the use of unipolar electrolytes, in which only the cations carry charges, but these have not broadly studied. Until now, the motion of free anions within PEMs results in polarization so the charge/discharge rate of the batteries is greatly limited. As a result, the future research avenues include the synthesis and characterization of new PEMs with fixed negative charges to avoid the depletion of salts.

References

1. Wee, J.-H. *Renewable Sustainable Energy Rev.* **2007**, *11*, 1720–1738.
2. Smitha, B.; Sridhar, S.; Khan, A. A. *J. Membr. Sci.* **2005**, *259*, 10–26.
3. Li, Y.; Tan, B.; Wu, Y. *Nano Lett.* **2008**, *8* (1), 265–270.
4. *Advances in Lithium-Ion Batteries*; van Schalkwijk, W., Scrosati, B., Eds.; Kluwer Academic/Plenum: Boston, 2004.
5. Wang, Y.; Chen, K. S.; Mishler, J.; Cho, S. C.; Adroher, X. C. *Appl. Energy* **2011**, *88*, 981–1007.
6. Agrawal, R. C.; Pandey, G. P. *J. Phys. D: Appl. Phys.* **2008**, *41*, 223001–2230018.
7. Arico, A. S.; Bruce, P.; Scrosati, B.; Tarascon, J.-M.; van Schalkwijk, W. *Nat. Mater.* **2005**, *4*, 366–377.
8. Kim, S. Y.; Kim, S. H.; Park, M. J. *Nat. Commun.* **2010**, *1*, 88.

9. Kim, S. Y.; Park, M. J.; Balsara, N. P.; Jackson, A. *Macromolecules* **2010**, *43*, 8128–8135.
10. Kim, S. Y.; Yoon, E. Y.; Joo, T.; Park, M. J. *Macromolecules* **2011**, *44*, 5289–5298.
11. Oriall, M. C.; Wiesner, U. *Chem. Soc. Rev.* **2011**, *40*, 520–535.
12. Kreuer, K. -D.; Paddison, S. J.; Spohr, E.; Schuster, M. *Chem. Rev.* **2004**, *104*, 4637–3678.
13. Meyer, W. H. *Adv. Mater.* **1998**, *10* (6), 439–448.
14. Peckham, T. J.; Holdcroft, S. *Adv. Mater.* **2010**, *22*, 4667–4696.
15. Choi, P.; Jalani, N. H.; Datta, R. *J. Electrochem, Soc.* **2005**, *152*, E123–130.
16. Park, M. J.; Downing, K. H.; Jackson, A.; Gomez, E. D.; Minor, A. M.; Cookson, D.; Weber, A. Z.; Balsara, N. P. *Nano Lett.* **2007**, *7* (11), 3547–3552.
17. Agrawal, R. C.; Pandey, G. P. *J. Phys. D: Appl. Phys.* **2008**, *41*, 223001–2230018.
18. Meyer, W. H. *Adv. Mater.* **1998**, *10*, 439–448.
19. Armand, M. *Solid State Ionics* **1994**, *69*, 309–319.
20. Fenton, D. E.; Parker, J. M.; Wright, P. V. *Polymer* **1973**, *14*, 589.
21. Elabd, Y. A.; Hickner, M. A. *Macromolecules* **2011**, *44*, 1–11.
22. Ghosh, A.; Wang, C.; Kofinas, P. *J. Electrochem. Soc.* **2010**, *157* (7), A846–B849.
23. Cho, B. K.; Jain, A.; Gruner, S. M.; Wiesner, U. *Science* **2004**, *305*, 1598–1601.
24. Simone, P. M.; Lodge, T. P. *ACS Appl. Mater. Interfaces* **2009**, *1* (12), 2812–2820.
25. Wanakule, N. S.; Panday, A.; Mullin, S. A.; Gann, E.; Hexemer, A.; Balsara, N. P. *Macromolecules* **2009**, *42*, 5642–5651.
26. Devanathan, R. *Energy Environ. Sci.* **2008**, *1*, 101–119.
27. Sone, Y.; Ekdunge, P.; Simonsson, D. *J. Electrochem. Soc.* **1996**, *143* (4), 1254–2359.
28. Schmidt-Rohr, K.; Chen, Q. *Nature* **2008**, *7*, 75–83.
29. Park, M. J.; Balsara, N. P. *Macromolecules* **2008**, *41* (10), 3678–3687.
30. Tsang, E. M. W.; Zhang, Z.; Shi, Z.; Soboleva, T.; Holdcroft, S. *J. Am. Chem. Soc.* **2007**, *129*, 15106–15107.
31. Shi, Z. Q.; Holdcroft, S. *Macromolecules* **2005**, *38*, 4193–4201.
32. Peckham, T. J.; Schmeisser, J.; Rodgers, M.; Holdcroft, S. *J. Mater. Chem.* **2007**, *17*, 3255–3268.
33. Lee, S. J.; Park, M. J. *Soft Matter* **2011**, *7*, 8838–8846.
34. Ding, J.; Chuy, C.; Holdcroft, S. *Chem. Mater.* **2001**, *13* (7), 2231–2233.
35. Tsang, E. M. W.; Zhang, Z.; Yang, A. C. C.; Shi, Z.; Peckham, T. J.; Narimani, R.; Frisken, B. J.; Holdcroft, S. *Macromolecules* **2009**, *42*, 9467–9480.
36. Elabd, Y. A.; Napadensky, E.; Walker, C. W.; Winey, K. I. *Macromolecules* **2006**, *39*, 399–407.
37. Moore, H. D.; Saitoab, T.; Hickner, M. *J. Mater. Chem.* **2010**, *20*, 6316–6321.

Downloaded by UNIV OF GUELPH LIBRARY on June 14, 2012 | http://pubs.acs.org
Publication Date (Web): May 7, 2012 | doi: 10.1021/bk-2012-1096.ch008

Downloaded by UNIV OF GUELPH LIBRARY on June 14, 2012 | http://pubs.acs.org
Publication Date (Web): May 7, 2012 | doi: 10.1021/bk-2012-1096.ch008

38. Ingratta, M.; Jutemar, E. P.; Jannasch, P. *Macromolecules* **2011**, *44* (7), 2074–2083.
39. Roy, A.; Yu, X.; Dunn, S.; McGrath, J. E. *J. Membr. Sci.* **2009**, *327*, 118–124.
40. Li, J.; Park, J. K.; Moore, R. B.; Madsen, L. A. *Nat. Mater.* **2011**, *10*, 507–511.
41. Park, M. J.; Balsara, N. P. *Macromolecules* **2010**, *43* (1), 292–298.
42. Chen, L.; Hilmyer, M. A. *Macromolecules* **2009**, *42* (16), 6075–6085.
43. Kim, S. Y.; Park, M. J.; Balsara, N. P.; Jackson, A. *Macromolecules* **2010**, *43* (19), 8128–8135.
44. Li, Q.; He, R.; Gao, J. A.; Jensen, J. O.; Bjerrum, N. J. *J. Electrochem. Soc.* **2003**, *150* (12), A1599–A1605.
45. Schuster, M. F. H.; Meyer, M. H. *Annu. Rev. Mater. Res.* **2003**, *33*, 233–261.
46. Zhang, J.; Xie, Z.; Zhang, J.; Tang, Y.; Song, C.; Navessin, T.; Shi, Z.; Song, D.; Wang, H.; Wilkinson, D. P.; Liu, Z. S.; Holdcroft, S. *J. Power Sources* **2006**, *160*, 872–891.
47. Armand, M.; Endres, F.; MacFarlane, D. R.; Ohno, H.; Scrosati, B. *Nat. Mater.* **2009**, *8*, 621–629.
48. Sekhon, S. S.; Park, J. S.; Cho, E. K.; Yoon, Y.-G.; Kim, C.-S.; Lee, W.-Y. *Macromolecules* **2009**, *42* (6), 2054–2062.
49. Cho, E. K.; Park, J.-S.; Sekhon, S. S.; Park, G.-G.; Yang, T.-H.; Lee, W.-Y.; Kim, C.-S.; Park, S.-B. *J. Electrochem. Soc.* **2009**, *156* (2), B197–B202.
50. Gwee, L.; Choi, J. H.; Winey, K. I.; Elabd, Y. A. *Polymer* **2010**, *51*, 5516–5524.
51. Chen, H.; Choi, J. H.; Cruz, D. S. D. L.; Winey, K. I.; Elabd, Y. A. *Macromolecules* **2009**, *42*, 4809–4816.
52. Hoarfrost, M. L.; Segalman, R. A. *Macromolecules* **2011**, *44*, 5281–5288.
53. Chen, Y.; Thorn, M.; Christensen, S.; Versek, C.; Poe, A.; Hayward, R. C.; Tuominen, M. T.; Thayumanavan, S. *Nat. Chem.* **2010**, *2*, 503–508.
54. Weber, R. L.; Ye, Y.; Schmitt, A. L.; Banik, S. M.; Elabd, Y. A.; Mahathappa, M. K. *Macromolecules* **2011**, *44* (14), 5727–5735.
55. Paddison, S. J.; Kreuer, K.-D.; Maier, J. *Phys. Chem. Chem. Phys.* **2006**, *8*, 4530–4542.
56. Tayouo, R.; David, G.; Ameduri, B.; Roziere, J.; Roualdes, S. *Macromolecules* **2010**, *43*, 5269–5276.
57. Fukuzaki, N.; Nakabayashi, K.; Nakazawa, S.; Murata, S.; Higashihara, T.; Ueda, M. *J. Polym. Sci., Part A: Polym. Chem.* **2011**, *49* (1), 93–100.
58. Lee, S.-I.; Yoon, K.-H.; Song, M.; Peng, H.; Page, K. A.; Soles, C. L.; Yoon, D. Y. *Chem. Mater.* 2011, ASAP.
59. Parvole, J.; Jannasch, P. *Macromolecules* **2008**, *41*, 3893–3903.
60. Brown, R. H.; Duncan, A. J.; Choi, J. H.; Park, J. K.; Wu, T.; Leo, D. J.; Winey, K. I; Moore, R. B.; Long, T. E. *Macromolecules* **2010**, *43*, 790–796.
61. Lee, S.-I.; Schomer, M; Peng, H. G.; Page, K. A.; Wilms, D.; Frey, H.; Soles, C. L.; Yoon, D. Y. *Chem. Mater.* **2011**, *23* (11), 2685–2688.
62. Zhang, C.; Gamble, S.; Ainsworth, D.; Slawin, A. M. Z.; Andreev, Y. G.; Bruce, P. G. *Nat. Mater.* **2009**, *8*, 580–584.
63. Singh, M.; Odusanya, O.; Wilmes, G. M.; Eitouni, H. B.; Gomez, E. D.; Patel, A. J.; Chen, V. L.; Park, M. J.; Fragouli, P.; Iatrou, H.;

Hadjichristidis, N.; Cookson, D.; Balsara, N. P. *Macromolecules* **2007**, *40* (13), 4578–4585.

64. Panday, A.; Mullin, S.; Gomez, E. D.; Wanakule, N.; Chen, V. L.; Hexemer, A.; Pople, J.; Balsara, N. P. *Macromolecules* **2009**, *42* (13), 4632–4637.
65. Choi, I.; Ahn, H.; Park, M. J. *Macromolecules* **2011**, *44* (18), 7327–7334.
66. Gomez, E. D.; Panday, A.; Feng, E. H.; Chen, V.; Stone, G. M.; Minor, A. M.; Kisielowski, C.; Downing, K. H.; Borodin, O.; Smith, G. D.; Balsara, N. P. *Nano Lett.* **2009**, *9* (3), 1212–1216.
67. Li, J.; Kamata, K.; Komura, M.; Yamada, T.; Yoshida, H.; Iyoda, T. *Macromolecules* **2007**, *40* (23), 8125–8128.

Downloaded by UNIV OF GUELPH LIBRARY on June 14, 2012 | http://pubs.acs.org
Publication Date (Web): May 7, 2012 | doi: 10.1021/bk-2012-1096.ch008

Downloaded by CORNELL UNIV on June 14, 2012 | http://pubs.acs.org
Publication Date (Web): May 7, 2012 | doi: 10.1021/bk-2012-1096.ch009

Chapter 9

An Overview of Polymer Electrolyte Membranes for Fuel Cell Applications

Kirt A. Page* **and Brandon W. Rowe**

Polymers Division, National Institute of Standards and Technology,
Gaithersburg, MD 20899
***kirt.page@nist.gov**

While fuel cells have received considerable attention over the last 10 years to 20 years, the history of hydrogen fuel cells dates back to 1838. It would take more than a century before polymers would be implemented as an electrolyte for proton transport (1955) and another 40 years after that before a real renaissance would be sparked that would finally make polymer electrolyte membrane (PEM) fuel cells a conceivable means of electrochemical energy conversion. This chapter covers a brief history of the fuel cell and the use of polymer electrolytes as an ion-transport medium. In addition to an overview of the materials challenges, the various types of polymeric materials being pursued as potential fuel cell membranes are presented. Although this chapter is not an exhaustive review of the literature, it is our hope that it will give the reader an appreciation for the history of PEM fuel cells and the approaches that polymer chemists are taking in order to address the major impediments for wide-spread commercialization of PEM fuel cells.

Introduction

A fuel cell is an electrochemical device that is capable of converting the stored, chemical energy of a fuel into electrical energy, *i.e.*, electricity, through electrochemical processes. A typical fuel cell consists of three major components including (*1*, *2*):

Not subject to U.S. Copyright. Published 2012 by American Chemical Society
In Polymers for Energy Storage and Delivery: Polyelectrolytes for Batteries and Fuel Cells; Page, K., et al.;
ACS Symposium Series; American Chemical Society: Washington, DC, 2012.

1) a fuel electrode, or anode
2) an oxidant electrode, or cathode; and
3) an electrolyte.

For a PEM fuel cell, the electrolyte consists of a polymer membrane that is capable of charge transport; a generic scheme is shown in FIGURE 1. In general, the fuel is catalytically oxidized at the anode to produce electrons and ions. While the electrons are diverted to an external circuit to create a current, the positively charged ions are transported through the electrolyte to the cathode where they recombine with the electrons and an oxidant to form exhaust. Fuel cells are typically distinguished by the type of electrolyte used in charge transport. The major classes of fuel cells include: alkaline fuel cells (AFC), solid oxide fuel cells (SOFC), phosphoric acid fuel cells (PAFC), molten carbonate fuel cells (MCFC), and proton-exchange (or polyelectrolyte) membrane fuel cells (PEMFCs). The latter class, PEMFCs, is the principle subject of the studies presented in this book. It should be noted that some AFCs use polymer membranes and will also be discussed in subsequent chapter(s). Before going into further detail, it is important that the reader have at least a general knowledge of the history of fuel cells and the use of polymers in fuel technology. A detailed historical account of this technological area is beyond the scope of a single introductory chapter on PEMFCs; however, this introduction will serve to give the reader an appreciation for the long history of fuel cell technology. While it is nearly a decade old, Perry and Fuller (*3*) offer an excellent historical perspective on fuel cell technology in the 20th century. Moreover, the Smithsonian Institution is collecting information and developing a website dedicated to the history and workings of fuel cell technology (*4*).

Downloaded by CORNELL UNIV on June 14, 2012 | http://pubs.acs.org
Publication Date (Web): May 7, 2012 | doi: 10.1021/bk-2012-1096.ch009

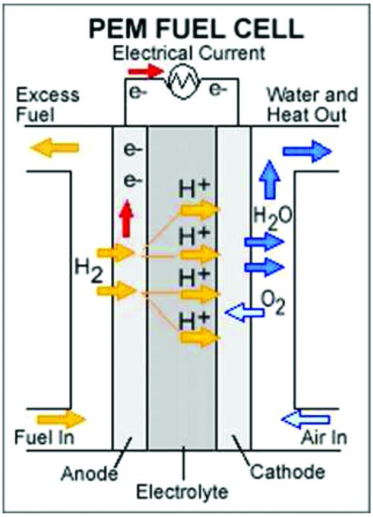

Figure 1. Generic PEM fuel cell schematic (5).

Downloaded by CORNELL UNIV on June 14, 2012 | http://pubs.acs.org
Publication Date (Web): May 7, 2012 | doi: 10.1021/bk-2012-1096.ch009

History of the Fuel Cell

Advances in the understanding of electrochemistry and catalysis in the early 18th and 19th centuries helped to nurture the discovery of the fuel cell effect and the ultimate invention of the fuel cell (*6*). The origin of this specific technology, however, can really be credited to the work by Christian Friederich Schönbein (1799-1868) and Sir William Robert Grove (1811-1896). It was the talent and vision of these two scientists that gave the world a technology with significant potential for solving the energy needs of today and tomorrow (*3*, *7–9*).

Schönbein was the first person to report and accurately describe the fuel cell effect in his early 1839 paper entitled "On the Voltaic Polarization of certain Solid and Fluid Substances" in which he reported a current produced through the combination of hydrogen and oxygen, thus the first reported hydrogen fuel cell (*10*). This publication was followed shortly by an article in which Grove suggested, in a short postscript, that he had found a means to produce electricity through the combination of the constituents of water, that is, hydrogen and oxygen (*11*).

Despite Schönbein's early discovery of the fuel cell effect, it is often Sir William Robert Grove to whom credit of the invention of the fuel cell is given. Both men made significant contributions to the understanding of the electrochemistry underlying the fuel cell effect in the early 1840's leading up to Grove's 1845 publication that demonstrated the first working 10-cell power generator. An excellent historical account of these events and evidence of the remarkably close and personal relationship that developed between these two men can be found in the book, The Birth of the Fuel Cell by Ulf Bossel (*7*). Bossel most aptly and succinctly states that to be historically accurate, and fair, one would characterize the events in a way that gives Schönbein the credit for discovery of the fuel cell effect and Grove credit for inventing the fuel cell. In essence, in the years between 1838 and 1845, Schönbein delighted in developing a fundamental understanding of the phenomena giving rise to the effect that he had observed, while Grove put this understanding to use in the development of an energy technology that had, and still has, the potential to revolutionize the way humans produce/convert and consume energy.

Interestingly, it was in 1894 that a scientist named Friedrich Wilhelm Ostwald, later a Nobel Laureate, in his address to the Deutschen Electrochemischen Gesellschaft that was later published as an article in the Zeitschrift für Elektrotechnik und Elektrochemie entitled "The Electrochemistry of Today and the Technology of the Future," spoke about the inefficiency and potential harm of using combustion for producing electricity (*12*). He saw the potential for storing and producing energy through electrochemical processes, which were quite efficient given the infantile nature of the field at that time. He demanded that mankind must replace the heat engine with electrochemical cells, such as the fuel cell, as a means to convert the stored energy in combustible materials, *i.e.*, coal, into electrical energy. The echoes of Ostwald's vision can be heard, 117 years later, in the voices of people today who demand that we find alternative, clean, and sustainable means of energy conversion.

Downloaded by CORNELL UNIV on June 14, 2012 | http://pubs.acs.org
Publication Date (Web): May 7, 2012 | doi: 10.1021/bk-2012-1096.ch009

History of PEM Fuel Cells

For the most part, the earliest fuel cells used platinum (Pt) as electrodes and a liquid electrolyte that was usually acidic in nature (*e.g.*, dilute sulfuric acid). In the early work by Schönbein and Grove, the fuel was typically hydrogen with oxygen being the oxidant. However, at the dawn of the 20th century, researchers were also pursuing direct-coal fuel cells due to the use of coal as a fuel in combustion engines.

It would not be until the 1950s that polymer materials, or solid-polymer electrolytes, would find their way into a working fuel cell and would be developed and eventually put to use in a technological application. In large part, the development of polyelectrolyte membrane technology was stimulated by the energy needs of space exploration. Because fuel cells operate with relatively high efficiency and are light-weight, they were poised to meet the auxiliary power needs of spacecraft. The first practical fuel cell for this application was invented in 1955 by W. T. Grubb (*13–15*), a scientist working for General Electric Company, and used an ion exchange (*13*, *14*) resin membrane as the electrolyte. The specific resins used changed in the years from 1959-1967, but ranged from membranes synthesized from the polymerization of phenol-sulfonic acid with formaldehyde, in the early years, to variations of polystyrene sulfonic acid in the mid-to-late 1960s. The patent on this technology, issued in 1959, purported that the fuel cell, using a solid-polymer electrolyte, was capable of operating at room temperature and under atmospheric pressures. The list of properties Grubb ascribed to this cation exchange resin, which gave it the ability to perform well in a fuel cell, would become the target for which decades of polymer chemists since have focused their aim while devising new synthetic routes towards higher performing polymer membranes for fuel cell applications. These attributes include, but are not limited to:

1) a good electrolyte (*i.e.*, high ion conductivity)
2) a negligible electrical conductivity
3) permeable to ions but allow only one type of charge
4) resistive to permeation of uncharged gases
5) variable membrane area and thickness; and
6) good mechanical strength.

Despite their famed use in NASA’s Gemini program, these PEMFCs suffered from insufficient proton conductivity, which resulted in poor power output (< 100 $mWcm^{-2}$), and poor durability, due to the oxidative instability of the C-H bonds in the polymer chain. To use a term by Costamanga (*16*, *17*), the ‘quantum leap’ in fuel cell performance and durability hinged on the invention of the perfluorosulfonic acid membrane, Nafion, by E.I. Du Pont de Nemours & Company, Inc. in 1962 (*18*, *19*). Nafion was initially used as a membrane separator in chloralkali cells and it was not until 1966 that Nafion was implemented in an H_2/O_2 fuel cell. Nafion met the originally-stated criteria for an ideal solid-polymer electrolyte, and it surpassed all other materials in its specific conductivity and its durability – increasing the conductivity by at least a factor of two and the lifetime by nearly four orders of magnitude – and remains the industry benchmark for PEMFC performance to this day. The specific properties of this material will be discussed in greater detail in later sections.

One would intuit, after such successful demonstrations of the practical use of PEMFC technology, that polymer-based fuel cells would enjoy widespread technological advancements and commercial use as power supplies for any number of applications ranging from portable electronic devices and back-up power stations to fuel cell-powered automobiles. However, this reality did not manifest itself. In fact, if one examines the time-line of patent and publication activity for polymer-based fuel cells (FIGURE 2), there is a surprisingly vast dormancy in activity after the developments of the 1960s and 1970s. In large part, durability and the cost of the membrane materials and the platinum catalyst in the electrodes were, and continue to be, critical factors that inhibited further commercial success.

Downloaded by CORNELL UNIV on June 14, 2012 | http://pubs.acs.org
Publication Date (Web): May 7, 2012 | doi: 10.1021/bk-2012-1096.ch009

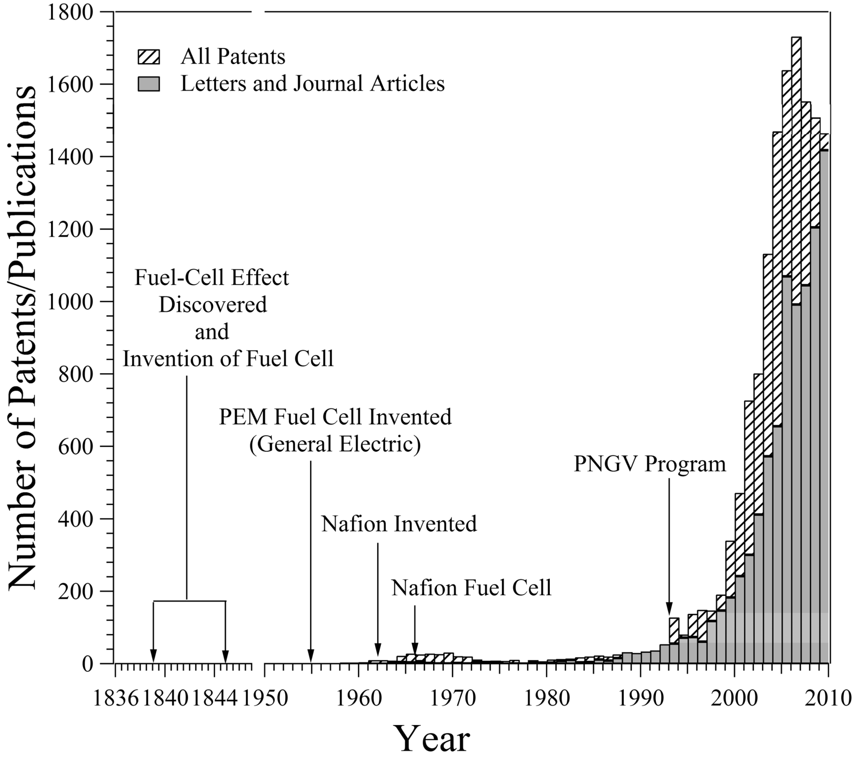

Figure 2. Historical perspective of fuel cell development.

A particularly salient feature of FIGURE 2 is the rapid rise in the number of patents and publications (referencing polymer fuel cells) that occurred in the mid-1990s. There are several factors, both societal and technological, that were

In Polymers for Energy Storage and Delivery: Polyelectrolytes for Batteries and Fuel Cells; Page, K., et al.;
ACS Symposium Series; American Chemical Society: Washington, DC, 2012.

Downloaded by CORNELL UNIV on June 14, 2012 | http://pubs.acs.org
Publication Date (Web): May 7, 2012 | doi: 10.1021/bk-2012-1096.ch009

responsible for the genesis of this renaissance in PEMFC technological research. While fuel cell research did not afford any particular prominence during the height of the Energy Crisis of the 1970s, it is likely that means of alternative energy were on the minds of politicians and researchers alike. However, this fact did not stimulate any advancement in fuel cell technology, at least with regards to PEM fuel cells. Undoubtedly, the origins in the rise of PEMFC research activity (circa 1996) can be traced back to the advancements in the fabrication of membrane electrode assemblies (MEA) by researchers at Los Alamos National Laboratory (LANL). Ian Raistrick, Supramaniam Srinivasan, and others developed methods capable of reducing the membrane electrode assembly (MEA) platinum content from $4x10^{-3}$ gcm^{-2} to $3.5x10^{-4}$ gcm^{-2}, a significant advancement in reducing the overall cost of the fuel cell (*20*, *21*). From the mid-1980s to the early 1990s the research team at LANL continued to refine the MEA manufacturing process and made several seminal contributions to understanding the kinetics of the electrochemical processes in PEMFCs, durability testing, and modeling of PEMFC performance.

On the heels of these technological and scientific breakthroughs, the Clinton administration established the Partnership for a New Generation of Vehicles (PNGV) program (*22*). This large-scale program was a concerted effort sponsored by the United States Federal government and the U.S. Council for Automotive Research (including DaimlerChrysler, Ford, and General Motors (GM)) with a mission to oversee the research and development (R&D) activities for the advancement of state-of-the-art technologies that could lead to increased fuel economy and reduced emissions of a wide range of vehicles. While there were several Federal agencies that participated in the program, the Department of Commerce, Office of the Under Secretary for Technology, was tasked with leading the Federal government's participation. This program was followed by the Bush administration's announcement of the FreedomCAR program in January of 2002. The Department of Energy (DoE) continues to support R&D in the area of fuel cell technology. It is reasonable to infer that these investments helped to spur further technological innovation and development as evidenced by the rapid increase in the number patent and literature publications pertaining to PEMFCs. With this history in mind, several questions come to mind including:

> What is the current state-of-art in membrane technology?
> What are the materials challenges?
> What are the alternative membrane materials?
> What are the future directions?

We hope to offer an overview of these guiding questions in the following sections.

Membrane Technologies and Challenges

The most cited impediments to world-wide commercialization of PEMFCs in the areas of transportation, stationary, and portable power applications are the high cost and poor durability of PEMFC stacks (*23–25*). The MEA constitutes

Downloaded by CORNELL UNIV on June 14, 2012 | http://pubs.acs.org
Publication Date (Web): May 7, 2012 | doi: 10.1021/bk-2012-1096.ch009

a significant portion of this cost due to the high production cost of the polymer membrane and the use of precious metals, notably platinum, in the catalyst layers (CL). The cost and durability targets for transportation and stationary power applications have been set by the DoE and are shown in TABLE 1. As of 2009 and 2005, respectively, a lifetime of *ca.* 2,500 h has been achieved for transportation (equivalent to *ca.* 75,000 miles) and 20,000 h for station fuel cells. The cost of fuel cell stacks has been reduced drastically over the last decade, dropping from \$275/kW in 2002 to \$51/kW in 2010.

Table 1. DoE cost and durability performance targets for fuel cell stacks. Goal years in parentheses

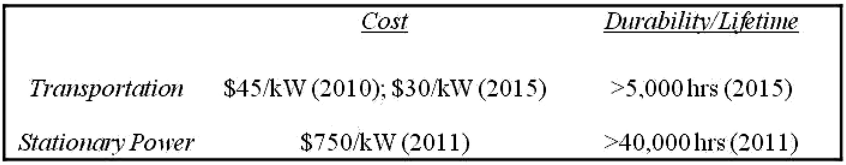

	Cost	*Durability/Lifetime*
Transportation	\$45/kW (2010); \$30/kW (2015)	>5,000 hrs (2015)
Stationary Power	\$750/kW (2011)	>40,000 hrs (2011)

Researchers are tackling the cost of PEMFCs in a number of ways. The materials used in the catalyst layers (and the catalyst support) and the membranes themselves can be expensive and represent a significant fraction of the cost of a fuel cell stack. Three strategies for reducing the catalyst layer cost that have been identified and are being pursued: 1) reduction of Pt loading (*i.e.*, more efficient use of the catalyst materials), 2) replacing Pt with new, cheaper catalyst materials and alloys (*e.g.*, ruthenium and palladium) and 3) to replace Pt, or other precious metals, with non-precious metal catalysts. In addition, the perfluorosulfonic acid membranes materials typically used can also be expensive because of the chemistry used to synthesize them. For example, a review of solid polymer electrolytes for fuel cells written in 2005 placed the cost of Nafion at \$700 per m^2 (*24*). The membrane performance targets for transportation applications set by the DoE can be seen in TABLE 2 (*26*, *27*). Polymer chemists are searching for alternative membrane materials that are cheaper to synthesize, but still meet the high performance criteria demanded by the harsh fuel cell operating conditions and that, to date, have been met by perfluorosulfonic acid ionomer-based materials. The various types of membranes are described in a later section.

While durability and cost are identified as two separate challenges facing commercialization of fuel cells, the two factors are actually inter-dependent. While the base cost of the materials is not necessarily a reflection, or related to, the durability of the materials, the overall operating costs of a fuel cell are intimately tied to durability issues. The more often a stack, or stack components, must be replaced, the more expensive it is to operate. Therefore, a more appropriate term might be the *durability-cost* factor of fuel cell commercialization.

Downloaded by CORNELL UNIV on June 14, 2012 | http://pubs.acs.org
Publication Date (Web): May 7, 2012 | doi: 10.1021/bk-2012-1096.ch009

Table 2. DoE technical targets for membranes for transportation applications

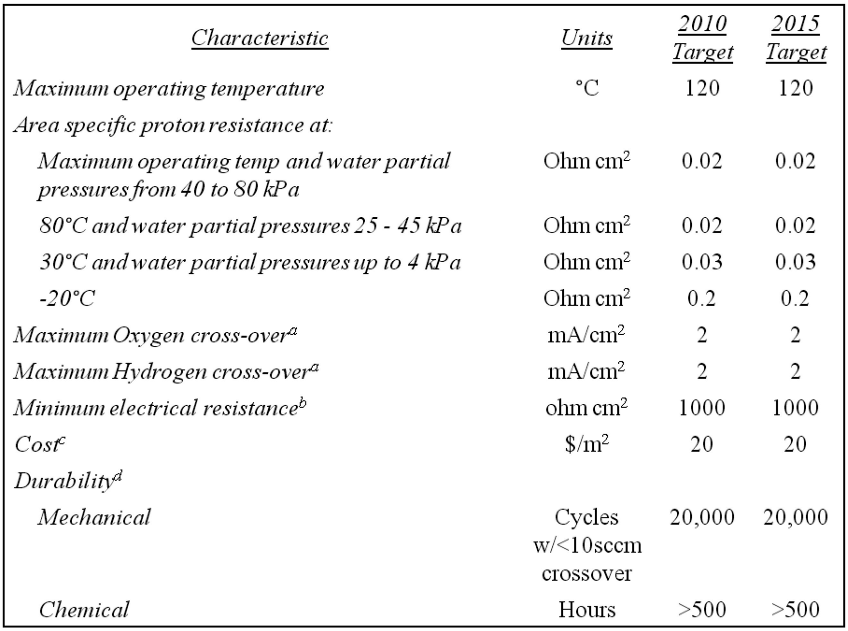

Characteristic	*Units*	*2010 Target*	*2015 Target*
Maximum operating temperature	°C	120	120
Area specific proton resistance at:			
Maximum operating temp and water partial pressures from 40 to 80 kPa	Ohm cm^2	0.02	0.02
80°C and water partial pressures 25 - 45 kPa	Ohm cm^2	0.02	0.02
30°C and water partial pressures up to 4 kPa	Ohm cm^2	0.03	0.03
-20°C	Ohm cm^2	0.2	0.2
Maximum Oxygen cross-over[a]	mA/cm^2	2	2
Maximum Hydrogen cross-over[a]	mA/cm^2	2	2
Minimum electrical resistance[b]	ohm cm^2	1000	1000
Cost[c]	\$/m^2	20	20
Durability[d]			
Mechanical	Cycles w/<10sccm crossover	20,000	20,000
Chemical	Hours	>500	>500

a) Tested in MEA at 1 atm O_2 or H_2 at nominal stack operating temperature, humidified gases at 0.5V DC.

b) Measure in humidified N_2/N_2 at 0.5V DC at 80°C.

c) Based on 2002 dollars and costs projected to high volume production (500,000 stacks per year).

d) Based on MEA chemical stability and metrics and membrane mechanical cycle and metrics.

The durability of the MEA can mean several things. First, one must consider the durability of each component independently and the variety of factors that can lead to degradation. All of the materials in the MEA are subject to chemical, electrochemical, and mechanical degradation processes (*23*). The catalyst and the catalyst support undergo electrochemical degradation, which can ultimately lead to mechanical failure. Likewise, the membrane lifetime is reduced due to chemical and electrochemical degradation (*23–25*, *28–30*). Ultimately, this molecular-level degradation can lead to mechanical failure of the membrane as well. In addition to the functional segments of the MEA, the durability of other components that are part of fuel cell operations, including gaskets and seals need to be carefully understood.

Another key factor when considering the durability and performance of a PEMFC is the effect of contaminants on performance (*23*, *30*). Again, contamination can occur throughout the MEA and come from the fuel (hydrogen), the oxidant (air), or other components present in the cell stack. At the anode, impurities in the fuel feed can lead to degradation and low performance. Typical impurities include CO, CO_2, H_2S, NH_3, and CH_4. At the cathode, NO_x and SO_x are the foremost causes of contamination. Lastly, metal ions such as Fe^{3+}, Ni^{2+}, Cu^{2+}, and Cr^{3+} coming from the bipolar plates can leach into the PEM causing chemical and mechanical degradation and failure. The most recent review by Zamel and Li cover these issues in detail (*30*).

Polyelectrolyte Membranes for Fuel Cell Applications

A wide variety of polymer types have been developed and studied for application as proton exchange membranes. These materials include, but are not limited to, poly(perfluorosulfonic acid)s, polystyrene derivatives, poly(arylene ether)s, polysulfones, polyimides, and engineered block copolymers (*31*)–(*38*). Although different applications for proton exchange fuel cells, *i.e.*, stationary, portable, or automotive power, have specific operational and material requirements, several material properties are key to high performance membranes. In all applications, materials with high proton conductivity, low fuel crossover, good mechanical and chemical stability, and manufacturability are needed for optimal performance. In addition to these requirements, materials must have low enough costs for commercial viability. Anion exchange materials containing ammonium, phosphonium, and sulfonium groups, which are being studied for application in alkaline fuel cells, must also meet analogous requirements as their proton exchange membrane counterparts.

One particularly difficult challenge for PEM materials development is achieving high proton conductivity with low water content. Because of the nature of proton mobility in these materials, there is an inherent tradeoff between water content and conductivity (*39*). For example, there is a minimum level of hydration to achieve a desirable conductivity (*e.g.*, $\sigma = 0.1$ S/cm, λ (moles of H_2O/moles of SO_3H) = 22). However, maintaining a high water content during fuel cell operation complicates water management issues and associated support systems. These issues are a large part of the motivation to develop high performance anhydrous membrane materials (*40*). A similar tradeoff between ionic conductivity and methanol permeability is an important issue in the design of materials for direct methanol fuel cells.

A broad overview of the basic material classes used in fuel cell membranes is presented here as an introduction to the development milestones in the area. This section is not an exhaustive review, and the reader is referred to additional resources for more detailed information. These material classes represent a sampling of the range of materials studied for application in PEMFCs. Extensive efforts to modify and improve these base materials continues to drive further development in this field.

Perfluorosulfonic Acid Ionomers (PFSA)

Nafion, a poly(perfluorosulfonic acid), is the most widely studied proton exchange material; its chemical structure is shown in FIGURE 3. Nafion exhibits

Downloaded by CORNELL UNIV on June 14, 2012 | http://pubs.acs.org
Publication Date (Web): May 7, 2012 | doi: 10.1021/bk-2012-1096.ch009

excellent thermal and chemical stability. Nafion consists of a perfluoroethylene backbone with flexible perfluorinated vinyl ether side chains terminated by a sulfonic acid group. Many studies have investigated the molecular-scale structure of this complex material, which contains ionic clusters and crystallites in an amorphous perfluorinated, Teflon-like, matrix (*41*)–(*44*). The specific morphology of Nafion can strongly influence its performance characteristics, and the reader is referred to additional information on this subject (*35*). Similar materials to Nafion have been developed by other chemical manufactures, including Flemion by Asahi Glass, Aciplex by Asahi Chemical, and Aquivion by Solvay Solexis (*45*, *46*).

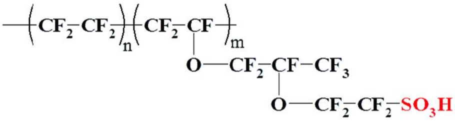

Figure 3. Nafion chemical structure.

Nafion is also available as dispersions in a range of solvents, most commonly in water and alcohol mixtures. These dispersions are used to create thin films of Nafion and in the preparation of catalyst layers in MEAs. The properties of these “re-cast” Nafion materials depend on the preparation conditions and can be significantly different than the commercial melt-processed films (*47*)–(*49*). Early work by Moore and Martin showed that recast Nafion material, without thermal annealing, had poor mechanical properties as compared to the melt processed films (*50*). Ma *et al.* have shown that the molecular conformations of Nafion in dilute dispersions and the morphology of the membranes prepared from these dispersions are strongly influenced by the solvent quality (*51*). While these studies focused on recast materials of bulk-like thickness, work continues on understanding the properties of thin films created using these dilute dispersions (*52*).

Despite Nafion’s strengths, the material is expensive and exhibits poor proton conductivity at low water contents and high temperatures, which limits the ideal operating range. Extensive efforts have focused on improving the performance of Nafion, including blends, patterning, nanofiber formation, and the incorporation of moieties, such as zeolites, silica and titanium dioxide, to improve water retention (*53*)–(*55*). Reinforced PFSA membranes, such as those developed by Gore Fuel Cell Technologies based on e-PTFE, have been shown to improve the durability of Nafion by up to an order of magnitude and are considered state-of-the-art materials (*56*, *57*). Because of its unique performance characteristics and the extensive studies focused on this material, Nafion is likely to remain the primary benchmark for PEM materials for the foreseeable future. New multiple acid side chain (MASC) polymers with low equivalent weight are being developed by 3M (*58*). By adding acidic groups to the side chains, the backbone regions of these perfluorinated materials are still able to crystallize and thus maintain mechanical strength. The use of nanofiber supports has also been shown to reduce swelling and increase the mechanical strength of these MASC polymers under hydrated conditions (*59*). This approach is aimed at developing

Downloaded by CORNELL UNIV on June 14, 2012 | http://pubs.acs.org
Publication Date (Web): May 7, 2012 | doi: 10.1021/bk-2012-1096.ch009

materials with enhanced conductivity as compared to Nafion while maintaining mechanical integrity in very low equivalent weight materials.

Polysulfones and Phosphazenes

Researchers seeking novel materials that are competitive with Nafion have made significant progress in the development of novel hydrocarbon PEMs based on sulfonated aromatic polymers, including polystyrenes, polysulfones, polyimides, polyphosphazenes, poly(arylene-ether)s, and others (*34*, *60*, *61*). These hydrocarbon-based materials offer promising routes to high performance PEMs at lower cost than the perfluorinated Nafion.

The most common method for preparing these materials uses electrophilic aromatic sulfonation to modify existing polymers. A classic example of this material class is sulfonated and crossklinked polystyrenes, which were part of the Gemini space program. This post-polymerization modification technique offers limited control over the location and degree of sulfonation, and may create undesired byproducts or degrade the polymer structure. However, the relative simplicity and applicability of this technique have driven many studies focused on understanding the influences of this modification on material properties.

To circumvent the problems associated with post-modification methods, McGrath's research group at Virginia Tech popularized the direct copolymerization of sulfonated monomers (*34*). Using mono- and di-sulfonated monomers, copolymers could be synthesized in any composition desired. This technique was used to create a wide range of sulfonated poly(arylene ether) materials. The conductivity and water uptake of these materials were shown to be directly related to the degree of sulfonation. Phase separation and significant swelling were observed in materials with high sulfonation levels, thus highlighting the need to balance water uptake and mechanical stability with proton conductivity. The variety of monomers available for this synthetic route has led to many variations in the chemistry of these materials. Because many of the monomers used to create these materials are also available at low prices and easily produced on a commercial scale, these materials offer potentially less expensive proton exchange membranes. Efforts have also been extended to include fluorinated monomers (*32*).

Another class of PEM materials that offers a wide range of possible macromolecular architectures is polyphosphazenes, which consist of a backbone of alternating phosphorus and nitrogen atoms with side groups attached to each phosphorus atom. The first PEM materials based on polyphosphazene chemistry were from sulfonated poly(aryloxy phosphazenes) (*62*). Additionally, Allcock *et al.* synthesized phosphonated poly(aryloxy phosphazenes), which showed significantly lower methanol crossover as compared to Nafion (*63*).

It is important to keep in mind that when comparing the performance characteristics of materials that have significantly different densities, such as hydrocarbon-based and perfluorinated materials, it is often more appropriate to use volume-based parameters, rather than mass-based parameters (*64*). Kim and Pivovar have developed a methodology for making meaningful comparisons between dramatically different materials. The effects of morphology on proton

Downloaded by CORNELL UNIV on June 14, 2012 | http://pubs.acs.org
Publication Date (Web): May 7, 2012 | doi: 10.1021/bk-2012-1096.ch009

conductivity and performance should also be considered in any comparison. Many hydrocarbon polymers show sufficiently high proton conductivities only in materials with high ion-exchange capacities, which exhibit significant water uptake and decreased mechanical strength due to swelling. Improving the dimensional stability and proton conductivity of aromatic polymers are critical issues in the design of new materials.

Block Copolymers and Blends

It is generally understood that proton transport through ionomers is associated with the ionic network within a material, and the transport properties are intimately related to morphology of this network, *i.e.*, poorly connected ionic domains do not facilitate fast proton transport while materials with an interconnected path through ionic channels can exhibit high conductivities. In many random copolymers and post-sulfonated materials, the size and connectivity of these ionic nanostructures are poorly controlled. One approach to create and control nanophase separation is through the use of block copolymers with concentrated ionic blocks along the polymer backbone (*31*). This type of structural architecture, with the ionic block facilitating transport and the nonionic block providing mechanical strength, enables the development of specifically engineered materials. By decoupling these performance requirements into different segments of the polymer chain, one can start to unravel how specific molecular structures affect different aspects of the material. Furthermore, by controlling the molecular mass of each component, the size scale of the phase separated regions can be tailored to some degree. Balsara and Beers recently summarized efforts to determine the ideal size and geometry of proton conducting channels; they report that channels with dimensions less than 6 nm in width are ideal for proton transport (*65*).

While sulfonated block copolymers generally show increases in proton conductivity with IEC and hydration, consistent with other polymer systems, changes in morphology with IEC or hydration can also significantly influence transport and performance properties. A morphological transition from periodic lamellar to a nonperiodic structure in sulfonated poly(styrene-b-(ethylene-r-butylene)-b-styrene) increased proton conductivity by an order of magnitude, as reported by Kim *et al.* (*66*). This significant increase in proton conductivity was realized by adding methanol to tetrahydrofuran as the casting solvent. Similar changes in conductivity with morphology were reported for sulfonated poly(styrene-b-isobutylene-b-styrene) (*67*). Although these non-equilibrium structures are difficult to predict, it is important to develop an understanding of the factors that control these kinetically trapped morphologies due to their strong influence on performance. Through systematic studies on a series of polystyrene sulfonate-b-polymethylbutylene (PSS–PMB) block copolymers, Balsara *et al.* have established relationships between morphology, water uptake, and ionic conductivity (*68–71*).

With aims to harness possible synergistic effects of miscible polymer blends, blended systems have also been studied for application as fuel cell membranes (*72*). For example, poly(vinylidene fluoride) (PVdF) is miscible under certain conditions with Nafion; however, the addition of PVdF reduces water uptake and

Downloaded by CORNELL UNIV on June 14, 2012 | http://pubs.acs.org
Publication Date (Web): May 7, 2012 | doi: 10.1021/bk-2012-1096.ch009

proton conductivity. Song *et al.* demonstrated improved performance of Nafion/PVdF blends by chemical modification of the PVdF phase (*73*). Studies on other materials such as blends of sulfonated poly(ether ketone ketone) polymers with different ionic exchange capacity showed that the ratio of proton conductivity to water sorption could be optimized. Optimization of the tradeoff between these two factors was attributed to percolative pathways for proton transport, which were created by the co-continuous morphology of the blended system (*74*, *75*).

Anhydrous Proton Conducting Membranes

Elevated temperature fuel cell operation, >120 °C, offers several advantages over lower temperature operation, including: increased tolerance to contaminates such as carbon monoxide, faster electrode kinetics, and streamlined water/heat management (*40*). However, because water contributes to the network for proton conduction in PEMs, conductivity decays rapidly at temperatures above 100 °C as the material dehydrates. Two possible ways to resolve this issue are to replace the water with a higher boiling point solvent or to immobilize a proton solvent within the material. Furthermore, membrane stability can also be compromised at high operating temperatures; requiring development of materials with improved high-temperature strength for these applications (*23*).

One of the most prominent candidates for high-temperature PEM fuel cell applications is phosphoric acid doped polybenzimidazole (PBI) membranes (*40*). Early development of these materials at Case Western Reserve University in the 1990s showed their promise in fuel cell membrane applications (*76*). PBI is capable of incorporating large amounts of phosphoric acid from dilute aqueous solutions. Increasing acid concentration in PBI membranes increases conductivity, but also lowers mechanical strength. Wainright *et al.* reported that the mechanical properties of the membrane are no longer sufficient at acid concentrations higher than five acid molecules per polymer repeat unit (*76*). While early work on these materials incorporated acid molecules by immersing preformed membranes in solutions, more recently, doped PBI films were synthesized using a sol-gel process; these materials showed promising fuel cell performance at temperatures above 150 °C using a non-humidified feed gas (*77*). Additionally, this material was shown to give stable operation for > 1000 h. Some concerns regarding the low temperature performance of these material types question their performance under cold start-up conditions in applications such as transportation. Also, the long term retention of phosphoric acid in such materials also has to be proven under appropriate operating conditions.

Another approach to creating anhydrous proton conducting membranes is to covalently link heterocyclic molecules to polymeric materials. Heterocycles such as imidazole, benzimidazole, and pyrazole are good proton solvents and due to their amphoteric nature and high boiling temperatures, they are suitable replacements for water within a PEM material (*78*). Because proton transport in these materials is likely facilitated by structural diffusion, flexible spacers are often used to attach these molecules to increase their mobility within the system. Studies on model compounds, including phosphonic acid groups, sulfonic acid groups, and imidazole groups, at low humidity and temperatures from 120 °C

Downloaded by CORNELL UNIV on June 14, 2012 | http://pubs.acs.org
Publication Date (Web): May 7, 2012 | doi: 10.1021/bk-2012-1096.ch009

Downloaded by CORNELL UNIV on June 14, 2012 | http://pubs.acs.org
Publication Date (Web): May 7, 2012 | doi: 10.1021/bk-2012-1096.ch009

to 160 °C identified phosphonic acid groups as the most suitable additive for improving proton conductivity (*79*). The high proton conductivity in the dry state of this material was attributed to high degrees of self-dissociation and dynamical hydrogen bonding. A straightforward addition of phosphonic acid into a polymer system is poly(vinylphosphonic acid) (PVPA) (*80*). Although PVPA exhibits good proton conductivity, it has poor mechanical properties due to its low glass transition temperature; therefore, researchers are continuing along this path by incorporating aromatic groups into the polymer structure to improve material stability needed for practical applications (*81*, *82*).

Anion Exchange Membranes

The potential advantages of alkaline fuel cells as compared to proton exchange membrane fuel cells have recently generated great interest in anion exchange membranes (AEM)s. In addition to benefits of reduced fuel crossover, improved water management, and a wide range of fuels, perhaps the greatest benefit of alkaline fuel cells is that they have the capability to operate with non-noble metal catalysts (*9*, *83*). The cost savings opportunity associated with using catalysts other than platinum is a significant factor in the drive for development of AEM materials. A recent review categorized the current AEM materials of interest into three classes:

1) heterogeneous membranes containing ion-solvating polymers; organic-inorganic membranes
2) interpenetrating polymer network membranes, and
3) homogeneous membranes (*9*)

Each material type has specific advantages and disadvantages for application in alkaline fuel cells, and a dominant high performance material, such as Nafion in the case of PEM fuel cells, is not apparent.

One of the most critical issues with the use of AEMs in alkaline fuel cells is chemical stability. Commercially produced AEMs are typically created by radiation-induced grafting and mostly based on crosslinked polystyrene materials (*9*). Unfortunately, these materials are not highly stable in electrochemical or alkaline environments. Due to the nucleophilicity of the hydroxide anion, the cations present in these materials are susceptible to several degradation mechanisms. Furthermore, the formation of carbonates from CO_2 that may be present during operation can reduce conductivity; however, because there are no mobile cations, the formation of solid precipitate is eliminated by using a membrane instead of a liquid electrolyte. In addition to the development of novel polymers that are resistant to these degradation pathways, several crosslinking strategies have been applied to improve chemical and thermal stability of AEM materials (*83*).

Understanding the transport behavior of AEM materials is also important in developing optimized materials for this application. Hibbs *et al.* compared the transport properties of AEMs synthesized from chloromethylated polysulfone and PEMs such as sulfonated polyphenylenes and Nafion (*84*). Although water

In Polymers for Energy Storage and Delivery: Polyelectrolytes for Batteries and Fuel Cells; Page, K., et al.;
ACS Symposium Series; American Chemical Society: Washington, DC, 2012.

mobility was higher in the AEMs—based on water self-diffusion behavior—they exhibited lower conductivity and water permeability than the sulfonated PEMs. The phase-separated morphology of the PEM materials was hypothesized as the reason for the greater conductivity of these materials despite slower local water mobility as compared to the AEMs. Clearly, understanding the influence of morphology on transport and performance characteristics is essential for further development of all material types for fuel cell applications.

Summary and Outlook

Fuel cells have the potential to become an important large-scale energy conversion technology for a variety of applications including stationary and portable power and transportation. Significant achievements in the development of polymer electrolyte materials and membrane electrode assemblies have greatly improved the viability of this technology at an industrial scale. A wide variety of materials have been studied for application in PEM fuel cells, all with some advantages and disadvantages. One of the most significant road blocks to the commercialization of current PEM fuel cells is cost; however, if production volume discount projections are correct, the price of PEM fuel cells will decrease dramatically as they begin to enter the market in larger quantities. Furthermore, researchers are investigating the design and synthesis of new polymeric materials that can be produced at a lower cost while maintaining the criteria for high performance PEM materials. Durability continues to be another significant issue that is being addressed by researchers by seeking to understand the complex degradation mechanisms of these materials under operational conditions in order to find ways to mitigate failure. Support for continued materials and device development, in addition to support for fuel infrastructure, will be required for fuel cell technologies to reach their full potential.

Downloaded by CORNELL UNIV on June 14, 2012 | http://pubs.acs.org
Publication Date (Web): May 7, 2012 | doi: 10.1021/bk-2012-1096.ch009

References

1. Li, X. *Principles of Fuel Cells*; Taylor & Francis: New York, 2006.
2. Vielstich, W. *Fuel Cells: Modern Processes for the Electrochemical Production of Energy*; John Wiley & Sons Ltd.: London, 1970.
3. Perry, M. L.; Fuller, T. F. *J. Electrochem. Soc.* **2002**, *149*, S59.
4. Collecting the History of Fuel Cells. http://americanhistory.si.edu/fuelcells/index.htm.
5. This image is a work of a United States Department of Energy (or predecessor organization) employee, taken or made as part of that person's official duties. As a work of the U.S. federal government, the image is in the public domain.
6. Sandstede, G.; Cairns, E. J.; Bagotsky, V. S.; Wiesener, K. History of Low Temperature Fuel Cells. In *Handbook of Fuel Cells*; Vielstich, W., Lamm, A., Gasteiger, H. A., Eds.; John Wiley & Sons Ltd: West Sussex, U.K., 2003; Vol. 1, pp 145−218.
7. Bossel, U. *The Birth of the Fuel Cell: 1835-1845*; European Fuel Cell Forum: Oberrohrdorf, Switzerland, 2000.

8. Eikerling, M.; Kornyshev, A. A.; Kucernak, A. R. *Phys. Today* **2006**, *59* (10), 38–44.
9. Merle, G.; Wessling, M.; Nijmeijer, K. *J. Membr. Sci.* **2011**, *377* (1−2), 1–35.
10. Schönbein, C. F. *Philos. Mag. (III)* **1839**, *14*, 43.
11. Grove, W. R. *Philos. Mag. (III)* **1839**, *14*, 127.
12. Ostwald, F. W. *Zeitschrift fuer Elektrotechnik und Elektrochmie* **1894**, *4*, 122–125.
13. Grubb, W. T. *J. Phys. Chem.* **1959**, *63* (1), 55–58.
14. Grubb, W. T.; Niedrach, L. W. *J. Electrochem. Soc.* **1960**, *107*, 131.
15. Grubb, W. T. U.S. Patent 2,913,511, 1959.
16. Costamagna, P.; Srinivasan, S. *J. Power Sources* **2001**, *102*, 253–269.
17. Costamagna, P.; Srinivasan, S. *J. Power Sources* **2001**, *102*, 242–252.
18. Certain commercial equipment, instruments, or materials are identified in this paper in order to specify the experimental procedure adequately. Such identification is not intended to imply recommendation or endorsement by the National Institute of Standards and Technology, nor is it intended to imply that the materials or equipment identified are necessarily the best available for the purpose.
19. Grot, W. *Chem. Ind. (London)* **1985**, 647–649.
20. Raistrick, I. D. *J. Electrochem. Soc.* **1986**, *133* (3), C123–C123.
21. Ticianelli, E. A.; Derouin, C. R.; Redondo, A.; Srinivasan, S. *J. Electrochem. Soc.* **1988**, *135* (9), 2209–2214.
22. Partnership for a New Generation of Vehicles. http://www.pngv.org/main/.
23. Borup, R.; Meyers, J.; Pivovar, B.; Kim, Y. S.; Mukundan, R.; Garland, N.; Myers, D.; Wilson, M.; Garzon, F.; Wood, D.; Zelenay, P.; More, K.; Stroh, K.; Zawodzinski, T.; Boncella, J.; McGrath, J. E.; Inaba, M.; Miyatake, K.; Hori, M.; Ota, K.; Ogumi, Z.; Miyata, S.; Nishikata, A.; Siroma, Z.; Uchimoto, Y.; Yasuda, K.; Kimijima, K.-I.; Iwashita, N. *Chem. Rev.* **2007**, *107*, 3904–51.
24. Smitha, B.; Sridhar, S.; Khan, a. a. *J. Membr. Sci.* **2005**, *259*, 10–26.
25. Wang, Y.; Chen, K. S.; Mishler, J.; Cho, S. C.; Adroher, X. C. *Appl. Energy* **2011**, *88*, 981–1007.
26. U.S. Department of Energy; Hydrogen and Fuel Cells Program. http://www.hydrogen.energy.gov/.
27. Research and Development of Fuel Cells for Stationary and Transportation Applications. http://web.mit.edu/mitei/docs/rfp-pdf/DE-FOA-0000360.pdf.
28. Beuscher, U.; Cleghorn, S. J. C.; Johnson, W. B. *Int. J. Energy Res.* **2005**, *29*, 1103–1112.
29. Bose, S.; Kuila, T.; Nguyen, T. X. H.; Kim, N. H.; Lau, K.-t.; Lee, J. H. *Prog. Polym. Sci.* **2011**, *36*, 813–843.
30. Zamel, N.; Li, X. *Prog. Energy Combust. Sci.* **2011**, *37*, 292–329.
31. Elabd, Y.; Hickner, M. *Macromolecules* **2011**, *44*, 1–11.
32. Lee, H.-S.; Roy, A.; Lane, O.; Lee, M.; McGrath, J. E. *J. Polym. Sci., Part A: Polym. Chem.* **2010**, *48* (1), 214–222.
33. Lee, H.-S.; Roy, A.; Lane, O.; McGrath, J. E. *Polymer* **2008**, *49* (25), 5387–5396.

Downloaded by CORNELL UNIV on June 14, 2012 | http://pubs.acs.org
Publication Date (Web): May 7, 2012 | doi: 10.1021/bk-2012-1096.ch009

34. Hickner, M.; Ghassemi, H.; Kim, Y. S.; Einsla, B. R.; McGrath, J. E. *Chem. Rev.* **2004**, *104*, 4587–4611.
35. Mauritz, K.; Moore, R. *Chem. Rev.* **2004**, *104*, 4535–4585.
36. Wang, X.; Beers, K. M.; Kerr, J. B.; Balsara, N. P. *Soft Matter* **2011**, *7* (9), 4446–4452.
37. Chen, L.; Hallinan, D. T.; Elabd, Y. A.; Hillmyer, M. A. *Macromolecules* **2009**, *42* (16), 6075–6085.
38. Hae-Seung, L.; Anand, S. B.; Abhishek, R.; James, E. M. *J. Polym. Sci., Part A: Polym. Chem.* **2007**, *45* (21), 4879–4890.
39. Robeson, L. M.; Hwu, H. H.; McGrath, J. E. *J. Membr. Sci.* **2007**, *302* (1−2), 70–77.
40. Schuster, M. F. H.; Meyer, W. H. *Annu. Rev. Mater. Res.* **2003**, *33*, 233–261.
41. Schmidt-Rohr, K.; Chen, Q. *Nat. Mater.* **2008**, *7*, 75–83.
42. Krueger, J. J.; Simon, P. P.; Ploehn, H. J. *Macromolecules* **2002**, *35*, 5630–5639.
43. Haubold, H. *Electrochim. Acta* **2001**, *46*, 1559–1563.
44. Rubatat, L.; Rollet, A. L.; Gebel, G.; Diat, O. *Macromolecules* **2002**, *35*, 4050–4055.
45. Shiroki, H.; Hiyoshi, T.; Ohta, T. *Mod. Chlor-Alkali Technol.* **1992**, *5*, 117–29.
46. Gebert, M.; Merlo, L.; Arcella, V. *ECS Trans.* **2011**, *30*, 91–95.
47. Laporta, M.; Pegoraro, M.; Zanderighi, L. *Macromol. Mater. Eng.* **2000**, *282* (1), 22–29.
48. Siroma, Z.; Kakitsubo, R.; Fujiwara, N.; Ioroi, T.; Yamazaki, S.-i.; Yasuda, K. *J. Power Sources* **2009**, *189* (2), 994–998.
49. Lee, K.; Ishihara, A.; Mitsushima, S.; Kamiya, N.; Ota, K.-i. *J. Electrochem. Soc.* **2004**, *151* (4), A639–A645.
50. Moore, R. B.; Martin, C. R. *Macromolecules* **1988**, *21* (5), 1334–1339.
51. Ma, C.-H.; Yu, T. L.; Lin, H.-L.; Huang, Y.-T.; Chen, Y.-L.; Jeng, U. S.; Lai, Y.-H.; Sun, Y.-S. *Polymer* **2009**, *50* (7), 1764–1777.
52. Dura, J. A.; Murthi, V. S.; Hartman, M.; Satija, S. K.; Majkrzak, C. F. *Macromolecules* **2009**, *42* (13), 4769–4774.
53. Yildirim, M. H.; te Braake, J.; Aran, H. C.; Stamatialis, D. F.; Wessling, M. *J. Membr. Sci.* **2010**, *349* (1-2), 231–236.
54. Dong, B.; Gwee, L.; Salas-de la Cruz, D.; Winey, K. I.; Elabd, Y. A. *Nano Lett.* **2010**, *10* (9), 3785–3790.
55. Yildirim, M. H.; Curos, A. R.; Motuzas, J.; Julbe, A.; Stamatialis, D. F.; Wessling, M. *J. Membr. Sci.* **2009**, *338* (1-2), 75–83.
56. Liu, W.; Ruth, K.; Rusch, G. *J. New Mater. Electrochem. Syst.* **2001**, *4* (4), 227–232.
57. Wu, J.; Yuan, X. Z.; Martin, J. J.; Wang, H.; Zhang, J.; Shen, J.; Wu, S.; Merida, W. *J. Power Sources* **2008**, *184* (1), 104–119.
58. Yandrasits, M. A.; Hamrock, S. J. Membranes for PEM Fuel Cells. In *Fuel Cell Chemistry and Operation*; Herring, A. M.,; Zawodzinski, T. A., Hamrock, S. J., Eds.; American Chemical Society: Washington, DC, 2010; Vol. 1040, pp 15−29.

Downloaded by CORNELL UNIV on June 14, 2012 | http://pubs.acs.org
Publication Date (Web): May 7, 2012 | doi: 10.1021/bk-2012-1096.ch009

Downloaded by CORNELL UNIV on June 14, 2012 | http://pubs.acs.org
Publication Date (Web): May 7, 2012 | doi: 10.1021/bk-2012-1096.ch009

59. Hamrock, S.; Schaberg, M.; Abulu, J.; Haugen, G.; Emery, M.; Yandrasits, M.; Xiong, P. *Polym. Prepr.* **2011**, *52* (1).
60. Peron, J.; Shi, Z.; Holdcroft, S. *Energy Environ. Sci.* **2011**, *4*, 1575.
61. Rozière, J.; Jones, D. J. *Annu. Rev. Mater. Res.* **2003**, *33*, 503–555.
62. Wycisk, R.; Pintauro, P. N. *J. Membr. Sci.* **1996**, *119* (1), 155–160.
63. Allcock, H. R.; Wood, R. M. *Polymer* **2006**, *44*, 2358–2368.
64. Kim, Y. S.; Pivovar, B. S. *Annu. Rev. Chem. Biomol. Eng.* **2010**, *1* (1), 123–148.
65. Balsara, N. P.; Beers, K. M. *Eur. Polym. J.* **2011**, *47* (4), 647–650.
66. Kim, J.; Kim, B.; Jung, B.; Kang, Y. S.; Ha, H. Y.; Oh, I.-H.; Ihn, K. J. *Macromol. Rapid Commun.* **2002**, *23* (13), 753–756.
67. Elabd, Y. A.; Napadensky, E.; Walker, C. W.; Winey, K. I. *Macromolecules* **2005**, *39* (1), 399–407.
68. Kim, S. Y.; Park, M. J.; Balsara, N. P.; Jackson, A. *Macromolecules* **2010**, *43* (19), 8128–8135.
69. Wang, X.; Yakovlev, S.; Beers, K. M.; Park, M. J.; Mullin, S. A.; Downing, K. H.; Balsara, N. P. *Macromolecules* **2010**, *43* (12), 5306–5314.
70. Park, M. J.; Nedoma, A. J.; Geissler, P. L.; Balsara, N. P.; Jackson, A.; Cookson, D. *Macromolecules* **2008**, *41* (6), 2271–2277.
71. Park, M. J.; Balsara, N. P. *Macromolecules* **2009**, *43* (1), 292–298.
72. Kerres, J. a. *Fuel Cells* **2005**, *5*, 230–247.
73. Song, M.-K.; Kim, Y.-T.; Fenton, J. M.; Kunz, H. R.; Rhee, H.-W. *J. Power Sources* **2003**, *117* (1-2), 14–21.
74. Swier, S.; Shaw, M. T.; Weiss, R. a. *J. Membr. Sci.* **2006**, *270*, 22–31.
75. Marino, L.; Giuseppe, M.; Giuseppe, S.; Montgomery, T. S.; Steven, S.; Robert, A. W. *J. Polym. Sci., Part B: Polym. Phys.* **2007**, *45* (4), 395–404.
76. Wainright, J. S.; Wang, J. T.; Weng, D.; Savinell, R. F.; Litt, M. *J. Electrochem. Soc.* **1995**, *142* (7), L121–L123.
77. Xiao, L.; Zhang, H.; Scanlon, E.; Ramanathan, L. S.; Choe, E.-W.; Rogers, D.; Apple, T.; Benicewicz, B. C. *Chem. Mater.* **2005**, *17* (21), 5328–5333.
78. Kreuer, K.-D.; Paddison, S. J.; Spohr, E.; Schuster, M. *Chem. Rev.* **2004**, *104* (10), 4637–4678.
79. Schuster, M.; Rager, T.; Noda, A.; Kreuer, K. D.; Maier, J. *Fuel Cells* **2005**, *5* (3), 355–365.
80. Bingol, B.; Meyer, W. H.; Wagner, M.; Wegner, G. *Macromol. Rapid Commun.* **2006**, *27* (20), 1719–1724.
81. Jiang, F.; Kaltbeitzel, A.; Meyer, W. H.; Pu, H.; Wegner, G. *Macromolecules* **2008**, *41* (9), 3081–3085.
82. Parvole, J.; Jannasch, P. *Macromolecules* **2008**, *41* (11), 3893–3903.
83. Couture, G.; Alaaeddine, A.; Boschet, F.; Ameduri, B. *Prog. Polym. Sci.* **2011**, *36* (11), 1521–1557.
84. Hibbs, M. R.; Hickner, M. A.; Alam, T. M.; McIntyre, S. K.; Fujimoto, C. H.; Cornelius, C. J. *Chem. Mater.* **2008**, *20* (7), 2566–2573.

Downloaded by PENNSYLVANIA STATE UNIV on June 14, 2012 | http://pubs.acs.org
Publication Date (Web): May 7, 2012 | doi: 10.1021/bk-2012-1096.ch010

Chapter 10

Polymer Materials for Charge Transfer in Energy Devices

Adam D. Miller, Matthieu Gervais, Jai Krishnamurthy, Leon Dyers, Xiaobing Zhu, Ravindra Potrekar, Xin Fei, Adam Weber, and John B. Kerr*

Lawrence Berkeley National Laboratory, MS 62R0203, 1 Cyclotron Road, Berkeley, CA 94720
***JBKerr@lbl.gov**

Charge transfer through the bulk and across the electrode interfaces is of fundamental importance for use of polymers in energy devices. Protons or lithium ions are transported by means of a solvent or solvating groups incorporated in the polymer, without which no charge can be passed. Typically the solvent groups for protons are water and carbonates or ethylene oxide units for lithium ions. The choice of a good solvent for transport through the bulk membrane may not be the best for charge transfer at the interfaces. This chapter describes efforts to develop alternative solvation methods particularly for proton transfer in fuel cells where the reduction of dependence on external humidification is a major goal. The design, synthesis and characterization of proton conducting polymers containing heterocylic bases and phosphonic acids will be described. The roles of the solvating groups, molecular architecture and morphology of the polymers is discussed.

Introduction

Polymer electrolyte membrane (PEM) fuel cells and lithium ion batteries are of considerable interest as power sources for transportation and stationary applications. These devices have several properties in common which are responsible for inadequate performance and ultimate failure. They include bulk transport of ions across a separator, mass transport resistance to the electrode

In Polymers for Energy Storage and Delivery: Polyelectrolytes for Batteries and Fuel Cells; Page, K., et al.;
ACS Symposium Series; American Chemical Society: Washington, DC, 2012.

surfaces for ions and substrates and most importantly the impedance to charge transport across the interfaces which is often the process that leads to poor performance and failure. For example, the poor kinetics of the electrochemical reactions of lithium ions at the electrodes leads to large impedances, the generation of heat and inefficient side reactions and ultimately the failure of the battery. Similarly, the sluggish oxygen reduction reaction in PEM fuel cells results in the generation of heat instead of electrical current and which is difficult to reject at temperatures below 100°C. Presently used membrane materials such as perfluorinated sulfonic acids (e.g. Nafion®) require the presence of liquid water to provide adequate conductivity and hence complex heat and water management systems are required. This is but one example of where better kinetics of charge transfer at the electrode would solve many of the issues that impede the introduction of fuel cells.

For fuel cells an alternative approach involves membrane materials that contain no or little free solvent but are conductive at low temperatures as well as high temperatures under dry conditions. The use of alternative solvent molecules such as imidazole, triazole and phosphonic acids have been considered as the proton conducting medium instead of water in PEM fuel cells (*1*, *2*). The need to operate fuel cells at higher temperatures (120°C) to facilitate heat rejection has moved the operating conditions to a range where the remarkable properties of the perfluorosulfonic acids [PFSAs] no longer satisfy the requirements. A proton conducting system with practical proton conductivities for fuel cell separator membranes has been a challenge to realize. In the past decade, several studies have been conducted by different groups that have successfully achieved proton conductivities on the order of 10^{-3} S/cm at 200°C (*3*). This paper outlines some syntheses, characterization and properties of homopolymers and copolymers with tethered imidazole groups which may be of interest for high temperature PEM fuel cells operating under dry conditions.

Figure 1 shows the general design of a material that shows a phase separated polymer backbone with covalently tethered imidazole groups and acid groups so that the solvating molecules are not washed out of the membrane by the product water. The acid groups provide the excess protons and the imidazoles provide the solvation for the proton to allow the proton to hop from one solvent site to the next without the need for the solvent molecule to move with it. This mechanism, commonly called the Grotthuss mechanism (*4*), is a low energy pathway and is different from ionic conduction assisted by the segmental motion of the polymer. The two types of ionic motion can be distinguished by the dependence of conductivity upon temperature with the Grotthuss motion having a low dependence while the segmental motion exhibits a typical WLF dependence that increases as the temperature decreases. The Grotthuss mechanism is therefore favored by phase separation of the backbone from the acid and solvating heterocyclic bases so that the proton hopping mechanism is not impeded by the polymer side chains. Thus self-organization of the polymer is important and this dictates the length of the tethers for the solvent and acid moieties. Ideally the organization should provide sufficient connectivity across the whole membrane to provide high conductivity and the design and synthesis of such well controlled materials represents a major challenge. This paper describes the effects of the

Downloaded by PENNSYLVANIA STATE UNIV on June 14, 2012 | http://pubs.acs.org
Publication Date (Web): May 7, 2012 | doi: 10.1021/bk-2012-1096.ch010

backbone identity, side chain length and concentration of the acid groups on the proton conduction both under dry conditions and humidified states. The backbones studied are polystyrene, polysulphone, polyether, polysiloxane and PTFE.

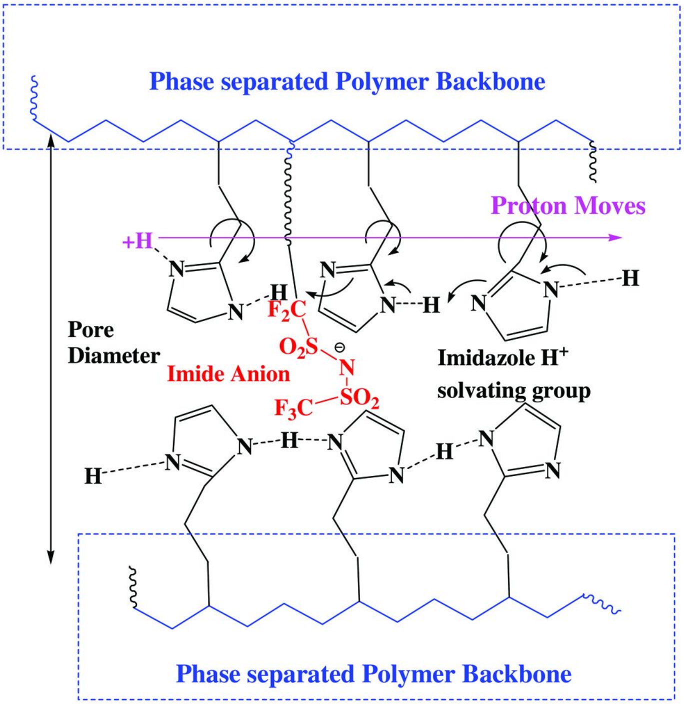
Phase separated Polymer Backbone
Proton Moves
+H
N
N
H
F_2C
O_2S
⊖
N
F_3C
SO_2
N
N
H
H
N
N
Pore
Diameter
Imide Anion
Imidazole H^+
solvating group
H
N
N
H
N
N
H
N
N
Phase separated Polymer Backbone

Figure 1. Ideal design of water-free proton conducting polymer

Downloaded by PENNSYLVANIA STATE UNIV on June 14, 2012 | http://pubs.acs.org
Publication Date (Web): May 7, 2012 | doi: 10.1021/bk-2012-1096.ch010

Results and Discussion

Covalent tethering of the imidazole to the polymer backbones is not easy as it is complicated by the need for protecting groups for the imidazole. Benzyl, Tosyl and Trityl groups are among the groups that have been examined. Figure 2 shows the general synthetic route followed to prepare an imidazole tethered to a polystyrene backbone. In order for the imidazole to support Grotthuss transport the tether must be accomplished via the 2-position rather than the 1-position and this introduces much synthetic difficulty. In order to reduce the synthetic complications this polymer was blended with Nafion 1100 to give films that have measurable conductivities. The conductivities of the dry and humidified blended polymers are shown in Figure 3.

Downloaded by PENNSYLVANIA STATE UNIV on June 14, 2012 | http://pubs.acs.org
Publication Date (Web): May 7, 2012 | doi: 10.1021/bk-2012-1096.ch010

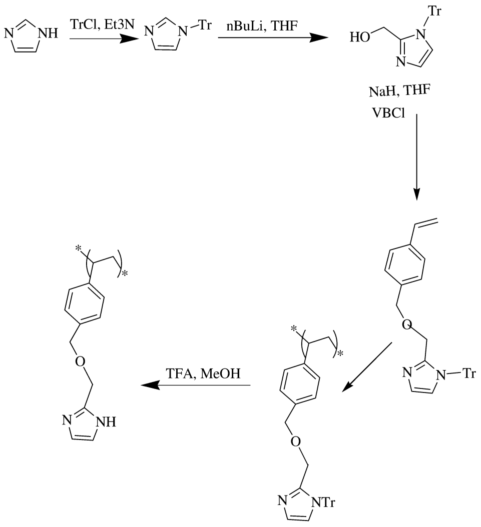

Figure 2. Synthetic route to obtain tethered imidazole polystyrene polymers (IMVBCl)

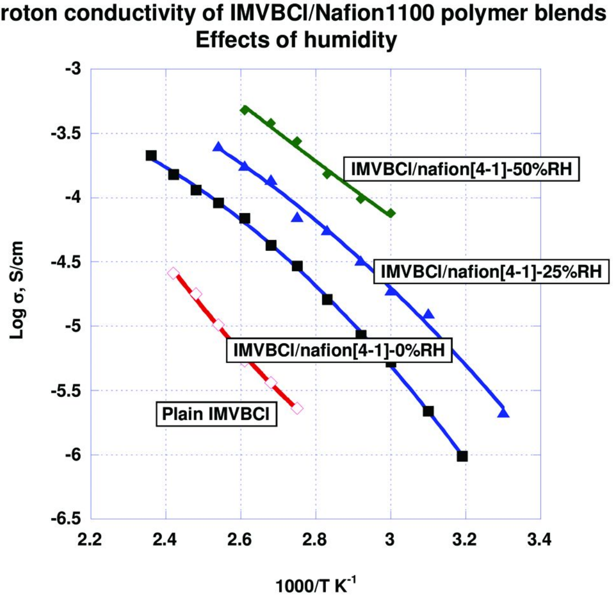

Figure 3. Conductivity as a function of temperature of imidazole tethered polystyrene polymers blended with Nafion under dry and humidified conditions.

Downloaded by PENNSYLVANIA STATE UNIV on June 14, 2012 | http://pubs.acs.org
Publication Date (Web): May 7, 2012 | doi: 10.1021/bk-2012-1096.ch010

The neat polymer is conductive due to the self-ionization of the imidazole but conductivity is enhanced due to the addition of the PFSA polymer. Humidification of the polymer results in increases in the conductivity as shown in Figure 3. However, the conductivity is somewhat lower than that of Nafion alone under these conditions because the presence of the imidazole suppresses the uptake of water and the effective equivalent weight of the acid is over 2000 resulting in a low concentration of charge carriers. The use of blends leads to this problem since there is a greater preponderance of backbone in the medium than would be the case if the bases and acids were attached to the same chain.

It can be seen from Figure 3 that the dependence of conductivity upon temperature is very similar to typical WLF dependences which indicates that the mechanism is dominated by segmental motion of the polymer. This conclusion is also supported by the DMA behavior which is shown in Figure 4.

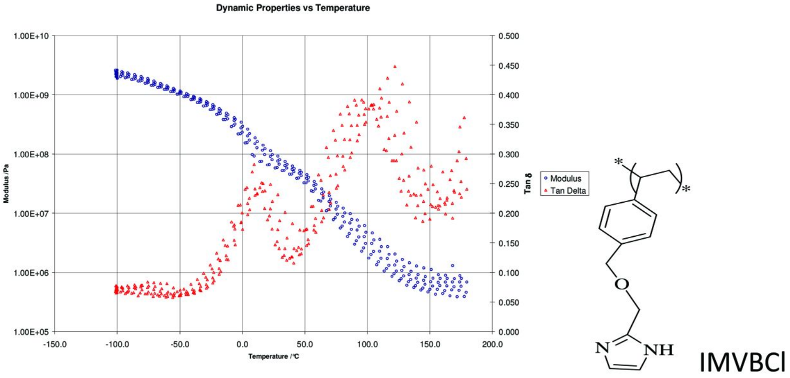

Figure 4. DMA of IMVBCl short side chain polymer blend with Nafion in the ratio 4:1.

The DMA shows considerable plasticization of the backbone by the imidaziole and SAXS measurements also indicate a lack of pahse separation.

Figure 5 shows methods of attaching imidazoles and acids to polysulfones and Figure 6 shows the conductivity of the proton and lithium ion conducting acid polymer under dry conditions and in the presence of water. The dry polymers exhibit Arrhenius behaviour as is expected due to the lack of solvent but upon addition of solvent water the conductivity increases markedly and the temperature dependence is consistent with Grotthuss transport. This appears to support the notion of the importance of phase separation in order to facilitate Grotthuss transport of protons. The DMA measurement shown in Figure 6b shows a single transition with no sign of mobility in the backbone again indicating a very stiif material with strong phase separation.

In Polymers for Energy Storage and Delivery: Polyelectrolytes for Batteries and Fuel Cells; Page, K., et al.;
ACS Symposium Series; American Chemical Society: Washington, DC, 2012.

Downloaded by PENNSYLVANIA STATE UNIV on June 14, 2012 | http://pubs.acs.org
Publication Date (Web): May 7, 2012 | doi: 10.1021/bk-2012-1096.ch010

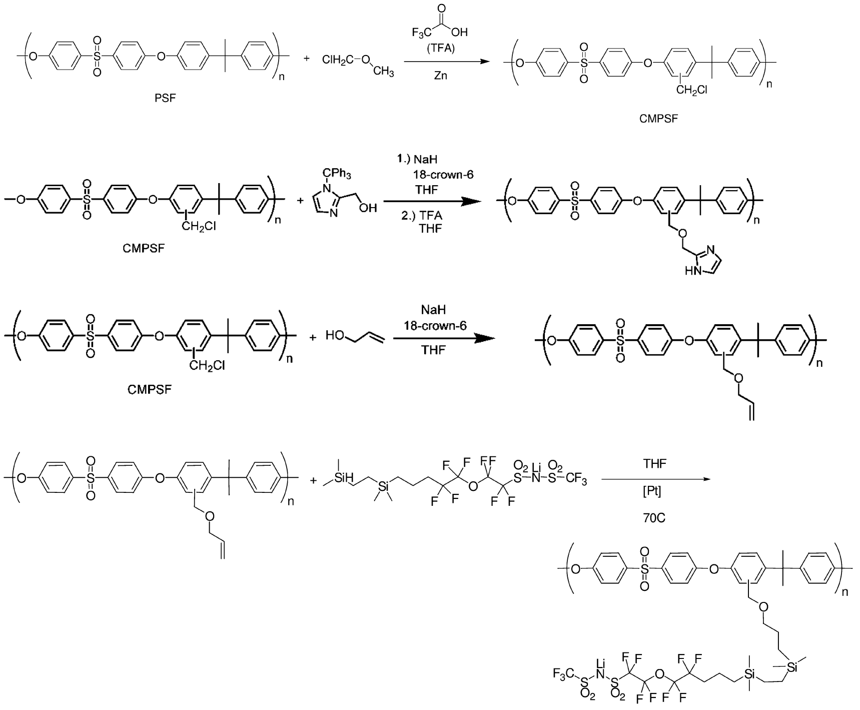

Figure 5. Synthetic routes to attach imidazoles and acid groups to polysulfones.

Moving on to an alternative protogenic group which can act as the proton donating species as well as the solvating species (*2*), Figure 7 shows the synthetic scheme for attaching phosphonic acid groups to the polysulfone backbone. The initial functionalization reaction gives mopno-functionalization after one day and bi-functionalization after 7 days. Increase of the functionalization density leads to a much more satisfactory concentration of the active functions. The conductivity of the bi-functional phophonic acid polymer (DPPSU) is shown in Figure 8 as a function of relative humidity and temperature. The remarkable lack of effect of humidity of the conductivity is striking as is the low dependence of conductivity on the temperature. These results are quite consistent with the Grotthuss mechanism of proton transport that is promoted by the strong phase separation. Water uptake measurements made on this polymer show only an uptake of 15% by weight even at 100% RH at 25 °C indicating that thewater is not critical to the conduyction mechanism. These membranes appear to have considerable promise for high temperature operation under dry conditions.

Downloaded by PENNSYLVANIA STATE UNIV on June 14, 2012 | http://pubs.acs.org
Publication Date (Web): May 7, 2012 | doi: 10.1021/bk-2012-1096.ch010

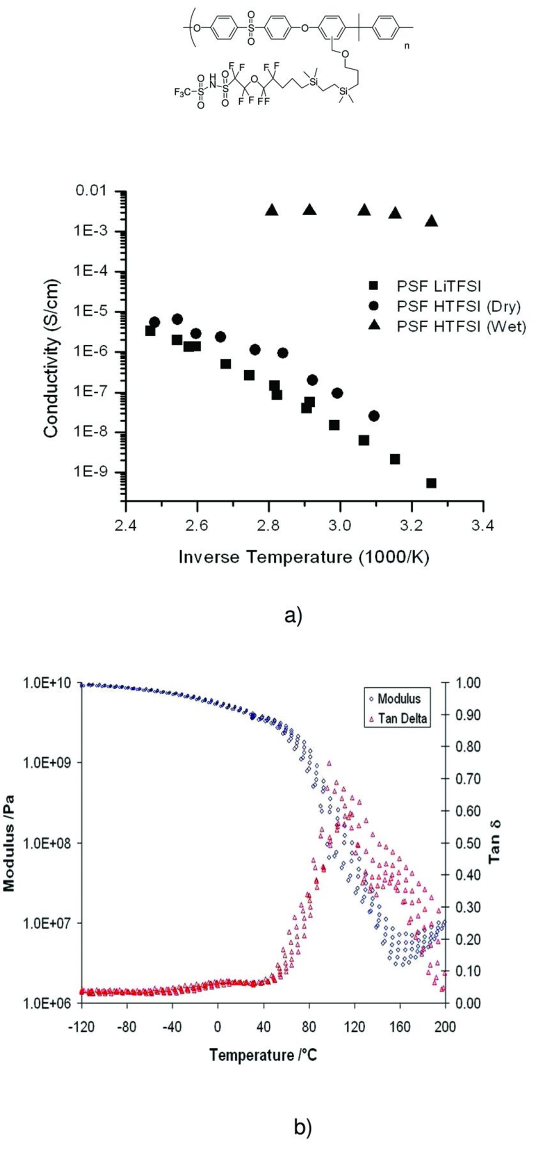

Figure 6. Conductivity and mechanical properties of Polyetherpolysulfone modified with a fluoroalkylimide side chain; a) conductivities of dry(Li$^+$ and H$^+$ forms) and wet(H$^+$)polymers; b) DMA of H$^+$ form

Downloaded by PENNSYLVANIA STATE UNIV on June 14, 2012 | http://pubs.acs.org
Publication Date (Web): May 7, 2012 | doi: 10.1021/bk-2012-1096.ch010

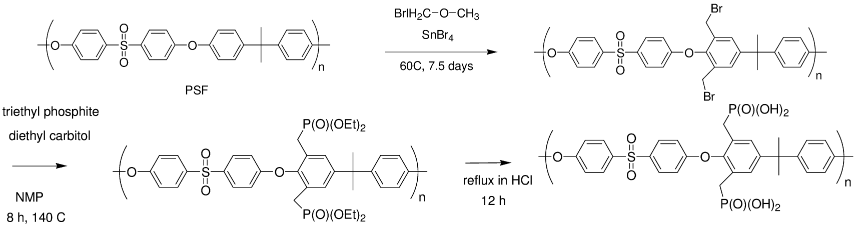

Figure 7. Synthesis route to Phosphonic acid functionalized polysulfone(DPPSU).

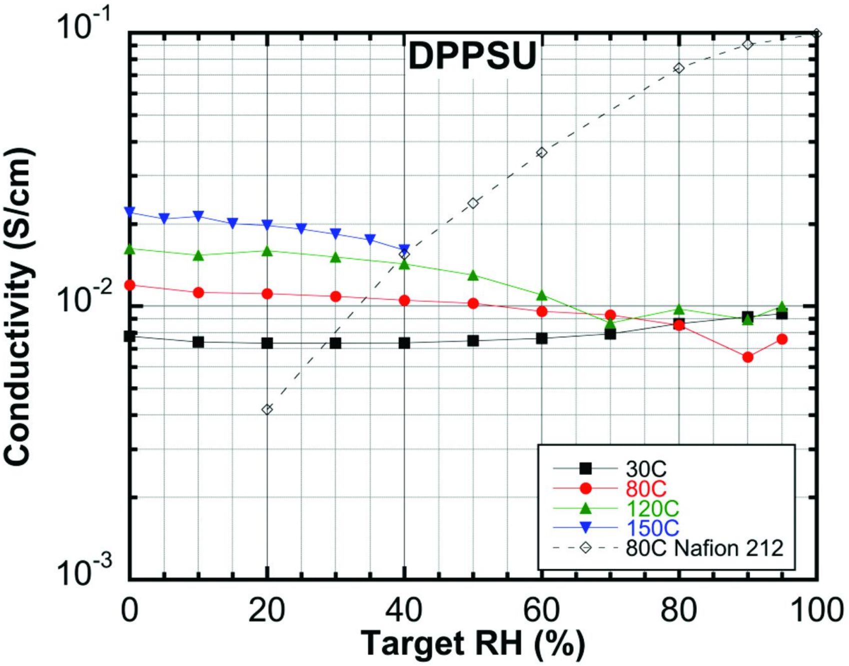

Figure 8. Conductivity of Polysulfone phosphonates(DPPSU) as a function of temperatyre and humidity (Nafion 212 included for comparison)

To investigate the role of morphology in the promortion of proton hopping or Grotthuss-type transport a number of systems have been investigated using block copolymers to try to control the morphology. Some of these systems have used proton conducting ionic liquids based on imidazolium bis(trifluoromethylsullfonyly)imide as the conducting medium (*5*, *6*). Recent measurements using pulsed field gradient nmr has shown large enhancements of the proton diffusion rates over the diffusion of the supporting ionic liquid when the liquid is confined in the nanochannels of the block copolymer (*7*). Similar effects have been observed with water in block copolymers (*8*) where enhanced proton transport has been observed with nano-separated polymers. However, it has been observed that these effects are often greatly reduced upon cycling the humidity and/or temperature which indicates that the morphology is not stable to the change in conditions. The provision of the correct morphology and its stabilization throughout the conditions that the membrane may see during operation is a severe challenge for polymer scientists.

$$\frac{\kappa_{\mathrm{eff}}}{\kappa_{\mathrm{Grot}}} = \frac{1}{1-\left(1+\dfrac{\kappa_{\mathrm{Vehicle}}}{\kappa_{\mathrm{Grot}}}\right)\dfrac{\delta_{\mathrm{Vehicle}}}{\delta_{\mathrm{Membrane}}}}$$

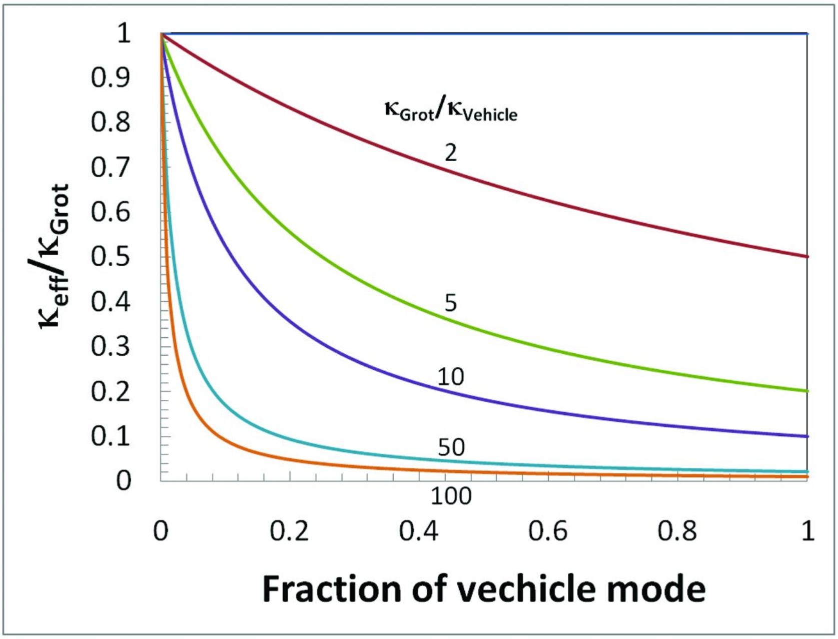

Figure 9. Effect of loss of connectivity on the overall conductivity, K_{eff}*, for different ratios of Grotthus conductivity ,* K_{Grott}*. and vehicular or segmental conductivity,* $K_{Vehicle}$*.*

The importance of providing and maintaining the appropriate connectivity through the membrane is illustrated by Figure 9 which shows the effect of discontinuities of the connectivity across the membrane. The conductivity of the entire membrane is estimated according to the equation whereby the effective conductivity K_{eff} divided by the Grotthuss conductivity, K_{Grott}, is plotted against the proportion of vehicular (or segmental) motion, K_{Vehicle}. The different curves

Downloaded by PENNSYLVANIA STATE UNIV on June 14, 2012 | http://pubs.acs.org
Publication Date (Web): May 7, 2012 | doi: 10.1021/bk-2012-1096.ch010

assess the effect for different ratios of the K_{Grott} to the $K_{Vehicle}$. The modeling shows that for a ratio of 100 the effect of a small loss of connectivity is very significant. For a comparison ofwith segnmental motion this ratio is more like 10,000 so the effect is likely to be even worse for a polymer m embrane with no mobile solvent in it. This model is a worst case scenario since it only considers a single one-dimensional motion and this is greatly alleviated by 2-d and 3-d pathways that provide alternative pathwatys around a bottleneck. However it very clearly shows the need for great control of the membrane morphology and this represents a major chjallnge for the synthetic chemicts as well as the polymer physics community.

Downloaded by PENNSYLVANIA STATE UNIV on June 14, 2012 | http://pubs.acs.org
Publication Date (Web): May 7, 2012 | doi: 10.1021/bk-2012-1096.ch010

Acknowledgments

This work was supported by the Assistant Secretary for Energy Efficiency and Renewable Energy, Office of Hydrogen, Fuel Cells and Infrastructure Technologies of the U.S. Department of Energy under Contract No. DE-AC02-05CH11231.

References

1. Kreuer, K. D.; Paddison, S. J.; Spohr, E.; Schuster, M. Transport in Proton Conductors for Fuel-Cell Applications: Simulations, Elementary Reactions, and Phenomenology. *Chem. Rev.* **2004**, *104*, 4637–4678.
2. Schuster, M.; Rager, T.; Noda, A.; Kreuer, K. D.; Maier, J. About the choice of the protogenic group in PEM separator materials for intermediate temperature, low humidity operation: A critical comparison of sulfonic acid, phosphonic acid and imidazole functionalized model compounds. *Fuel Cells* **2005**, *5*, 355–365.
3. Herz, H. G.; et al. New fully polymeric proton solvents with high proton mobility. *Electrochim. Acta* **2003**, *48*, 2165–2171.
4. Agmon, N. The Grotthuss Mechanism. *Chem. Phys. Lett.* **1995**, *244*, 456–462.
5. Hoarfrost, M. L.; Segalman, R. A. Ionic Conductivity of Nanostructured Block Copolymer/Ionic Liquid Membranes. *Macromolecules* **2011**, *44*, 5281–5288.
6. Virgili, J. M.; Hoarfrost, M. L.; Segalman, R. A. Effect of an Ionic Liquid Solvent on the Phase Behavior of Block Copolymers. *Macromolecules* **2010**, *43*, 5417–5423.
7. Hoarfrost, M.; Tyagi, M.; Reimer, J.; Segalman, R. Presented at the APS March Meeting, Boston, 2011.
8. Wang, X.; Beers, K. M.; Kerr, J. B.; Balsara, N. P. Conductivity and water uptake in block copolymers containing protonated polystyrene sulfonate and their imidazolium salts. *Soft Matter* **2011**, *7*, 4446–4452.

Chapter 11

Water Transport and Sorption in Nafion Membrane

Ahmet Kusoglu and Adam Z. Weber*

Lawrence Berkeley National Laboratory, 1 Cyclotron Road, Berkeley, CA 94720, USA
***Corresponding Author Email: azweber@lbl.gov**

Downloaded by STANFORD UNIV GREEN LIBR on June 14, 2012 | http://pubs.acs.org
Publication Date (Web): May 7, 2012 | doi: 10.1021/bk-2012-1096.ch011

Understanding the sorption behavior of perfluorinated ionomer membranes and its effects on the membrane's transport properties remains an important issue in the development of ion-conducting materials. In this chapter, the current state of understanding of water-transport mechanisms in Nafion membranes are explained by summarizing the relevant studies in the literature as well as including some of our experimental results. A large discrepancy in the reported diffusion coefficient exists due to a number of techniques measuring the mobility of water molecules at different time- and lengthscales. In addition, morphological changes in the membrane during water uptake provide insight into the additional mechanisms of water transport and incorporation in the membrane. By analyzing the time constants from different experiments it is possible to draw key conclusions that shed light onto the multiple swelling and transport processes in membranes.

Introduction

Ionomers are, in essence, multi-functional materials that can be used in applications ranging from micro-fluidics (*1*) and soft actuators (*2*) to electrochemical devices, especially polymer-electrolyte-membrane fuel-cells (PEMFCs) (*3*, *4*). Perfluorinated-sulfonic-acid (PFSA) membranes are ionomers that possess a good combination of physiochemical properties and thermo-mechanical stability, which makes them suitable candidates as the ion-conducting, gas-separating electrolytes in PEMFCs (*3*–*6*). Nafion® membrane

In Polymers for Energy Storage and Delivery: Polyelectrolytes for Batteries and Fuel Cells; Page, K., et al.;
ACS Symposium Series; American Chemical Society: Washington, DC, 2012.

is a commercially available PFSA ionomer developed by DuPont in the late 1960s. Since then, Nafion® membranes have been the most widely studied material for PEMFC applications and is still used as the baseline membrane for developing ion-conducting systems for energy applications. Nafion is composed of a polytetrafluoroethylene (PTFE) backbone, providing mechanical support, and (perfluorovinyl ether) side-chains terminated with sulfonic acid end-groups (SO_3^-), where exchangeable ions (e.g., H^+) attach. When exposed to an external water source, ionic groups in the membrane are hydrated, resulting in enhanced ion (e.g. proton) conductivity (Figure 1), which is critical to sustain desirable cell performance (*7–13*). Once hydrated, Nafion membrane has a phase-separated nanostructure where water-swollen ionic-domains facilitate water and ion transport (see Figure 1) (*4*, *6*, *12*). So far, water domains in Nafion have been described as inter-connected spheres (*11*, *14*) or more random pores (*15*, *16*) and cylinders (*17*) embedded in the polymer matrix, or water pools surrounding polymer rods (*18*, *19*), all of which are interrelated to the membrane's water-uptake behavior. The water-uptake behavior of Nafion membranes have been under investigation over the past few decades (see Table I). Selected data are also shown in Fig. 2 as a function of water content, λ (the number of water molecules per mole of sulfonic acid group, λ = mol H_2O/mol SO_3^-) (*7*), which is determined from the reported values (of water-mass uptake, concentration, *etc.*) from the same group, if available, or using the values in literature for the most similar condition (temperature and membrane type and pretreatment).

Water diffusivity in membranes is generally determined using experimental methods such as dynamic vapor sorption (DVS), steady-state (SS) diffusion or permeability, pulsed-field gradient spin-echo (PGSE) nuclear magnetic resonance (NMR), and time-resolved Fourier transform infrared-attenuated total reflectance (FTIR). In addition, conductivity, using AC impedance, and surface properties, using conductive atomic force microscopic (cAFM), provided insight into the transport mechanisms. The growth of water domains with water uptake and water mobility have also been studied using small-angle X-ray scattering (SAXS) experiments (*11*, *14*, *16*) and quasi-elastic neutron scattering (QENS) (*64–66*). The findings in these studies provide useful information on the processes of water transport in Nafion membranes, yet a complete understanding of the water-transport mechanisms is still under investigation due to the complex and ill-defined nanostructure of the membrane and its surfaces. For example, water diffusivity reported in the literature varies up to four-orders-of-magnitude, i.e. D ~ 10^{-10} to 10^{-6} cm^2/s (Figure 2) due to the varying testing methods focusing on certain time- and lengthscales. Large differences in water diffusivities obtained in dynamic and steady-state experiments is an indication of fundamentally different processes for water transport and water sorption. Thus, understanding the water-transport mechanisms requires a systematic investigation that bridges the studies conducted at multiple length and timescales via different experimental techniques. In the following, first the theoretical background of water-transport phenomena will be presented and then steady-state and dynamic water transport will be discussed based on the experimental findings. It should be noted that this chapter focuses on chemical-potential-derived fluxes and transport properties and not those associated with other fluxes and gradients (e.g., electro-osmotic flow).

Downloaded by STANFORD UNIV GREEN LIBR on June 14, 2012 | http://pubs.acs.org
Publication Date (Web): May 7, 2012 | doi: 10.1021/bk-2012-1096.ch011

Downloaded by STANFORD UNIV GREEN LIBR on June 14, 2012 | http://pubs.acs.org
Publication Date (Web): May 7, 2012 | doi: 10.1021/bk-2012-1096.ch011

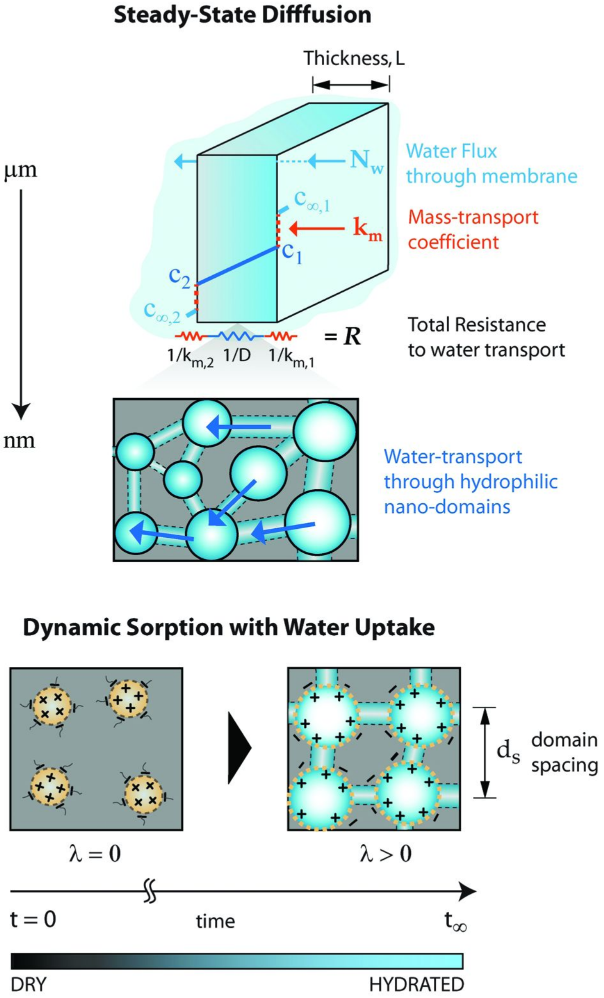
Steady-State Diffusion
Thickness, L
μm
nm
N_w
Water Flux through membrane
$c_{\infty,1}$
k_m
Mass-transport coefficient
c_1
c_2
$c_{\infty,2}$
= R
$1/k_{m,2}$ $1/D$ $1/k_{m,1}$
Total Resistance to water transport
Water-transport through hydrophilic nano-domains
Dynamic Sorption with Water Uptake
d_s domain spacing
λ = 0
λ > 0
t = 0
time
t_∞
DRY
HYDRATED

Figure 1. Water-transport and sorption processes in the membrane at multiple lengthscales.

Table I. Studies relevant to Diffusivity of Water in Nafion® Membrane[a]

Reference	*Diffusion Coefficient D [cm^2/s]*
Steady-State and Permeability Experiments	
Zelsmann et al. (*20*)	$D(\lambda) = 1 - 5 \times 10^{-7}$
Springer et al. (*7*)	$D(\lambda) = 1 - 3 \times 10^{-6}$
Fuller (*21*)	$D(\lambda) = 1 - 9 \times 10^{-6}$
Okada et al. (*22*)	$D(\lambda) = 1 - 5 \times 10^{-6}$
Grossi et al. (*23*)	$D(\lambda) = 2 - 9 \times 10^{-8}$
Rivin et al. (*24*)	$D(\lambda) = 1 - 7 \times 10^{-7}$
Ye and LeVan (*25*)	$D(\lambda) = 1 - 8 \times 10^{-6}$
Ge et al. (*26*)	$D(\lambda,T) = 1 - 8 \times 10^{-6}$
Majsztrik et al. (*27*)	$D(\lambda) = 1.5 - 7 \times 10^{-6}$ (30 °C), $4 - 25 \times 10^{-6}$ (80 °C)
Monroe et al. (*28*)	$D \sim 10^{-6}$
Onishi (*29*)	$D(\lambda) = 1 - 4 \times 10^{-6}$
Schneider and Rivin (*30*)	$D(\lambda) = 0.1 - 8 \times 10^{-6}$
Kienitz et al. (*31*)	$D(\lambda) = 2.7 \times 10^{-5}$
Reference	*Diffusion Coefficient D [cm^2/s]*
NMR	
Zawodzinski et al. (*9*)	$D_{self}(\lambda) = 1 - 19 \times 10^{-6}$
Hietala et al. (*32*)	$D_{self} = 8 \times 10^{-6}$
Gong et al. (*33*)	$D_{self}(\lambda,T) = 0.5 - 6 \times 10^{-7}$
Edmondson et al. (*34*)	$D(\lambda) = 2 - 5 \times 10^{-6}$
Giotto et al. (*35*)	$D(T) = 0.1 - 1 \times 10^{-6}$
Jayakody et al. (*36*)	$D_{self}(\lambda) = 0.5 - 6 \times 10^{-6}$
Saito et al. (*37*)	$D_{self}(T) = 6 - 7 \times 10^{-6}$
Tsushima et al. (*38*)	$D(\lambda) = 3 - 7.5 \times 10^{-6}$
Saito et al. (*39*)	$D(T) = 6 - 7 \times 10^{-6}$
Zhang et al. (*40*)	$D_{self}(\lambda) = 3 - 7 \times 10^{-6}$
Hensley et al. (*41*)	$D(T) = 1 - 2.5 \times 10^{-5}$ at 100%RH
Ohkubo et al. (*42*)	$D(T) = 0.34 - 5 \times 10^{-4}$
Ochi et al. (*43*)	$D_{self}(\lambda,T) = 10^{-6} - 10^{-7}$
Guillermo et al. (*44*)	$D_{self}(\lambda,T) = 10^{-5} - 10^{-7}$
Kidena et al. (*45*)	$D(\lambda,T) = 2 - 10 \times 10^{-6}$

Continued on next page.

Downloaded by STANFORD UNIV GREEN LIBR on June 14, 2012 | http://pubs.acs.org
Publication Date (Web): May 7, 2012 | doi: 10.1021/bk-2012-1096.ch011

Table I. (Continued). Studies relevant to Diffusivity of Water in Nafion® Membrane[a]

Reference	*Diffusion Coefficient D [cm²/s]*
NMR	
Zhao et al. (*46*)	$D_{self}(\lambda,T) = 1 - 9 \times 10^{-6}$
Tabuchi et al. (*47*)	$D(\lambda) = 0.1 - 4 \times 10^{-6}$
Reference	*Diffusion Coefficient D [cm²/s]*
Dynamic Water Uptake / Sorption-Desorption Experiments	
Yeo and Eisenberg (*48*)	$D(T) = 1.8 - 7 \times 10^{-6}$
Takamatsu et al. (*49*)	$D(T) = 1.8 - 6 \times 10^{-6}$ in water $D(T) = 2 \times 10^{-8}$ in vapor
Zelsmann et al. (*20*)	$D(\lambda) = 1 - 2 \times 10^{-6}$
Morris and Sun (*50*)	$D(\lambda) = 2 - 1.4 \times 10^{-7}$
Rivin et al. (*24*)	$D \sim 7.7 \times 10^{-9}$ for sorption $D \sim 2.6 \times 10^{-8}$ for desorption
Legras et al. (*51*)	$D(\lambda) = 0.3 - 22 \times 10^{-7}$
Burnett et al. (*52*)	$D(\lambda) = 0.5 - 2 \times 10^{-7}$
Hallinan et al. (*53*, *54*)	$D(\lambda) = 4 - 5 \times 10^{-6}$ (with FTIR) $D(\lambda) = 4 - 7 \times 10^{-7}$
Hallinan and Elabd (*55*)	$D(\lambda) = 3 - 8.5 \times 10^{-7}$
Majsztrik et al. (*56*)	$D = 3 \times 10^{-9}$ at 30 °C $D = 1 \times 10^{-7}$ at 80 °C
Satterfield et al. (*57*)	5×10^{-8} (254μm), 5×10^{-9} (51μm) for sorption 5×10^{-9} (254μm), 5×10^{-8} (51μm) for desorption
Damay and Klein (*58*)	$D = 0.5 - 2 \times 10^{-6}$
Onishi (*29*)	$D(\lambda) = 1 - 7 \times 10^{-7}$
Kongkanand (*59*)	$1 - 2 \times 10^{-4}$ cm/s for sorption $3 - 6 \times 10^{-4}$ cm/s for desorption
Mangiagli (*60*)	$D(\lambda) = 0.3 - 3 \times 10^{-9}$
Reference	*Diffusion Coefficient D [cm²/s]*
Radiotracer (a), QENS (b) and SANS (c)	
Yeager and Steck (*61*) (a)	$D_{self}(T) = 1 - 4 \times 10^{-6}$
Zelsmann et al. (*20*) (a)	$D_{self}(\lambda) = 1.5 - 2.5 \times 10^{-6}$
Verbrugge et al. (*62*) (a)	$D_{self}(T) = 8 - 30 \times 10^{-6}$ in water
Suresh et al. (*63*) (a)	$D_{self}(\lambda,T) = 1.8 - 9 \times 10^{-6}$
Volino et al. (*64*) (b)	$D(T) = 0.8 - 2.5 \times 10^{-5}$

Continued on next page.

Downloaded by STANFORD UNIV GREEN LIBR on June 14, 2012 | http://pubs.acs.org
Publication Date (Web): May 7, 2012 | doi: 10.1021/bk-2012-1096.ch011

Table I. (Continued). Studies relevant to Diffusivity of Water in Nafion® Membrane[a]

Reference	*Diffusion Coefficient D [cm²/s]*
Radiotracer (a), QENS (b) and SANS (c)	
Pivovar and Pivovar (*65*) (b)	$D(\lambda) = 0.5 - 2 \times 10^{-5}$
Perrin et al. (*66*) (b)	$D(\lambda) = 0.5 - 2 \times 10^{-5}$
Page et al. (*67*) (b)	$D = 1 - 4 \times 10^{-7}$
Kim et al. (*16*) (c)	$D = 1 - 2.4 \times 10^{-7}$

[a] Notes: Use of T and/or λ in diffusivity values show if that study investigated the temperature and/or water content dependence, and does not necessarily imply a functional relationship. Reader is recommended to see the original articles for details about the membrane types, experimental methods and exact diffusivity values.

Theory

The water content, λ (= mol H_2O/mol SO_3^-), of the membrane can be calculated from the water mass uptake of the membrane as

$$\lambda = \frac{M_\mathrm{w} / \bar{V}_\mathrm{w} \rho_\mathrm{w}}{M_\mathrm{p} / \mathrm{EW}} \qquad [1]$$

where EW is equivalent membrane [g/mol] of the membrane, $\bar{V}_\mathrm{w}$ is the (partial) molar volume of water (~18 [cm³/mol]), and M_w and M_p are the mass of water and dry polymer, respectively. The water concentration in the membrane is

$$c_\mathrm{w} = \frac{\lambda}{\lambda \bar{V}_\mathrm{w} + \bar{V}_p} = \frac{\lambda}{\lambda \bar{V}_\mathrm{w} + \mathrm{EW} / \rho_p}, \qquad [2]$$

where $\bar{V}_p$ and ρ_p are the molar volume and density of dry polymer, respectively. The volume fraction of water in the hydrated membrane is also commonly used, which is simply

$$\varphi_\mathrm{w} = c_\mathrm{w} \bar{V}_\mathrm{w} \qquad [3]$$

In most experimental setups, the controlled parameter is the water-vapor activity, a_w, (or relative humidity) instead of water content. Thus, the relationship between the water content and a_w at a given temperature, so-called sorption isotherms, must be determined. Fig 3 shows a sample of the data for such a plot.

Downloaded by STANFORD UNIV GREEN LIBR on June 14, 2012 | http://pubs.acs.org
Publication Date (Web): May 7, 2012 | doi: 10.1021/bk-2012-1096.ch011

Downloaded by STANFORD UNIV GREEN LIBR on June 14, 2012 | http://pubs.acs.org
Publication Date (Web): May 7, 2012 | doi: 10.1021/bk-2012-1096.ch011

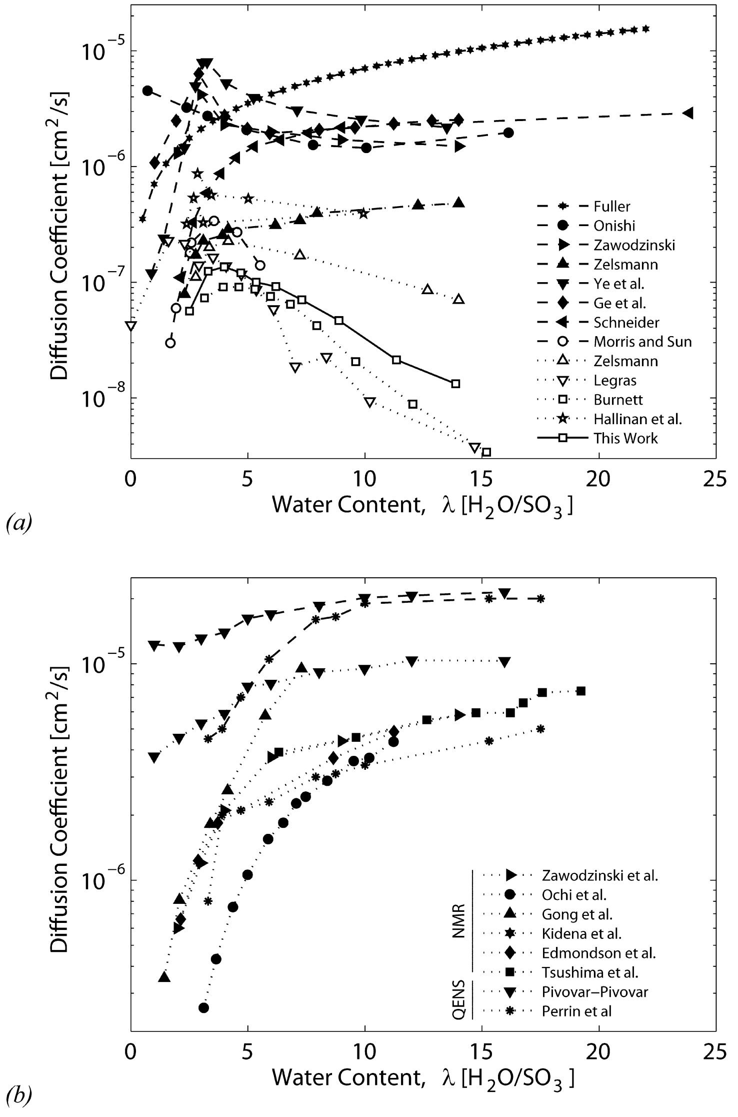

Figure 2. Water diffusivity of PFSA reported in the literature based on (a) dynamic (20, 50–52, 55) (open symbols) and steady-state (20, 21, 25, 26, 29, 30, 68) (filled symbols) and (b) NMR (33, 34, 38, 43, 45, 68) and QENS (38, 65, 66) measurements.

Downloaded by STANFORD UNIV GREEN LIBR on June 14, 2012 | http://pubs.acs.org
Publication Date (Web): May 7, 2012 | doi: 10.1021/bk-2012-1096.ch011

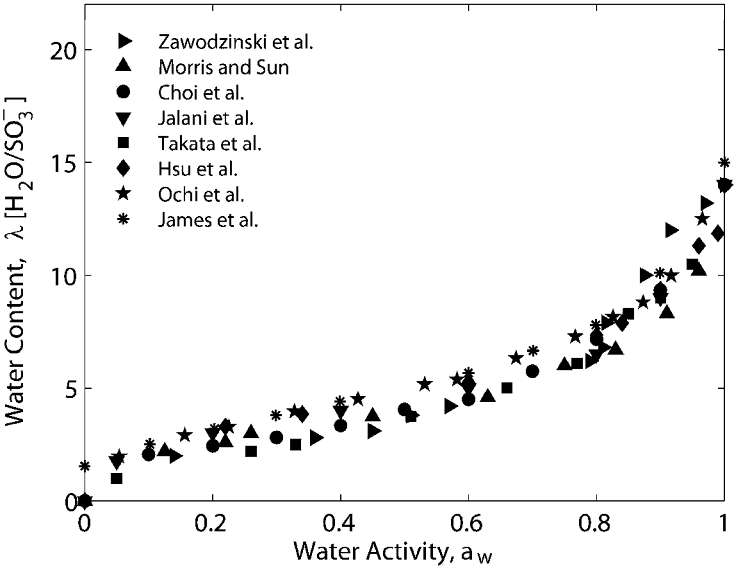

Figure 3. Membrane water content, λ, as a function of water activity at ambient temperature from various experimental data (9, 10, 43, 50, 69–72).

The literature is rich with theoretical and experimental studies correlating the water content and water-vapor activity for PFSA membranes (*7–9*, *43–45*, *50*, *69–92*). In addition, sorption isotherms have been modeled using empirical relationships (*7*, *84*), mass-transfer equations (*93*), Flory-Huggins theory (*70*, *94–97*), or equilibrium between water and hydrated protons in the membrane and vapor (*98–101*). In addition, there is an observable difference in the water content of membranes in fully saturated water vapor and liquid water. This difference is known as Schroeder's paradox, which probably stems from different polymer morphologies (*6*, *8*, *9*, *29*, *89*, *90*, *102–104*). A full review on $\lambda(a_\mathrm{w})$ relationship is beyond the scope of this work, the focus of which is water transport and sorption. In the ensuing discussions, water content will be used as the main parameter.

In the following, water diffusivities will be defined as: D_d for dynamic diffusion (although, as discussed, it is not really just a diffusive process), D_f for steady-state Fickian diffusion, D_μ for thermodynamic diffusion, and D_κ for diffusion derived from ionic mobility (e.g. conductivity).

Water transport can be described mathematically using the overall water mass balance and transport equations

$$\frac{\mathrm{d}\rho_\mathrm{w}}{\mathrm{d}t} = M_\mathrm{w}\left(\nabla \cdot \mathbf{N}_\mathrm{w}\right) \qquad [4]$$

and

$$\mathbf{N}_w = -\alpha \nabla \mu_w \qquad [5]$$

respectively, where N_w is water flux, ρ_w is the mass density of water in the system, α is the transport coefficient, and $\nabla\mu_w$ is the gradient of chemical potential of water (at constant temperature)

$$\nabla\mu_w = RT\nabla \ln a_w + \bar{V}_w \nabla p \,, \qquad [6]$$

where a_w is the activity of water, R is the universal gas constant, T is the absolute temperature, and p is the pressure. The transport coefficient can be related to the thermodynamic diffusion coefficient by (*8*)

$$D_\mu = \alpha \frac{RT}{c_w(\lambda+1)} \,. \qquad [7]$$

Often, Fick's law is used for the water-transport equation,

$$\mathbf{N}_w = -D_f \nabla c_w \qquad [8]$$

where D_f is diffusion coefficient for steady-state (Fickian) diffusion and c_w is the concentration of water, which can also be concentration-dependent. The two diffusivities defined above are related by the Darken factor,

$$D_f = \frac{\partial \ln a_w}{\partial \ln c_w} D_\mu \,. \qquad [9]$$

Similarly, for time-dependent, transient water transport, Fick's second law is often assumed,

$$\frac{dc_w}{dt} = -\nabla \cdot \mathbf{N}_w = -\nabla \cdot D_d(c_w) \nabla c_w \,, \qquad [10]$$

where D_d is considered a concentration-dependent dynamic diffusivity. The equation above can be solved with the initial and boundary conditions reflecting the nature of the water transport. For thin membranes where thickness is much smaller than the other dimensions, diffusion in the plane is negligible and diffusion in the thickness direction controls the overall mass uptake. Therefore, it is a common practice to use the thickness of the membrane, L, as the characteristic length for the diffusion process in ionomer membranes and thin films. An accurate boundary condition for Eq. [10] is the flux at the surface of the membrane,

$$D_d \frac{dc}{dz} = k_m (c_\infty - c_0) \quad \text{at } z = \pm L/2 \qquad [11]$$

where k_m is the mass-transport coefficient and c_∞ is the concentration of water in the environment. k_m is inversely proportionally to the interfacial resistance to water

Downloaded by STANFORD UNIV GREEN LIBR on June 14, 2012 | http://pubs.acs.org
Publication Date (Web): May 7, 2012 | doi: 10.1021/bk-2012-1096.ch011

Downloaded by STANFORD UNIV GREEN LIBR on June 14, 2012 | http://pubs.acs.org
Publication Date (Web): May 7, 2012 | doi: 10.1021/bk-2012-1096.ch011

transport at the membrane surface, i.e. $R_{\text{int}} = 1/k_m$. For example, for a membrane with negligible interfacial resistance ($R_{\text{int}} \rightarrow 0$, $k_m \rightarrow \infty$), Eq. [11] reduces to fixed concentration boundary condition, i.e. $c = c_\infty$, at the surface. Solution of Eq. [10] using the boundary condition given by [11] is (*105*):

$$\frac{M(t)-M_0}{M_\infty - M_0} = 1 - \sum_{n=1}^{\infty} \frac{8\sin^2(\beta_n/2)}{\beta_n{}^2 + \beta_n \sin(\beta_n)} \exp\left(-\beta_n{}^2 \frac{D_d}{L^2} t\right) \qquad [12]$$

where $M(t)$, M_0, and M_∞ are the current, initial, and final (steady-state) values of the membrane mass, respectively, and β_n is the roots of the equation

$$\beta_n \tan\frac{\beta_n}{2} = \text{Bi}, \qquad [13]$$

where Bi is dimensionless Biot number. The term D_d/L^2 can be interpreted as the sorption rate with units of 1/s, or reciprocal of time constant for sorption and diffusion, $\tau_{\text{diffusion}}$ (= L^2/D_d). The Biot number is the ratio of the characteristic time for water diffusion through the bulk membrane, $\tau_{\text{diffusion}}$, to that for mass transport through the membrane surface, $\tau_{\text{interface}}$, and therefore can be written in the following form

$$\text{Bi} = \frac{k_m L}{D} = \frac{L^2/D}{L/k_m} = \frac{\tau_{\text{diffusion}}}{\tau_{\text{interface}}} \qquad [14]$$

The Biot number shows which process dominates (or limits) the diffusion. If, for example, water transport is limited by the interfacial resistance at the membrane/vapor interface with very low k_m, then the characteristic time constant for mass-transport becomes high ($\tau_{\text{interface}} >> \tau_{\text{diffusion}}$) making the Biot number small ($Bi<<1$). As a limiting case, using $Bi = 0$ for a solely diffusion-controlled problem simplifies Eq. [12] to

$$\frac{M(t)-M_0}{M_\infty - M_0} = 1 - \frac{8}{\pi^2} \sum_{n=1}^{\infty} \frac{1}{(2n+1)^2} \exp\left(-\frac{\pi^2}{4}(2n+1)^2 \frac{D_d}{L^2} t\right) \qquad [15]$$

On the other hand, for $\tau_{\text{diffusion}} >> \tau_{\text{interface}}$ water transport is limited by the bulk diffusion and interfacial effects are negligible. In this case, the Biot number becomes large enough ($Bi>>1$) to give $\beta 1 \rightarrow \pi$ for Eq. [12]. The critical value for Biot number that determines which process dominates the water transport is around 10. Lastly, swelling of the Nafion membrane with water uptake (*3*, *46*, *53*, *106*, *107*) must be taken into consideration for the diffusion analysis. Increase in the thickness of a Nafion membrane upon water absorption can be written as (assuming isotropic swelling)

$$L(\lambda) = L_{\mathrm{dry}}\left(1+\lambda\frac{\overline{V}_{\mathrm{w}}}{\overline{V}_{\mathrm{p}}}\right)^{1/3} . \qquad [16]$$

If multiple time constants or diffusivities exist for the system, the above analysis becomes very complicated and it is easiest and more straightforward to assume an empirical approach of additive time constants with each term representing a different time-dependent process for water transport and uptake,

$$\frac{M(t)-M_0}{M_\infty - M_0} = 1-\sum_m A_m \exp\left(-\frac{t}{\tau_m}\right) \text{ with } \sum_{m=1} A_m = 1 \qquad [17]$$

where A_m is an arbitrary constant and τ_{m} is the characteristic time constant for the process m. For example, using one term might be sufficient for classical Fickian diffusion problem, where $\tau_{\mathrm{diffusion}}$ is proportional to the L^2/D_{d}. Eq. [17] reduces to following form if only two time constants are used:

$$\frac{M(t)-M_0}{M_\infty - M_0} = 1-A\exp\left(-\frac{t}{\tau_1}\right)-(1-A)\exp\left(-\frac{t}{\tau_2}\right) \qquad [18]$$

This form can also be used to characterize the diffusion-relaxation process in the membrane by associating the second time constant with the relaxation of the polymer backbone during water sorption. Alternatively, interfacial resistance can be implemented into the equation by setting $\tau_2 = \tau_{\mathrm{interface}} = k_m/L$.

Steady-State Water Transport

Diffusion

Steady-state diffusion in the membrane is generally investigated using a diffusion cell where the membrane is exposed to a chemical-potential gradient by controlling the water-activity or pressure (typically done with liquid water) at both surfaces of the membrane. For gases, one measures the water flux, N_{w}, for different water-vapor activity gradients across the membrane, $\Delta a_{\mathrm{w}} = a_1 - a_2$. Then, the diffusivity can be determined from a transport as a function of average water activity in the membrane. Similarly, one can use a pressure gradient to drive the water flux and calculate the permeability of the membrane (*21–25*, *56*, *57*, *108*, *109*). In general, the water transport coefficient from liquid-water permeation studies is higher than that from humidified water vapor for a given μ_w, although the actual flux is often lower due to a smaller accessible range of chemical-potential gradients. Steady-state diffusivities reported for Nafion membrane are generally consistent and within the same order-of-magnitude (see Table I and Figure 2). Determining the steady-state water diffusivity is actually measuring the resistance to water transport through the membrane. However, as the test setups and cell designs vary among these studies, careful attention must

Downloaded by STANFORD UNIV GREEN LIBR on June 14, 2012 | http://pubs.acs.org
Publication Date (Web): May 7, 2012 | doi: 10.1021/bk-2012-1096.ch011

Downloaded by STANFORD UNIV GREEN LIBR on June 14, 2012 | http://pubs.acs.org
Publication Date (Web): May 7, 2012 | doi: 10.1021/bk-2012-1096.ch011

be used to ascertain that the correct value is being reported and analyzed and not a combination of effects (e.g., it includes membrane/vapor interfacial resistances).

The interfacial resistance and the bulk resistance to water transport can be determined from a steady-state diffusion experiment by measuring the water flux through the membrane at different water activity gradients and using samples with different thicknesses. Then, the water flux can be written as

$$N_w = \frac{\Delta a_w}{R} = \frac{\text{Activity-Gradient}}{\text{Resistance}} = \frac{\Delta a_w}{\dfrac{1}{k_{m,1}} + \dfrac{L}{D} + \dfrac{1}{k_{m,2}}}, \qquad [19]$$

where the resistance is the sum of the interfacial resistance ($1/k_m$) at both sides of the membrane and the bulk resistance, which is inversely proportional to the diffusivity (1/D). Thus, the plot of the measured membrane resistance as a function of membrane thickness, L, gives a straight line where the slope gives the diffusivity and the non-zero intercept, if it exists, gives the interfacial resistance. Note that if the intercept is zero, then the interfacial resistance does not exist, meaning that Biot number is 0 (see eq [14]) and the diffusion process is not limited by interfacial mass transport (k_m >>1). A typical resistance vs. thickness plot is demonstrated in Figure 4 using the experimental data of Kienitz et al. (*31*).

Interfacial Resistance

As noted above, a nonzero intercept, as shown in Figure 4, allows for the calculation of the mass-transport coefficient. From Figure 4, one can write the mass-transport coefficient of the form

$$k_m = 6.8 \cdot 10^{-4} (\lambda - \lambda_0)^{1.6}, \qquad [20]$$

although other functional relationships can also be used (e.g., exponential form) with dependences on water fraction or concentration (using Eq. [2]). Eq. [20] accounts for the residual water in the membrane, λ_0, if there is any due to the pretreatment method or thermal history. In any case, mass transport through the membrane/vapor interface should be enhanced when the membrane surface is more hydrated. The mass-transport coefficients reported in the literature are summarized in Table II. In general, k_m increases with increasing water content suggesting reduced interfacial resistance for hydrated membranes.

The existence and origin of the interfacial resistance is due to polymer surface reorganization during swelling, which can be investigated using conductive AFM. The surface of the PFSA membrane is hydrophobic, especially in low humidities, as has been shown through contact-angle (*111*) and AFM (*71*, *112–116*) measurements. In addition, conductive AFM studies (*113*, *115*, *117*) indicate an increase in the conductive surface area with humidity, which can be an indication of an increase in overall hydrophilicity of the surface. Bass et al. (*19*, *118*) recently suggested using grazing-incidence SAXS (GISAXS) that while the surface of PFSA membrane is hydrophobic in vapor it becomes

Downloaded by STANFORD UNIV GREEN LIBR on June 14, 2012 | http://pubs.acs.org
Publication Date (Web): May 7, 2012 | doi: 10.1021/bk-2012-1096.ch011

hydrophilic when the membrane is in liquid water altering the surface morphology (*19*, *118*). It is very probable that hydrophilicity of the surface has a direct role in both the surface conductivity and water transport through the membrane surface. The effect of interfacial resistance at the membrane/vapor interface on the water-transport mechanisms in Nafion membrane has been investigated using steady-state and transient diffusion measurements (*26*, *28*, *46*, *56*, *57*, *104*). For instance, interfacial resistance was shown to be the limiting mechanism for water transport at low temperatures and for thinner membranes (*56*, *57*) and at high humidities (*46*). Zhao et al. (*46*) reported a humidity-independent interfacial resistance. However, data by Kienitz et al. (*31*) suggest a decrease in mass-transport coefficient with humidity (see eq. [20]). Moreover, a correlation exists between the mass-transport coefficient and the fraction of hydrophilic surface area, f_a, determined from conductive AFM (*117*):

$$k_m \propto f_a^{0.5}\,, \qquad [21]$$

which indicates that it is the inaccessible hydrophilic groups at the membrane surface that is controlling the interfacial resistance.

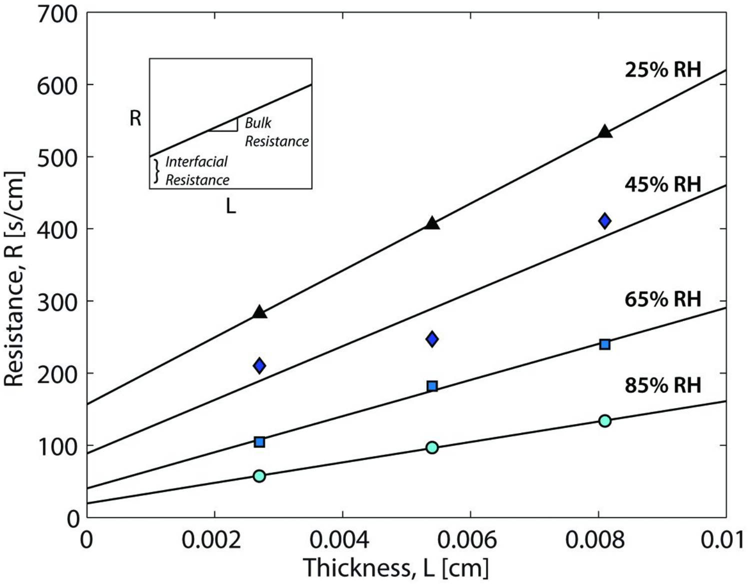

Figure 4. Resistance to steady-state water transport in the membrane as a function of membrane thickness (lines are fitting based on Eq. [19] and symbols are measured experimental data taken from literature (31)).

Table II. Interfacial Resistance of Nafion membrane

Reference	*Method*	*Mass-Transport Coefficient* *k_m [cm/s]*
Okada et al. (*110*)	model	$1 - 9 \times 10^{-4}$
Ge et al. (*26*)	steady-state permeability	Sorption: 3.53×10^{-3} φw Desorption: 1.42×10^{-2} φw
Satterfield et al. (*57*)	sorption	2.8 to 10.6 (50 to 250 μm thick)
Kienitz et al. (*31*)	steady-state	See Eq. [20]
Kongkanand (*59*)	sorption	Sorption: 2×10^{-4} Desorption: 5.9×10^{-4}
Zhao et al. (*46*)	permeability	$1.2 - 3.8 \times 10^{-3}$ (30 to 80 °C)
Adachi et al. (*109*)	permeability	4.5×10^{-4} 70 °C
Tabuchi et al. (*47*)	Raman spectroscopy	$1.25 - 10 \times 10^{-4}$ at 70 °C
Monroe et al. (*28*)	permeability	0.63 – 0.75

Another approach to understand the interfacial phenomenon is investigating the water transport through thin-films, where nominally they are almost entirely interface. Krtil et al. (*119*) reported that diffusion is lower for thin films (as low as 0.02 micron). Recently, Kongkanand (*59*) studied the water uptake and sorption mechanism in thin films and evidenced interfacial resistance and mechanical relaxation.

Liquid-Water Permeability

For a membrane in contact with liquid water on both sides, a flux can happen if the two liquid have different pressures and hence different chemical potentials (eq. [6]) since the water concentration at both sides becomes equal. In this case, the transport coefficient used is derived from Darcy's law

$$\alpha = \frac{k}{\mu \bar{V}_w^2} \qquad [22]$$

where k is the permeability of the membrane and μ is the viscosity of water inside the membrane. Thus, liquid/liquid permeability experiments are different in nature than the steady-state diffusion experiments in vapor. In addition, it seems that liquid/liquid conditions result in no appreciable interfacial resistance (*25*, *27*, *28*, *57*, *109*), owing to the arrangement of the membrane's surface hydrophilic groups. The values for the permeabilities of Nafion are very close and only vary due to various pretreatment or chemical and/or mechanical modifications.

Downloaded by STANFORD UNIV GREEN LIBR on June 14, 2012 | http://pubs.acs.org
Publication Date (Web): May 7, 2012 | doi: 10.1021/bk-2012-1096.ch011

Despite the similarities among the reported permeability data, there are difficulties in explaining and analyzing date with both liquid and vapor boundaries due to the presence of Schroeder's paradox, which affects the morphology and transport properties (*6*, *8*, *9*, *29*, *89*, *90*, *102–104*). The effect of water phase on sorption behavior has been attributed to the thermal history (*89*) and the distinct processes for water transport from liquid and vapor phases (*8*, *9*, *88*), where the latter is related to the interfacial resistance at the membrane/vapor interface (*88*, *118*) and surface nanostructure (*19*, *118*).

Nuclear Magnetic Resonance

NMR can be used to determine the thermodynamic diffusion coefficient, D_μ, directly, which is often termed self-diffusion coefficient in these experiments. NMR tracks the mobility of the water molecules in the membrane at smaller lengthscales. The reported self-diffusion coefficients of water are consistent and all increase with increasing water content (Figure 2). Some NMR studies also reported ionic conductivity, κ, of the membrane from which another diffusion coefficient, D_κ, can be determined using the Nernst-Einstein relationship (*120*),

$$D_\kappa = \kappa \frac{RT}{zF} \qquad [23]$$

where F is Faraday's constant and z is the charge of ion. Comparison of the water mobility (D_μ) and ionic mobility (D_κ) provides an understanding of the role of water in ion transport. It has been found that the measured D_μ, so-called intra-diffusion coefficient of water, is lower than the diffusion coefficient of H^+ obtained from proton conductivity (*34*, *43*, *45*, *68*). This was attributed to that fact that, mechanisms of water and ion transport are different, especially at high water contents. In addition to the vehicular transport of hydrated protons, hopping, or the Grotthuss mechanism, provides an additional path for ion movement (*121*). Thus, ion and water transport are related through the chemical structure and morphology of the membrane even though their mobilities are different ($D_\mu > D_\kappa$). Of course, another source of discrepancy is that eq [24] is only rigorously valid for diluet solutions, of which the membrane system is not. Thus, there is error in such an analysis and extreme care is necessary to try and relate the conductivity to the water diffusion. Another technique to probe the mobility of water at small scales is quasi-elastic neutron scattering (QENS) (*64–67*) which provides a diffusion coefficient based on "jump" and "local" movement of ions that is similar to those obtained from NMR (Figure 2b).

Dynamic Water Transport

Dynamic Vapor Sorption

Dynamics of water transport in PFSA membranes are commonly investigated using time-dependent gravimetric measurements, for example using a dynamic vapor sorption (DVS) analyzer. Most studies rely on measuring the change in

In Polymers for Energy Storage and Delivery: Polyelectrolytes for Batteries and Fuel Cells; Page, K., et al.;
ACS Symposium Series; American Chemical Society: Washington, DC, 2012.

Downloaded by STANFORD UNIV GREEN LIBR on June 14, 2012 | http://pubs.acs.org
Publication Date (Web): May 7, 2012 | doi: 10.1021/bk-2012-1096.ch011

the mass of the membrane with time at a given temperature and humidity from which the diffusivity of water is determined (see eqs. [10] and [12]). Thus, the time to reach the equilibrium mass (or water content) at a given humidity provides information on the timescales for the dynamics of water transport in the membrane. As seen in Table I and Fig 2, the values for the dynamic studies are often much lower than those for the steady-state ones which is due to the additional need for incorporation of the water and swelling of the membranes. Therefore, the process of sorption is actually much more complicated than just diffusion as it also involves swelling, polymer relaxation, morphological changes, etc. and a term such as diffusion coefficient is not really appropriate. However, the much lower measured values of the transport processes during dynamic studies demonstrate that interfacial resistance is no longer dominant (i.e., a very large Biot number, see eq [14]), and for most cases can be ignored for the dynamic measurements. Determination of the diffusion coefficient from a DVS experiment from dry to saturated conditions could be cumbersome. Mathematical modeling of dynamic water transport in PFSA membranes requires a careful examination of thickness, mass-transport coefficient, and diffusivity, the competition among which determines the dominant (or limiting) process in the membrane. Moreover, all these parameters change with concentration and time, which makes it challenging to characterize the dynamics of diffusion. Due to the high number of unknown time constants representing various processes and interrelated parameters, the equations outlined above become coupled and therefore have to be solved numerically.

By conducting a differential DVS experiment (i.e., small humidity intervals), the change in diffusion coefficient, D_d, due to concentration can be minimized (Figure 5). This way, the time-dependent diffusion problem can be solved at different humidity intervals assuming a constant D_d. The results of our DVS experiment conducted by measuring the water-vapor uptake by increasing the humidity step by step up to the saturation vapor pressure are shown in Figure 5. The data suggest that diffusion coefficient decreases with increasing humidity and reaches its lowest value (10^{-9} cm^2/s) at saturation (Figure 2), which is in agreement with references (*51*, *52*, *60*). The decrease in diffusivity at high humidities is opposite to those observed in steady-state and NMR experiments, in which diffusivity generally increases with increasing humidity. Moreover, in some studies the steady-state diffusivity exhibits a sharp peak around $\lambda = 3$ to 5 and then slowly increases with additional water (Figure 2).

As mentioned, the dynamic diffusion involves water uptake in addition to water transport (Figure 1). Thus, the membrane's nanostructure has to accommodate the growth of water domains while providing a pathway for the mobility of water molecules. For example, the decrease in dynamic diffusivity was attributed to growth of water clusters which reduce the water mobility (*51*).

Downloaded by STANFORD UNIV GREEN LIBR on June 14, 2012 | http://pubs.acs.org
Publication Date (Web): May 7, 2012 | doi: 10.1021/bk-2012-1096.ch011

Downloaded by STANFORD UNIV GREEN LIBR on June 14, 2012 | http://pubs.acs.org
Publication Date (Web): May 7, 2012 | doi: 10.1021/bk-2012-1096.ch011

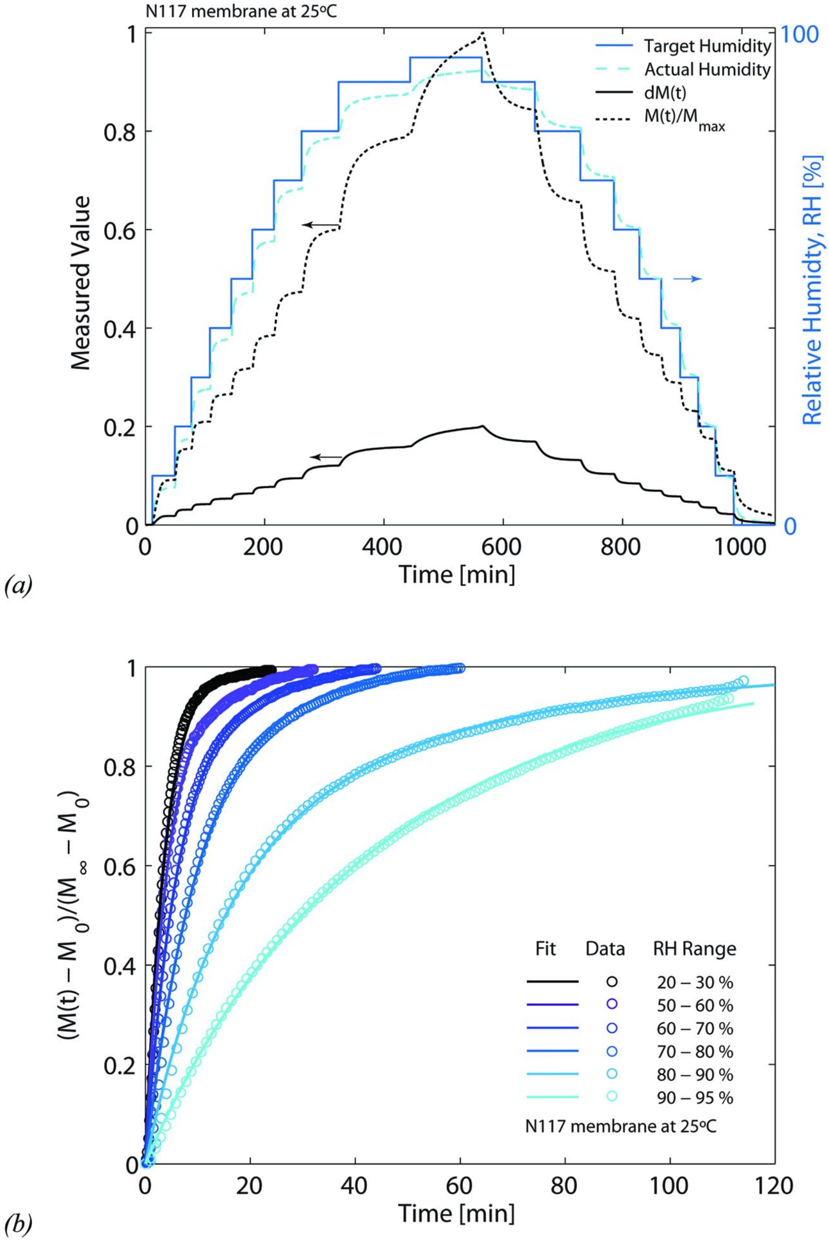

Figure 5. (a) Water-uptake profile for the step-changes in humidity during a dynamic vapor sorption test, and (b) normalized water uptake with model fit.

Downloaded by STANFORD UNIV GREEN LIBR on June 14, 2012 | http://pubs.acs.org
Publication Date (Web): May 7, 2012 | doi: 10.1021/bk-2012-1096.ch011

One can also examine the sorption/desorption behavior of the membrane. From Figure 5, it seems that desorption is faster than sorption although relatively similar. In Table I, some studies measure faster desorption rates and others do not; there is no consensus in the literature. The issue is probably due to several differences between sorption and desorption stemming from the polymer surface rearrangement and differences in the initial and final morphological states of the two processes. For example, one can explain a faster desorption rate in that it is easier to expel and contract the water domains rather than expand them. In other words, the surface and internal morphology of well-connected and open pores at higher water contents facilitates water removal, whereas the sorption process is retarded by the need for the structure to reorganize. Another possible reason is due to condensation/evaporation in that for sorption, there is an increase in temperature, due to the heat of condensation of the vapor, which has the effect of lowering the water-vapor activity relative to the higher membrane temperature, and therefore decreasing the sorption rate (*24*). A reason why one could observe faster sorption than desorption rates could be in experiments where the interfacial resistance is limiting and changes substantially. For example, upon contact with liquid water, the membrane interface rearranges fast and allows water to transport in immediately, whereas upon contact with dry gas, the rearrangement of the interface is slow and limits the desorption rate.

The diffusion-relaxation model as defined in Eq. [18] has been adopted by Satterfield (*57*) and Kongkanand (*59*) to investigate the interfacial effects during water transport in Nafion membranes and thin films, respectively. Even though additional terms can easily be incorporated to include other processes controlling the water transport a two-term expression has been shown to be sufficient to reproduce the time-dependent water-uptake behavior of Nafion membranes (*29*, *57*, *59*). However, it is possible to attribute different processes to the time constants. One such process is the time-dependent deformation of the polymer matrix. During water uptake, growth of water domains in the membrane deforms the polymer matrix generating a swelling pressure (*97*, *122*). Assigning the second time constant to polymer relaxation, $\tau_{\mathrm{relaxation}}$, generally gives two- to three- orders-of-magnitude higher values than the diffusion time constant (*29*), meaning that the overall transport process becomes controlled by the polymer relaxation. It is also possible correlate the interfacial effects to the interplay between the swelling of water domains and the generation and subsequent relaxation of swelling pressure generated in the matrix during water uptake (*57*). Water uptake was suggested to be limited by the interfacial transport during the earlier times of the sorption whereas relaxation of polymer matrix with time allows more water to be absorbed (*57*).

Lastly, Elabd, Hallinan and co-workers (*53–55*) investigated the dynamics of water sorption in Nafion membranes using time-resolved Fourier transform infrared-attenuated total reflectance (FTIR). FTIR measures both the molecular changes in the water/polymer and the molecular interactions between the water and polymer through shifts in the infrared spectra (*54*). It was evidenced, using dynamic infrared data, that water-induced relaxation in the polymer backbone is critical for the diffusion-relaxation mechanism during dynamic sorption at high humidities (*54*).

In Polymers for Energy Storage and Delivery: Polyelectrolytes for Batteries and Fuel Cells; Page, K., et al.;
ACS Symposium Series; American Chemical Society: Washington, DC, 2012.

Downloaded by STANFORD UNIV GREEN LIBR on June 14, 2012 | http://pubs.acs.org
Publication Date (Web): May 7, 2012 | doi: 10.1021/bk-2012-1096.ch011

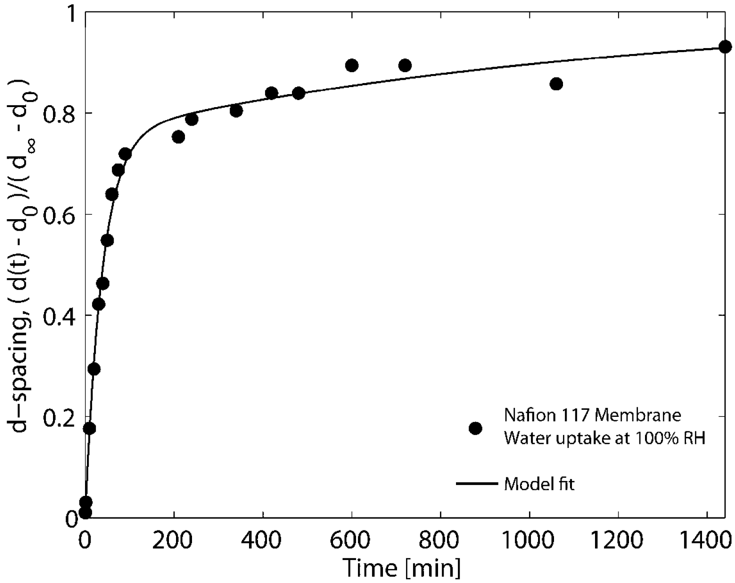

Figure 6. Swelling of water domains with time for a membrane exposed to saturated water vapor at ambient temperature.

Sorption at Nanoscales

Most of the analysis above is predicated on some interpretation of phenomena occurring at the nanoscale. The above macroscale experiments are unable to capture these nanoscale effects. However there are some techniques suited to study nanoscale phenomena including small-angle X-ray and neutron scattering. Kim et al. (*16*) studied the sorption behavior of a Nafion membrane using small-angle neutron scattering (SANS) and determined the change in the spacing between water domains as a function of time during water uptake. Using the classical Fickian diffusion problem (Eq. [12] with fixed concentration boundary condition) they calculated the coefficient for the growth of water domains as 1 to 2.4×10^{-7} cm^2/s.

To understand better the nanoscale dynamics of water transport, we carried out SAXS experiments at Advance Light Source (ALS) at Lawrence Berkeley National Laboratory. The timescale investigated was varied from minutes to days. Our results indicate that inter-domain spacing and consequently the size of the water domains increase with time consistent with the macroscopic diffusion process (Figure 6). Fitting of normalized domain spacing using Eq. [12] gives ~10^{-6} cm^2/s, faster than reported by Kim et al. (*16*). However, it is questionable whether Fickian diffusion can be used for the growth of water domains as it involves processes like absorption of water molecules and accommodation of domains in the deformed polymer matrix. In addition, it is hard to analyze the data in terms of D/L^2 as the lengthscales in the SAXS experiment is lower than the macroscopic membrane size (Figure 1) (i.e., L is poorly defined). A very good fit to the measured data, however, can be obtained using Eq. [18] with time constants of 10^5 and 10^3 seconds (Figure 6). These time constants probably correspond to the processes for water-domain growth at nanoscales. Even though more studies are needed to understand fully the water transport at smaller lengthscales, there is evidence to suggest that microscopic diffusion processes are generally faster than the macroscopic ones.

Temperature Effect

Water-transport studies (steady-state and dynamic) conducted at various temperatures (Table II) provide additional information on the temperature-induced kinetics of water mobility (*45*, *72*, *78*, *79*, *81*, *83–85*, *87*, *123*). Most studies agree that temperature results in an increase in water transport independent of the test method. That is not to say that the final water content is higher at higher temperatures, just that the rate of water diffusion and/or sorption is higher. The water-content and temperature-dependence of the diffusivity is generally separated for simplicity, i.e. $D(\lambda,T) = D_0(T)f(\lambda)$. Even though polynomial (*7*) and linear (*8*) dependences on water content were developed for the steady-state and thermodynamic diffusivities, respectively, the highly nonlinear water-content dependence of diffusivity (Figure 2) makes it difficult to develop a functional relationship for $f(\lambda)$. However, the temperature dependence is commonly represented by an Arrhenius expression,

$$D_0(T) \propto \exp\left(-\frac{E_a}{RT}\right), \qquad [24]$$

where E_a is the activation energy of water transport. The activation energy has been reported to be in the range of 20 to 30 kJ/mol (*48–50*, *57*, *62*) for sorption experiments, and 13 to 30 kJ/mol (*33*, *39*, *44–46*, *59*, *61*, *124*) for NMR experiments conducted at different temperatures. Of course, the sorption studies are also complicated by the change in the polymer properties and relaxation with temperature.

Concluding Remarks

The current state of understanding of the sorption behavior of Nafion membranes is investigated using the reported data in the literature. A number of techniques are commonly used to determine the characteristic time constants for water transport at macroscopic and nanoscopic scales. The large discrepancy in diffusivity can be attributed to differences in test setups, variation in environmental condition, membrane types, and even the pretreatment of the samples prior to the tests. However, some similarities are observed when the reported data is compared for each experimental procedure which indicates the following order for the diffusion coefficient, $D_\kappa > D_\mu > D_f > D_d$. In general, diffusion coefficients from steady-state and permeability measurements (D_f) are close, yet a few orders-of-magnitude higher than those obtained from dynamic

Downloaded by STANFORD UNIV GREEN LIBR on June 14, 2012 | http://pubs.acs.org
Publication Date (Web): May 7, 2012 | doi: 10.1021/bk-2012-1096.ch011

vapor sorption (D_d). Also, experiments probing the mobility of ions and water molecules, such as conductivity (D_κ) or NMR (D_μ) and QENS, generally indicate a faster diffusion process. In addition, interfacial resistance to water transport at membrane/vapor interfaces might have a critical role in the overall diffusion process. However, interfacial effects seem to be more influential in steady-state water transport. Dynamic swelling behavior of a PFSA membrane, on the other hand, is a complex process involving time-dependent nanostructural changes to accommodate the growing water domains and polymer surface reorganization, which together control water transport. Therefore, classical Fickian diffusion or polymer relaxation mechanisms alone are not sufficient to characterize the experimental dynamic water-sorption data. Hence, dynamics of sorption is very different than the steady-state water transport which can be attributed to the swelling and relaxation processes in the membrane occurring at multiple scales during water uptake.

Downloaded by STANFORD UNIV GREEN LIBR on June 14, 2012 | http://pubs.acs.org
Publication Date (Web): May 7, 2012 | doi: 10.1021/bk-2012-1096.ch011

References

1. Ramirez-Garcia, S.; Diamond, D. *Sens. Actuators, A* **2007**, *135* (1), 229–235.
2. Shahinpoor, M. *Math. Mech. Solids* **2003**, *8* (3), 281–288.
3. Mathias, M. F.; Makharia, R.; Gasteiger, H. A.; Conley, J. J.; Fuller, T. J.; Gittleman, C. J.; Kocha, S. S.; Miller, D. P.; Mittelsteadt, C. K.; Xie, T.; Van, S. G.; Yu, P. T. *Electrochem. Soc. Interface* **2005**, *14* (3), 24–35.
4. Hickner, M. A.; Pivovar, B. S. *Fuel Cells* **2005**, *5* (2), 213–229.
5. Rajendran, R. G. *MRS Bull.* **2005**, *30* (8), 587–590.
6. Mauritz, K. A.; Moore, R. B. *Chem. Rev.* **2004**, *104* (10), 4535–4585.
7. Springer, T. E.; Zawodzinski, T. A.; Gottesfeld, S. *J. Electrochem. Soc.* **1991**, *138* (8), 2334–2342.
8. Weber, A. Z.; Newman, J. *J. Electrochem. Soc.* **2004**, *151* (2), 311–325.
9. Zawodzinski, T. A.; Derouin, C.; Radzinski, S.; Sherman, R. J.; Smith, V. T.; Springer, T. E.; Gottesfeld, S. *J. Electrochem. Soc.* **1993**, *140* (4), 1041–1047.
10. Hsu, W. Y.; Gierke, T. D. *J. Membr. Sci.* **1983**, *13* (3), 307–326.
11. Gebel, G. *Polymer* **2000**, *41* (15), 5829–5838.
12. Eikerling, M.; Kornyshev, A. A.; Kucernak, A. R. *Phys. Today* **2006**, *59* (10), 38–44.
13. Weber, A. Z.; Newman, J. *Chem. Rev.* **2004**, *104* (10), 4679–4726.
14. Gierke, T. D.; Munn, G. E.; Wilson, F. C. *J. Polym. Sci., Polym. Phys. Ed.* **1981**, *19* (11), 1687–1704.
15. Elliott, J. A.; Wu, D.; Paddison, S. J.; Moore, R. B. *Soft Matter* **2011**, *7* (15), 6820–6827.
16. Kim, M. H.; Glinka, C. J.; Grot, S. A.; Grot, W. G. *Macromolecules* **2006**, *39* (14), 4775–4787.
17. Schmidt-Rohr, K.; Chen, Q. *Nat. Mater.* **2008**, *7* (1), 75–83.
18. Rubatat, L.; Rollet, A. L.; Gebel, G.; Diat, O. *Macromolecules* **2002**, *35* (10), 4050–4055.

19. Bass, M.; Berman, A.; Singh, A.; Konovalov, O.; Freger, V. *Macromolecules* **2011**, *44* (8), 2893–2899.
20. Zelsmann, H. R.; Pineri, M.; Thomas, M.; Escoubes, M. *J. Appl. Polym. Sci.* **1990**, *41* (7−8), 1673–1684.
21. Fuller, T. F. Solid-polymer-electrolyte fuel cells. Ph.D. dissertation, University of California - Berkeley, Berkeley, CA, 1992.
22. Okada, T.; Xie, G.; Gorseth, O.; Kjelstrup, S.; Nakamura, N.; Arimura, T. *Electrochim. Acta* **1998**, *43* (24), 3741–3747.
23. Grossi, N.; Espuche, E.; Escoubes, M. *Sep. Purif. Technol.* **2001**, *22-3* (1−3), 255–267.
24. Rivin, D.; Kendrick, C. E.; Gibson, P. W.; Schneider, N. S. *Polymer* **2001**, *42* (2), 623–635.
25. Ye, X. H.; LeVan, M. D. *J. Membr. Sci.* **2003**, *221* (1−2), 147–161.
26. Ge, S. H.; Li, X. G.; Yi, B. L.; Hsing, I. M. *J. Electrochem. Soc.* **2005**, *152* (6), A1149–A1157.
27. Majsztrik, P.; Bocarsly, A.; Benziger, J. *J. Phys. Chem. B* **2008**, *112* (51), 16280–16289.
28. Monroe, C. W.; Romero, T.; Merida, W.; Eikerling, M. *J. Membr. Sci.* **2008**, *324* (1−2), 1–6.
29. Onishi, L. Equilibrium and transport properties of a proton-exchange membrane for fuel cells. Ph.D. dissertation, University of California, Berkeley, Berkeley, CA, 2009.
30. Schneider, N. S.; Rivin, D. *Polymer* **2010**, *51* (3), 671–678.
31. Kientiz, B.; Yamada, H.; Nonoyama, N.; Weber, A. Z. *J. Fuel Cell Sci. Technol.* **2011**, *8* (1), 011013.
32. Hietala, S.; Maunu, S. L.; Sundholm, F. *J. Polym. Sci., Polym. Phys.* **2000**, *38* (24), 3277–3284.
33. Gong, X.; Bandis, A.; Tao, A.; Meresi, G.; Wang, Y.; Inglefield, P. T.; Jones, A. A.; Wen, W. Y. *Polymer* **2001**, *42* (15), 6485–6492.
34. Edmondson, C. A.; Fontanella, J. J. *Solid State Ionics* **2002**, *152*, 355–361.
35. Giotto, M. V.; Zhang, J. H.; Inglefield, P. T.; Wen, W. Y.; Jones, A. A. *Macromolecules* **2003**, *36* (12), 4397–4403.
36. Jayakody, J. R. P.; Stallworth, P. E.; Mananga, E. S.; Farrington-Zapata, J.; Greenbaum, S. G. *J. Phys. Chem. B* **2004**, *108* (14), 4260–4262.
37. Saito, M.; Arimura, N.; Hayamizu, K.; Okada, T. *J. Phys. Chem. B* **2004**, *108* (41), 16064–16070.
38. Tsushima, S.; Teranishi, K.; Hirai, S. *Energy* **2005**, *30* (2−4), 235–245.
39. Saito, M.; Hayamizu, K.; Okada, T. *J. Phys. Chem. B* **2005**, *109* (8), 3112–3119.
40. Zhang, J. H.; Giotto, M. V.; Wen, W. Y.; Jones, A. A. *J. Membr. Sci.* **2006**, *269* (1−2), 118–125.
41. Hensley, J. E.; Way, J. D.; Dec, S. F.; Abney, K. D. *J. Membr. Sci.* **2007**, *298* (1−2), 190–201.
42. Ohkubo, T.; Kidena, K.; Ohira, A. *Macromolecules* **2008**, *41* (22), 8688–8693.
43. Ochi, S.; Kamishima, O.; Mizusaki, J.; Kawamura, J. *Solid State Ionics* **2009**, *180* (6-8), 580–584.

Downloaded by STANFORD UNIV GREEN LIBR on June 14, 2012 | http://pubs.acs.org
Publication Date (Web): May 7, 2012 | doi: 10.1021/bk-2012-1096.ch011

44. Guillermo, A.; Gebel, G.; Mendil-Jakani, H.; Pinton, E. *J. Phys. Chem. B* **2009**, *113* (19), 6710–6717.
45. Kidena, K.; Ohkubo, T.; Takimoto, N.; Ohira, A. *Eur. Polym. J.* **2010**, *46* (3), 450–455.
46. Zhao, Q. A.; Majsztrik, P.; Benziger, J. *J. Phys. Chem. B* **2011**, *115* (12), 2717–2727.
47. Tabuchi, Y.; Ito, R.; Tsushima, S.; Hirai, S. *J. Power Sources* **2011**, *196* (2), 652–658.
48. Yeo, S. C.; Eisenberg, A. *J. Appl. Polym. Sci.* **1977**, *21* (4), 875–898.
49. Takamatsu, T.; Hashiyama, M.; Eisenberg, A. *J. Appl. Polym. Sci.* **1979**, *24* (11), 2199–2220.
50. Morris, D. R.; Sun, X. D. *J. Appl. Polym. Sci.* **1993**, *50* (8), 1445–1452.
51. Legras, M.; Hirata, Y.; Nguyen, Q. T.; Langevin, D.; Metayer, M. *Desalination* **2002**, *147* (1-3), 351–357.
52. Burnett, D. J.; Garcia, A. R.; Thielmann, F. *J. Power Sources* **2006**, *160* (1), 426–430.
53. Hallinan, D. T.; Elabd, Y. A. *J. Phys. Chem. B* **2007**, *111* (46), 13221–13230.
54. Hallinan, D. T.; De Angelis, M. G.; Baschetti, M. G.; Sarti, G. C.; Elabd, Y. A. *Macromolecules* **2010**, *43* (10), 4667–4678.
55. Hallinan, D. T.; Elabd, Y. A. *J. Phys. Chem. B* **2009**, *113* (13), 4257–4266.
56. Majsztrik, P. W.; Satterfield, M. B.; Bocarsly, A. B.; Benziger, J. B. *J. Membr. Sci.* **2007**, *301* (1−2), 93–106.
57. Satterfield, M. B.; Benziger, J. B. *J. Phys. Chem. B* **2008**, *112* (12), 3693–3704.
58. Damay, F.; Klein, L. C. *Solid State Ionics* **2003**, *162*, 261–267.
59. Kongkanand, A. *J. Phys. Chem. C* **2011**, *115* (22), 11318–11325.
60. Mangiagli, P. M.; Ewing, C. S.; Xu, K.; Wang, Q.; Hickner, M. A. *Fuel Cells* **2009**, *9* (4), 432–438.
61. Yeager, H. L.; Steck, A. *J. Electrochem. Soc.* **1981**, *128* (9), 1880–1884.
62. Verbrugge, M. W.; Schneider, E. W.; Conell, R. S.; Hill, R. F. *J. Electrochem. Soc.* **1992**, *139* (12), 3421–3428.
63. Suresh, G.; Scindia, Y. M.; Pandey, A. K.; Goswami, A. *J. Phys. Chem. B* **2004**, *108* (13), 4104–4110.
64. Volino, F.; Pineri, M.; Dianoux, A. J.; Degeyer, A. *J. Polym. Sci., Polym. Phys.* **1982**, *20* (3), 481–496.
65. Pivovar, A. A.; Pivovar, B. S. *J. Phys. Chem. B* **2005**, *109* (2), 785–793.
66. Perrin, J. C.; Lyonnard, S.; Volino, F. *J. Phys. Chem. C* **2007**, *111* (8), 3393–3404.
67. Page, K. A.; Park, J. K.; Moore, R. B.; Sakai, V. G. *Macromolecules* **2009**, *42* (7), 2729–2736.
68. Zawodzinski, T. A.; Neeman, M.; Sillerud, L. O.; Gottesfeld, S. *J. Phys. Chem.* **1991**, *95* (15), 6040–6044.
69. Jalani, N. H.; Datta, R. *J. Membr. Sci.* **2005**, *264* (1−2), 167–175.
70. Choi, P.; Jalani, N. H.; Datta, R. *J. Electrochem. Soc.* **2005**, *152* (3), E84–E89.
71. James, P. J.; Elliott, J. A.; McMaster, T. J.; Newton, J. M.; Elliott, A. M. S.; Hanna, S.; Miles, M. J. *J. Mater. Sci.* **2000**, *35* (20), 5111–5119.

Downloaded by STANFORD UNIV GREEN LIBR on June 14, 2012 | http://pubs.acs.org
Publication Date (Web): May 7, 2012 | doi: 10.1021/bk-2012-1096.ch011

72. Takata, H.; Mizuno, N.; Nishikawa, M.; Fukada, S.; Yoshitake, M. *Int. J. Hydrogen Energy* **2007**, *32* (3), 371–379.
73. Kreuer, K. D. *Solid State Ionics* **1997**, *97* (1-4), 1–15.
74. Alberti, G.; Narducci, R. *Fuel Cells* **2009**, *9* (4), 410–420.
75. Freger, V.; Korin, E.; Wisniak, J.; Korngold, E. *J. Membr. Sci.* **1997**, *133* (2), 255–267.
76. Collette, F. M.; Lorentz, C.; Gebel, G.; Thominette, F. *J. Membr. Sci.* **2009**, *330* (1−2), 21–29.
77. Park, Y. S.; Hatae, T.; Itoh, H.; Jang, M. Y.; Yamazaki, Y. *Electrochim. Acta* **2004**, *50* (2-3), 595–599.
78. Broka, K.; Ekdunge, P. *J. Appl. Electrochem.* **1997**, *27* (2), 117–123.
79. Park, M. J.; Downing, K. H.; Jackson, A.; Gomez, E. D.; Minor, A. M.; Cookson, D.; Weber, A. Z.; Balsara, N. P. *Nano Lett.* **2007**, *7* (11), 3547–3552.
80. Pineri, M.; Volino, F.; Escoubes, M. *J. Polym. Sci., Polym. Phys.* **1985**, *23* (10), 2009–2020.
81. Gates, C. M.; Newman, J. *AIChE J.* **2000**, *46* (10), 2076–2085.
82. Mauritz, K. A.; Rogers, C. E. *Macromolecules* **1985**, *18* (3), 483–491.
83. Futerko, P.; Hsing, I. M. *J. Electrochem. Soc.* **1999**, *146* (6), 2049–2053.
84. Hinatsu, J. T.; Mizuhata, M.; Takenaka, H. *J. Electrochem. Soc.* **1994**, *141* (6), 1493–1498.
85. Alberti, G.; Narducci, R.; Sganappa, M. *J. Power Sources* **2008**, *178* (2), 575–583.
86. Laporta, M.; Pegoraro, M.; Zanderighi, L. *Phys. Chem. Chem. Phys.* **1999**, *1* (19), 4619–4628.
87. Zawodzinski, T. A.; Springer, T. E.; Davey, J.; Jestel, R.; Lopez, C.; Valerio, J.; Gottesfeld, S. *J. Electrochem. Soc.* **1993**, *140* (7), 1981–1985.
88. Choi, P. H.; Datta, R. *J. Electrochem. Soc.* **2003**, *150* (12), E601–E607.
89. Onishi, L. M.; Prausnitz, J. M.; Newman, J. *J. Phys. Chem. B* **2007**, *111* (34), 10166–10173.
90. Bass, M.; Freger, V. *Desalination* **2006**, *199* (1−3), 277–279.
91. Escoubes, M.; Pineri, M.; Robens, E. *Thermochim. Acta* **1984**, *82* (1), 149–160.
92. Thompson, E. L.; Jorne, J.; Gu, W. B.; Gasteiger, H. A. *J. Electrochem. Soc.* **2008**, *155* (6), B625–B634.
93. Siegel, N. P.; Ellis, M. W.; Nelson, D. J.; von Spakovsky, M. R. *J. Power Sources* **2003**, *115* (1), 81–89.
94. Futerko, P.; Hsing, I. M. *J. Electrochem. Soc.* **1999**, *146* (6), 2049–2053.
95. Futerko, P.; Hsing, I. M. *Electrochim. Acta* **2000**, *45* (11), 1741–1751.
96. Hsing, I. M.; Futerko, P. *Chem. Eng. Sci.* **2000**, *55* (19), 4209–4218.
97. Kusoglu, A.; Santare, M. H.; Karlsson, A. M. *Polymer* **2009**, *50* (11), 2481–2491.
98. Meyers, J. P.; Newman, J. *J. Electrochem. Soc.* **2002**, *149* (6), A710–A717.
99. Weber, A. Z.; Newman, J. *J. Electrochem. Soc.* **2004**, *151* (2), A311–A325.
100. Thampan, T.; Malhotra, S.; Tang, H.; Datta, R. *J. Electrochem. Soc.* **2000**, *147* (9), 3242–3250.
101. Choi, P.; Datta, R. *J. Electrochem. Soc.* **2003**, *150* (12), E601–E607.

Downloaded by STANFORD UNIV GREEN LIBR on June 14, 2012 | http://pubs.acs.org
Publication Date (Web): May 7, 2012 | doi: 10.1021/bk-2012-1096.ch011

102. Freger, V. *J. Phys. Chem. B* **2009**, *113* (1), 24–36.
103. Vallieres, C.; Winkelmann, D.; Roizard, D.; Favre, E.; Scharfer, P.; Kind, M. *J. Membr. Sci.* **2006**, *278* (1−2), 357–364.
104. Bass, M.; Freger, V. *Polymer* **2008**, *49* (2), 497–506.
105. Crank, J. *The mathematics of diffusion*; Clarendon Press: 1975.
106. Tang, Y.; Karlsson, A. M.; Santare, M. H.; Gilbert, M.; Cleghorn, S.; Johnson, W. B. *Mater. Sci. Eng. A* **2006**, *425* (1−2), 297–304.
107. Majsztrik, P. W.; Bocarsly, A. B.; Benziger, J. B. *Macromolecules* **2008**, *41* (24), 9849–9862.
108. Romero, T.; Merida, W. *J. Membr. Sci.* **2009**, *338* (1−2), 135–144.
109. Adachi, M.; Navessin, T.; Xie, Z.; Li, F. H.; Tanaka, S.; Holdcroft, S. *J. Membr. Sci.* **2010**, *364* (1−2), 183–193.
110. Okada, T. *J. Electroanal. Chem.* **1999**, *465* (1), 1–17.
111. Zawodzinski, T. A.; Gottesfeld, S.; Shoichet, S.; Mccarthy, T. J. *J. Appl. Electrochem.* **1993**, *23* (1), 86–88.
112. McLean, R. S.; Doyle, M.; Sauer, B. B. *Macromolecules* **2000**, *33* (17), 6541–6550.
113. Aleksandrova, E.; Hiesgen, R.; Friedrich, K. A.; Roduner, E. *Phys. Chem. Chem. Phys.* **2007**, *9* (21), 2735–2743.
114. Takimoto, N.; Wu, L.; Ohira, A.; Takeoka, Y.; Rikukawa, M. *Polymer* **2009**, *50* (2), 534–540.
115. Van Nguyen, T.; Nguyen, M. V.; Lin, G. Y.; Rao, N. X.; Xie, X.; Zhu, D. M. *Electrochem. Solid-State Lett.* **2006**, *9* (2), A88–A91.
116. Affoune, A. M.; Yamada, A.; Umeda, M. *Langmuir* **2004**, *20* (17), 6965–6968.
117. He, Q.; Kusoglu, A.; Lucas, I. T.; Clark, K.; Weber, A. Z.; Kostecki, R. *J. Phys. Chem. B* **2011**, *115* (40), 11650–11657.
118. Bass, M.; Berman, A.; Singh, A.; Konovalov, O.; Freger, V. *J. Phys. Chem. B* **2010**, *114* (11), 3784–3790.
119. Krtil, P.; Trojanek, A.; Samec, Z. *J. Phys. Chem. B* **2001**, *105* (33), 7979–7983.
120. Newman, J. S.; Thomas-Alyea, K. E. *Electrochemical systems*; J. Wiley & Sons: 2004.
121. Kreuer, K. D.; Rabenau, A.; Weppner, W. *Angew. Chem., Int. Ed. Engl.* **1982**, *21* (3), 208–209.
122. Freger, V. *Polymer* **2002**, *43* (1), 71–76.
123. Luo, Z. P.; Chang, Z. Y.; Zhang, Y. X.; Liu, Z.; Li, J. *Int. J. Hydrogen Energy* **2010**, *35* (7), 3120–3124.
124. Schlick, S.; Gebel, G.; Pineri, M.; Volino, F. *Macromolecules* **1991**, *24* (12), 3517–3521.

Downloaded by STANFORD UNIV GREEN LIBR on June 14, 2012 | http://pubs.acs.org
Publication Date (Web): May 7, 2012 | doi: 10.1021/bk-2012-1096.ch011

Downloaded by PENNSYLVANIA STATE UNIV on June 14, 2012 | http://pubs.acs.org
Publication Date (Web): May 7, 2012 | doi: 10.1021/bk-2012-1096.ch012

Chapter 12

Cross-Linked Low EW PFSA for High Temperature Fuel Cell

H. Ghassemi,*,[a] T. Zawodzinski,[b] D. Schiraldi,[a] and S. Hamrock[c]

[a]Department of Macromolecular Science and Engineering, Case Western Reserve University, Cleveland, OH 44106
[b]Department of Chemical and Biomolecular Engineering, University of Tennessee, Knoxville, TN 37996
[c]3M Fuel Cell Components Program, 3M Company, St. Paul, Minnesota 55144
***email: hossein.ghassemi@cwru.edu**

Several approaches have been studied to prepare ionomers for a high temperature proton exchange membrane (PEM) fuel cell. These ionomers were designed to be very low equivalent weight (EW), chemically stable, solvent resistant and highly conductive. The synthetic approaches include grafting, hybrid formation and cross-linking. The most interesting results were obtained from cross-linking of functionalized PFSA ionomers with various cross-linking compounds. New side-chain component multifunctional ionomers have been developed that were cross-linkable during or after membrane fabrication. As a result of this approach, a suite of polymers have been synthesized that, after membrane casting and cross linking show improved solvent resistant, low swelling and excellent proton conductivity.

An obvious approach to increase proton conductivity in PSFA materials is to lower the equivalent weight (EW) by increasing the number of protogenic groups. PFSA membranes with EW < 700 g/mol show conductivity of *ca* 0.1 S/cm at 120°C and <40% RH compared with conductivity of 0.05 S/cm for PFSA membranes with EW 1000 g/mol under similar conditions. Low EW gives high conductivity, but mechanical properties and durability are compromised. At low EW, membranes swell excessively and become nearly soluble in

In Polymers for Energy Storage and Delivery: Polyelectrolytes for Batteries and Fuel Cells; Page, K., et al.;
ACS Symposium Series; American Chemical Society: Washington, DC, 2012.

water at higher temperature. One way to stabilize polymers and prevent from dissolving is by chemical modification to form crosslinking structure. In this work low EW ionomers from the 3M Company were used to form cross-linked network using various crosslinking agents.

Introduction

Fuel cells are anticipated to be a basic building block in the transition toward a more sustainable energy economy in the 21st century. The use of fuel cells is envisioned in applications that range from portable electronics to transportation and stationary power generation. In the small to medium power markets (e.g., personal electronics and light duty vehicles), proton exchange membrane fuel cells (PEMFCs), also referred to as polymer electrolyte membrane fuels cells, have garnered a great deal of attention. The PEM serves as a solid electrolyte barrier to separate the fuel and oxidant streams, while providing a path for transport of protons resulting from anodic oxidation of the fuel. The PEM has to meet numerous requirements for robust fuel cell operation and has become one of the performance-limiting components in PEMFCs. Among these requirements are high proton conductivity, low electronic conductivity, low permeability to both fuel and oxidant, low water transport, high hydrolytic stability under the oxidative fuel cell environment, and excellent mechanical integrity, not to mention competitive cost. In the past two decades a great deal of effort has been focused on the development of membranes with improved performance and durability under hotter, drier operating conditions (*1*). Among these perfluorosulfonic acid (PFSA) polymer electrolyte membranes have been the platform of choice for the development of PEMFCs due to their high proton conductivity and good chemical stability (*2*); however, PFSA-based membranes have operational limitations such as relatively poor mechanical integrity in the hydrated state and sharp drop in proton conductivity at low relative humidity. Extensive research is underway to address these limitations and meet the aforementioned PEM requirements in order to devise affordable materials with enhanced performance and extended lifetime especially for fuel cells operating under hot and dry conditions (*3*, *4*).

Several methods for preparation of cross-linked PFSAs are reported in the literature such as acid-based interpenetrating PFSAs (*5*), radiation crosslinking (*6*), ionic crosslinking, blending with a cross-linkable polymer and organic/inorganic hybrid (*7*). Our approach was to prepare functionalized PFSAs suitable for crosslinking with covalent linkages. The general goal of this work is to develop proton exchange membranes with higher proton conductivity, improved durability under hotter and dryer conditions compared to current membranes. The desired membranes should be stable under high and low humidification conditions and at temperatures ranging from -20°C to 120°C in order to meet DOE commercialization targets for automotive fuel cells.

Downloaded by PENNSYLVANIA STATE UNIV on June 14, 2012 | http://pubs.acs.org
Publication Date (Web): May 7, 2012 | doi: 10.1021/bk-2012-1096.ch012

Downloaded by PENNSYLVANIA STATE UNIV on June 14, 2012 | http://pubs.acs.org
Publication Date (Web): May 7, 2012 | doi: 10.1021/bk-2012-1096.ch012

Cross-Linking PFSA with Various Cross-Linkers

Sulfonylfluoride Approach

PFSA ionomers before hydrolysis contain sulfonyl fluoride groups which were considered and studied as reactive sites. Sulfonyl fluoride is susceptible for nucleophilic attack to form sulfonate, sulfonamide or sulfonic ester. Since PFSA in the sulfonyl fluoride form is insoluble in almost any common solvents cross-linking under melt condition was investigated. A series of mono and difunctional aliphatic and aromatic molecules such as, arylsulfonamide, hexamethylene diamine, bisphenol-A and oxydianiline were examined. Various amounts of each of these compounds mixed with the waxy oligomer and pressed several times using a hot press. The temperature of the hot press varied between 100-200°C and each time the samples were hold around 3 minutes under the press. The amount of difunctional cross-linking compounds was calculated to be around 20 mol% of sulfonyl fluoride groups providing a condition for highly crosslinked products. After each press the films were removed and their mechanical behavior was compared with the blank sample. Figure 1 shows a typical structure of PFSA after cross-linking. Only membranes reacted with hexamethylene diamine and oxydianiline formed highly cross-linked products. However, the films were not homogenous due to poor mixing condition which prevent diamino compounds blend thoroughly with the oligomer.

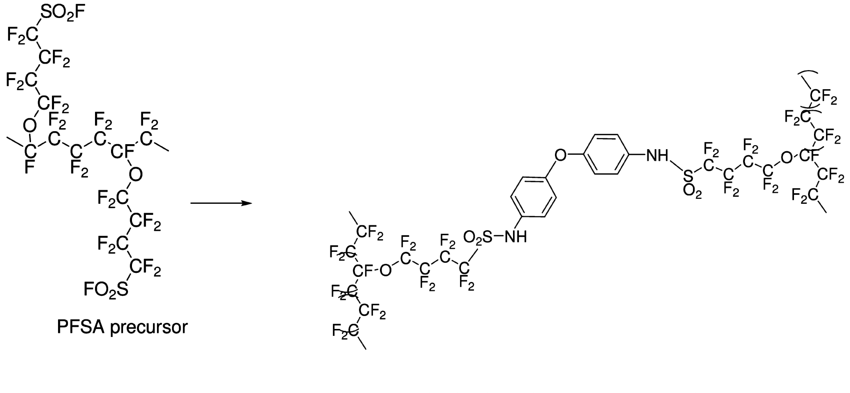

Figure 1. PFSA ionomer cross-linked with an aromatic diamine

Sulfonamide-Sulfonyl Chloride Approach

To overcome the problems of working with infusible PFSA precursor, new PFSAs with sulfonamide groups (PFSAmide) were employed. PFSAmides with various degree of functionalization were supplied by 3M which were prepared by partial ammonolysis of sulfonyl fluoride of PFSA precursor followed by hydrolysis of the remaining to sulfonic acid. A set of reactions was design between PFSAmide and functionalized polyethersulfones to form cross-linked membranes. In these experiments sulfonated polysulfones (SPES) with low level of sulfonation were selected as cross-linkers. Several reactions were set

Downloaded by PENNSYLVANIA STATE UNIV on June 14, 2012 | http://pubs.acs.org
Publication Date (Web): May 7, 2012 | doi: 10.1021/bk-2012-1096.ch012

up between PFSAmide with various percent of amide groups on the side-chain and SPES carrying sulfonyl chloride. Multiple sulfonyl chloride sites on SPES were expected to react with amide groups and generate sulfonimide cross-linked structure as shown in Figure 2. Qualitative swelling testing in hot water showed that in most cases the final products had better dimensional stability compared with the control. The highest degree of cross-linking occurred when PFSAmide with a high level of amide groups were used.

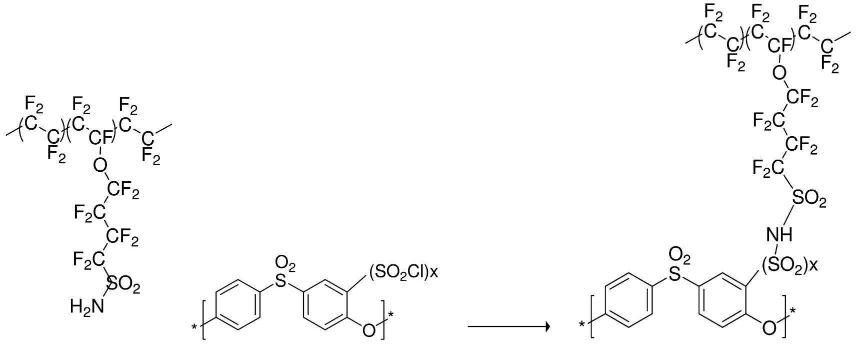

Figure 2. Cross-linking PFSA via sulfonamide-sulfonyl chloride approach

Sulfonamide-Activated Arylfluoride Approach

Decafluorobiphenyl reacts with bisphenols to form linear poly(arylene ether)s. The high reactivity of fluorine atoms in decafluorobiphenyl provides an easy route to carry out further chemistry and produce new materials (*8*). Two poly(arylene ether) oligomers with Mw of 3k and 5k were synthesized from 6F-bisphenol-A and decafluorobiphenyl. The molecular weight of the oligomers was controlled by using slight excess of decafluorobiphenyl which also serves as a reactive end-group. Reaction of PFSAmide (88% sulfonamide) with these two oligomers in N-methylpyrrolidone (NMP) resulted products which were insoluble in many organic solvents (Figure 3). Films cast from mixtures of PFSAmide and either of these oligomers remained flexible after heating at 120°C for one hour and showed a low degree of swelling after treating in hot water. Films prepared from 88% amide containing PFSAmide showed much better dimensional stability compared with those made from PFSAmide with 7% amide content. Proton conductivities of the samples made from low amide content materials were higher, however, and measured in the range of 80-250 mS/cm depending on the ratio of PFSAmide to oligomers.

Downloaded by PENNSYLVANIA STATE UNIV on June 14, 2012 | http://pubs.acs.org
Publication Date (Web): May 7, 2012 | doi: 10.1021/bk-2012-1096.ch012

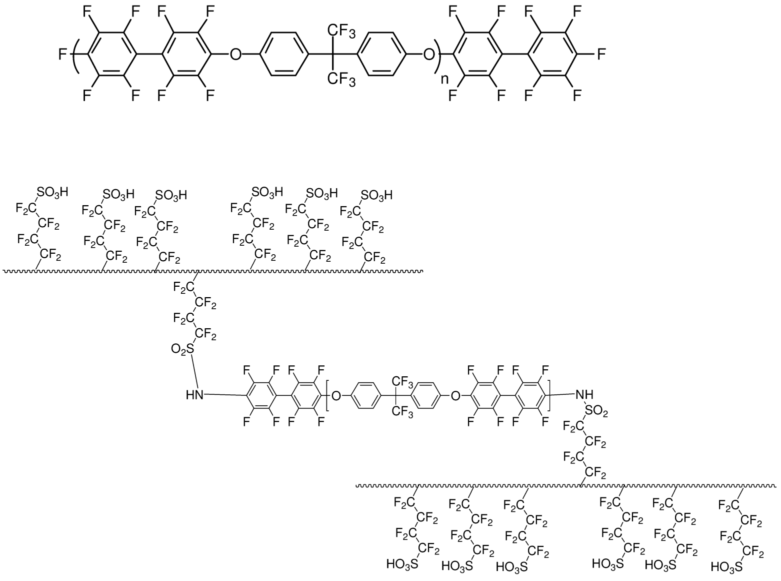

Figure 3. Cross-linking PFSA via sulfonamide-activated arylfluoride approach

PFSA with Pendent Fluorobenzene Rings

Two functionalized PFSA ionomers were prepared from PFSAmides and 4-fluorobenzenesulfonyl chloride and pentafluorosulfonyl chloride (Figure 4). Fluorobenzene groups are reactive sites toward phenolates (BP) and can be used for cross-linking. These functionalized PFSA materials, when reacted with various bisphenolate salts, such as biphenol dipotassium salt, form cross-linked products (Figure 5). The highest degree of cross-linking obtained when highly functionalized PFSA (89% amide content) with pentafluorobenzene groups reacted with biphenolate in DMSO. The amount of biphenolate was calculated to be about 8 wt% of the total ionomer and 30 mole% of the fluorobenzene groups. The whole process of casting and curing was complete in less than an hour, producing films that were clear and which exhibited a very low level of swelling before and after treating in boiling water. The conductivity of the cross-linked ionomer was 40 mS/cm (in water) and 7 mS/cm (at 60% RH). Cross-linked product was not soluble or even swelled in acetonitrile while the starting ionomer readily swelled and disintegrated in acetonitrile.

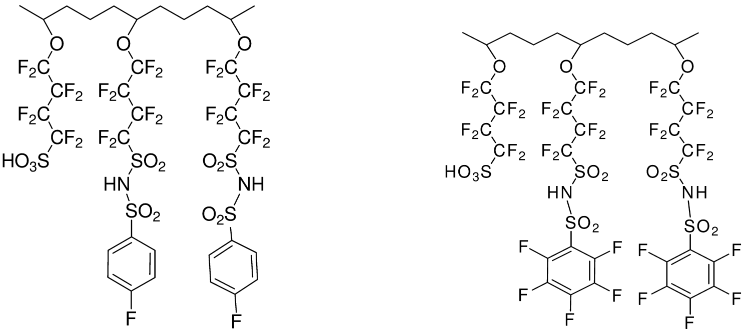

Figure 4. PFSA with fluorobenzene rings on the side-chain

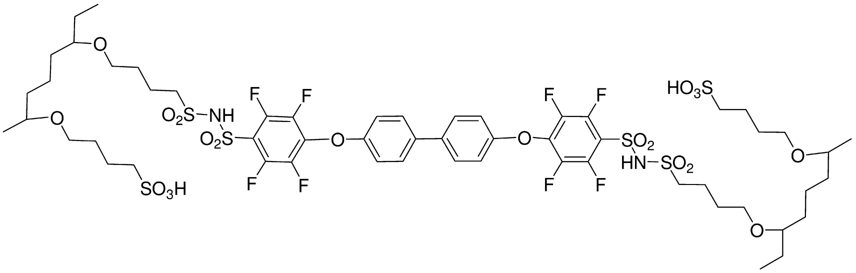

Figure 5. Proposed structure of cross-linked PFSA with biphenol

Downloaded by PENNSYLVANIA STATE UNIV on June 14, 2012 | http://pubs.acs.org
Publication Date (Web): May 7, 2012 | doi: 10.1021/bk-2012-1096.ch012

The membranes exhibiting the least dimensional stability were those made from low amide content (28%) and 4-fluorobenzenesulfonyl chloride which produced materials with lower cross-linked density. This instability can be explained by the fact that pentafluorobenzene has more reaction sites and its fluorine atoms are more reactive compared with those in the 4-fluoro derivative. As expected samples made from low amide content had relatively higher proton conductivity. Table 1 shows a summary of these results.

An alternative approach to generate bisphenolates in situ is to use masked bisphenols. Masked bisphenols are synthesized from bisphenols and an alkylisocyanate and easily purified by crystallization. Biscarbamates decompose at high temperature in the presence of carbonate ions and generate bisphenoxides and gases biproducts (*9*). To alleviate some of the problems associated with the preparation and introduction of biphenoxide ion in the reaction a masked biphenol (Figure 6) was utilized. Masked bisphenol and functionalized PFSA (with pentafluorobenzene) formed transparent film after casting and curing at 230°C for 3 minutes. The presence of small voids were noticed in all cured membranes which were caused probably by evolution of volatile gases generated during decomposition of the masked bisphenol. Samples made from highly functionalized PFSAs showed lower swelling in hot water compared with those made from low imide content materials.

Downloaded by PENNSYLVANIA STATE UNIV on June 14, 2012 | http://pubs.acs.org
Publication Date (Web): May 7, 2012 | doi: 10.1021/bk-2012-1096.ch012

Table 1. Summary of curing experiments between functionalized PFSA and biphenolate

Exp	Imide	BP wt%	Rx condition	Film quality	Conductivity (mS/cm) in 100% RH
1	89-F5	8	Gelled in solution, hot pressed at 190°C	Lot of small gel particles	
2	89-F5	8	Two sol. Mixed and cast. Dried at 120°C	Clear, low swelling	40
3	28-p-F	4	Two sol. Mixed and cast. Dried at 120°C	Opaque, high Swelling	
4	28-F5[1]	4	No gel in solution	Semi-transparent High swelling	90-110
5	28-F5	4	Two sol. Mixed and cast. Dried at 120°C	Transparent High swelling	90-110

1) conductivity: 110 mS/cm (100%), 6 mS/cm (75%), 1 mS/cm (60%)

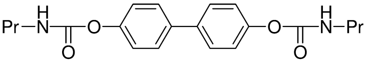

Figure 6. Structure of masked biphenol

Sulfinated Polyarylenes (S-Alkylation)

Sulfinate groups of sulfinated aliphatic or aromatics compounds react with activated halides to form sulfone linkage (*10*). To study the possibility of using sulfinated aromatic compounds as cross-linker, UDEL® polysulfone was converted into sulfinated polysulfone through lithiation followed by reaction with sulfur dioxide. The degree of sulfination was estimated by NMR to be at least two sulfinate groups per diphenylsulfone moiety (Figure 7). The reactivity of sulfinated polymer toward fluorinated aromatic compounds was demonstrated by performing a model reaction between sulfinated UDEL and decafluorobiphenyl. A solution of these two compounds in NMP at 100°C turned into gel in just a few minutes (Figure 8).

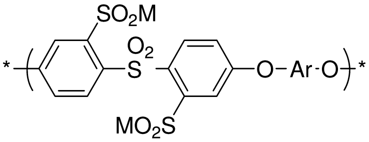

Figure 7. Structure of a sulfinated poly(arylene ether)

In Polymers for Energy Storage and Delivery: Polyelectrolytes for Batteries and Fuel Cells; Page, K., et al.; ACS Symposium Series; American Chemical Society: Washington, DC, 2012.

Downloaded by PENNSYLVANIA STATE UNIV on June 14, 2012 | http://pubs.acs.org
Publication Date (Web): May 7, 2012 | doi: 10.1021/bk-2012-1096.ch012

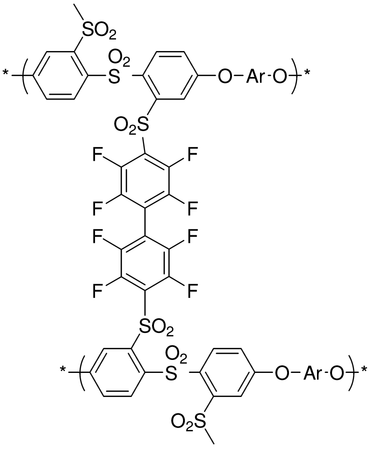

Figure 8. Proposed structure of sulfinated poly(arylene ether) cross-linked with decafluorobiphenyl

Reaction of PFSA containing 7% pentafluorophenylsulfonimide groups with 5 wt% sulfinated polysulfone formed a membrane which showed high swelling. When PFSA with higher level of functional groups was used resulting product showed slightly better swelling properties. Increasing the curing temperature up to 260°C improved the swelling properties of the membrane. Discoloration of the membranes after exposing to high temperature even for short period of time (< 3 min) was noticeable.

1,3,5-Benzenetrisulfonyl Chloride

Another method of cross-linking was designed so that sulfonamide groups of PFSAmide react with 1,3,5-benzenetrisulfonyl chloride (BTS) to generate a cross-linked network. Reaction of PFSAmide with BTS in the presence of triethylamine (TEA) in NMP at 60°C produces a gel within a few minutes. Controlled addition of PFSAmide to excess BTS in the presence of TEA at room temperature, however, generates a soluble polymer with benzene disulfonic acid side-groups (Figure 9). Proton NMR of this product shows two peaks at 7.9 and 8.8 ppm with the ratio of 2 to 1 assigned as aromatic protons and the broad peak at 8.9 is assigned to the exchangeable acidic protons of NH and SO_3H (Figure 10).

Downloaded by PENNSYLVANIA STATE UNIV on June 14, 2012 | http://pubs.acs.org
Publication Date (Web): May 7, 2012 | doi: 10.1021/bk-2012-1096.ch012

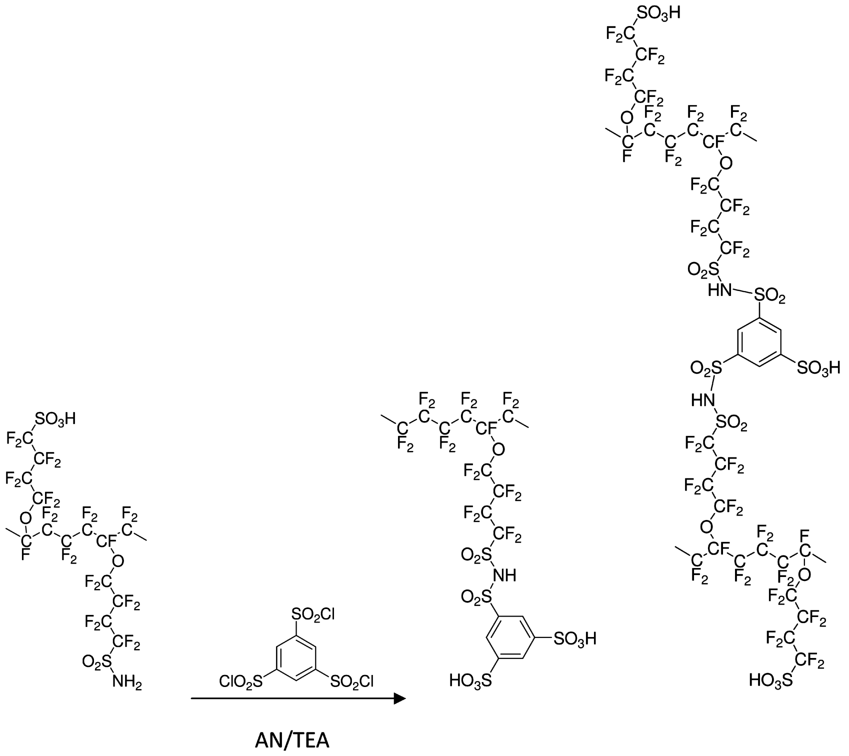

Figure 9. Reaction of PFSA with 1,3,5-benzenetrisulfonyl chloride

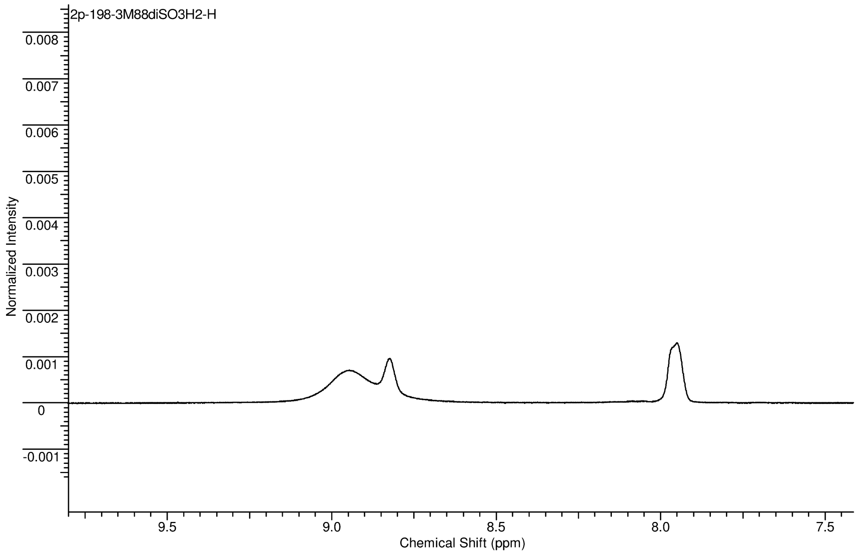

Figure 10. Proton NMR spectrum of PFSA cross-linked with 1,3,5-benzenetrisulfonyl chloride

Downloaded by PENNSYLVANIA STATE UNIV on June 14, 2012 | http://pubs.acs.org
Publication Date (Web): May 7, 2012 | doi: 10.1021/bk-2012-1096.ch012

To form cross-linked membranes, PFSAmides and controlled amounts of BTS were reacted at low temperature (< 0°C). Acetonitrile was a typical solvent for both reactants during the reaction and casting. Reaction between sulfonamide and sulfonyl chloride presumably occurs during the mixing of reactant at low temperature for a few minutes and casting at room temperature for 24 hours. Films were dried after heating at 60°C for 2 hours and 170°C for 1 hour. Films were evaluated for the extent of cross-linking by soaking in acetonitrile at 40°C for several days, recording weights before and after treatment in. The membranes made from high SO_2NH_2 content (89%) polymers showed almost zero weight loss and only little swelling after soaking in acetonitrile. Those made from low SO_2NH_2 content (28%) polymers, however, only swelled in acetonitrile with little weight loss. Cured membranes also showed significant improvement in their dimensional stability before and after treatment in hot water. The level of swelling depended upon the sulfonamide content and the amount of BTS used in each case. Figure 9 suggests a possible structure for the cross-linking group. Proton conductivity of the cross-linked membranes in water at room temperature showed a wide range from 3 - 340 mS/cm. The highest values were recorded for membranes with low sulfonamide content. Table 2 shows summarizes all of these results.

Table 2. Properties of PFSA cross-linked with 1,3,5-benzenetrisulfonyl chloride

Exp	SO_2NH_2 Content (%)	SO_2NH_2/ SO_2Cl	Solubility in acetonitrile[1]	Solubility in boiling water	Conductivity (S/cm) at 18°C and 100% RH
1	89	1.7	100% insoluble	Insoluble	0.008
2	89	1	100% insoluble	Insoluble	-
3	89	2.4	100% insoluble	Insoluble	-
4	28	1	Mostly soluble in acetonitrile	Mostly insoluble	0.30
5	28	0.5	95% insoluble	Mostly insoluble	0.34
6	28	1	88% insoluble	Mostly insoluble	0.25
7	-	1	100% insoluble	Insoluble	0.12

1) Starting PFSAmide is soluble in acetonitrile and the degree of insolubility of the products in acetonitrile was used as an indication of degree of cross-linking.

4-(Sulfonylfluoride)butyryl Fluoride (SFBF)

A new functionalized ionomer was synthesized by reaction of PFSAmide with 4-(sulfonylfluoride)butyryl fluoride (Figure 11). The main idea underlying this approach was to take advantage of reactivity difference between the two functional groups in SFBF and to synthesize a cross-linked membrane in two steps. In first step, the sulfonamide groups of PFSAmide react with excess acylfluoride of SFBF to form an extended side chain with a new $-CF_2-SO_2-NH-CO-CF_2-$ linkage (Figure 11). Fluorine NMR showed complete disappearance of sulfonamide groups and formation of imide linkage. This intermediate was then reacted with the starting PFSAmide to form a cross-linked product (Figure 12). The final product contained one unsymmetrical imide and a symmetrical sulfonamide on every connecting linkage between two main chains. Acyclic imides are generally known for their poor hydrolytic stability under basic or acidic environment. This stability was tested by treatment of intermediate product in 0.5 M sulfuric acid at 60°C for 48 hours. The results showed complete hydrolysis of unsymmetrical imide. Fluorine NMR spectra of the starting PFSAmide, SFBF and intermediate before and after hydrolysis are shown in Figure 13. The top spectrum in Figure 13 is for the crude SFBF and the middle and bottom spectra are for intermediate product before and after hydrolysis, respectively. The new peaks highlighted by arrows in the middle spectrum indicate formation of extended side-chain which completely disappeared after hydrolysis.

Perfluoropropylene Disulfonyl Fluoride (PPDSF)

A symmetrical difunctional PPDSF was next used as a cross-linking agent. Reaction between sulfonamide containing PFSAmide and sulfonyl fluoride of PPDSF in acetonitrile produced intermediate B with sulfonimide linkages (Figure 14). Nearly complete conversion of sulfonamide groups into imide was evidenced by ^{19}F NMR (Figure 15) which showed disappearance of sulfonamide peak at -115 ppm. A mixture of the intermediate B and starting ionomer A in acetonitrile formed a clear film after casting under IR lamp followed by heat treatment at 170°C for one hour. All films prepared using various ratio of A and B became insoluble in water, methanol and acetonitrile after curing indicating formation of cross-linked structure (membranes swell up to 75% after soaking in water). The extent of cross linking was qualitatively examined by monitoring the swelling behavior of the films in hot water. Films produced with a high ratio of ionomer A to B showed little swelling and hence a high degree of cross linking and the film made with low ratio of ionomer A showed relatively high swelling resulting from a lower level of cross linking.

Downloaded by PENNSYLVANIA STATE UNIV on June 14, 2012 | http://pubs.acs.org
Publication Date (Web): May 7, 2012 | doi: 10.1021/bk-2012-1096.ch012

Downloaded by PENNSYLVANIA STATE UNIV on June 14, 2012 | http://pubs.acs.org
Publication Date (Web): May 7, 2012 | doi: 10.1021/bk-2012-1096.ch012

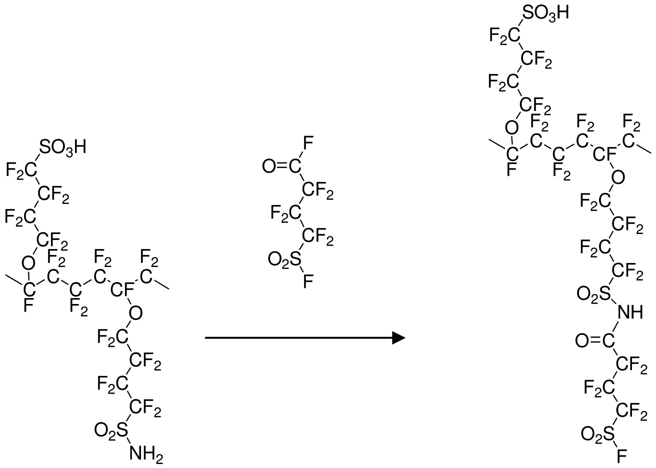

Figure 11. *Reaction of PFSA with SFBF; formation of intermediate*

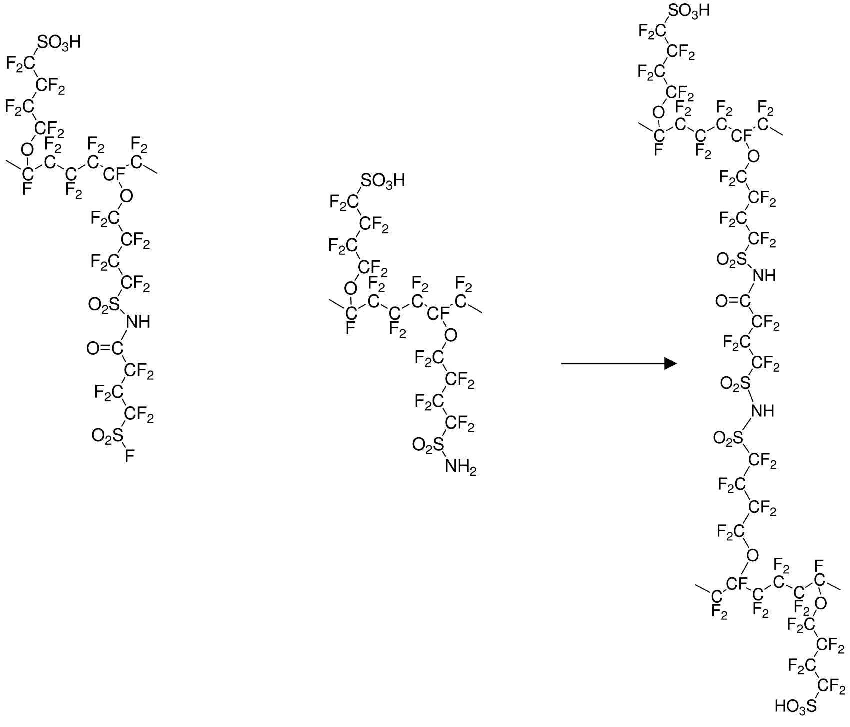

Figure 12. *Cross-linked PFSA*

Downloaded by PENNSYLVANIA STATE UNIV on June 14, 2012 | http://pubs.acs.org
Publication Date (Web): May 7, 2012 | doi: 10.1021/bk-2012-1096.ch012

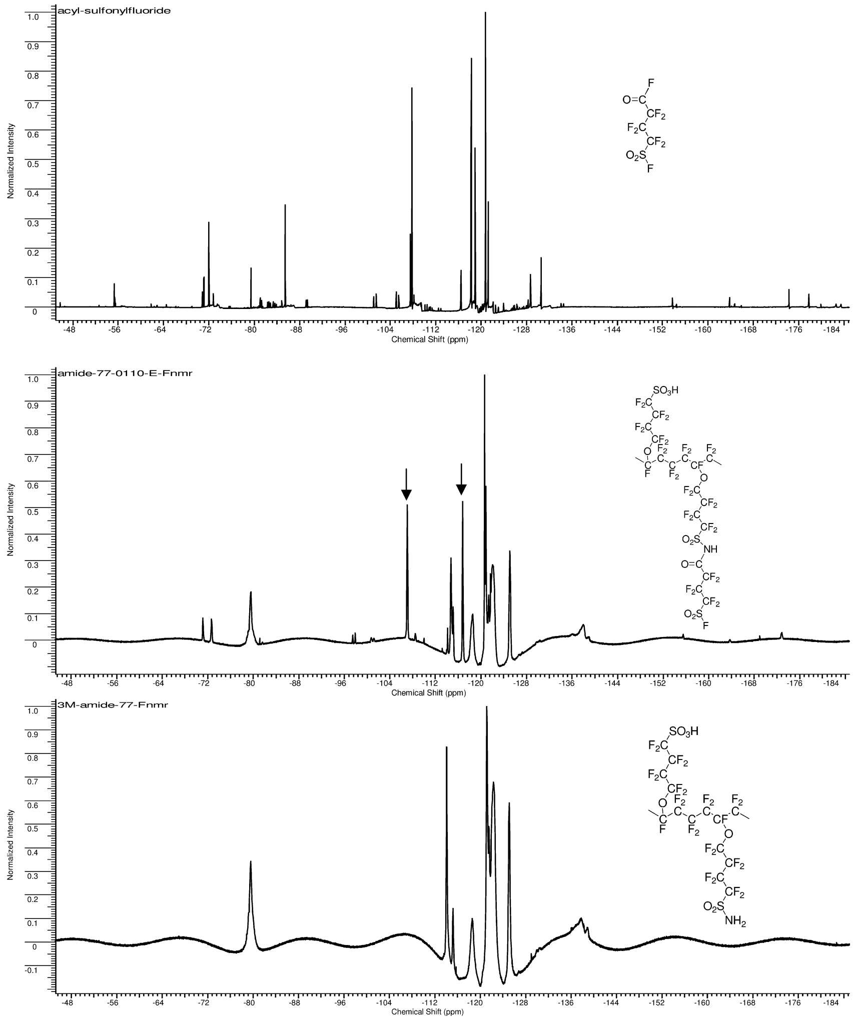

Figure 13. Fluorine NMR spectra of SFBF (top), PFSA intermediate before (middle) and after (bottom) hydrolysis

Downloaded by PENNSYLVANIA STATE UNIV on June 14, 2012 | http://pubs.acs.org
Publication Date (Web): May 7, 2012 | doi: 10.1021/bk-2012-1096.ch012

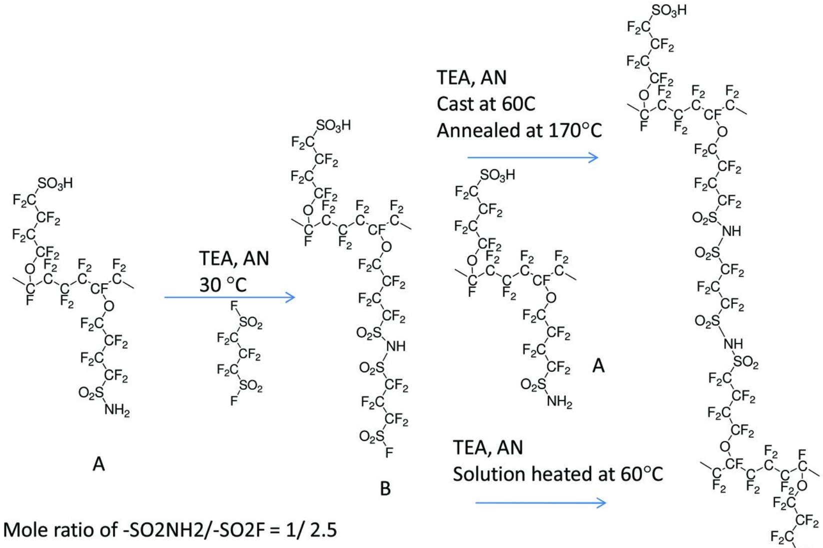
TEA, AN
30 °C
A
B
TEA, AN
Cast at 60C
Annealed at 170°C
A
TEA, AN
Solution heated at 60°C
Mole ratio of -SO2NH2/-SO2F = 1/ 2.5

Figure 14. Reaction of PPDSF with PFSA

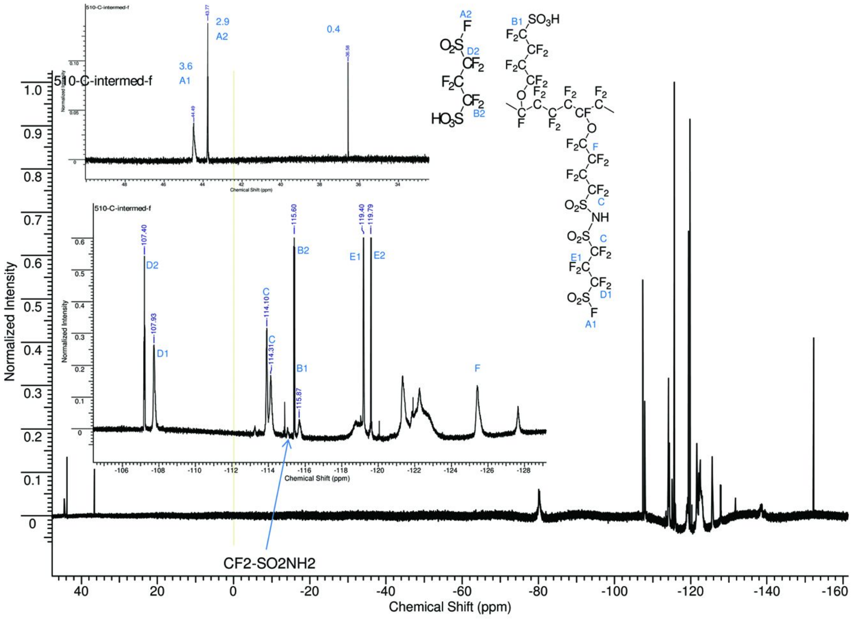

Figure 15. ^{19}F NMR spectrum of the intermediate B

Downloaded by PENNSYLVANIA STATE UNIV on June 14, 2012 | http://pubs.acs.org
Publication Date (Web): May 7, 2012 | doi: 10.1021/bk-2012-1096.ch012

When intermediate B and ionomer A were mixed in acetonitrile and heated at 60°C for several hours the mixture became viscous and finally gelled. The fluorine NMR spectrum of the solution-cured product showed no trace of sulfonamide group which appears around -114.8 ppm and revealed new peaks assigned for sulfonimide linkages (Figure 16). It is obvious that the cured products contain at least three acid functional groups that include sulfonimide, sulfonic acids from starting PFSA and intermediate B. Peaks labeled as A at -115.8 and D at -115.3 ppm were assigned as CF_2 groups next to sulfonic acids on the short and long side-chain, respectively. The fluorine NMR of samples cured in solid phase and solution looks almost identical (Figure 17). Equivalent weights of the cross-linked membranes determined by titration show higher values compared with theoretical numbers. Presence of residual triethylamine or sulfonamide groups might be the reason for this deviation. Proton conductivity of the membranes at 15°C and 100% RH was around 0.12 S/cm (thickness of the membranes in fully hydrated condition used in calculation). Summary of the results is tabulated in Table 3.

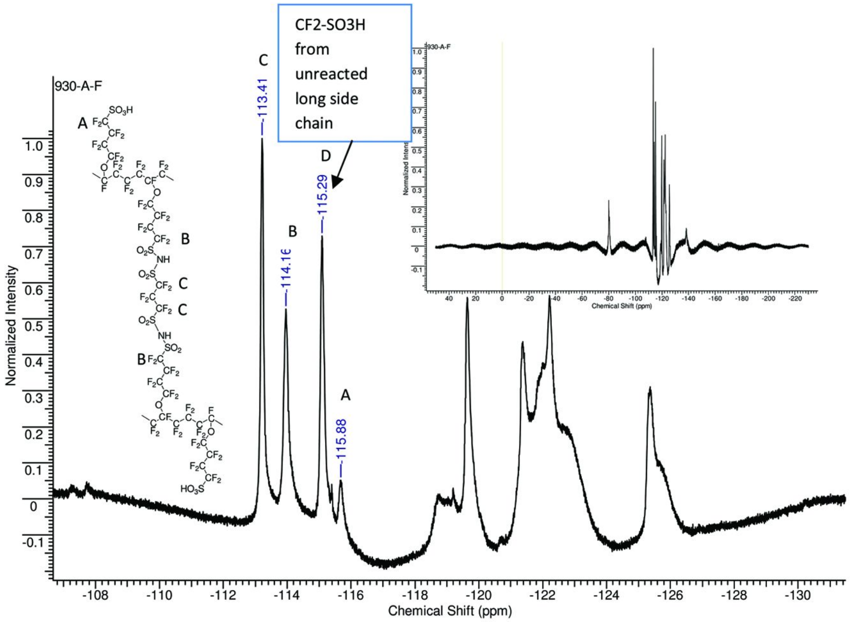

Figure 16. ^{19}F NMR spectrum of the crosslinked ionomer made in solution

Downloaded by PENNSYLVANIA STATE UNIV on June 14, 2012 | http://pubs.acs.org
Publication Date (Web): May 7, 2012 | doi: 10.1021/bk-2012-1096.ch012

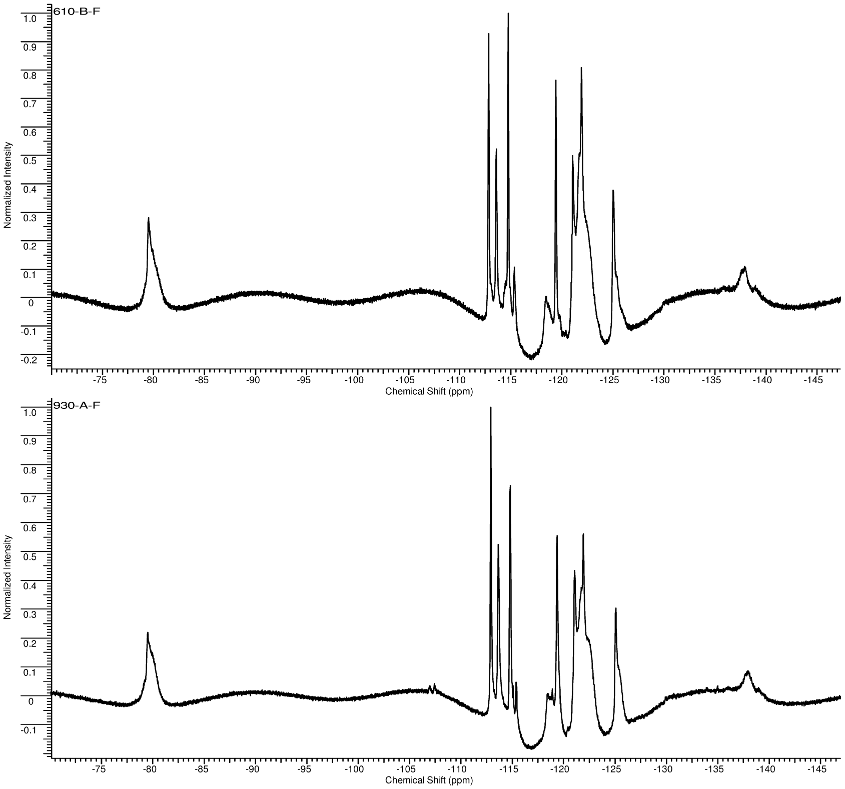

Figure 17. Comparing ^{19}F NMR spectra of the crosslinked ionomers in solid state (top) and in solution (bottom)

Table 3. Properties of ionomers cross-linked with PPDSF

Sample	EW (g/mol)		Conductivity[3]	Swelling[4]	Solubility[5]		
	Calc.	Exp.	(S/cm)	(%)	AN	MeOH	Water
640-77[1]	470	585	0.12	60	NS	NS	SW
640-77[2]	470	570	-	75	NS	NS	SW

1) Sample cured in solid state. 2) Sample cured in solution. 3) Measured at 15°C and 100% RH. 4) By measuring dimension after soaking the sample in water for 24 hr and dried in ambient condition for 24 hr. 5) NS= not soluble, SW= swelled, AN=acetonitrile.

Downloaded by PENNSYLVANIA STATE UNIV on June 14, 2012 | http://pubs.acs.org
Publication Date (Web): May 7, 2012 | doi: 10.1021/bk-2012-1096.ch012

(Trifluorovinyl oxy)benzene (TFVOB)

Trifluorovinyl ethers are usually prepared from substituted phenols in two steps which include fluoroalkylation with $BrCF_2CF_2Br$ and a zinc mediated elimination of ‘FBr’. One of the most interesting properties of [(trifluorovinyl)oxy] benzene is the thermal [2π+2π] cyclodimerization at temperatures up to 150°C (Figure 18) (*11*). TFVOB prepared from bis- and tris-phenols were thermocyclopolymerized into linear or thermoset polymers endowed with good thermal stability and mechanical properties.

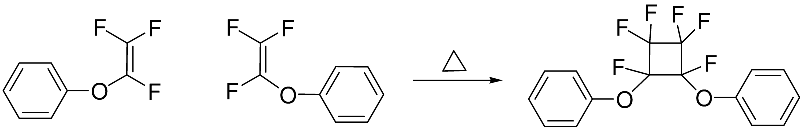

Figure 18. Thermal [2+2] cyclization of trifluorovinyl aryl ether

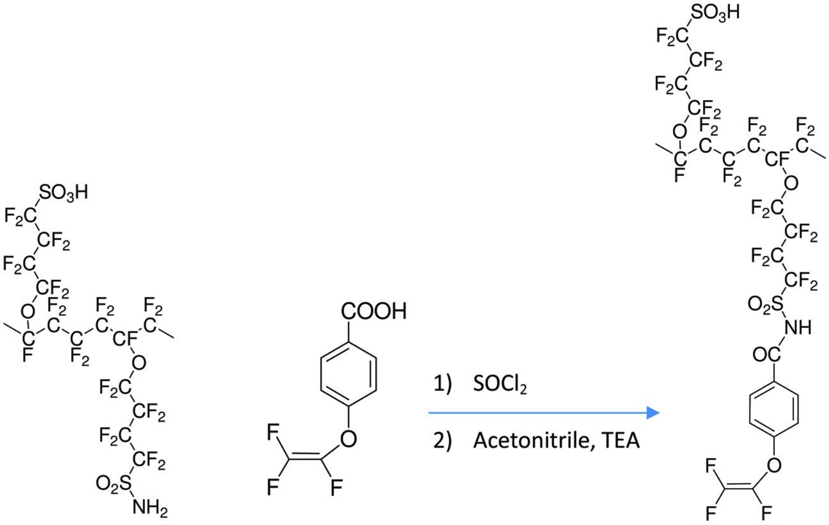

Figure 19. Synthesis of PFSA with trifluorovinylether group

Downloaded by PENNSYLVANIA STATE UNIV on June 14, 2012 | http://pubs.acs.org
Publication Date (Web): May 7, 2012 | doi: 10.1021/bk-2012-1096.ch012

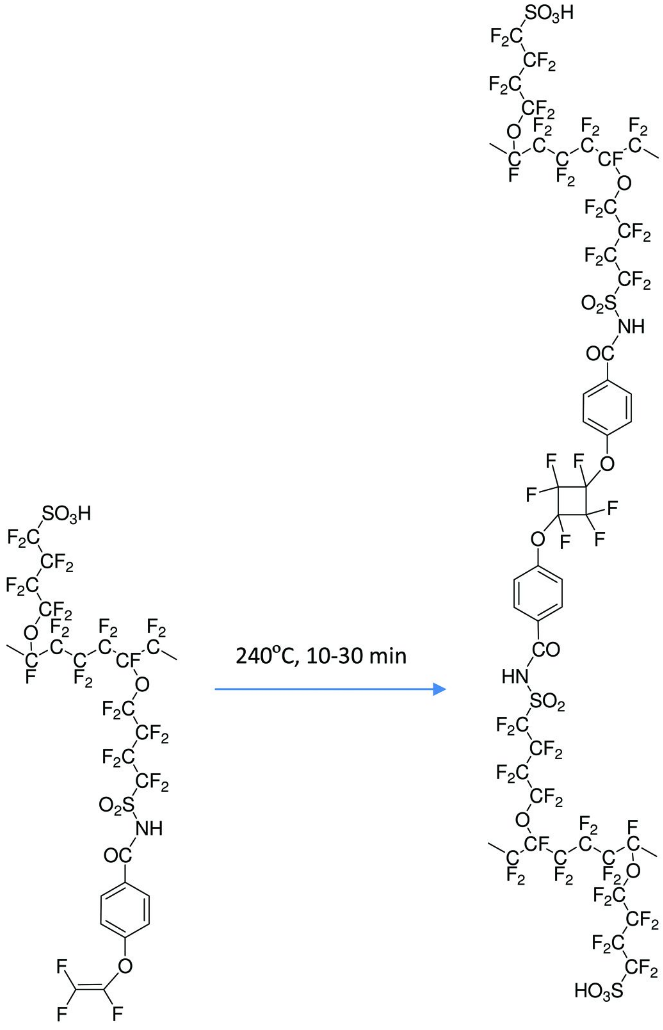

Figure 20. Curing reaction of PFSA with trifluorovinylether group

In this approach, 4-(trifluorovinyl oxy)benzoyl chloride was used to convert PFSAmide into a new, thermally cross-linkable polymer. Reaction between PFSAmide (28% sulfonamide) and 4-(trifluorovinyloxy)benzoyl chloride in acetonitrile in the presence of triethylamine produced PFSA with TFVOB units (Figure 19). The benzoyl chloride was prepared from its benzoic acid precursor by reacting with thionyl chloride. The ionomer at this stage is very soluble in acetonitrile and partially soluble in boiling water. Thin films were prepared by casting from acetonitrile solution which then heated at 240°C for 10-30 min. The curing condition caused two vinyl groups to react and form a cyclobutane structure (Figure 20). F-NMR spectrum of the material before curing shows three distinct signals assigned to three vinyl fluorines. These signals totally disappeared after curing which indicates complete cyclization reaction (Figure 21); no clear signals could be assigned to fluorinated cyclobutane which are expected around -120 to -130 ppm. The fluorine signals from cyclobutane might be overlapped by the signals from other fluorine atoms in the backbone. These membranes, after curing, became insoluble in acetonitrile and only swelled in water, another indication that the membranes were cross-linked. The degree of swelling varied between 30-50% depending on the curing time. Unsymmetrical imide linkage in the final product unlike the material described in section 7 was hydrolytically stable and no apparent degradation was observed after heating the cured membrane in 0.5 M sulfuric acid for one month. Proton conductivity of the cross-linked membrane at 15°C and 100% RH was measured to be approximately 0.18 S/cm.

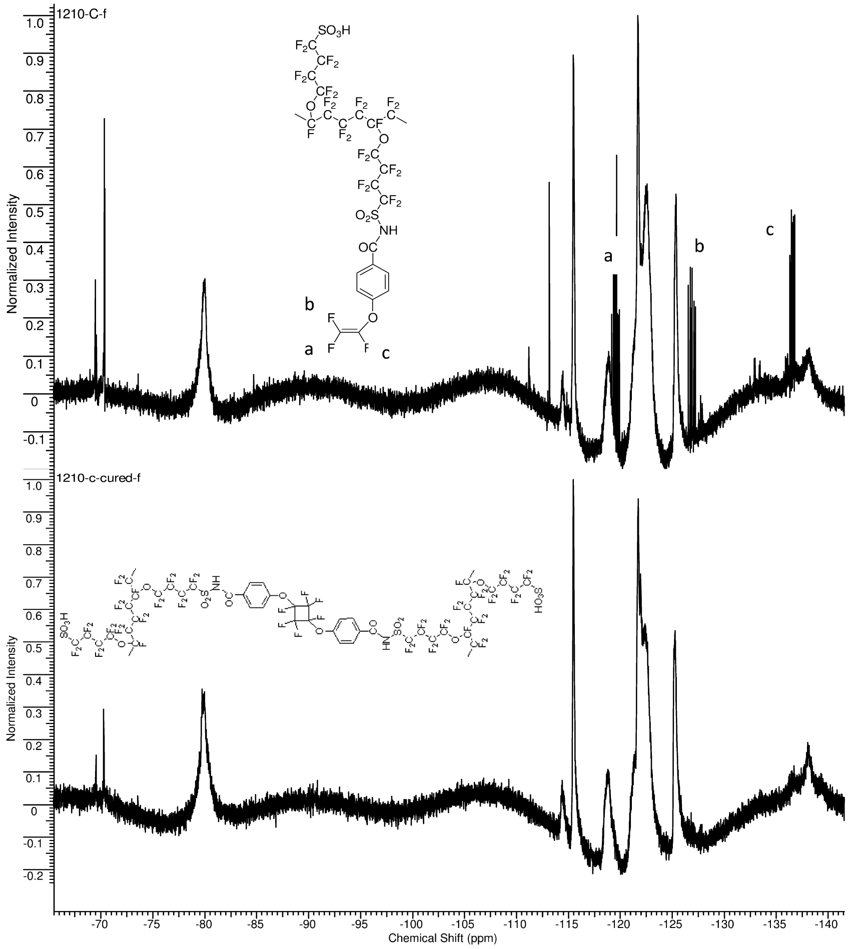

Figure 21. ^{19}F NMR spectra of PFSA ionomer with trifluorovinyl groups before (top) and after curing (bottom)

Downloaded by PENNSYLVANIA STATE UNIV on June 14, 2012 | http://pubs.acs.org
Publication Date (Web): May 7, 2012 | doi: 10.1021/bk-2012-1096.ch012

Downloaded by PENNSYLVANIA STATE UNIV on June 14, 2012 | http://pubs.acs.org
Publication Date (Web): May 7, 2012 | doi: 10.1021/bk-2012-1096.ch012

Conclusions

Several methods for preparation of proton exchange membranes for high temperature fuel cells were investigated. The goal of this work was to generate low EW cross-linked PFSAs by utilizing sulfonamide functional groups of PFSAs and di- and tri-functional crosslinkers. Fluorine and proton NMR revealed high conversion sulfonamide indication of formation of crosslinked structure. Cross-linked membranes made from 1,3,5-benzenetrisulfonyl chloride (BTS), perfluoropropylene disulfonyl fluoride (PPDSF) and (trifluorovinyl oxy)benzene (TFVOB) demonstrated improved resistance toward organic solvents and water and show high proton conductivity, while those made from 4-(sulfonylfluoride)butyryl fluoride (SFBF) showed poor stability toward hydrolysis. Other approaches to cross-link and convert low EW PFSA ionomers into insoluble membranes were also examined which in some cases were partially successful and highly cross-linked membranes formed. Cross-linked membranes in many cases were good proton conductors and values up to 0.34 S/cm was recorded at room temperature and 100% relative humidity. These materials need to be further evaluated and tested under various conditions and the best candidates should be selected for structural optimization.

Acknowledgments

This research was supported in part by the U.S. Department of Energy, Cooperative Agreement No. DE-FG36-07GO17006. DOE support does not constitute an endorsement by DOE of the views expressed in this presentation.

References

1. Hickner, M. A.; Ghassemi, H.; Kim, Y. S.; Einsla, B. R.; McGrath, J. E. *Chem. Rev.* **2004**, *104*, 4587.
2. Hamrock, S.; Schaberg, M.; Sharma, N., S.; Abulu, J. WO2009132241, 2009.
3. Schiraldi, D. A. *Polym. Rev.* **2006**, *46* (3), 315.
4. Zhou, C.; Guerra, M. A.; Qiu, Z.-M.; Zawodzinski, T., Jr.; Schiraldi, D. A. *Macromolecules* **2007**, *40* (24), 8695.
5. Pan, H.; Pu, H.; Jin, M.; Wan, D.; Chang, Z. *Polymer* **2010**, *51* (11), 2305.
6. Tsao, C.; Chang, H.*Current Development of Radiation-Induced Graft in Membranes*; 2008; p 133.
7. Greso, A. J.; Moore, B.; Cable, K. M.; Jarrett, W. L.; Mauritz, K. A. *Polymer* **1997**, *38* (6), 1345.
8. Ghassemi, H.; McGrath, J. E.; Zawodzinski, T. A. *Polymer* **2006**, *47*, 4132.
9. Wang, Z. Y.; Carvalho, H. N.; Hay, A. S. *J. Chem. Soc., Chem. Commun.* **1991**, 1221–1222.
10. Ghassemi, H.; Zawodzinski, T. A. Presented at the 232nd ACS National Meeting, San Francisco, CA, United States, Sept. 10−14, 2006.
11. Spraul, B. K.; Suresh, S.; Jin, J.; Dennis, W., Jr. *J. Am. Chem. Soc.* **2006**, *128* (21), 7055–7064.

Downloaded by UNIV OF DELAWARE MORRIS LIB on June 14, 2012 | http://pubs.acs.org
Publication Date (Web): May 7, 2012 | doi: 10.1021/bk-2012-1096.ch013

Chapter 13

High Ion Exchange Capacity, Sulfonated Polybenzimidazoles

Mahesh P. Kulkarni, Owen D. Thomas, Timothy J. Peckham, and Steven Holdcroft*

Department of Chemistry, Simon Fraser University, 8888 University Drive, Burnaby BC V5A 1S6, Canada
***Email: holdcrof@sfu.ca**

A novel, highly sulfonated, polybenzimidazole (sOPBI) was successfully prepared from poly[2,2′-(p-oxydiphenylene)-5,5′-bibenzimidazole] (OPBI) through two complementary sulfonation methods: grafting of a pendant sulfonic acid chain *via* reaction with 1,3-propane sultone, and direct sulfonation of the aromatic rings in the polymer backbone. These membranes possess an IEC of 4.1 $mmol{\cdot}g^{-1}$, are soluble in organic solvents, and display high proton conductivity (40.1 $mS{\cdot}cm^{-1}$) at elevated temperatures (80 °C, 95 % RH). Fuel cell testing of these membranes provided good performance, comparable to Nafion 112, with a peak power density of 700 $mW{\cdot}cm^{-2}$ at 80 °C using humidified H_2 and O_2.

Introduction

Proton exchange membrane fuel cells (PEMFC) have attracted great attention due to their promising applications in power conversion and generation (*1*). In order to replace current sulfonated perfluorinated polymers, new materials, with high proton conductivity, good mechanical strength and high thermo-chemical stability, are urgently needed.

Polybenzimidazoles (PBIs) have currently been proposed as an alternative polymer for high temperature PEMFCs (*2–9*) because of their outstanding thermal, oxidative, chemical, and hydrolytic stability under fuel cell operating conditions, particularly when exposed to high temperatures. PBI can only conduct protons if it is modified to contain acidic groups, either through doping with acid (*10–12*) or

In Polymers for Energy Storage and Delivery: Polyelectrolytes for Batteries and Fuel Cells; Page, K., et al.;
ACS Symposium Series; American Chemical Society: Washington, DC, 2012.

Downloaded by UNIV OF DELAWARE MORRIS LIB on June 14, 2012 | http://pubs.acs.org
Publication Date (Web): May 7, 2012 | doi: 10.1021/bk-2012-1096.ch013

by introduction of bound acidic groups. Covalently bound acidic groups have the advantage in that these groups do not leach from the membrane upon contact with water, as can occur with doped acids (*13*).

Three main approaches to prepare sulfonated polybenzimidazoles (sPBI) are being developed: (a) direct sulfonation of the PBI backbone (*14–17*); (b) chemical grafting of functional monomers such as propanesultone, butanesultone, and sodium (4-bromomethyl) benzenesulfonate via N-linkages (*18*, *19*); (c) co-polycondensation of sulfonated aromatic diacids (e.g., 5-sulfoisophthalic acid and 2-sulfoterephthalic acid) with aromatic tetraamines (*20*, *21*).

Direct sulfonation of the PBI backbone and characterization of post-sulfonated polybenzimidazoles using sulfuric acid and post-sulfonated thermal treatments were reported by Arija et al. (*14*) and Staiti et al. (*16*), but the conductivity of the membranes prepred is not sufficiently high for practical PEMFC applications. Roziere et al. (*22*) report the direct sulfonation of a poly-[(1-(4, 4′-diphenylether)-5-oxybenzimidazole)-benzimidazole] (PBI-OO) in sulfuric acid under mild reaction conditions. In PBI-OO, the presence of electron donor ether bridges offers four rings per repeat unit for sulfonation, which enables IECs of upto 4.2 mequiv.g^{-1} to be achieved, providing membranes with proton conductivities of up to 0.05 S/cm. Derivatization of PBI by chemical grafting of sulfonated monomer groups at the N-site of the imidazole ring of the polymer backbone was reported by Reynolds et al. (*23*, *24*) and Glipa et al (*18*, *25*). However, the grafting reaction has to be performed under strict anhydrous conditions and 100% degree of grafting is difficult to achieve. Glipa et al. (*18*) grafted sulfonated aryl groups onto polybenzimidazole. They achieved a degree of sulfonation up to 75% based on available sites. Sulfonation increases the conductivity from 10^{-4} S/cm in non-modified PBI to 10^{-2} S/cm at room temperature for highly sulfonated PBI, doped in 1 mol H_3PO_4.

The direct polycondensation method was invented by Uno et al. (*26*). In contrast to other methods, direct polycondensation provides advantages in that the the structure of resulting ionomers can be tailored. In recent years many researchers have used this route to synthesize sulfonated polybenzimidazoles using different sulfonated aromatic diacids, such as 5-sulfoisophthalic acid and 4,8-disulfonyl-2,6-naphthalenedicarboxylic acid (*27–29*), 3,3′-disulfonate-4,4′-dicarboxylbiphenyl (*30*), 4′-sulfonate-2,5-dicarboxyphenyl sulfone (*31*), 2,2′-disulfonate- 4,4′-oxydibenzoic acid (*32*), and 4,6-bis(4-carboxyphenoxy)benzene-1,3-disulfonate (*33*). However, membranes prepared from the majority of these SPBI membranes shows relatively low conductivities since the vast proportion of the sulfonic acid groups are neutralized by the basic imidazole groups (*34*, *35*) and do not contribute to proton conductivity. To achieve higher proton conductivity in SPBI membranes, the degree of sulfonation of PBI must be above 3 to provide a sufficient concentration of "free" protons following neutralization of a proportion of them by basic imidazole groups.

In this work, we report the combined use of two approaches, chemical grafting and post-sulfonation of OPBI, to achieve high IEC polymers. The physical properties and proton conductivities of membranes prepared from sOPBI and preliminary testing in H2/O2 PEMFCs are reported.

In Polymers for Energy Storage and Delivery: Polyelectrolytes for Batteries and Fuel Cells; Page, K., et al.;
ACS Symposium Series; American Chemical Society: Washington, DC, 2012.

Downloaded by UNIV OF DELAWARE MORRIS LIB on June 14, 2012 | http://pubs.acs.org
Publication Date (Web): May 7, 2012 | doi: 10.1021/bk-2012-1096.ch013

Experimental

Materials

OPBI was prepared by polycondensation of 3,3′ diaminobenzidine and 4,4′-oxy-bis-benzoic acid, both purchased from Aldrich. Sulfuric acid (98%), dimethylsulfoxides (DMSO) were obtained from Caledon Laboratory Chemicals, Canada. Lithium hydride, calcium hydride, 1, 3-propane sultone and 20% fuming sulphuric acid were purchased from Aldrich.

Synthesis of Sultone-Substituted OPBI

In a 500 mL round bottom flask, equipped with a stirrer, gas inlet and a guard tube, OPBI (0.5 g, 1.25 mmol) was dissolved in dry DMSO (180 mL). The solution was heated to 70 °C with stirring under a stream of argon. Lithium hydride (131.1 mg, 16.5 mmol) was added to the solution and the reaction mixture was heated overnight. 1,3-propane sultone (2.015 g, 16.5 mmol) was added slowly and reaction was continued for 48 h. After cooling, the polymer was precipitated in acetone and washed with acetone several times to remove DMSO. The precipitated polymer was isolated by filtration and dried under vacuum overnight at 120 °C. The product, sultone-modified OPBI, was characterized by ^{1}H NMR with no additional purification which indicated that the 1.9-1.95 out of 2.0 N-imidazole units reacted.

Post-Sulfonation of Sultone-Substituted OPBI

A 50 mL, single necked round bottom flask, equipped with a magnetic stirrer, argon gas inlet and a guard tube, was charged with 15 mL of H_2SO_4 and 5mL 20% oleum sultone-modified OPBI (1g) in powder form was added slowly and the mixture was heated to 80 °C with stirring under a stream of argon. The sultone modified OPBI dissolved in 1 h, providing a homogeneous solution. The solution was heated to 120 °C and maintained at this temperature for 48 h. The resulting viscous solution was cooled and poured into 100 mL water to precipitate the polymer as fiber. As the polymer was water soluble, excess NaCl was added to the solution to precipitate it. The polymer precipitate was filtered, and dissolved in 5% KOH solution for further purification by dialysis.

Membrane Preparation and Characterization

Membranes were prepared by dissolving the sulfonated OPBI in DMSO and triethylamine and casting on a levelled glass plate maintained at a temperature of 80 °C. Polymer films were dried at 120 °C under vacuum overnight. The membranes (~40 μm thick) were converted to the protonic form by immersing in 2 M HCl overnight. The protonated membranes were washed several times with deionized water and were dried at 120 °C under vacuum overnight, to promote

Downloaded by UNIV OF DELAWARE MORRIS LIB on June 14, 2012 | http://pubs.acs.org
Publication Date (Web): May 7, 2012 | doi: 10.1021/bk-2012-1096.ch013

acid-base self-crosslinking, and placed in water overnight to uptake water. The pre-treated membranes (acidic form) were equilibrated in 2 M NaCl for overnight to release the protons, which were subsequently titrated with 0.001 M NaOH to a phenolphthalein end point. Acid-base control titrations were performed on 2 M NaCl solutions with no membranes present to determine the blank titration volume. After titration, the membranes were immersed in 2 M HCl for a minimum of 4 h to reprotonate the sulfonic sites. After drying at 70 °C under vacuum overnight, the membranes' "dry" weight was measured. The ion exchange capacity (IEC, mmol/g) of the membrane was calculated by

$$IEC = \frac{V_{NaOH} \times M_{NaOH}}{W_{dry}}$$

where V_{NaOH} and M_{NaOH} are the blank-corrected volume (mL) and molar concentration (mol/L) of NaOH solution, respectively. W_{dry} is the dry weight of the membrane. The membranes were equilibrated in deionized water overnight at room temperature and blotted with a Kimwipe to remove surface water prior to determining the "wet" weight. The water uptake was calculated as the percentage increase in mass over the "dry" weight and given by

$$Water\ Uptake = \frac{W_{wet} - W_{dry}}{W_{dry}} \times 100$$

where W_{wet} and W_{dry} are the wet and dry weight of the membrane, respectively.

Instrumentation

^{1}H NMR spectra were obtained using a Bruker AVANCE III spectrometer operating at 500 MHz. In-plane proton conductivity was measured by ac impedance spectroscopy with a Solartron 1260 frequency response analyzer (FRA) employing a two-electrode configuration, according to a procedure described elsewhere (*36*). A membrane (5-10 mm) was placed between two Pt electrodes of a conductivity cell, and a 100 mV sinusoidal ac voltage over a frequency range of 10 MHz-100 Hz was applied. The resulting Nyquist plots were fitted to the standard Randles equivalent circuit to determine the membrane resistance. Proton conductivity (σ) was calculated using

$$\sigma = \frac{L}{RA}$$

where L (cm) is the distance between electrodes, R (Ω) is the membrane resistance, and A (cm^2) is the cross-sectional area of the membrane.

In Polymers for Energy Storage and Delivery: Polyelectrolytes for Batteries and Fuel Cells; Page, K., et al.;
ACS Symposium Series; American Chemical Society: Washington, DC, 2012.

Membrane Electrode Assembly (MEA) Fabrication and Fuel Cell Test Conditions

A 5 cm^2 membrane-electrode assembly (MEA) was composed of commercial gas diffusion layers (SIGRACET® GDL 24 BC, SGL Group) on either side of a catalyst-coated membrane (CCM). The CCM was prepared by using an automatic spray coater (Ultra™ 325TT, EFD) to deposit a catalyst ink to form anode and cathode catalyst layers on the sOPBI membrane. The catalyst ink components included platinum on high surface area carbon (46.4% Pt by weight, TEC10E50E, Tanaka Kikinzoku Kogyo K.K.), 5% by weight commercial Nafion® dispersion (D-520, E. I. du Pont de Nemours and Company) and a dispersant mixture of water (18.2 MΩ) and methanol (>99.8%, Fisher Scientific). All components were used as-received. The ratio of methanol to water was 9:1 by weight. The solid Pt, carbon and Nafion accounted for ~ 1% of the total ink weight; Nafion, itself, accounted for 30% of the total solid mass. After spray coating, the cell was assembled into 5 cm^2 single cell hardware (Fuel Cell Technologies) with single serpentine flow fields. SIGRACET® GDL 24 BC (SGL Group) was used for both the anode and cathode GDL. After assembly, the cell was installed on a Teledyne Medusa® fuel cell test station (Teledyne Energy Systems) with a Scribner 890CL load. For performance testing, hydrogen and oxygen were supplied to the anode and cathode, respectively, at a constant flow rate of 200 mL/min. The cell was heated to 80 °C and polarization curves were generated with anode and cathode gases supplied at 100%, 70%, 50% and 30% relative humidity. Curves were generated by increasing the current stepwise from 0 A to the maximum achievable current for a given humidity.

Downloaded by UNIV OF DELAWARE MORRIS LIB on June 14, 2012 | http://pubs.acs.org
Publication Date (Web): May 7, 2012 | doi: 10.1021/bk-2012-1096.ch013

Results and Discussion

OPBI was synthesized by the solution polymerization in PPA by condensing 3,3′ diaminobenzidine and 4,4′-oxy-bis-benzoic acid. The post-modification of OPBI was further carried out as shown Figure 1. Poly[2,2′-(p-oxydiphenylene)-5,5′-bibenzimidazole] (OPBI) was dissolved in dry DMSO by heating at 70 °C with stirring under a stream of argon. After complete dissolution of OPBI in DMSO, the solution was cooled to room temperature and lithium hydride added in a 2.2 molar ratio and the reaction mixture heated overnight. 1,3-Propane sultone was added slowly and the reaction was continued for 48 h. After cooling, the solution was precipitated in acetone and washed with acetone several times to remove DMSO. The precipitated polymer was filtered and dried under vacuum overnight at 120 °C.

The product, sOPBI, was characterized by ^{1}H NMR spectroscopy (Figure 2). The disappearance of proton signals at 13.30 δ, assigned to the N-H hydrogen of the imidazole ring, and the emergence of aliphatic protons at 2.3–4.6 δ substantiates the reaction of the sultone with N-H groups in OPBI. ^{1}H-NMR spectroscopy indicated that ~95-97.5% of the total number of the N-H groups reacted with the sultone. From the 1H NMR spectrum, it was calculated that the IEC of the sultone-substituted OPBI is 2.95 mmole/g. The sulfonated OPBI prepared by the chemical grafting method alone was soluble in DMSO, and provided good film forming ability, and excellent mechanical strength. However, despite the high IEC, the room temperature proton conductivity of these fully-hydrated membranes was only 7 × 10^{-3} S/cm. The relatively low proton conductivity is due to the self-neutralization of the sulfonic acid groups by the basic imidazole. Thus, no further analysis of this particulalr membrane was undertaken, and the sultone substituted OPBI was further post-sulfonated to increase the IEC.

To achieve post-sulfonation of the sultone-substituted OPBI, the polymer was dissolved in a mixture of conc.H_2SO_4 and 20% oleum at 80 °C with stirring under a stream of argon for 1h and further heated at 120 °C for 48 h. The resulting viscous solution was cooled and poured into 100 mL of water containing excess NaCl. The polymer precipitate was filtered, and dissolved in 5 wt% KOH solution for further purification by dialysis. After dialysis, the water was evaporated. The polymer was dissolved in a DMSO/water mixture and films were cast. The post-sulfonated modified sOPBI also showed solubility in DMSO and good film forming ability.

Downloaded by UNIV OF DELAWARE MORRIS LIB on June 14, 2012 | http://pubs.acs.org
Publication Date (Web): May 7, 2012 | doi: 10.1021/bk-2012-1096.ch013

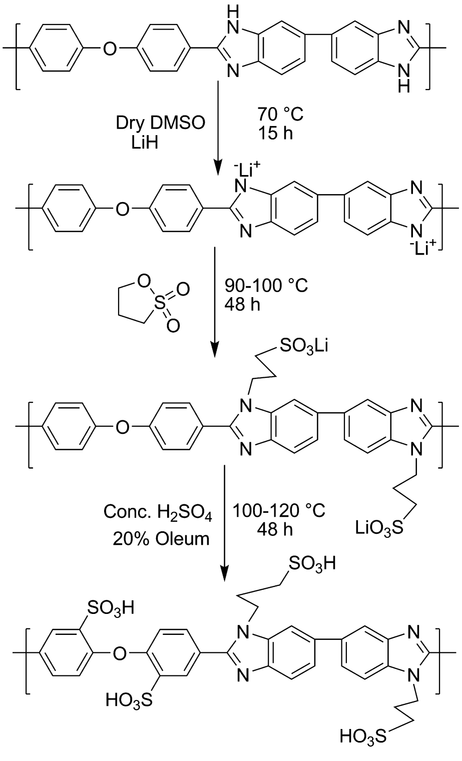

Figure 1. Synthesis of the sulfonated OPBI, sOPBI.

Downloaded by UNIV OF DELAWARE MORRIS LIB on June 14, 2012 | http://pubs.acs.org
Publication Date (Web): May 7, 2012 | doi: 10.1021/bk-2012-1096.ch013

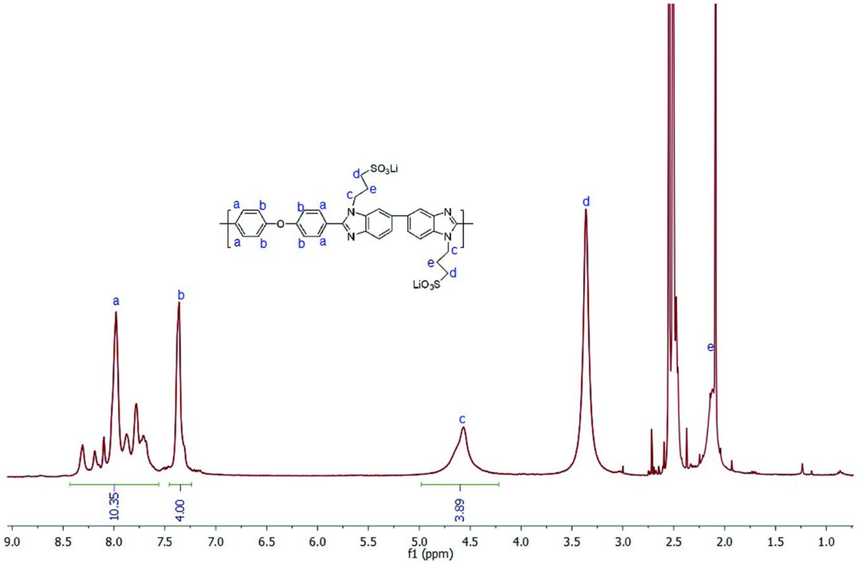

Figure 2. ^{1}H-NMR spectrum of sultone-substituted OPBI.

The IEC of the post-sulfonated OPBI, sOPBI, was calculated, using a combination of ^{1}H-NMR spectrum of the sultone-substituted polymer and the IEC titration of sOPBI to be 4.2mmole/g. However, titration alone, in which only free H^+ ions are detected gave a value of only 1.7mmol/g, because acid-base complex formation between benzimidazole and the sulfonic acid groups (*34*, *35*) binds a large fraction of the H+ ions.

Water content and water uptake are important parameters that in some instances can provide indirect insights into the connectivity of hydrophobic domains and the ability of the polymer matrix to resist osmotic pressure. Water uptake also has a profound effect on proton conductivity, mechanical properties and long term performance of the membrane in a fuel cell (*37*). High water uptake leads to higher proton conductivity but excessive water uptake results in unacceptable dimensional instability, which creates weakness between the membrane and electrode in the MEA. The sOPBI membrane exhibit 82 wt% water uptake and 91 vol% swelling. This translates into a water content of 44 wt%. However, because the IEC is high, lambda values, λ, are 11, when considering the total IEC (4.1 mmole/g) and 26, when considering only “free” protons. Similarly, the [H+] is 3.04 M when taking the total IEC into account and 1.3 M when considering the free IEC (1.7 mmole/g)

The proton conductivity of the sOPBI was measured at various conditions and compared to Nafion 112. Figure 3 and Table 1 show the conductivity of sOPBI and Nafion 112 under various relative humidity and temperatures. For a given temperature, the proton conductivity increases with increasing relative humidity. sOPBI membrane yield proton conductivities between 2.3×10^{-3} to 4.0×10^{-2} S/cm for increases in RH from 65% to 95% at 80 °C, which is lower than Nafion 112. sOPBI shows a decrease in proton conductivity at 90 °C and 95 % RH which indicates that its conductivity is highly water dependent. The room temperature, proton conductivity of hydrated membranes is 3 × 10^{-2} S/cm.

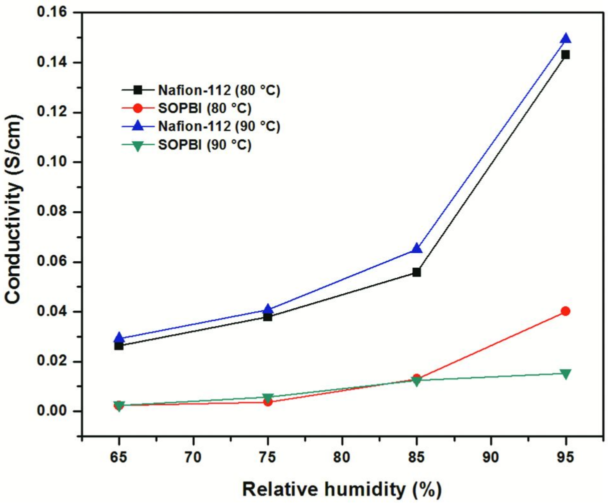

Figure 3. Variation in proton conductivity of sOPBI and Nafion 112 membranes as a function of relative humidity.

Table 1. Proton conductivity values of sOPBI and Nafion 112 at 80 and 90 °C under different RH

Relative Humidity (%)	*sOPBI σ at 80 °C*	*Nafion-112 σ at 80 °C*	*sOPBI σ at 90 °C*	*Nafion-112 σ at 90 °C*
65	2.28 × 10^{-3}	2.62 × 10^{-2}	2.49 × 10^{-3}	2.92 × 10^{-2}
75	3.80 × 10^{-3}	3.79 × 10^{-2}	5.79 × 10^{-3}	4.07 × 10^{-2}
85	1.30 × 10^{-2}	5.57 × 10^{-2}	1.25 × 10^{-2}	6.51 × 10^{-2}
95	4.01 × 10^{-2}	1.43 × 10^{-1}	1.54 × 10^{-2}	1.49 × 10^{-1}

I–V power output characteristics at 80 °C were measured for sOPBI by using CCMs prepared as described in experimental section. Polarization curves are shown in Figure 4. Pure hydrogen and pure oxygen gases were used as the fuel and the oxidant, respectively. The RH of the cathode and anode were maintained at 100% and the gas flow was maintained at 0.2 lpm. A maximum power output of 700mW/cm^2 was obtained at 2.1 A/cm^2 current density with cell voltage of 0.30 V. The I-V characteristics of Nafion112 are shown as a comparison. Despite the lower proton conductivities determined ex-situ, the I-V characteristics of the sOPBI membranes are comparable to Nafion-112 under these operating conditions. The reasons for this are not yet understood but might be due to compression of the

Downloaded by UNIV OF DELAWARE MORRIS LIB on June 14, 2012 | http://pubs.acs.org
Publication Date (Web): May 7, 2012 | doi: 10.1021/bk-2012-1096.ch013

more hydrated sOPBI membrane, which would effectively squeeze water out of the membrane, increase the acid concentration, and increased conductivity.

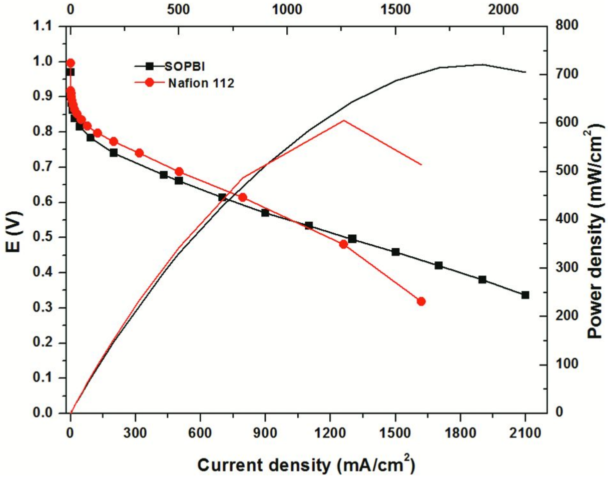

Figure 4. I–V characteristics of sOPBI and Nafion 112 with Pt/C electrodes (ETEK, Pt loading 0.4 mg/cm^2) at 80 °C by using pure hydrogen and oxygen gases, 0.2 lpm flow. RH, 100%.

Conclusions

A novel, sulfonated polybenzimidazole, sulfonated poly[2,2′-(p-oxydiphenylene)-5,5′-bibenzimidazole] (sOPBI), was successfully prepared by chemical grafting and post-sulfonation reaction of parent polymer, poly[2,2′-(p-oxydiphenylene)-5,5′-bibenzimidazole] (OPBI). sOPBI showed good solubility in DMSO, good film forming ability and proton conductivities of up to 4.1×10^{-2} S/cm at 80 °C. Though these membranes offered no improved performance as compared to Nafion in ex-situ conductivity analyses, they displayed displayed good fuel cell performance in initial tests that were comparable to Nafion 112, despite their showing lower ex-situ proton conductivity. The results are encouraging and provide motivation for further investigation of high IEC PBIs.

Acknowledgments

The authors of this paper would like to thank Natural Sciences and Engineering Research Council of Canada for financial support of this research. The authors are grateful to Mark Haldane and Paul Le Marquand of NRC-IFCI, Vancouver, for assistance in fuel cell polarization tests.

Downloaded by UNIV OF DELAWARE MORRIS LIB on June 14, 2012 | http://pubs.acs.org
Publication Date (Web): May 7, 2012 | doi: 10.1021/bk-2012-1096.ch013

References

1. Carrette, L.; Friedrich, K. A.; Stimming, U. *ChemPhysChem* **2000**, *1* (4), 162–193.
2. Savinell, R. F.; Wainright, J. S.; Litt, M. *Proceedings of the Second International Symposium on Proton Conducting Membrane Fuel Cell II* **1999**, *98* (27), 81–90.
3. Wainright, J. S.; Savinell, R. F.; Litt, M. H. *New Mater. Fuel Cell Mod. Battery Syst. II* **1997**, 808–817.
4. Wainright, J. S.; Wang, J. T.; Savinell, R. F. *IECEC 96 - Proc. 31st Intersoc. Energy Convers. Eng. Conf.* **1996**, *1−4*, 1107–1111.
5. Wainright, J. S.; Wang, J. T.; Weng, D.; Savinell, R. F.; Litt, M. *J. Electrochem. Soc.* **1995**, *142* (7), L121–L123.
6. Fontanella, J. J.; Wintersgill, M. C.; Wainright, J. S.; Savinell, R. F.; Litt, M. *Electrochim. Acta* **1998**, *43* (10−11), 1289–1294.
7. Yu, S.; Benicewicz, B. C. *Macromolecules* **2009**, *42* (22), 8640–8648.
8. Yu, S.; Xiao, L.; Benicewicz, B. C. *Fuel Cells* **2008**, *8* (3−4), 165–174.
9. Xiao, L.; Zhang, H.; Jana, T.; Scanlon, E.; Chen, R.; Choe, E. W.; Ramanathan, L. S.; Yu, S.; Benicewicz, B. C. *Fuel Cells* **2005**, *5* (2), 287–295.
10. Jones, D. J.; Rozière, J. *J. Membr. Sci.* **2001**, *185* (1), 41–58.
11. Kawahara, M.; Morita, J.; Rikukawa, M.; Sanui, K.; Ogata, N. *Electrochim. Acta* **2000**, *45* (8-9), 1395–1398.
12. Xing, B.; Savadogo, O. *Electrochem. Commun.* **2000**, *2* (10), 697–702.
13. Aricò, A. S.; Srinivasan, S.; Antonucci, V. *Fuel Cells* **2001**, *1* (2), 133–161.
14. Ariza, M. J.; Jones, D. J.; Rozière, J. *Desalination* **2002**, *147* (1−3), 183–189.
15. Asensio, J. A.; Borrós, S.; Gómez-Romero, P. *Electrochim. Acta* **2004**, *49* (25), 4461–4466.
16. Staiti, P.; Lufrano, F.; Aricò, A. S.; Passalacqua, E.; Antonucci, V. *J. Membr. Sci.* **2001**, *188* (1), 71–78.
17. Kuder, J. E.; Chen, J. C. Chemical modification of preformed polybenzimidazole semipermeable membrane. U.S. Patent 4,634,530, 1987.
18. Glipa, X.; El Haddad, M.; Jones, D. J.; Rozière, J. *Solid State Ionics* **1997**, *97* (1−4), 323–331.
19. Bae, J. M.; Honma, I.; Murata, M.; Yamamoto, T.; Rikukawa, M.; Ogata, N. *Solid State Ionics* **2002**, *147* (1−2), 189–194.
20. Carraher, C. E.; Swift, G. G.; Sakaguchi, Y.; Kitamura, K.; Nakao, J.; Hamamoto, S.; Tachimori, H.; Takase, S. Preparation and Properties of Sulfonated or Phosphonated Polybenzimidazoles and Polybenzoxazoles. *Functional Condensation Polymers*; Springer: 2002; pp 95−104.
21. Juan Antonio, A.; Salvador, B.; Pedro, G.-R. *J. Polym. Sci., Part A: Polym. Chem.* **2002**, *40* (21), 3703–3710.
22. Peron, J.; Ruiz, E.; Jones, D. J.; Rozière, J. *J. Membr. Sci.* **2008**, *314* (1-2), 247–256.
23. Gieselman, M. B.; Reynolds, J. R. *Macromolecules* **1992**, *25* (18), 4832–4834.

Downloaded by UNIV OF DELAWARE MORRIS LIB on June 14, 2012 | http://pubs.acs.org
Publication Date (Web): May 7, 2012 | doi: 10.1021/bk-2012-1096.ch013

24. Gieselman, M. B.; Reynolds, J. R. *Macromolecules* **1993**, *26* (21), 5633–5642.
25. Rozière, J.; Jones, D. J.; Marrony, M.; Glipa, X.; Mula, B. *Solid State Ionics* **2001**, *145* (1−4), 61–68.
26. Uno, K.; Niume, K.; Iwata, Y.; Toda, F.; Iwakura, Y. *J. Polym. Sci., Polym. Chem. Ed.* **1977**, *15* (6), 1309–1318.
27. Qing, S.; Huang, W.; Yan, D. *Eur. Polym. J.* **2005**, *41* (7), 1589–1595.
28. Qing, S.; Huang, W.; Yan, D. *React. Funct. Polym.* **2006**, *66* (2), 219–227.
29. Bai, H.; Ho, W. S. W. *J. Taiwan Inst. Chem. Eng.* **2009**, *40* (3), 260–267.
30. Kang, S.; Zhang, C.; Xiao, G.; Yan, D.; Sun, G. *J. Membr. Sci.* **2009**, *334* (1-2), 91–100.
31. Tan, N.; Xiao, G.; Yan, D.; Sun, G. *J. Membr. Sci.* **2010**, *353* (1−2), 51–59.
32. Jouanneau, J.; Gonon, L.; Gebel, G.; Martin, V.; Mercier, R. *J. Polym. Sci., Part A: Polym. Chem.* **2010**, *48* (8), 1732–1742.
33. Sheng, L.; Xu, H.; Guo, X.; Fang, J.; Fang, L.; Yin, J. *J. Power Sources* **2011**, *196* (6), 3039–3047.
34. Jouanneau, J.; Mercier, R. g.; Gonon, L.; Gebel, G. r. *Macromolecules* **2007**, *40* (4), 983–990.
35. Thomas, O. D.; Peckham, T. J.; Thanganathan, U.; Yang, Y.; Holdcroft, S. *J. Polym. Sci., Part A: Polym. Chem.* **2010**, *48* (16), 3640–3650.
36. Xie, Z.; Song, C.; Andreaus, B.; Navessin, T.; Shi, Z.; Zhang, J.; Holdcroft, S. *J. Electrochem. Soc.* **2006**, *153* (10), E173–E178.
37. Zawodzinski, J. T. A.; Springer, T. E.; Davey, J.; Jestel, R.; Lopez, C.; Valerio, J.; Gottesfeld, S. *J. Electrochem. Soc.* **1993**, *140* (7), 1981–1985.

Downloaded by UNIV OF DELAWARE MORRIS LIB on June 14, 2012 | http://pubs.acs.org
Publication Date (Web): May 7, 2012 | doi: 10.1021/bk-2012-1096.ch013

Downloaded by OHIO STATE UNIV LIBRARIES on June 14, 2012 | http://pubs.acs.org
Publication Date (Web): May 7, 2012 | doi: 10.1021/bk-2012-1096.ch014

Chapter 14

Chemical Stability of Anion Exchange Membranes for Alkaline Fuel Cells

Yuesheng Ye and Yossef A. Elabd*

**Department of Chemical and Biological Engineering, Drexel University,
3141 Chestnut Street, Philadelphia, PA 19104
*elabd@drexel.edu**

Solid-state alkaline fuel cells (AFCs), which utilize anion exchange membranes (AEMs) as their electrolytes, have the potential to provide society with low-cost, long-lasting renewable portable power. However, the chemical stability of AEMs poses a critical challenge that limits the wide scale use of AFCs. This chapter reviews literature findings on the chemical stability of recently developed hydroxide conducting AEMs with various backbone and cation chemical structures, where covalently attached cations in AEMs, include ammonium, phosphonium, sulfonium, guanidinium, imidazolium, pyridinium, quaternized 1,4-diazabicyclo(2,2,2)octane (DABCO), and piperidinium. However, limited chemical analysis has been conducted regarding the chemical stability of AEMs, therefore, this chapter will also discuss earlier work on the chemical stability of small molecule cation analogs in alkaline conditions. In the future, a more fundamental understanding of the chemical stability of AEMs will be required to adequately design robust solid-state AFCs.

Introduction

The alkaline fuel cell (AFC), classified by electrolyte type (i.e., electrolytes that conduct hydroxide anions (OH^-)), is among the oldest and most powerful fuel cell (*1*). The AFC technology was first patented by Reid in 1903 (*2*), demonstrated by Bacon in 1932 (*3*), utilized in NASA's Apollo space missions in the mid-1960s (*1*), and developed by Kordesch for AFC-powered motorcycles (*4*). However,

In Polymers for Energy Storage and Delivery: Polyelectrolytes for Batteries and Fuel Cells; Page, K., et al.;
ACS Symposium Series; American Chemical Society: Washington, DC, 2012.

the use of liquid electrolytes (e.g., KOH(aq)) in AFCs has significantly limited its wide scale use due to the durability issues encountered with electrolyte leakage and the precipitation of carbonate crystals, such as potassium carbonate (K_2CO_3), due to carbonation (i.e., exposure to CO_2 in the fuel) (*5*). The acid fuel cell, however, mitigated problems associated with liquid electrolytes in the 1950s with the incorporation of solid-state electrolytes that can readily transport protons. This work led to the development of the proton exchange membrane fuel cell (PEMFC) and was utilized in NASA's Gemini space missions (*6*). Furthermore, the development of Nafion®, a PEM with excellent properties developed by DuPont in 1960s (*7*), significantly accelerated research and development of PEMFCs for wide scale application in portable power (e.g., automobiles).

Similarly, a robust solid-state membrane that can conduct hydroxide ions (i.e., anion exchange membrane (AEM)) could replace liquid electrolytes in AFCs. This would eliminate leakage and carbonate precipitation issues associated with liquid electrolytes and accelerate the development of long-lasting AFCs. To date, recent advances in the PEM counterpart, the alkaline AEM (*8*, *9*), have significantly renewed interest in the AFC. The AEM AFC not only circumvents problems encountered with liquid-based alkaline electrolytes, but also provides significant advantages over PEMFCs, including enhanced electrokinetics that allows for the use of non-noble metal catalysts, reduced fuel crossover, and improved water management (*10*). Most importantly, a solid-state AFC using AEMs holds the promise of a low-cost, long-lasting fuel cell.

Recently, a number of AEMs have been developed for the AFC (several examples shown in Table 1). However, the chemical stability of AEMs is still a critical and challenging factor that limits the wide scale use of solid-state AFCs. Specifically, the high nucleophilicity and basicity of OH^- ions can trigger the degradation of a covalently attached counter cation, as well as the polymer backbone. Therefore, it is essentially important to understand the chemical stability of AEMs under various conditions. However, studies on the chemical stability of AEMs are still relatively scarce. Particularly, recent stability studies on AEMs for AFCs have mainly focused on evaluating ion exchange capacity (IEC) or ionic conductivity over a designated period of time after an AEM sample is immersed in a concentrated alkaline solution at a certain temperature (see literature results in Table 2). These results suggest that a change or lack thereof in IEC or ionic conductivity provides an understanding of the chemical stability of the AEM under a chosen test condition. However, this approach has several shortcomings. For instance, IEC or conductivity may not truly represent the chemical stability of the AEM in OH^- form since hydroxide ions may quickly convert to carbonate (CO_3^{2-}) and/or bicarbonate (HCO_3^-) ions in the presence of ambient air (i.e., carbonation due to ~ 400 ppm of CO_2 in air) (*11*). Furthermore, this approach does not provide a quantitative chemical analysis or a deep understanding of chemical stability of AEMs, e.g., degradation mechanisms and kinetics.

Downloaded by OHIO STATE UNIV LIBRARIES on June 14, 2012 | http://pubs.acs.org
Publication Date (Web): May 7, 2012 | doi: 10.1021/bk-2012-1096.ch014

Downloaded by OHIO STATE UNIV LIBRARIES on June 14, 2012 | http://pubs.acs.org
Publication Date (Web): May 7, 2012 | doi: 10.1021/bk-2012-1096.ch014

Table 1. Examples of AEMs for the AFC

AEM Chemical Structure	Ref.
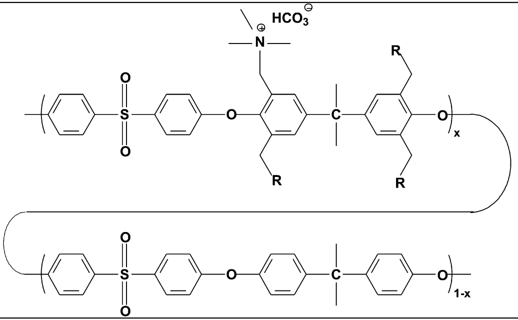	Hickner et. al.[11] 2010
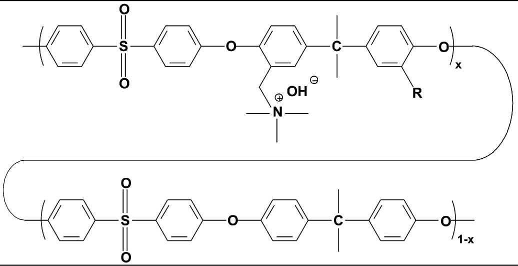	Kohl et al.[16] 2010
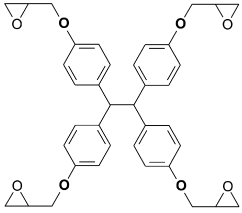 (crosslinker)	
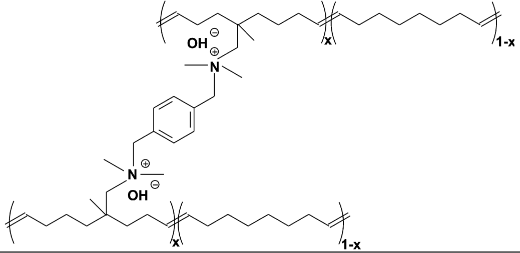	Coates et al.[17] 2010
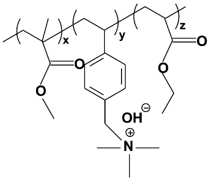	Wang et al.[18] 2010
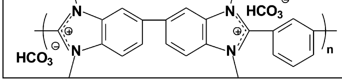	Holdcroft et al.[19] 2011

Downloaded by OHIO STATE UNIV LIBRARIES on June 14, 2012 | http://pubs.acs.org
Publication Date (Web): May 7, 2012 | doi: 10.1021/bk-2012-1096.ch014

Table 2. Summary of chemical stability studies on AEMs for the AFC

AEM Chemical Structure	Chemical Stability				
	[OH$^-$] (M)	T (°C)	t (h)	Remarks[a]	Ref.
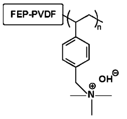	Water	50	> 2400	ΔIEC < 13%	Slade et al.[20] 2003
	Water	60	2856	ΔIEC = 18%	Slade et al.[9] 2003
	Water	100	~ 336	ΔIEC ≈ 18%	
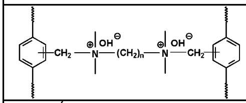	2	40	240	ΔIEC = 28%	Stamatialis et al.[21] 2004
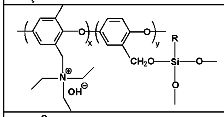	2	25	2-192	ΔIEC ≈ 17-32%	Xu et al.[22] 2009
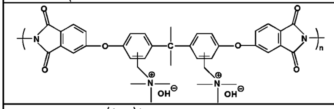	1	80	24	$\Delta\sigma \approx 0$	Chen et al.[23] 2009
	2	25	24	$\Delta\sigma \approx 0$	
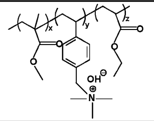	1	60	120	$\Delta\sigma \approx 0$	Fang et al.[24] 2010
	6	60	120	$\Delta\sigma \approx$ 50%	
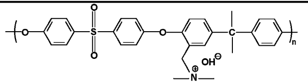	2	75	120	$\Delta\sigma \approx 0$	Zhuang et al.[25] 2010
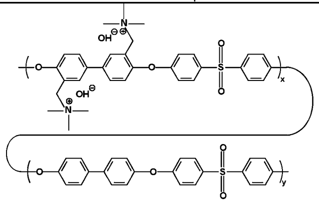	4	20	> 48	ΔIEC ≤ 3%	Zhang et al.[26] 2011
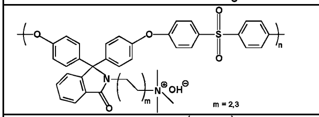	10	30	24	ΔNMR ≈ 16%-57%	Zhang et al.[27] 2010
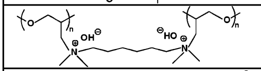	1-8	30	24	$\Delta\sigma \approx 0$	Liu et al.[28] 2011
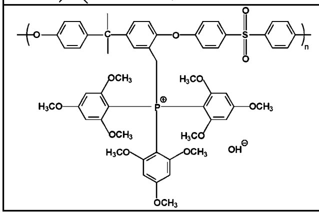	1-10	25	48	$\Delta\sigma \approx 0$	Yan et al.[29] 2009

Continued on next page.

Downloaded by OHIO STATE UNIV LIBRARIES on June 14, 2012 | http://pubs.acs.org
Publication Date (Web): May 7, 2012 | doi: 10.1021/bk-2012-1096.ch014

Table 2. (Continued). Summary of chemical stability studies on AEMs for the AFC

AEM Chemical Structure	Chemical Stability				
	$[OH^-]$ (M)	T (°C)	t (h)	Remarks[a]	Ref.
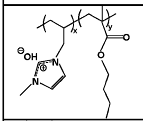	6	60	120	$\Delta\sigma = 8\%$	Fang et al.[30] 2010
	6	80	120	$\Delta\sigma = 56\%$	
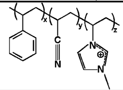	1	60	400	$\Delta\sigma \approx 0$	Yan et al.[31] 2010
	10	72	48	$\Delta\sigma \approx 0$	
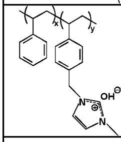	10	60	120	$\Delta\sigma \approx 0$	Fang et al.[32] 2011
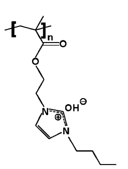	0	80	168	ΔNMR = 0	Elabd et al.[33] 2011
	1	80	168	ΔNMR = 38%	
	10	25	24	ΔNMR = 50%	
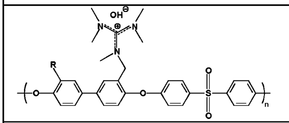	1	60	48	$\Delta\sigma \approx 0$	Zhang et al.[34] 2010
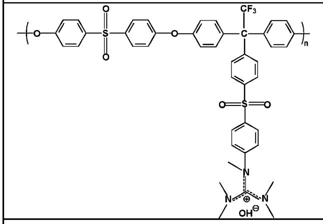	0.5	80	382	$\Delta\sigma \approx 30\%$	Kim and Kim[35] 2010
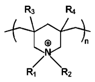	1.8	80	500	ΔIEC ≤ 10%	Daikoku et al.[36] 2011

[a] ΔIEC and Δσ denote a negative change in ion exchange capacity and ionic conductivity, respectively. ΔNMR denotes the degree of degradation estimated from NMR spectroscopy results.

In contrast to the limited studies on chemical stability of AEMs, the chemical stability of small molecule organic cations in the presence of alkaline solutions have been extensively investigated in the past. Although the current status of AEM development for AFCs has been reviewed (*1*, *10*, *12–15*), including two recent comprehensive review articles (*1*, *15*), the chemical stability of AEMs

Downloaded by OHIO STATE UNIV LIBRARIES on June 14, 2012 | http://pubs.acs.org
Publication Date (Web): May 7, 2012 | doi: 10.1021/bk-2012-1096.ch014

was not thoroughly discussed in these review articles. Therefore, in this chapter, results on the chemical stability of AEMs, as well as the chemical stability of small molecule organic cations will be reviewed. Both non-cyclic cations (e.g., ammonium, phosphonium, sulfonium, guanidinium) and cyclic cations (e.g., imidazolium, pyridinium, quaternized 1,4-diazabicyclo(2,2,2)octane (DABCO), and piperidinium) will be discussed. A brief summary of the chemical stability of the polymer backbone in AEMs will also be discussed.

Chemical Stability of Ammonium-Based AEMs

The chemical stability of ammonium-based AEMs has its origins in early work on using AEMs for desalination (*37*) and as ion exchangers (*38*, *39*). Two major degradation reactions are generally accepted for ammonium-based AEMs: 1) a nucleophilic displacement (substitution) from the attack of OH^- on the α carbons via a S_N2 reaction resulting in two byproducts (amine and alcohol) (Scheme 1), and 2) an E2 (Hofmann) elimination from the abstraction of β hydrogen by OH^- resulting in two byproducts (amine and alkene) (Scheme 2). Note that the S_N2 reaction and E2 elimination occur in competition with one another, often leading to a mixture of byproducts. Different chemical structures associated with the ammonium cation may favor one degradation mechanism over the other. For instance, the steric hindrance of bulky chemical groups near the α carbon of the ammonium cation preferentially leads to the E2 elimination reaction. Alternatively, if the β hydrogen is not present, the degradation prefers a S_N2 pathway. For example, the benzyltrimethylammonium cation with no β hydrogen undergoes a S_N2 reaction and yields trimethylamine (65%) and benzyldimethylamine (35%) (see Scheme 1) (*37*).

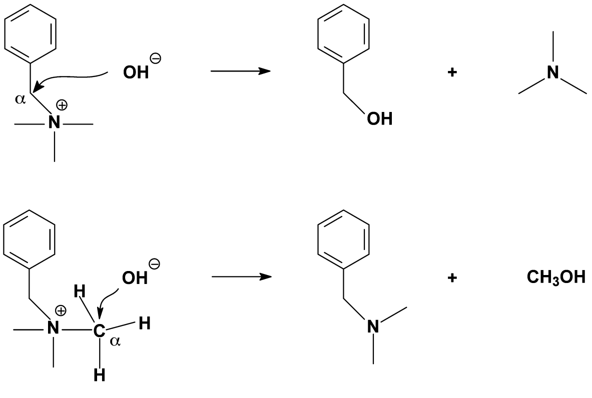

Scheme 1. Nucleophilic displacement (substitution) of benzyltrimethylammonium cation (37)

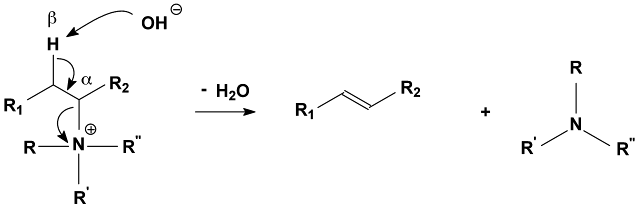

Scheme 2. E2 (Hofmann) elimination reaction of a quaternary ammonium cation (37)

Downloaded by OHIO STATE UNIV LIBRARIES on June 14, 2012 | http://pubs.acs.org
Publication Date (Web): May 7, 2012 | doi: 10.1021/bk-2012-1096.ch014

The development of ammonium-based AEMs have received the most attention for solid-state AFCs, as well as the study of chemical stability. Most ammonium-based AEMs (*20–27*) (See Tables 1 and 2) contain an arylammonium (e.g., benzylammonium) group. Although a few recent studies have quantified the degree of degradation using ^{1}H NMR (*27*), most stability studies were based on the results of IEC or ionic conductivity (See Table 2). Table 2 shows test conditions of alkaline concentration, temperature, and immersion time in an alkaline solution ranging from 0 (water) to 10 M, 25 to 80 °C, and 2 to 2856 h, respectively. Early stability studies were conducted in water for long periods of time (e.g., 2856 h) (*9*), while more recent ones were conducted in concentrated alkaline solutions (*21–28*). Also, most stability tests were carried out at either a low temperature (< 60 °C) or a low alkaline concentration (~ 1 M), indicating that both high temperature (≥ 60 °C) and high alkaline concentration (≥ 1 M) will significantly accelerate degradation reactions. For example, at 6 M and 60°C, the benzyltrimethylammonium-based AEM experienced a 50% loss in conductivity after 2 h (*30*).

Compared to the work on the chemical stability of ammonium-based AEMs over the past decade, the chemical stability of small molecule ammonium cations has been studied more extensively for more than a century. Work on the stability of the ammonium cation dates back to the 1850s when August Wilhelm von Hofmann pioneered the synthesis of ammonium and phosphonium bases (*40*, *41*). Subsequently, the Hofmann (E2) elimination was named after the scientist for his work on amines and ammonium bases and organic phosphorus compounds. In addition to the E2 elimination, other major degradation mechanisms include the Stevens and Sommelet-Hauser rearrangement reactions.

The Stevens rearrangement reaction (Scheme 3) was first discovered by Stevens and coworkers (*42*) in 1928 when treating phenacylbenzyldimethylammonium bromide with aqueous sodium hydroxide. The reaction was recognized as an intramolecular migration with a 1,2-rearrangment based on crossover experiments (*43*), and confirmed by ^{13}C labeling (*44*). As for the reaction mechanism, it is clear that the rearrangement reaction begins with the abstraction of the α proton by the base to give an ylide intermediate and this was isolated by others (*45*). However, regarding the further reaction of the ylide intermediate, several mechanisms including ion-pair (*44*), concerted shift (*46*) and radical-pair (*47*) pathways were proposed. Note that the Stevens rearrangement of benzyltriammonium cation results in tertiary benzylamines (Scheme 4) that are different from the products obtained from the nucleophilic displacement (S_N2) pathway (Scheme 1).

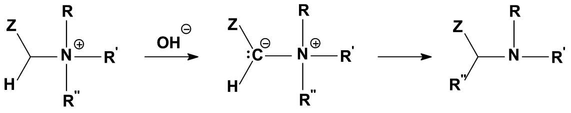

Scheme 3. Stevens rearrangement of an ammonium cation (42)

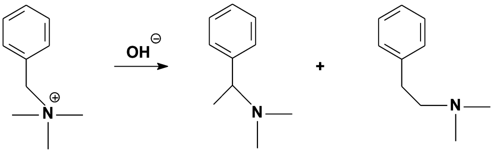

Scheme 4. Stevens rearrangement of benzyltrimethylammonium cation (42)

Another mechanism, the Sommelet-Hauser rearrangement (Scheme 5), was first observed by Sommelet in 1937 with observations on the rearrangement of benzhydryltrimethylammonium hydroxide to *o*-benzylbenzyldimethylamine upon heating with concentrated sodium hydroxide (*48*). These results were confirmed with further investigations by Kantor and Hauser in 1951 (*49*). The Sommelet-Hauser rearrangement occurs only with certain quaternary benzyl ammonium cations. The reaction mechanism is simpler than the Stevens rearrangement, and was confirmed by intermediate isolation (*50*, *51*) and ^{13}C labeling experiments (*52*). For the benzyltrimethylammonium cation, both Stevens (Scheme 4) and Sommelet-Hauser (Scheme 5) rearrangement reactions are possible, and it was reported that the Stevens rearrangement is favored at high temperatures, while the Sommelet-Hauser is favored at lower temperatures (*53*).

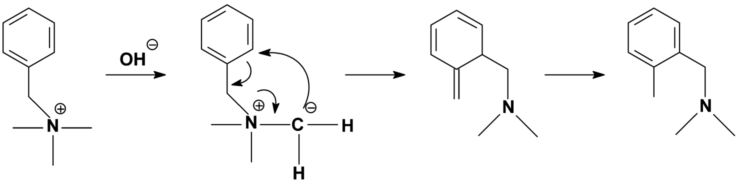

Scheme 5. Sommelet–Hauser rearrangement of benzyltrimethylammonium cation (49)

In addition to these rearrangement pathways, Pivovar and coworkers (*54*) recently reported that the direct degradation of an ylide intermediate results in alcohol and amine byproducts (Scheme 6), suggesting that the degradation pathway of nucleophilic displacement via a S_N2 reaction (Scheme 1) is not the only pathway to produce alcohol and amine byproducts.

Downloaded by OHIO STATE UNIV LIBRARIES on June 14, 2012 | http://pubs.acs.org
Publication Date (Web): May 7, 2012 | doi: 10.1021/bk-2012-1096.ch014

Downloaded by OHIO STATE UNIV LIBRARIES on June 14, 2012 | http://pubs.acs.org
Publication Date (Web): May 7, 2012 | doi: 10.1021/bk-2012-1096.ch014

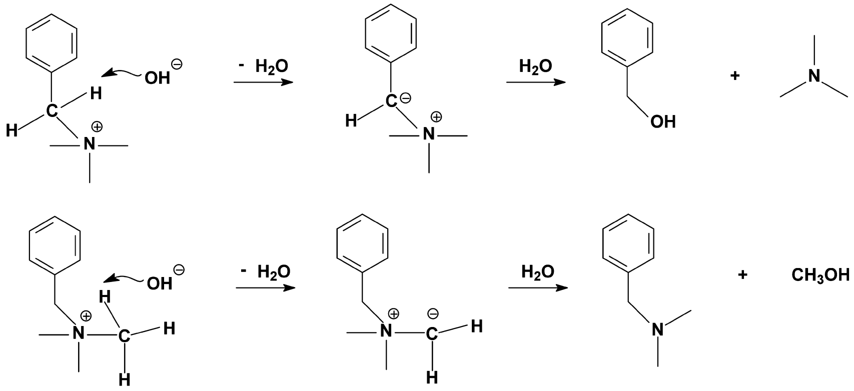

Scheme 6. Ylide degradation pathway of benzyltrimethylammonium cation (54)

Degradation studies on small molecule quaternary ammonium ions in alkaline conditions suggest that the degradation of ammonium-based AEMs is not a simple process and may include a number of degradation pathways, such as nucleophilic displacement (S_N2), E2 (Hofmann) elimination, Stevens and Sommelet-Hauser rearrangements, and direct ylide degradation. However, the chemical stability of ammonium-based AEMs involving the Stevens and Sommelet-Hauser rearrangement reactions has not been experimentally investigated. Thus, more detailed and fundamental studies are necessary to gain better understanding of the possible degradation pathways and the extent of degradation for ammonium-based AEMs under various alkaline conditions.

Chemical Stability of Phosphonium-Based AEMs

Compared to the work on ammonium-based AEMs, there are fewer investigations on phosphonium-based AEMs for the AFCs. This may be due to the much lower chemical stability of small molecule quaternary phosphonium cations compared to their ammonium analogs (*55*). For example, the instability of phosphonium-based AEMs was evidenced by a complete loss of water sorption capacity when poly(benzyltrialkylphosphonium chloride) ion exchange resins were exposed to 4% aqueous NaOH for 24 h (*55*).

However, recent work showed that 2,4,6-trimethoxyphenyl bulky groups surrounding the phosphonium cation can significantly enhance chemical stability of phosphonium-based AEMs compared to quaternary ammonium-based AEMs (*29*). Ionic conductivity results on this AEM suggest high chemical stability after immersion in concentrated alkaline solutions (1-10 M) at room temperature for 48 h (see Table 2). The enhanced chemical stability was attributed to the strong electron-donating groups (*o*-methoxy (*o*-OCH_3) and *p*-methoxy (*p*-OCH_3)) in the benzene ring and the steric hindrance of the bulky trimethoxyphenyl groups in the cation (*29*). Although there is continued work on phosphonium-based AEMs (*56*, *57*), their degradation mechanisms, in general, have not been well investigated.

In contrast, the degradation of small molecule organic phosphonium cations has been explored extensively by Hofmann and Cahours (*58*), Ingold and coworkers (*59*, *60*), and other researchers, such as McEwen and coworkers (*61*, *62*). The degradation of a quaternary phosphonium cation in alkaline conditions results in phosphine oxide and a hydrocarbon as byproducts and is referred to as the Cahours-Hofmann reaction (*63*).

According to the work of McEwen and coworkers (*61*), the degradation of a phosphonium cation in alkaline conditions consists of the following steps (Scheme 7): 1) rapid, reversible attack by the hydroxide anion at a face of the phosphonium tetrahedron to produce a hydroxyphosphorane; 2) rapid, reversible removal of a proton from the hydroxyphosphorane to generate a phosphoranyl anion; 3) irreversible, rate-determining expulsion of a carbanion to form a tertiary phosphine oxide, where the expulsion and protonation of the carbanion probably occur simultaneously rather than as separated steps. The degradation of the benzyltrimethylphosphonium cation (Scheme 7) results in toluene and trimethylphosphine oxide as byproducts. Therefore, one would expect that the degradation of benzyltrimethylphosphonium-based AEMs would yield poly(4-methyl styrene).

Downloaded by OHIO STATE UNIV LIBRARIES on June 14, 2012 | http://pubs.acs.org
Publication Date (Web): May 7, 2012 | doi: 10.1021/bk-2012-1096.ch014

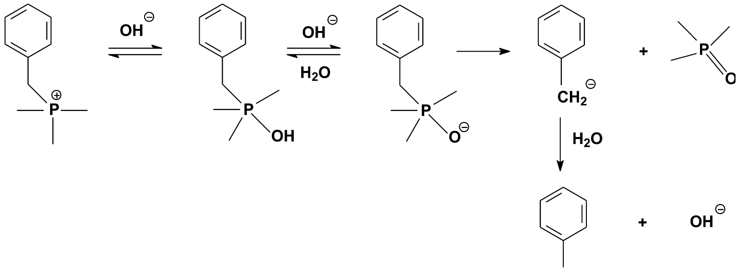

Scheme 7. Degradation of benzyltrimethylphosphonium cation (61)

Note that the significant difference in chemical stability between the benzyltri(2,4,6-trimethoxyphenyl) phosphonium cation and a more conventional quaternary phosphonium cation suggests that the chemical groups attached to the phosphonium cation can greatly affect the chemical stability of the cation. For example, for the benzyltriarylphosphonium cation, electron-withdrawing groups, such as *m*-Cl, *p*-Cl and *m*-OCH_3 (methoxy), can accelerate the degradation reaction. This acceleration was attributed to an increase in the concentration of the intermediate (Scheme 7) (*64*). In contrast, electron-withdrawing groups, such as *p*-OCH_3 and *o*-OCH_3, can inhibit the degradation reaction and enhance the chemical stability. For example, the introduction of a single *o*-OCH_3 group into the benzyltriphenylphosphonium structure reduces the rate of alkaline cleavage to only 1/37 of its value compared to the unsubstituted benzyltriphenylphosphonium cation. The introduction of one more *o*-OCH_3 group into the same benzene ring (i.e., benzyl(2,6-dimethoxyphenyl)diphenylphosphonium cation) can reduce the degradation rate to 1/380 compared to the unsubstituted cation. Notice that the newly developed phosphonium-based AEMs, containing three 2,4,6-trimethoxyphenyl groups with electron-donating groups of *o*-OCH_3 and *p*-OCH_3, greatly enhance the stability of the phosphonium cation (*29*). In other words, the chemical stability can be significantly altered by designing the chemistry around the cation to inhibit the degradation reaction.

Chemical Stability of Sulfonium-Based AEMs

There are only a few reports on the chemical stability of sulfonium-based AEMs (*55*, *65*). Trostyanskaya and Makarova (*55*) investigated the chemical stability of ion exchange resins that contain ammonium, phosphonium and sulfonium cations. This study showed that when the resins were exposed to 4% aqueous NaOH for 24 h, the poly(benzyldialkylsulfonium chloride) ion exchange resin retained 40% of its water sorption capacity, while the poly(benzyltrialkylphosphonium chloride) ion exchange resin completely lost its water sorption capacity. This work suggests that chemical stability may follow the order: sulfonium > phosphonium. They also reported that the degradation of the benzyldialkylsulfonium cation yields dialkyl sulfide and benzylalkyl sulfide as byproducts. Prior work on the degradation of small molecule organic sulfonium cations shows that the main degradation reaction is the Stevens rearrangement reaction (*42*, *43*) (Schemes 8 and 9), which is similar as the Stevens rearrangement of an ammonium cation (Scheme 3 and 4). To the authors' best knowledge, the relatively poor chemical stability of the sulfonium cation in alkaline conditions, may be a primary reason that sulfonium-based AEMs have not been developed for the AFCs.

Downloaded by OHIO STATE UNIV LIBRARIES on June 14, 2012 | http://pubs.acs.org
Publication Date (Web): May 7, 2012 | doi: 10.1021/bk-2012-1096.ch014

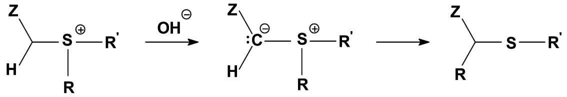

Scheme 8. Stevens rearrangement of a sulfonium cation (42)

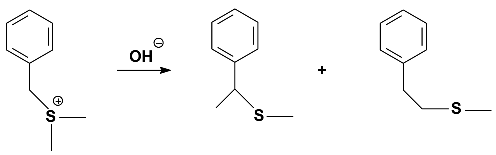

Scheme 9. Stevens rearrangement of benzyldimethylsulfonium cation (42)

Chemical Stability of Guanidinium-Based AEMs

Recent studies (*34*, *35*) show that guanidinium-based AEMs have good chemical stability in alkaline solutions. The conductivity was maintained after immersion in 1 M KOH solution at 60 °C for 48 h (*34*) or it reduced by only 30% after immersion in 0.5 M KOH at 80 °C solution for 382 h (*35*) (Table 2). Unfortunately, there are few investigations on the chemical stability of the small molecule organic guanidinium cation. A recent study showed that the degradation of guanidinium cation undergoes a S_N2 reaction (Scheme 10) (*66*).

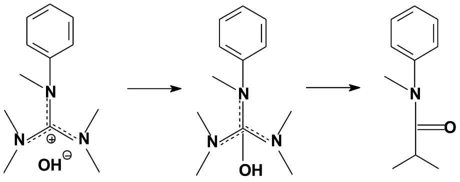

Scheme 10. Degradation of a guanidinium-based cation (66)

Chemical Stability of Imidazolium-Based AEMs

There are far less studies on AEMs with cyclical cations (e.g., imidazolium, pyridinium, and quaternized DABCO, piperidinium) compared to AEMs with non-cyclical cations (e.g., ammonium). Imidazolium-based AEMs are of interest due to the five-membered heterocyclic ring and π conjugated structure of the imidazolium cation. Several recent studies (*30–32*) developed imidazolium-based AEMs and reported good chemical stability based on conductivity results. For example, the conductivity of a 1-allyl-3-methylimidazolium-based random copolymer reduced by only 8% after immersion in 6 M NaOH solution at 60 °C for 120 h, and a 1-vinyl-3-methylimidazolium-based block copolymer retained its conductivity after immersion in 1 M KOH solution at 60 °C for 400 h (See Table 2). However, a detailed stability analysis (e.g., degradation mechanisms) on these imidazolium-based AEM were not conducted.

However, a recent study (*33*) provides a thorough analysis of chemical stability for an imidazolium-based polymerized ionic liquid (PIL). A combination of conductivity and NMR experiments were utilized to comprehensively characterize and quantify the chemical stability of the AEM over a broad range of humidities, temperatures, and alkaline concentrations. In this study, high chemical stability was observed under dry conditions (10% RH) at 30 °C, humid and saturated conditions up to 80 °C, and even in mild alkaline conditions ([KOH] < 1 M) at 25 °C. Degradation was only observed under more vigorous conditions: dry conditions (10% RH) at 80 °C or at higher alkaline concentrations ([KOH] > 1 M). A ring-opening degradation pathway was suggested for the imidazolium cation based on a detailed analysis of the NMR spectra (Scheme 11).

Downloaded by OHIO STATE UNIV LIBRARIES on June 14, 2012 | http://pubs.acs.org
Publication Date (Web): May 7, 2012 | doi: 10.1021/bk-2012-1096.ch014

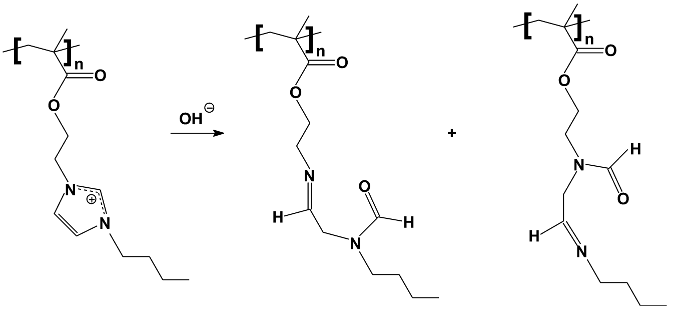

Scheme 11. Degradation of imidazolium-based AEMs (33)

Downloaded by OHIO STATE UNIV LIBRARIES on June 14, 2012 | http://pubs.acs.org
Publication Date (Web): May 7, 2012 | doi: 10.1021/bk-2012-1096.ch014

The enhanced chemical stability of the imidazolium-based AEM was largely attributed to the steric hindrance and the presence of the π conjugated structure that reduce the S_N2 and Hofmann elimination reactions. Furthermore, the deprotonation of a 1,3-alkyl-substituted imidazolium hydroxide can result in a relatively stable carbene. For example, stable imidazolium-based carbenes, such as 3-bis(adamantyl)imidazol-2-ylidene have been synthesized and isolated by others (*67*). It was reported that carbenes with large bulky substitutes are even more stable, and more importantly, the stable alkyl-substituted carbenes resulting from deprontonation can be reversely protonated by water (*68*). As a comparison, deprotonation of the tetraalkyl quaternary ammonium cation has been shown to result in the formation of a relatively unstable ylide intermediate and the ylide intermediate undergoes further degradation through direct degradation (Scheme 6) and/or ylide rearrangements, such as Stevens rearrangement (Scheme 4) and Sommelet-Hauser rearrangement (Scheme 5).

The stable structure of imidazolium cations has also been demonstrated with a number of hydroxide-based ionic liquids (ILs) that have been synthesized and dried for use as catalysts (i.e., stable under dry conditions), such as 1-butyl-3-methylimidazolium hydroxide (*69*) and 1-butyl-2,3-dimethylimidazolium hydroxide (*70*). As a comparison, ammonium counterparts, such as tetrabutylammonium hydroxide, are commercially available, but always stored in a liquid form at a low concentration (< 40 wt %) (i.e., requires solvation for stability) (*71*).

In contrast to the work on ammonium and phosphonium cations, the chemical stability of small molecule imidazolium cations is relatively scarce. The degradation of purines, compounds that consist of a pyrimidine ring fused to an imidazole ring, appears to be the only relevant work reported. For example, several studies (*72*, *73*) reported that 7-methylguanosine undergoes ring-opening reactions in a strong aqueous base due to a nucleophilic attack by the hydroxide anion (Scheme 12). One characteristic of the ring opening reaction is the formation of isomer products since there are two possible sites available in the imidazolium ring. This study showed the formation of isomers, which agrees with literature (*74*, *75*).

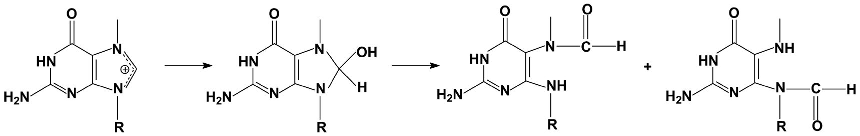

Scheme 12. *Ring opening reaction of 7-methylguanosine under alkaline conditions (75)*

Chemical Stability of Pyridinium-Based AEMs

There are a few studies on pyridinium-based AEMs (*76–80*). However, only several of these were for the application of the AFC (*78*, *79*). Xiao et al. (*78*) synthesized a copolymer of vinylpyridinium and styrene, which revealed high conductivity (0.8 mS/cm at 25 °C), but poor fuel cell performance. They attributed this to a possible chemical degradation of the AEM. Several studies indicate that the benzyltrimethylammonium cation may have better chemical stability than the pyridinium cation (*37*, *79*). The possible instability of the pyridinium cation may be attributed to the enhanced susceptibility for nucleophilic addition and displacement at the α- and γ-positions (Scheme 13) (*81*).

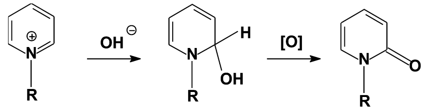

Scheme 13. *Degradation reaction of a pyridinium cation under alkaline conditions followed by oxidization (81).*

Chemical Stability of Other Cyclic Cation-Based AEMs

The incorporation of other cyclic cations such as quaternized 1,4-diazabicyclo(2,2,2)octane (DABCO), and piperidinium in AEMs has been also investigated in literature. Due to the chemical stability, the quaternized DABCO cation-based AEMs (*37*, *82*) has received relatively more attention. It was reported that both Hofmann elimination reaction and nucleophilic displacement reaction can be reduced due to the merit of the DABCO molecule (*37*). The absence of Hofmann elimination was attributed to internal steric constraints from an anti-periplanar conformation of C(β)-H and C(α)-N. Moreover, the second nitrogen atom in the para position, reduces the acidity of the molecule and thus reduces the effect of the positively charged nitrogen facing the hydroxide group.

The DABCO molecule process two amine groups and can be converted to either a mono-quaternized cation or a bis-quaternized ammonium cation. Bauer et al. indicated that the mono-quaternized one was much more stable ($t_{1/2}$ = 42 min) than the bis-quaternized DABCO-based polymer ($t_{1/2}$ = 2.3 min) in 2M KOH at 160 °C under nitrogen atmosphere. The higher degradation rate of bis-quaternized DABCO was attributed to a rapid elimination according to the

Downloaded by OHIO STATE UNIV LIBRARIES on June 14, 2012 | http://pubs.acs.org
Publication Date (Web): May 7, 2012 | doi: 10.1021/bk-2012-1096.ch014

monomolecular E1 mechanism. For the degradation pathways, mono-quaternized DBCO undergoes a nucleophilic displacement reaction (Scheme 14), while the bis-quaternized DABCO cations convert into a piperazine structure (Scheme 15).

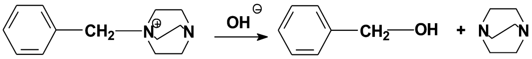

Scheme 14. Degradation reaction of a mono-quaternized DABCO cation under alkaline conditions (37).

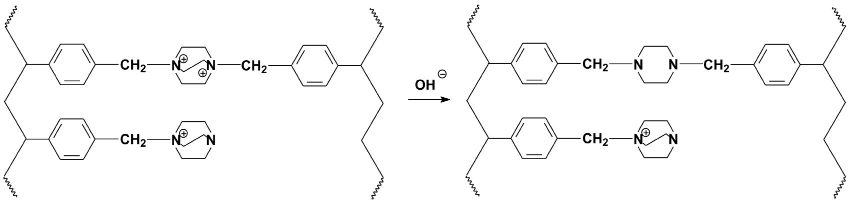

Scheme 15. Degradation reaction of a bis-quaternized DABCO cation under alkaline conditions (37).

Recent patented work (*36*) showed the IEC of the piperidinium-cation based AEMs can be well retained (> 90%) even at a high temperature (80 °C) in a strong alkaline condition (~ 1.8 M KOH). However, more investigation is needed to better understand the chemical stability of piperidium cation.

Chemical Stability of AEM Polymer Backbones

The alkaline chemical stability of the polymer backbone in AEMs should also be considered. However, studies on AEM polymer backbone chemical stability have received less attention compared to the cation since it is generally assumed that it is more stable than the cation. Previous studies indicated that backbone instability can largely be related to an attack by the hydroxide anion (*9*, *83*) or oxygen (*38*). For example, Slade et al. observed decreased CH_2 signal and decreased nitrogen signal from ^{13}C $\{^1H\}$ and ^{15}N $\{^1H\}$ cross polarization and magic angle spinning (CP-MAS) NMR spectra, which was due to the degradation of the poly(vinylidene fluoride) (PVDF) backbone (*9*, *76*). This instability in alkaline conditions was attributed to the attack of OH^-, which resulted in an E2 elimination (Scheme 16). Other studies showed that the byproduct can undergo further degradation reactions, such as hydroxylation and carbonyl formation (*84*). In the presence of oxidants, the styrenic backbone may undergo oxidization and form carboxylic acid (Scheme 17) (*15*).

In Polymers for Energy Storage and Delivery: Polyelectrolytes for Batteries and Fuel Cells; Page, K., et al.; ACS Symposium Series; American Chemical Society: Washington, DC, 2012.

Downloaded by OHIO STATE UNIV LIBRARIES on June 14, 2012 | http://pubs.acs.org
Publication Date (Web): May 7, 2012 | doi: 10.1021/bk-2012-1096.ch014

Downloaded by OHIO STATE UNIV LIBRARIES on June 14, 2012 | http://pubs.acs.org
Publication Date (Web): May 7, 2012 | doi: 10.1021/bk-2012-1096.ch014

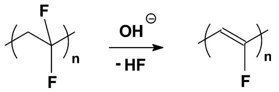

Scheme 16. Degradation of PVDF polymer backbone (1)

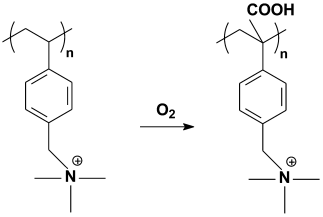

Scheme 17. Oxidization of polymer backbone (15)

Conclusions

In summary, the chemical stability of AEMs poses a critical challenge that limits the wide scale use of AFCs. This instability stems from the highly nucleophilic and basic nature of the hydroxide anion. All covalently attached conducting cation groups that have been studied thus far are prone to some level of degradation by OH^- attack, particularly at high alkaline concentrations and high temperatures. Generally, ammonium has shown better chemical stability compared to phosphonium and sulfonium, while heterocyclic cations, such as imidazolium, can enhance the chemical stability compared to non-cyclical cations due to their conjugated structure and steric hindrance.

Recent studies on the development of AEMs for the AFC have primarily focused on measuring changes in ion exchange capacity and ionic conductivity under certain conditions over a period of time to assess chemical stability. Among these studies, the ammonium cation has received the most attention. Although more recent studies have shown enhanced stability (e.g., imidazolium-based AEMs), a deep fundamental understanding of AEM chemical stability is still lacking. In the future, the same approach as in the investigation of small molecule organic cations should be applied to AEMs (e.g., the use of advanced characterization techniques, such as nuclear magnetic resonance and isotope labeling). For example, understanding the electron-withdrawing nature of *o*-, and *p*-methoxy groups in phosphonium-based AEMs (e.g., benzyltri(2,4,6-trimethoxyphenyl) phosphonium cation) could aid in the design of new AEMs with high chemical stability. Overall, more fundamental investigations on the chemical stability of AEMs will be beneficial in the design of chemically robust AEMs that could result in long-lasting, high-performing AFCs.

In Polymers for Energy Storage and Delivery: Polyelectrolytes for Batteries and Fuel Cells; Page, K., et al.;
ACS Symposium Series; American Chemical Society: Washington, DC, 2012.

Downloaded by OHIO STATE UNIV LIBRARIES on June 14, 2012 | http://pubs.acs.org
Publication Date (Web): May 7, 2012 | doi: 10.1021/bk-2012-1096.ch014

Acknowledgments

The authors gratefully acknowledge the U.S. Army Research Office for the financial support (grant W911NF-07-1 0452, Ionic Liquids in Electro-Active Devices (ILEAD) MURI).

References

1. Couture, G.; Alaaeddine, A.; Boschet, F.; Ameduri, B. *Prog. Polym. Sci.* **2011**, *36*, 1521.
2. Reid, J. H. U.S. Patent 736,016, 1903.
3. Varga, Á. In *Fuel cell electronics packaging*; Kuang, K., Easler, K., Eds.; Springer: New York, 2007; p 5.
4. Kordesch, K. V. In *Fuel Cells*; Mitchell, W., Jr., Ed.; Academic Press: New York, 1963; Vol. 1, pp 329−70.
5. Rolla, A.; Sadkowski, A.; Wild, J.; Zoltowski, P. *J. Power Sources* **1980**, *5*, 189.
6. Rikukawa, M.; Sanui, K. *Prog. Polym. Sci.* **2000**, *25*, 1463.
7. Grot, W. G. U.S. Patents 3,718,627, 1968; 3,969,285, 1976; 4,026,783, 1977; 4,030,988, 1977.
8. Agel, E.; Bouet, J.; Fauvarque, J. F. *J. Power Sources* **2001**, *101*, 267.
9. Danks, T. N.; Slade, R. C. T.; Varcoe, J. R. *J. Mater. Chem.* **2003**, *13*, 712.
10. Varcoe, J. R.; Slade, R. C. T. *Fuel Cells* **2005**, *5*, 187.
11. Yan, J.; Hickner, M. A. *Macromolecules* **2010**, *43*, 2349.
12. Jagur-Grodzinski, J. *Polym. Adv. Technol.* **2007**, *18*, 785.
13. Yu, E. H.; Krewer, U.; Scott, K. *Energies* **2010**, *3*, 1499.
14. Elabd, Y. A.; Hickner, M. A. *Macromolecules* **2011**, *44*, 1.
15. Merle, G.; Wessling, M.; Nijmeijer, K. *J. Membr. Sci.* **2011**, *377*, 1.
16. Zhou, J.; Ünlü, M.; Anestis-Richard, I.; Kohl, P. A. *J. Membr. Sci.* **2010**, *350*, 286.
17. Robertson, N. J.; Kostalik, H. A., IV; Clark, T. J.; Mutolo, P. F.; Abruña, H. D.; Coates, G. W. *J. Am. Chem. Soc.* **2010**, *132*, 3400.
18. Luo, Y.; Guo, J.; Wang, C.; Chu, D. *J. Power Sources* **2010**, *195*, 3765.
19. Thomas, O. D.; Soo, K. J. W. Y.; Peckham, T. J.; Kulkarni, M. P.; Holdcroft, S. *Polym. Chem.* **2011**, *2*, 1641.
20. Herman, H.; Slade, R. C. T.; Varcoe, J. R. *J. Membr. Sci.* **2003**, *218*, 147.
21. Komkova, E. N.; Stamatialis, D. F.; Strathmann, H.; Wessling, M. *J. Membr. Sci.* **2004**, *244*, 25.
22. Wu, Y.; Wu, C.; Xu, T.; Lin, X; Fu, Y. *J. Membr. Sci.* **2009**, *338*, 51.
23. Wang, G.; Weng, Y.; Chu, D.; Xie, D.; Chen, R. *J. Membr. Sci.* **2009**, *326*, 4.
24. Xu, H.; Fang, J.; Guo, M.; Lu, X.; Wei, X.; Tu, S. *J. Membr. Sci.* **2010**, *354*, 206.
25. Pan, J.; Lu, S.; Li, Y.; Huang, A.; Zhuang, L.; Lu, J. *Adv. Funct. Mater.* **2010**, *20*, 312.
26. Wang, J.; Wang, J.; Li, S.; Zhang, S. *J. Membr. Sci.* **2011**, *368*, 246.
27. Zhang, Q.; Zhang, Q.; Wang, J; Zhang, S.; Li, S. *Polymer* **2010**, *51*, 5407.

28. Guo, T.; Zeng, Q.; Zhao, C.; Liu, Q.; Zhu, A.; Broadwell, I. *J. Membr. Sci.* **2011**, *371*, 268.
29. Gu, S.; Cai, R.; Luo, T.; Chen, Z. W.; Sun, M. W.; Liu, Y.; He, G. H.; Yan, Y. S. *Angew. Chem., Int. Ed.* **2009**, *48*, 6499.
30. Guo, M.; Fang, J.; Xu, H.; Li, W.; Lu, X.; Lan, C.; Li, K. *J. Membr. Sci.* **2010**, *362*, 97.
31. Lin, B.; Qiu, L.; Lu, J.; Yan, F. *Chem. Mater.* **2010**, *22*, 6718.
32. Li, W.; Fang, J.; Lv, M.; Chen, C.; Chi, X.; Yang, Y.; Zhang, Y. *J. Mater. Chem.* **2011**, *21*, 11340.
33. Ye, Y.; Elabd, Y. A. *Macromolecules* **2011**, *44*, 5727.
34. Wang, J.; Li, S.; Zhang, S. *Macromolecules* **2010**, *43*, 3890.
35. Kim, D. S.; Kim, Y. S. *ECS Trans.* **2010**, *33*, 1867.
36. Daikoku, Y; Isomura, T.; Fukuta, K.; Yanagi, H.; Yamaguchi, M. Eur. Patent, EP 2,351,785 A1, 2011.
37. Bauer, B.; Tirathmann, H.; Effenberger, F. *Desalination* **1990**, *79*, 125.
38. Neagu, V.; Bunia, I.; Plesca, I. *Polym. Degrad. Stab.* **2000**, *70*, 463.
39. Zagorodni, A. A.; Kotova, D. L.; Selemenev, V. F. *React. Funct. Polym.* **2002**, *53*, 157.
40. Hofmann, A. W. *Philos. Trans. R. Soc., London* **1851**, *141*, 357.
41. Hofmann, A. W. *Proc. R. Soc. London* **1857**, *9*, 287.
42. Stevens, T. S.; Creighton, E. M.; Gordon, A. B.; MacNicol, M. *J. Chem. Soc.* **1928**, 3193.
43. Stevens, T. S. *J. Chem. Soc.* **1930**, 2107.
44. Johnstone, R. A. W.; Stevens, T. S. *J. Chem. Soc.* **1955**, 4487.
45. Puterbaugh, W. H.; Hauser, C. R. *J. Am. Chem. Soc.* **1964**, *86*, 1105.
46. Hauser, C. R.; Kantor, S. W. *J. Am. Chem. Soc.* **1951**, *73*, 1437.
47. Schöllkopf, U.; Ludwig, U.; Ostermann, G.; Patsch, M. *Tetrahedron Lett.* **1969**, *10*, 3415.
48. Sommelet, M. *Compt. Rend.* **1937**, *205*, 56.
49. Kantor, S. W.; Hauser, C. R. *J. Am. Chem. Soc.* **1951**, *73*, 4122.
50. Hauser, C. R.; Van Eenam, D. N. *J. Am. Chem. Soc.* **1957**, *79*, 5512.
51. Pine, S. H.; Sanchez, B. L. *Tetrahedron Lett.* **1969**, *10*, 1319.
52. Jones, F.; Hauser, C. R. *J. Org. Chem.* **1961**, *26*, 2979.
53. A. R. Lepley, A. R.; Becke, R. H. *Tetrahedron* **1965**, *21*, 2365.
54. Chempath, S.; Boncella, J. M.; Pratt, L. R.; Henson, N.; Pivovar, B. S. *J. Phys. Chem. C* **2010**, *114*, 11977.
55. Trostyanskaya, E. B.; Makarova, S. B. *Zhurnal Prikladnoi Khimii* **1966**, *39*, 1754.
56. Gu, S.; Cai, R.; Luo, T.; Jensen, K.; Contreras, C.; Yan, Y. *ChemSusChem* **2010**, *3*, 555.
57. Arges, C. G.; Kulkarni, S.; Baranek, A.; Pan, K.-J.; Jung, M.; Patton, D.; Mauritz, K. A.; Ramani, V. *ECS Trans.* **2010**, *33*, 1903.
58. Hofmann, A. W.; Cahours, A. *Philos. Trans. R. Soc., London* **1857**, *147*, 575.
59. Fenton, G. W.; Ingold, C. K. *J. Chem. Soc.* **1929**, 2342.
60. Hey, L.; Ingold, C. K. *J. Chem. Soc.* **1933**, 531.

Downloaded by OHIO STATE UNIV LIBRARIES on June 14, 2012 | http://pubs.acs.org
Publication Date (Web): May 7, 2012 | doi: 10.1021/bk-2012-1096.ch014

61. McEwen, W. E.; VanderWerf, C. A.; Zander, M. *J. Am. Chem. Soc.* **1959**, *81*, 3806.
62. Keldsen, G. L.; McEwen, W. E. *J. Am. Chem. Soc.* **1978**, *100*, 7312.
63. Wang, Z. *Comprehensive Organic Name Reactions and Reagents*, 1st ed.; Wiley-Interscience: 2009.
64. McEwen, W. E.; Axelrad, G.; Zanger, M.; VanderWerf, C. A. *J. Am. Chem. Soc.* **1965**, *87*, 3948.
65. Dewi, E. L.; Oyaizu, K.; Nishide, H.; Tsuchida, E. *J. Power Sources* **2003**, *115*, 149.
66. Kim, D. S.; Labouriau, A.; Guiver, M. D.; Kim, Y. S. *Chem. Mater.* **2011**, *23*, 3795.
67. Arduengo, A. J., III; Harlow, R. L.; Kline, M. *J. Am. Chem. Soc.* **1991**, *113*, 361.
68. Amyes, T. L.; Diver, S. T.; Richard, J. P.; Rivas, F. M.; Toth, K. *J. Am. Chem. Soc.* **2004**, *126*, 4366–4374.
69. Ranu, B. C.; Banerjee, S. *Org. Lett.* **2005**, *7*, 3049.
70. Mehnert, C. P.; Dispenziere, N. C.; Schlosberg, R. H. U.S. Patent 6,552,232, 2003.
71. Kagimoto, J.; Fukumoto, K.; Ohno, H. *Chem. Commun.* **2006**, 2254.
72. Hecht, S. M.; Adams, B. L.; Kozarich, J. W. *J. Org. Chem.* **1976**, *41*, 2303.
73. Chetsanga, C. J.; Bearie, B.; Makaroff, C. *Chem.-Biol. Interact.* **1982**, *41*, 235.
74. Smith, C. W.; Rasmussen, R. S.; Ballard, S. A. *J. Am. Chem. Soc.* **1949**, *71*, 1082.
75. Chetsanga, C. J.; Makaroff, C. *Chem.-Biol. Interact.* **1982**, *41*, 235.
76. Sata, T.; Yamane, Y.; Matsusaki, K. *J. Polym. Sci., Part A: Polym. Chem.* **1998**, *36*, 49.
77. Sata, T.; Tsujimoto, M.; Yamaguchi, T.; Matsusaki, K. *J. Membr. Sci.* **1996**, *112*, 161.
78. Huang, A.; Xia, C.; Xiao, C.; Zhuang, L. *J. Appl. Polym. Sci.* **2006**, *100*, 2248.
79. Hnát, J.; Paidar, M.; Schauer, J.; Žitka, J.; Bouzek, K. *J. Appl. Electrochem.* **2011**, *41*, 1043.
80. Kang, M.-S.; Choi, Y. J.; Moon, S. H. *AIChE J.* **2003**, *49*, 3213.
81. Joule, J. A.; Mills, K. *Heterocyclic Chemistry. Chapter 5. Pyridines: Reactions and Synthesis*, 4th ed.; 2000.
82. Altmeier, P. U.S. Patents 5,746,917, 1998; 5,936,004.
83. Danks, T. N.; Slade, R. C. T.; Varcoe, J. R. *J. Mater. Chem.* **2002**, *12*, 3371.
84. Ross, G. J.; Watts, J. F.; Hill, M. P.; Morrissey, P. *Polymer* **2001**, *42*, 403.

Downloaded by OHIO STATE UNIV LIBRARIES on June 14, 2012 | http://pubs.acs.org
Publication Date (Web): May 7, 2012 | doi: 10.1021/bk-2012-1096.ch014

Downloaded by OHIO STATE UNIV LIBRARIES on June 14, 2012 | http://pubs.acs.org
Publication Date (Web): May 7, 2012 | doi: 10.1021/bk-2012-1096.ch015

Chapter 15

Block Copolymers Containing Quaternary Benzyl Ammonium Cations for Alkaline Anion Exchange Membrane Fuel Cells (AAEMFC)

Tsung-Han Tsai,[a] Craig Versek,[b] Michael Thorn,[b] Mark Tuominen,[b] and E. Bryan Coughlin[a,*]

[a]Department of Polymer Science and Engineering, University of Massachusetts Amherst, 120 Governors Drive, Amherst, MA, USA 01003
[b]Department of Physics, University of Massachusetts Amherst, 411 Hasbrouck Laboratory, Amherst, MA 01003
***Corresponding author. Phone: +1 413-577-1616, Fax: +1 413-545-0082, E-mail: Coughlin@mail.pse.umass.edu**

Block copolymers of polystyrene-*b*-poly (vinylbenzyltrimethylammonium tetrafluoroborate) (PS-*b*-[PVBTMA][BF_4]) were synthesized by sequential monomer addition using atom transfer radical polymerization (ATRP). Block copolymers of polystyrene-b-poly (vinylbenzyltrimethylammonium hydroxide) (PS-b-[PVBTMA][OH]) was prepared as polymeric alkaline anion exchange membranes (AAEMC) materials by ion exchange from PS-b-[PVBTMA][BF_4] with hydroxide in order to investigate the morphology relationship to ion conductivity. Membranes of the block copolymers were made by drop casting from dimethylformamide. Initial evaluation of the microphase separation in these PS-*b*-[PVBTMA][BF_4] materials via SAXS revealed the formation of spherical, cylindrical and lamellar morphologies. Studies of humidity (RH)-dependent conductivity at 80°C showed that a strong effect of microstructures on conductivity. Moreover, the investigation of the temperature-dependent conductivity at RH = 50%, 70% and 90% showed a significant effect of grain boundaries in the membranes against the formation of continuous conductive channels which is an important requirement for achieving high ion conductivity.

In Polymers for Energy Storage and Delivery: Polyelectrolytes for Batteries and Fuel Cells; Page, K., et al.;
ACS Symposium Series; American Chemical Society: Washington, DC, 2012.

Downloaded by OHIO STATE UNIV LIBRARIES on June 14, 2012 | http://pubs.acs.org
Publication Date (Web): May 7, 2012 | doi: 10.1021/bk-2012-1096.ch015

Introduction

Fuel cells, which convert chemical energy to electrical energy through redox reactions have gained renewed attention for renewable energy devices because of their high efficiency, high energy density and low formation of pollutants (*1*, *2*). Among different types of fuel cells, the most well-developed is the proton exchange membrane fuel cell (PEMFC) containing sulfonic acid groups as ion transport moieties. Commercially available Nafion® (*3*), a perfluorosulfonic acid ionomer, has been widely used and investigated as a proton exchange membrane because of its good chemical stability, suitable mechanical properties and high proton conductivity. However, due to the high cost of the membranes and their need for noble metal (i.e. platinum) based electrocatalysts, the commercialization of PEMFCs is still limited. Additionally, oxygen reduction and fuel (hydrogen or alcohol) oxidation are sluggish under the cell's acidic condition, and the noble metal catalysts are easily poisoned by carbon monoxide at low temperature. These are serious obstacles to the extensive application of PEMFCs as energy devices (*4*).

Alkaline anion exchange membrane fuel cells (AAEMFCs) that can overcome these limitations are regarded as promising energy devices (*5*, *6*). An important advantage of AAEMFCs over PEMFCs is that the oxygen reduction and fuel oxidation overpotentials can be reduced leading to the use of non-noble metal catalysts (i.e. nickel and silver) and longer chain alcohol fuels. Moreover, metal catalysts are more resistant to corrosion under the cell's basic conditions. When using methanol as the fuel, issues with fuel crossover can be reduced because the hydroxide conduction direction is opposite to the methanol crossover direction.

The major challenge for AAEMFCs is the chemical durability of the polycation ion transport groups, and the polymeric backbone of the conductive membranes under alkaline condition. Benzyltrimethylammonium cations have been proven to be stable cations under basic condition because of the absence of β-hydrogen, preventing Hoffmann elimination (*7*). Recently, Varcoe and co-workers demonstrated radiation-grafted PVDF, ETFT and FEP containing polymeric benzyltrimethylammonium hydroxide ions for AAEMFCs (*8–11*). Additionally, chloromethylated poly(sulfone)s quaternized by treatment with trimethylamine are another popular type of AAEMFCs because of their good mechanical, thermal and chemical stability (*12–14*). Brominated benzylmethyl-containing poly(sulfone)s for AAEMFCs investigated by Hickner's group avoid the chloromethylation which is known to be a toxic and carcinogenic process (*15*). Cross-linked tetraalkylammonium-functionalized polyethylenes have been synthesized by ring opening metathesis copolymerization of tetraalkylammonium-functionalized cyclooctenes copolymerization with unfunctionalized cyclooctenes (*16*). These cross-linked structures provide good mechanical properties and allow higher incorporation of ion conductive groups. Until now, all of the studies on AAEMFCs have been based on random copolymers containing conductive polycation moieties.

Microphase separation in block copolymers can provide versatile platforms for the fabrication of nanostructure materials with a wide range of morphologies such as cylinders, lamellas and gyroids (*17*, *18*). Polymeric conductive membranes made from block copolymers can provide more well-oriented and

Downloaded by OHIO STATE UNIV LIBRARIES on June 14, 2012 | http://pubs.acs.org
Publication Date (Web): May 7, 2012 | doi: 10.1021/bk-2012-1096.ch015

continuous conductive microdomain to enhance ion conductivity than membranes made from random copolymers. Because of the presence of the hydrophobic domain in the membranes, the mechanical strength can be enhanced and enables the incorporation of more ion conductive groups (higher ion exchange capacity). Several studies about structure-morphology-property relationships of block copolymers for PEM have shown that the morphology of the conductive membranes strongly influences their proton conductivity (*19–25*). However, fundamental investigation about the relationship between morphology and conductivity in AAEM made from well-defined block copolymer is still lacking.

In the present work, we synthesized block copolymers of polystyrene-*b*-poly (vinylbenzyltrimethylammonium tetrafluoroborate) (PS-*b*-[PVBTMA][BF_4]) via sequential monomer addition atom transfer radical polymerization (ATRP). Polystyrene-*b*-poly (vinylbenzyltrimethylammonium hydroxide) (PS-*b*-[PVBTMA][OH]) was subsequently prepared by ion exchange with hydroxide to produce the AAEMFC materials. Conductivity measurements were made using impedance spectroscopy to better understand the fundamental relationships between the morphology and conductivity of the materials.

Experimental

Materials

Styrene (>99%, Aldrich) was passed through a column of basic alumina. Anhydrous N,N-dimethylformamide (DMF) (99.8%, Alfa Aesar), (vinylbenzyl)trimethylammonium chloride [VBTMA][Cl] (99%, Aldrich), sodium tetrafluoroborate ($NaBF_4$) (97%, Alfa Aesar), copper(I) bromide (CuBr) (99.999%, Aldrich), (1-bromoethyl)benzene (97%, Alfa Aesar) and 1,1,4,7,10,10-hexamethyltriethylenetetramine (HMTETA) (97%, Aldrich) were used as received. All solvents were of ACS grade.

Characterizations

^{1}H-NMR spectroscopy was performed on a Bruker DPX-300 FT-NMR. Gel permeation chromatography (GPC) was performed in THF on a Polymer Laboratories PL-GPC 50 Integrated GPC system. Infrared spectroscopy was performed on a Perkin-Elmer Spectrum 100 FTIR spectrometer with universal ATR sampling accessory. SAXS experiments were performed at the synchrotron X-ray beamline X27C at the National Synchrotron Light Source (NSLS) in Brookhaven National Laboratory (BNL). The wavelength of the X-ray beam was 0.1366 nm. A MAR CCD X-ray detector (MAR) was used to collect the 2D SAXS patterns. The scattering angle of the SAXS pattern was calibrated using silver docosanoate.

Conductivity Measurement

Ion conductivity measurements were made by employing impedance spectroscopy using custom electrode assemblies and automation software within

Downloaded by OHIO STATE UNIV LIBRARIES on June 14, 2012 | http://pubs.acs.org
Publication Date (Web): May 7, 2012 | doi: 10.1021/bk-2012-1096.ch015

the humidity and temperature controlled environment of an ESPEC SH-241 test chamber. The free standing membrane samples of irregular areas were lightly compressed between two gold-plated stainless steel electrodes, the top having an area of A=0.07917 cm^2 (1/8 inch diameter) and bottom having a 1/2 inch diameter, such that there was exposed material on the top surface. The impedance spectra were sampled at regular intervals of 20 minutes using a Solartron 1260 Impedance/Gain Phase Analyzer over a range of 10 MHz to 0.1Hz in logarithmic steps of 10 points per decade; the portion of each spectrum forming a "plateau" in the impedance magnitude and corresponding to the first local phase minimum nearest the low frequency range was fitted to a constant magnitude function and interpreted as the bulk resistance R to ion transport within the membrane. The thickness t of each membrane was measured with a micrometer and effective area for the conductance measurement was estimated as the area of the smaller top electrode A, so that conductivity was computed as conductivity (σ) = t/(A*R). The thickness of the membranes are 189μm, 242μm and 310μm for PS-b-[PVBTMA][BF_4]-1 to 3 respectively.

Ion Exchange of Vinylbenzyltrimethylammonium Tetrafluoroborate [VBTMA][BF_4]

The ion exchange of [VBTMA][Cl] was performed as previously reported (*26*). [VBTMA][Cl] (2.2 g, 10.39 mmol) and $NaBF_4$(1.255 g, 11.43 mmol) were dissolved in 200 ml acetonitrile and stirred at ambient temperature overnight. The solution was filtered, and the filtrate was concentrated. White crystals were obtained by precipitation in anhydrous diethyl ether and then dried in vacuum at 40 °C.

Synthesis of Poly(vinylbenzyltrimethylammonium tetrafluoroborate) ([PVBTMA][BF_4]) by ATRP

Nitrogen purged DMF (2 ml), (1-bromoethyl)benzene (7.03 mg, 0.038 mmol) and HMTETA (8.75 mg, 0.038 mmol) were added to a Schlenk tube containing a mixture of [VBTMA][BF_4] (1g, 3.8 mmol) and copper(I) bromide (5.45 mg, 0.038 mmol). The mixture was put under vacuum and refilled with nitrogen 3 times. The mixture was degassed by 3 freeze-pump-thaw cycles followed by stirring at 90 °C. Aliquot samples were taken and analyzed to determine conversion of the reaction by ^{1}H-NMR.

Synthesis of Polystyrene (PS-Br) by ATRP

The polymerization of styrene was performed as reported in the literature (*27*). Styrene (36.36 g, 348.8 mmol) was added to a Schlenk tube containing a mixture of CuBr (74.5 mg, 0.519 mmol), (1-bromoethyl)benzene (99.0 mg, 0.519 mmol) and HMTETA (119.6 mg, 0.519 mmol). The mixture was degassed by 3 freeze-pump-thaw cycles followed by stirring at 110 °C for 5h. After polymerization, the reaction solution was quenched in an ice bath then passed through a pad of basic

In Polymers for Energy Storage and Delivery: Polyelectrolytes for Batteries and Fuel Cells; Page, K., et al.;
ACS Symposium Series; American Chemical Society: Washington, DC, 2012.

alumina to remove the copper catalyst and, precipitated in methanol three times to obtain polystyrene as a white powder.

Synthesis of PS-*b*-[PVBTMA][BF$_4$] by ATRP

Nitrogen purged DMF (4 ml) and HMTETA (4.6 mg, 0.05 mmol) were added to a Schlenk tube containing a mixture of PS-Br (700 mg, M_n=35 kg/mol), [VBTMA][BF$_4$] (700 mg, 2.67 mmol) and copper(I) bromide (2.86 mg, 0.02 mmol). The mixture was degassed by 3 freeze-pump-thaw cycles followed by stirring at 90°C. The polymer was precipitated into methanol.

Membranes Preparation of PS-*b*-[PVBTMA][BF$_4$]

PS-*b*-[PVBTMA][BF$_4$] membranes were drop cast from DMF (10 wt% solution) onto a Teflon sheet. The membranes were first dried at ambient temperature, and then under vacuum at 40 °C.

Ion Exchange of PS-*b*-[PVBTMA][OH]

PS-*b*-[PVBTMA][BF$_4$] membranes were soaked in 1M KOH aqueous solution for 3 days. The solution was changed several times, then the membranes were immersed in water for 1day.

Result and Discussion

Synthesis of PS-*b*-[PVBTMA][BF$_4$]

Amphiphilic block copolymers PS-*b*-[PVBTMA] have been synthesized by quaternization with trimethylamine of polystyrene-*b*-polyvinyl benzyl chloride (PVBCl) synthesized by sequential stable free radical polymerization (SFRP) (*28*). However, complete conversion of the quaternization was difficult to achieve, and the polycation block was a random copolymer, [PVBTMA]-ran-PVBCl. Therefore, in order to obtain a ture block copolymer PS-*b*-[PVBTMA][OH], we synthesized PS-*b*-[PVBTMA][BF$_4$] first by sequential ATRP in DMF followed by ion exchange with hydroxide because PS and [PVBTMA][BF$_4$] are soluble in DMF. First, the ATRP of [PVBTMA][BF$_4$] was investigated to confirm its living character. As shown in Scheme 1, [VBTMA][BF$_4$] was made by ion exchange from commercially available [VBTMA][Cl], then polymerized by ATRP catalyzed by a CuBr/HMTETA complex at 90 °C. The linear increase of conversion versus time (shown in Figure 1a) was observed when the conversion was kept below 50%. Conversion reaches a plateau at 50% probably due to the poor solubility of the highly concentrated polymer chains in the reaction mixture. The ^{1}H-NMR spectra in Figure 1b confirmed the presence of [PVBTMA][BF$_4$] resonances.

Downloaded by OHIO STATE UNIV LIBRARIES on June 14, 2012 | http://pubs.acs.org
Publication Date (Web): May 7, 2012 | doi: 10.1021/bk-2012-1096.ch015

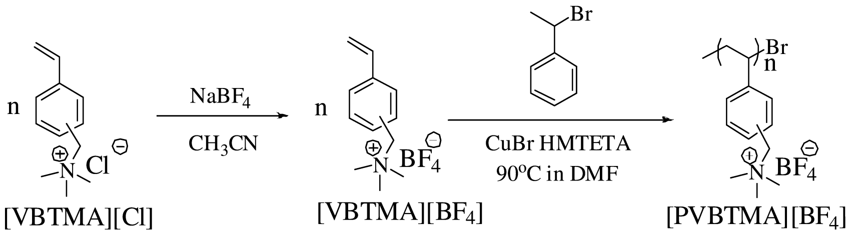
n
NaBF4
CH3CN
n
Br
CuBr HMTETA
90°C in DMF
Br
n
Cl
BF4
BF4
[VBTMA][Cl]
[VBTMA][BF4]
[PVBTMA][BF4]

Scheme 1. Synthesis of poly (vinylbenzyltrimethylammonium tetrafluoroborate) [PVBTMA][BF_4] homopolymers.

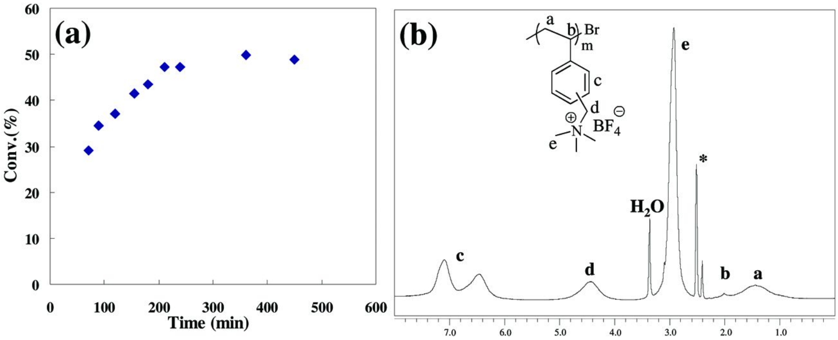

Figure 1. (a) Time dependence of conversion for polymerization of [VBTMA][BF_4] by ATRP. [[VBTMA][BF_4]]$_0$/[initiator]$_0$/[CuBr]$_0$/[HMTETA]$_0$ = 100:1:1:1, [[VBTMA][BF_4]] = 1.9M. (b) ^{1}H-NMR spectra of [PVBTMA][BF_4] in DMSO-d_6.

Downloaded by OHIO STATE UNIV LIBRARIES on June 14, 2012 | http://pubs.acs.org
Publication Date (Web): May 7, 2012 | doi: 10.1021/bk-2012-1096.ch015

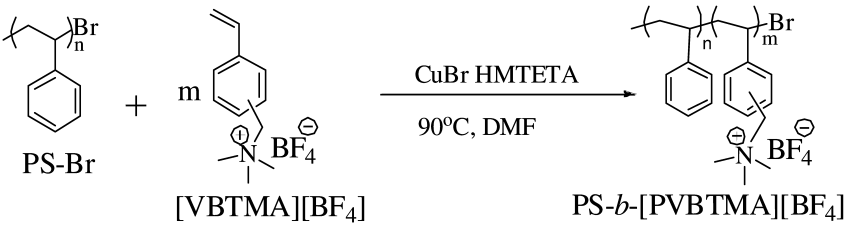
Br
n
PS-Br
+
m
BF4
[VBTMA][BF4]
CuBr HMTETA
90°C, DMF
n
Br
m
BF4
PS-b-[PVBTMA][BF4]

Scheme 2. Synthesis of poly (styrene-b-vinylbenzyltrimethylammonium tetrafluoroborate) PS-b- [PVBTMA][BF_4] block copolymers.

The synthetic route for PS-*b*-[PVBTMA][BF_4] is shown in Scheme 2. PS-Br materials with M_n = 35 kg/mol and dispersity (Đ) = 1.13 were synthesized via ATRP catalyzed by a CuBr/HMTETA complex. PS-*b*-[PVBTMA][BF_4] materials were synthesized by a chain extension ATRP of [VBTMA][BF_4] using the PS-Br as macroinitiator in DMF at 90°C (Table I). After the copolymerization, aliquots of solution were analyzed by ^{1}H-NMR in DMSO-d_6 to measure the conversion of the polymerization. The M_n of the [PVBTMA][BF_4], and the composition and ion exchange capacity (IEC) of PS-*b*-[PVBTMA][BF_4] were calculated based on the conversion. The Đ and M_n of the resulting block copolymers cannot be readily measured by GPC due to lack of a suitable solvent systems to serve as the eluent.

Table I. Samples of PS-*b*-[PVBTMA][BF_4]

Sample	*Starting Polystyrene*					
	M_n[a] (kg/mol)	*Đ[a]*	*Conv.[b] (%)*	*M_n of [PVBTMA]-[BF_4][c]*	*PS mole%*	*IEC[d] (meq/g)*
PS-*b*-[PVBTMA][BF_4]-1	35.0	1.13	56.2	19659	64	1.36
PS-*b*-[PVBTMA][BF_4]-2	35.0	1.13	35.7	16065	68	1.19
PS-*b*-[PVBTMA][BF_4]-3	35.0	1.13	15.7	6280	84	0.58

[a] M_n and Đ of PS were measured by GPC versus narrow linear PS standards. [b] The conversion was calculated by ^{1}NMR spectra of reaction mixture after copolymerization in DMSO-d_6. [c] M_n of [PVBTMA][BF_4] was calculated by the conversion. [d] Ion exchange capacity (IEC) of the samples were calculated from the composition ratio between PS and [PVBTMA][BF_4].

The ^{1}H-NMR spectra (Figure 2) of PS-*b*-[PVBTMA][BF_4]-2 in DMF-d_7 confirmed the presence of the quaternary ammonium group in [PVBTMA][BF_4] block with the methylene resonances (d) at δ = 4.3 ppm and the methyl group (e) adjacent to the quaternary ammonium resonances at δ = 3.1 ppm.

Morphology Studies on the PS-*b*-[PVBTMA][BF_4] by SAXS

Originally, the membranes of the PS-*b*-[PVBTMA][BF4] were made by drop casting from dichloromethane (DCM), chloroform, tetrahydrofuran and dimethylformamide (DMF). Small angle X-ray scattering experiments were performed at room temperature to determine the self-assembly behavior these of PS-b-[PVBTMA][BF_4] membranes. SAXS data (log (I) vs q) for the membranes cast from different solvents show that scattering from the membranes cast from DMF, a good solvent for both blocks, show a lower degree of order. On the contrary, SAXS data for the membranes cast from DCM, a selective solvent for the PS; showed distinctly higher order peaks. Therefore, well-defined membrane morphologies can be obtained by choosing a selective solvent to drop cast the

Downloaded by OHIO STATE UNIV LIBRARIES on June 14, 2012 | http://pubs.acs.org
Publication Date (Web): May 7, 2012 | doi: 10.1021/bk-2012-1096.ch015

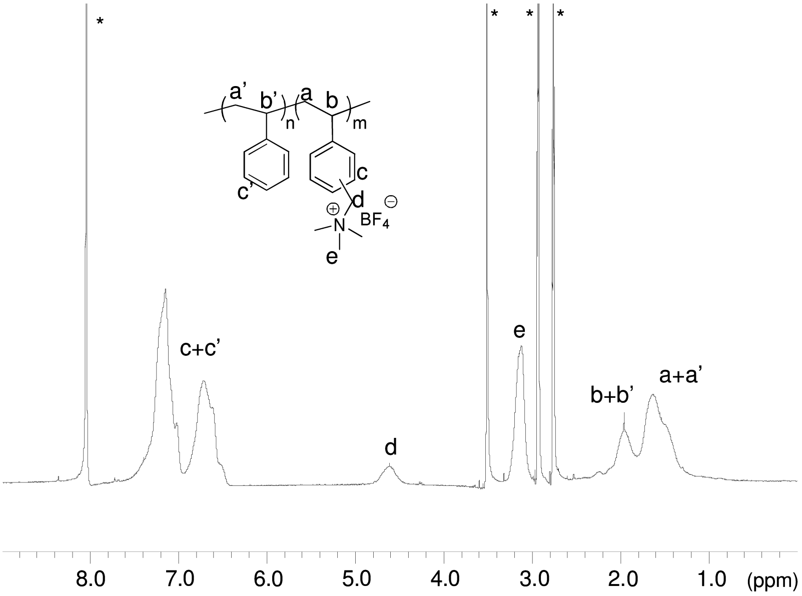

Figure 2. ^{1}H-NMR spectrum of PS-b-[PVBTMA][BF$_4$]-2 in DMF-d$_7$.

membranes. However, the ion exchange to hydroxide anion for the membranes made by drop casting from DCM failed. This may have occurred because PS-*b*-[PVBTMA][BF$_4$] forms micelle like structures (with PS as corona and [PVBTMA][BF$_4$] as core) in DCM, disturbing the formation of continuous ion conductive channels when drop casting the membranes from DCM. Membranes from DMF, while less ordered, undergo successful conversion to the hydroxide counter ion.

SAXS data of different PS-*b*-[PVBTMA][BF$_4$] samples are shown in Figure 3. For samples PS-*b*-[PVBTMA][BF$_4$]-1 and 2, the SAXS data shows two scattering peaks at q* and 2q*, making it difficult to determine the actual morphology of the membranes. However, the SAXS data confirm the existence a degree of orientation (cylinders or lamellas) in these membranes. The larger d-spacing of sample PS-*b*-[PVBTMA][BF$_4$]-1 and 2 (around 46 nm) compared to sample PS-*b*-[PVBTMA][BF$_4$]-3 (28.8 nm) is due to the phase transition to spherical morphology, which is supported by presumably decreasing [PVBTMA][BF$_4$] content from sample 1 to 3.

Ion Exchange for PS-b-[PVBTMA][BF$_4$]

In order to determine the conversion of ion exchange, these membranes were characterized by FTIR. Figure 4 shows the FTIR spectrum of PS-*b*-[PVBTMA][BF$_4$] before and after ion exchange in 1M KOH aqueous solution for 3 days. The disappearance of the characteristics band at 1048cm^{-1} corresponding to the tetrafluoroborate anion and the presence of the characteristic signal of hydroxide anion (O-H stretching at around 3500 cm^{-1}) indicates complete ion exchange.

Downloaded by OHIO STATE UNIV LIBRARIES on June 14, 2012 | http://pubs.acs.org
Publication Date (Web): May 7, 2012 | doi: 10.1021/bk-2012-1096.ch015

Downloaded by OHIO STATE UNIV LIBRARIES on June 14, 2012 | http://pubs.acs.org
Publication Date (Web): May 7, 2012 | doi: 10.1021/bk-2012-1096.ch015

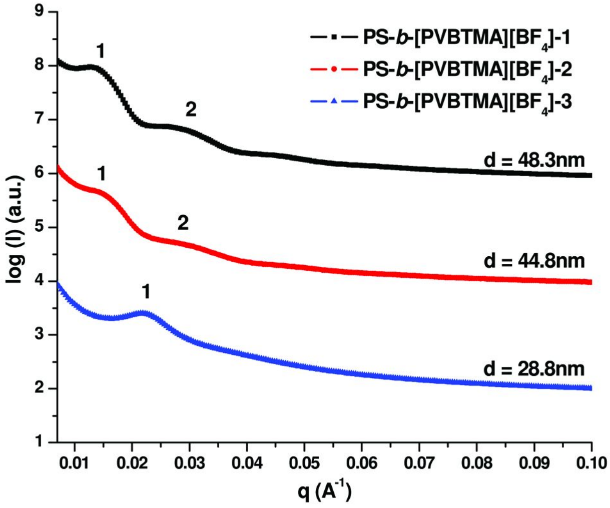

Figure 3. SAXS profiles for PS-b-[PVBTMA][BF$_4$] membranes cast from DMF.

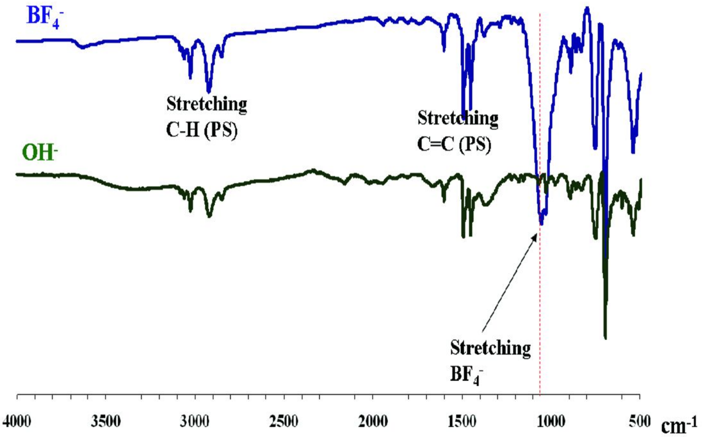

Figure 4. FTIR spectra for the PS-b-[PVBTMA][BF$_4$]-2 membrane (upper trace) and the PS-b-[PVBTMA][OH]-2 membrane (lower trace).

Morphology-Conductivity Relationships

The humidity-dependent conductivity of PS-b-[PVBTMA][OH] membranes at 80 °C are shown in Figure 5. From the log conductivity versus humidity plot, the conductivity increase with increasing humidity for all three samples because water uptake in the membrane facilitates ion conduction. Additionally, the conductivity increase with increasing IEC of the materials (from PS-b-[PVBTMA][OH]-3, IEC = 0.58 meq/g to PS-b-[PVBTMA][OH]-1, IEC = 1.36 meq/g); however, it does not increase proportionally. The conductivity increase 4-fold (0.36 mS/cm to

12.5mS/cm) at RH = 90% and approximately 5-fold (0.05mS/cm to 0.23mS/cm) at RH = 30% when IEC change from 0.57 meq/g to 1.36 meq/g. This unexpected relationship between conductivity and IEC may result from inherent types of microstructures in the materials. For PS-*b*-[PVBTMA][OH]-3 (IEC = 0.58 meq/g), self-assembly into spherical morphology which is a inferior structure for ion conduction compared to PS-*b*-[PVBTMA][OH]-1 that formed a cylindrical or a lamellar microstructure.

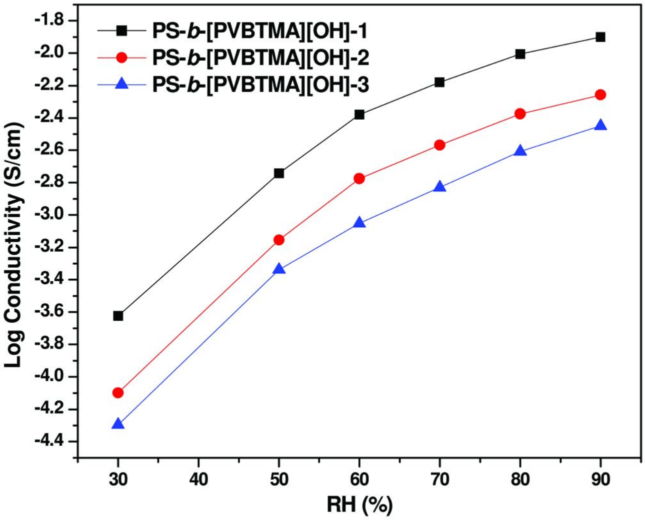

Figure 5. Humidity (RH)-dependent conductivity for PS-b-[PVBTMA][OH] membranes at 80°C.

Conductivity data as a function of temperature of PS-*b*-[PVBTMA][OH] membranes at different humidity conditions are shown Figure 6. The ion conductivity of these there samples increase with elevated temperature at humidity levels of 50%, 70% and 90%. As shown in Figure 6a, the conductivity of PS-b-[PVBTMA][OH]-1 and -2 are higher then that of [PVBTMA][OH]-3 at temperature above 45°C, so-called refraction temperature, because of higher IEC leading to higher conductivity. The conductivity among these samples follow a reverse order at temperature below 45 °C. This unexpected behavior may result from a grain boundary effect of the PS-*b*-[PVBTMA][OH]-1 and -2 at temperature below 45 °C. The PS-*b*-[PVBTMA][OH]-1 and -2 self-assemble into cylindrical or lamellar microstructure having grain boundaries at room temperature because of poor order SAXS pattern shown in Figure 3. At temperatures below 45 °C and humidity 50%, the existence of grain boundaries may hinder the ion transport resulting in low conductivity. These grain boundaries in sample PS-*b*-[PVBTMA][OH]-1 and -2 are broken to generate a more continuous conductive channels when temperature is above 45°C as a consequence of water swelling in the membranes at higher temperature. Because

Downloaded by OHIO STATE UNIV LIBRARIES on June 14, 2012 | http://pubs.acs.org
Publication Date (Web): May 7, 2012 | doi: 10.1021/bk-2012-1096.ch015

Downloaded by OHIO STATE UNIV LIBRARIES on June 14, 2012 | http://pubs.acs.org
Publication Date (Web): May 7, 2012 | doi: 10.1021/bk-2012-1096.ch015

the PS-*b*-[PVBTMA][OH]-3 sample exhibit spherical morphology, the conductive channels are built by the stacking of spherical [PVBTMA][OH] domains which are less influenced by the grain boundaries and increasing temperature. Moreover, the refraction temperature at 70% humidity (35°C, shown in Figure 6b) is lower than that at humidity 50% (45 °C, shown in Figure 6a) because more water swelling of the membrane at humidity 70% than at humidity 50% facilitates the elimination of grain boundaries.

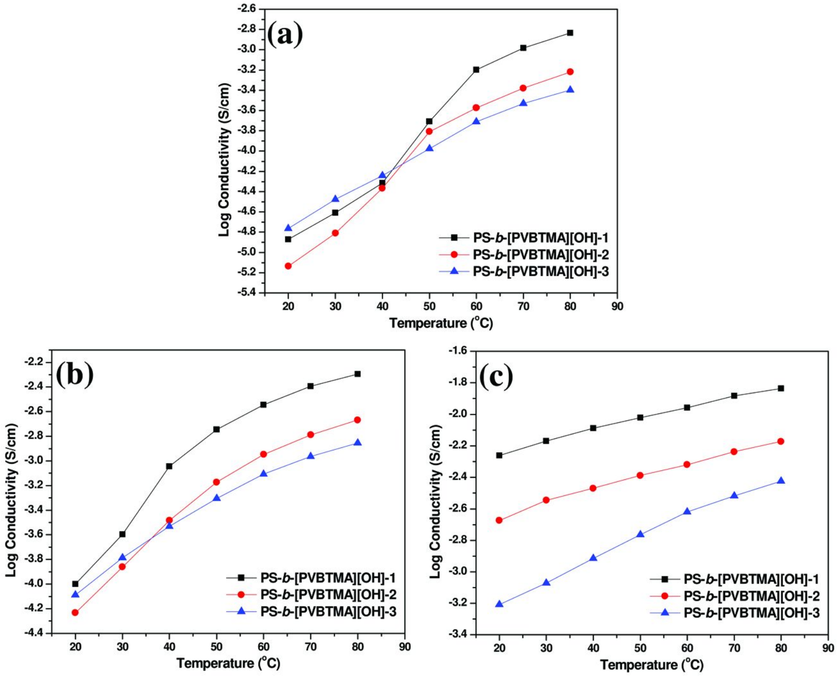

Figure 6. Temperature-dependent conductivity for PS-b-[PVBTMA][OH] membranes at (a) RH = 50%, (b) RH = 70% and (c) RH = 90%.

Conclusions

In this study, block copolymers PS-*b*-[PVBTMA][OH] were synthesized by sequential monomer addition ATRP of styrene and [VBTMA] [BF_4] followed by anion exchange from tetrafluoroborate counter anion to hydroxide anion. The total disappearance of the characteristics stretching band of tetrafluoroborate anion indicated the complete conversion of ion exchange. Microphase separation of the PS-*b*-[PVBTMA][BF_4] samples into spherical, cylindrical or lamellar microstructure were determined by SAXS. The investigation of humidity (RH)-dependent conductivity at 80 °C showed that the conductivity increase with increasing humidity due to water uptake in the membrane facilitating ion conduction. Additionally, the non-linearly increasing conductivity (12.5

mS/cm to 3.5 mS/cm at RH = 90%) with increasing IEC of the materials (from PS-*b*-[PVBTMA][OH]-3, IEC = 0.58 meq/g to PS-*b*-[PVBTMA][OH]-1, IEC = 1.36 meq/g) may result from the different types of microstructures formed in the materials. Moreover, the temperature-dependent conductivity at RH = 50%, 70% and 90% showed that the ion conductivity of these three samples increase with elevated temperature. The conductivity of PS-*b*-[PVBTMA][OH]-1 and -2 are higher then that of [PVBTMA][OH]-3 at temperatures above 45°C because of higher IEC leading to higher conductivity. The conductivity among these samples follow a reverse order at temperature below 45 °C. This unexpected behavior may result from the presence of grain boundary effect on the PS-*b*-[PVBTMA][OH]-1 and -2 samples at temperature below 45 °C. From the above observations, we concluded that it is crucial for achieving high conductivity of AAEM made by block copolymers to self-assemble into the well-connected and defect-free lamellar or cylindrical microstructures.

Downloaded by OHIO STATE UNIV LIBRARIES on June 14, 2012 | http://pubs.acs.org
Publication Date (Web): May 7, 2012 | doi: 10.1021/bk-2012-1096.ch015

Acknowledgments

Funding was provided by the US Army MURI on Ion Transport in Complex Heterogeneous Organic Materials (W911NF-10-1-0520). Partial support was provided by the National Science Foundation Center for Hierarchical Manufacturing (CMMI-1025020) and an IGERT program (DGE-0504485) The SAXS synchrotron X-ray beamline X27C at the National Synchrotron Light Source (NSLS) in Brookhaven National Laboratory (BNL) is supported by the Department of Energy. We thank Zhao Wei and Professor T. P. Russell for help with SAXS experiments.

References

1. Carrette, L.; Friedrich, K. A.; Stimming, U. *Fuel Cells* **2001**, *1* (1), 5–39.
2. Steele, B. C. H.; Heinzel, A. *Nature* **2001**, *414* (6861), 345–352.
3. Diat, O.; Gebel, G. *Nat. Mater.* **2008**, *7* (1), 13–14.
4. Borup, R.; Meyers, J.; Pivovar, B.; Kim, Y. S.; Mukundan, R.; Garland, N.; Myers, D.; Wilson, M.; Garzon, F.; Wood, D.; Zelenay, P.; More, K.; Stroh, K.; Zawodzinski, T.; Boncella, J.; McGrath, J. E.; Inaba, M.; Miyatake, K.; Hori, M.; Ota, K.; Ogumi, Z.; Miyata, S.; Nishikata, A.; Siroma, Z.; Uchimoto, Y.; Yasuda, K.; Kimijima, K.-i.; Iwashita, N. *Chem. Rev.* **2007**, *107* (10), 3904–3951.
5. Couture, G.; Alaaeddine, A.; Boschet, F.; Ameduri, B. *Prog. Polym. Sci.* **2011**, *36* (11), 1521–1557.
6. Varcoe, J. R.; Slade, R. C. T. *Fuel Cells* **2005**, *5* (2), 187–200.
7. Sata, T.; Tsujimoto, M.; Yamaguchi, T.; Matsusaki, K. *J. Membr. Sci.* **1996**, *112* (2), 161–170.
8. Danks, T. N.; Slade, R. C. T.; Varcoe, J. R. *J. Mater. Chem.* **2003**, *13* (4), 712–721.
9. Herman, H.; Slade, R. C. T.; Varcoe, J. R. *J. Membr. Sci.* **2003**, *218* (1−2), 147–163.

10. Varcoe, J. R.; Slade, R. C. T. *Electrochem. Commun.* **2006**, *8* (5), 839–843.
11. Varcoe, J. R.; Slade, R. C. T.; Lam How Yee, E.; Poynton, S. D.; Driscoll, D. J.; Apperley, D. C. *Chem. Mater.* **2007**, *19* (10), 2686–2693.
12. Hibbs, M. R.; Hickner, M. A.; Alam, T. M.; McIntyre, S. K.; Fujimoto, C. H.; Cornelius, C. J. *Chem. Mater.* **2008**, *20* (7), 2566–2573.
13. Wang, G.; Weng, Y.; Chu, D.; Chen, R.; Xie, D. *J. Membr. Sci.* **2009**, *332* (1−2), 63–68.
14. Wang, J.; Zhao, Z.; Gong, F.; Li, S.; Zhang, S. *Macromolecules* **2009**, *42* (22), 8711–8717.
15. Yan, J.; Hickner, M. A. *Macromolecules* **2010**, *43* (5), 2349–2356.
16. Robertson, N. J.; Kostalik, H. A.; Clark, T. J.; Mutolo, P. F.; Abruña, H. c. D.; Coates, G. W. *J. Am. Chem. Soc.* **2010**, *132* (10), 3400–3404.
17. Khandpur, A. K.; Foerster, S.; Bates, F. S.; Hamley, I. W.; Ryan, A. J.; Bras, W.; Almdal, K.; Mortensen, K. *Macromolecules* **1995**, *28* (26), 8796–8806.
18. Bates, F. S. *Science* **1991**, *251* (4996), 898–905.
19. Elabd, Y. A.; Napadensky, E.; Walker, C. W.; Winey, K. I. *Macromolecules* **2006**, *39* (1), 399–407.
20. Elabd, Y. A.; Napadensky, E.; Sloan, J. M.; Crawford, D. M.; Walker, C. W. *J. Membr. Sci.* **2003**, *217* (1−2), 227–242.
21. Peckham, T. J.; Holdcroft, S. *Adv. Mater. (Weinheim, Ger.)* **2010**, *22* (42), 4667–4690.
22. Park, M. J.; Balsara, N. P. *Macromolecules* **2009**, *43* (1), 292–298.
23. Park, M. J.; Downing, K. H.; Jackson, A.; Gomez, E. D.; Minor, A. M.; Cookson, D.; Weber, A. Z.; Balsara, N. P. *Nano Lett.* **2007**, *7* (11), 3547–3552.
24. Park, M. J.; Balsara, N. P. *Macromolecules* **2008**, *41* (10), 3678–3687.
25. Elabd, Y. A.; Hickner, M. A. *Macromolecules* **2010**, *44* (1), 1–11.
26. Tang, J.; Tang, H.; Sun, W.; Plancher, H.; Radosz, M.; Shen, Y. *Chem. Commun.* **2005** (26), 3325–3327.
27. Xia, J.; Matyjaszewski, K. *Macromolecules* **1997**, *30* (25), 7697–7700.
28. Wendler, U.; Bohrisch, J.; Jaeger, W.; Rother, G.; Dautzenberg, H. *Macromol. Rapid Commun.* **1998**, *19* (4), 185–190.

Downloaded by OHIO STATE UNIV LIBRARIES on June 14, 2012 | http://pubs.acs.org
Publication Date (Web): May 7, 2012 | doi: 10.1021/bk-2012-1096.ch015

Downloaded by STANFORD UNIV GREEN LIBR on June 14, 2012 | http://pubs.acs.org
Publication Date (Web): May 7, 2012 | doi: 10.1021/bk-2012-1096.ch016

Chapter 16

Structure and Properties of Proton Exchange Membrane Fuel Cells at Interfaces

Sangcheol Kim,* Kirt A. Page,* and Christopher L. Soles

**Polymers Division, National Institute of Standards and Technology,
100 Bureau Dr, Gaithersburg, MD 20899
*sangcheol.kim@nist.gov; kirt.page@nist.gov**

Although substantial improvements have been demonstrated for fuel cell technology over the past decade, challenges associated with cost and durability need to be overcome to compete in real markets and achieve wide-spread commercial success. Most researchers agree that the catalyst and the membrane are key components for which significant improvement could lead to solutions to these issues. However, as a potential route to solve cost and durability problems, structures and properties at interfaces have not been appropriately understood due to a lack of experimental methods to characterize these complex systems. Recently, in an effort to understand the transport and structural properties of the triple phase interfaces within polyelectrolyte membrane (PEM) fuel cells, thin PEM films cast on flat substrates have been investigated with a variety of techniques to understand the structure and transport at vapor and catalyst surfaces. Since fuel cells are highly integrated systems of heterogeneous materials, the structure and activity at the various interfaces affect the overall performance as much as the individual components. In this review, we review recent efforts to measure structures and physical properties not only at the bulk PEM surface, but also at the heterogeneous interfaces found within the catalyst layers. To overcome longstanding experimental limitations, neutron reflectometry has been deomonstrated as a powerful tool to probe the buried interfacial structure of the PEM within the catalyst layer.

Not subject to U.S. Copyright. Published 2012 by American Chemical Society
In Polymers for Energy Storage and Delivery: Polyelectrolytes for Batteries and Fuel Cells; Page, K., et al.;
ACS Symposium Series; American Chemical Society: Washington, DC, 2012.

Downloaded by STANFORD UNIV GREEN LIBR on June 14, 2012 | http://pubs.acs.org
Publication Date (Web): May 7, 2012 | doi: 10.1021/bk-2012-1096.ch016

Introduction

Since their first emergence as auxiliary power sources in the Gemini space flights, proton exchange membrane fuel cells (PEMFCs) have shown promise due to high efficiency in a wide range of applications such as transportation, stationary and portable power generation. Although substantial improvements in performance have been realized over the past decades, PEMFCs need to overcome two key challenges, cost and durability, to achieve wide-spread commercial success (*1*). The membrane electrode assembly (MEA) is central component of PEMFC and consists of several layers including: a proton exchange or polyelectrolyte membrane (PEM), triple phase anode and cathode catalyst layers, two gas diffusion layers (GDLs), and two sets of sealing gaskets. Generally, the catalyst loaded electrodes are put onto each side of a proton exchange membrane and hot pressed at 111 °C at 3.45 MPa for (2 to 3) minutes. Platinum is the typical catalyst for both the anode and the cathode and is dispersed as (5 to 20) nm particles supported on porous and conductive carbon supports. These porous layers conduct protons to the PEM to complete the ionic path while the electrons move through the conductive carbon to complete the fuel cell circuit. It is important that these layers have optimized transport of gases, water/ions, and electrons in such a way that resistive losses are reduced for the overall fuel cell performance. At high production volumes, the catalyst ink account for nearly half of the fuel cell stack cost due to the expensive platinum (Pt) particles. Another contributor to the cost is the proton exchange membrane, especially at low production volumes. The term “triple phase” means that all of these transport media need to be intimately interfaced at the catalytically active sites. Managing the interfaces of these different phases is extremely important for the ultimate performance of the fuel cell, as well as the overall cost of the system.

Among the many polymeric materials that have been developed for PEMFCs, Nafion (*2*) remains the most suitable membranes due to its thermal stability, chemical stability, and excellent transport properties. Nafion is a copolymer that consists of a polytetrafluoroethylene backbone with randomly distributed perfluorinated-vinyl-polyether side chains terminated with sulfonic acid end groups. In addition to being used as the active PEM material, Nafion is also integrated into the catalyst layers as a binder in the composite structure of carbon supported Pt catalyst particles. As ions must be able to reach the Pt catalyst particles, it is critical that the binder also be an ion conductor. The use of Nafion in the catalyst layer was pioneered by researchers at Los Alamos National Laboratory (*3*, *4*). While early PEM fuel cells required electrodes containing a high platinum loading (4 mg/cm^2) for a high level of performance, Srinivasan *et al.* (*3*) impregnated Nafion into the porous gas diffusion electrode structure and reduced platinum loading by a order of magnitude (to 0.35 mg Pt/cm^2). The reduction of the Pt loading was achieved mainly by extending the three-dimensional reaction zone and optimizing the amount of Nafion impregnated into the electrode structure (*4*). This technical break-through is one of the events that led to the renaissance in PEMFC research over the last 15 years.

For protonic conduction to occur, it is essential that the Nafion be hydrated. It is generally accepted that the kinetics of water transport in Nafion reliably reflects the protonic conductivity which occurs via an aqueous enviroment. There have, however, been several fundamental studies of water diffusion in Nafion membranes under different conditions and the results are generally all over the map. This is because the water transport kinetics are a function of several factors including temperature, membrane water content, the processing condtions for creating the Nafion film, and even the membrane thickness. There are well documented changes in the water diffusion coefficients for Nafion films in the thickness range of (50 to 250) μm, length scale at which finite size effects are generally not observed (*5–7*). Clearly the water and proton transport processes in Nafion are very complicated. The need for high power and energy density is pushing the industry towards thinner membranes in order to reduce the impedance of the fuel cell. As the membrane become increasingly thinner, the mass transport properties across the membrane are more strongly dominated by the interfacial resistance. It was recently suggested that, in a thin PEM, the interfacial resistance could be responsible for a significant portion of the net water transport (*8–11*) and that a less water permeable skin might be formed at the interface (*12*). As the membrane is cast in a very thin film, phase separation of the polymer electrolyte is limited and the interaction with the substrate is significant (*13*)(*14*). This in turn can affect the water content and transport properties of the membrane.

The role of interfacial properties becomes even more dominant in the MEA and with the large quantity of interfaces between the heterogeneous materials. In the composite anodes and cathodes where Nafion is used as a binder, the thickness of the Nafion coatings that actually hold the particles together is on the order of tens of nanometers. In this region, all of the Nafion can be classified as “interfacial” and bulk properties are meaningless. There is a strong need to understand the interplay between components and how the interactions and interfaces between these components affect the transport properties and performance of the fuel cell system. For instance, in the anode, the catalyst particles must participate in three transport functions: (1) adsorbing molecular hydrogen, (2) conducting electrons to the electrode via the catalyst support, and (3) transport of protons into the PEM. Within the catalyst layers, such electrochemical and electrocatalytic processes are most likely affected by the reactions occurring at the triple phase interface consisting of the PEM, vapor, and catalyst surface. To date, a complete understanding of the structures and transport properties at the PEM/metal interface does not exist. However, since impregnated Nafion was shown to significantly enhance the methanol electro-oxidation reaction (*15*), hydrogen anodic oxidation (*15*) and oxygen cathodic reduction reaction (*16–18*) over the bare Pt electrodes, it can be concluded that Nafion strongly interacts with Pt surface and modifies the interfacial properties (*19*, *20*). Difficulty of understanding the true nature of such interfaces has been attributed to a lack of experimental methods for preparing and characterizing well-defined triple phase interface-like systems for electrochemical studies.

Here, we review recent efforts to investigate molecular phenomena and structures not only at the bulk PEM surface but also at the heterogeneous interfaces within the catalyst layers. To overcome longstanding experimental limitations, we discuss in more detail a promising approach using neutron reflectivity which can probe the buried interfaces within the thin film at nanoscale. Understanding

Downloaded by STANFORD UNIV GREEN LIBR on June 14, 2012 | http://pubs.acs.org
Publication Date (Web): May 7, 2012 | doi: 10.1021/bk-2012-1096.ch016

the interfacial structure of the PEM within the catalyst layer is important for shedding light on water transport, proton transport and the oxygen reduction reaction mechanism occurring at the triple-phase interface.

Interfacial Structures and Transport Properties in PEMFC

Interfacial Phenomena in PEM

Over a century ago, von Schroeder (*21*) observed that gelatins would absorb more water under liquid immersion as compared to under 100 % relative humidity (RH) at the same temperature. This phenomenon, which appears to violate the laws of thermodynamics, is now commonly referred to Schroeder's Paradox. While the basis for these observations remains controversial, the explainations typically invoke a structure or phenomenon at the surface of the absorbing material which is different from that of the bulk. Similar observations of Schroeder's Paradox have been reported in the general class of polyelectrolyte membranes that are used for fuel cell applications. A better understanding of the interfacial phenomena in Nafion and Nafion-like materials is of significant importance to the fuel cell membrane community. Reports of this paradox in Nafion have led to fundamental questions about the nature of the interfacial thermodynamics and molecular structure of the material and how they affect the transport properties at the interface with water vapor or with liquid water.

Early AFM work by McLean *et al.* (*22*) suggested that the surface of Nafion is enriched by a thin fluorine rich layer which would seemingly be a barrier to moisture absorption. However X-ray photoelectron spectroscopy (XPS) and dynamic water contact angle measurements by Kim *et al.* (*23*) reported that the surface composition changes upon exposure to liquid water. It was Weber *et al.* (*24*) who first suggested that the surface composition of Nafion could have a major impact on the transport of water through Nafion membranes. While the structure of bulk Nafion is still debated, Weber and coworkers invoked the modified cluster-network model where ionic clusters are connected by hydrophobic channels that have different properties depending of the state of the water in contact with the membrane. They suggested that the surface of Nafion membranes reorganizes from hydrophobic fluorocarbon-rich skin under dry conditions to a hydrophilic sulfonic acid-rich surface in the presence of water.

Majsztrik *et al.* (*12*) argued that water permeation and sorption for thin Nafion membranes at low temperature are controlled by interfacial mass transport at the membrane/air interface. When water vapor is present at both interfaces, the water transport is governed by diffusion kinetics through the membrane. But, the rate-limiting step becomes interfacial transport at the vapor/membrane interface when liquid water is present at just one interface (*25*). This phenomenon was pursued further by Goswami *et al.* (*26*) with advancing and receding contact angle measurements on Nafion and Teflon films. Teflon showed an advancing contact angle of 110° and a receding contact angle of 95°, demonstrating a nonwetting surface for water. In contrast, the receding contact angle on Nafion was between 20° and 30° while the advancing contact angle was 105° to 110°, comparable to the Teflon surface. They attributed this unusual behavior of

Downloaded by STANFORD UNIV GREEN LIBR on June 14, 2012 | http://pubs.acs.org
Publication Date (Web): May 7, 2012 | doi: 10.1021/bk-2012-1096.ch016

Downloaded by STANFORD UNIV GREEN LIBR on June 14, 2012 | http://pubs.acs.org
Publication Date (Web): May 7, 2012 | doi: 10.1021/bk-2012-1096.ch016

Nafion to molecular rearrangements at the polymer-fluid interface. The authors, however, were not able to probe how deep below the surface this structural rearrangement occurs. This concept of dynamic rearrangement near the surface was recently explored using water contact angle measurements, AFM and *in-situ* grazing-incidence small-angle X-ray scattering (GI-SAXS) of Nafion under wet and humid conditions (*27*). These measurements showed preferential alignment of micellar-like structures near the interface. The advancing contact angle measured in Figure 1 shows that the Nafion surface is hydrophobic under water vapor but becomes hydrophilic under water immersion. These authors also characterized the Nafion surface after water exposure with AFM and found that the surface roughness increases significantly (Figure 1). The rougher surface topography demonstrates drastic structural variations, which is consistent with the proposed liquid-induced restructuring. These studies are discussed in detail in the chapter entitled "Thermodynamics, microstructure and interfacial effects in hydrated Nafion" of this book.

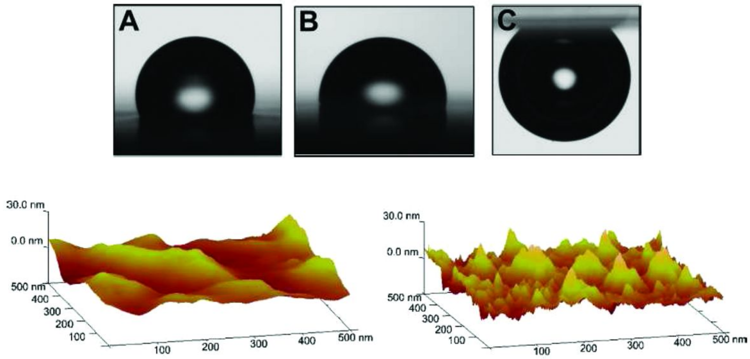

Figure 1. Water droplets in air on Nafion, dry film (upper left) and equilibrated at RH = 97 % (upper middle), and air bubble attached from below Nafion in water (upper right). Surface topography of Nafion measured by AFM in air (lower left) and under water (lower right). Reprinted with permission from (27) © 2010 American Chemical Society.

Zhao and co-workers (*28*) used pulse field gradient spin echo nuclear magnetic resonance (PGSE-NMR) to quanitify self-diffusion coefficient of water within a Nafion membrane and interpreted their findings in terms of the tortuosity of the hydrophilic water conduction channels. They argue that surface energy is minimized by having the water transport channels buried beneath the surface in geometries that are non-conductive for interfacial transport when the membrane surface is in contact with a water vapor. However, these water transport channels extend directly to the interface when the Nafion is in contact with liquid water. Their interpretation of the NMR data is consistent with the notion that the nanophase-separated structure of Nafion, driven by the hydrophilic side-chain segregation from the hydrophobic backbone, is responsible for its complex interfacial transport behaviors. To date, however, a clear molecular-level understanding of interfacial mass transport resistance has not emerged. For example, there has been no determination of the length scale over which the interfacial resistance persists. This can only be determined from a detailed molecular-level understanding of this phenomenon.

Interfacial Phenomena in MEA

As the polymer electrolyte membrane material is also used as an active binder in the electrode catalyst layers, the nature of the triple phase interface between heterogeneous materials needs to be well understood. However, it is very difficult to measure or quantify these interfaces especially when the Pt catalyst is usually a nanoparticle, the electron conductor is a combination of graphitic or nanofiber form of carbon and the Nafion binder is a poorly defined layer holding these components together. Due to such a complicated and poorly defined geometry, it is difficult to describe accurately the molecular-level structure of the triple phase interface and its effect on electrochemical processes. The measurements are just too complicated. To simplify the situation, researchers have started to utilize model thin PEM films cast on flat substrates. This approach has made it much easier to quantify the role of the interfaces; thin film measurements are relatively well established.

Pt is the most common catalyst for the oxygen reduction in a hydrogen fuel cell and there have been several attempts to indentify this reaction mechanism on model planar Pt interfaces using both electrochemical X-ray photoelectron spectroscopy (EC-XPS) (*29*), which has high sensitivity and specificity of the O_{1s} spectra, and *in-situ* attenuated total reflectance-Fourier transform infrared (ATR-FTIR) (*30*). There are also recent reports of utilizing half-membrane-electrode assembly type cells by Kunimatsu *et al.* (*31*) to conduct ATR-FTIR measurements at the Pt/Nafion interface under humidified N_2/O_2 atmosphere. An infrared absorption band observed near 1400 cm^{-1} to 1403 cm^{-1} under humidified oxygen atmosphere is assigned as the O-O vibration of the adsorbed oxygen molecule O_2.

There have also been attempts to develop a molecular-level structural description of the triple phase interface through a combination of *in-situ* infrared reflection absorption spectroscopy (IRRAS) and cyclic voltammetry on model Pt(111)/Nafion interfaces in $HClO_4$ acid solutions (*32*). Analysis of the infrared data revealed that proton mobility inside the membrane is enhanced with the deprotonation of sulfonic groups near the electrode surface in the presence of higher potentials. The authors attributed this effect to an electric field induced orientation of the membrane morphology. They also observed that the character of CO absorption and oxidation at Pt(111) is affected by the presence of polymer electrolyte membrane. The nature of the Pt-Nafion interface for both polycrystalline and single crystal Pt surfaces was probed by Subbaraman *et al.* (*33*) using a voltammetric fingerprinting approach. A CO charge displacement technique identified that the sulfonate anions of Nafion adsorb onto the Pt surface. They report that the nature and strength of the adsorption is significantly influenced by the presence of the native interactions of these anions with their host polymer matrix. The adsorption behavior of the sulfonate anions at the interface is consistent with the elucidation by the cooperative efforts using *operando*

Downloaded by STANFORD UNIV GREEN LIBR on June 14, 2012 | http://pubs.acs.org
Publication Date (Web): May 7, 2012 | doi: 10.1021/bk-2012-1096.ch016

(actual reactor conditions) infrared (IR) spectroscopy, polarization modulated IR spectroscopy (PM-IRRAS) of Nafion-Pt interfaces, ATR-FTIR spectroscopy of bulk Nafion, and density functional theory (DFT) calculations of the resulting spectra (*34*). As illustrated in Figure 2, sulfonate and CF_3 co-adsorbates of the Nafion side chain are anchored at the Nafion-Pt interface and reduce the degrees of freedom available for backbone and side chain dynamics. Such adsorption partially orders the Nafion backbone and/or side-chain CF_2 groups relative to the Pt surface.

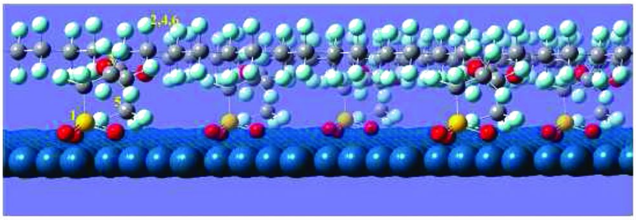

Figure 2. A model for Nafion functional group adsorption to Pt: carbon (gray), fluorine (light blue), sulfur (yellow), oxygen (red), and Pt (dark blue) (color online). Reprinted with permission from (34) © 2010 American Chemical Society.

Quartz-crystal microbalance (QCM) measurements have been used to quantify the water content (λ) of thin Nafion membranes (0.033 μm to 3 μm thick) on Pt substrates over a range of temperatures and and relative humidities (RHs) (*35*). For films down to approximately 500 nm, the measured water uptakes are very similar to that of a thick Nafion membrane. However, when the thickness drops below 33 nm, these measurements indicate that the membrane water content is slightly reduced, especially at higher vapor water activities. These authors speculate that the lower water content results from either interactions of the ionomers with the substrate, surface confinement, or a water-impermeable layer at the gas/ionomer interface. Their observations did not appear to depend on specific substrate-ionomer interactions as identical results were obtained on both Au-coated and Pt-coated quartz crystals.

Molecular simulations to characterize the structure and dynamics of the processes at Nafion interfaces have the potential to provide new insights into the electrochemical processes within the catalyst layers. Selvan *et al.* (*36*) performed molecular dynamics (MD) simulations and observed a region of water depletion in Nafion membrane near the vapor interface. They concluded that there is no additional resistance to mass transport of the vehicular component of water and hydronium due to the interface. However, there is a decrease in the fraction of fully hydrated hydronium ions at the interface. MD simulations were also performed by Liu *et al.* (*37*) to investigate the structural and dynamical behavior of water and hydronium ions at the electrode/electrolyte interface in PEMFCs. As shown in Figure 3, they observed significant wetting of the catalyst surface (Pt(111)) and no wetting of the catalyst support surface (graphite). The degree of wetting depended strongly on the level of the water content. However, no more than a monolayer of surface structure was observed. This monolayer was

Downloaded by STANFORD UNIV GREEN LIBR on June 14, 2012 | http://pubs.acs.org
Publication Date (Web): May 7, 2012 | doi: 10.1021/bk-2012-1096.ch016

Downloaded by STANFORD UNIV GREEN LIBR on June 14, 2012 | http://pubs.acs.org
Publication Date (Web): May 7, 2012 | doi: 10.1021/bk-2012-1096.ch016

composed of a mixture of water, Nafion, and hydronium ions. Because the catalyst support shows no significant wetting, this work implies that the catalyst particles must be in intimate contact with the hydrated membrane, or with recast hydrated polymer electrolyte membrane in the electrode that provides a pathway for protons to move from the catalyst surface into the bulk hydrated membrane.

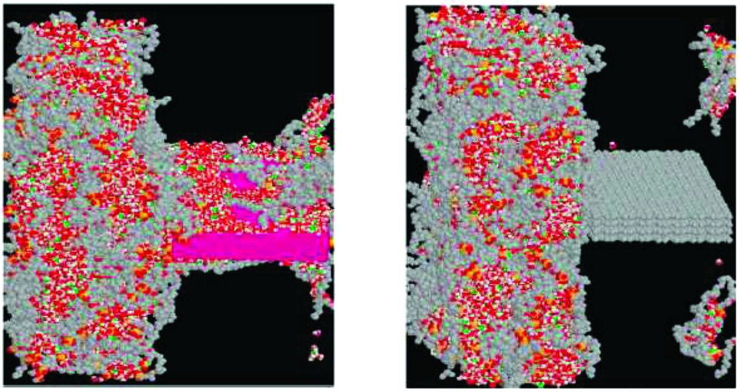

Figure 3. Final snapshots of simulations containing the Pt catalyst surface (left) and the carbon catalyst support surface (right) for water contents of 20 % by mass: CF_x groups (gray), sulfur (orange), oxygen of H_2O and SO_3^- (red), oxygen of H_3O^+ (green), hydrogen (white), Pt (pink), and graphitic carbon (gray) (color online). Reprinted with permission from (37) © 2008 American Chemical Society.

Interfacial Structure Characterization in MEA

While interfacial phenomena are commonly invoked to describe an unusual response or performance of fuel cell membranes, there have been relatively few studies that directly correlate this response to an actual interfacial structure. This is in part because such interfacially selective measurements have been difficult, especially with the added complexity that the bulk structure of PEMs like Nafion are still debated. However, there appears now an increasing number of reports in the literature that directly address this interfacial structure issue. In this section we review several of these recent advances.

Neutron reflectivity (NR) and X-ray reflectivity (XR) are powerful tools to characterize swelling dynamics and distribution of water at interfaces and in thin films (*38–41*). For details on the NR technique, please refer to the chapter entitled “In situ neutron techniques for studying lithium ion batteries” in this book. Some early examples illustrate how NR can be used to quantify the equilibrium concentration of water at the buried interfaces between an amorphous polyimide film and silicon substrate. These measurements showed an excess of water, dependent upon the substrate hydrophilicity, at the polymer/substrate interfaces (*38*, *39*). This excess of interfacial moisture in a polymer film on a hydrophilic substrate is manifest through an increased degree of swelling of the entire film when the film thickness approaches the length scale of the interfacial enhancement: this effect nominally becomes visible for films thinner than approximtately 50 nm (*40*). It was further shown that this interfacial uptake could be reduced by making the substrate interface more hydrophobic than the polymer film (*42*). These authors coupled these interfacial moisture absorption studies with *in-situ* QCM measurements that demonstrated significantly reduced uptake kinetics in both thin polymer (*42*) and polyelectroyte films (*43*).

There have been attempts to perform *in-situ* NR measurements of water penetration into thin sulfonated polyphenylene (sPP) ionomer films as a function of time, ionic strength, and film thickness (*44*). NR measurements are typically too slow to track the swelling response of a thin film *in-situ*, so these authors focused on fiting only the low *q* data of the reflectivity curve (where counting statistics are higher) to acquire partial curves. sPP films with an initial thicknesses of 131 Å, 218 Å and 567 Å with 33.4 % sulfonation were exposed to D_2O vapors and subsequently measured by NR in time-averaged 10 min intervals. The data were analyzed by fitting a 3-layer model as illustrated in Figure 4. The scattering length density (SLD) is profiled as a function of the distance (Z) from Si substrate. At steady state, nonuniform distributions of water molecules were observed with D_2O-rich layers (higher SLD) at the both air/polymer interface and polymer/SiO_x substrate interface. The formation of a thin water-rich layer is somewhat unusual since the hydrophobic thin layer is preferred at the air interface, especially in case of fluorinated ionomers (e.g., Nafion) (*45*). Generally, the lower surface tension component tends to segregate predominantly to the air interface for the lowest energy configuration. However, the authors speculated that the rigidity of the sPP backbone may not be sufficient to allow chain folding to bury the ionic groups. Figure 4 also suggests that a water rich interface exists near the SiO_x substrate in the 131 Å thick film, but for some reason this preferential accumulation is lost for the 567 Å thick film. It is not immediately clear why this preferential accumulation would disappear in the thicker film, but it needs to be noted that film thickness, roughness, and SLD become highly convoluted when fitting NR data for films on the order of 131 Å. By only fitting the low *q* data the authors would not be able to separate these effects for their thinnest films.

Wood and coworkers (*14*) also used NR to characterize the interfacial morphology of Nafion on smooth and idealized glassy carbon (GC) substrates coated with device relevant Pt or Pt oxide (PtO) layers. The spin cast Nafion films were thermally processed following the electrode preparation method developed by Wilson and Gottesfeld (*46*, *47*). It resulted in Nafion films on top of either hydrophobic Pt or hydrophilic PtO substrates. When the Nafion was equilibrated with saturated D_2O on the Pt surface, the best fit to the data (Figure 5) showed a dip in the SLD profile near the hydrophobic substrate: a thin water depletion region (SLD = 4.6 x 10^{-6} Å^{-2}, thickness = 74 Å) beneath a thicker hydrated (SLD = 5.1 x 10^{-6} Å^{-2}, thickness = 619 Å) layer of Nafion. After conversion of the Pt surface to PtO, the interfacial depletion region disappeared and the resulting hydrated film could be modeled with a bilayer structure. In this bilayer, the Nafion adjacent the hydrophilic PtO absorbed more D_2O (SLD = 5.0 x 10^{-6} Å^{-2}, thickness = 372 Å) while the Nafion adjacent to the air interface is comparatively more hydrophobic layer (SLD = 4.7 x 10^{-6} Å^{-2} thickness = 333 Å).

Downloaded by STANFORD UNIV GREEN LIBR on June 14, 2012 | http://pubs.acs.org
Publication Date (Web): May 7, 2012 | doi: 10.1021/bk-2012-1096.ch016

Downloaded by STANFORD UNIV GREEN LIBR on June 14, 2012 | http://pubs.acs.org
Publication Date (Web): May 7, 2012 | doi: 10.1021/bk-2012-1096.ch016

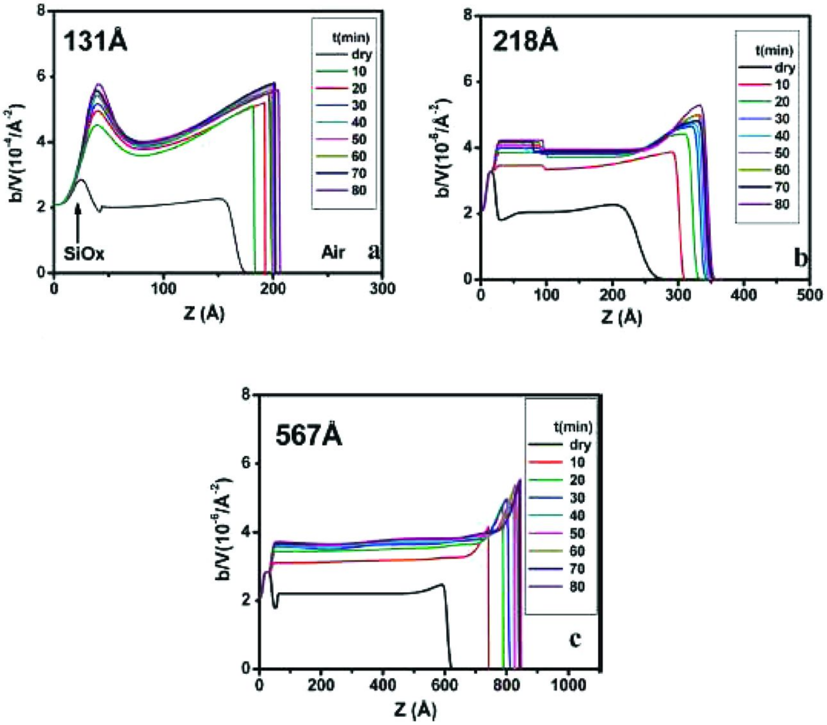

Figure 4. NR Scattering length density profiles of sPP thin films with initial thickness of 131 Å (upper left), 218 Å (upper right), and 567 Å (lower) as a function of exposure time to D_2O vapor. Z is the distance from Si substrate at Z = 0. Reprinted with permission from (44) © 2008 American Chemical Society.

Reversible restructuring of Nafion morphology at the interface with Pt was previously proposed by ultramicroelectrode studies. When Nafion is in contact with a bare Pt surface, the hydrophilic sulfonate-containing side chains are driven away from the hydrophobic Pt surface. When the Pt surface becomes hydrophilic PtO, the sulfonate-containing side chains are drawn back into the interface, leaving hydrophobic fluorinated segments at the surface. While the NR data presented above seem to support this general picture, it is hard to imagine how such a phase segregation of the different domains could occur for a random copolymer like Nafion over length scales as large as 600 Å to 700 Å: the short-range average distance between the different segments in a polymer chain would seemingly prevent phase demixing at such large length scale. Furthermore, this proposed surface templating effect is inconsistent with other interpretations that Nafion is anchored onto the Pt surface using sulfonate anion groups (*33*, *35–37*). The nature of the interfacial interactions between Pt, PtO, and Nafion are clearly very complicated.

Downloaded by STANFORD UNIV GREEN LIBR on June 14, 2012 | http://pubs.acs.org
Publication Date (Web): May 7, 2012 | doi: 10.1021/bk-2012-1096.ch016

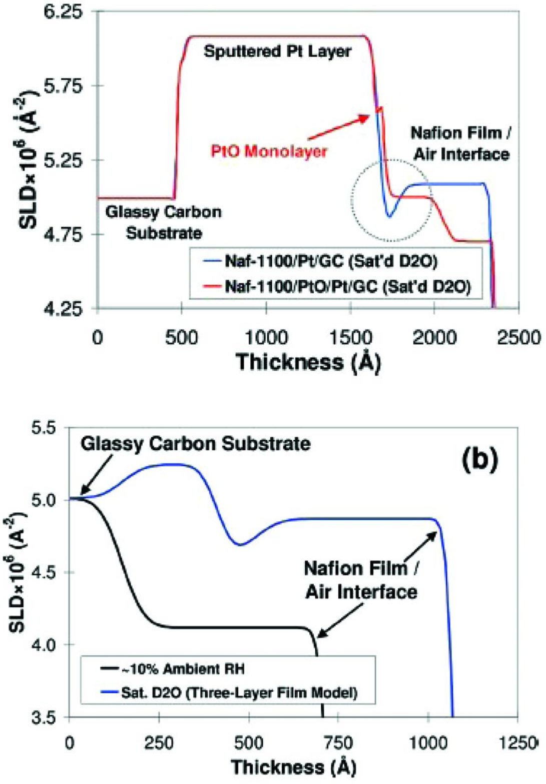

Figure 5. NR scattering length density (SLD) profiles of Nafion: on Pt surface or PtO surface in a saturated D_2O environment (upper); on glassy carbon surface in saturated D_2O and ambient 10 % RH environments (lower). Reprinted with permission from (14) © 2009 American Chemical Society.

When the Nafion film on GC surface was measured in a saturated D_2O environment, different multilayer structures of Nafion were found. As shown in Figure 5, reasonable agreement is achieved by three-layer heterogeneous model consisting of a thin, rough intermediate "more hydrophobic" zone between two thicker, more hydrophilic layers. Like Nafion on the Pt surface, the thickest hydrophilic layer existes at the air interface. However, the most hydrophilic layer is additionally found at the GC interface and the total thickness of the three zones increased nearly 60 %. These results are in contradiction to what Liu *et al.* (*37*) observed with molecular dynamics simulations and the structural rearrangement of Nafion surface proposed by Bass *et al.* (*27*) as a extension of Schroeder's Paradox.

NR was also used by Dura and coworkers (*13*) to demonstrate that lamellar layers of thin alternating water-rich and Nafion-rich domains are induced at the interface of hydrated Nafion with native Si oxide substrates. Nafion solution were spin cast onto various substrates and then immediately annealed at either 60 °C or

Downloaded by STANFORD UNIV GREEN LIBR on June 14, 2012 | http://pubs.acs.org
Publication Date (Web): May 7, 2012 | doi: 10.1021/bk-2012-1096.ch016

150 °C for 1 h. As shown in Figure 6a, the Nafion spin-cast onto SiO_2 shows a peak at $Q_z = 0.21$ Å^{-1} at RH = 97 %. The position and intensity of the peak are strongly dependent on sample hydration level, which suggests that water is inducing the structure. Transverse scans to probe the in-plane structure suggest that the high-Q peak stems from extended two-dimensional planes or lamellae running parallel to the substrate. The best fit SLD profiles to the experimental data are presented in Figure 6b and show excellent agreement with the specular reflectivity data. The cartoon schematic in Figure 6b illustrates corresponding layer structures. For Nafion on SiO_2 at RH=97 %, the layers in the model correspond to the Si substrate, the native Si oxide layer, and then the lamellae consisting of three water-rich layers alternating with two Nafion-rich layers. The composition of the lamellae decayed from nearly 100 % by volume H_2O to a final layer of ≈ 60 % by volume H_2O with increasing distance from the interface. The "bulk" layer on top of the lamellae is consistent with Nafion that has a water content (λ) of (5.0 ± 0.2) water molecules per sulfonic acid. Upon dehydration, as shown in Figure 6b (green), the lamellar structure has been reduced in extent and only three layers are observed. It is notable that this interfacial lamellar structure is not observed for the Nafion/Pt or Nafion/Au interfaces except a thin partially hydrated single interfacial layer. But, the thickness decreases to a few Å as humidity is reduced to zero. This indicates that Au and Pt surfaces have a lower affinity for the sulfonic acid of Nafion/water phase than the more hydrophilic SiO_2 surface.

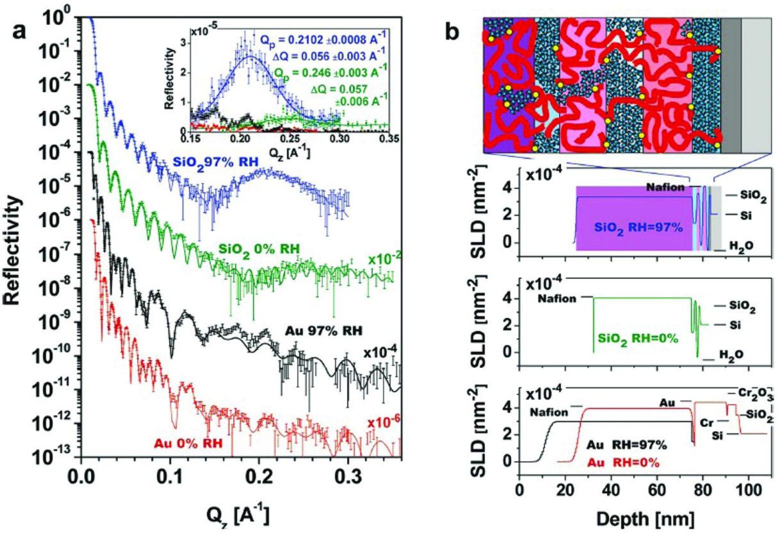

Figure 6. (left) Specular NR data and model fits showing a high-Q peak for SiO_2 at RH = 97 % (blue), a smaller high-Q peak for SiO_2 at RH = 0 % (green) and no high-Q peak for Au at RH =97 % (black) or Au at RH = 0 % (red). (right) NR scattering length density profiles and the model corresponding to SiO_2 at RH =97 %: Nafion fluorocarbon backbone (red), sulfonic acid group (yellow), and water (blue) (color online). Reprinted with permission from (13) © 2009 American Chemical Society.

Downloaded by STANFORD UNIV GREEN LIBR on June 14, 2012 | http://pubs.acs.org
Publication Date (Web): May 7, 2012 | doi: 10.1021/bk-2012-1096.ch016

Currently, we are investigating the origins of the interfacial lamellar formation and its impact on transport properties using NR, GISAXS, and QCM. Our approach has been to measure the structure and transport properties of Nafion thin films spin cast onto model substrates having various surface energies (*48*). The interfacial structures of Nafion and water appears to be strongly dependent on the surface energy of the substrate. We generally do not observe interfacial lamella in hyrdrated Nafion cast on hydrophobic surfaces. However, strongly hydrophilic surface tend to show interfacial lamella formation for fully hydrated Nafion films. These results seem reasonably consistent with previous observations of wetting on catatlyst layer surfaces (*37*) and an excess of water at the interfaces of polymers with hydrophilic surfaces (*38–40*, *42–44*). Our systematic approach can give an insight into the premature but controversial debates on the interfacial Nafion behavior as discussed above.

Summary and Outlook

To be competitive in commercial markets, fuel cells technology should overcome technical challenges associated with cost and durability. The catalyst ink account for nearly half of the fuel cell stack cost due to the expensive Pt particles. Another major contributor to the cost is the proton exchange membrane. Most researchers agree that the catalyst and the membrane are key components for which significant improvement could lead to a solution to these issues. Although impressive advances on individual components have been achieved, the importance of understanding the interfaces has not been adequately addressed. Since the fuel cell is a highly integrated system of heterogeneous materials, the structure and (transport) activity at the interface affect the overall performance as much as the individual components. Innovations in the characterization and analysis techniques aimed at improving our understanding of the electrochemical processes, the structure and the transport at interfaces present in PEMFCs have been developed and are hoped to make efficient progress in eliminating cost and durability challenges that the current fuel cell technology faces. In this review, we introduced recent efforts to investigate structures and properties not only at the PEM interface but also at the heterogeneous interfaces within the catalyst layers.

References

1. Martin, K. E.; Kopasz, J. P.; McMurphy, K. W. Fuel Cell Chemistry and Operation. *ACS Symp. Ser.* **2010**, *1040*, 1–13.
2. Certain commercial equipment, i., or materials are identified in this paper in order to specify the experimental procedure adequately. Such identification is not intended to imply recommendation or endorsement by the National Institute of Standards and Technology, nor is it intended to imply that the materials or equipment identified are necessarily the best available for the purpose.
3. Ticianelli, E. A.; Derouin, C. R.; Redondo, A.; Srinivasan, S. *J. Electrochem. Soc.* **1988**, *135*, 2209–2214.

4. Paik, W.; Springer, T. E.; Srinivasan, S. *J. Electrochem. Soc.* **1989**, *136*, 644–649.
5. Zawodzinski, T. A.; Neeman, M.; Sillerud, L. O.; Gottesfeld, S. *J. Phys. Chem.* **1991**, *95*, 6040–6044.
6. Rivin, D.; Kendrick, C. E.; Gibson, P. W.; Schneider, N. S. *Polymer* **2001**, *42*, 623–635.
7. Burnett, D. J.; Garcia, A. R.; Thielmann, F. *J. Power Sources* **2006**, *160*, 426–430.
8. Satterfield, M. B.; Benziger, J. B. *J. Phys. Chem. B* **2008**, *112*, 3693–3704.
9. Merida, W.; Romero, T. *J. Membr. Sci.* **2009**, *338*, 135–144.
10. Navessin, T.; Adachi, M.; Xie, Z.; Li, F. H.; Tanaka, S.; Holdcroft, S. *J. Membr. Sci.* **2010**, *364*, 183–193.
11. Tabuchi, Y.; Ito, R.; Tsushima, S.; Hirai, S. *J. Power Sources* **2011**, *196*, 652–658.
12. Majsztrik, P. W.; Satterfield, M. B.; Bocarsly, A. B.; Benziger, J. B. *J. Membr. Sci.* **2007**, *301*, 93–106.
13. Dura, J. A.; Murthi, V. S.; Hartman, M.; Satija, S. K.; Majkrzak, C. F. *Macromolecules* **2009**, *42*, 4769–4774.
14. Wood, D. L.; Chlistunoff, J.; Majewski, J.; Borup, R. L. *J. Am. Chem. Soc.* **2009**, *131*, 18096–18104.
15. Maruyama, J.; Inaba, M.; Katakura, K.; Ogumi, Z.; Takehara, Z. *J. Electroanal. Chem.* **1998**, *447*, 201–209.
16. Gottesfeld, S.; Raistrick, I. D.; Srinivasan, S. *J. Electrochem. Soc.* **1987**, *134*, 1455–1462.
17. Floriano, J. B.; Ticianelli, E. A.; Gonzalez, E. R. *J. Electroanal. Chem.* **1994**, *367*, 157–164.
18. Watanabe, M.; Miyatake, K.; Omata, T.; Tryk, D. A.; Uchida, H. *J. Phys. Chem. C* **2009**, *113*, 7772–7778.
19. Watanabe, M.; Yano, H.; Higuchi, E.; Uchida, H. *J. Phys. Chem. B* **2006**, *110*, 16544–16549.
20. Ohma, A.; Fushinobu, K.; Okazaki, K. *Electrochim. Acta* **2010**, *55*, 8829–8838.
21. von Schroeder, P. *Z. Phys. Chem.-Stoch. Ve* **1903**, *45*, 75–117.
22. McLean, R. S.; Doyle, M.; Sauer, B. B. *Macromolecules* **2000**, *33*, 6541–6550.
23. Kim, Y. H.; Oblas, D.; Angelopoulos, A. P.; Fossey, S. A.; Matienzo, L. J. *Macromolecules* **2001**, *34*, 7489–7495.
24. Weber, A. Z.; Newman, J. *J. Electrochem. Soc.* **2003**, *150*, A1008–A1015.
25. Majsztrik, P.; Bocarsly, A.; Benziger, J. *J. Phys. Chem. B* **2008**, *112*, 16280–16289.
26. Goswami, S.; Klaus, S.; Benziger, J. *Langmuir* **2008**, *24*, 8627–8633.
27. Bass, M.; Berman, A.; Singh, A.; Konovalov, O.; Freger, V. *J. Phys. Chem. B* **2010**, *114*, 3784–3790.
28. Zhao, Q. A.; Majsztrik, P.; Benziger, J. *J. Phys. Chem. B* **2011**, *115*, 2717–2727.
29. Wakisaka, M.; Suzuki, H.; Mitsui, S.; Uchida, H.; Watanabe, M. *J. Phys. Chem. C* **2008**, *112*, 2750–2755.

Downloaded by STANFORD UNIV GREEN LIBR on June 14, 2012 | http://pubs.acs.org
Publication Date (Web): May 7, 2012 | doi: 10.1021/bk-2012-1096.ch016

30. Shao, M. H.; Liu, P.; Adzic, R. R. *J. Am. Chem. Soc.* **2006**, *128*, 7408–7409.
31. Kunimatsu, K.; Yoda, T.; Tryk, D. A.; Uchida, H.; Watanabe, M. *Phys. Chem. Chem. Phys.* **2010**, *12*, 621–629.
32. Gomez-Marin, A. M.; Berna, A.; Feliu, J. M. *J. Phys. Chem. C* **2010**, *114*, 20130–20140.
33. Subbaraman, R.; Strmcnik, D.; Stamenkovic, V.; Markovic, N. M. *J. Phys. Chem. C* **2010**, *114*, 8414–8422.
34. Kendrick, I.; Kumari, D.; Yakaboski, A.; Dimakis, N.; Smotkin, E. S. *J. Am. Chem. Soc.* **2010**, *132*, 17611–17616.
35. Kongkanand, A. *J. Phys. Chem. C* **2011**, *115*, 11318–11325.
36. Selvan, M. E.; Liu, J.; Keffer, D. J.; Cui, S.; Edwards, B. J.; Steele, W. V. *J. Phys. Chem. C* **2008**, *112*, 1975–1984.
37. Liu, J. W.; Selvan, M. E.; Cui, S.; Edwards, B. J.; Keffer, D. J.; Steele, W. V. *J. Phys. Chem. C* **2008**, *112*, 1985–1993.
38. Wu, W. L.; Orts, W. J.; Majkrzak, C. J.; Hunston, D. L. *Polym. Eng. Sci.* **1995**, *35*, 1000–1004.
39. Tan, N. C. B.; Wu, W. L.; Wallace, W. E.; Davis, G. T. *J. Polym. Sci., Polym. Phys.* **1998**, *36*, 155–162.
40. Vogt, B. D.; Soles, C. L.; Jones, R. L.; Wang, C. Y.; Lin, E. K.; Wu, W. L.; Satija, S. K.; Goldfarb, D. L.; Angelopoulos, M. *Langmuir* **2004**, *20*, 5285–5290.
41. Mukherjee, M.; Singh, A.; Daillant, J.; Menelle, A.; Cousin, F. *Macromolecules* **2007**, *40*, 1073–1080.
42. Vogt, B. D.; Soles, C. L.; Lee, H. J.; Lin, E. K.; Wu, W. *Polymer* **2005**, *46*, 1635–1642.
43. Vogt, B. D.; Soles, C. L.; Lee, H. J.; Lin, E. K.; Wu, W. L. *Langmuir* **2004**, *20*, 1453–1458.
44. He, L. L.; Smith, H. L.; Majewski, J.; Fujimoto, C. H.; Cornelius, C. J.; Perahia, D. *Macromolecules* **2009**, *42*, 5745–5751.
45. Zawodzinski, T. A.; Gottesfeld, S.; Shoichet, S.; Mccarthy, T. J. *J. Appl. Electrochem.* **1993**, *23*, 86–88.
46. Wilson, M. S.; Gottesfeld, S. *J. Appl. Electrochem.* **1992**, *22*, 1–7.
47. Wilson, M. S.; Gottesfeld, S. *J. Electrochem. Soc.* **1992**, *139*, L28–L30.
48. Kim, S.; Dura, J. A.; Page, K. A.; Soles, C. L. *Abstr. Pap., Am. Chem. Soc.* **2011**, *241*.

Downloaded by STANFORD UNIV GREEN LIBR on June 14, 2012 | http://pubs.acs.org
Publication Date (Web): May 7, 2012 | doi: 10.1021/bk-2012-1096.ch016

Downloaded by PENNSYLVANIA STATE UNIV on June 14, 2012 | http://pubs.acs.org
Publication Date (Web): May 7, 2012 | doi: 10.1021/bk-2012-1096.ch017

Chapter 17

Thermodynamics, Microstructure and Interfacial Effects in Hydrated Nafion

Viatcheslav Freger[*]

The Wolfson Department of Chemical Engineering, Technion - Israel Institute of Technology, Technion City, Haifa 32000, Israel
[*]e-mail: vfreger@tx.technion.ac.il

Hydration of Nafion is known to profoundly effect its performance, however, measurements of hydration and its modeling and relation to other characteristics have been subject to puzzling controversies such as Schroeder's paradox. This chapter analyzes Nafion hydration based on a new model that consistently relates hydration to microstructure. The hydration equilibrium is interpreted as a balance of 3 pressures: osmotic, elastic and a special interfacial-elastic Laplace pressure, which clarifies the role of relaxation and the origin of non-equilibrium phenomena such as Schroeder's paradox. The predicted structural variation of microstructure with hydration shows a good agreement with available data. The model is also used to analyze microstructure and orientation of Nafion micelles in the surface region exposed to different environments. The predicted variations of surface structure in vapor and water fully agree with GISAXS, AFM and contact angle measurements for Nafion membranes and thin films on different substrates. The external medium and substrate are shown to strongly affect the orientation of micelles in their vicinity. This suggests attractive possibilities of enhancing transport characteristics of Nafion.

Introduction: Transport Properties, Hydration, and Microstructure of Nafion

Nafion and similar perfluorinated ionomers have been widely used as ion-conductive barrier materials in membrane electrolysis, polymer electrolyte

In Polymers for Energy Storage and Delivery: Polyelectrolytes for Batteries and Fuel Cells; Page, K., et al.;
ACS Symposium Series; American Chemical Society: Washington, DC, 2012.

Downloaded by PENNSYLVANIA STATE UNIV on June 14, 2012 | http://pubs.acs.org
Publication Date (Web): May 7, 2012 | doi: 10.1021/bk-2012-1096.ch017

membrane fuel cells (PEMFC) and other electrochemical applications since their invention in 70s. Their remarkable chemical stability and high ionic conductivity have made them benchmark material in the field for nearly 4 decades. Unique characteristic of Nafion stimulated a large number of studies with the purpose to understand the thermodynamics and structure and their relation to functioning of these materials. Apart from fundamental interest, an important driver for this research was the need to find substitutes for perfluorinated materials, in view of their well-recognized limitations, such as high cost, substantial cross-over of liquid fuels such as methanol and potential difficulties with their recycling or reuse.

The remarkable transport characteristics of Nafion are illustrated in Figure 1 comparing its proton mobility and water diffusivity as function of water content to a few more “regular” polymers. It is seen that Nafion requires much less water fraction (“mobile microphase” within the polymer) than “regular” materials to achieve the same macroscopic mobility of the diffusing species. This superior trend of conductivity vs. degree of hydration exhibited by Nafion and other perfluorinated ionomers, is apparently a manifestation of the unique microphase-separated microstructure. The evidence for microphase separation in Nafion using scattering experiments was obtained already in the early studies by Gierke et al. (*1*) and was subsequently extended and thoroughly elaborated by the Grenoble group (*2*–*6*). In particular, findings of the last decade demonstrated that the water microphase is arranged within well-connected aggregates or micelles with elongated (2D) morphology, as opposed to “regular” materials exhibiting a random isotropic (3D) micromorphology. The elongated micelle morphology well explains the exceptionally high ionic conductivity and water diffusion in Nafion (*7*, *8*), which may be further enhanced in the desired direction by stretching (*9*). This behavior is analogous to the larger conductivity and reduced percolation threshold of composites containing elongated conductive particles dispersed in an insulting matrix, e.g., in carbon nanotube-filled polymer composites (*10*).

Figure 1 also emphasizes the relation of transport characteristics to hydration. For this reason “water management” is commonly recognized as an important aspect of PEMFC design. Although the dependence of conductivity on water content is not as steep for Nafion as for other proton conductors, it is still strong enough to critically affect the performance of a working PEMFC, given extensive dry-out of the anode side of the membrane by electroosmosis. The electroosmotic flux of water is counterbalanced by back diffusion from the cathode side, as described by the equation

$$J_w = -\frac{D_w C_w}{RT}\nabla\mu_w + \chi J_{H^+}, \tag{1}$$

where J_w, D_w, C_w, and μ_w are, respectively, total flux, local diffusivity, local concentration, and local chemical potential of water, J_{H+} the proton flux (current), and χ is the electro-osmotic coefficient. Integration of Eq. 1 across the membrane for a given hydration conditions determines the current, above which the water diffusion cannot keep up with electro-osmosis and dry-out occurs. The use of

In Polymers for Energy Storage and Delivery: Polyelectrolytes for Batteries and Fuel Cells; Page, K., et al.;
ACS Symposium Series; American Chemical Society: Washington, DC, 2012.

Downloaded by PENNSYLVANIA STATE UNIV on June 14, 2012 | http://pubs.acs.org
Publication Date (Web): May 7, 2012 | doi: 10.1021/bk-2012-1096.ch017

eq. 1 or analogous equations requires knowledge of the hydration isotherm of the membrane material, i.e., chemical potential μ_w or activity of water a_w as a function of water concentration C_w. This isotherm is usually obtained by equilibrating Nafion with a vapor. i.e., isopiestically, in a range of activities and such measurements have long been an integral part of Nafion-related research.

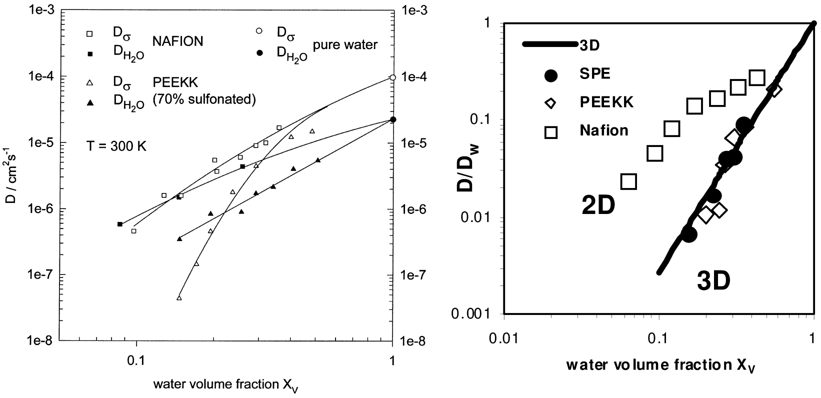

A **B**

Figure 1. A - The proton diffusivity D_σ (calculated from conductivity using the Einstein equation) and water self-diffusivity D_w in Nafion and poly(ether-ether-ketone-ketone) as a function of water volume fraction. Reproduced from ref. (8) with permission by the publisher. Copyright 2001 Elsevier. B - Water self-diffusion relative to bulk water in Nafion and two ionomer materials, poly(ether-ether-ketone-ketone) and sulfonated polyethylene as a function of water volume fraction. The solid line summarizes the results for non-aqueous non-ionic polymer-solvent systems, representative of random isotropic (3D) composites. After (7).

Unfortunately, measurements of equilibrium hydration of Nafion and other ionomer materials have often been puzzled by a controversial phenomenon called Schroeder's paradox, whereby equilibration in contact with saturated vapor and liquid water yields different results. Bass and Freger (*11*) extended liquid equilibration to under saturation using solutions of an osmotic stressor to show that discrepancies may be observed at all activities, as shown in Figure 2. Obviously, these results may seem to contradict the fundamental principles of thermodynamics. In particular, they preclude unambiguous determination of a chemical potential of water for a given hydration and rigorous modeling of water transport. No explanation was found to this puzzling phenomenon until the last decades and it was often ascribed to various artifacts. A few attempts to find genuine physical reasons appeared only relatively recently, even though the controversy is still not fully removed.

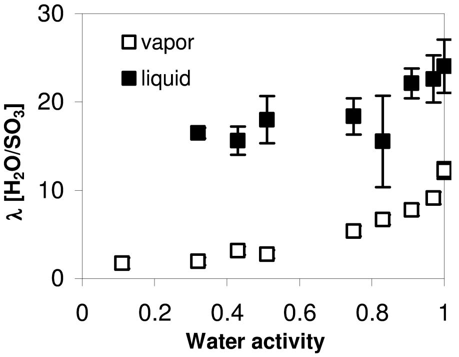

Figure 2. Water uptake isotherms by the Li form of Nafion 117 membrane at 30°C based on dimensional changes in vapor- and liquid-equilibration modes. Liquid isotherm was measured using Nafion samples immersed in a solution of an osmotic stressor Li-poly(vinylsulfonate). After ref. (11).

Downloaded by PENNSYLVANIA STATE UNIV on June 14, 2012 | http://pubs.acs.org
Publication Date (Web): May 7, 2012 | doi: 10.1021/bk-2012-1096.ch017

Vallieres et al. (*12*) hypothesized that this effect could result from multiple minima that are possible in the free energy expression given by the Frenkel-Flory-Rehner theory of swollen polymeric gels (*13*) for certain combinations of parameters. Their assumption should however predict a swelling hysteresis rather than dependence of the equilibrium state on the phase state of the external medium, which was not experimentally observed.

Nearly all models that addressed Schroeder's paradox attributed its origin to interfacial effects and an additional capillary or Laplace pressure exerted on the internal aqueous microphase. The idea was apparently first suggested by Zawodzinski et al. (*14*). A decade later in mid-2000s Choi and Datta (*15*, *16*), Weber and Newman (*17*, *18*) and Elfring and Struchtrup (*19*) proposed a few slightly different but conceptually related models. All of them essentially view the interfacial (Laplace) pressure as an additional contribution that together with the mechanical pressure exerted by the elastic matrix counterbalances the osmotic pressure by the ions within the polymer. Presence of the Laplace pressure in vapor equilibration and its absence in liquid equilibration may explain the difference between hydration in the two modes and the observed hydration behavior and water transport in Nafion could be reasonably well described. Remarkably, these models, especially the one by Choi and Datta (*15*, *16*), indicate the connection between the hydration behavior and microstructure, the two most puzzling properties of Nafion.

However, closer inspection of these models reveals a few weaknesses fixed through *ad hoc* assumptions. For instance, the model of Choi and Datta views the polymer as a network of permanent pores that are filled with water and open to the environment, vapor or liquid, at the surface. Existence of the aqueous microphase in Nafion is well established, yet its microscopic dimension does not follow from the model and the experimentally known area of the interface is used to calculate the pore radius. Since a permanent pore cannot exert a Laplace pressure, the latter is actually assumed to arise from the liquid-vapor interface at the open mouths of

Downloaded by PENNSYLVANIA STATE UNIV on June 14, 2012 | http://pubs.acs.org
Publication Date (Web): May 7, 2012 | doi: 10.1021/bk-2012-1096.ch017

the pores at the surface. As pointed out by Vallieres et al. (*12*), such an *ad hoc* assumption clearly ignores the fact that the open mouth configuration at the surface should be unstable. Similar flaws may be found in other models.

Finally it needs to be stressed that equilibrium Laplace pressure must always vanish and the curvature of a liquid interface must become zero at saturation. Therefore, even though incorporation of a Laplace or similar pressure in the above models seems to explain the observed difference under saturation, this still cannot resolve the controversy of Schroeder's paradox at saturation. Again, this point is circumvented and experimental results are explained in the above models by *ad hoc* assumptions.

The main purpose of this chapter is to clarify the questionable points and controversies related to Schroeder's paradox and microstructure. The second section presents a new thermodynamic model that ultimately produces a transparent connection between the equilibrium hydration and microstructure. Subsequently, in the third section the model predictions are compared versus the structural data for the bulk and surface of Nafion. It is shown that, despite its crudeness, the model may explain and correctly describe the structural evolution of Nafion at various hydration conditions.

Thermodynamics of Hydrated Nafion

Bulk Free Energy of Microphase-Separated Ionomer

All equilibrium properties of a polymer-solvent system, including chemical potentials, can be in general derived from an appropriate expression for the free energy. A number of methods are available that can be used to carry out such calculations in rather general cases and many of them have been applied to Nafion, such as self-consistent mean-field (SCMF) calculations (*20*, *21*), molecular dynamics (*22*, *23*), dissipative particle dynamics (*24*), or atomic structure calculations (*25–27*). These methods may usually fairly adequately address molecular interactions using appropriate intermolecular potentials, therefore, they all successfully demonstrate the formation of microscopic phase-separated domains within Nafion with the size and morphology of the aggregates varying with degree of hydration. However, these models usually rely on ideal Gaussian statistics of long polymer chains (*28*) and may encounter difficulties when effects, such as presence of relatively short chains, crystallinity or transient elasticity due to slow relaxation, become critical for adequate description.

In this situation, which is characteristic of Nafion, a transparent model calculating the total free energy of the system using some physically correct "effective" expressions and values of parameters, may offer advantages over sophisticated first-principle computations. The optimal level of complexity would be the one just sufficient to contain all necessary physics, in particular, microscopic phase separation. For instance, the latter requirements was not fully met by the model of Choi and Datta that assumed phase separation but contained no physics to ensure it would remain microscopic.

The model proposed recently (*29*) appears to meet the above criteria. Similar to previous phenomenological models it explicitly assumes that the perfluorinated matrix and (hydrated) ionic groups are highly incompatible and strongly segregate within the matrix. The total change of the free energy upon mixing the polymer and water *per unit dry volume* is written as follows:

$$\Delta F = \Delta F_o + \Delta F_s + \Delta F_e, \tag{2}$$

where ΔF_o is the osmotic term that accounts for hydration of polar group and all interactions within the aggregates, i.e., between ionic groups, counter-ions and water, ΔF_s is the interfacial energy associated with the interface between the aggregates and matrix, and ΔF_e is the elastic energy of the matrix polymer. The interfacial term may be approximately viewed as the residual free energy associated with incomplete (microscopic) phase separation and presence of an interface. Equation 2 neglects the residual translational entropy of aggregates, which is small, when aggregates are large.

Downloaded by PENNSYLVANIA STATE UNIV on June 14, 2012 | http://pubs.acs.org
Publication Date (Web): May 7, 2012 | doi: 10.1021/bk-2012-1096.ch017

Given the volume density of polar groups in dry polymer n or, alternatively, the dry polymer volume per group $v_e = 1/n$, the macroscopic state of the system, as well as composition of the aggregates, is uniquely determined by the average number of water molecules per ionic group λ. This parameter is then assumed to determine the hydration term ΔF_o, just as for a macroscopic solution. The hydration energy change ΔF_o *per group* is then written as

$$f_o = \Delta F_o / n = g_o(\lambda), \tag{3}$$

where $g_o(\lambda)$ is some decreasing function of λ. For instance, an ideal solution, a Debye–Hückel electrolyte solution or a BET sorption isotherm (*15*, *29*, *30*) could be used as approximations, yet the specific form is inessential for the following analysis.

The second interfacial term in eq. 2 is customarily written as (*31*, *32*)

$$f_s = \Delta F_s / n = \gamma A / n = \gamma \sigma, \tag{4}$$

where γ is the interfacial tension and A is the total interfacial area per unit dry polymer volume. Similar to eq. 3, eq. 4 gives this energy per ionic group, where σ is the interfacial area per group. The value of γ will be in general dependent on λ, but should weakly change for the more important range of moderate and large λ.

The elastic term ΔF_e may arise in two different principal ways. First, the matrix is strained upon swelling, which raises its elastic energy. In the present case of a microphase-separated system water is added to aggregates but does not penetrate inside the surrounding hydrophobic matrix, thus the incompressible matrix will be non-affinely “inflated”, i.e., squeezed or stretched between growing aggregates (*33*). Note that this mode of deformation differs from the classic Flory-Rehner or related models that assumes affine deformation, i.e., uniform hydration and swelling of the whole polymer with increasing spacing between individual chains (*13*, *34*)). As hydration increases, the matrix gradually transforms from a network of thinning partitions separating isolated aggregates to a network of rods embedded in a continuous aqueous phase and, ultimately, to a liquid dispersion at very high hydrations. However, in a limited range, the energy of strained partitions or rods will be analogous to that of a spring, which is a quadratic function of strain. It may then be shown that, as long as the matrix

Downloaded by PENNSYLVANIA STATE UNIV on June 14, 2012 | http://pubs.acs.org
Publication Date (Web): May 7, 2012 | doi: 10.1021/bk-2012-1096.ch017

remains connected, this part of the elastic energy per group may be approximately calculated using the following relation (*33*)

$$f_d = \Delta F_d / n \approx G_{ef} v_e (1-\phi_o)(\phi_w - \phi_o)^2 \cdot \quad (5)$$

Here G_{ef} is the effective elastic modulus, $\phi_w = v\lambda/(v_e+v\lambda)$ is the water volume fraction in the polymer, v the volume of water molecule, and ϕ_0 is the value of ϕ_w corresponding to the relaxed state of the matrix.

Since Nafion is not cross-linked but its relaxation is very slow, G_{ef} and ϕ_0 may be viewed as transient characteristics that depend on the thermal and/or hydration history. Note that eq. 5 predicts that the elastic pressure, proportional to 1st derivative of f_d with respect to ϕ_w (see below), vanishes at $\phi_w = \phi_0$ whereas in the classic Flory-Rehner or related models of homogeneous gels it is always finite, since the elastic energy is roughly a linear and not quadratic function of ϕ_w (*13*, *34*). It is seen that, similar to the osmotic term, the energy f_d roughly depends only on the *volume* change, i.e., λ or ϕ_w, but not on σ or aggregate size.

A different type of elastic contribution ΔF_c is related to the presence of a *microscopic interface*. It is particularly characteristic of ionomers and strongly segregated block-copolymers and is associated with the so-called "corona" region adjacent to the interface, in which backbone chains have to be stretched to allow aggregation of ionic groups (see Figure 3A) (*31*, *32*, *35*). The "corona" chains gets more crowded and stretched and the associated elastic energy rapidly increases with the size of aggregate, which ensures that the phase separation remains microscopic. This important contribution was not previously considered in phenomenological models of Nafion, even though it was obviously inherently present in some simulations, e.g., self-consistent field calculations (*20*, *21*). The following relation could reasonably well describe this energy per group (*31*, *32*, *36*)

$$f_c = \Delta F_c / n = BR/\sigma, \quad (6)$$

where B is a polymer-specific elastic parameter and R is the radius of curvature of the microscopic interface. Rigorous derivation of eq. 6 may be found elsewhere (*31*, *32*, *36*), however, it can be easily understood by noting that R represents the distance from the interface, over which the corona chains are stretched, and R_σ is the volume of a stretched chain connected to one group. The latter is approximately constant (see next) and it is immediately seen that f_c is a quadratic function of R, analogous to the energy of a stretched ideal Gaussian chain or a spring. For ideal "corona" chains the "spring constant" B may be related to the geometry of the monomer and persistence length and is weakly dependent of the morphology and type of the aggregates (micelles). In general, it is convenient to view B as a polymer-specific phenomenological parameter.

The variables λ (or ϕ_w) and σ and R in eq. 6 are not independent. Indeed, in the full range of hydrations the interfacial area per unit total volume may be approximately calculated

$$\sigma(1-\phi)/v_e = a\phi(1-\phi)/R, \quad (7)$$

Downloaded by PENNSYLVANIA STATE UNIV on June 14, 2012 | http://pubs.acs.org
Publication Date (Web): May 7, 2012 | doi: 10.1021/bk-2012-1096.ch017

Here $\phi = (v_g+v\lambda)/(v_e+v\lambda)$ is the total volume fraction of the aqueous phase including the ionic groups, v_g the volume of an ionic group with counter-ion, and a is a numerical coefficient depending on the aggregate dimensionality and geometry. The left side of eq. 7 is the total interfacial area calculated as the product of σ and the total number of groups per unit hydrated volume $(1-\phi)/v_e$, while the right side is the same quantity calculated using a general geometric expression often utilized in analysis of random two-phase media (*37*, *38*). The values $a = 1.455$ and $a = 2$ valid for 3D and 2D Voronoi tessellations (*39*) could be good approximations for, respectively, spherical and rod-like micelles. Equation 7 then yields

$$R = av_e\phi/\sigma. \tag{8}$$

and, ultimately,

$$f_c = BR^2/av_e\phi = Bav_e\phi/\sigma^2, \tag{9}$$

Note that eqs. 6 to 9 assume the so-called strong segregation regime, in which stretching of corona may vary. It was postulated (*31*, *40*) that in ionomers a situation is possible whereby the interfacial area per group may reach the limit σ_{min} imposed by the densest packing of the groups or maximal stretching of the corona chains. This regime called the super-strong segregation regime (*31*) will modify the relations above and below and make $\sigma \approx \sigma_{min}$ independent of λ. In particular, the balance between the interfacial and corona energy (see next) will be somewhat different. It appears however that such correction will not change any principal conclusion therefore its discussion is omitted here.

It is to be stressed that the corona energy is inherently associated with microphase separation and arises regardless of the presence or absence of cross-links in the matrix. On the other hand, the inflation terms only arises when the matrix possesses a permanent or transient rigidity, e.g., due to crystallinity, glassiness, entanglements etc. If both inflation and corona strains are simultaneously present they are superimposed. In the direction(s) normal to the interface the strain will mainly be the corona stretching described by eq. 9, while in the other direction(s) it will mainly be determined by inflation. Since to the lowest order the elastic energy is proportional to the sum of the three principle strain components squared, additivity of the corona and inflation energies is expected for small strains, thus the total elastic energy is approximately given by

$$f_e = \Delta F_e/n \approx f_d + f_c \tag{10}$$

thus the total (Helmholtz) free energy per ionic group of the ideal ionomer is written as follows

$$f \approx f_o + f_s + f_d + f_c \approx g_o(\lambda) + \gamma\sigma + G_{ef}v_e(1-\varphi_o)(\varphi_w-\varphi_o) + Bav_e\varphi/\sigma^2 \tag{11}$$

Within the approximations used f_o and f_d depend only on λ, while f_c depend on λ and σ, thereby, eq. 9 manifests the crucial fact that the total free energy may be split to σ-dependent and σ-independent parts.

Equilibrium Characteristics of Ionomer Bulk

The equilibrium values of microscopic parameters σ and R at given hydration λ are determined by minimizing with respect to σ the Gibbs energy per group $g = f - \mu\lambda$, where μ is the chemical potential of water, i.e., using the relation

$$\hat{\gamma} = \left(\frac{\partial g}{\partial \sigma}\right)_{\lambda} = \left(\frac{\partial f}{\partial \sigma}\right)_{\lambda} = \left(\frac{\partial f_{\sigma}}{\partial \sigma}\right)_{\lambda} = 0 \quad , \tag{12}$$

where $f_\sigma = f_c + f_s$ is the σ-dependent part of the free energy viewed here as a composite interfacial energy including elastic corona contribution. Since all groups are assumed to be located at the interface and their total number is fixed, comparison with the thermodynamic definition of surface tension shows that $\hat{\gamma}$ has the meaning of the total interfacial tension of the matrix-aggregate interface and $\hat{\gamma} = 0$ furnishes a necessary condition for the thermodynamic stability of the microscopic interface.

Equations 11 and 12 yield relations of σ and R to λ or ϕ

$$\sigma(\lambda) = (2av_e B/\gamma)^{1/3}\phi^{1/3} = \sigma_\infty \phi^{1/3}, \tag{13}$$

$$R(\lambda) = (a^2 v_e^2 \gamma/2B)^{1/3}\phi^{2/3} = R_\infty \phi^{2/3}. \tag{14}$$

It is seen that both σ and R increase with hydration and local corona stretching decreases. The relation $\sigma \sim \gamma^{-1/3}$ was earlier derived and tested experimentally by Adelbert et al. (*2*) and $R \sim v_e^{2/3}$ is equivalent to the well-known dependence of the microdomain size for block copolymers in strong-segregation regime (*36*, *41*).

The parameters σ_∞ and R_∞ have the meaning of limiting values at very high hydrations, i.e., when $\lambda \to \infty$ and $\phi \to 1$ and σ and R become independent of λ. The aggregates in this situation assume the configuration of *normal micelles* and the ideal ionomer breaks up to a colloidal dispersion. The existence of such micelles in solution was confirmed for Nafion and similar ionomers (*2*, *3*, *42*). Nevertheless, the effective values of σ_∞ and $R_\infty = av_e/\sigma_\infty$ may somewhat vary with hydration, if effective values of parameters B and γ vary. In such case it may be more convenient to consider σ_∞ and R_∞, accessible from scattering experiments (*4*), as phenomenological parameters that may replace "molecular" parameters B and γ.

Using eqs. 13 and 14, the total free energy (eq. 10) becomes

$$f \approx f_o + f_s + f_d + f_c \approx g_o(\lambda) + G_{ef} v_e (1-\phi_o)(\phi_w - \phi_o) + \tfrac{3}{2}\gamma\sigma_\infty \phi^{1/3}. \tag{15}$$

The last term of eq. 15 represents a combined contribution of the interfacial and corona energy. Minimization of $g = f - \mu\lambda$ with respect to λ yields the chemical potential of water for a given λ

$$\mu(\lambda) = \frac{df}{d\lambda} = \mu_0(\lambda) + 2vG_{ef}(\phi_w - \phi_0) + \tfrac{1}{2}\gamma\sigma_\infty \frac{v}{v_e - v_g}\phi^{-2/3}(1-\phi)^2 = -v\pi_0 + v\pi_d + v\pi_s \tag{16}$$

where $\mu_o(\lambda) = dg_o/d\lambda$ is the osmotic (hydration) part of the chemical potential of water that is subsequently expressed as the product $-v\pi_o$., where π_o is the intra-

In Polymers for Energy Storage and Delivery: Polyelectrolytes for Batteries and Fuel Cells; Page, K., et al.;
ACS Symposium Series; American Chemical Society: Washington, DC, 2012.

Downloaded by PENNSYLVANIA STATE UNIV on June 14, 2012 | http://pubs.acs.org
Publication Date (Web): May 7, 2012 | doi: 10.1021/bk-2012-1096.ch017

Downloaded by PENNSYLVANIA STATE UNIV on June 14, 2012 | http://pubs.acs.org
Publication Date (Web): May 7, 2012 | doi: 10.1021/bk-2012-1096.ch017

polymer osmotic pressure. Similarly, the second and third terms in eq. 16 are also expressed through two pressures exerted on the aqueous microphase, π_d, the elastic pressure, and π_s that may be interpreted as a "Laplace" pressure modified with the elastic contribution of the corona. The former is given by the expression

$$\pi_d \approx 2G_{ef}\left(\phi_w - \phi_0\right). \tag{17}$$

It is to be stressed that, since Nafion is not chemically cross-linked, this pressure in Nafion is transient and must always vanish at true equilibrium. However, given the extremely slow relaxation in Nafion, especially, at ambient temperatures, this pressure may be very significant and strongly dependent on the sample history and the time and mode of equilibration. For this reason in realistic conditions this non-equilibrium pressure and parameters G_{ef} and ϕ_0 present the greatest uncertainty in Nafion hydration.

In contrast, the interfacial-elastic "Laplace" pressure is given by

$$\pi_s = \tfrac{1}{2}\frac{\gamma\sigma_\infty}{v_e - v_g}\phi^{-2/3}(1-\phi)^2 = \frac{v_e}{v_e - v_g}(1-\phi)^2\frac{a\gamma}{2R} \tag{18}$$

is a true equilibrium characteristics, since it arises from the balance between interfacial tension and corona stretching, both inherent to the microscopic phase separation in Nafion. Formally, this pressure is similar to the Laplace pressure used by Choi and Datta; for instance, both pressures are inversely proportional to the pore (i.e., aggregate) radius R. However, a principal difference is that here π_s is related to a different interface – between matrix and hydrated ion aggregates - and is a true equilibrium property.

As hydrations increases, the elastic pressure π_d should increase (eq. 17), however, G_{ef} is expected to decrease with ϕ, therefore π_d is only expected to increase in a limited hydration range and at times much less that relaxation time. At very high hydrations ($\phi \to 1$) when the matrix loses connectivity G_{ef} should vanish thereby π_d should vanish as well. On the other hand, the "Laplace" pressure π_s stays constant for a given λ and does not relax, but it decreases with hydration and vanishes at $\phi \to 1$ (eq. 18). It may be then concluded that *the true equilibrium state of Nafion at saturation is an (infinitely) dilute dispersion of micelles*, in which case both π_d and π_s are zero (*43*). Obviously, no Schroder's paradox is expected for liquid dispersion. However, as long as Nafion remains solid-like, a finite π_d will keep $\phi << 1$, which will also keep π_s finite. As shown in the next section, this will result in Schroeder's paradox.

Equilibrium at Ionomer Surface and Schroeder's Paradox

The situation at the surface is complicated by the presence of an external phase. Therefore there are three different phases involved: the hydrophobic matrix, the internal aqueous phase (interior of ionic aggregates), and vapor (if the polymer contacts water vapor) or external solution (if the polymer contacts a liquid phase). Correspondingly, there are three types of interfaces and three interfacial tensions: solution-vapor γ_1, matrix-vapor γ_2 and matrix-solution γ_{12} (Figure 3B). If three different phases meet and form a 3-phase contact line, as

Downloaded by PENNSYLVANIA STATE UNIV on June 14, 2012 | http://pubs.acs.org
Publication Date (Web): May 7, 2012 | doi: 10.1021/bk-2012-1096.ch017

in Figure 3B, the 3 tensions must balance each other forming a force triangle (the so-called Neumann construction (*44*)), otherwise the 3-phase contact may not exist and one interface will disappear. It is then immediately seen that a hypothetical "open" inverted micelle at the surface of an ionomer facing a vapor phase, as shown in Figure 3B, will always be unstable. Indeed, γ_{12} is identified with $\hat{\gamma}$ that must be *zero at equilibrium* (see eq. 12). Since in general $\gamma_1 \neq \gamma_2$, the Neumann construction is impossible. As the surface tension of water is much higher than that of a hydrophobic matrix, $\gamma_1 > \gamma_2$, in vapor the matrix phase must "spread" over the unstable "open" micelle, i.e., the latter must "sink" under the surface to become a regular "closed" bulk micelle (Figure 3C). Disregarding fluctuations, the surface will then be entirely composed of the hydrophobic matrix phase, which indeed agrees with experimental observations (*14*, *45*).

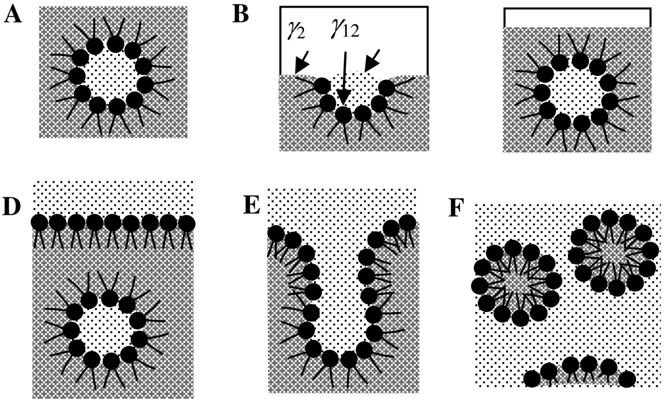

Figure 3. Schematic representation of micelles in the bulk and at the ionomer surface: A - a 2D or 3D inverted micelle in the bulk composed of aggregated and hydrated ionic groups connected through corona chains to the surrounding matrix; B - a hypothetical open micelle at the surface facing a vapor phase; C - an equilibrium micelle "buried" under the surface facing a vapor phase; D - a hypothetical "flat" surface facing a liquid; E - a transitional or methastable state at the surface facing a liquid; F - equilibrium state at the surface facing a liquid (dispersed normal micelles). After reference (29).

In the case of liquid equilibration the relation between γ_1 and γ_2 is opposite. Since $\gamma_1 = 0$, γ_2 will be the largest interfacial tension in the system. The interface between the matrix and external fluid will have to disappear and the internal interface will get exposed to the external liquid phase. The corresponding re-arrangement will resemble "adsorption" of the ionic groups on the polymer surface, like that of surfactant molecules on water-vapor interface. However, unlike a surfactant monolayer on water, a flat external surface ($R = \infty$) schematically shown in Figure 3D will have interfacial and corona energies unbalanced and will tend to curve to the same extent as the internal interface (Figure 3E) and in water will eventually break up to dispersion (Figure 3F). Even if the breakup is not complete, the external surface facing a large volume of liquid will tend to assume the limiting values $\sigma = \sigma_\infty$ and $R = R_\infty$ of the dilute dispersion and the configuration of normal micelles. On the other hand, since the ionic groups at the surface and inside the polymer are exchangeable, their chemical potential η must be equal throughout, as well as chemical potential of water μ. Since both $\mu = df/d\lambda$ and $\eta = f - \mu\lambda = f - \lambda(df/d\lambda)$ are derived from the same free energy f for a given μ, it is easily shown that the interface configuration at the surface as well as in the bulk must be identical. As there can be no "Laplace" pressure for the groups on the surface, the internal aqueous phase should not be subject to any such pressure as well. The volume-dependent (but σ-independent) elastic pressure π_d may still restrict polymer expansion; a reduced chemical potential of water in the external liquid will have a similar effect. However, the restrictive effect of the "Laplace" pressure will vanish in liquid.

The vanishing of π_S in liquid equilibration may be interpreted as follows. The whole matrix phase, everywhere bounded by the matrix-solution interface, is under a pressure lower by π_S than the solution phase, external or internal. In the process of equilibration with a liquid solution (i.e., transition from Figure 3C to 3E and 3F) external and internal interfaces have to adopt the same configuration to equalize the pressure in the matrix. The excess pressure π_S inside the aqueous aggregates in the bulk is then exactly compensated by the pressure in the matrix lower by $\Delta P = \pi_S$ than in the external solution then the external and internal liquid phases are under the same pressure. The final equilibrium state in liquid will obviously be different from the hydration in vapor of the same μ. In vapor equilibration the external surface is approximately flat to minimize the surface energy (Figure 3C) and the matrix will be under the same pressure as the external medium ($\Delta P = 0$), whereas the pressure inside the aggregates will be larger by π_S. This will result in Schroeder's paradox.

In this respect, two points are to be emphasized. First, at saturation ($\mu = 0$ and $a_w = 1$) thermodynamics clearly prohibits Schroeder's paradox. Therefore it will only be observed as a transient quasi-equilibrium phenomenon under two conditions:

(1) slow relaxation prevents dissolution of the matrix in liquid keeping the surface structure as in Figure 3E;
(2) the surface in vapor is in a metastable state shown in Figure 3C, in which it is hydrophobic and has no liquid film on it. As long as excessive condensation is prevented, this state can also last very long, even at saturation, since it may only be broken through a slow activation-relaxation process involving nucleation of many water droplets on the hydrophobic surface followed by "pulling" of the ionic groups out of the bulk to the surface to create a continuous surface liquid phase. Since activation energy required for nucleation of water on a hydrophobic surface is larger, this whole process may be very slow.

Both conditions have been routinely realized in most hydration experiments with Nafion, yet in some this could not be the case. For instance, in very long vapor-equilibration experiments at saturation by Onishi et al. (*46*) the second condition could be violated, which may explain why no paradox was observed.

Downloaded by PENNSYLVANIA STATE UNIV on June 14, 2012 | http://pubs.acs.org
Publication Date (Web): May 7, 2012 | doi: 10.1021/bk-2012-1096.ch017

Second, Schroeder's paradox may be perfectly legitimate from the thermodynamics viewpoint under saturation ($\mu < 0$ and $a_w < 1$), if the equilibrium hydration in liquid is low enough so that no dissolution occurs. This equilibrium hydration is given by the relation $\mu = -v\pi_0$, i.e., eq. 16 without elastic and "Laplace" terms. In this case the finite π_s that exists but does affect hydration in liquid equilibration will show up in vapor-equilibration and result in differences between the two modes. A transient rigidity, i.e., a finite π_d, will only enhance the difference, since it will further reduce ϕ and R and increase π_s (cf. eq. 18). This effect of finite π_d may also completely obscure the "twilight" range of water activities just under saturation, in which $\pi_s = 0$, since the polymer should still form a dispersion with water content rapidly rising as a_w approaches 1. Obviously, the experimentally measured hydration of (unrelaxed) solid Nafion ($\pi_s > 0$) in this range should be highly sensitive to water activity and relaxation history. Indeed, such enhanced sensitivity is well observed in recent thorough measurements by Jeck et al., presented in Fig. 4 (*47*).

Downloaded by PENNSYLVANIA STATE UNIV on June 14, 2012 | http://pubs.acs.org
Publication Date (Web): May 7, 2012 | doi: 10.1021/bk-2012-1096.ch017

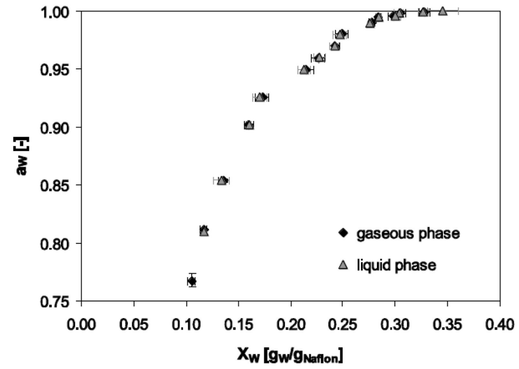

Figure 4. Vapor equilibration isotherm for Nafion showing a high sensitivity of hydration to water activity in the range just under $a_w = 1$. Reproduced from ref. (47) with permission by the publisher. Copyright 2011 Elsevier.

Comparison with Experiments

Bulk Microstructure: Microscopic and Microscopic Swelling and Morphology

Gebel proposed a general scheme for the evolution of the Nafion structure with hydration, mainly based on scattering data (*3*, *5*, *6*, *48*). According to it, aqueous phase undergoes transition from isolated spherical aggregates (inverted micelles) at low hydration to "cluster network" (*49*) that is transformed to a network of rod-like normal micelles around $\phi \sim 0.5$ and breaks up to a liquid dispersion of individual rod-like micelles at still higher hydrations. Recently, Schmidt-Rohr and Chen (*50*) modified this scheme and concluded that the aqueous aggregates at low hydration have the form of elongated cylindrical channels, apparently stabilized by the stiffness and partial crystallinity of the matrix polymer. The present model cannot predict whether the micelles are 2D or 3D, but the dimensionality can

Downloaded by PENNSYLVANIA STATE UNIV on June 14, 2012 | http://pubs.acs.org
Publication Date (Web): May 7, 2012 | doi: 10.1021/bk-2012-1096.ch017

be viewed as a parameters that is to be found by comparison with experimental data. It is shown below that the model with a 2D morphology "plugged in" shows good agreement with structural data. Thus it well agrees with the observation that "microscopic swelling", i.e., increase in the Bragg spacing *d* relative to the dry state (d_0) shows an approximately linear relation to the macroscopic linear expansion ratio ("macroscopic swelling"). It has been already pointed out and shown by simulations (*20*, *27*) that such relation between the two may result from the evolution of the microstructure and does not necessarily indicate a lamellar (1D) morphology, as was previously assumed (*51*).

Indeed, the volume of a unit cell enclosing one aggregate scales as d^D, where $D = 2$ for rods or channels and $D = 3$ for spherical aggregates. On the other hand, the aggregate surface area scales as R^{D-1}. Using eq. 7 for area per volume we obtain

$$\frac{R^{D-1}}{d^D} \cong \frac{b\phi(1-\phi)}{R}, \tag{19}$$

and, using eq. 14,

$$d_0 = d_\infty \phi^{n-1/D}(1-\phi)^{-1/D}, \tag{20}$$

where $d_\infty \cong b^{-1/D}R_\infty$ and n should vary between 2/3 (strong segregation) and 1 (super-strong segregation). Since ϕ includes the group volume, $\phi = \phi_w + \phi_g(1-\phi_w)$, where $\phi_g = v_g/v_e$ is the volume fraction of the ionic groups in the dry polymer. This yields the microscopic swelling for the full range of ϕ

$$\frac{d-d_0}{d_0} = \left(\frac{\phi}{\phi_g}\right)^{n-1/D}\left(\frac{1-\phi}{1-\phi_g}\right)^{-1/D} - 1 = \left(\frac{\phi}{\phi_g}\right)^{n-1/D}\left(1-\phi_w\right)^{-1/D} - 1. \tag{21}$$

On the other hand, for isotropic swelling the macroscopic linear expansion ratio is $(1-\phi_w)^{-1/3} - 1$ thereby the slope of microscopic versus macroscopic swelling is given by

$$slope = \frac{(d-d_0)/d_0}{\left(1-\phi_w\right)^{-1/3}-1} \approx 3\left[\left(n-\frac{1}{D}\right)\frac{1-\phi_g}{\phi_g}+\frac{1}{D}\right], \tag{22}$$

where the last approximate expression is the initial slope for small hydrations. Figure 5 compares thus calculated microscopic versus macroscopic swelling with Gebel's data (*3*). The volume of sulfonic group $v_g = 68$ Å^3 and the dry volume per group of Nafion 117 $v_e = 870$ Å^3 were used in calculations (*1*, *52*). It is seen that a good agreement is obtained for $D = 2$ and n = 2/3 using a constant d_∞ adjusted to fit the Bragg spacing $d = 2.7$ nm for dry Nafion (*3*). Still better agreement, especially, at high hydrations was obtained when the d_∞ was allowed to vary linearly with ϕ_w (the "D = 2 var" curve in Figure 5A). The calculated initial slope equal to 7.4 for $D = 2$ and n = 2/3 was also reasonably close to the measured value 5.5-6 (*3*, *53*). The scattering data are then reasonably explained by the present model assuming a 2D morphology in the whole hydration range, i.e, gradual transformation from aligned nanochannels to rod- or spaghetti-like micelles as the hydration increases. Since nanochannels within aligned domains bear similarity to the bore spaces

Downloaded by PENNSYLVANIA STATE UNIV on June 14, 2012 | http://pubs.acs.org
Publication Date (Web): May 7, 2012 | doi: 10.1021/bk-2012-1096.ch017

of a bundle of stuck-together macaroni, this transformation may be conveniently termed "macaroni-spaghetti" transition (*54*).

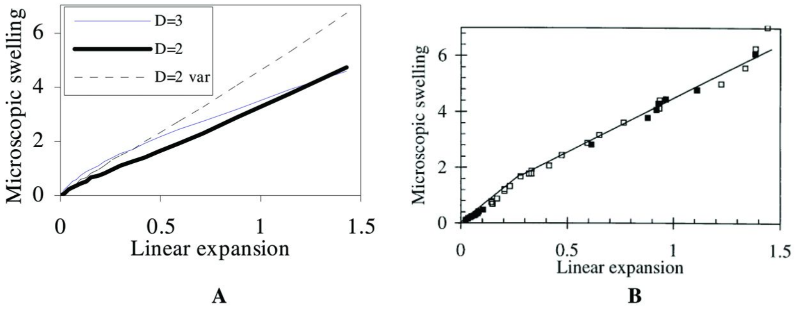

Figure 5. Microscopic vs. macroscopic swelling: A - calculated based on the present model for D = 2 and D = 3, B - experimental data presented by Gebel, reproduced with permission from ref. (3). Copyright 2000 Elsevier. For solid curves in A d_∞ was adjusted to yield the value d = 2.7 nm for dry polymer, for dotted curve d_∞ was allowed to vary linearly from 1.8 at $\phi_w = 0$ to 5.5 nm at $\phi_w = 1$.

Surface of Nafion as a Special Region

A "macaroni-spaghetti" transition is supposed to occur when a solid Nafion is placed in water and approaches thermodynamic equilibrium. However, the macroscopic relaxation times of Nafion at ambient temperatures may exceed 10^5 – 10^6 s (*55*, *56*), i.e., months or years. In ambient conditions Nafion may then remain in a quasi-equilibrium solid state virtually infinitely. Such quasi-equilibrium swelling only requires a local rearrangement along the shortest dimension of the micelles (macaroni or spaghetti), i.e., a few nm, and thus occurs fairly rapidly, in a matter of hours or less. In contrast, the relaxation required for dissolution apparently requires complete disentanglement of long individual micelles from the matrix, which involves much longer timescales.

The true equilibrium in water may however be approached closely in a few nanometers-thick outermost surface region, which is subject to much weaker topological constraints and strong and localized surface tension forces. As a result, partial disentanglement may occur fairly rapidly, at timescales typical of swelling rather than complete disentanglement. Based on the present model and 2D morphology, the expected structural changes at the surface upon transfer from vapor to liquid are schematically depicted in Figure 6. In vapor the hydrophobic surface will tend to flatten and thus minimize its finite surface tension; macaroni-like micelles will tend to align along the surface and bury hydrophobic bores under the hydrophobic "crust" (cf. Figure 3C). In contrast, in water the surface tension is zero and the entropy will randomize the loose ends of surface micelles that face infinite solution and become spaghetti-like. The surface will become hydrophilic and rough and loose spaghetti-like micelles may freely extend away from the surface but remain anchored to the surface and laterally

Downloaded by PENNSYLVANIA STATE UNIV on June 14, 2012 | http://pubs.acs.org
Publication Date (Web): May 7, 2012 | doi: 10.1021/bk-2012-1096.ch017

constrained (cf. Figure 3E). This will result in overall preferential alignment normal to the surface, while in vapor it will be along the surface (Figure 6).

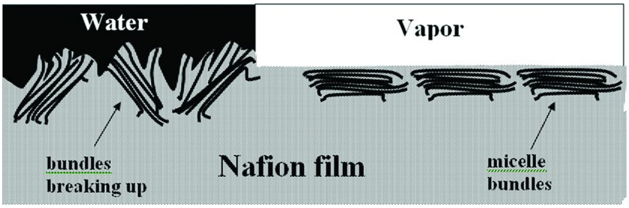

Figure 6. Schematic representation of the micelle arrangement at the Nafion surface in liquid (left) and vapor (right). Aqueous phase is black, matrix is grey, and vapor is white.

This picture was verified by examining the surface of Nafion using grazing incidence SAXS (GISAXS), AFM and contact angle of Nafion in vapor and in water (*54*, *57*). The contact angle was used to quantify hydrophilicity of the surface in vapor and liquid using, respectively, sessile drop and captive bubble methods. The result clearly demonstrated that hydrophobic surface of dry or vapor-equilibrated Nafion 117 membranes (contact angle >92°) turns hydrophilic (<28°) under water irrespective of the ionic form. Concurrently with change in hydrophilicity, AFM showed that the surface of Nafion turns significantly rougher. To rule out artifacts related to multi-scale roughness of Nafion 117 membranes, topographic AFM images of high clarity and resolution were acquired using very flat ~100 nm think films of Nafion spin-cast on Si wafers with a native hydrophilic oxide surface and with a C18-capped hydrophobic surface. The use of the hydrophobicized wafers prevented detachment of the films and allowed AFM scanning in water. Figure 7 compares topographic AFM images of identical Nafion films in air and under water. A drastic 5-fold increase of RMS roughness from 0.35 nm in air to 1.85 nm under water and appearance of protruding features is well observed, in full agreement with the mechanism depicted in Figure 6.

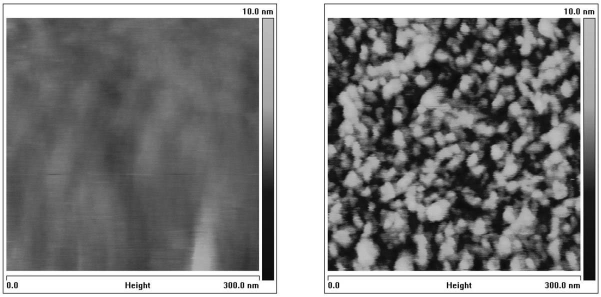

Figure 7. Topographic AFM images of the surface of a Nafion film in vapor (left) and under water (right). After (54).

The high flatness of the spin-cast samples allowed analysis of micelle orientation using GISAXS. A remarkable feature of GISAXS is that both surface and bulk structures may be probed depending on whether the incidence angle α_i is below or near/above the critical angle α_c. When $\alpha_i < \alpha_c$, the thickness of the probed depth is commensurate with depth of penetration d_p given by (*58–60*)

$$d_p \approx \frac{2d_{\min}}{\sqrt{1-(\alpha_i/\alpha_c)^2}}, \tag{23}$$

where d_{min} is the minimal penetration depth of X-rays, equal for Nafion surface to about 3.5 nm in vapor and 5.3 nm under water. For $\alpha_i/\alpha_c \leq 0.9$ the region probed GISAXS- stays within first 15-20 nm nanometers and for $\alpha_i/\alpha_c \leq 0.6$ within 10-13 nm from the surface, i.e., within the thickness of a very few micelles. On the other hand, at or above α_c GISAXS probes the whole thickness of the film.

Downloaded by PENNSYLVANIA STATE UNIV on June 14, 2012 | http://pubs.acs.org
Publication Date (Web): May 7, 2012 | doi: 10.1021/bk-2012-1096.ch017

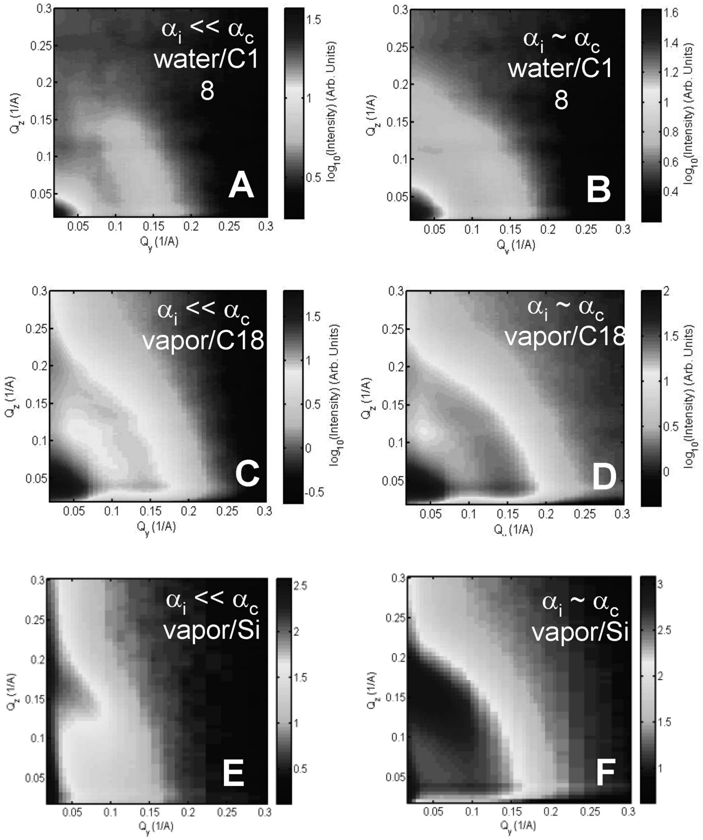

Figure 8. Two-dimensional GISAXS maps for Nafion films on a C18-capped (A to D) and native (E, F) Si substrates in water and vapor. The sustrate and environment are indicated in each spectrum. A, C, E were recorded at subcritical and B, D, F at near-critical incidence angles. After (54, 57).

Figure 8 shows the results obtained in water and vapor for Nafion films cast on native and C18-capped Si wafers. (On untreated Si wafers measurements were possible only in vapor.) The preferential orientation of the micelles is indicated by the anisotropy of the ionomer ring at Q ~ 0.15-0.2 Å in the scattering maps. The intensity is weakened and the Q value decreases in the direction of orientation. This feature has been often used to analyze anisotropy of mechanically stretched Nafion membranes (*9*, *61*). At subcritical incidence angles the surface micelles under water show preferential orientation normal to the surface (Figure 8A), while the spectrum at near-critical incidence angles shows no significant anisotropy. In vapor spectra C and E acquired at subcritical angles the anisotropy of the ionomer ring indicates preferential orientation parallel to the surface, regardless of the substrate and the micelle orientation in the bulk (spectra D and F). These results appear to fully conform to the mechanism depicted in Figure 6.

An unexpected result observed in spectra D and F in Figure 8 that were recorded in vapor is that preferential micelle orientation in the bulk of the films appears to depend on the type of substrate. Thus spectrum D recorded on a C-18 capped substrate shows micelle orientation normal to the substrate, while spectrum F of the film prepared on native substrate shows that the predominant orientation is parallel. The reason for the observed normal orientation on C18-capped substrate is not clear and may originate from preferential orientation of C18 tails or from micro-heterogeneities of self-assembled C18 monolayer. However, parallel orientation on native Si is apparently due to strong preference of the substrate by the hydrated phase and is in good agreement with recent neutron reflectivity data by Dura et al. (*62*). In either case the orienting effect of the substrate is another manifestation of the interactions that a surface or interface impose on Nafion micelles, similar to the effect of water or vapor phases at the external surface. It was reported recently that orientation of Nafion micelles may significantly enhance transport properties in a desired direction (*9*). The use of appropriate substrates for orienting micelles may then be beneficial for developing highly ion- and water-conductive Nafion based materials.

Downloaded by PENNSYLVANIA STATE UNIV on June 14, 2012 | http://pubs.acs.org
Publication Date (Web): May 7, 2012 | doi: 10.1021/bk-2012-1096.ch017

Acknowledgments

The author thanks Israel Science Foundation for financial support of this research.

References

1. Gierke, T. D.; Munn, G. E.; Wilson, F. C. *J. Polym. Sci., Part B: Polym. Phys.* **1981**, *19*, 1687–1704.
2. Aldebert, P.; Dreyfus, B.; Gebel, G.; Nakamura, N.; Pineri, M.; Volino, F. *J. Phys.* **1988**, *49*, 2101–2109.
3. Gebel, G. *Polymer* **2000**, *41*, 5829–5838.
4. Gebel, G.; Diat, O. *Fuel Cells* **2005**, *5*, 261–276.
5. Rubatat, L.; Gebel, G.; Diat, O. *Macromolecules* **2004**, *37*, 7772–7783.
6. Rubatat, L.; Rollet, A. L.; Gebel, G.; Diat, O. *Macromolecules* **2002**, *35*, 4050–4055.

7. Freger, V.; Korin, E.; Wisniak, J.; Korngold, E.; Ise, M.; Kreuer, K. D. *J. Membr. Sci.* **1999**, *160*, 213–224.
8. Kreuer, K. D. *J. Membr. Sci.* **2001**, *185*, 29–39.
9. Li, J.; Park, J. K.; Moore, R. B.; Madsen, L. A. *Nat. Mater.* **2011**, *10*, 507–511.
10. Regev, O.; ElKati, P. N. B.; Loos, J.; Koning, C. E. *Adv. Mater.* **2004**, *16*, 248–+.
11. Bass, M.; Freger, V. *Polymer* **2008**, *49*, 497–506.
12. Vallieres, C.; Winkelmann, D.; Roizard, D.; Favre, E.; Scharfer, P.; Kind, M. *J. Membr. Sci.* **2006**, *278*, 357–364.
13. Flory, P. J. *Principles of polymer chemistry*; Cornell University Press: Ithica, NY, 1953.
14. Zawodzinski, T. A.; Derouin, C.; Radzinski, S.; Sherman, R. J.; Smith, V. T.; Springer, T. E.; Gottesfeld, S. *J. Electrochem. Soc.* **1993**, *140*, 1041–1047.
15. Choi, P.; Jalani, N. H.; Datta, R. *J. Electrochem. Soc.* **2005**, *152*, E84–E89.
16. Choi, P. H.; Datta, R. *J. Electrochem. Soc.* **2003**, *150*, E601–E607.
17. Weber, A. Z.; Newman, J. *J. Electrochem. Soc.* **2003**, *150*, A1008–A1015.
18. Weber, A. Z.; Newman, J. *J. Electrochem. Soc.* **2004**, *151*, A311–A325.
19. Elfring, G. J.; Struchtrup, H. *J. Membr. Sci.* **2007**, *297*, 190–198.
20. Galperin, D. Y.; Khokhlov, A. R. *Macromol. Theory Simul.* **2006**, *15*, 137–146.
21. Krueger, J. J.; Simon, P. P.; Ploehn, H. J. *Macromolecules* **2002**, *35*, 5630–5639.
22. Mologin, D. A.; Khalatur, P. G.; Kholhlov, A. R. *Macromol. Theory Simul.* **2002**, *11*, 587–607.
23. Vishnyakov, A.; Neimark, A. V. *J. Phys. Chem. B* **2001**, *105*, 9586–9594.
24. Yamamoto, S.; Hyodo, S. A. *Polym. J.* **2003**, *35*, 519–527.
25. Elliott, J. A.; Paddison, S. J. *Phys. Chem. Chem. Phys.* **2007**, *9*, 2602–2618.
26. Paddison, S. J.; Elliott, J. A. *J. Phys. Chem. A* **2005**, *109*, 7583–7593.
27. Wescott, J. T.; Qi, Y.; Subramanian, L.; Capehart, T. W. *J. Chem. Phys.* **2006**, *124*.
28. de Gennes, P. G. *Scaling concepts in polymer physics*; Cornell: Ithaca, 1991.
29. Freger, V. *J. Phys. Chem. B* **2009**, *113*, 24–36.
30. Freger, V.; Korin, E.; Wisniak, J.; Korngold, E. *J. Membr. Sci.* **1997**, *128*, 151–162.
31. Nyrkova, I. A.; Khokhlov, A. R.; Doi, M. *Macromolecules* **1993**, *26*, 3601–3610.
32. Semenov, A. N.; Nyrkova, I. A.; Khokhlov, A. R. In *Ionomers: Characterization, Theory and Applications*; Schlick, S., Ed.; CRC Press: Boca Raton, 1996, pp 251−279.
33. Freger, V. *Polymer* **2002**, *43*, 71–76.
34. Osada, Y.; Khokhlov, A. R. *Polymer Gels and Networks*; Marcel Dekker: New York, 2002.
35. Dreyfus, B. *Macromolecules* **1985**, *18*, 284–292.
36. Semenov, A. N. *Zhurnal Eksperimentalnoi I Teoreticheskoi Fiziki* **1985**, *88*, 1242–1256.

Downloaded by PENNSYLVANIA STATE UNIV on June 14, 2012 | http://pubs.acs.org
Publication Date (Web): May 7, 2012 | doi: 10.1021/bk-2012-1096.ch017

37. Mohanty, K. K.; Ottino, J. M.; Davis, H. T. *Chem. Eng. Sci.* **1982**, *37*, 905–924.
38. Talmon, Y.; Prager, S. *J. Chem. Phys.* **1982**, *76*, 1535–1538.
39. Meijering, J. L. *Philips Res. Rep.* **1953**, *8*, 270–290.
40. Semenov, A. N.; Nyrkova, I. A.; Khokhlov, A. R. *Macromolecules* **1995**, *28*, 7491–7500.
41. Bates, F. S.; Fredrickson, G. H. *Annu. Rev. Phys. Chem.* **1990**, *41*, 525–557.
42. *Ionomers: Characterization, Theory, and Applications*; Schlick, S., Ed.; CRC Press: Boca Raton, FL, 1996.
43. Note that the same will be true for other microphase-separated non-crosslinked systems, e.g., diblock-copolymers with one hydrophilic block, which are expected to dissolve by forming micelles or vesicles. Their size and morphology should depend on the molecular weight and the ratio between the blocks, but is typiclly controlled by nonequilibrium aspects of the formation process (e.g., Discher, D. E.; Eisenberg, A. *Science* **2002**, *297*, 967−973). As for Nafion, dissolution of such polymers may take excessively long, especially, for larger and symmetrical block-copolymers that form larger vesicles.
44. de Gennes, P.-G.; Brochard-Wyart, F.; Quere, D. *Capillarity and Wetting Phenomena: Drops, Bubbles, Pearls, Waves*; Springer: New York, 2004.
45. McLean, R. S.; Doyle, M.; Sauer, B. B. *Macromolecules* **2000**, *33*, 6541–6550.
46. Onishi, L. M.; Prausnitz, J. M.; Newman, J. *J. Phys. Chem. B* **2007**, *111*, 10166–10173.
47. Jeck, S.; Scharfer, P.; Kind, M. *J. Membr. Sci.* **2011**, *373*, 74–79 (Note that the authors presented two isotherms designated as “liquid” and “gaseous”, but in their liquid equilibration experiments there was no actual contact between liquid and Nafion, therefore both isotherms shown in Fig. 4 represent vapor equilibration.).
48. Van Der Heijden, P.; Bouzenad, F.; Diat, O. *J. Polym. Sci., Part B: Polym. Phys.* **2004**, *42*, 2857–2870.
49. Hsu, W. Y.; Gierke, T. D. *J. Membr. Sci.* **1983**, *13*, 307–326.
50. Schmidt-Rohr, K.; Chen, Q. *Nat. Mater.* **2008**, *7*, 75–83.
51. Litt, M. *Abstracts of Papers of the American Chemical Society* **1997**, *213*, 33-POLY.
52. Gebel, G.; Moore, R. B. *Macromolecules* **2000**, *33*, 4850–4855.
53. Fujimura, M.; Hashimoto, T.; Kawai, H. *Macromolecules* **1982**, *15*, 136–144.
54. Bass, M.; Berman, A.; Singh, A.; Konovalov, O.; Freger, V. *Macromolecules* **2011**, *44*, 2893–2899.
55. Barclay Satterfield, M.; Benziger, J. B. *J. Phys. Chem. B* **2008**, *112*, 3693–3704.
56. Barclay Satterfield, M.; Benziger, J. B. *J. Polym. Sci., Part B: Polym. Phys.* **2009**, *47*, 11–24.
57. Bass, M.; Berman, A.; Singh, A.; Konovalov, O.; Freger, V. *J. Phys. Chem. B* **2010**, *114*, 3784–3790.
58. Als-Nielsen, J.; McMorrow, D. *Elements of modern X-ray physics*; John Wiley & Sons: New York, 2001.

Downloaded by PENNSYLVANIA STATE UNIV on June 14, 2012 | http://pubs.acs.org
Publication Date (Web): May 7, 2012 | doi: 10.1021/bk-2012-1096.ch017

59. Dosch, H.; Batterman, B. W.; Wack, D. C. *Phys. Rev. Lett.* **1986**, *56*, 1144.
60. Vineyard, G. H. *Phys. Rev. B: Condens. Matter* **1982**, *26*, 4146.
61. Rubatat, L.; Diat, O. *Macromolecules* **2007**, *40*, 9455–9462.
62. Dura, J. A.; Murthi, V. S.; Hartman, M.; Satija, S. K.; Majkrzak, C. F. *Macromolecules* **2009**, *42*, 4769–4774.

Downloaded by PENNSYLVANIA STATE UNIV on June 14, 2012 | http://pubs.acs.org
Publication Date (Web): May 7, 2012 | doi: 10.1021/bk-2012-1096.ch017

Subject Index

A

AAEMFC. *See* alkaline anion exchange membrane fuel cells (AAEMFC)
AFC. *See* alkaline fuel cells (AFC)
Alkaline anion exchange membrane fuel cells (AAEMFC), 253
Alkaline fuel cells (AFC), 233
  AEM, chemical stability, 236*t*
  AEM, examples, 235*t*
Ammonium-based AEM, 238, 238*s*, 239*s*, 240*s*, 241*s*
Anhydrous proton conducting membranes, 159
Anion-cation interaction potential energy surface, 21*f*
Anion exchange membranes (AEM), 160
  ammonium-based, 238, 238*s*, 239*s*, 240*s*, 241*s*
  bis-quaternized DABCO cation, 247*s*
  cyclic cation-based, 246
  guanidinium-based, 244, 244*s*
  imidazolium-based, 244, 245*s*, 246*s*
  mono-quaternized DABCO cation, 247*s*
  overview, 233
  phosphonium-based, 241, 242*s*
  polymer backbones, 247
    degradation, 248*s*
    oxidization, 248*s*
  pyridinium-based, 246, 246*s*
  sulfonium-based, 243, 243*s*
Aromatic diamine, 203*f*

B

1,3,5-Benzenetrisulfonyl chloride, 208, 209*f*, 210*t*
Biphenol, 206*f*, 207*f*, 207*t*
Bis-quaternized DABCO cation, AEM, 247*s*
Block copolymers
  characterizations, 255
  conductivity measurement, 255
  morphology-conductivity relationships, 261
  overview, 253
  polystyrene synthesis, 256
  poly(vinylbenzyltrimethylammonium tetrafluoroborate) synthesis, 256, 258*s*
  PS-b-[PVBTMA][BF_4] ion exchange, 260
  PS-b-[PVBTMA][BF_4] membrane preparation, 257, 261*f*
  PS-b-[PVBTMA][BF_4] morphology, 259, 260*f*
  PS-b-[PVBTMA][BF_4] synthesis, 257, 258*s*, 259*t*
  PS-b-[PVBTMA][OH] ion exchange, 257, 262*f*, 263*f*
  vinylbenzyltrimethylammonium tetrafluoroborate ion exchange, 256

C

Charge transfer, energy devices
  overview, 165
  tethered imidazole polystyrene polymers, 168*f*
  water-free proton conducting polymer, 167*f*
Conductivity concentrations, polyelectrolytes, 4*f*
Conductivity measurement, block copolymers, 255
Cross-linked low equivalent weight PFSA, 212*f*
  aromatic diamine, 203*f*
  1,3,5-benzenetrisulfonyl chloride, 208, 209*f*, 210*t*
  biphenol, 206*f*, 207*f*, 207*t*
  ionomers, 215*f*, 216*f*
  overview, 201
  pendent fluorobenzene rings, 205, 206*f*
  perfluoropropylene disulfonyl fluoride, 211, 214*f*, 216*t*
  sulfinated polyarylenes, 207, 207*f*, 208*f*
  sulfonamide-activated arylfluoride approach, 204, 205*f*
  sulfonamide-sulfonyl chloride approach, 203, 204*f*
  sulfonylfluoride approach, 203
  4-(sulfonylfluoride)butyryl fluoride, 211, 212*f*, 213*f*
  (trifluorovinyl oxy)benzene, 217, 217*f*, 218*f*, 219*f*
Cyclic cation-based AEM, 246

Downloaded by 89.163.35.42 on June 14, 2012 | http://pubs.acs.org
Publication Date (Web): May 7, 2012 | doi: 10.1021/bk-2012-1096.ix002

Downloaded by 89.163.35.42 on June 14, 2012 | http://pubs.acs.org
Publication Date (Web): May 7, 2012 | doi: 10.1021/bk-2012-1096.ix002

D

Density-functional theory (DFT), 22, 28*t*
Department of Energy (DoE)
  cost and durability performance targets, fuel cell stacks, 153*t*
  technical targets, transportation applications, 154*t*
DFT. *See* density-functional theory (DFT)
Dimethyl ether, 36, 38*f*, 39*f*
Dipole moments, ionomers, 23*t*, 24*f*
Dynamic water transport, nafion membrane
  nanoscale sorption, 193
  vapor sorption, 189, 191*f*
  water swelling, 193*f*

E

Equilibrium pair structures, ionomers, 29*f*

F

Fast segmental motion *vs.* ion transport, 85
Four-state model, ionomers, 39
Fuel cell
  history, 149, 151*f*
  PEM, 148*f*, 150
  test conditions, sOPBI, 225
Fuel cell applications, PEM, 155
  anhydrous proton conducting membranes, 159
  anion exchange membranes, 160
  block copolymers, 158
  PFSA, 155
  phosphazenes, 157
  polysulfones, 157

G

Guanidinium-based AEM, 244, 244*s*

I

Imidazolium-based AEM, 244, 245*s*, 246*s*
Inelastic neutron scattering, polyelectrolytes
  cross-sections, 71*f*
  data interpretation, 78
  energy exchange, 70*f*
  fast segmental motion *vs.* ion transport, 85
  high flux backscattering spectrometer, 77*f*
  inelastic fixed window energy, 85*f*
  INS data interpretation, 78
  instrumentation, 74
  intermediate scattering function, 82*f*
  Li^+ ion conductivity, 87*f*
  overview, 67
  relaxations, 80
  time-of-flight, 75*f*
In situ neutron techniques
  neutron depth profiling, 92, 93*f*, 95*f*
  neutron imaging, 102, 102*f*, 104*f*
  neutron reflectivity, 96, 97*f*, 98*f*
  overview, 91
  small angle neutron scattering, 99, 100*f*, 101*f*
Ionomers, facile ion transport
  anion-cation interaction potential energy surface, 21*f*
  computational methods, 22
  DFT, 28*t*
  dimethyl ether, 36, 38*f*, 39*f*
  dipole moments, 23*t*, 24*f*
  equilibrium pair structures, 29*f*
  four-state model, 39
  ion pair interaction energies, 30*t*
  isolated ion pairs, 28
  Li^+ cations, 25*f*, 26*t*, 40*t*
  $Li\text{-}(C_6H_5)SO_3$ species, 41*f*
  Na^+ cations, 40*t*
  overview, 19
  PCM, 32, 33*f*, 34*t*, 35*f*, 36*f*
  ZPVE, 22, 35*f*, 36*f*
Ion pair interaction energies, ionomers, 30*t*
Isolated ion pairs, ionomers, 28

L

Li^+ cations, 25*f*, 26*t*, 40*t*
$Li\text{-}(C_6H_5)SO_3$ species, 41*f*
Li-methyl carboxylate, 29*f*
Li-methyl phosponate, 29*f*
Li-methyl sulfonate, 29*f*
Liquid-water permeability, 188
Li-tetraphenylborate, 29*f*
Lithium salt content effect
  dynamical mechanical analysis, 59
  electrical impedance spectroscopy, 58
  Fourier-transform infrared spectroscopy, 59
  lithium triflate salt, 58*f*

Downloaded by 89.163.35.42 on June 14, 2012 | http://pubs.acs.org
Publication Date (Web): May 7, 2012 | doi: 10.1021/bk-2012-1096.ix002

  overview, 55
  photopolymerization, 57
  thermosets' conductivity, 62
  thermosets' mechanical properties, 60
Lithium triflate salt, 58*f*

M

Membrane electrode assembly fabrication, sOPBI, 225
Membrane preparation, sOPBI, 223
Membrane technologies, 152
Mono-quaternized DABCO cation, AEM, 247*s*
Morphology-conductivity relationships, block copolymers, 261

N

Na^+ cations, 40*t*
Nafion, 116*f*, 168*f*, 169*f*
  117 membrane, 286*f*
  112 membranes, 228*f*, 229*f*
  chemical structure, 156*f*
  films, 298*f*, 299*f*
  functional group adsorption, 273*f*
  hydrated
    bulk microstructure, 295
    hydration, 283
    ionomer bulk, equilibrium characteristics, 291
    ionomer surface equilibrium, 292
    micelles, 293*f*, 298*f*
    microphase-separated ionomer, 287
    microstructure, 283
    overview, 283
    proton diffusivity, 285*f*
    Schroeder's paradox, 292
    surface, 297
    thermodynamics, 287
    transport properties, 283
    vapor equilibration isotherm, 295*f*
  scattering length density, 277*f*
  water droplets, 271*f*
Nafion membrane
  dynamic water transport
    nanoscale sorption, 193
    vapor sorption, 189
  overview, 175
  steady-state water transport
    diffusion, 185
    interfacial resistance, 186
    liquid-water permeability, 188
    nuclear magnetic resonance, 189
  temperature effect, 194
  water content, 182*f*
  water diffusivity, 178*t*, 181*f*
Nanostructure role
  fuel cell
    anhydrous ionic conductivity improvement, 136, 137*f*, 138*f*
    ion conduction, 131, 132*f*, 133*f*
    ion guidance, 134
    ion transport mechanisms, 130
    ionic aggregates break up, 134, 135*f*
    overview, 129
  lithium batteries
    ion conduction, 140, 141*f*, 142*f*, 143*f*
    ion guidance, 142
NDP. *See* neutron depth profiling (NDP)
Neutron depth profiling (NDP), 92, 93*f*, 95*f*
Neutron imaging (NI), 102, 102*f*, 104*f*
Neutron reflectivity, 96, 97*f*, 98*f*
NI. *See* neutron imaging (NI)

O

OPBI. *See* poly[2,2′-(p-oxydiphenylene)-5,5′-bibenzimidazole] (OPBI)

P

PCM. *See* polarizable continuum model (PCM)
PEM. *See* polymer electrolyte membranes (PEM)
PEMFC. *See* proton exchange membrane fuel cells (PEMFC)
Pendent fluorobenzene rings, 205, 206*f*
PEO. *See* polyethylene oxide (PEO)
PEO/$LiClO_4$ SPE, 3*f*
Perfluoropropylene disulfonyl fluoride, 211, 214*f*, 216*t*
Perfluorosulfonic acid ionomers (PFSA), 155
PFSA. *See* perfluorosulfonic acid ionomers (PFSA)
Phosphazenes, 157
Phosphonic acid functionalized polysulfone, 172*f*
Phosphonic acid grafted PEM, 139*f*
Phosphonium-based AEM, 241, 242*s*
Polarizable continuum model (PCM), 32, 33*f*, 34*t*, 35*f*, 36*f*
Polyelectrolytes, batteries, 1
  conductivity concentrations, 4*f*

In Polymers for Energy Storage and Delivery: Polyelectrolytes for Batteries and Fuel Cells; Page, K., et al.;
ACS Symposium Series; American Chemical Society: Washington, DC, 2012.

Downloaded by 89.163.35.42 on June 14, 2012 | http://pubs.acs.org
Publication Date (Web): May 7, 2012 | doi: 10.1021/bk-2012-1096.ix002

  conductivity increase, 8*f*
  inelastic neutron scattering
    cross-sections, 71*f*
    data interpretation, 78
    energy exchange, 70*f*
    fast segmental motion *vs.* ion transport, 85
    high flux backscattering spectrometer, 77*f*
    inelastic fixed window energy, 85*f*
    instrumentation, 74
    intermediate scattering function, 82*f*
    Li^+ ion conductivity, 87*f*
    overview, 67
    relaxations, 80
    time-of-flight, 75*f*
  nanostructure role, fuel cell
    anhydrous ionic conductivity improvement, 136
    ion conduction, 131
    ion guidance, 134
    ion transport mechanisms, 130
    ionic aggregates break up, 134
    overview, 129
  nanostructure role, lithium batteries
    ion conduction, 140
    ion guidance, 142
Polyetherpolysulfone, 171*f*
Polyethylene oxide (PEO), 2
Poly(galvinoxylstyrene), 48*f*
Polymer backbones, AEM, 247
  degradation, 248*s*
  oxidization, 248*s*
Polymer electrolyte membranes (PEM), 129
  DoE cost and durability performance targets, fuel cell stacks, 153*t*
  DoE technical targets, transportation applications, 154*t*
  fuel cell applications, 155
    anhydrous proton conducting membranes, 159
    anion exchange membranes, 160
    block copolymers, 158
    PFSA, 155
    phosphazenes, 157
    polysulfones, 157
  membrane technologies, 152
  overview, 147
Poly[2,2′-(p-oxydiphenylene)-5,5′-bibenzimidazole] (OPBI), 221
  See also sulfonated polybenzimidazoles (sOPBI)
Polystyrene synthesis, 256
Polysulfones, 157, 170*f*
Poly(TEMPO-substituted norbornene), 48*f*
Poly(vinylbenzyltrimethylammonium tetrafluoroborate) synthesis, 256, 258*s*
Proton conductivity, sOPBI, 228*f*, 228*t*
Proton exchange membrane fuel cells (PEMFC)
  interfacial structures, 270
  overview, 267
  transport properties, 270
PS-b-[PVBTMA][BF_4] ion exchange, 260
PS-b-[PVBTMA][BF_4] membrane preparation, 257, 261*f*
PS-b-[PVBTMA][BF_4] morphology, 259, 260*f*
PS-b-[PVBTMA][BF_4] synthesis, 257, 258*s*, 259*t*
PS-b-[PVBTMA][OH] ion exchange, 257, 262*f*, 263*f*
Pyridinium-based AEM, 246, 246*s*

R

Redox-active radical polymers
  nitroxide, 47*f*
  overview, 45
  p, n-type, 47
  phenoxyl radicals, 47*f*
  poly(galvinoxylstyrene), 48*f*
  poly(TEMPO-substituted norbornene), 48*f*

S

SANS. *See* small angle neutron scattering (SANS)
Small angle neutron scattering (SANS), 99, 100*f*, 101*f*
Solid polymer electrolytes (SPE), 2
  filler surface, 7*f*
SOPBI. *See* sulfonated polybenzimidazoles (sOPBI)
SPE. *See* solid polymer electrolytes (SPE)
Steady-state water transport, Nafion membrane, 177*f*
  diffusion, 185
  interfacial resistance, 186
  liquid-water permeability, 188
  nuclear magnetic resonance, 189
  resistance, 187*f*, 188*t*
Sulfinated polyarylenes, 207, 207*f*, 208*f*
Sulfonamide-activated arylfluoride approach, cross-linked PFSA, 204, 205*f*
Sulfonamide-sulfonyl chloride approach, cross-linked PFSA, 203, 204*f*

In Polymers for Energy Storage and Delivery: Polyelectrolytes for Batteries and Fuel Cells; Page, K., et al.;
ACS Symposium Series; American Chemical Society: Washington, DC, 2012.

Downloaded by 89.163.35.42 on June 14, 2012 | http://pubs.acs.org
Publication Date (Web): May 7, 2012 | doi: 10.1021/bk-2012-1096.ix002

Sulfonated polybenzimidazoles (sOPBI)
  characterization, 223
  fuel cell test conditions, 225
  instrumentation, 224
  membrane electrode assembly fabrication, 225
  membrane preparation, 223
  Nafion 112 membranes, 228*f*, 229*f*
  overview, 221
  proton conductivity, 228*f*, 228*t*
  sultone-substituted OPBI post-sulfonation, 223
  sultone-substituted OPBI synthesis, 223, 226*f*, 227*f*
Sulfonated polyphenylene (sPP) ionomer films, 275, 276*f*
Sulfonium-based AEM, 243, 243*s*
Sulfonylfluoride approach, cross-linked PFSA, 203
4-(Sulfonylfluoride)butyryl fluoride, 211, 212*f*, 213*f*
Sultone-substituted OPBI post-sulfonation, 223
Sultone-substituted OPBI synthesis, 223, 226*f*, 227*f*

T

Tethered imidazole polystyrene polymers, 168*f*
Totally organic rechargeable battery, 45
  charge/discharge curves, 50*f*
(Trifluorovinyl oxy)benzene, 217, 217*f*, 218*f*, 219*f*

V

Vanadium redox flow batteries (VRFB)
  assembly principle, 113*f*
  flow-battery technology, 109
  high power density, 114
  membrane challenges, 123
  membrane separators, 116
  membrane tested, 119*t*
  Nafion, 116*f*
  overview, 107
  power density, 115*f*
  vanadium ions crossover, 117*f*
  voltage loss, 124*f*
  vs. conventional, 111*t*
  vs. PEMFC applications, 117*t*
Vinylbenzyltrimethylammonium tetrafluoroborate ion exchange, 256
VRFB. *See* vanadium redox flow batteries (VRFB)

W

Water swelling, 193*f*
Water-free proton conducting polymer, 167*f*

Z

Zero-point vibrational energy (ZPVE), 22, 35*f*, 36*f*
Zwitterionic-type block copolymer, 139*f*